CLRC
COUNCIL FOR THE CENTRAL LABORATORY
OF THE RESEARCH COUNCILS

Central Laser Facility

Rutherford Appleton Laboratory

Annual Report 2001-2002

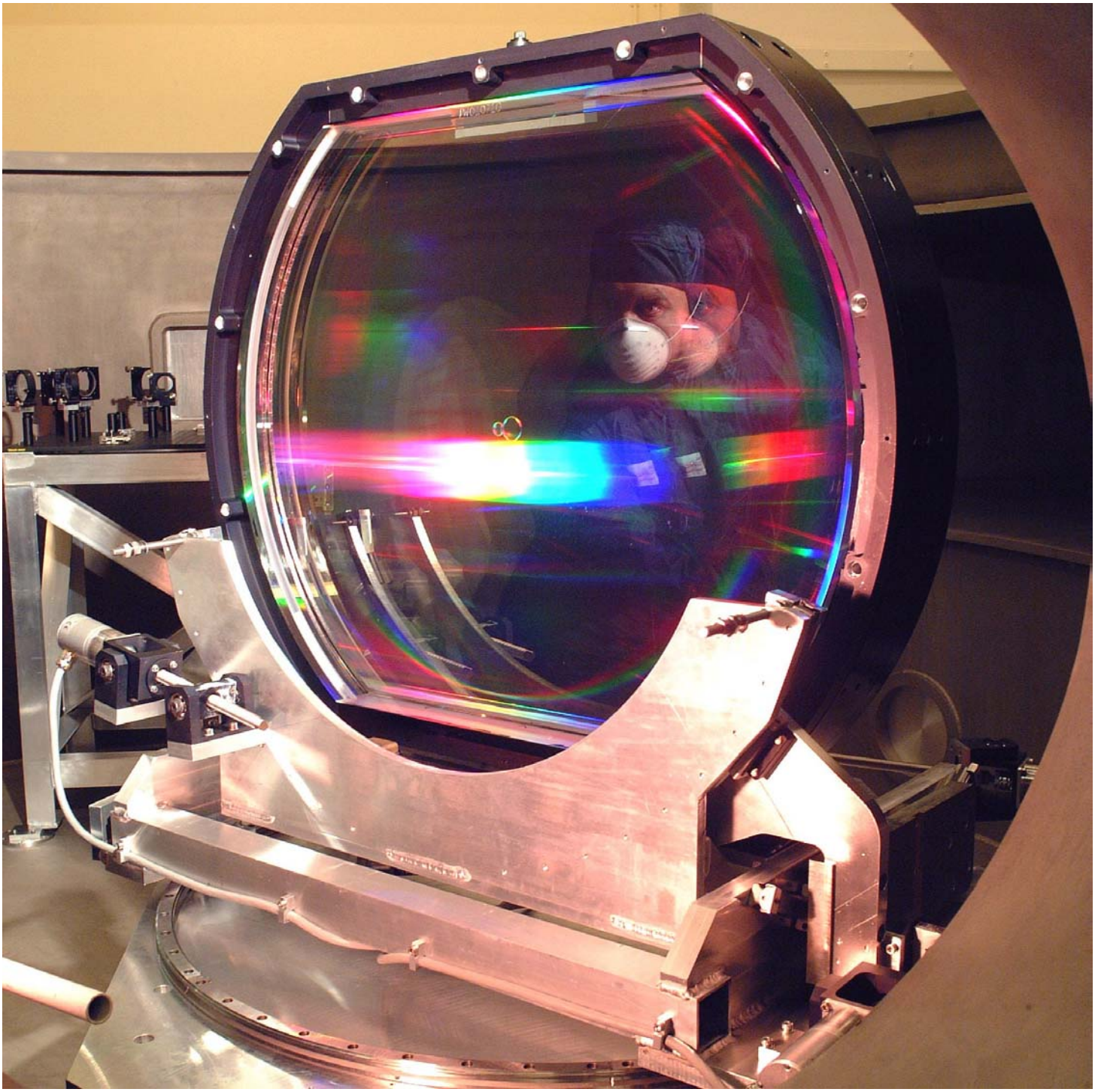

Enquiries about copyright, reproduction and requests for additional copies of this report should be addressed to:

The Central Laboratory of the Research Councils
Library and Information Services
Rutherford Appleton Laboratory
Chilton
Didcot
Oxfordshire
OX11 0QX
Tel: 01235 445384 Fax: 01235 446403
E-mail: library@rl.ac.uk

ISSN 1358-6254

Central Laser Facility

Rutherford Appleton Laboratory

Annual Report 2001/2002

Central Laser Facility
Rutherford Appleton Laboratory
Chilton, Didcot
Oxfordshire OX11 0QX
Tel. 44 (0) 1235 445655
Fax. 44 (0) 1235 445888
E-mail. clf@rl.ac.uk
Web site. http://www.clf.rl.ac.uk

RAL Report No. RAL-TR-2002-013

The front cover shows a large aperture compression grating being inspected by Trevor Winstone after its installation in the Vulcan Petawatt Compression Chamber.
(Photograph courtesy of RAL Photographic Section).

ISBN 0902376217

Acknowledgements

The production team for this Annual Report was as follows:

Editor	Brian Wyborn
Overall Co-ordination	Alison Brown
Production	Dave Burgess
Chapter Editors	David Neely, Tony Parker, Colin Danson, Graeme Hirst
Section Editors	Rob Clarke, David Neely, Margaret Notley, Roger Evans, Andrew Langley, Pavel Matousek, Stan Botchway, Waseem Shaikh, Colin Danson, Mike Towrie, Cristina Hernandez-Gomez, Ian Ross
Technical Support	Chris Reason, RAL BITD.

This report is available on the CLF's Web Page Ref. http://www.clf.rl.ac.uk/.

The document has been reproduced by the RAL Reprographics Section.

Thanks to all the above for their contribution towards producing this report and of course to all the authors for their submissions.

Contents

Lasers for Science Facility Programme - Biology

Lasers for Science Facility Programme - Physics

Laser Science and Development - Astra

Laser Science and Development - Lasers for Science Facility

Laser Science and Development - Laser Optics and Laser Design

Laser Science and Development - Instrumentation

Foreword

M H R Hutchinson

Central Laser Facility, CLRC Rutherford Appleton Laboratory, Chilton, Didcot, Oxon., OX11 0QX, UK

Email address: *H.Hutchinson@rl.ac.uk*

This report contains scientific accounts of the work which has been carried out at the Central Laser Facility (CLF) of the CCLRC's Rutherford Appleton Laboratory by its users and staff during the financial year 2001-02. The year has again been extremely productive with very strong scientific programmes carried out in Vulcan, Astra and the Lasers for Science Facility (LSF).

The Vulcan laser has continued to provide the focus of the very strong international research programme in laser plasma interactions. The short-pulse, high-intensity programme has benefited from further increases in the available intensity to 10^{20}W/cm^2 using the technique of chirped pulse amplification. Areas of study have included the physics relevant to fast ignition for inertial fusion energy, photo-induced nuclear physics, proton production for applications in imaging, plasma diagnostics and medicine and the production and measurement of ultra-high magnetic fields. Complementary studies in high-intensity physics have also been carried out using the high repetition rate Astra laser. A strong scientific programme on the development and application of X-ray lasers pumped by Vulcan operating in the long pulse mode has also been carried out.

The unique laser and diagnostic facilities provided by the LSF has continued to enable a diverse programme of research across a broad range of topics in physics, chemistry and biology. Using the Picosecond Infrared Absorption and Transient Excitation (PIRATE) laser system and the Kerr gate technique for fluorescence suppression, time-resolved resonance Raman and absorption spectroscopy of a wide range of molecules of basic chemical and biological interest have been studied. In addition, the laser loan pool has continued to enable a wide range of research in UK university research groups through the provision of specialist lasers and their technical support.

The research being carried out within the CLF by scientists from UK universities, and, through international agreements, from Europe and the USA, continues to be of the highest quality. The next years will bring new opportunities and challenges. The completion of the Petawatt upgrade for Vulcan will increasingly provide an international focus for research on ultra-high field physics and, with the wide range of facilities and expertise within the CLF, we can again look forward to exciting research across a broad range of science.

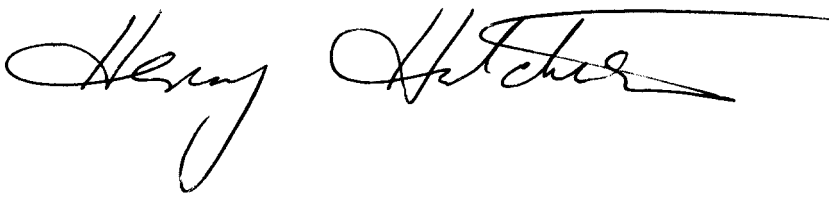

Overview of the Central Laser Facility

C B Edwards

Central Laser Facility, CLRC Rutherford Appleton Laboratory, Chilton, Didcot, Oxon, OX11 0QX, UK

Main contact email address: *c.b.edwards@rl.ac.uk*

Laser Facilities for Users

The Central Laser Facility (CLF) is a world leading centre for research using lasers. Facilities available to users include the Vulcan Nd: glass laser which delivers multi- TW beams to two target areas, the Astra ultra- short pulse interaction facility based on titanium sapphire laser technology, a range of state of the art table top laser systems and specialised diagnostic instruments within the Lasers *for* Science Facility and the Laser Loan Pool.

Vulcan

Vulcan is a highly versatile large scale Nd: glass laser installation which delivers a maximum of 2.5 kJ of energy in its six 10 cm and two 15 cm beamlines to two target areas, each of which is equipped with frequency conversion optics to enable both 1μm and 0.5 μm operation of all beams. A range of pulse durations are available from 100 ps to 20 ns in various geometries.

A short pulse (700 fs) high irradiance (~10^{20} W cm^{-2}) chirped pulse amplification (CPA) capability is available, with vacuum propagation to target and reflective beam focusing optics. Additional low energy beams, including sub- picosecond CPA probes, are provided for diagnostics with high temporal resolution. The system is fully characterised and equipped with advanced diagnostics.

Vulcan Petawatt Upgrade

A 3 year development of Vulcan's CPA beamline to the Petawatt level began in April 1999. The project involves the addition of 20 cm disc amplifiers, the construction of a large aperture vacuum beam compressor and a new target chamber within a new target area building.

The new building was handed over in January 2001. The vacuum compressor and target chamber were delivered in August and commissioned by December 2001. Following vacuum tests and thorough cleaning of the chambers, the large aperture mirror mounts, beam optics and compression gratings were installed during the first quarter of 2002.

The first Petawatt user experiment is scheduled for beamtime during November and December 2002.

Lasers for Science Facility (LSF)

The LSF operates a suite of state of the art table- top laser systems and associated instrumentation giving users access to highly tunable (vuv - ir) and variable pulse width (ns to fs) laser radiation. This includes lasers for ns and ps time- resolved studies. The time resolved resonance Raman (TR^3) facility offers a unique 4 ps optical shutter fluorescence rejection system and a state-of-the-art dual wavelength kHz femtosecond synchronised pump-probe apparatus based on OPA technology. There is also a high average power laser plasma x-ray source and a fast gated (100 ps) confocal microscopy laboratory.

The high brightness PIRATE facility (Picosecond Infrared Absorption and Transient Excitation) provides two independently tunable beams across the mid infra red region of the spectrum for pump / probe experiments. Pirate and the ps-TR^3 apparatus is used for a wide range of experiments in chemistry, physics, biological and material sciences.

Laser Loan Pool

Commercial laser systems are available from the Laser Loan Pool for periods of up to 4 months at the user's home laboratory. Systems available include nanosecond tunable YAG pumped dye lasers (with frequency up-conversion and down-conversion covering the spectral region from 205 nm to 4500 nm), an excimer laser operating down to 157 nm, a CW frequency doubled argon ion laser and an all solid-state femtosecond Titanium Sapphire laser tunable between 680 nm and 1020 nm. A wide range of ancillary and diagnostic equipment is also available to support user experiments.

Astra

The Astra facility is based on titanium sapphire laser technology which gives users access to high intensity laser pulses at 10 Hz repetition rate.

The facility supplies laser pulses to two target areas simultaneously. Target Area I provides pulses of 50fs duration with an energy of 10 mJ, producing irradiance on target in excess of 10^{16} W.cm^{-2}. The Target Area II currently delivers 300 mJ in 50fs with target irradiance at 10^{18} W.cm^{-2} regime.

Engineering Services

Mechanical, electrical and computing support is provided for the operation of the laser facilities at the CLF, for the experimental programmes on these facilities and for the CLF's research and development activities. Access to mechanical and electrical CAD tools and workshop facilities enable a rapid response to be provided to users.

Access to Facilities

The mechanism for awarding access to beamtime at all CCLRC facilities is changing following the conclusion of the second stage of the Quinquennial Review of the CCLRC. From April 2003, beamtime will be awarded and funded by CCLRC. For the latest information please visit the CCLRC Web site at: www.clrc.ac.uk/QReview/QR_FacilityAccess_07_02.htm. For further information, please contact Mrs. Alison Brown (a.j.brown@rl.ac.uk).

During the period covered by this report, beamtime at all CLF facilities has been available for European researchers and their collaborators through the EU Access to Large Scale Infrastructure programme. The CLF hopes to continue this arrangement in the forthcoming Sixth Framework Programme through a joint application with other European laser facilities. For information on calls for proposals, eligibility criteria, etc. please contact Colin Danson (c.danson@ rl.ac.uk).

Hiring of the facilities and access to CLF expertise is also available on a commercial basis for industrial research and development. Please contact Mrs. Alison Brown for further information.

CLF Web site

Further information on the CLF, its facilities and the scientific programmes is available on the CLF Web site at http://www.clf.rl.ac.uk.

High Power Laser Programme

1) Short Pulse Plasma Physics

2) X-ray Laser and Long Pulse Plasma Physics

3) Theory and Computation

4) Femtosecond Pulse Physics

Fast Electron Generation and Transport in Solid Matter Irradiated at Relativistic Intensities by Rear-Side Self-Radiation Diagnostics — Evidence of vxB Electron Acceleration

J J Santos, F Amiranoff, S D Baton, M Koenig, E Martinolli, L Gremillet, H Popescu

Laboratoire pour l'Utilisation des Lasers Intenses, UMR 7605, CNRS-CEA-Univ. Paris VI-Ecole Polytechnique, Palaiseau, France

D Batani, A Bernardinello, E Perelli, F Scianitti

Dipartimento de Fisica G. Ochialini, Università degli Studi di Milano-Bicocca and INFM, Milan, Italy

T Hall

University of Essex, Colchester, UK

M H Key, A J Mackinnon

Lawrence Livermore National Laboratory, Livermore, CA, USA

R R Freeman, R A Snavely, C Andersen, J King, J M Hill

Department of Applied Sciences, University of California-Davis, Davis, CA, USA

R B Stephens, T E Cowan

General Atomics, San Diego, CA, USA

D Neely, R J Clarke

Central Laser Facility, CLRC Rutherford Appleton Laboratory, Chilton, Didcot, Oxon, OX11 0QX, UK

Main contact email address: *joao-jorge.santos@polytechnique.fr*

Introduction

For several years now we have been studying the generation and the transport of fast electrons in solid matter[1-4] within the context of the fast ignitor scheme in inertial confinement fusion[5]. This concept is based on relativistic electrons generation by the interaction of an ultra-intense laser pulse with a dense plasma, electron transport in the over-critical matter and finally its energy deposition in the region wrapping the nuclear fuel. Understanding of the physical mechanisms involved in these steps is crucial for the success of fuel ignition.

Our main goal has been to characterize the energy distribution of the fast electrons produced by short and intense laser irradiation and the geometry of its transport through solid matter. For that purpose we have implemented different diagnostics of the target rear side visible emission. Time-integrated and time-resolved images obtained in previous experiments performed on the LULI 100 TW laser facility had already shown a very bright and short signal preceding the long emission of the cooling and expanding plasma heated by the fast electrons flux [3,6]. Because of the very short duration of the initial burst - less than 2 ps for a 100 μm Al target [6] - it is interpreted as a signature of fast electron jets crossing the target-vacuum boundary. The measured signal spreading half-angle was ~17°. This signal has been explained as Optical Transition Radiation (OTR) emitted by electrons crossing the target/vacuum boundary, or by the synchrotron-like radiation emitted by these electrons when they circulate outside the target before being forced back by the electrostatic field. The estimated ~10^{13} electrons population would have a temperature of a few hundred keV corresponding to a total kinetic energy of ~1 J [3].

In this report we present results on time-integrated images and time-resolved spectra of the optical self-emission of flat targets rear side, from the RAL-CLF experimental campaign. As at LULI[6], a 2ω bright component, corresponding to the second harmonic of the laser light, has been observed. This emission is explained by the acceleration of short bunches of electrons by the **vxB** force in front of the target.

Experimental Setup and Results

The experiment was performed on the RAL-CLF Vulcan laser facility. The 1 ps, 1.054 μm laser pulse with an energy up to 90 J was focused by a *f/3.5* off-axis parabola at normal incidence onto either pure Al, or Cu-buried and CH-buried targets. The laser focal spot was 10 μm in diameter corresponding to a maximum intensity of a 1-5 x 10^{19} W/cm^2. The optical radiation (400 – 750 nm) of the rear side of the target was collected on axis with a *f/4* optical system. The emitting region was imaged on both a CCD camera and the entrance slit of a Bentham spectrometer coupled to a Hadland S20 streak camera, as shown in Figure 1.

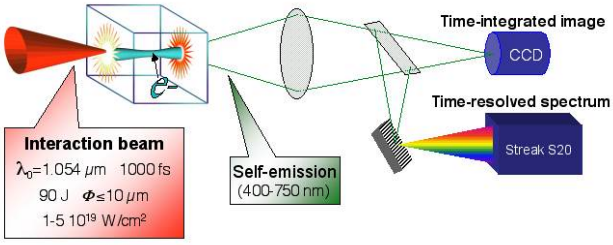

Figure 1. Experimental setup.

A typical time resolved spectrum of the target rear side self-emission is presented in Figure 2a, as well as the spectral profiles (time integration of the spectral images) for two different thickness CH-buried targets (Figures 2b-2c). An intense contribution at ~530 nm (second harmonic of the laser light) is clearly visible over a wide spectrum. We explain the wide spectrum by the incoherent part of the radiation produced by a random electron population, while the 2ω line is attributed to coherent transition radiation CTR (a coherent synchrotron-type radiation might also explain the results), emitted by very high-energy electron bunches separated by half of the laser pulse period. In the LULI experiment severe tests had been made to ensure that the 2ω light does not come from the front side of the target, so that this signal really comes from the rear side of the foils.

The integrated energy collected in the 2ω spectral line is plotted in Figure 3 for the different kinds of used targets. As can be seen it decreases very rapidly for small thickness but the line is still visible after 500 μm. The full triangles in the plot stand for signal evolution with target total thickness, whereas the empty triangles stand for evolution with Al-equivalent thickness, i.e., they take into account the different density of all the different layers of each target. In this last case a slight separation of the

CH-buried targets (in blue) from the completely metallic ones is visible, which could be interpreted as a higher inhibition for electron flux in the CH-layers.

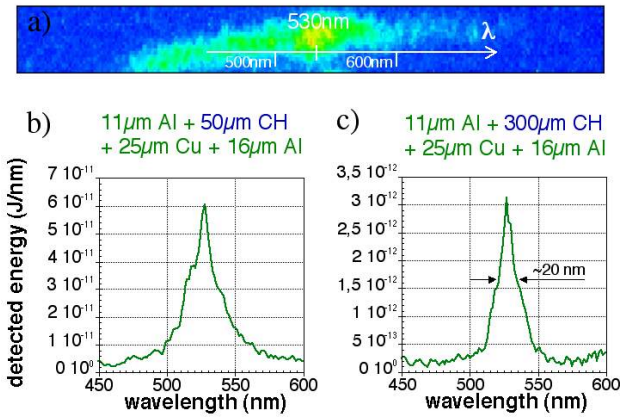

Figure 2. a) Typical time-resolved spectrum showing an intense contribution at 530 nm. The lower graphics are the spectral profiles integrated in time for CH-buried targets with total thickness: **b)** 102 μm. **c)** 352 μm.

The coherent light at 2ω is also seen on the time-integrated images (cf. Figure 4): a bright ring-shape interference pattern, which could only be produced by coherent radiation, was seen when acquisition was made in all the optical range (top images Figure 4). If we suppress the 2ω component by means of a magenta filter, the interference pattern disappears (bottom images on Figure 4), leaving just a weaker and wide smooth cloud.

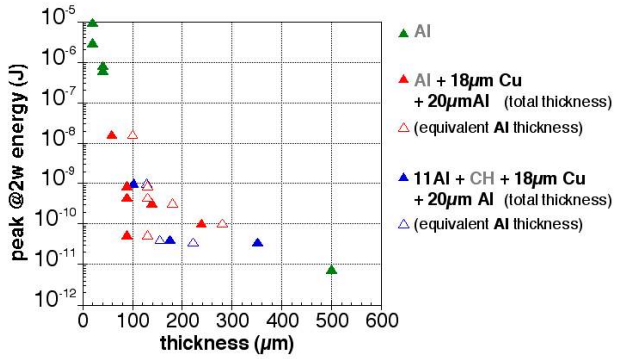

Figure 3. 2ω coherent radiation integrated energy as function of the target total thickness (full triangles) or as function of the Al-equivalent thickness (empty triangles).

Discussion

When interacting with a plasma, the energy of a laser beam can be absorbed by various mechanisms. In particular, at relativistic regimes of interaction, the electrons' quiver velocity in the laser field is so high that the Lorentz component of the force (the so-called **v**x**B** force) can accelerate them longitudinally. This acceleration mechanism can generate ultra short bunches of relativistic electrons separated by half the period of the laser field (see Figure 5 on the left). Such electron bursts emitted at the rate of two per laser period had already been observed in particle-in-cell simulations of fast electron transport through dense matter[7,8]. If the electrons do not dephase and remain bunched in their propagation till they reach the target-vacuum boundary (and we expect it at least from the more relativistic), the individual fields due to each electron add coherently for wavelengths much larger than the bunch length. This leads to a much higher emitted power proportional to the square of the number of electrons N^2, instead of N in the incoherent case. In the case electrons are bunched in successive short bunches separated by a time delay δT, the emission is coherent for wavelengths close to $c\delta T$.

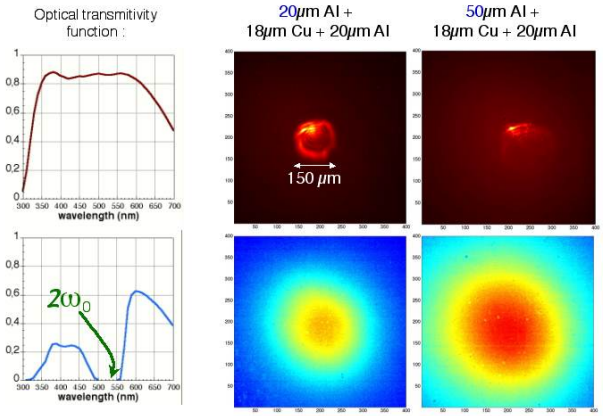

Figure 4. CCD time-integrated images. The upper images were acquired using all the visible spectral range and show a ring-shape interference pattern. The lower ones were acquired filtering off the 2ω component. The corresponding transmissivity functions are shown on the left.

The plot presented on Figure 5 on the right is the result of a pure ballistic calculation for the evolution within the target of two successive electron bunches separated by half the laser pulse period. Each bunch had an electron distribution with a temperature of 2 MeV. The normalized electron flux through the rear surface is plotted, for three target thicknesses, as a function of the time delay relative to the arrival of the fastest particles. We can see that the electron bunches broaden and merge for large target thickness. This calculation allows us to conclude that only the more relativistic electrons, with a kinetic energy higher than twice the electron distribution temperature, remain bunched and have a significant contribution to the coherent signal emitted at the target rear side.

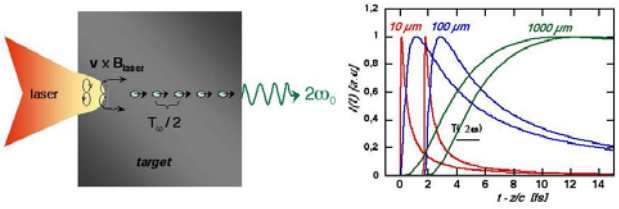

Figure 5. Schematic illustration of the **v**x**B** acceleration of relativistic electron bunches (left). Evolution of the electronic flux through the rear surface for three target thicknesses and a 2 MeV electron temperature (right).

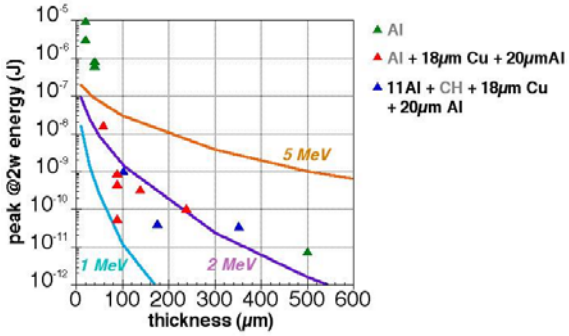

Figure 6. Evolution of the 2ω coherent energy with target total thickness for three temperatures of the electron distribution. The triangles are the experimental points for the different kinds of targets.

The evolution of this signal's absolute energy with target thickness is represented in Figure 6 for three different electron distribution temperatures.

In this purely ballistic model the energy contained in the 2ω peaks is basically given by the expression:

$$E_{2\omega} \propto N^2 \left| P(2\omega) \right|^2$$

where N is the total number of electrons within the bunches and $\left| P(2\omega) \right|$ depends on the target thickness, the electron energy distribution and on the radiation model energy conversion efficiency (we have considered a transition radiation model). From the width of the observed spectral lines at 2ω (~ 20 nm FWHM) we can estimate the number of the bunches involved to be ~ 30. Comparing with experimental data (represented by the triangles, as in Figure 3) we see that data is well fitted for a temperature of ~2MeV and an energy of 12 μJ per bunch.

Conclusions

The emission at 2ω from the back of thick targets irradiated by a laser beam at high intensity has been detected, both by spectral analysis and by a circular interference pattern in time-integrated images. This is the evidence for the acceleration of ultra-short relativistic electron bunches at 2ω by the **v**x**B** force in the interaction region. It could also be the second harmonic due to bunches of electrons emitted at ω. However, there are no physical mechanisms which could explain such electron emission. First estimates show that the total energy in those electron bunches is a modest fraction (~10^{-5}) of the laser energy, and that they have an energy distribution with a temperature of a few MeV. These high energy electron bunches are then distinct from the lower energy population detected in a previous experiment[3)], where we had filtered off the 2ω component of the spectra, and could be responsible for the jets observed before by shadowgraphy[1)].

Acknowledgments

The authors would like to thank the technical staff of the CLF for their help in running this experiment. This work has been supported by the European Laser Facility Access Program (contract HPRI-CT-1999-00010). One of us (J.J.S.) was financed by MCT (Portugal) under the contact PRAXIS XXI BD/18108/98.

References

1. L. Gremillet *et al.*
Phys. Rev. Lett. 83, 24, 5015 (1999)

2. F. Pisani *et al.*
Phys. Rev. E 62, 5, R5927 (2000)

3. J.J. Santos *et al.*
Phys. Rev. Lett. 89, 2, 025001 (2002)

4. E. Martinolli *et al.*
Submitted to Phys. Rev. Lett. (2002)

5. M. Tabak *et al.*
Phys. Plasmas 1, 5 1626 (1994)

6. S.D. Baton *et al.*
Rapport d'Activité LULI 2001, Ecole Polytechnique, France, 2002

7. B. F. Lasinski *et al.*
Phys. of Plasmas 6, 5, 2041 (1999)

8. A.J. Mackinnon *et al.*
Phys. Rev. Lett. 88, 215006 (2002)

Experimental Observations of the Weibel Instability in High Intensity Laser Solid Interactions

M S Wei, F N Beg, A E Dangor, A Gopal, M Tatarakis, K Krushelnick

Blackett Laboratory, Imperial College of Science, Technology and Medicine, London SW7 2BZ, UK

E L Clark

Radiation Physics department, AWE plc, Aldermaston, Reading, RG7 4PR, UK

P A Norreys, R J Clarke, K Lancaster

Central Laser Facility, CLRC Rutherford Appleton Laboratory, Chilton, Didcot, Oxon, OX11 0QX, UK

K W D Ledingham, P McKenna, T McCanny, I Spencer

Department of Physics and Astronomy, University of Glasgow, Glasgow G12 8QQ, UK

M Zepf

Department of Pure and Applied Physics, The Queen's University Belfast, UK

Main contact email address: *wei.mingsheng@ic.ac.uk*

Introduction

Recently, there has been significant interest in the study of fast electron propagation in solid density plasmas particularly due to potential applications with regard to the fast ignition scheme[1)] for inertial confinement fusion, in which laser-produced energetic electrons are envisaged to penetrate into the pre-compressed fuel core to ignite the fusion spark. In this way, the separation of the heating and compression stages in inertial confinement fusion significantly reduces the total energy requirements for the driving beams and greatly relaxes the symmetry conditions as well.

Electron beams having energies of tens of MeV have already been produced in short pulse high intensity laser solid interactions[2)]. The number of hot electrons is of the order of 10^{13} with a temperature of 1~2 MeV. The current carried by these electron beams is significantly above the Alfvén current:

$$I_A = 1.7\times10^4 \beta\gamma \approx 30\text{KA for } \gamma = 2$$

Here I_A is the limiting electron beam current in vacuum, $\beta = v/c$ and γ is the relativistic Lorenz factor $(\gamma = (1-\beta^2)^{-1/2}$.

When the fast electron beam generated by a high intensity short pulse laser near the vacuum plasma interface penetrates into a solid target, the return current induced in the bulk cold plasma effectively balances the fast electron current so that currents larger than the Alfvén current limit can propagate. Such two counter-propagating streams are subject to the well-known Weibel instability[2)], which can generate strong magnetic fields transverse to the fast electron beam direction. These magnetic fields can consequently cause the electron beam to break up into small filaments. Linear analysis of the Weibel instability in the two-fluid model has studied the dynamics of this instability[3,4)]. Considerable numerical simulation work has been done on such fast electron propagation and the related formation of magnetic channels in the overdense plasmas[4-7)]. An essential feature of these simulations is the break-up of the current into very small current filaments in the overdense plasma and the subsequent coalescence of these filaments.

A single highly collimated electron beam has already been confirmed experimentally inside transparent glass targets and at the rear surface of the plastic targets in high intensity laser solid interactions[8)]. However, until now, filamentary structures resulting from the Weibel Instability have not yet been observed experimentally.

In this report, we present the first experimental observations of the fine structures of the Weibel instability induced in a high intensity laser produced fast electron beam. The speckle-like off-normal electron filaments have consistently been observed in our high intensity laser interaction experiments using thin gold foil targets.

Experimental Set-up and Diagnostic Tools

The experiments were performed at the Rutherford Appleton Laboratory using the Vulcan Nd:Glass laser operating in the CPA mode. The 1.054 μm laser beam, 1ps in duration, was split into two beams, CPA1 & CPA2. These beams were focused to 10 μm diameter spots at 41^0 and 20^0 to the target normal by two f/4.5 off-axis parabolic mirrors from opposite directions. The targets were thin 5 mm × 8 mm gold foils with varied thickness. Both beams were p-polarized. Up to 30 J and 20 J on the target from CPA1 and CPA2 produce a peak intensity of 2×10^{19} W/cm^2.

The main diagnostics used in the experiments were multi-layered stacks consisting of layers of radiochromic film (RCF) and CR-39 particle track detectors. RCF is a type of radiation dosimeter that contains a thin active layer on the clear polyester substrate. When exposed to any kind of ionizing radiation, the active organic dye reacts to form a blue coloured polyester. The films have been absolutely calibrated to give absorbed radiation dose in kRad (10^{-2} J/g). CR-39 nuclear track detectors are only sensitive to energetic ions. In the experiments, the stacks were positioned on both sides of the target and aligned so that the faces of the detector were parallel to the surface of the target.

The detailed experimental arrangement is shown in Figure 1. A frequency doubled green beam, split from the uncompressed main beam, was used as a probe. The probe passed transversely across the target, both surfaces being in the field of view. The

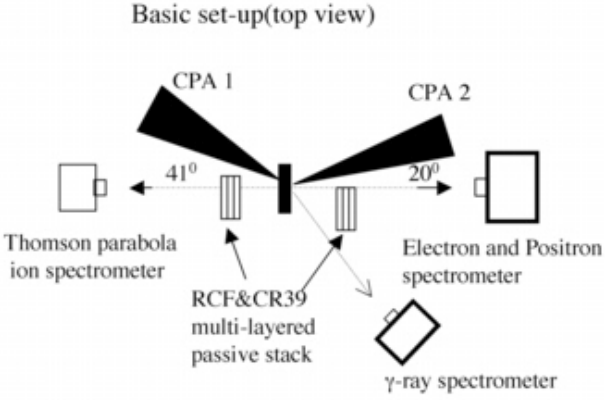

Figure 1. Schematic of the double-sided illumination experimental arrangement. The left hand stack and the right one only collect the top half and right half emissions, respectively.

probe was used to check that the two laser focal spots were in line along the target normal. In addition, single sided illuminations were also carried out with CPA1 laser pulse.

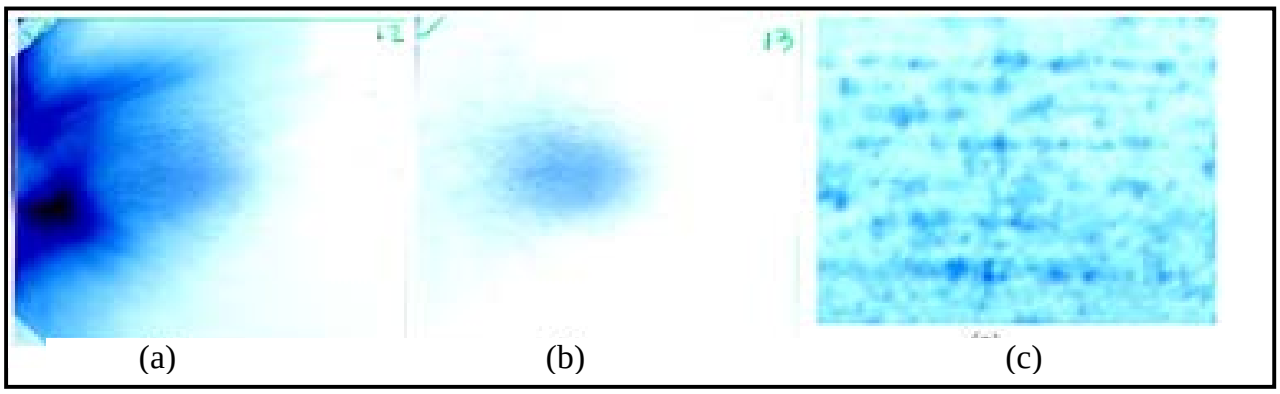

Figure 2. Scanned RCF images show the existence of the speckle-like off normal electron beam when two CPA beams were coincident in time. The left edge of (a) is at target normal direction. (a) and (b) are the front and deeper layers in the right stack respectively. (c) is a magnified view of a small region of (b) with magnification 1000. The detectors were 5 cm by 5 cm.

Experimental Results

Typical images of the radiochromic films are presented in Figure 2 which show the existence of an off-normal electron beam. Scanned RCF images (a) and (b) are from the same shot when the target was illuminated on both sides with two laser beams coincident in time. Except for the lower energy electron and proton emission due to the CPA2 laser produced plasma (only seen in the first two front layers of the RC films), there was the higher energy off-normal electron beam recorded on all the RC films in the stack, which is on the right side 5 cm from the targets. The evidence that the beam consists of electrons rather than ions was obtained by comparing the signals on the RC film and the subsequent CR39 pieces in the stack, which did not show any signal. The collimated off-normal off-axis intense electron beam was emitted at 20^0 from the target normal with full emission cone angle of 11^0. A distinct feature of the electron beam is that it has a very fine speckle-like emission pattern which can be seen in Figure 2 (c). Image (c) is a closer view of a small square region of (b) with magnification 1000.

Such electron beams were also observed when the delay between CPA1 and CPA2 laser pulses was varied by up to 2 ps. It is noted that these variations did not affect the behaviour of the electron beam. From the RCF absorbed dose, it is estimated that the beam consists of 10^{12} electrons.

Experiments with only CPA1 laser beam single sided illumination were carried out with similar laser energy as that in the double sided shots. Figure 3 presents the raw scanned images of the RCF of the stack which was positioned behind the target. In this shot the centre of the detector was at the target normal. Two separate signals are clearly visible. The significant emission along target normal is mainly due to energetic protons, which was confirmed by the CR39 data. The off-normal off-axis signals are due to electrons. These are at the same direction as the off-normal electron beams observed in double illumination cases. The beam was formed by dozens of separated large speckle-like electron jets. The biggest speckle has a radius of approximately 500 μm and is seen almost in the centre of the off-normal beamlets surrounded by relatively smaller speckles with diameters of the order of 250 μm. In the deeper RCF layers of the stack, only a couple of large speckles exist. The angular spread of the off-normal electron beam produced in the single sided illumination is similar to those produced by the double sided illuminations. The only significant difference is the speckle size. Therefore, it is reasonable to assume that all the off-normal electron beams were produced by the CPA1 laser pulse which then propagated through the solid density plasma reaching the detectors on the other side. The different emission structures in the double and single sided illuminations are very likely due to the significant changes of the conditions for fast electron transport inside the solid density plasma in the two different schemes.

TLD dosimeter measurement[9)] indicated that CPA1 laser pulse has much higher energy than that of CPA2. The ratio was about 3/2, which confirmed that CPA1 took the dominant role during the double sided illuminations.

It should also be noted that the electron spectra measured by an electron spectrometer[10)] along the target normal in both schemes are very similar in terms of energy and temperature. But the number of the electrons in double sided illumination seemed to be reduced by a factor of 3 compared to that from single sided shots.

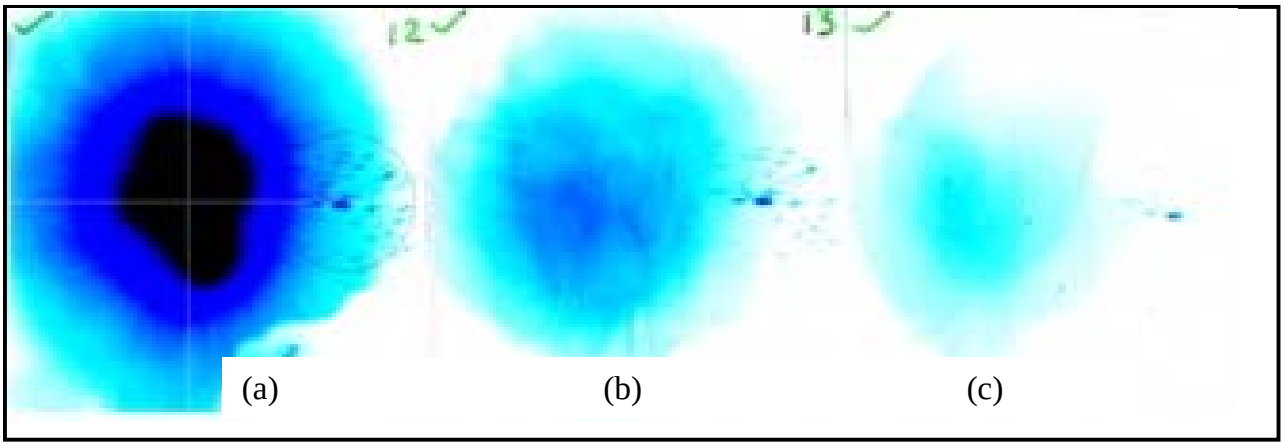

Figure 3. The raw scanned RCF images in the single sided illumination shot with only CPA1. Two separated emissions are shown. The detector stack was 5 cm behind a 20 μm thick gold target. (a) is the front layer of the stack, (b) and (c) are in the deeper layers. The big electron beamlets are clearly visible at the similar off-normal direction as that in double illumination shots.

Discussion

These observations are consistent with the fast electron beam breaking into filaments due to the Weibel instability as they propagate in the overdense plasma.

Linear analysis of the Weibel instability including electron kinetic effects and resistivity and 2-D PIC simulations done by Sentoku et al [5)], which include relativistic binary collisions, suggests that the growth rates of shorter wavelengths are significantly reduced when the initial plasma temperature is high. In a collisional plasma, the growth rates of the fast modes are suppressed due to the plasma kinetic effects and the spectral peak of the growth rate shifts to long wavelength modes in the later stage due to the coalescence of the quasistatic magnetic channels.

Comparing this analysis with our experiments in the single illumination case, the background plasma can be assumed to be cold. Consequently, plasma kinetic effects are very important in the evolution of the Weibel instability. The much larger electron beamlets seem to agree well qualitatively with the simulation results. On the other hand, the fast electron propagation in the overdense plasma in the double sided scheme can be compensated at least partially by the counter propagating hot electron beam produced on the other side. The plasmas in such cases are much hotter than in the single sided scheme. Therefore, the filament sizes are much smaller. From this point of view, our experimental data agrees very well with the simulation predictions.

It is worth pointing out that the direction of the off-normal electron beam in the single sided illumination shots became random when the laser energy was increased. The emission pattern also changed from one having a large speckle structure to a very fine structure pattern. More experiments are needed to study this intriguing phenomenon.

Acknowledgements

The author would like to acknowledge the assistance of the staff of the Central Laser Facility of the Rutherford Appleton Laboratory. This work was funded by UK Engineering and Physical Sciences Research Council (EPSRC).

References

1. M. Tabak *et al*., Phys. Plasmas. 1, 1626 (1994)
2. M. I. K. Santala *et al*., Phys. Rev. Lett. 84, 1459 (2000); K. B. Wharton *et al*., Phys. Rev. Lett. 81, 995 (1998); G. Malka *et al*., Phys. Rev. Lett. 78, 3314 (1997); M. H. Key *et al*., Phys. Plasma. 5, 1966 (1998)
3. E.S.Weibel, Phys. Rev. Lett. 2, 83 (1959)
4. F. Pegoraro *et al*., Phys. Rev. E 56, 963 (1997); F. Califano *et al*., Phys. Rev. E. 57, 7048 (1998)
5. Y. Sentoku *et al*., Phys. Plasmas. 7, 689 (2000); Y. Sentoku *et al*., Phys. Rev. E. 65, 046408 (2002)
6. M. Honda, J. Meyer-ter-Vehn, and A.Pukhov, Phys. Plasma. 7, 1302 (200); Pukhov and J.Meyer-ter-Vehn, Phys. Rev. Lett. 79, 2686 (1997); B. F. Lasinski *et al.*, Phys. Plasmas. 6, 2041 (1999)
7. L. Gremillet *et al*., Phys. Plasmas. 9, 941 (2002)
8. M. Tatarakis *et al*., Phys.Rev.Lett. 81, 999 (1998); M. Borghesi *et al*., Phys. Rev. Lett. 83, 4309 (1999); L. Gremillet *et al*., Phys. Rev. Lett. 83,,5015 (1999)
9. R D Edwards, private communication, 2001
10. P McKenna *et al*, Central Laser Facility Annual Report 2001/2002, RAL-TR-2002-013, 16, (2002)

Fast electron heating in ultra-intense laser-solid interaction using high brightness shifted Kα spectroscopy

E Martinolli, M Koenig, L Gremillet, J J Santos, F Amiranoff, S D Baton

Laboratoire pour l'Utilisation des Lasers Intenses, Ecole Polytechnique, Palaiseau, 91128, France

D Batani, F Scianitti, E Perelli-Cippo

Dipartimento di Fisica G Occhialini, Università degli Studi di Milano-Bicocca, Milano, 20126, Italy

T A Hall

University of Essex, Colchester, Essex, CO4 3SQ, UK

M H Key, A J Mackinnon,

Lawrence Livermore National Laboratory, Livermore, CA 94550-9234, USA

R R Freeman, R A Snavely, J A King, C Andersen, J M Hill

University of California Davis, Davis, CA 95616, USA

R B Stephens, T E Cowan

General Atomics, San Diego, CA 92121-1122, USA

A Ng, T Ao

Department of Physics & Astronomy, University of British Columbia, Vancouver, B.C. V6T 1Z1, Canada

D Neely, R J Clarke

Central Laser Facility, CLRC Rutherford Appleton Laboratory, Chilton, Didcot, Oxon, OX 0Q11, UK

Main contact email address: *emanuele.martinolli@polytechnique.fr*

Introduction

In the fast ignition[1)] approach to the inertial confinement fusion a few kJ of fast electrons produced by an intense laser pulse should deposit their energy in the dense DT fuel in a small area (≈ 10 μm size) and heat it to a high temperature (≈ 10 keV), enough to ignite thermonuclear reactions[2)]. One of the key issues is therefore the amount of energy which can be carried and deposited in the target by the electrons. Several experiments have been performed in order to study fast electron transport in solid targets by means of optical techniques[3, 4)], X-ray diagnostics[5-9)], proton measurements[10, 11)] and magnetic field measurements[12)]. Important results have already been obtained on some geometric aspects of the electron transport: the presence of fast-electron jets, the directionality of the beam, the huge self-generated magnetic fields associated with the fast electron current, the role of the target conductivity. However, only a few experiments have been performed regarding a quantitative measurement of the heating induced in the target bulk[13, 14)]. Only X-ray diagnostics can give a direct insight into this process.

In our experiment, Kα line emission spectroscopy (at ≈ 8 Å) has been successfully used to determine the ionization stage and infer the temperature of an aluminium fluorescer layer (buried in a multilayer target), which was heated by the fast electron current. We note that in the same experiment other diagnostics such as time-resolved, rear side, optical imaging and X-ray Kα imaging were also implemented, which results are described in other contributions to this report (see J J Santos, M H Key). As the emitting atoms are ionized by collision with fast electrons, the Kα line is shifted towards shorter wavelength by several tens of mÅ, due to the lower screening of the nucleus by the bound electrons[15)]. The fast electron range and temperature were also inferred from the total Kα yield emitted by the aluminium layer and by an additional copper fluorescent layer. The results were compared with simulations performed with the 3D hybrid collisional electromagnetic transport code PâRIS[16)]. As the intensity of the shifted lines is usually weak for the expected range of temperature (≈ 10 – 50 eV) [17)] and the bremsstrahlung noise level can be high, a good photon collection efficiency is required as well as a high S/N ratio. Therefore, we designed for this experiment a Bragg spectrograph based on a conically bent crystal, which provides a high brightness and a good spectral resolution over a wide spectral range (7 - 8.5 Å), chosen to include the Kα, the He-α and Ly-α region. Contrary to traditional flat crystals, the conical one strongly focuses the spectrum onto a narrow focus line, as first described by Hall[18)].

Experimental set-up

The Vulcan laser CPA pulse was focused at normal incidence by a f/3.5 off-axis parabolic mirror onto a flat multilayer target, shown in Figure 1. The small focal spot (≈ 10 μm) allows a high irradiance (1-5 10^{19} Wcm^{-2}) to be reached. About 10-40 % of the laser energy is expected to be transferred to electrons[7, 8)], which are accelerated to several 100 keV. The target is typically composed of three layers. The front propagation layer is made of aluminium of varying thickness in the range 10 - 300 μm. We do not detect the X-rays coming from this layer. Two 20 μm-thick fluorescer layers were also buried in the target. The first one is copper, whose bright Kα line is detectable at the 5th order (at 1.5 Å) by the spectrograph. This layer also stops the X-rays coming from the first layer. The second fluorescer is aluminium and emits the shifted Kα lines (at ≈ 8Å). The effect of the photoionization of the Al layer by the X-rays from the Cu layer was also considered.

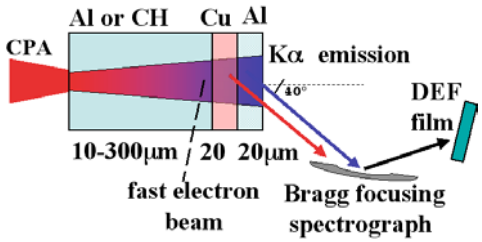

Figure 1. Experimental set-up for Kα spectroscopy of Al and Cu fluorescent layers buried into multilayer targets.

The spectrograph looks at the target rear side at a 40 degrees angle from the laser axis and at 31 cm from the target. We used a 7 cm by 4 cm potassium acid phtalate (KAP) crystal (2d = 26.64 Å, integrated reflectivity = 8 10^{-4} at 8 Å), whose surface is bent about a conical surface (half angle 17.48 degrees), which corresponds to an average bending radius

of 9 cm. The dispersion of the spectrograph is 26.9 mm / Å, while the spectral resolution ($\lambda / \Delta\lambda$) is ≈ 500, mainly limited by the finite size of the emission region (up to 200 μm). On the spatial axis the spectrograph forms an image of the emission region with a magnification of 1. However, the spatial resolution (above 200 μm) is limited by the intrinsic aberrations associated with the focusing of the conical geometry and by the crystal defects. Because of the high radiation field typical of short pulse-solid interaction, a DEF X-ray film was used as a detector instead of a CCD camera and positioned at 62 cm from the target. The film was then analyzed using a 16-bit densitometer. As the conical geometry is cumbersome to study analytically, a 3D-ray tracing code was used to choose all the parameters of the spectrograph in order to maximize the focusing.

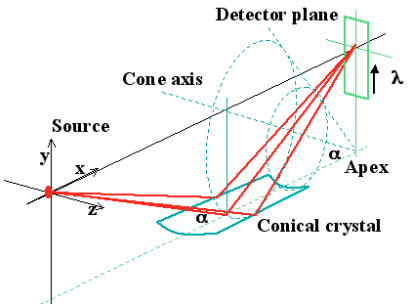

Figure 2. Simplified diagram of the conical crystal.

Due to the high sensitivity of the spectrograph performance to the crystal alignment, a two-step procedure was used. First, a 10 μm diameter fiber optic was used as a point source on a separate optical bench. The fiber emits visible laser rays which are then reflected by the crystal surface and focused onto a CCD camera. The relative positions and angles are adjusted to obtain the best focalization, i.e. the narrowest possible line focus, according to the ray-tracing code This is found to be approximately 200 μm (500 μm including the low intensity lateral wings) over the whole dispersion range. The spectrograph as a whole is then positioned into the vacuum chamber so that the alignment pin (corresponding to the source) is brought onto a point corresponding to the centre of the target rear surface, by means of target alignment viewers.

Experimental results

We present in Figure 3 an example of the spectra obtained, corresponding to an Al 11μm - Cu 25μm - Al 16 μm target.

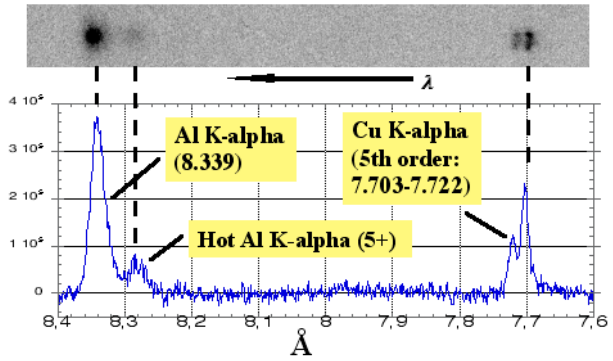

Figure 3. Experimental spectrum obtained with a Al 11 - Cu 25 - Al 16 μm target. Energy on target was 45 J.

The Al Kα line appears at the left of the spectrum as well as the first shifted line, which corresponds to the 5+ ionization state (oxygen like). The Al 0+ to Al 4+ transitions are blended in the big "cold" peak. At the right side, the cold Cu Kα I and II lines (reflected at 5th order) are present. Their separation being ≈ 19 mÅ, the corresponding spectral resolution is at least 500, as expected. Looking at the whole series of shots on multilayer targets, we found that the 5+ shifted line is visible in targets with a front layer thickness up to 100 μm. The 6+ is visible only in the thinnest targets, with no front layer. The intensity of the cold and 5+ lines is plotted vs. the thickness of the front layer in Figure 4. The copper Kα line (not shown) shows a similar exponential decay to the aluminum one. From these data we can estimate the (exponential) range of the fast electron current, which is ≈ 250 μm.

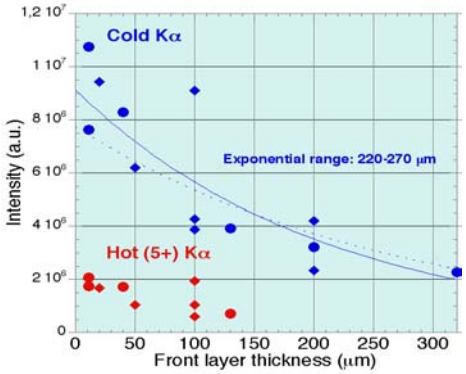

Figure 4. Kα line intensity from the aluminium fluorescent layer (Al-Cu-Al targets) as a function of the thickness of the front aluminium layer. Laser energy on target was in the range 30-45 J.

We compared the measured fast electron range with a Monte Carlo simulation. A Maxwellian electron distribution with an initial 0° divergence was supposed and the experimental values of energy and spot size were used. We obtained the best agreement for a 300-400 keV distribution temperature.

The experimental intensity ratio of the hot Kα line to the cold one (shown in Figure 5 left) was 20% and does not show any particular time trend vs. the thickness.

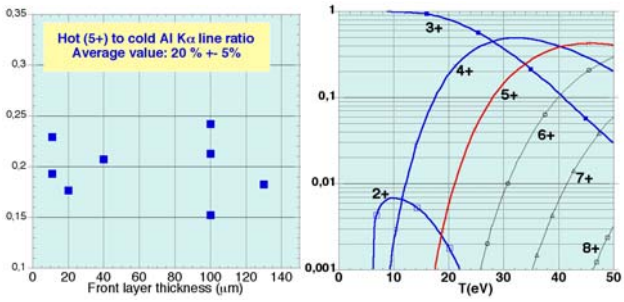

Figure 5. (Left) Experimental ratio of the hot (5+) to cold Al Kα line obtained on Al-Cu-Al targets. Laser energy is in the range 30-45 J. (Right) Ionic fractions of solid density aluminium vs. the temperature from UBCAM code[19].

We briefly note that there is another process, besides the 5+ ionization, not distinguishable with our spectral resolution, which may contribute to the observed shifted peak. It is the double KL ionization, in which the initial state has two electron vacancies instead of one. The intensity of this transition line was measured in short pulse laser-solid experiments, although under different conditions, and found to be ≈ 10% of the ordinary Kα peak weakly temperature dependent[20]. In our conditions, the 5+ ionization due to the fast electron target heating is supposed to be the dominant process.

We therefore used the atomic physics UBCAM code to compute the ionic fractions of solid aluminium heated up to a few times 10 eV at LTE. The 5+ state appears to progressively account for 1% up to 20% of the ratio to the cold line (2+ - 4+ states), if the target is heated in the range 20 - 35 eV. Therefore we can assume 20 eV as a lower limit for the temperature. However,

the experimental situation is more complicated for several reasons. First, the heated spot at target rear side is smaller than the fast electron beam size: Kα photons coming from more external cold regions contribute to the cold peak, lowering the observed line ratio. Second, fast electrons both heat and produce Kα (pump = probe), so the dynamics of this highly transient process should be considered in a self-consistent transport model. We performed a preliminary analysis with the help of the PâRIS hybrid transport code, in which an on-line calculation of the ionic fractions (based on the UBCAM code) and the corresponding Kα emission were added. In the case of bare aluminium targets (the only ones currently handled by the code) and for the experimental conditions, the code shows that a temperature of 30 eV at target rear side would be in agreement with the observed ratio. However, the femtosecond time step used in the code in order to describe the relativistic electrons transport (which lasts 1-2 ps for a typical target), would not allow *a priori* to use LTE ionization for the heating and the Kα emission. This is because the electron-ion relaxation time (approximately 5 fs for cold aluminium) is greater than the time step. A time-dependent heating model is currently being studied.

Conclusions

Kα emission spectroscopy of an aluminium fluorescer layer has been successfully used to study the fast electron transport and heating in sub-picosecond laser interaction with multilayer solid targets. This work is relevant in the context of the fast ignition studies. In particular the spectrally shifted Kα lines have been observed as a diagnostic for the target heating due to the fast electron current. A high brightness conical crystal Bragg spectrograph has been designed for this experiment, in order to detect the expected weak signal.

Acknowledgements

The authors gratefully acknowledge the Vulcan laser, target area and target fabrication staff of the Central Laser Facility. This work has been supported by the EU Laser Facility Access Program (contract N° HPRI-CT-1999-00010) and by the Femto Program of the European Science Foundation. One of us (JJS) was supported by a grant of the Portuguese Government (MCT, PRAXIS XXI BD/18108/98).

References

1. M Tabak *et al*.
Phys. of Plasmas 1, 1626, (1994)
2. S Atzeni *et al*.
Jap. J. Appl.Phys. 34, 1980 (1995)
3. M Tatarakis *et al*.
PRL 5, 999, (1998)
4. L Gremillet *et al*.
PRL 83, 5015, (1999)
5. M I K Santala *et al*.
PRL 84, 1459, (2000)
6. D Batani *et al*.
PRE 61, 5725, (2000)
7. F Pisani *et al*.
PRE 62, R5927, (2000)
8. M H Key *et al*.
Phys. of Plasmas 5, 1966, (1998)
9. K B Wharton *et al*.
PRL 81, 822, (1998)
10. M Zepf *et al*.
Phys. of Plasmas 8, 2323, (2001)
11. R A Snavely *et al*.
PRL 85, 2945, (1999)
12. M Tatarakis *et al*.
Phys. of Plasmas 9, 2244, (2002)
13. J A Koch *et al*.
PRE 65, 016410, (2001)
14. E Martinolli *et al*.
submitted to PRL, (2002)
15. L L House
Astrophys. J. Suppl. Ser. 18, 21, (1969)
16. L Gremillet *et al*.
Phys. of Plasmas 9, 941, (2002)
17. A Rousse *et al*.
PRE 50, 2200, (1994)
18. T A Hall
J.Phys.E:Sci.Instrum. 17, 110, (1984)
19. G Chiu and A Ng
PRE 59, 1024, (1999)
20. J C Gauthier *et al*.
PRE 52, 2963, (1995)

Determination of high energy proton origin in laser-solid interaction

M Zepf

Physics Department, School of Mathematics and Physics, Queen's University, Belfast, BT7 1NN, UK

F N Beg, AE Dangor, A Gopal, K Krushelnick, M Tatarakis, U Wagner, M S Wei

Blackett Laboratory, Imperial College of Science, Technology and Medicine, London SW7 2BZ, UK

P A Norreys, R J Clarke

Central Laser Facility, CLRC Rutherford Appleton Laboratory, Chilton, Didcot, Oxon, OX11 0QX, UK

E L Clark,

AWE, Aldermaston, UK

Main contact email address: *m.zepf@qub.ac.uk*

Introduction

If a solid target is irradiated with relativistic intensities high energy protons can be observed at the rear of the target[1)]. A significant amount of the incident laser energy (>10%)[2)] is converted into protons with E_p>1 MeV, giving rise to a compact and reasonably efficient source of protons which may be of interest to a range of applications. However, there is still some disagreement as to the precise mechanism underlying the acceleration and also the proton source.

Acceleration mechanisms which have been suggested include sheath acceleration which generates large electric fields at the rear of the target[2)] and fields set up at the front or inside the target[1,3)] . The origin of the accelerating field at the rear of the target is readily understood. During the interaction the high intensity laser light couples its energy efficiently into a beam of fast electrons. These fast electrons then propagate to the rear of the target and set up a strong electrostatic field upon exiting which forces the electrons back into the target and drags protons and ions out of the target. Charge separation also occurs at the critical surface over short distances at the front of the target, due to the ponderomotive force of the laser pulse. This accelerates protons to approximately the ponderomotive energy of the laser (up to 4 MeV for 10^{20}Wcm^{-2}) as a result of hole boring and/or the propagation of an electrostatic shock[4)]. Toupin *et al*[5)], for example, predict a collimated, multi-MeV ion beam that is directed into the target for small density scale-lengths, predictions that are supported by some experimental evidence[6)]. The predicted ion energies are low compared to those that have been observed to emerge from the rear of the target, but these acceleration processes may be the origin of some of the fastest protons that receive an initial 'kick' and that are accelerated more efficiently in subsequent fields[7)].

Strong fields are also set up inside the target in response to the hot electrons propagating into the target, since charge neutrality must be maintained by a suitable return current. The electric field required to set-up this return current will also accelerate ions and protons inside the target. The return current is strongly affected by collisions and the resulting electric field can be estimated from the target resistivity[8)]. These fields can extend over large distances in the target (the penetration depth of the hot electron beam) and their magnitude depends strongly on the resistivity experienced by the return current.

Present computational modeling of these plasmas is only of limited use in elucidating the question of the relative strength of the accelerating electric fields. Particle--in--Cell codes (PIC) frequently do not include collisions, assume that the plasma is already hot (electron temperature ~ 1 keV) for numerical reasons and at ~10% of solid density to reduce computation time. By contrast in the experiments the target is initially a cold solid. Consequently there is some doubt as to the validity of PIC simulations for predicting material conditions and electron transport inside a target which is rapidly evolving from a cold solid to hot dense plasma. However, PIC codes typically provide accurate predictions for high intensity short pulse laser experiments in low density plasmas or at surfaces of solid targets. Results from three dimensional simulations[9)] show protons accelerated up to 6 MeV for $I\lambda^2 = 10^{19}$ Wcm^{-2} μm^2, by fields at the rear of the target, where the PIC code should be reasonably accurate. This is lower than the experimental observation of 10 MeV at 6×10^{18} Wcm^{-2}μm^2 and 20 MeV at 10^{19} Wcm^{-2}μm^2. They also predict a divergence of around 10° full width angle for the lower energy protons rather than the 40-60° observed experimentally. It is worth noting that 2D codes predict higher energies due to the lower dimensionality and should therefore not be directly compared to the experimental results. Alternative modeling techniques such as hybrid PIC/fluid codes[8)] are capable of capturing the transition from cold solid to plasma and do predict large accelerating electric fields in the target. The fields predicted to exist inside the target are, however, not large enough to explain the large proton energies observed experimentally. Since the resistivity is not calculated self-consistently (typically approximated by the Spitzer expression), the code may well underestimate the magnitude of the fields. Effects such as the lower hybrid instability[10)] are expected to result in enhanced resistivity and thus higher field strengths.

The most direct evidence for the origin of the protons and the acceleration mechanism involved comes from experiments by Maksimchuk *et al*.[3)], using selective deuterium contamination of the target, where the origin of the protons was determined to be from the front surface. Furthermore, the energy of protons was found to increase with increasing target thickness in the range of 0.1-10 μm, which is consistent with an acceleration mechanism near the front of the target.

On the other hand the proton beam tends to be aligned to the rear target surface normal in most experiments and experiments using wedge shaped targets have observed a proton beam from both rear surfaces[2)]. This suggests that the rear surface strongly influences the proton acceleration and that acceleration directly from the rear surface may dominate. Further support for this hypothesis has come from recent experiments, which show that the proton beam can be suppressed by forming a plasma on the rear surface[11)]. Clearly, it is possible that several acceleration mechanisms are operating simultaneously. A fundamental difficulty is to measure the various acceleration mechanisms independently. In a typical experiment, hydrogen is present on all target materials in the form of surface contaminants (and possibly trapped within the lattice structure of the target), which makes it difficult to determine the various contributions.

Experiment

The protons were detected using stacks of CR39 nuclear track detectors, radio-chromic film (RCF) and materials for nuclear activation. Since the protons are decelerated as they pass through subsequent layers of the detector stack, one can obtain images of the proton angular distributions at different energies on a single shot[1)].

The approach taken in the experiment described here is to selectively contaminate one side of the target with hydrogen by

coating it with a suitable compound while minimising the general hydrocarbon surface contamination by heating the target. The temperature at which all surface contamination boils off reliably is in excess of 1000°C. Unfortunately, such temperatures are above the typical boiling point of most hydrocarbon compounds, which could be used to coat the target. Consequently, the temperature was chosen as a compromise between boiling off the contaminants while retaining the coating. Therefore, some contamination is still present on all surfaces during the experiment. The target temperature was typically 300-400°C. At this temperature we observed that the hydrocarbon contamination was significantly reduced and the integrity of the coating was maintained. The coating consisted of PEEK (Polyetheretherketone), which has a melting point of 250°C but retains a high viscosity far beyond the melting point. Figure 1 shows a comparison of the ion spectra taken from a heated and an unheated pure aluminum target showing a significant reduction in the overall proton signal.

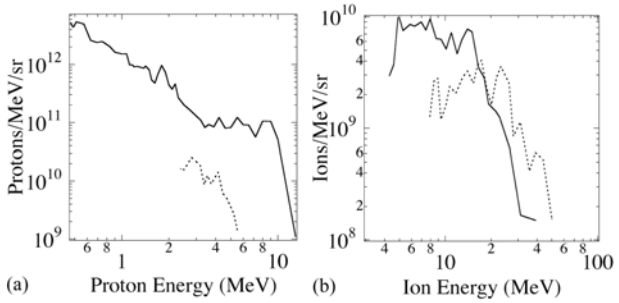

Figure 1. (a) Comparison of proton spectra from the heated (dotted line) and unheated Al targets (solid line). **(b)** comparison of the carbon^{6+} spectrum from heated and unheated Al targets. A clear reduction in proton and carbon numbers is visible. Carbon energies are enhanced due to the reduction of protons. These spectra were measured at the front side of the target using a Thomson parabola.

Our measurements indicate that this reduction of the contamination is sufficient to distinguish between the signal from the front and the back. Figure 2 a-c shows typical proton data recorded with RCF and CR39 detector stacks from an interaction with a square, unheated Al target of 100 µm thickness. The features can be categorised into three qualitatively distinct regions. First, there is a cross--like pattern that extends to very large angles from the centre of symmetry. Secondly there is a ring of enhanced signal, which is clearly visible on the CR39 track detector data and thirdly there is a feature at the centre of the ring that corresponds to the area of highest exposure on the RCF. The ring structure contracts with increasing proton energy, while the feature at the centre appears to contain no high energy contribution and is only visible on the low energy layer at the front of the detector stack.

The cross structure is found to be dependent on the shape, transverse size and orientation of the target. In the case of a square target the cross is aligned to the principal axes of the target and is only visible if the targets are sufficiently small (< 1 cm). The protons responsible for the cross pattern appear to originate from the front of the target and are then transported around the target, as is evidenced by the shadow that corresponds to the glass target mounting stalk in the bottom arm of the feature in Figure 2 a. When the target is rotated the cross pattern rotates correspondingly. Also, the intensity of the crosspattern diminishes with increasing target size, as can be seen by comparing Figures 2 a and d. In this case, the acceleration takes place by well understood mechanisms at the front of the target during the plasma expansion and the protons are deflected around the target by magnetic fields.

By contrast, the ring structure and central feature do not depend on the size and orientation of the target, and are therefore not generated in the same manner, but rather are emitted from the rear surface of the target.

However, in this case the use of heated targets can aid our understanding of the observed signal. Figure 3 contrasts two targets consisting of 100 µm Al and 20 µm of PEEK. The top of Figure 3 shows the data taken from a shot with the PEEK on the front of the target and the bottom shows a shot when the PEEK was on the back. The ring structure is only clearly visible when the PEEK is on the front of the heated target. The rings in this case are quite broad, which is characteristic of plastic targets under all conditions. When the PEEK is on the rear of the heated target the signal in the ring structure is significantly reduced and gives way to a faint signal on the CR39. This suggests that the protons that form the rings originate on or near the front surface. Since the ring structure also contains the highest energy protons, it appears that the overall accelerating potential experienced by these protons is larger than for those at the rear of the target. The total potential may well consist of contributions from several or all the mechanisms outlined above. This result agrees well with the finding that the ring structure gives way to uniform disks of emitted protons as the target thickness is reduced below 25 µm[12]. This behavior can be understood in terms of the magnetic fields that are generated inside the solid density plasma as the electron beam propagates through it. In order to deflect all protons of a given energy by the same amount, regardless of their initial radial position, they have to pass through the same length of magnetic field. The angular spread of up to 60° full width of the rings is also in reasonably good agreement with deflection anticipated from fields predicted to be present inside the target[1]. By contrast PIC simulations predict fields at the rear of the target that are only sufficient to create ring structures of <10° full width[9]. It is also interesting to note that the ring structure is not always centred on the target normal. Particularly for thinner targets there can be substantial deviations (~20°) from the target normal of the ring (or disk in the case of thin targets) structure[12], providing further evidence that rings and the central feature are generated separately.

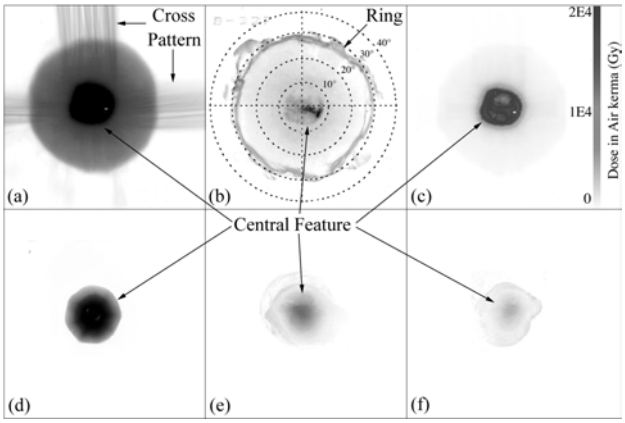

Figure 2. (a-c) images from a detector stack showing the typical features observed for cold targets. Parameters were I= 10^{19}Wcm^{-2}, 100 µm Al target. **(a)** data taken using RCF film (Proton energy E>3 MeV. **(b)** CR39 data (E=5MeV). (**c)** dose derived from (a). Three spatially distinct contributions are indicated.

(**d-e)** series of corresponding data taken from a heated Al target under otherwise identical conditions. (**d)** E> 1 MeV (RCF) (**e)**E=3 MeV (CR39) and **(f)** E=6 MeV (CR39). The signal level is significantly reduced on the heated target and the rings visible in b) have (almost) disappeared. The absence of the cross pattern is due to the significantly larger spatial extent of the heated target. Angles in (b) are half angles and apply to (a)-(f).

The central feature is typically responsible for the bulk of the signal at low ion energies (<5 MeV). These low energy protons are typically well collimated (< 10°) in contrast to the low energy component of the ring structure. This feature is reliably centred on the target normal from the rear of the target. When the target was heated the feature remained visible on all shots and was enhanced by a factor of 30 when the PEEK was on the back facing the detector stack. This suggests that the protons in the central feature originate from the rear surface of the target.

The central feature does not extend to very high energies (although still substantial). In fact, the peak energy and the angular spread of the protons in the central feature are in very good agreement with the protons accelerated by fields at the rear of the target in detailed PIC simulations[9], lending support to this interpretation of our data.

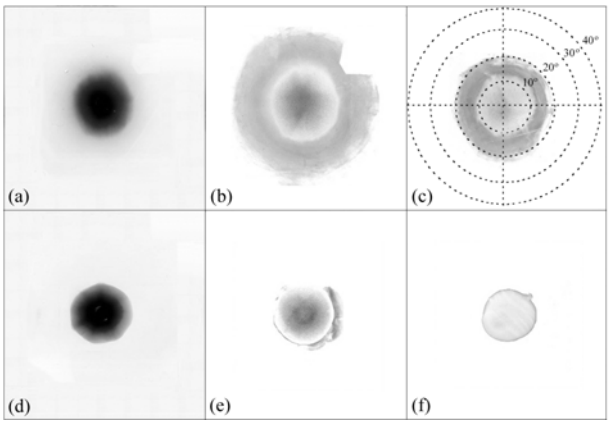

Figure 3. Comparison of data from heated target (20 µm PEEK on 100 µm Al). The PEEK coating was on the front side in the first case (a-c) and on the back side of the target (d-f) in the second. Proton energies: a,d) 1 MeV (RCF behind 25 µm Al filter), b,e) 3MeV (CR39) c,f) 6MeV (CR39). Angles indicated in c) are half angles and apply to a)-f).

In conclusion, we have presented experimental data that allows us to distinguish between the origin of various structures present in the energetic proton signal at the rear of the target in high power laser--solid interactions. We have identified three distinct proton populations that contribute to the signal observed on the detectors. The ring structure that contains the highest energy particles consists of protons that originate from the front surface, strongly supporting the original hypothesis by Clark *et al.*[1]. The low divergence, lower energy central feature is accelerated by fields at the rear of the target and agrees well in structure and energy with simulation results for protons accelerated from the rear surface.

References

1. E L Clark *et al*., Phys. Rev. Lett. 84, 670 (2000).
2. R. Snavely *et al*., Phys. Rev. Lett. 85, 2945 (2000).
3. A. Maksimchuk *et al*., Phys. Rev. Lett. 84, 4108 (2000); K. Nemoto it *et al*., Appl. Phys. Lett. 78,595 (2001).
4. S.C. Wilks *et al*., Phys. Rev. Lett. 69, 1383 (1992).
5. C. Toupin *et al*., Phys. Plas. 8, 1011 (2001).
6. N. Izumi *et al*., Phys. Rev. E 65, 036413 (2002).
7. J.T. Mendonca *et al*., Meas. Sci. Technol., 12, (2001); J.R. Davies, Laser and Part. Beams, to be published.
8. A.R. Bell *et al*., Plasma Phys. Contr. F., 39, 653 (1997). JR Davies *et al*., Phys. Rev. E 56, 7193 (1997).
9. A. Pukhov, Phys. Rev. Lett., 86, 3562 (2001).
10. M.G. Haines, Phys. Rev. Lett., 78, 25 (1997).
11. A.J. MacKinnon *et al*., Phys. Rev. Lett. 86, 1769 (2001).
12. M. Zepf *et al*., Phys. Plas. 8, 2323 (2001).

Double-sided laser illumination of high Z targets using Vulcan

P McKenna, K W D Ledingham*, I Spencer, T McCanny, R P Singhal
Department of Physics and Astronomy, University of Glasgow, Glasgow G12 8QQ, UK

** also at AWE plc, Aldermaston, Reading RG7 4PR, UK*

F N Beg, K Krushelnick, M S Wei, A Gopal, A E Dangor
Blackett Laboratory, Imperial College, London SW7 2BZ, UK

P A Norreys, K L Lancaster, R J Clarke, S Hawkes
Central Laser Facility, CLRC Rutherford Appleton Laboratory, Chilton, Didcot, Oxon, OX11 0QX, UK

M Zepf
Department of Pure and Applied Physics, The Queen's University of Belfast, Belfast BT7 1 NN, UK

E L Clark, R D Edwards
AWE plc, Aldermaston, Reading RG7 4PR, UK

Main contact email address: *p.mckenna@physics.gla.ac.uk*

Introduction

The Vulcan laser, focused to intensities up to 10^{20} Wcm^{-2} and interacting with solid and gaseous targets, has proven to be an efficient, bright source of energetic particles, including electrons[1)], protons[2)], heavy ions[3)], neutrons[4)], and γ-rays[5)]. Energetic particles so-generated are finding applications in many traditional areas of science including nuclear physics[6)]. With the imminent upgrade of Vulcan to Petawatt status and intensities of the order of 10^{21} Wcm^{-2}, these particle beams will become even brighter, and more exotic particles will be produced.

Of current interest is the search for novel methods of producing intense (>10^{10} Bq) positron beams for use in many diverse applications including surface science, positronium spectroscopy and positron interaction physics[7)]. Ultra-intense lasers may provide a solution to the difficulties of producing positron sources by conventional methods. In principle the electric field at the focus of a laser could pull electron-positron pairs from a vacuum. An $\boldsymbol{E}$ field of the order of 10^{16} V/cm is required, which corresponds to a focused intensity of 5×10^{28} Wcm^{-2}, orders of magnitude higher than is currently achievable. The hot plasma created at a laser focus however provides a practical medium for pair production. For laser irradiance $I\lambda^2 \approx 10^{19}$ Wcm^{-2}μm^2 , the electron quiver motion in a laser field increases beyond $2m_0c^2$ (where m_0 is the rest mass of the electron), the pair production threshold is exceeded, and electron/positron pairs are produced. This occurs directly via trident electron-ion collisions and indirectly via the creation of Bremsstrahlung gamma radiation, which interacts with nuclei to produce electron/positron pairs (the Bethe-Heitler process). These processes are discussed further in[8,9)] .

To date, positron production has been demonstrated at LLNL[10)] and Garching[11)] using single ultra-intense pulses focused onto solid targets and gaseous targets with a high Z converter, respectively. In the present study we have sought to test experimentally a new arrangement involving double-sided illumination of a high Z foil target to enhance pair production rates. The possibility of using counter-propagating ultra-intense (>10^{19} Wcm^{-2}) laser pulses in this way has been modelled by a number of groups[12-14)] . In this arrangement the hot electron-positron plasma produced at the laser focus is confined by the laser ponderomotive pressure on the front and back of the target, with additional confinement in the lateral direction due to the induced magnetic fields. A sufficiently confined hot dense plasma should lead to an increased pair production rate. Electron-positron plasmas exist in a variety of astrophysical environments including neutron stars, pulsars and quasars, and the production of these plasmas in the laboratory is therefore also of great interest from an astrophysical point of view [9)].

This report describes our first experiment involving this novel high intensity double-sided illumination arrangement. Spectrometers have been developed to measure both electron and positron energy distributions up to 15 MeV. Electron energy spectra are compared for single and double illumination of Au foil targets. It is planned to extend the experiment to the higher intensities available on the Petawatt branch of Vulcan in the near future.

Experimental

The experiment used the ultra-intense CPA beam-line of the Vulcan laser[15)]. The CPA beam was split after the final amplifier and the two halves of the beam were focused onto either side of the gold foil target. Various target thicknesses in the range 1 to 50 μm were studied. A maximum energy of 40 J in each laser pulse limited the focused intensity on each side of the target to below 10^{19} Wcm^{-2}. The arrangement is shown schematically in Figure 1.

After irradiation of the foil with the laser pulses the plasma produced expands freely. A number of diagnostics were used to detect the high energy particle and radiation produced, including two magnetic spectrometers with fields of the order 2.5 kGauss. Plastic collimators were used at the entrance of the spectrometers to stop electrons without producing unwanted Bremsstrahlung radiation. The spectrometers, which were each surrounded in 6 ton of lead to shield against the flash of X-rays from the laser plasma, were positioned 40 degrees apart to obtain angular information on the electron and positrons produced.

Figure 2 shows the design of the spectrometers in more detail, including the particle trajectories within the magnetic field as

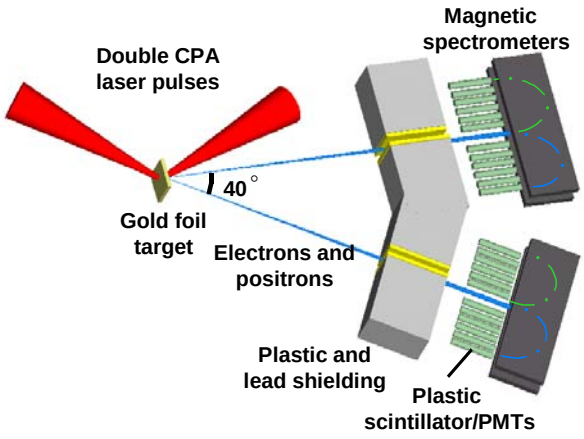

Figure 1. Experiment arrangement.

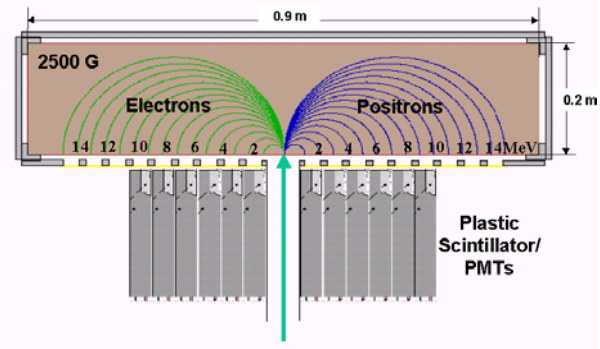

Figure 2. Schematic of the electron/positron spectrometer.

computed using the SIMION code. The electrons and positrons from the expanding laser-produced plasma are separated according to their charge and momentum and deflected through 180°. This is necessary in order to distinguish from other types of radiation, including γ-rays, ions and neutrons, and to separate the much higher flux of fast electrons from the weak positron signal. Electrons and positrons with energy up to 15 MeV are deflected over a dispersion range of 40 cm and detected using light-tight plastic scintillator coupled to photomultiplier tubes. Each detector produces a signal corresponding to the total energy deposited in the scintillator. The level of the background is determined in two ways, firstly by blocking the collimator with plastic and secondly by replacing the magnetic pole pieces with iron plates of similar dimension and spacing.

Results and Discussion

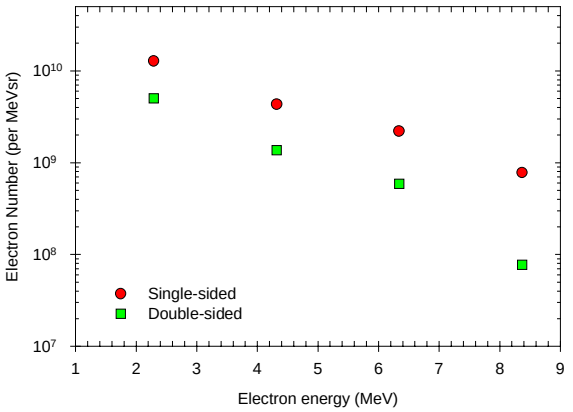

Figure 3. Electron spectra obtained for a 1 μm Au target under single- and double-sided illumination. The electron flux is significantly lower for the latter case.

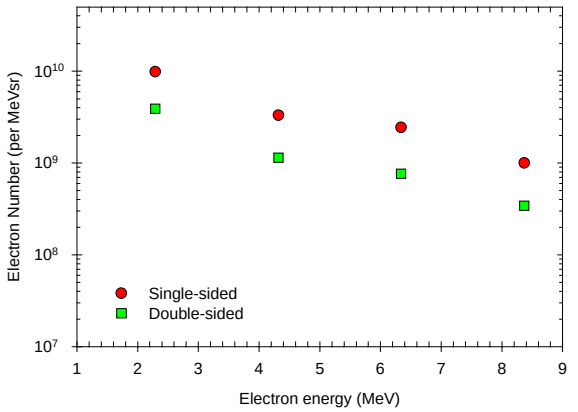

Figure 4. Electron spectra obtained for a 50 μm Au target under single- and double-sided illumination.

The final focused intensity of each laser pulse was below 10^{19} Wcm^{-2} and as a result no significant positron signal was observed above the background level. However, the electron energy distributions measured for both single- and double-sided illumination of the gold foil targets have yielded interesting results.

Figures 3 and 4 compare the electron spectra for single- and double-sided illumination shots on a 1 μm and a 50 μm gold target respectively. The plots have been normalised to the total pulse energy on target. Similar energy distributions are observed with a temperature of the order of 1 MeV. The flux of electrons observed for the double-sided illumination is lower than for single beam shots. The spectra in Figures 3 and 4 are typical examples from a large number of shots on a variety of targets with thicknesses from 1 to 50 μm. In all cases the flux of electrons observed for the double-sided illumination is consistently a factor of 3 to 4 lower than the single-sided equivalent. An initial analysis of the bremsstrahlung gamma spectra indicates a similar trend.

The interaction processes occurring when counter-propagating beams are incident on a foil target are likely to depend on a number of target parameters including its thickness. Electron energy distributions for double-sided shots were measured as a function of target thickness as shown in Figure 5. No significant target thickness dependence in the range 1 to 50 μm was observed.

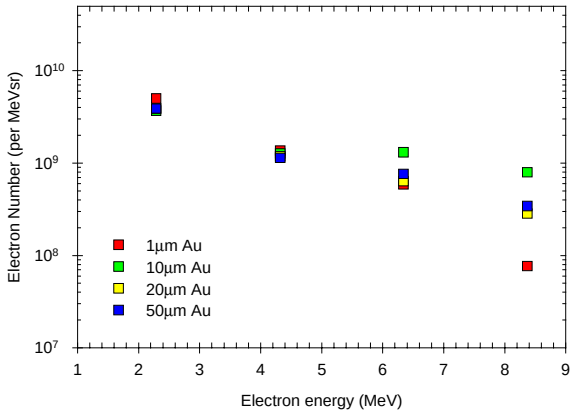

Figure 5. Electron energy distributions for double-sided illumination of a range of target thicknesses.

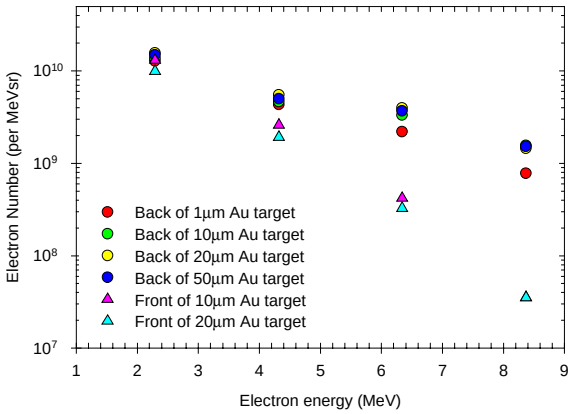

Figure 6. Electron energy distributions measured in front of and behind targets for single-sided irradiation.

Finally, a comparison of the electron energy distributions from each side of the target was made for single-sided illumination shots. Previous measurements of ions in particular have shown that ions measured at the back of an irradiated solid target exhibit higher luminosity, energy conversion efficiency and

well defined beam characteristics, compared to ions detected from the laser illuminated side (see Reference 16 and other references therein). As shown in Figure 6, in the present study higher electron temperatures were consistently observed from the back of the target regardless of its thickness. The flux of high energy electrons was also considerably higher than that measured from the irradiated side.

Conclusions

A first experimental study involving high-intensity double-sided irradiation of solid targets has been undertaken. Double-sided illumination has been found to materially change the dynamics of the laser-solid interaction, as compared to single beam shots. This is manifested in a reproducible change in the flux of electrons detected. The techniques and experience developed during this experiment will be used on a future experiment on the Petawatt branch of Vulcan and will seek to verify plasma confinement and enhance electron-positron pair production.

References

1. M. I. K. Santala *et al*., Phys. Rev. Lett. 86, 1227 (2001).
2. E. L. Clark *et al*., Phys. Rev. Lett. 84, 670 (2000).
3. E. L. Clark *et al*., Phys. Rev. Lett. 85, 1654 (2000).
4. P. A. Norreys *et al*., Plasma. Phys. Control. Fusion 40, 175 (1998).
5. P. A. Norreys *et al*., Phys. Plasmas. 6 , 2150 (1999).
6. K. W. D. Ledingham *et al*., Phys. Rev. Lett. 84, 899 (2000).
7. T. D. Steiger *et al*., Nucl. Inst. Meth. A 299, 255 (1990).
8. H. Takabe, Progress of Theoretical Physics Supplement 143, 202 (2001).
9. K. Nakashima and H. Takabe, Phys. Plasmas. 9, 1505 (2002).
10. T. E. Cowan *et al*., Nucl. Inst. Meth. A455, 130 (2000).
11. C. Gahn *et al*., Appl. Phys. Lett. 77 , 2662 (2000).
12. E. P. Liang, S. C. Wilks, and M. Tabak, Phys. Rev. Lett. 81, 4887 (1998).
13. B. Shen and J. Meyer-ter-Vehn, Phys. Rev E 65, 016405 (2001).
14. H. M. Fried *et al*., Phys. Rev. D. 63 , 125001 (2001).
15. C.N. Danson *et al*., J. Mod. Opt. 45, 1653 (1998).
16. M. Zepf *et al*., Phys. Plasmas. 8, 2323 (2001).

Medical Isotope Production using Proton Beams Generated by Vulcan

I Spencer, K W D Ledingham*, R P Singhal, T McCanny, P McKenna

Department of Physics and Astronomy, University of Glasgow, Glasgow G12 8QQ, UK

** also at AWE plc, Aldermaston, Reading RG7 4PR, UK*

E L Clark

AWE plc, Aldermaston, Reading RG7 4PR, UK

K Krushelnick, M Zepf, F N Beg, M Tatarakis, A E Dangor

Blackett Laboratory, Imperial College, Prince Consort Road, London SW7 2BZ, UK

P A Norreys, R J Clarke, R M Allott, I N Ross

Central Laser Facility, CLRC Rutherford Appleton Laboratory, Chilton, Didcot,, Oxon OX11 0QX, UK

Main contact email address: *i.spencer@physics.gla.ac.uk*

Introduction

In the last four years, gamma rays of energies up to 100 MeV have been generated when intense lasers interact with thick high Z solid targets[1-5] . These gamma-rays are generated via bremsstrahlung emission from energetic electrons, implying electrons of similar energies. Hence a high intensity laser can produce energetic electrons similar to that of a low-energy linear accelerator. These laser-generated gamma-rays have been used to produce radioactive nuclei (decaying by electron capture/positron emission) via (γ,mn) reactions. The development of this technique for "table-top" production of radio-nuclides is a natural extension of this work.

One of the potential applications of this new technology is to produce short-lived (2 minutes - 2 hours) positron emitters for Positron Emission Tomography (PET) [6] . This is a form of medical imaging, where a patient receives by injection a pharmaceutical labelled with a short-lived β^+ emitting source. This radio-pharmaceutical is taken up wherever it is used in the body, and specific sites in the body can be imaged by detecting the back-to-back 511 keV positron annihilation gamma rays emitted. Among the principal applications for this important diagnostic technique are imaging of blood flow, amino acid transport and brain tumours. The main positron emitting nuclei used as tracers are ^{11}C, ^{13}N, ^{15}O and ^{18}F, with the latter being the most widely used positron source. These sources are usually produced using energetic proton beams produced by cyclotrons or van de Graaff accelerators via (p,n) and (p,α) reactions. The reactions used, the thresholds for these, the half-life of the product and the peak reaction cross sections are listed in Table 1. The reason that proton induced nuclear reactions are favoured is because the isotope produced has a different atomic number from the reactant, and hence these can be separated using fast chemistry. This makes it possible to produce carrier free sources allowing patients to be injected with the minimum of foreign material.

This report discusses the generation of energetic proton beams of up to 37 MeV via ultra-intense laser solid interactions. These beams are then used to produce the PET isotopes ^{11}C and ^{13}N. Activities of 200 kBq have been measured from a single laser pulse of 5x10^{19} Wcm^{-2} interacting with a thin aluminium target. Various methods of increasing the induced activity and the possibility of using lasers for commercial applications are discussed.

Experimental

The experiment used the ultra-intense beam line of the Vulcan Nd: Glass laser [7] incident on a thin aluminium or CH foil target, at 45° incidence with p-polarised light within an evacuated target chamber. This system delivered pulses of energies up to 120 J, duration 0.9-1.2 ps with a wavelength of 1.053 μm. When focused to a spot size of radius 6 μm onto target using a f/4 off-axis parabolic mirror, intensities up to 10^{20} Wcm^{-2} were achieved.

Nuclear reaction	Half-life	Q (MeV)	Peak cross-section (mb)	Radiation measured
^{11}B(p,n)^{11}C	20.34 mins	2.76	430	β^+ 99%
^{14}N(p,α)^{11}C	20.34 mins	2.92	250	β^+ 99%
^{16}O(p,α)^{13}N	9.96 mins	5.22	140	β^+ 100%
^{15}N(p,n)^{15}O	123 seconds	3.53	200	β^+ 100%
^{18}O(p,n)^{18}F	109.7 mins	2.44	700	β^+ 97%

Table 1. PET isotope production reaction data.

The Vulcan laser pulse has a pre-pulse associated with it, with intensity roughly 10^{-6} that of the main pulse, arriving between 300 ps and 1 ns before the main pulse. This is sufficient to ionise the target surface, generating a plasma that expands out in front of the target, which is known as "blow-off" plasma, consisting of electrons and ions. The type of ion depends on the target. The main pulse then interacts with this plasma, and causes electrons to be accelerated into the target and exit through the rear of the target. Protons, originating from hydrocarbon or water impurity layers on the target surfaces are then "dragged" by the fast electrons via charge separation. Proton beams are therefore obtained in front of the target in the "blow-off" direction, and behind the target, in the "straight through" direction. A schematic of the experimental arrangement is shown in Figure 1. The experiment was conducted within a target chamber which was evacuated to a modest vacuum of about 10^{-5} torr.

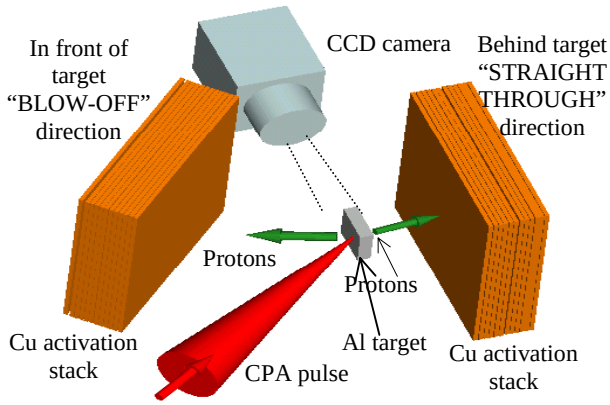

Figure 1. Schematic of the experimental arrangement.

Results and Discussion

To characterise the proton beam, and to produce radioisotopes, different activation samples were placed in the target chamber, behind the target, in the "straight through" direction at a distance 10 mm from the target, and in front of the target, directed along the target normal, at a distance 50 mm from the target, in the "blow-off" direction. The time taken to extract the samples from the target chamber after irradiation was a few minutes, as the chamber must be returned to atmospheric pressure before the samples could be removed. These samples were then transferred to a nuclear laboratory for analysis limiting the lifetimes of the activated samples that could be measured to a few minutes or more. These practicalities are a temporary inconvenience, and will be resolved in future experiments.

The energy spectrum of the accelerated protons were determined by placing activation stacks in both the "blow-off" and "straight through" directions. These consisted of 9 pieces of copper foil, 100 μm thick, plus a 1 mm piece.

Previous results from Clark *et al.* [8] show that the protons are emitted in the "straight through" direction in a cone half angle of 30°. The protons in the "blow-off" direction are emitted in a cone half angle of 20°. The copper activation stacks were positioned such that all of the protons were incident on the stacks and hence a spatially integrated measurement was made.

Copper undergoes the nuclear reaction $^{63}Cu(p,n)^{63}Zn$ when bombarded with protons of energies greater than 4.15 MeV. The resulting Zn isotope is radioactive, and decays via β^+ emission with a half life of 38.1 mins. Positrons slow down in solids, and annihilate at rest with free electrons, producing two photons of 511 keV, at 180° to each other. These annihilation photons were detected using two 3 inch x 3 inch NaI scintillation detectors, set up to detect 511 keV photons, and operated in coincidence. The efficiency of the coincidence system was measured using a calibrated ^{22}Na source, and hence the absolute activity, i.e. the number of (p,n) reactions induced in each copper piece in the stack, could be determined.

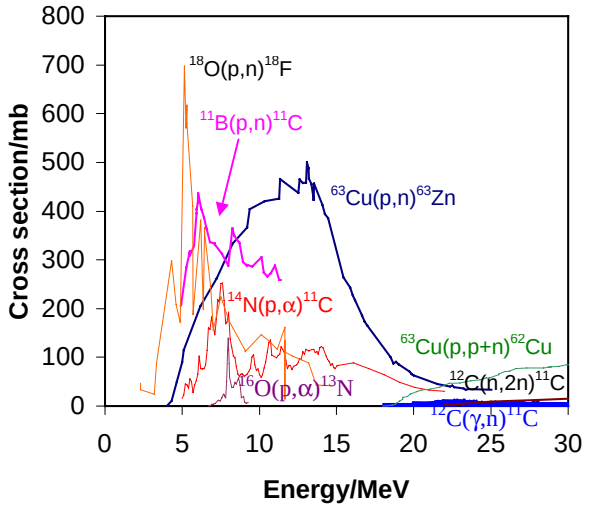

Figure 2. Cross sections for the reactions discussed.

Knowing the $^{63}Cu(p,n)^{63}Zn$ cross section, which is shown in Figure 2 [9], the number of protons incident on each piece of copper in the stack can be found, and hence a proton energy spectrum can be built up. Each piece of copper in the stack represents an energy "bin", because protons are slowed down in copper. Figure 3 shows typical energy spectra of the emitted protons from the front and rear of the target. It is clear that more energetic protons are observed in the "straight through" direction, having energies up to a diagnostic limit of 37 MeV. The proton beam in the blow-off direction has a maximum energy of 25 MeV. Fitting a non-relativistic Maxwellian or exp(-E/kT) distribution to the spectra where E is the proton energy and T is the proton temperature, the temperatures for the front and back proton beams are 1.4 and 2.9 MeV respectively. Care has to be taken when taking these activity measurements to account for contributions from competing reactions. The reaction $^{63}Cu(p,p+n)^{62}Cu$ takes place for proton energies above 10.9 MeV, but the isotope ^{62}Cu can be distinguished from ^{63}Zn as it has a much shorter half life of 9.8 mins. The cross section for this reaction is also much lower compared to the reaction $^{63}Cu(p,n)^{62}Cu$. The contribution from this reaction was accounted for when calculating the proton energy spectrum and found to have a negligible effect on the shape of the calculated spectrum.

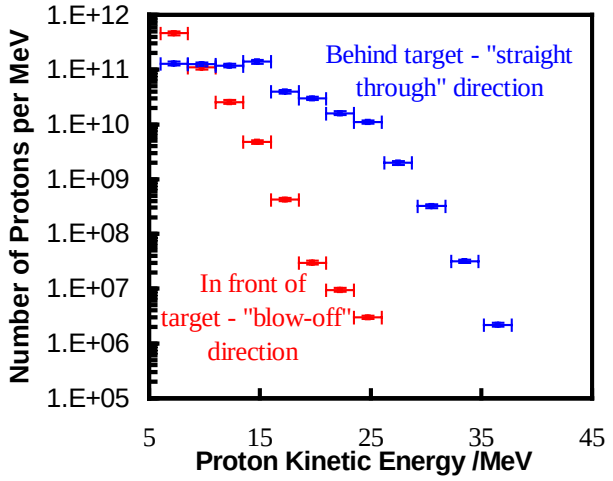

Figure 3. Proton spectra obtained from copper activation stacks in front of and behind the target.

It can be seen from the spectra shown in Figure 3 that around 8×10^{12} protons are produced in the "straight through" direction (and around 5×10^{12} in the blow-off). As stated previously, these protons are present as hydrocarbon or water impurity layers on the rear target surface. Preliminary static SIMS analysis have revealed a hydrocarbon layer of about 5 nm on the surfaces of the aluminium targets. A simple calculation assuming that the impurity layer consists of water molecules shows that to produce 10^{12} protons, the area involved must be greater than 55x55 μm, which is a factor of 10 greater than the laser focal spot region.

Different samples were placed in the target chamber and were bombarded with energetic protons from the intense laser-solid interaction. Samples were chosen to produce isotopes of relevance to the nuclear medicine community.

First, a boron sample of circular geometry with diameter 50 mm and 3 mm thick was placed in front of the target, in the "blow-off" direction, prior to the laser irradiation. The induced activity in the boron sample was then measured in the coincidence unit following the laser interaction. From the decay curve obtained (Figure 4) it is clear from the measured half-life of 20.3±0.4 mins that the isotope produced was ^{11}C (accepted value 20.34 mins) which is used in medical imaging for Positron Emission Tomography, or PET. The ^{11}B nuclei undergo (p,n) reactions to form ^{11}C, and the cross section for this reaction is shown in Figure 2. By extrapolating the curve, it can be seen that the activity at the time of laser irradiation was 200 kBq.

A sample of silicon nitride (SiN_4) of dimensions 20x20 mm and thickness 1.75 mm was placed in front of the target. The silicon nuclei, when bombarded with protons in the present energy range, produce isotopes with lifetimes of a few seconds, and a small amount of the 2.5 min ^{30}P isotope. Hence because of the

finite transfer time they could not be detected in our current arrangement, and can therefore be neglected.

The activity of the silicon nitride sample as a function of time was measured following laser irradiation, and is shown in Figure 4. As with the boron activation, the isotope ^{11}C was produced, but this time via the reaction $^{14}N(p,\alpha)^{11}C$. The activity at time zero (laser irradiation) was two orders of magnitude lower than the boron activation, at 2 kBq, but this is not surprising, since the cross section for this reaction is much lower (Figure 2).

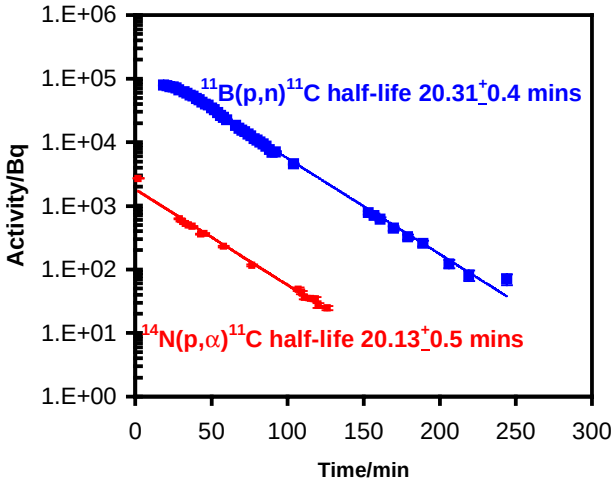

Figure 4. Decay curves for the activated boron and silicon nitride samples, showing that the isotope ^{11}C was produced via the reactions $^{11}B(p,n)^{11}C$ and $^{14}N(p,\alpha)^{11}C$.

Conclusions

It has been shown that protons of energies up to 37 MeV can be generated when an ultra-intense laser interacts with solid targets. These energetic protons can then be used to induce (p,n) and (p,α) reactions in various materials, to produce radioisotopes that are used in nuclear medicine, specifically Positron Emission Tomography (PET). Activities of $2x10^5$ Bq of the isotope ^{11}C have been measured.

Although ^{11}C is a useful isotope for PET, the favoured isotope at the moment is ^{18}F. The reaction usually employed to produce this isotope is $^{18}O(p,n)^{18}F$. The cross section for this reaction is shown against the $^{11}B(p,n)^{11}C$ reaction in Figure 2. The integrated cross section for the ^{18}F producing reaction is about half that of the ^{11}C reaction, hence it is feasible that the Vulcan laser could produce 10^5 Bq of ^{18}F per shot, operating at 10^{20} Wcm^{-2}.

A typical patient dose for PET is 5 mCi ($1.85x10^8$ Bq) although up to 20 mCi ($7.4x10^8$ Bq) sources are necessary so that fast chemistry can be performed to separate the tracer from the inactive carrier. Assuming that a Vulcan type laser could deliver 10 Hz, then the integrated activity after 500 seconds is about 10^9 Bq, or 27 mCi. If this source was generated by a 1 J pulse typical of table-top lasers then a kHz repetition rate would be required. Further improvement in the production rate will be achieved by optimising the laser pre-pulse, and as stated previously, the target material and surface treatment. Also, it has been shown that the proton spectrum from the back of the target is more energetic, which could also lead to higher activities since the cross-sections for the relevant reactions extend to this current limit of 37 MeV. Yamigiwa and Koga [10] have estimated that ^{18}F yields as high as 10^{14} Bq ($2.7x10^3$ Ci), two orders of magnitude higher than standard cyclotrons can be generated if the laser intensity were increased to 10^{21} Wcm^{-2}.

At present a smaller scale laser operating at 1kHz and 0.2 J per pulse is proposed[11] which would approach the required irradiance on target to provide sufficiently intense ^{18}F sources. The proposed design contains a Nd: YLF laser system (100 ps mode-locked oscillator and several diode-pumped amplifiers) operating at a wavelength of 1.047 µm and generating 1 J pulses at 1 kHz repetition rate using a total peak pump power of 100 kW (quasi-cw). The output of this laser is used to pump an optical parametric chirped pulse amplifier (OPCPA) which amplifies chirped pulses at a wavelength of 2 µm up to an energy of 0.3 J. These pulses are compressed to 30 fs and focused to a sub-10 µm spot size to generate intensities in excess of 10^{19} Wcm^{-2}. Although this laser is based on current technology and the basis of the proton generation process has been established, the complete system will operate in a regime at the forefront of laser physics and technology. A full study of such a system described here is the basis of a new research proposal[11].

Finally, it has been shown that beams of cyclotron produced energetic protons can be used to treat tumours, with greater efficiency than conventional X-radiotherapy, because protons have more suitable dE/dx curves than gamma-rays. Protons with their characteristic "Bragg Peak"[12] deposit almost all of their energy just before coming to rest in materials . This means that proton beam energies can be tuned to efficiently treat tumours, once the position of the tumour is determined by techniques such as PET. The energy required for proton oncology is typically 150 MeV. The irradiance required to generate protons of energies of 150 MeV required for proton oncology is 5×10^{21} $Wcm^{-2}\mu m^2$ [13]. There have been a number of numerical simulations that confirm that protons with energies of 150 MeV or larger are generated with these intensities on target. These intensities, however, require energies on target of 100 J in 30 fs in a 10 µm diameter focal spot with lasers operating at 1 µm wavelength. These parameters are extreme but one possible development of an oncology laser might be based on an upgrade of the PET laser described earlier. This laser will operate at 2 µm rather than 1 µm, and consequently the energy required to reach an irradiance of 5×10^{21} $Wcm^{-2}\mu m^2$ is reduced to 25 J per pulse. This is a significant saving on the energy requirement compared with the Ti-S laser, but is still two orders of magnitude larger than the 0.2 J level of the PET laser.

In summary, it has been shown that high-intensity lasers can be used to produce short-lived positron-emitting nuclei, and the commercial applications of this new science are well within reach in the next few years.

References

1. P. A. Norreys *et al.*, Phys. Plasmas. 6, 2150 (1999).
2. T. W. Phillips *et al.*, Rev. Sci. Inst. 70, 1213 (1999).
3. K. W. D. Ledingham and P. A. Norreys, Contemp. Phys 40, 367 (1999).
4. K. W. D. Ledingham *et al.*, Phys. Rev. Lett. 84, 899 (2000).
5. T. E. Cowan *et al.*, Phys. Rev. Lett. 84, 903 (2000).
6. R. Nutt, Mol. Imag. Biol. 4, 11 (2001).
7. C. Danson *et al.*, J. Mod. Opt. 45, 1653 (1998).
8. E. L. Clark *et al.*, Phys. Rev. Lett. 84, 670 (2000).
9. EXFOR www nuclear reaction database, http://iaeand.iaea.or.at/exfor/
10. M. Yamigiwa and J. Koga, J. Phys. D. 32, 2526 (1999).
11. N. Ross, to be published.
12. Indiana University Cyclotron Facility Website, http://www.Iucf.indiana.edu/MPRI/about.htm
13. E. L. Clark *et al.*, Phys. Rev. Lett. 85, 1654 (2000).

A Nearly Real Time Electron Temperature Diagnostic using Isotope Production in Tantalum

I Spencer, K W D Ledingham*, P McKenna, R P Singhal, T McCanny

Department of Physics and Astronomy, University of Glasgow, Glasgow G12 8QQ, UK
**also at AWE plc, Aldermaston, Reading RG7 4PR, UK*

K Krushelnick, F N Beg, M Tatarakis, A E Dangor

Blackett Laboratory, Imperial College, Prince Consort Road, London SW7 2BZ, UK

M Zepf

Queen's University Belfast, University Road, Belfast BT7 1NN, UK

E L Clark, R D Edwards, M A Sinclair

AWE plc, Aldermaston, Reading RG7 4PR, UK

P A Norreys, R J Clarke, R M Allott

Central Laser Facility, CLRC Rutherford Appleton Laboratory, Chilton, Didcot, Oxon OX11 0QX, UK

Main contact email address: *i.spencer@physics.gla.ac.uk*

Introduction

For the last four years, ultra-intense lasers have been used to generate photo-nuclear reactions [1-5]. This has been made possible since electrons can be accelerated to energies as high as 100 MeV when a laser of intensity 10^{20} Wcm^{-2} interacts with matter. These relativistic electrons can be converted to γ-rays via bremsstrahlung in a thick, high Z radiator, and these high-energy photons are then capable of producing photo-nuclear reactions, typically (γ,mn) (m=1,2,3…) and (γ,fission) reactions.

An important application of this new technology is the use of nuclear reactions to diagnose fundamental parameters of the laser-plasma interaction. This report describes a method of measuring the temperature of the fast electrons produced in ultra-intense laser-plasma interactions using a single tantalum target, by utilising (γ,n) and (γ,3n) reactions in tantalum and measuring the radiation emitted by the products of these reactions via γ-ray spectroscopy. The technique can yield results on large laser systems on a shot-to-shot basis, and it is possible to carry out this process while other experiments are being conducted. This technique has been applied at a preliminary level[6] in the characterisation of a self-modulated laser wakefield accelerator, i.e. in under-dense laser-plasma interactions. The technique is described in greater detail herein.

Experimental

The experiment employed the ultra-intense beam-line of the Vulcan Nd: Glass laser system[7] at the Rutherford Appleton Laboratory, UK, operating in the Chirped Pulse Amplification (CPA)[8,9] mode. The beam was incident on a tantalum target, of dimensions 10×10 mm and 1.75 mm thick, and at an angle of 45°. The light was p-polarised, and the target was maintained in a vacuum of ~10^{-4} Torr. When operated in this manner, the laser delivered pulses of energy up to 120 J and 1 ps duration, and provided intensities up to 10^{20} Wcm^{-2}. A more detailed description of the experimental set-up and the principal diagnostics involved can be found in[1]. The main-pulse/pre-pulse contrast ratio was measured by a third-order autocorrelator and found to be 1 : 10^{-6}.

Once the tantalum was irradiated with the Vulcan pulse, the target chamber was restored to atmospheric pressure and the tantalum target was extracted. The time taken to restore the chamber to atmospheric pressure was a few minutes, after which the sample was transferred to a nuclear laboratory for analysis. This limited the measurable lifetimes of the unstable isotopes produced to a few minutes or more. The γ-radiation emitted from the tantalum target was measured in an intrinsic germanium detector. The efficiency of the detector was calibrated as a function of energy using sources of known energy and activity (^{57}Co, ^{22}Na, ^{137}Cs, ^{60}Co and ^{152}Eu). This made it possible to measure the energy and activity of any γ-rays incident on the detector.

Results and Discussion

The tantalum target was composed of 100 % ^{181}Ta, the stable tantalum isotope. The two reactions of interest are ^{181}Ta(γ,n)^{180}Ta and ^{181}Ta(γ,3n)^{178m}Ta. ^{180}Ta decays via electron capture with a half-life of 8.1 hours to an excited state of ^{180}Hf, which then achieves stability via the emission of a γ-ray of 93 keV. Hf X-rays are also emitted in the decay (K_α=55.7 keV, K_β=63.2 keV). The competing decay to EC is β^-, again with a characteristic half-life of 8.1 hours. This produces an excited state of ^{180}W, which achieves stability via the emission of a γ-ray of 103 keV plus Hf X-rays[10,11].

^{178m}Ta decays via EC with a characteristic half-life of 2.36 hours to excited states of ^{178}Hf which then achieves stability via the emission of a number of γ-rays of various energies, plus Hf X-rays. The relevant portions of the decay schemes for ^{180}Ta and ^{178m}Ta are shown in Figure 1. The cross sections for these reactions are shown in Figure 2 [12].

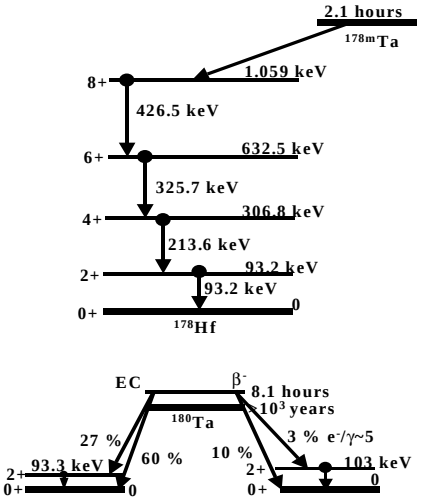

Figure 1. Relevant decay schemes for ^{180}Ta and ^{178m}Ta.

The product of the reaction ^{181}Ta(γ,2n)^{179}Ta (Q=-14.2 MeV) has a half-life of 600 days, which is too long for the type of analysis undertaken in this study, and the principal radiation is Hf X-rays, making it impossible to distinguish from other (γ,mn) reactions. This was why the reaction was not studied in detail in the present case, although the cross section for this

reaction is shown in Figure 2 for comparison with the (γ,n) and (γ,3n) processes.

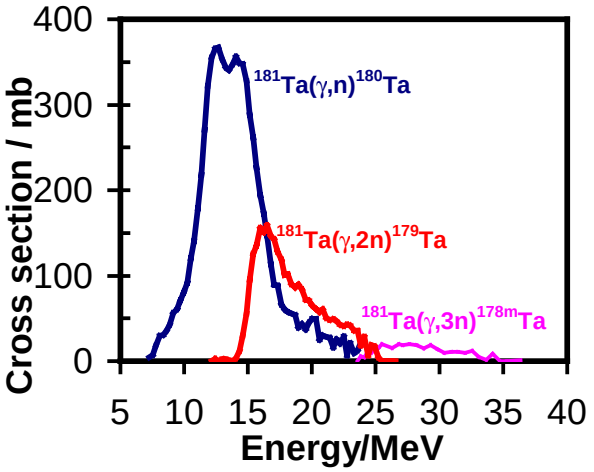

Figure 2. Cross sections for the reactions studied.

The tantalum sample was analyzed using the germanium detector described above which was shielded in lead and coupled to a multi-channel analyzer (MCA). The sample was measured for 1 hour. It is also important to measure the contribution from any background radiation. The background spectrum was taken over a period of 12 hours to improve the counting statistics, then the overall counting rate was divided by 12 to show its strength relative to the tantalum signal. Figure 3 shows a typical spectrum obtained in the region 0-500 keV with the background contribution overlapped. Many lines are observed, most notably the 93.6 keV peak (accepted value 93.3 keV) which is emitted by both ^{180}Ta and ^{178m}Ta, and the 103.3 keV peak which is emitted solely by ^{180}Ta.

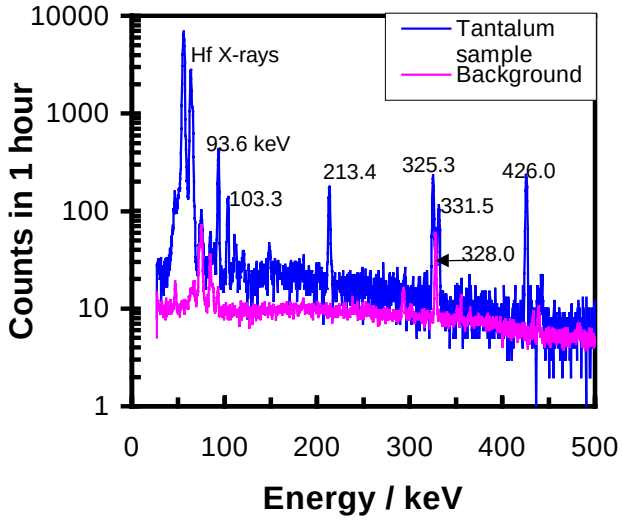

Figure 3. Tantalum spectrum in the region 0-500 keV.

A strong case for the presence of ^{178m}Ta can be made by examining an interesting feature of the decay scheme for this isotope [10,11]. There is a cascade of transitions from the 8+ level of ^{178}Hf to 6+, 4+, 2+, then to the ground state via the emission of γ-rays of energies 426.5, 325.7, 213.6 and 93.2 keV. The intensities of these peaks are all equal, and these peaks are evident in Figure 3 (experimentally measured values 426.0, 325.3, 213.4 and 93.6 keV). This gives an automatic efficiency calibration for the detector, in addition to the measurement made using calibration sources. These lines are also a unique fingerprint and evidence of the presence of ^{178m}Ta. Even though the 93.6 keV peak has a contribution from ^{180}Ta, the observation of the other three lines provides proof of the presence of ^{178m}Ta, meaning that γ-rays of energy greater than 22 MeV - the energy threshold for the reaction ^{181}Ta(γ,3n)^{178m}Ta - were produced in the laser-plasma interaction.

The 328 keV peak is a background peak, and its source has been identified as ^{207}Bi. In future experiments, this peak will be eliminated by improved shielding of the germanium detector. The peaks at 111.0, 121.0 and 148.4 keV are as yet unidentified, but since this study requires signals from ^{180}Ta and ^{178m}Ta alone, they do not cause any ambiguity.

As well as measuring the energies of the γ-rays emitted from the tantalum sample, another method for isotope identification is to measure the decay of the sample. Since radioisotopes all have characteristic half-lives, a positive measurement coupled with the energy measurements increases the reliability of the identification.

To measure the decay of the γ-ray activity of the sample, four measurements lasting one hour were taken. The areas of the peaks were then measured as a function of time. The most useful peaks are at 103 keV (^{180}Ta) and 426 keV (^{178m}Ta) since these are unique to the two isotopes in question, and occur in areas of the spectrum which are uncontaminated from background contributions. Figure 4 shows the areas of these peaks as a function of time, where t=0 is the time of laser irradiation. From this decay data, the half-lives of the peaks were established. The 103 keV peak half-life was found to be 7.4±0.3 hours. The accepted value for ^{180}Ta is 8.1 hours. The decay was only measured over one half-life. To yield more accurate results the decay should have been monitored for longer, but this was not possible due to experimental constraints. A more detailed measurement will be carried out in future studies. The half-life measurement obtained however, coupled with the energy measurement of the peak is more than adequate to identify the source of this radiation as ^{180}Ta, produced via the reaction ^{181}Ta(γ,n)^{180}Ta. The half-life of the 426 keV peak was found to be 2.2±0.2 hours (accepted value for ^{178m}Ta=2.36 hours). This provides unambiguous evidence that the source of this peak is ^{178m}Ta, produced via the reaction ^{181}Ta(γ,3n)^{178m}Ta. The result obtained is closer to the accepted value than for the ^{180}Ta peak because the decay was monitored for almost ten half-lives, as opposed to just one for the previous measurement.

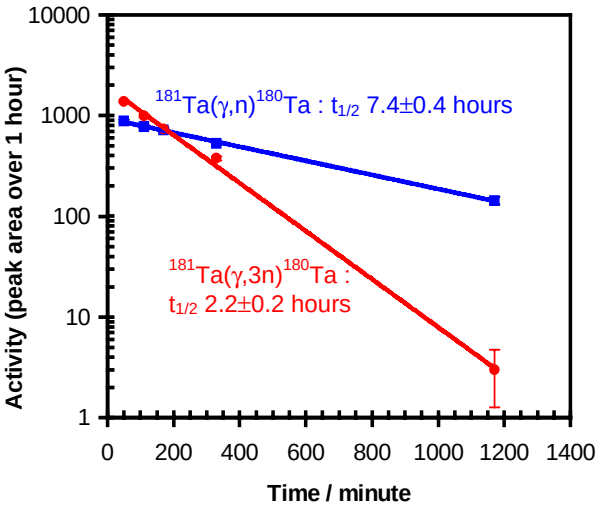

Figure 4. Decay plots of the two peaks in question. Half-life measurements confirm the presence of ^{180}Ta and ^{178m}Ta.

The long analysis time described is only to ascertain the procedure, whereas once established, temperature measurements can be made in a few minutes and certainly before the next pulse in large laser systems.

Now that the presence of ^{180}Ta and ^{178m}Ta was established, the activity ratio of these isotopes was measured. This was done by measuring the areas of the peaks in question and taking into account their relative intensities which are 0.78 % for the 103 keV peak and 97 % for the 427 keV peak[10,11]. In addition, the efficiency of the detector had to be included in the calculation, since this varied with incident energy.

Another important factor to take into consideration is the absorption of γ-rays in the tantalum target. The mass attenuation coefficient varies with γ-ray energy[13], and the fraction of γ-rays absorbed was calculated for the relevant energies. The importance of making this correction was made obvious by looking at the 426 and 213.4 keV peaks. According to the decay scheme of ^{178m}Ta, these should be almost equal in intensity. After taking account of the detector efficiency, it was found that the area of the 426 keV peak was greater than that of the 213.4 keV peak by a factor 1.7. After correcting for absorption effects, the peak areas were found to differ by a factor of 1.1. Correcting for the 426 and 103 keV peaks in addition to branching ratios and the detector efficiency gave an experimentally measured ^{178m}Ta/^{180}Ta activity ratio of $(1.78\pm0.44)\times10^{-3}$. This measurement was then fitted to the theoretical activity ratio calculated as a function of kT.

The theoretical ^{178m}Ta/^{180}Ta activity ratio was calculated in the following way: the relativistic Maxwellian electron energy distribution in η dimensions is given by

$$N(E) \propto \gamma(\gamma^2-1)^{\frac{\eta}{2}-1} e^{-\left(\frac{E}{kT}\right)} \qquad (1)$$

where N(E) is the number of electrons of energy E, $\gamma = 1 + E/mc^2$, k is Boltzmann's constant and T is the electron temperature. In the ultra-relativistic limit and three-dimensional space, this tends to the form [1,4,14]

$$N(E) = N_0 E^2 e^{-\left(\frac{E}{kT}\right)} \qquad (2)$$

where N_0 is a constant. Figure 5 shows this distribution for E=0 to 50 MeV, kT=2.3 MeV and N_0=1.

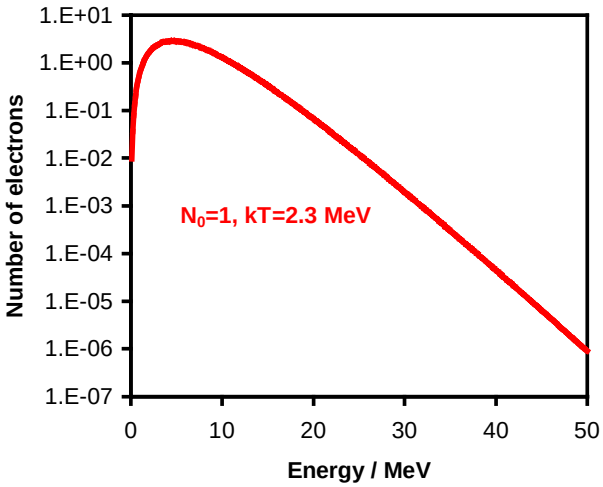

Figure 5. The shape of the relativistic electron energy distribution for N_0=1, kT=2.3 MeV.

Electrons of energy E MeV produce a γ-ray spectrum in tantalum via bremsstrahlung. This spectrum was calculated using an analytical representation for bremsstrahlung spectra developed by D J S Findlay[15].

Figure 6 shows the calculated bremsstrahlung yield for photons produced along the electron propagation (and hence the laser) direction by electrons of energy 10 and 25 MeV.

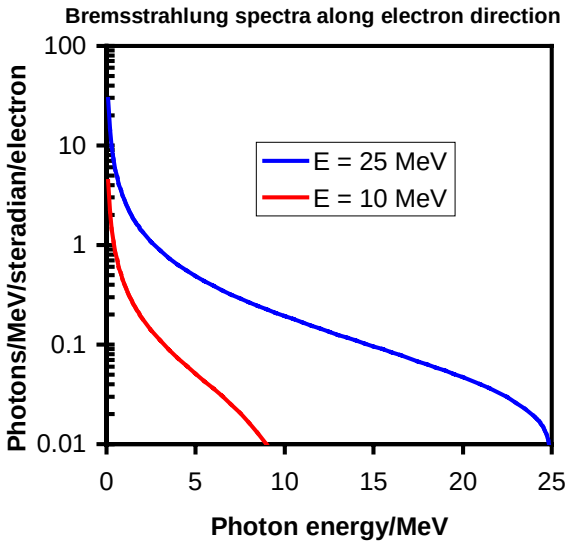

Figure 6. Bremsstrahlung spectra along relativistic electron beam direction for electrons of energy 10 MeV and 25 MeV.

The induced activity of a sample when bombarded with high-energy photons may be obtained from

$$A = \left(\frac{\ln(2)}{t_{1/2}}\right)\sum_{E_\gamma} N(E_\gamma)\sigma_\gamma(E_\gamma)N \qquad (3)$$

where $t_{1/2}$ is the half-life of the radioisotope, $N_\gamma(E_\gamma)$ is the number of photons in the energy bin of width 0.5 MeV at energy E_γ, $\sigma_\gamma(E_\gamma)$ is the photo-nuclear reaction cross section at energy E_γ and N is the number of nuclei present / cc. The results are shown in Figure 7.

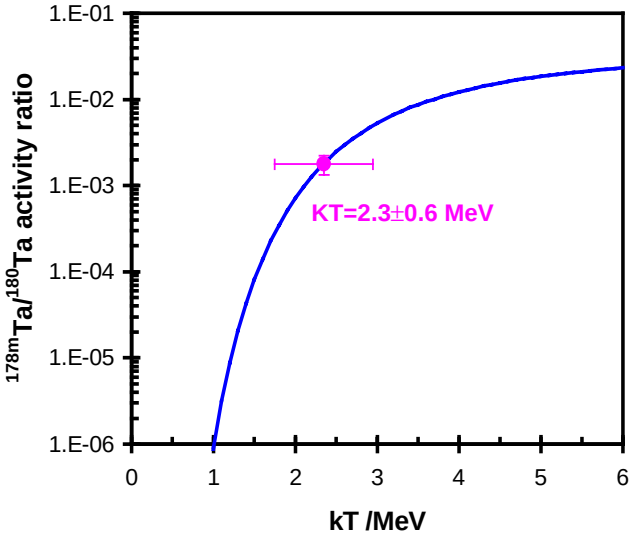

Figure 7. (Blue line) theoretical ^{178m}Ta/^{180}Ta activity ratio as a function of kT. The experimentally measured ratio (pink point) corresponds to the kT value of 2.3±0.6 MeV.

The experimentally measured activity ratio of $(1.78\pm0.44)\times10^{-3}$ corresponds to kT=2.3±0.6 MeV on this plot. The intensity on target was ~10^{20} Wcm^{-2}. This measurement is in agreement with measurement made using the Cu/C technique[4] at a slightly lower intensity. This is in reasonable agreement with the electron spectrum reported by Cowan *et al* [5] – a rough analysis of this spectrum shows that the temperature is ~3.5 MeV for an intensity greater than 10^{20} Wcm^{-2}. Measurements of proton beam temperatures[16] give kT=5-6 MeV. The measurement is

in good agreement with the **j×B** ponderomotive model described by Wilks *et al* [17] and confirmed experimentally by Malka and Miquel[18], where, for p-polarization and oblique incidence, kT is of the order $0.511(\sqrt{\{1+I\lambda^2/1.37\times10^{18}/2\}}-1)$ MeV. For $I\lambda^2=10^{20}$ $Wcm^{-2}\mu m^2$, kT is calculated to be 2.6 MeV. Measurements made by Santala *et al.*[6] using a similar technique at a preliminary level gave a kT value of 4.4 MeV at similar intensities, although this experiment involved a laser-gas interaction which is known to give higher electron temperatures than laser-solid interactions[19]. If the data were not corrected for absorption effects, the kT value measured would be of the order 5 MeV, which, for a laser-solid interaction at intensities up to 10^{20} Wcm^{-2} would be higher than expected and observed in other measurements. Therefore, the measurement made appears to be reasonable.

Conclusions

It has been shown that higher-order photo-nuclear reactions can be used to measure the electron temperature when an ultra-intense laser pulse interacts with a solid tantalum target. Analysis of the specific peaks described is recommended since they are unambiguous for the isotopes ^{180}Ta and ^{178m}Ta. For higher laser intensities and hence higher electron and photon energies, this technique should still be applicable since one simply looks for evidence of higher order reactions using the same spectroscopic technique and choosing thoughtfully the reactions that will yield unambiguous peaks. In particular, ^{181}Ta(γ,4n)^{177}Ta (Q=29.0 MeV) and ^{181}Ta(γ,5n)^{176}Ta (Q=37.3 MeV) look like very useful reactions for this technique. ^{177}Ta has a half life of 2.36 days, and unambiguous γ-ray lines at 113.0 and 208.4 keV. ^{176}Ta has a half-life of 8.08 hours, and a cascade of transitions with the highest energy 1115.9 keV, then many others of lower energy with the same intensity, yielding a unique fingerprint similar in nature to that of ^{178m}Ta shown above, but with different γ-ray lines. This technique can provide temperature measurements on a shot-to-shot basis, even while other experiments (e.g. angular distribution measurements) are being conducted. The technique is also applicable for gas target interactions if the tantalum sample is placed in the path of the fast electron beam. Other activation samples may also prove useful, and a full study involving higher order reactions in other high Z materials is planned for the future in order to find the most suitable material for the electron spectra obtained at various laser intensities.

References

1. P. A. Norreys *et al.*, Phys. Plasmas. 6**,** 2150 (1999).
2. T. W. Phillips *et al.*, Rev. Sci. Inst. 70**,** 1213 (1999).
3. K. W. D. Ledingham and P. A. Norreys, Contemp. Phys 40**,** 367 (1999).
4. K. W. D. Ledingham *et al.*, Phys. Rev. Lett. 84**,** 899 (2000).
5. T. E. Cowan *et al.*, Phys. Rev. Lett. 84**,** 903 (2000).
6. M. I. K. Santala *et al.*, Phys. Rev. Lett. 86**,** 1227 (2001).
7. C. Danson *et al.*, J. Mod. Opt. 45**,** 1653 (1998).
8. M. D. Perry and G. Mourou, Science 264**,** 917 (1994).
9. D. Strickland and G. Mourou, Opt. Comm. 56**,** 219 (1985).
10. R. B. Firestone, V. S. Shirley, and C. M. Chu, Table of Isotopes 8th Edition 1998 update, (Wiley, New York, 1998).
11. J. Magill, Nuclides 2000 (2000)
12. IAEA, EXFOR www nuclear reaction database, http://iaeand.iaea.or.at/exfor/ (2000)
13. J. H. Hubbell and S. M. Seltzer, NIST X-ray mass attenuation coefficients, http://aeldata.phy.nist.gov/PhysRefData/XrayMassCoef/cover.html (2002)
14. J. R. Davies, Phys. Rev E 65**,** 026407 (2002).
15. D. J. S. Findlay, Nucl. Inst. Meth. A276**,** 598 (1989).
16. M. Roth *et al.*, Phys. Rev. Lett. 86**,** 436 (2001).
17. S. C. Wilks *et al.*, Phys. Rev. Lett. 69**,** 1383 (1992).
18. G. Malka and J. L. Miquel, Phys. Rev. Lett. 77**,** 75 (1996).
19. D. Umstadter, Phys. Plasmas. 8**,** 1774 (2001).

Imaging of thin solid objects with a laser produced proton beam via multiple scattering

L Romagnani, M Borghesi

Department of Pure and Applied Physics, The Queen's University, Belfast

O Willi

Institut für Laser-und-Plasmaphysic,Heinrich-Heine-Universität, Düsseldorf, Germany

D H Campbell, A Schiavi

The Blackett Laboratory, Imperial College of Science, Technology and Medicine, London

Main contact email address: *l.romagnani@qub.ac.uk*

Introduction

The idea of using proton beams for radiography purposes has circulated for several years[1,2]. Conventional accelerators have been employed as suitable sources of protons for these applications. Charged particle optics was used to obtain parallel beams and only radiographs of macroscopic objects could be realized. Basically three different proton radiography techniques have been developed in the past. The first and most obvious one is based on the stopping of protons when they encounter an obstacle thicker than their stopping range. A second method is based on the energy loss of protons when they cross an object thinner than their stopping range but still thick enough to absorb a detectable fraction of their energy. Finally a third method is possible that is based on multiple small angle scattering due to Coulomb collisions in the obstacle. Since this method doesn't require stopping or energy loss of the protons, it is clearly suitable for radiography of very thin objects.

We present here a possible application of laser produced proton beams to imaging of thin solid objects via multiple small angle scattering. The term imaging rather than radiography applies since the intrinsic magnification properties of the diverging laser produced proton beams play an important role [3-5].

We then present a quantitative interpretation of the experimental results based on Monte Carlo simulations of the propagation of protons in matter. Numerical simulations have been performed using the SRIM simulation code [6,7]. We have developed PV Wave routines to elaborate the results from simulations.

Finally proton imaging technique is briefly compared with previous experiments on proton radiography with conventional accelerators.

Experimental set-up

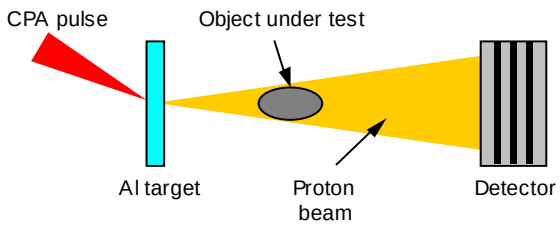

Figure 1. Experimental set-up for proton imaging.

The Vulcan Nd:glass laser operating in the Chirped Pulse Amplification mode (CPA) has been used in the experiment. This laser provides pulses at 1.054 µm in wavelength, 1ps in duration and with energies up to 100 J. To generate the proton beam [3-5] the laser beam is focused in the centre of a thin metallic target by an F/3.5 off-axis parabola. In order to avoid undesired reflections back to the laser cavity an incident angle of 15° with the target normal is chosen. The focal spot is between 8 and 10 µm in diameter at full width at half maximum, containing 30-40% of the total energy and giving intensities up to 5-7 x 10^{19} W/cm^2. The targets mainly used to generate the proton beam were 1-2 mm wide and 3-25 µm thick Al foils. Even if the targets nominally do not contain hydrogen, hydrocarbon contaminants that are always present on the target surfaces ensure a suitable source of protons. The detector used to reveal the proton beam is typically placed at 20-22 mm from the main target. The object under test, i.e. the object to be imaged, is usually placed 1-2 mm after the proton source. This leads to a geometrical magnification between 10 and 22. A picture of a typical experimental set-up is shown in Figure 1.

The detector used to reveal the proton beams consists of a stack of several layers of radiochromic films (RCF)[3-5]. Each RCF contains one or more layers of active gel, sensitive to ionizing radiation, sandwiched between polyester foils and eventually kept together by thin adhesive substrates. The RCF, transparent before irradiation, develops a blue color upon exposure to ionizing radiation. The change in the optical density can be measured with transmission densitometers, film scanners or spectrophotometers.

Experimental results

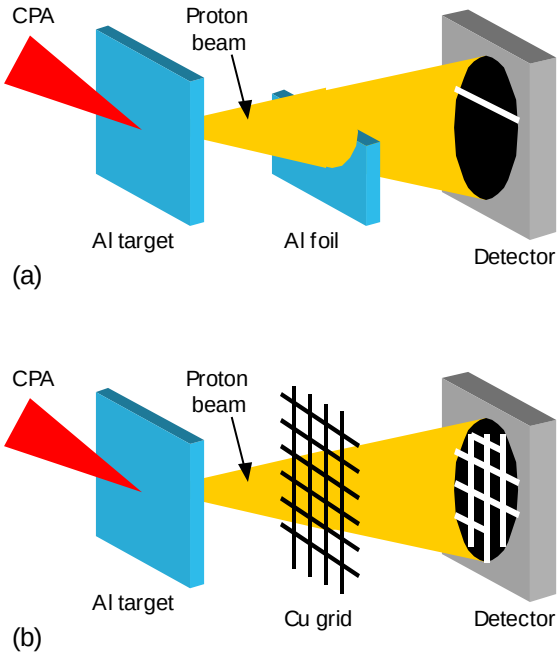

Figure 2. Experimental set-up for proton imaging of an Al foil (a) and of a Cu grid (b).

Imaging of several objects of different material, thickness and shape has been realized. In Figure 2 (a) the experimental set-up for the imaging of a 25 µm Al foil is shown. The foil was perpendicular to the proton beam propagation axis covering about 3/4 of the proton beam cross section. The distance between the proton source and the foil was 2 mm while the

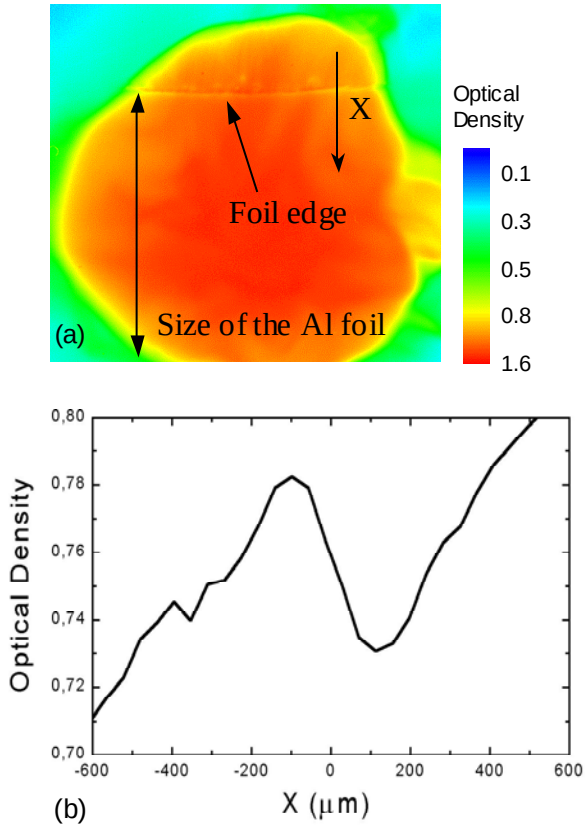

Figure 3. (a) Image of the Al foil obtained with 20 Mev protons. (b) Correspondent optical density variation across the beam cross-section.

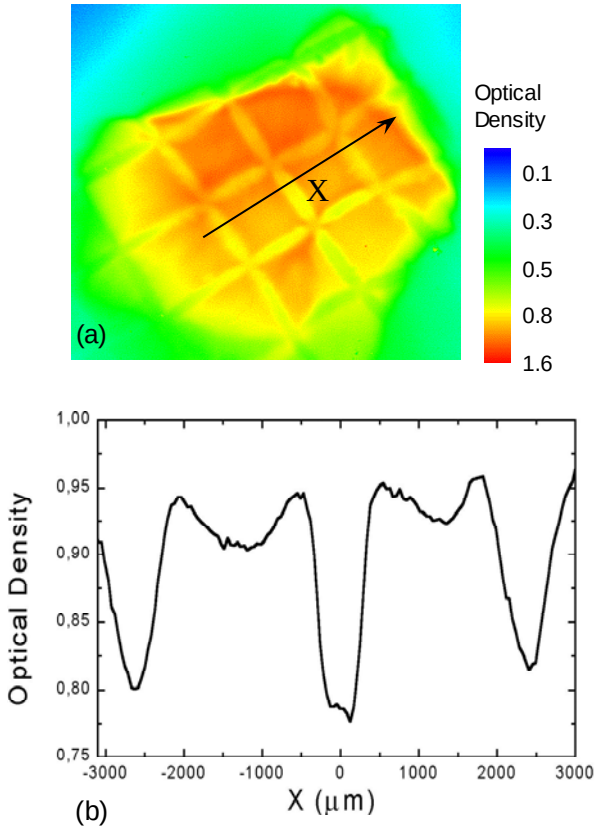

Figure 4. (a) Image of the Cu grid obtained with 20 Mev protons and (b) correspondent optical density variation across the beam cross-section. The whole shape of the grid can be distinguished in the image and deep minima can be observed in the optical density variation.

detector was positioned at 22 mm from the source. In Figure 3 (a) the image of the Al foil on the detector obtained with 20 Mev protons is reported. In Figure 3 (b) the corresponding optical density variation across the beam cross-section is shown. Only the edge of the Al foil produces a perturbation in the proton beam cross section. Far away from the edge the proton beam is not perturbed by the presence of the Al foil. This is expected since the stopping range of 20 MeV protons in Al is about 2.1 mm, i.e. far more than the foil thickness. The origin of the beam perturbation in correspondence with the foil edge will be explained later.

In Figure 2 (b) the experimental set-up for the imaging of a Cu mesh is shown. The mesh was formed by 25 μm wires with 100 μm spacing and was placed 1 mm after the proton source. The detector was at 22 mm from the source giving a geometrical magnification of 22. In Figure 4 (a) the image of the grid on the detector obtained with 20 Mev protons is reported. In Figure 4 (b) the corresponding optical density variation across the beam cross-section is shown. In this case a complete image of the mesh can be distinguished. This cannot be due to the stopping of the protons when crossing the mesh wires. In fact the stopping range of 20 MeV protons in Cu is about 800 μm, i.e. far larger than the thickness of the mesh wires. The image cannot be due to the energy loss of protons when crossing the wires either. In fact the energy loss of 20 MeV protons after a path of 25 μm in Cu is just $\Delta E/E \approx 10^{-2}$. Taking into account the detector response this would lead to a variation in the optical density of ~ 10^{-4}, the observed variation being ~ 0.2.

Data interpretation and modeling

In previous publications[3-4], the shadow of the mesh in the proton beam cross section was tentatively attributed to electrical charge-up, possibly due to precursor electrons. In reality such an effect does not seem to be required to explain the observations, as scattering alone can produce patterns that are qualitatively similar to the ones observed experimentally.

A possible interpretation of the experimental data is as follows. Because of multiple small angle scattering by the ions inside the object under test, protons that propagate through the object suffer a larger lateral spread compared to protons that propagate in vacuum. At the edges of the object the difference in the lateral spreads produces a perturbation in the beam intensity profile. Far away from the edges the beam is unperturbed, provided that the object is much thinner than the proton stopping range. If the transverse size of the object is larger than the perturbation width then the perturbations due to different edges do not superimpose and only the contour of the object is visible in the image. This corresponds to the foil case, where actually only one edge intercepted the beam. If instead the transverse size of the object is smaller than the perturbations' width then the perturbations due to two adjacent edges can superimpose producing deep minima in the intensity profile. This corresponds to the mesh case, where the two edges of a single wire are only 25 μm far from each other. As a consequence the whole mesh structure can be recognized in the image while deep minima can be observed in the optical density variation across the beam cross section.

Numerical modeling of the experimental results has been carried out. The SRIM (Stopping Range of Ions in Matter) code[6,7] was used to simulate the propagation of protons in vacuum or through the object and to calculate their final distributions in the detector for a given angle of emission from the source. We developed numerical routines that superimpose the proton distributions corresponding to the different angles of emission so reconstructing portions of the beam cross-section.

Portions of the image of the object on the detector and the correspondent optical density variation can so be obtained. It should be pointed out that SRIM appears to underestimate somehow the lateral spread due to multiple scattering[8-10].

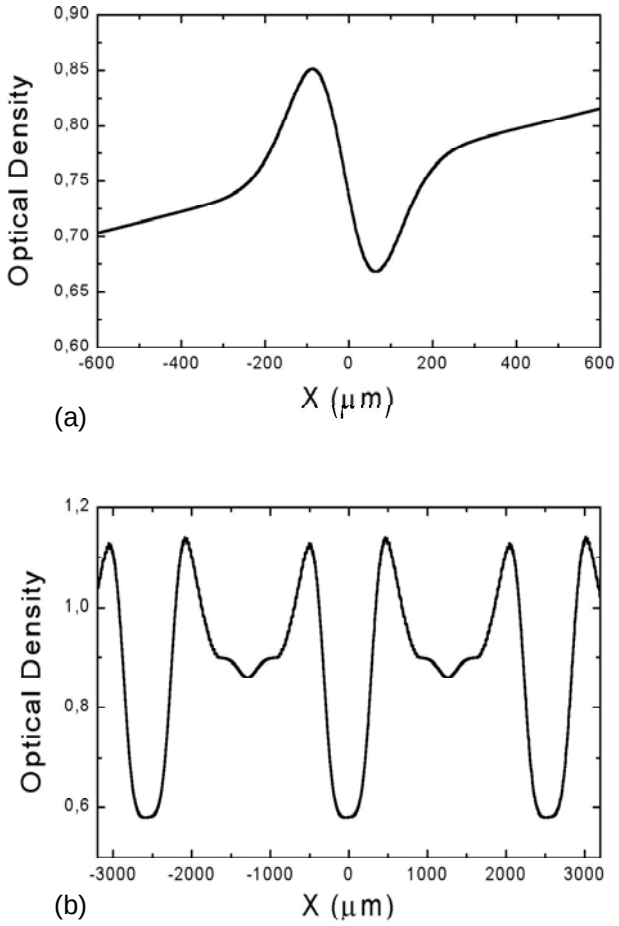

Figure 5. Calculated optical density variation across the beam cross-section for the foil case (a) and for the grid case (b).

As an example of results from numerical modeling in Figure 5 the optical density variations across the beam cross-section calculated for the Al foil (a) and for the Cu mesh (b) are shown. The graphs reproduce well the experimental data from a qualitative point of view, even if the contrast values are higher. The difference can be imputed mainly to the not perfect estimation of the lateral spread by SRIM and to some physical effects not included up to now in the numerical model, such as the finite size of the proton source and the broad proton spectrum. It is expected that, when included in the model, both these effects should contribute to keep down the contrast to values closer to the experimental values.

Comparison with previous experiments

Proton radiography using proton beams from conventional accelerators has been reported[1,2] where charged particle optics was used to obtain parallel beams. When using a parallel beam the distance between the object under test and the detector has to be chosen properly. In fact the width of the perturbation corresponding to a single edge of the object is proportional to $l\theta_s$, where l is the distance between the object and the detector and θ_s is the angular spread of protons that propagates through the object. If too large a distance l is chosen then perturbations originating from more than two edges can superimpose, so destroying the image of the object on the detector. Moreover only radiographs of macroscopic objects can be realized since the magnification of a parallel beam is 1.

By contrast using diverging beams the distance of the detector from the object is not a critical parameter because the beam divergence can compensate for the angular spread due to scattering. Moreover imaging of microscopic objects can be performed thanks to the intrinsic magnification properties of the beam. The combination of the beam divergence with the possibility of placing the detector far away from the object leads to a large freedom in the values of the magnification that can be reached. In the experiment magnification between 10 and 22 have been used, but higher magnification values can be easily reached. Laser produced proton beams are particularly suitable for proton imaging since they are divergent and apparently originating from a point source less than 10 μm in diameter.

Conclusion

It has been shown that proton imaging via multiple scattering is a sensitive technique for imaging of very thin solid objects. Overall it appears to be a promising and sensitive technique for the detection of density perturbations of relatively small amplitude. In a laser-plasma context there is scope, for example, for its application to detect the growth of hydrodynamic instability. In particular the use of protons can be useful in conditions (e.g. the interior of a dense target) in which other, more established techniques (i.e. x-ray radiography) may be of difficult application.

References

1. A M Koheler
Science, 160 303, (1968)
2. D West and A C Sherwood
Nature, 239 157, (1972)
3. M Borghesi *et al*, CLF RAL Annual Report (2000-2001)
4. M Borghesi *et al*, Plasma Phys. Control. Fusion 43 A267, (2001)
5. M Borghesi *et al*, Phys. Plasmas 9 2214, (2002)
6. J F Ziegler, The Stopping and Range of Ions in Matter, Vol 1, Pergamon Press, New York (1985)
7. www.srim.org
8. C Michelet *et al*, Nucl. Instr. And Meth. B 181 157, (2001)
9. G Kuri *et al*, Nucl. Instr. And Meth. B 111 234, (1996)
10. J H Liang, Nucl. Instr. and Meth.. B 134 157, (1998)

Nuclear Physics and Potential Transmutation with the Vulcan Laser

J Galy, J Magill, R Schenkel

European Commission, Institute for Transuranium Elements, Postfach 2340, 76125 Karlsruhe, Germany

P McKenna, K W D Ledingham*, I Spencer, T McCanny, R P Singhal

Department of Physics and Astronomy, University of Glasgow, Glasgow G12 8QQ UK
**also at AWE plc Aldermaston, Reading RG7 4PR, UK*

F N Beg, K Krushelnick, M S Wei,

Blackett Laboratory, Imperial College, London SW7 2BZ, UK

P A Norreys, K L Lancaster, R J Clarke

Central Laser Facility, CLRC Rutherford Appleton Laboratory, Chilton, Didcot, Oxon, OX11 0QX,UK

E L Clark

AWE plc Aldermaston, Reading RG7 4PR, UK

Main contact email address: *jean.galy@itu.fzk.de*

Introduction

One of the biggest challenges facing the nuclear community is the safe disposal of nuclear waste. During the normal operation of nuclear reactors, various hazardous by-products are formed which are long-lived and highly radiotoxic. The main by-products are plutonium, the "minor" actinides neptunium, americium and curium and long-lived fission products of the elements technetium, iodine and caesium. The preferred solution for the disposal of this waste is to isolate it from the biosphere for periods of hundreds of thousands of years in deep underground geological repositories.

An alternative approach is to transmute this nuclear waste into shorter-lived or stable isotopes and thereby minimise the very long times during which the waste must be isolated. One way of doing this is through neutron driven transmutation in special dedicated transmutation reactors. A detailed "Roadmap" for the development of this technology has been published recently[1)]. In this approach, high energy protons impinge upon a spallation target to produce copious amounts of neutrons. These neutrons then enter into a sub-critical blanket containing the plutonium, minor actinides and long-lived fission products to transmute these isotopes either through fission or neutron capture reactions followed by decay.

It is, however, not clear that neutron driven reactions are the best approach to transmutation. Through a collaboration with the Institute of Transuranium Elements in Germany, the University of Glasgow, Imperial College, AWE and the Rutherford Appleton Laboratory, an investigation of alternative nuclear reactions is underway using the high intensity laser radiation from Vulcan. By focusing the laser spot very high laser intensities in excess of 10^{19} W.cm^{-2} are produced. Under these conditions, matter in the focal spot is turned into a hot dense relativistic plasma with a temperature of several MeV. Under these extreme conditions, high energy electrons, photons (bremsstrahlung), and ions are produced. These particles can then be used to induce nuclear interactions in target materials. The results of the recent experiments performed with Vulcan are described here.

Laser Induced Heavy Ion Fusion

The interaction of the ultra-high laser radiation with matter results in the production of highly energetic electrons, gamma radiation and ions. In a recent series of experiments with the Vulcan laser, at intensities of 10^{19} W. cm^{-2}, beams of energetic ions were produced by firing the laser onto a thin foil primary target (Figure 1).

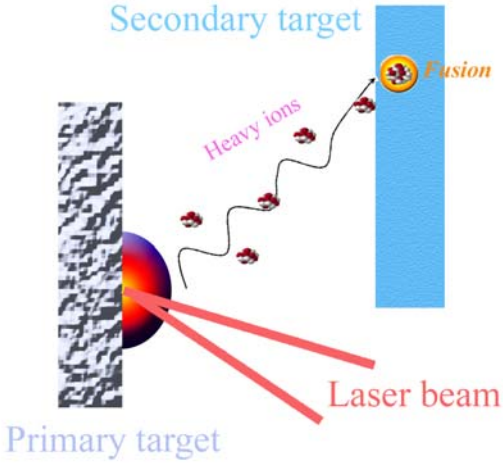

Figure 1. Setup of the heavy ion fusion experiment. The laser is focused onto a primary target (Al, C or other), where it generates a hot plasma on the surface. Heavy ions accelerated in the plasma are blown-off into the secondary target (Al, Ti, Zn, or other) inducing a fusion reaction.

The resulting ion beam then interacts with a secondary target. If the ions have enough kinetic energy, it is possible to produce fusion of the ions in the beam with atoms in the secondary target. Such fusion reactions did indeed occur and are reported for the first time in this article for a series of targets as a function of increasing Z. Heavy ion beams were generated from primary targets of iron, aluminium and carbon. Secondary target material consisted of aluminium, titanium, iron and zinc niobium and silver. The heavy ion "blow-off" fused with the atoms in the secondary target creating compound nuclei in highly excited states. The compound nuclei then de-excited to create fusion products in the secondary target foils.

These foils were then examined in a high efficiency germanium detector to measure the characteristic gamma radiation produced by the radioactive decay of short-lived fusion product nuclides. Typical spectra are shown in Figure 2.

Figure 2(B) shows the results of experiments involving cold and heated targets. The target here was aluminium, and the secondary titanium. The spectrum in blue is that taken for the aluminium target at room temperature, and the red spectrum is that of an aluminium target heated to 391°C. For the heated target, many more fusion products are evident which are not observed in the cold target. This is attributed to the heating of the target removing impurity layers responsible for proton production. When these layers are removed, heavier ions are accelerated more readily and to higher energies[2)].

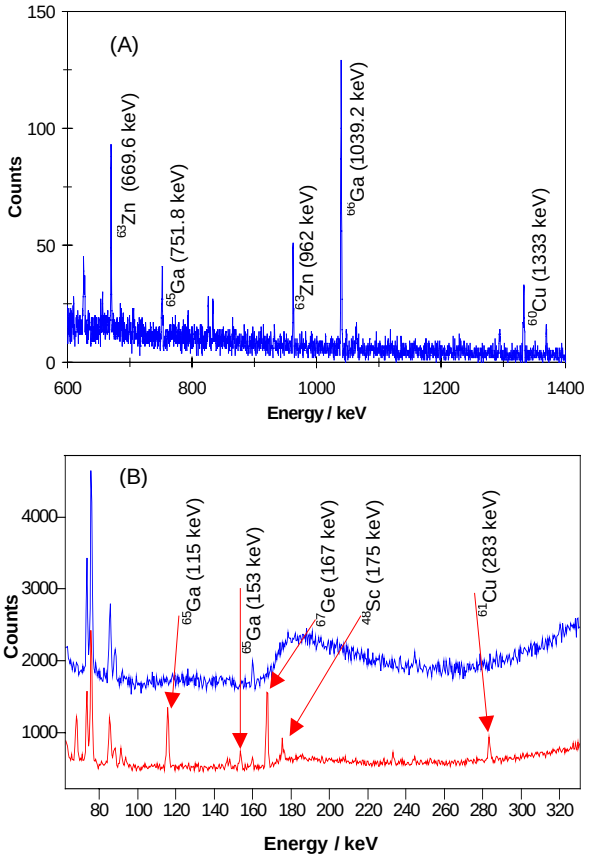

Figure 2. Characteristic emission lines observed in some heavy ion fusion experiments. (A) An Fe plate was exposed to C blow-off. (B) A Ti plate was exposed to an Al blow-off. Blue spectrum: "cold" target, red spectrum, heated target (391°C). Fusion products are much more evident in the heated target.

Some of the heavy ion beams used in these experiments together with the secondary targets materials are listed in Table 1. The main reaction products identified by their characteristic gamma emission are also shown. The measurements clearly show that fusion of the heavy ions with the target atoms, accompanied by the emission of neutrons and light particles, occurred.

Primary target material	Secondary target material	Nuclides identified in preliminary analysis
Al	Al	^{49}Cr, ^{27}Mg, ^{28}Al, ^{43}Sc, ^{34m}Cl
Al (heated)	Ti	^{48}V, ^{44}Sc, ^{48}Sc, ^{65}Ga, ^{67}Ge, , ^{61}Cu, ^{70}As
C	Fe	^{65,66}Ga, ^{67}Ge, ^{60}Cu, ^{63}Zn
C	Ag	^{117}Te, ^{115}Te, ^{119}I

Table 1. Heavy ions fusion measurement. The primary and secondary target material are given, with some of the measured and identified fusion products.

Previous measurements of the proton spectrum at similar intensities[3] showed that around 5×10^{12} protons were produced in the "blow-off" direction with a characteristic temperature of 1.4 MeV and a maximum energy of 25 MeV.

Laser Induced Photo-Fission of Actinides

Laser induced fission of metallic uranium was demonstrated[4] with the Vulcan laser in 2000. This was a world first for the Vulcan facility. In the same issue of Phys. Rev. Letts. a group at Lawrence Livermore reported laser induced fission with the NOVA laser systems[5].

In the latest experiments, laser induced fission of thorium has been demonstrated with the Vulcan laser. Similar experiments are being carried out with the high repetition rate tabletop laser at the University of Jena.

In the experiments on Vulcan, the laser beam was focused onto a 2 mm thick tantalum plate. In the focal spot, matter is turned into a hot dense relativistic plasma with a temperature of several MeV. Under these conditions the highly energetic electrons interact with the tantalum ions to produce high energy bremsstrahlung. It is this bremsstrahlung which gives rise to photo-fission in a nearby thorium sample. Following the laser shots, the sample is removed from the irradiation chamber and placed in front of a high efficiency gamma detector. The gamma spectrum showed a number of signatures of typical short-lived fission products (with half-lives from 30 min to several hours).

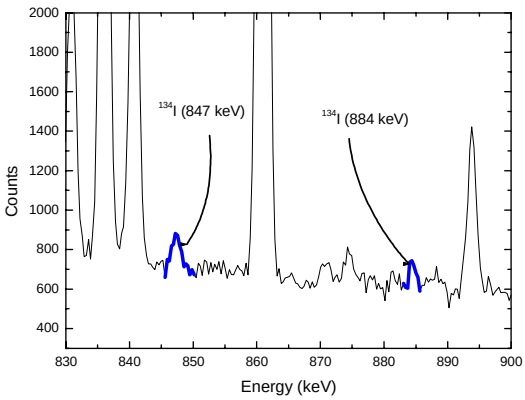

Figure 3. γ-spectrum of the irradiated ^{232}Th sample. Strong emission occurs from the ^{232}Th decay products, mainly ^{228}Ac and ^{208}Tl. Emission from fission products, in this case from ^{134}I at 847 keV and 884 keV, however, are clearly identifiable.

Laser Induced Photo-Nuclear Activation

One of the difficulties in characterising the very high energy density plasma produced in the focal spot of the laser radiation is that there are no standard techniques to determine the temperature, in particular the temperature of the resulting very high energy bremsstrahlung. A very useful method to determine this temperature is to use nuclear activation techniques. Nuclear reactions typically have a threshold energy. Below a certain energy the reaction does not proceed. Above the threshold energy, reaction products can be observed.

Several target materials with different thresholds for (γ, xn) reactions have been placed near the focus of the laser. In these reactions, a single gamma photon is absorbed by the nucleus which enters into an excited state. The excited nucleus can then de-excite by the emission of 1, 2, 3 or more neutrons, depending on the energy of the excitation. The tantalum (γ,3n) reaction has been measured. This reaction presents a gamma threshold of 22 MeV with a cross section at this energy of about 40 mb. Photonuclear reactions in tantalum have been used to measure the temperature of fast electrons produced in the laser-solid interaction[6].

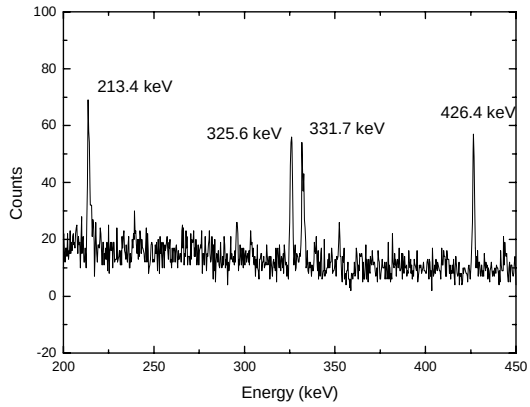

Figure 4. Characteristic γ rays emitted by ^{178m}Ta following the ^{181}Ta(γ,3n)^{178m}Ta reaction.

A praseodymium target with a 27 MeV threshold for the same (γ,3n) reaction did not show any significant signature on the measured spectra.

Transmutation of Technetium

Technetium was the first element to be produced artificially – there are no stable isotopes. Since its discovery by Perrier and Segre in Italy in 1937, searches for the element in terrestrial material have been made without success. The element is known to exist in stars. The isotope technetium-99 with a half-life of 211,000 years is produced through the fissioning of uranium in nuclear reactors. The Tc used in the present experiment was separated out of nuclear waste and fabricated into metal elements.

In the intense bremsstrahlung field produced by the Vulcan laser, photo-neutron reactions – (γ, n), (γ, 2n), (γ, 3n) etc.) are expected to occur. However both (γ,n) and (γ, 2n) result in Tc-98 and Tc-97 respectively which have even longer half-lives than Tc-99. Only with a (γ, 3n) reaction is Tc-96 produced with a short half-life of 4.28 d.

Since the tantalum (γ, 3n), which has a gamma threshold of 22 MeV and a cross section of 40 mb at this energy, was clearly observed in the present experiments, there was a chance that the Tc-99 (γ, 3n) could be detected.

The reported value of the (γ, 3n) threshold in the literature is 25.7 MeV with a maximum cross section of 6 mb at 30 MeV. Unfortunately no evidence for the reaction was detected. It is proposed to repeat these experiments with the new petawatt laser which will become available in November.

Conclusion

Through a collaboration with the Institute for Transuranium Elements in Karlsruhe, the University of Glasgow, Imperial College, AWE and the Rutherford Appleton laboratory, a basic investigation of nuclear reactions for transmutation of key components in nuclear waste has been initiated using the Vulcan laser facility. Under the extreme conditions produced in the focal spot, very high energy electrons, photons, and ions can be produced. These projectiles can be used to bombard target materials to induce fusion, fission, and activation reactions.

Acknowledgement

We would like to acknowledge the technical assistance of the Vulcan operations team.

References

1. C. Rubbia *et al*., "A European Roadmap for Accelerator Driven Systems for Nuclear Waste Transmutation", 2001.
2. E.L. Clark *et al*., CLF Annual Report 2001-2002, pp 35.
3. I. Spencer *et al.* Nucl. Inst. Meth. B. 183, 449 (2001).
4. K.W.D. Ledingham *et al*., Phys. Rev. Lett.. 84, 899 (2000).
5. T. Cowan *et. al.*, Phys. Rev. Lett. 84 903, (2000).
6. I. Spencer *et al.*, accepted for publication in Rev. Sci. Inst. (2002).

Proton Beam Generation from Double-sided Illuminations of Solid Target by High Intensity Short Pulse Lasers

M S Wei, F N Beg, A E Dangor, A Gopal, M Tatarakis, K Krushelnick

Blackett Laboratory, Imperial College of Science, Technology and Medicine, London SW7 2BZ, UK

E L Clark

Radiation Physics department, AWE plc, Aldermaston, Reading, RG7 4PR, UK

K W D Ledingham, P McKenna, T McCanny, I Spencer

Department of Physics and Astronomy, University of Glasgow, Glasgow G12 8QQ, UK

P A Norreys, R J Clarke, K L Lancaster

Central Laser Facility, CLRC Rutherford Appleton Laboratory, Chilton, Didcot, Oxon, OX11 0QX, UK

M Zepf

Department of Pure and Applied Physics, The Queen's University Belfast, UK

Main contact email address: *wei.mingsheng@ic.ac.uk*

Introduction

With the advance of the high intensity short pulse (tens of femto -second to pico-second) techniques, state-of-the-art lasers are able to achieve very high intensity, up to 10^{20} Wcm^{-2}. This opens up completely new research fields, such as, laser plasma accelerator for producing energetic particles, huge magnetic field generation, laser produced nuclear excitations and laser experiments for astrophysical purposes. Among them, energetic proton and heavy ion production have become a very interesting topic particularly because it is directly related to fast electron generation during the laser plasma interactions and the subsequent energy transfer to ions. This will greatly help us to understand the basic physics, still under exploration. On the other hand, these energetic protons and ions have many potential applications, for example, using proton beams to generate a fusion spark in fast ignition schemes[1)], proton produced short-lived positron emitting radioisotopes for medical imaging[2)], proton probing[3)], and compact ion sources [4)].

In experiments, energetic proton beams have been observed both in front of and behind the target[5-9)]. The proton beam emitted from the rear side has demonstrated higher quality in terms of higher energy and lower divergence with considerable luminosity. The established explanation for proton origin is that the protons come from a surface contamination layer formed by water, oil and vacuum grease as well as from bulk of the materials when plastic targets were used. These protons are accelerated by the electro-static field set up by fast electrons leaving the target[10)]. Protons can also be accelerated to energies greater than the temperature of electrons inside the target[11)].

Studies where a radiochromic film dosimeter was used as the proton detector[12)] have shown that plasma scale length at the rear surface has strong effects on proton beam production. In the unperturbed rear surface case, the authors reckoned that they observed up to 21.7 MeV proton beam. With the increase of the preformed plasma at rear surface, both the proton energy and beam quality were significantly reduced. No proton beam with energy greater than 5 MeV was produced when the plasma scale length was increased to 100 μm at back surface. The observations were interpreted by the proton rear surface sheath acceleration mechanism where the acceleration E field is proportional to $KT_H/ e \max(l_D, l_i)$.

In this paper, we report results from a novel experimental configuration using two short pulse Vulcan laser beams illuminating the solid target from both sides. We found that proton production in this double-sided irradiance (DSI) became very complex. Two (maybe more) highly collimated proton beams with peak energy about 8~9 MeV were consistently observed at the opposite side to the higher intensity laser beam even in the presence of a much larger plasma scale length due to another relatively lower intensity CPA beam. The proton emission in this scheme demonstrated completely different characteristics when compared with that produced by single side illumination alone.

Experiment

In the experiments reported here, the Vulcan short pulse CPA beam was split into two and fired onto a thin solid target from both sides. Up to 30 J and 20 J from CPA1 and CPA2 were focused down to 10 μm focal spots within 1 ps pulse duration at 1.053 μm wavelength by 2 off-axis parabolic mirrors. The laser beams were p-polarized and were incident on the target at angles of 41^0 and 20^0 from left and right sides respectively. CPA2 beam delivered relatively lower energy, about 2/3 of that from CPA1. The peak intensity was about 2×10^{19} Wcm^{-2}. The thin targets, 1 μm to 50 μm, were typically 5 mm by 8 mm gold plane foils.

Energetic protons were measured with the passive stack consisting of a few layers of radiochromic films (RCF) and particle track detectors (CR39), which were positioned 5 cm from the target. RCFs (model HD810) were used as the dosimeter. Care must be taken when interpreting the RCF data as the film responds to all kinds of ionization radiation. In contrast, track detector CR39 is only sensitive to protons in the stack arrangement as the first two RCFs (220 μm) can stop all the energetic heavy ions, such as carbon and oxygen ions. In fact, proton beams were only recorded by the track detectors in our experiment.

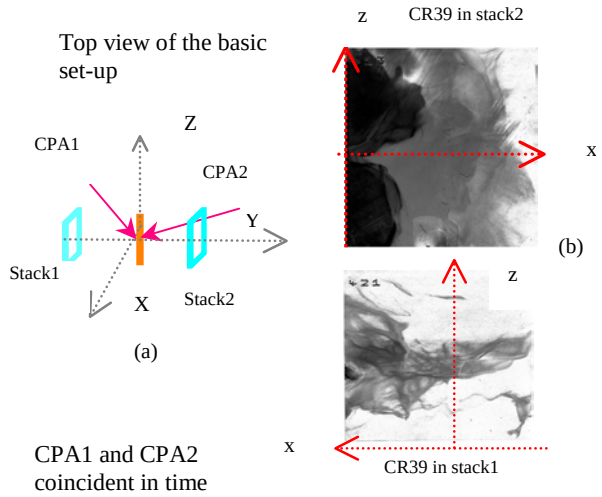

Figure 1. Schematic of the experiment arrangement (a) and the scanned CR39 data from both stacks (b).

Figure 1 shows the scanned images of proton emission when two laser beams were coincidently fired to a 20 μm gold target. Stack1 only looked at the top half proton emission as for CPA1 the beam came from the bottom. Also there was limited space for stack 2 and, therefore, it only collected half of the proton emission in most of the shots. From the data, it can be seen there were two proton beams on the right side with peak energy about 8 MeV. On the left side, only lower energy protons (~4.25 MeV) were observed with very irregular beam shapes.

To study the influence of CPA2 on proton production, a series of shots with CPA2 later than CPA1 in time (by up to 2 ps) were carried out with similar laser and target conditions. In all those shots two proton beams were consistently observed at the right side. Figure 2 presents two separated highly collimated proton beams observed in stack 2. One beam was above the middle plane and the other was below. Both beams have peak energy about 9 MeV. No protons with energy greater than 4.25 MeV were observed in stack 1. In this shot, CPA2 was 0.5 ps later than CPA1.

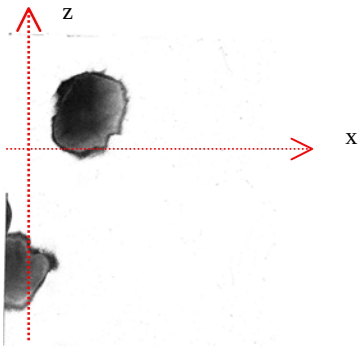

Figure 2. Scanned CR39 data in stack 2 showing the existence of two 9 MeV proton beams with CPA2 0.5 ps later than CPA1.

Figure 3 shows proton data when the CPA2 beam was focused onto the target 1 ps earlier than CPA1. Still, two 8 MeV proton beams were observed at the right side. In stack 1, on the first piece of CR39 detector, except the irregular shape protons, there was also one collimated weaker proton beam (4.25 MeV) at the left side, which is very likely produced by the CPA2 laser pulse.

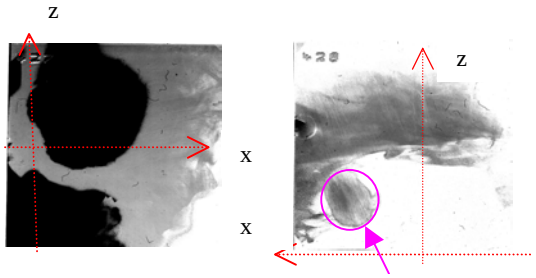

(a) 8 MeV proton beams in stack 2

(b) 4.25 MeV proton beam in stack 1

Figure 3. Scanned CR39 proton data with CPA2 1 ps earlier than CPA1.

Images of the independent probe beam, which was parallel to the target plane, indicate that the expanded plasmas on both sides were well aligned. This should eliminate the possibility of two proton beams produced by two laser pulses. Considering that CPA1 has the higher energy, we believe it took the dominant role during the interactions. Here we propose one possible explanation for more than one proton beams: high energy proton beams were initially produced by the dominant laser beam CPA1, then split and deflected by the charged rear surface. It is interesting to note that peak proton energy at the right side was much higher than that at the left side, which is opposite to the intensities of the two laser beams.

In the following, we will compare the experimental results of the peak proton energy measured at right side in DSI with that from SSI, where only CPA1 beam was used with similar energy as that in the double-sided case. A series of shots were taken with the thickness of the thin gold targets varied from 1 μm to 50 μm. Figure 4 presents the variation in peak proton energy versus target thickness. It clearly shows that maximum proton energy in the DSI case was reduced. Data also suggest that proton acceleration in the SSI case may depend on the thickness of the targets. Similar results have been reported by different groups on different laser facilities[7,13]. In our experimental conditions, 10 μm seems to be the optimum thickness for forward proton acceleration. Curiously, this correlation disappeared in the DSI case, which suggests electrostatic fields for proton acceleration may be reduced inside the target due to the decrease of the return current.

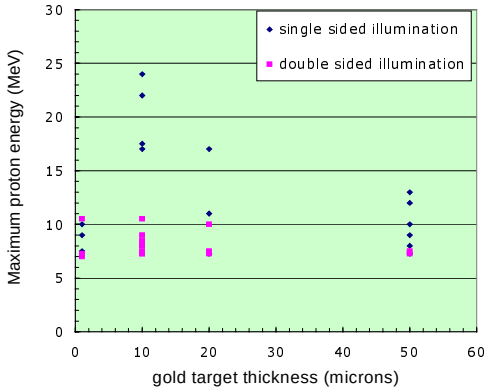

Figure 4. Maximum proton energies measured as a function of target thickness for gold.

In conclusion, proton beam production has been studied by a novel double-sided illumination scheme with two CPA beams. Due to the unbalance of the two laser pressures, proton production became very complex. However, two energetic proton beams were consistently observed at the opposite side to the higher intensity laser beam even with a much larger plasma scale length at target surface. The charged rear surface did affect the behavior of the proton beams. Both the peak proton energy and its direction have been changed.

Finally, our thanks extend to all the staff of the CLF for their help and assistance during the experiment. This work was supported by EPSRC, UK.

References

1. M Roth *et al.*, Phys. Rev. Lett. 85 1654 (2001)
2. I Spencer *et al.*, Nucl. Inst. Meth. B. 183, 449 (2001)
3. M Borghesi *et al.*, Plasma. Phys. Control. Fusion 43, A267 (2001)
4. K Krushelnick *et al.*, IEEE Trans. Plas. Sci. 28, 1184 (2000)
5. E L Clark *et al.*, Phys. Rev. Lett. 84, 670 (2000)
6. M Zepf *et al.*, Phys. Plasmas 7, 2055 (2000)
7. A Maksimchuk *et al.*, Phys. Rev. Lett. 84, 4108 (2000)
8. R A Snavely *et al.*, Phys. Rev. Lett. 85, 2945 (2000)
9. Y Murakami *et al.*, Phys. Plasmas 8, 4138 (2001)
10. S C Wilks *et al.*, Phys. Plasmas 8, 542 (2001)
11. J R Davies submitted to Laser and Particle beam, (2002)
12. A J Mackinnon *et al.*, Phys. Rev. Lett. 86, 1769 (2001)
13. I Spencer *et al.*, Submitted to Phys. Rev. Lett. (2002)

Ion heating and thermonuclear neutron production from high intensity subpicosecond laser pulses interacting with underdense plasmas

S Fritzler, V Malka

Laboratoire d'Optique Appliquee, ENSTA, UMR7639, CNRS, Ecole Polytechnique, 91761 Palaiseau, France

Z Najmudin, K Krushelnick, C Marle, B Walton, M S Wei, A E Dangor

Blackett Laboratory, Imperial College of Science, Technology and Medicine, London SW7 2BZ, UK

R J Clarke

Central Laser Facility, CLRC Rutherford Appleton Laboratory, Chilton, Didcot, Oxon, OX11 0QX, UK

Main contact email address: *kmkr@ic.ac.uk*

Introduction

The generation of energetic particles and radiation from intense laser-plasma interactions is a new and rapidly evolving branch of physics and of particular interest for two important reasons. Firstly, these plasmas are efficient sources of bright, energetic, and strongly collimated electron [1)], proton [2)], and gamma ray beams[3)] which may have a wide range of applications. Secondly, measurements of these beams provide a useful plasma diagnostic technique and can elucidate much of the fundamental physics which occurs in these interactions. Recently, there have been important observations and simulations of neutron generation during the interaction of high intensity lasers with matter at solid or near-solid densities [4)]. These neutrons are generated by laser produced ion beams in solid deuterated targets via D(d; n)^{3}He reactions and can provide information on the spectrum of the accelerated deuterons as well as heating processes which occur during these interactions. In contrast, the study of ion dynamics in the interaction of intense lasers with underdense plasmas has received less attention, even though it is well known that such interactions can produce energetic ions. For example, an intense laser pulse passing through a plasma causes the radial displacement of electrons due to its ponderomotive force, $F_p = - m_e c^2 (1 + a^2/2)^{1/2}$, where a is the normalized vector potential of the laser. This results in an impulsive acceleration of the ions, often called a "Coulomb explosion". The maximum ion energy that can be produced by this process is equal to their ponderomotive energy, $U = Zm_e c^2(\gamma-1)$, where γ is the relativistic quiver velocity of electrons in the laser field given by $\gamma = (1 + a^2/2)^{1/2}$. For modern laser systems which reach relativistic intensities ($a > 1$), the energy of "Coulomb explosion" ions can reach several MeV [5, 6)].

Furthermore, the interaction of intense laser pulses with underdense plasmas can generate extremely high current electron beams [7)]. It is well known that such intense electron beams, where the beam particle density n_b is comparable to the ambient plasma density n_e, have a stopping power in plasma several orders of magnitude greater than the classical Coulomb-collision stopping power. Much of this enhanced stopping can be attributed to heating of the ions either by the beam or by the self-generated return current. This can result in significantly higher ion plasma temperatures [8)].

In this report we present the first experimental evidence of neutron generation due to the interaction of an intense laser pulse with an underdense deuterium plasma. These results show that it is possible for the ions in these interactions to reach the keV energies required for the D(d, n)^{3}He reaction. Moreover, since the neutrons produced by these reactions have little interaction with the ambient matter, one can obtain information concerning the ion kinetics by studying the yield, spectrum and angular distribution of the emitted neutrons. From these studies, we find that the measured neutron yield cannot be explained solely by the propagation of the "Coulomb explosion" ions through the ambient D_2 gas. It is deduced that plasma ions are heated to fusion temperatures by a non-collisional heating mechanism.

Experiment

The experiment was performed on the Vulcan:CPA laser. The laser produced pulses with a duration of 0.8 to 1 ps and an energy of up to 62 J on target, at a wavelength of 1.05 µm. Using a f/4 off-axis parabolic mirror, the laser beam was focused onto the edge of a D_2 gas jet produced by a 1 mm diameter sonic nozzle, which was located 1 mm below the focus. The waist of the focal spot, w_0, was 20 µm, resulting in a peak intensity of up to 2×10^{19} W/cm^2. Interferometric studies were used to characterise both the density and gas profile [9)]. Plasma densities in the range 1×10^{19} to 1×10^{20}cm^{-3} could be selected by changing the gas-jet backing pressure. In addition, the density was verified on each shot by forward Raman Scattering measurements. In this way, the density and spatial dimensions of the plasma and gas were accurately known on each shot, in contrast with other experimental geometries, where these parameters are more difficult to accurately measure.

The time-of- flight (TOF) technique was used to obtain the neutron energy spectrum and angular distribution [10)]. For this measurement, the detectors used were 5 cm diameter cylindrical NE102 scintillators, which had a rise time of 1.5 ns. These were coupled to the windows of photomultiplier (PM) tubes. The output of the PM tubes were read by oscilloscopes, with a 500 ps sampling rate. Up to five of these detectors were used simultaneously at various distances from 1.9 to 5.5 m from the interaction region and at angles, of 0 to 180 degrees relative to the direction of propagation of the laser beam, z, in the horizontal (x; z)-plane. They were calibrated relative to one another by swapping their position for different shots under the same conditions. To suppress background signals due to scattered neutrons and those generated by other processes, up to 53 cm long tapered collimators of polyethylene and lead were used. These pointed directly towards the interaction region, ensuring only neutrons generated there reached the detectors. A typical TOF trace is shown in the inset of Figure 1. It is noted that all the detectors gave similar traces on any given shot, irrespective of their angle. The prompt signal is the flash due to Bremsstrahlung generated by the energetic electrons that are produced in this interaction [7)]. The peak at 187 ns is produced by neutron events having an energy E_n of 2:5 ± 0:2 MeV. This energy is characteristic for neutrons produced by thermonuclear D(d; n)^{3}He fusion reactions. The short neutron pulse confirms that these neutrons are not due to (γ, n) processes, which would produce a broader spectrum. To ensure that the peak was due to the D(d;n)^{3}He reaction, additional shots with helium as a target gas were performed. In this case, no neutron peak was observed. The TOF signals were converted to an energy spectrum. An example spectrum for a detector at an angle of 67 degrees, is shown by the solid line in Figure 1. Simulations with the Monte-Carlo neutron transportation code MCNP [11)] confirmed that no significant broadening of signal occurred once the neutrons passed the target chamber. Thus, the spectrum of the emitted neutrons is simply determined by the kinematics of the original D(d;n)^{3}He reaction [12)]. The isotropy and approximate Gaussian profile of the neutron spectrum is

what would be expected for an originally Maxwellian deuteron profile. Hence by assuming such an initial profile, the deuteron temperature required to produce the measured neutron energy spectrum can be deduced[13]. The neutron peak shown by the solid line in Figure 1 implies an ion temperature of about 1 keV.

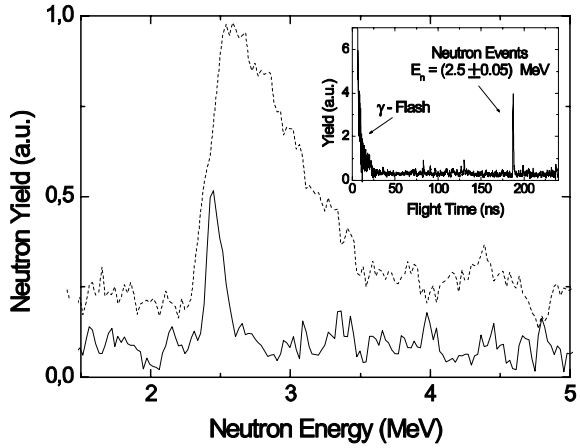

Figure 1. Neutron spectrum for detector at an angle of 67 degrees without the secondary CD_2 target (solid line), and with CD_2 (dashed line). The inset shows a TOF signal representative for all angles. For these shots, n_d was 5. $10^{19}cm^{-3}$ and the laser energy about 62 J.

Special attention was paid to a precise determination of the neutron yield. These additional measurements were made by nuclear activation of ^{115}In, where the resulting metastable ^{116}In decays with a half-life of 54 min to ^{116}Sn, by β- decay. The thickness of the activation target must be chosen to increase the efficiency of neutron capture, but not significantly affect the emitted electrons. The thickness used was 100 mg/cm^2, which is close to the optimum of 90 mg/cm^2 (see Reference 14 and references therein). The total cross-section, of ^{115}In is several hundred mb for thermal neutrons [15]. Therefore, the indium foils were stacked at different distances, within a polyethylene brick, which acted as a moderator. This brick was placed at closest 9 cm from the interaction, and at an angle of 90 degrees. To reduce measurement of scattered neutrons and those generated by other processes, the bricks were shielded by extra layers of polyethylene.

Since this activation can also be due to a resonance of the ^{115}In nucleus from epithermal neutrons of 1.46 eV, the foils were shielded with cadmium, which has an approximately 100 times higher cross-section for thermal neutrons. The difference in activity between shielded and unshielded indium foils gives the activation due to thermal neutrons. The β- decay was measured using a Geiger-Muller counter which had a very low background due to the special low-activity lead shielding used. The number of neutrons on the activation detector was then calculated from the activity, as a function of distance [14]. Since the angular distribution was also measured by the TOF detectors, and found to be almost isotropic for these shots, the total yield of neutrons can be estimated. A maximum of $1.0 \pm 0.2 \times 10^6$ neutrons per shot was observed. An estimate for the expected yield can be made for a Maxwellian velocity distribution [16]. Assuming that the confinement duration is about the plasma dissassembly time, one finds that the heated volume must be of the order of twice the original laser spot size times the gas-jet length. Since this calculation is extremely sensitive to the exact form of the deuteron energy profile, this order of magnitude agreement demonstrates that our initial assumption on the deuteron energy profile being Maxwellian was valid.

To assess if the observed neutron yield could be due to the Coulomb explosion accelerated ions, the spectrum of these ions was measured. This was performed using a Thomson parabola ion spectrometer positioned 40 cm from the focal spot and at an angle of 90 degrees. CR-39 nuclear track detectors recorded the dispersed ions. As has been previously measured, the energetic ion emission was sharply peaked in this direction[5]. This was confirmed by using radiochromic film, which is sensitive to the dose produced by the expelled ions. In these experiments about 2×10^{11} deuterons accelerated above 100 keV and up to a maximum energy of (1:2 ± 0:2) MeV were observed as can be seen in Figure 3. Equating this to the ponderomotive potential U indicates that the averaged intensities in the focal spot were as expected of the order 10^{19} W/cm^2.

Calculating the likely yield that these ions produce as they travel through the ambient gas surrounding the plasma, one finds that no more than 10^4 neutrons could have been produced in this way. To demonstrate this more clearly, a 200 μm thick and 5 mm wide solid deuterated plastic (CD_2) target was placed 2.5 mm away from the interaction at the same angle as the Thomson parabola. The purpose of this target is to simulate the beam-target interaction of the expelled ions as they pass through the stationary ambient gas, but obviously with a much higher reaction rate due to the higher density of deuterons in the solid. This resulted in a significant enhancement of the neutron signal, as expected. The increase in yield is more than one order of magnitude, as shown by the dashed line in Figure 1.

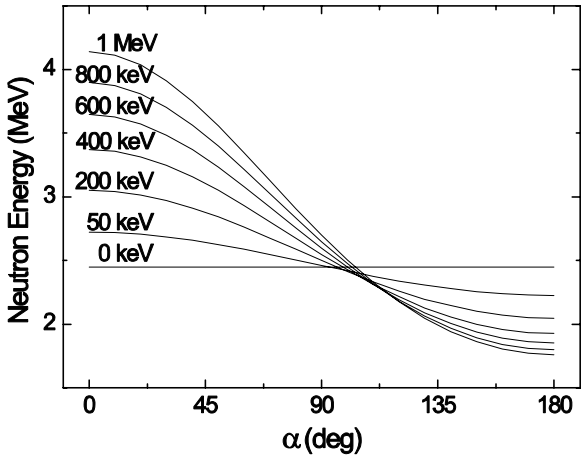

Figure 2. Neutron energy as a function of the relative angle of observation between incident deuteron and expelled neutron for D(d; n)^{3}He reactions.

As can be seen in Figure 2, the energy of the emitted neutron from a beam-target D(d; n)^{3}He reaction is a function of the relative angle of observation to the deuteron momentum. The broad neutron spectrum, when the deuterated target is present, reflects that there is a continuous deuteron distribution for the D(d; n)^{3}He reaction up to an energy of (1.0 ± 0.1) MeV. Furthermore, the distribution of the deuterons incident on the target can be calculated using the differential cross-section for the D(d;n)^{3}He reaction [10], and the stopping cross-section within the solid CD_2. This calculation reveals that the neutrons were produced by a Maxwellian distribution of deuterons with temperature T_{calc} of (186 ± 39) keV.

This compares with the ion temperature measured by the Thomson parabola T_{exp} of (216 ± 36) keV, as shown in Figure 3 below. Therefore, it is clear that the broad neutron spectrum with the solid target is the result of the radial beam of deuterons expelled from the plasma from the Coulomb explosion. However, it is also clear that the interaction of this distribution with the ambient deuterium gas cannot account for the narrow neutron spectrum obtained without the external target.

This is further emphasized by the angular dependence of the neutron emission with and without the external CD_2 target, as presented in Figure 4. In the case of (d; n) reactions with the beam of deuterons generated by the Coulomb explosion, an angular variation in the distribution can be observed with a minimum in the laser propagation direction, since this direction

is orthogonal to the motion of all of the accelerated ions [10]. In contrast the thermonuclear fusion neutrons generated directly in the plasma have a more isotropic emission profile in yield and temperature.

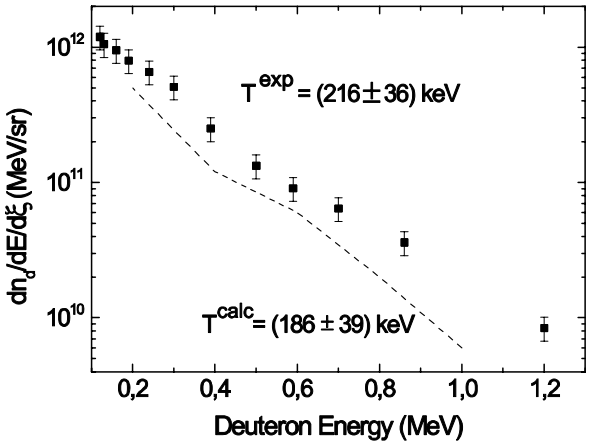

Figure 3. Deuteron spectrum from Coulomb explosion as measured by the Thomson parabola (squares) and as calculated from the TOF signal (dashed line).

From these measurements it is clear that the neutron production without an external target cannot be ascribed to a beam target reaction, but is the result of a much more isotropic thermal distribution of ions. Both the measurements of total neutron yield and its spectrum indicate that neither the yield nor the heating process exhibit a very strong dependence with the plasma deuteron density. Averaging the temperature over all these points gives a mean temperature of about 1 keV.

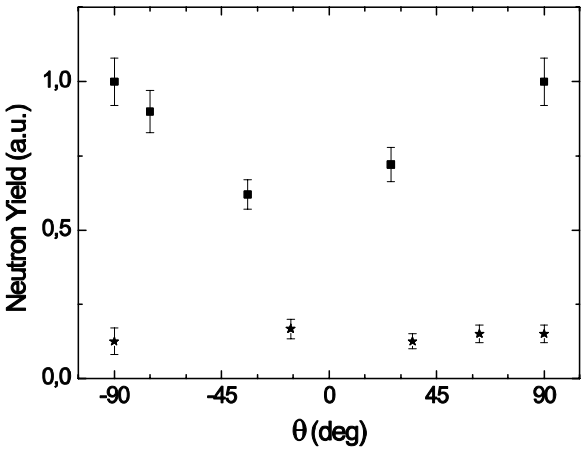

Figure 4. Angular distribution of neutrons with (squares)and without (stars) the solid CD_2 target, for two typical shots, the latter showing a more isotropic thermal distribution of ions.

It is well known that the interaction of an intense laser pulse with underdense plasma can result in efficient absorption of the laser pulse. This can lead to the production not only of beams of energetic electrons but also to a hot thermal bulk of electrons [17]. However it is also evident that for the range of densities explored in this study, the time for the electrons to equilibrate with the ions is well in excess of the disassembly time for the plasma. For our conditions, τ_{eq} is more than 1 ns. Hence this ion heating must be the result of direct non-collisional heating mechanisms that occur on the time scale of the laser pulse. The simplest explanation for the ion heating is due to variations in the Coulomb potential caused by the ponderomotive expulsion of charge by the laser pulse. This is quite likely due to the presence of self-focusing and other propagation instabilities under these conditions. However, it is also noted that by systematically varying the plasma density, a correlation was observed between the neutron yield and the generation of energetic electrons. As has been noted previously, the electrons are generated by wave-breaking [1] and result in a hot electron tail in the distribution with a total current approaching the Alfven limit [7]. At densities n_{WB} below the wavebreaking limit of about 1:5 x $10^{19}cm^{-3}$, both neutron and hot electron yields dropped dramatically. However above this deuteron density, the neutron yield showed no great variation with density. Recent simulations have shown that the filamentation and propagation instabilities of such high current electron beams in a plasma can result in collisionless heating of the ions [18]. Thus, this result may be of interest for such applications as fast-ignitor heating of fusion capsules, since it would allow for the use of higher intensity ignitor beams for which the laser coupling efficiency can be higher [19].

In summary, we have observed the generation of (1:0 ± 0:2) x 10^6 thermonuclear fusion neutrons from the interaction of an intense laser pulse with an underdense plasma. These neutrons are generated by D(d; n)^{3}He reactions in the plasma which is heated to fusion temperatures on the time-scale approaching the laser pulse duration. It is therefore possible to measure the ion temperature of the underdense plasma, which was found to be in the range of 1 keV. Finally it is noted that no special attention was given to maximizing the neutron yield in this experiment. It is expected that using a pulse guided over a longer distance can increase the efficiency of energy transfer to deuterons [6]. Moreover it has been demonstrated that a small CD_2 target can increase the neutron yield by over an order of magnitude. It is thought that a longer interaction length coupled to a solid CD_2 target, that stops all of the radially ejected deuterons, could significantly enhance the neutron production. This may make this interaction an attractive source for applications that require bright and short duration pulses of neutrons.

References

1. Modena *et al.*, Nature 377, 606 (1995).
2. E. L. Clark *et al.*, Phys. Rev. Lett. 85, 1654 (2000); S. P. Hatchett *et al.*, Phys. Plasmas 7, 2076 (2000).
3. M. H. Key *et al.*, Phys. Plasmas 5, 1966 (1998); P. A. Norreys *et al.*, Phys. Plasmas 6, 2150 (1999).
4. P. A. Norreys *et al.*, Plasma Phys. Contr. Fusion 40, 175 (1998); G. Pretzler *et al.*, Phys. Rev. E 58, 1165 (1998); L. Disdier *et al.*, Phys. Rev. Lett. 82, 1454 (1999); C. Toupin *et al.*, Phys. Plasmas 8, 1011 (2001); T. Ditmire *et al.*, Nature 398, 489 (1999).
5. K. Krushelnick *et al.*, Phys. Rev. Lett. 83, 737 (1999).
6. V. V. Goloviznin *et al.*, J. Phys. D 31, 3243 (1998).
7. M. I. K. Santala *et al.*, Phys. Rev. Lett. 86, 1227 (2001).
8. R. B. Miller, Intense Charged Particle Beams, Plenum Press, New York (1982).
9. V. Malka *et al.*, Rev. Sci. Inst. 71, 2329 (2000).
10. J. B. Marion, R. Fowler, Ed., Fast Neutron Physics, Part I, Interscience Publishers, Inc., New York (1960).
11. J. F. Briesmeister, Ed., Program MCNP , Los Alamos report LA-12625-M (1993).
12. H. Wepstra and A. Audi, Nucl. Phys. *A* 432, 1 (1985).
13. H. Hutchinson, Principles of Plasma Diagnostics, Cambridge University Press, Cambridge (1987).
14. E. Segre, Nuclei and Particles, (The Benjamin/Cummings Publishing Company, Reading, 1975).
15. Hughes, Neutron Cross Sections, BNL 325 (1958).
16. J. D. Huba, NRL Plasma Formulary, Washington (2000).
17. K.-C. Tzeng and W. B. Mori, Phys. Rev. Lett. 81, 104(1998).
18. M. Honda *et al.*, Phys. Rev. Lett. 85, 2128 (2000).
19. M. Tabak *et al.*, Phys. Plas. 5, 1626 (1994).

The production of energetic electrons from the interaction of an intense laser pulse with an underdense plasma

Z Najmudin, K Krushelnick, E L Clark, M Tatarakis, A Modena and A E Dangor

Plasma Physics, Imperial College of Science, Technology and Medicine, London, SW7 2BZ, UK

J Faure, V Malka

LULI, Ecole Polytechnique, Palaiseau, France

D Gordon, C Joshi

University of California, Los Angeles, CA 90095, USA

R Clarke

Central Laser Facility, CLRC Rutherford Appleton Laboratory, Chilton, Didcot, Oxon, OX11 0QX, UK

Main contact email address: *zn1@ic.ac.uk*

Introduction

The advent of Chirped-Pulse Amplification has pushed the maximum intensities that can be produced by pulsed lasers to new highs. Within the next few years, several lasers with powers greater than a Petawatt (10^{15} W) will come into operation in research laboratories around the world. It will be possible to focus these lasers to intensities greater than 10^{21} Wcm^{-2}. The interaction of such laser pulses with matter is of great interest not only because of the new frontiers of physics that can be investigated, but also because of the many applications which have been envisaged for such interactions. In particular, these interactions will be the source of energetic particles with energies of interest for nuclear physics applications.

For example, it has long been supposed that plasma may be an ideal medium for acceleration of particles to extremely high energies[1]. This is due to the large electric fields, which can be supported in plasmas. For a relativistic plasma wave (one with a phase velocity close to the speed of light), the wavenumber is simply $k_p = \omega_p/c$, where ω_p is the plasma frequency, $\omega_p = ne^2/\omega_0 m_e$. The electric field associated with a sinusoidal variation in charge density due to the plasma wave of this density and wavenumber is then simply:-

$$E_{\max} = c(m_e n_0/\varepsilon_0)^{1/2} \approx 0.96(n_0(\mathrm{cm}^{-3}))^{1/2}\mathrm{Vcm}^{-1}.$$

For $n_0 = 10^{19}$ cm^{-3}, E_{max} = 300 GeVm^{-1}, about 10^4 times greater than the electric field attainable in present day high energy accelerators, due to the limitations of electrical breakdown. Tajima and Dawson[1], when proposing the use of plasmas for acceleration purposes, suggested several methods of generating such relativistic plasma waves of high amplitude, using either lasers or particle beam drivers. They also noted that such large amplitude relativistic waves could be produced by instabilities of an intense laser pulse propagating in a plasma.

When an intense laser passes through a plasma, it can be scattered collectively by low level oscillations within the plasma. Such collective scattering is common in laser plasma interaction where the laser wavelength can be much greater than the Debye length of the initially cold and dense plasma. Such scattering can be thought of as a scattering off quanta of plasma oscillations, $\omega_s = \omega_0 \pm \omega_p$, where $\hbar\omega_s$ is the scattered photon energy and $\hbar\omega_0$ is the incident photon energy. The superposition of the incident and scattered photon can result in a modulation of the laser pulse at the plasma frequency, ω_p. This modulation through the action of the ponderomotive force can resonantly drive growth of the plasma waves. Since the plasma oscillations have to be in phase with the laser modulations, which travel at the laser group velocity, the plasma wave must have a phase velocity that equals the laser group velocity. For a sufficiently underdense plasma ($n_e << n_{cr} = \varepsilon_0 m_e \omega_p/e^2$), this will be close to the speed of light, (since in a plasma the dispersion relation for an electromagnetic wave is $c^2k^2=\omega_0^2\,(1 - n_e/n_{cr})^{1/2}$. As the plasma wave grows the scattering rate increases, resulting in a distribution of energy to satellites of the initial laser pulse, and a modulation of the laser pulse. Hence in analogy to the scattering from atomic media, this process is often called Stimulated Raman Scattering [2,3].

The result of this increasing unstable modulation of the laser pulse is an increasing growth in the plasma wave amplitude, so that it is possible for the amplitude of the plasma wave to reach a density perturbation close to the initial ambient density of the plasma. When this happens it becomes possible for the plasma wave to self-trap electrons with sufficient velocity relative to the correlated motion of electrons within the plasma wave. Indeed if the plasma wave amplitude greatly exceeds the intial ambient plasma density (as it may do, from non-linear steepening of the plasma wave), then a large bunch of electrons which form part of the plasma wave can become dephased (when excessively driven) from the plasma wave, and rather than feeling a returning force, will experience an acceleration from the next phase of the plasma wave. Since in this large amplitude electric field the electrons can reach relativistic speeds very quickly, these electrons can then remain in phase with the accelerating field and be accelerated to very high energies. This process is known as wavebreaking and can result in the production of a very large current of relativistic electrons[4].

Laser parameters, target area set-up, spectrometer and electron beam diagnostics

The experiments detailed in this report were performed at the Rutherford Appleton Laboratory with the Vulcan:CPA laser. The Vulcan:CPA laser can generate laser pulses with up to 100 J on target in a 1 ps pulse. Wavefront distortion in the beam due to thermal lensing in the amplifiers is corrected with a static adaptive optic. This allows the beam to be focused to a roughly 2 times diffraction limited beam. In the experiments detailed here the laser beam was focused to a spot diameter of roughly 10 µm (FWHM), resulting in intensities well in excess of 10^{19} Wcm^{-2}, when focused in vacuum.

To prevent ionisation defocusing of the laser beam before reaching focus, the laser beam is focused on the edge of a high-density gradient gas-jet. The density profile of the nozzle had been previously measured by interferometry [5]. The nozzle has been optimised to ensure that the vacuum-gas interface is as sharp as possible whilst retaining a flat density profile within the gas itself. The density of neutrals is varied by varying the backing pressure on the jet, and is found to vary almost linearly. Hydrogen or helium is generally used in these experiments, which ensures that the plasma density produced remains uniform, without the intensity dependent ionisation profile that characterises the interaction with other gases at these laser intensities. This also ensures that the gas jet is free from cluster formation. The gas jet densities measured in this experiment are consistent with the full ionisation of the neutrals (2 electrons per molecule) as measured by interferometry.

The spectrum of the beam transmitted through the gas jet is attenuated by reflecting off a glass plate before directing it out of the vacuum chamber. Reflecting optics are used for all transport of the beam, including the lens for collimation and focusing. This ensures a neutral response of the optical system, as well as reducing modifications in the spectrum that may arise from self-phase modulation of the beam passing through optics. Furthermore, the spectral response of the system is calibrated with a black-body emitter placed at the focal plane of the laser beam. The beam is focused on a spectrometer and the spectrum detected with a 16-bit (high dynamic range) CCD camera. The glass plate for collecting the transmitted light has a small hole in it to allow any electrons accelerated by the interaction to pass without scattering or energy absorption. The electron beam is passed into an electron spectrometer, which consists of an evacuated chamber placed between the poles of an electromagnet of radius 5 cm, which has a maximum magnetic field (uniform between the poles) of about 1 Tesla. The dispersed electrons are detected either with individual silicon barrier detectors (of circular area ≈ 1cm^2 each), or a series of 100 strip detectors, each 500 µm by 5 cm (total area 5 cm by 5 cm). In either case, the detectors are biased, and the current generated by ionising radiation in the diodes' depletion region is measured on oscilloscopes. When using the strip detectors, two sets of detectors were used simultaneously, one either side of the undeviated direction of the beam. Thus one set of detectors can be used to detect the accelerated electrons whilst the other gives a measure of the noise per shot, which principally is from x-rays produced in the collimator, and so is symmetric around the undeviated beam. Indeed the same detectors used to measure noise can be used to measure ion spectra as well, since due to their slower time-of-flight in reaching the detectors, they can be easily differentiated from the prompt x-ray noise on the oscilloscope traces. A combination of time-of-flight and magnetic deflection can determine the particular ion state detected. However it is noted that in these experiments with gaseous targets, one observes no ion signals in the directly forward direction. A schematic of the set-up is shown in Figure 1.

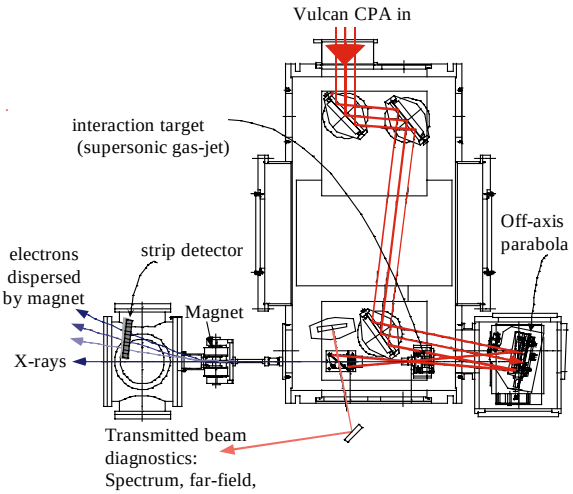

Figure 1. Experimental Set-up.

Raman scattering

The laser pulse is found to be highly unstable to plasma Raman type instabilities. In particular, the transmitted beam becomes heavily modulated due to Forward Raman Scattering (FRS). Indeed it has been found previously that as the pulse length decreases from around 3 ps to less than 1 ps with similar energies, Raman scattering at larger angles is suppressed in favour of direct forward Raman scattering[6]. But even at such high intensities, where FRS growth rates are at a maximum[7], it is predicted from the analytic growth rates that the direct Raman forward scattering cannot grow with sufficient e-foldings to completely modulate the laser pulse, if it were to grow directly from thermal noise[8]. Indeed irrespective of intensity, scattering of laser energy at larger angles (sideways, or directly backwards), should always have a greater growth rate than direct forward scattering. This is because laser light can be scattered directly by a 3-wave process for the large angle scattering, where the incoming photon and the scattered one can be wave-matched with a plasmon. However, this is not true of the FRS, which can only take place through the action of a four wave process – both upshifted and downshifted scattered waves are required in this mechanism for wavematching. Fortunately 3D particle-in-cell (PIC) simulations are now possible which can adequately describe the behaviour of the laser beam, including the complex interplay between several different instabilities[9,10].

It is observed in such simulations that off-angle Raman instabilities do indeed have a much larger growth rate, and can cause severe scattering from the front of the pulse, resulting in localised pump depletion. This large intensity ramp is then able to drive a large amplitude plasma wave, which can act as a sufficiently large seed to stimulate the growth of FRS. Once FRS is initiated, the smaller k_p plasma wave destroys the favourable long length uniform density plasma in which large angle instabilities thrive, and this, along with the plasma heating due to these initial instabilities, can effectively damp the large angle Raman Scattering at later times.

The evidence for this behaviour is clearly seen in Figure 2a.

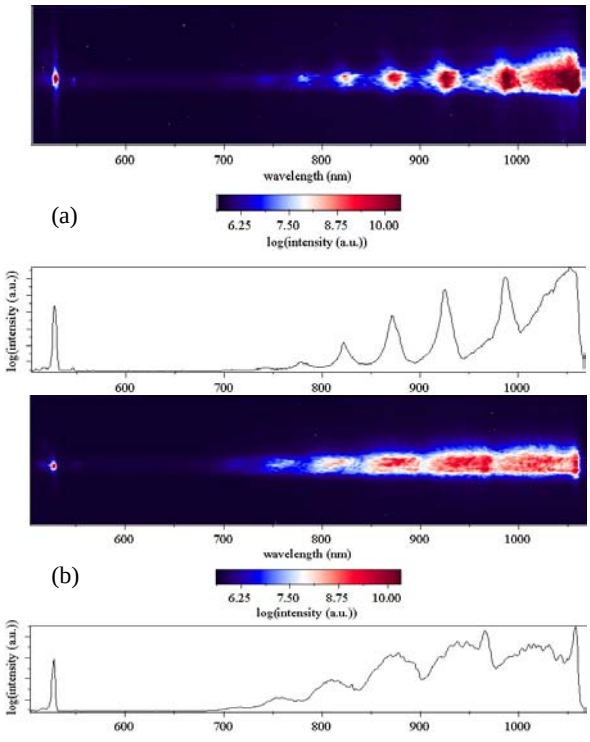

Figure 2. Transmitted beam spectra with :-
a) $n_e = 4 \ . \ 10^{18}$ cm^{-3} and I = 2 . 10^{19} Wcm^{-2}
b) $n_e = 7.5 \ . \ 10^{18}$ cm^{-3} and I = 1 . 10^{19} Wcm^{-2}

This shows the transmitted laser light spectrum for two different densities. Figure 2a shows up to 8 satellite frequencies of the transmitted light on the blue-shifted side of the fundamental laser frequency, plotted as log of intensity. The satellites are very clearly differentiated from one another, and are constantly spaced by intervals of the plasma frequency. The spectrum has a similar character on the red side of the fundamental.

However, one basic difference exists between plasma Raman scattering and molecular Raman scattering, and that is the excitation of the plasma wave. The plasmons that constitute the plasma wave are not fixed quantum states. As the plasma wave

grows to large amplitude, in particular when the plasma wave amplitude δn approaches the initial plasma density n_0, then the plasma wave can no longer be described as the linear superposition of the generated ω_p plasmons. Indeed the density highs tend to form peaks whereas the lows form shallow troughs. This non-linearly steepened plasma wave can be fourier-decomposed into its harmonic constituents as follows:-

$$\frac{n^m}{n_0} = \frac{m^m}{2^{m-1}m!}\left(\frac{\delta n}{n_0}\right)^m$$

where n^m is the amplitude of the m-th harmonic of the plasma wave of peak amplitude $\delta n/n_0$.

One can therefore see why sidebands are so efficiently generated even though the growth of the FRS predicts that in 1 ps there is barely enough time for the first electromagnetic sideband to grow to large amplitude. Evidently the cascading is evidence of scattering from the non-linear steepened plasma wave, rather than a step-wise scattering of the successive electromagnetic sidebands off a linear plasma wave (i.e. one that has a harmonic content only at ω_p).

Evidence of wavebreaking

Clearly increasing the growth of the plasma wave due to further increases in the FRS growth rate, cannot lead to an indefinitely increasing plasma wave amplitude. Mori *et al*. have derived the spatio-temoral growth rates for the FRS instability in the relativistic regime ($a_0 > 1$) [7]. They find that the FRS growth rate actually saturates with intensity and in this regime one can only achieve further plasma wave growth by its dependence on density. This is shown in Figure 2b, where a higher density is used with all other parameters the same as in Figure 2a. The sidebands can still be discerned in this Figure (with a slightly greater seperation due to the dependence of the plasma frequency on density $\omega_p = n_e e^2/ \varepsilon_0 m$. However, the sidebands are noticeably broader. This is even though the scattering is over the same pulse length as before. This increased width suggests that the scattering plasma wave is losing coherence.

Energetic electron production and the dependence on wavebreaking

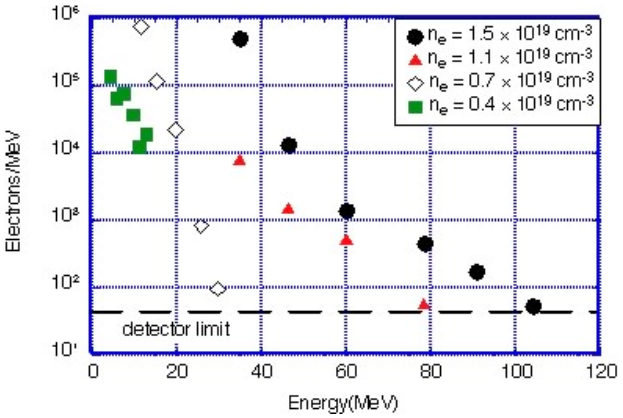

Figure 3. Electron spectra for a variety of different densities.

The exact reason for this loss of coherence is demonstrated by the spectrum of electrons accelerated by the generated plasma wave, Figure 3. Figure 3 shows that even at 4 x 10^{18} cm^{-3}, when the plasma wave is still coherent, there are a significant number of electrons accelerated to quite high energy (up to 13 MeV before they fall below the detection limit of our detector). This is necessarily due to the hot temperature that such plasmas can reach due to the optical field ionisation, and the presence of other large angle electron plasma oscillations. In the large electric fields of the plasma wave, it is possible to further accelerate these electrons to high energies, even if they are not trapped for long distances by the plasma wave. However one can see that as the density is increased to 7.5 x 10^{18} cm^{-3}, the number and maximum energy of the electrons increases markedly. This is even more so the case as the plasma wave growth rate is increased at yet higher densities. One can see that not only is the maximum energy of the electron distribution increasing, but that it is gaining a significant "tail" to the distribution that can no longer be fitted with a single Maxwellian profile. If one considers all the electrons accelerated, not just those within the acceptance cone of our detector, one finds upwards of 10^{12} relativistic electrons, or in other words practically all the electrons from within the focal volume over a Rayleigh length. Clearly such a huge fraction of accelerated electrons cannot be simply explained by trapping of hot electrons. The electrons are actually generated by wavebreaking[4]. The push on the electrons forming the peaks of the non-linear plasma wave is so great, that the restoring force they generate is no longer sufficient to return them to their initial displacement. Indeed charge sheets can cross longitudinally, such that instead of feeling a returning force, some of the electrons - those travelling in the same direction as the phase velocity of the plasma wave - can feel a continuing acceleration in the direction in which they were travelling. Once they can reach relativistic speeds, they can stay in phase with the plasma wave until they gain enough energy that they begin to outrun the wave and so become de-phased from it. A simple treatment that considers sinusoidal plasma wave, shows that the maximum energy to which electrons can be accelerated before de-phasing is of the order $2\gamma_p^2 \delta n/n_0 \cdot m_e c^2$, where γ_p is the relativistic factor of the plasma wave, and in the underdense regime is roughly given by $\gamma_p \approx \omega_0/\omega_p$. So for densities around 10^{19} cm^{-3}, $\gamma_p \approx 10$, and the maximum expected energy is approximately 100 MeV. Therefore once the wave fully breaks, one can see that a significant number of electrons are accelerated until they are de-phased from the wave.

Hence the broadening of the satellites in the transmitted spectra is a clear signature of the onset of wave-breaking. Indeed at the higher densities, the broadening is so severe that it becomes difficult to distinguish the individual satellites. Note also that there is clear evidence of the increased growth of the FRS at higher density from Figure 2a to Figure 2b even though the intensity of the second shot was slightly lower. This reiterates the weak dependence of the FRS growth rates on intensity in this regime.

Results using the strip detectors instead of the individual silicon barrier detectors

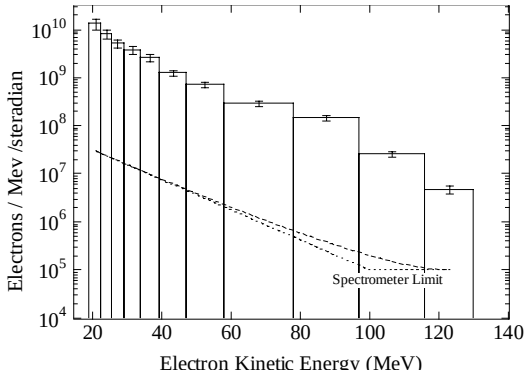

Figure 4. Highest energy electrons recorded using strip detectors.

The use of the strip array allows one to obtain a higher resolution energy spectrum of the accelerated electrons, and also allows a slightly greater collection and thus higher sensitivity, Figure 4. This particular shot was taken at a density of around 2 x 10^{19} cm^{-3}, for which the maximum expected linear dephased energy is 50 MeV. Clearly some electrons are accelerated beyond this energy. Indeed a few electrons are

accelerated at more than twice this energy. It has been suggested by Gordon *et al*.[11], that this acceleration beyond the linear dephasing limit may well be due to the influence of the large current of electrons initially accelerated by the wavebreaking. In effect this initial bunch of electrons can set-up a large wake in its tail as it travels through the plasma and can accelerate electrons trailing behind to even higher energies, in an almost two step process.

Discussion

It has been shown that an intense laser beam travelling through underdense plasma is highly susceptible to the Raman Forward Scatter Instability. This instability can grow to large amplitude due to the pulse erosion of the front of the intense pulse. The growth can be sufficient to fully modulate the laser beam and to grow a large amplitude plasma wave in its wake. Wave-breaking of this plasma wave can efficiently produce an intense source of energetic electrons. The possibility of using these intense electron sources has already been shown for many applications, such as the generation of short-lived radioisotopes[12], gamma-ray radiography[13] , and neutron production[14]. As higher repetition rate lasers with these intensities become progressively more available, the prospect of these uses with a high repetition rate electron source [15] becoming common appears to be possible.

References

1. T.Tajima and J. Dawson, "Laser electron accelerator," Physical Review Letters 43, 267 (1979).
2. J. F. Drake, P. K. Kaw, Y. C. Lee *et al*., "Parametric instabilities of electromegnetic waves in plasmas," Physics of Fluids 17 (4), 778 (1974).
3. D. W. Forslund, J. M. Kindel, and E. L. Lindman, "Theory of stimulated scattering processes in laser-irradiated plasmas," Physics of fluids 18 (8), 1002 (1975).
4. Modena, Z. Najmudin, A. E. Dangor *et al*., "Electron acceleration from the breaking of relativistic plasma waves.," Nature 377, 606 (1995).
5. V. Malka, C. Coulaud, J. P. Geindre *et al*., "Characterization of neutral density profile in a wide range of pressure of cylindrical pulsed gas jets," Review of Scientific Instruments 71 (6), 2329-2333 (2000).
6. Z. Najmudin, "Parametric Instabilities in the Interaction of High-Intensity Short-Pulse Lasers with Under-Dense Plasmas," , Imperial College, University of London, 1995.
7. W. B. Mori, C. D. Decker, D.E. Hinkel *et al*., "Raman forward scattering of short-pulse high-intensity lasers," Physical Review Letters 72 (10), 1482 (1994).
8. Z. Najmudin, R. Allott, F. Amiranoff *et al*., "Measurement of forward Raman scattering and electron acceleration from high-intensity laser-plasma interactions at 527 nm," IEEE Transactions On Plasma Science 28 (4), 1084-1089 (2000).
9. C. D. Decker, W. B. Mori, and T. Katsouleas, "Particle-in-Cell Simulations of Raman Forward Scattering from Short-Pulse High-Intensity lasers," Physical Review E 50, R3338-R3341 (1994).
10. D. F. Gordon, B. Hafizi, P. Sprangle *et al*., "Seeding of the forward Raman instability by ionization fronts and Raman backscatter," Physical Review E 64, 046404 (2001).
11. D. Gordon, K. C. Tzeng, C. E. Clayton *et al*., "Observation of electron energies beyond the linear dephasing limit from a laser-excited relativistic plasma wave," Physical Review Letters 80 (10), 2133-6 (1998).
12. M. I. K. Santala, Z. Najmudin, E. L. Clark *et al*., "Observation of a hot high-current electron beam from a self- modulated laser wakefield accelerator," Physical Review Letters 86 (7), 1227-1230 (2001).
13. R. D. Edwards, M. A. Sinclair, T. J. Goldsack *et al*., "Gamma - radiography using a laser-plasma accelerator," To appear in Applied Physics Letters (2002).
14. W. P. Leemans, D. Rodgers, P. E. Catravas *et al*., "Gamma-neutron activation experiments using laser wakefield accelerators," Physics of Plasmas 8, 2510 (2001)
15. V. Malka, J. Faure, J. R. Marques *et al*., "Characterization of electron beams produced by ultrashort (30 fs) laser pulses," Physics of Plasmas 8 (6), 2605-2608 (2001)

Magnetic field measurements from polarimetry of XUV harmonics

U Wagner, P Norreys, D Neely, R Clarke

Central Laser Facility, CLRC Rutherford Appleton Laboratory, Chilton, Didcot, Oxon, OX11 0QX, UK

R G Evans

Physics Department, University of York, York, YO10 5DD

M Tatarakis, F N Beg, A Gopal, I Watts, M S Wei, A E Dangor, K Krushelnick

Blackett Laboratory, Imperial College of Science, Technology and Medicine, London SW7 2BZ, UK

E L Clark

Radiation Physics department, AWE plc, Aldermaston, Reading, RG7 4PR, UK

M Zepf

Department of Pure and Applied Physics, The Queen's University Belfast, UK

Main contact email address: *kmkr@ic.ac.uk*

Introduction

The interaction of an ultra-strong electromagnetic wave with matter is of great interest for fundamental and applied physics. In particular, recent developments in high-power, short-pulse laser-technology have facilitated the construction of 100 Tera-Watt lasers. These machines have allowed fundamental interactions between an electromagnetic-field (with intensities up to 10^{20} W/cm^2) and a nearly solid-density plasma to be studied experimentally for the first time. The plasma is created quasi-instantaneously when the leading edge of the laser pulse irradiates the solid surface. The strongly non-linear interaction between the electromagnetic-field and the plasma gives rise to ultra-strong DC-magnetic fields. These fields can be generated by strong return currents due to charge-separation between electron and ions, caused by the ponderomotive force of the laser-pulse [1,2,3]. Consequently the measurement of these DC-fields is essential for understanding the fundamental nature of the laser solid-density-plasma interaction and the properties of the plasma itself. This report will discuss the development of a new method for measuring these fields which has been successfully implemented in an experiment [4,5]. In this experiment, magnetic fields up to 700 MG have been measured for the first time.

Experiment

The experimental set-up is shown in Figure 1.

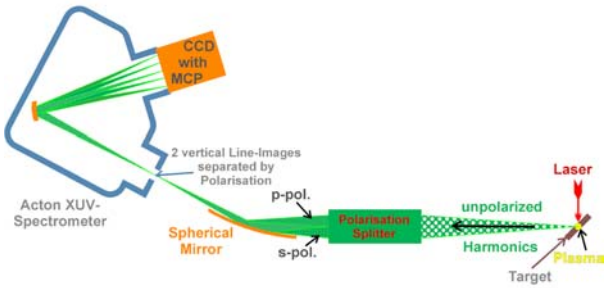

Figure 1. Experimental setup.

The CPA-beam from Vulcan (0.7-1 ps, 1054 nm, 100 J on target) is focused by an f/4.8 Parabola to a spot size of 7-10 µm, resulting in intensities up to 10^{20} W/cm^2. The magnetic field inside the plasma has been measured by observing the change of the polarisation properties of the self-generated harmonics emitted from the critical surface [6]. These harmonics propagate through the magnetised area inside the plasma. Computer simulations performed with a PIC-code show that for the chosen geometry the magnetic field is perpendicular to the propagation direction of the harmonics [3]. Therefore the change of the polarisation-properties is due to the Cotton-Mouton-effect. Hence the magnetic field inside the plasma can be determined by measuring the change of the polarisation properties. For this purpose a multi-channel VUV-polarimeter was constructed.

To perform magnetic-field measurements with harmonics of higher order than 5, a VUV-polarimeter is needed, as the wavelength of these harmonics are below 200 nm for the Nd-glass-laser Vulcan, that operates at 1053 nm. Such a polarimeter has been built and was successfully used in the experiment. The set-up of the instrument is shown in Figure 1. The VUV-polarisers are a triple-mirror-configuration, which are partially polarising due to the Fresnel-refection on the gold-coated mirror surfaces. Two VUV-polarisers were set-up orthogonally to measure the p- and the s-component of the harmonics. The polarised beams are then focused onto the slit of an Acton spectrometer, enabling the simultaneous measurement of the higher order harmonics. An open microchannel-plate (MCP) coupled to a charge-coupled-device (CCD) by a fiber-optic-bundle was used as the detector.

Results

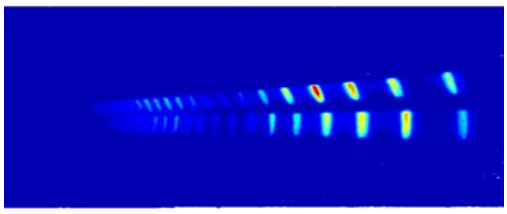

Figure 2. Raw data from MCP (7th to 25th harmonic).

The magnetic-field can be calculated from the measured s/p-ratio. The measurement of these high order harmonics was performed with the VUV-polarimeter described in the last section. A set of raw data acquired during the experiment is shown in Figure 2.

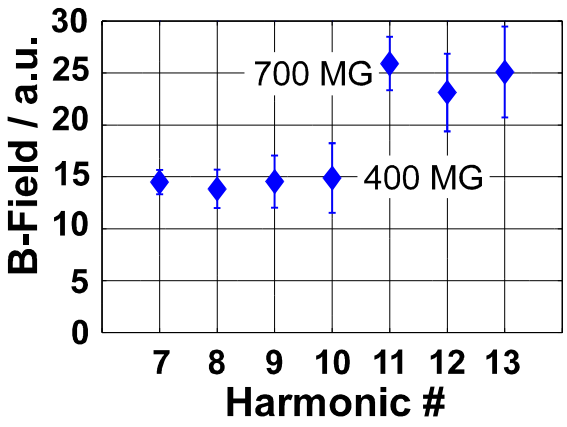

Figure 3. Magnetic field calculated from VUV data.

The magnetic field calculated from this data is shown in Figure 3. The most notable feature in the data obtained with this polarimeter is the jump from 14 a.u. to 25 a.u. in field strength at the 11^{th} harmonic. If we assume a field strength of 400 MG for the lower order harmonics (7^{th} to 10^{th}), as obtained from the optical-UV-polarimetric measurements [4], then the higher order harmonics propagate through a plasma with a magnetic field of 700 MG. Detailed 2.5-dimensional particle-in-cell-computer-simulations predict DC-fields of 650 MG, in good agreement with our observations [5].

Conclusion

The measurements described here have been the first detailed study of near GigaGauss magnetic fields in laser-produced-plasmas. A VUV-spectrometer was constructed and deployed to measure magnetic-fields in laser-produced-plasmas for the first time. These measurements indicate DC-fields up to 700 MG in good agreements with detailed computer simulations. The VUV-polarimeter is essential to diagnose multi-GigaGauss DC-magnetic-fields that are expected to be generated with the new Vulcan PetaWatt-laser. Moreover there are many interesting physical problems, such as the precise topology of the magnetic-field, generated around the critical surface, which need to be addressed in future experiments.

References

1. R. N. Sudan., Phys. Rev. Letters,70, 3075 (1993).
2. J. A. Stamper. *et al.,* Phys. Rev. Letters, 26, 1012 (1971).
3. Pukhov.A *et al.,* Phys. Rev. Letters, 76, 3975 (1996).
4. M. Tatarakis *et al.,* Nature, 415, 280 (2002).
5. M. Tatarakis *et al.,* Physics of Plasmas, 9, 2244 (2002).
6. P. A. Norreys. *et al.,* Phys. Rev. Letters, 76, 1832 (1996).

Absorption spectroscopy of Al XIII Ly-α Radiation by a Fe XXIV plasma

A Gouveia, J Hawreliak, I R Al'miev, P Sondhauss, J S Wark

Department of Physics, Clarendon Laboratory, University of Oxford, Parks Road, Oxford OX13PU, UK

O Renner

Institute of Physics, Czech Academy of Sciences. 18221 Prague, Czech Republic

D M Chambers, P A Pinto

Steward observatory, University of Arizona, Tucson, AZ85721, USA

R S Marjoribanks

Department of Physics, McLennan Physical Laboratories, University of Toronto, Toronto, Ontario M5S 1A7, Canada

Tianjiao Liang

Institute of physics,Beijing, China

Main contact email address: *gouveia@physics.ox.ac.uk*

Introduction

Photopumped X-Ray Lasers have posed a considerable experimental challenge for several decades. Although photopumping was one of the first X-Ray laser schemes to be proposed[1)] and despite simulations showing that lasing can be achieved with this scheme, its experimental demonstration has so far proved unsuccessful.

The photopumping scheme relies on having a frequency match between spectral lines of two different elements at different ionization stages. In this way the emission from a pump plasma should couple to the coincident transition in the second plasma and pump the populations of the upper level that should then decay to an intermediate level, thus achieving population inversion. A number of possible schemes has been noted in the literature[2)].

We performed a photopumping experiment in Target Area East with the Aluminium Iron Scheme[3)]. Even though we have not been able to observe lasing, we have observed absorption of the H-like Aluminium Ly-α radiation by the Li-like Iron 5-2 transitions – a necessary condition for the photopumped laser to occur.

The Aluminium Iron photopumping Scheme

This Scheme uses a line coincidence between the Al XIII 1s-2p transitions at 7.1749Å and 7.1695Å, and the Fe XXIV 2s-5p lines at 7.1667Å and 7.1726Å. The Al Ly-α emission couples to the iron transition exciting the 5p level. The remaining n=5 levels are then populated by collisional mixing. Lasing is expected to occur by the decay of the n=5 levels of the iron plasma into n=4 giving the XUV lasing lines at around 70Å.

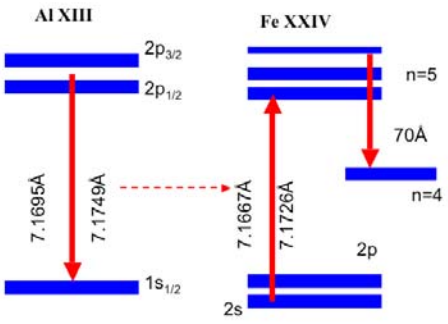

Figure 1. Simplified Grotrian diagram of the Aluminium-Iron photopumping scheme.

Previous simulations[4)] predicted that gain could be achieved in the lasing line. However we were unable to confirm this experimentally.

Experimental setup

Three of the Vulcan main six beams were set up in line focus geometries irradiating the target from one side and creating the line focus in the North-South direction of the chamber. The main diagnostic used was a vertical variant Johann spectrometer (VJS). This is a crystal spectrometer that allows very high resolution without compromise of luminosity[5)]. In the later part of the experiment this was replaced by a non-imaging flat field spectrometer in order to observe the expected lasing line in the XUV region. Both of these instruments were used on axis with the line focus direction on target surface.

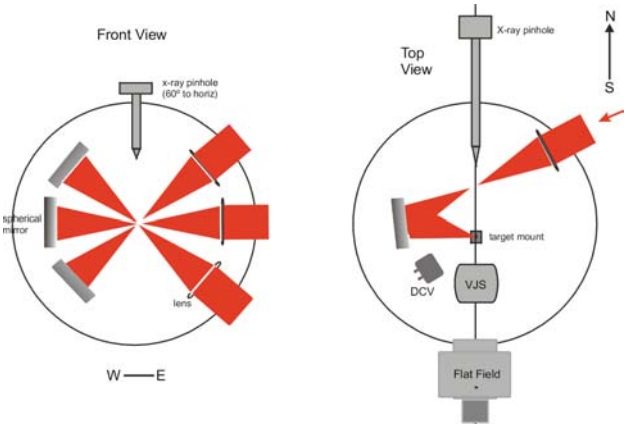

Figure 2. Experimental setup inside TAE target chamber VJS-Vertical Johann Spectrometer. DCV-Double Crystal Vertical dispersion spectrometer.

Absorption and fluorescence measurements

Prior to attempting a proper photopumped X-ray laser experiment we undertook a series of spectroscopic measurements in the 7Å region to try to characterize the pumping mechanism as best as possible.

Using a target geometry as seen in Figure 3 composite targets made of 0.2mm wide Aluminium foils on the side of Iron foils of variable width created two parallel streaming plasmas. This setup allowed us to observe the profile of the Al Ly-α emission as it crossed the different lengths of iron plasma.

For the proper photopumping experiment we used a different target geometry where an Al foil overlaps an Iron foil and the focal region is set over the intersection of the two materials (right hand side of Figure 3).

We also attempted to measure the fluorescence of the 5-2 Iron transitions as a function of the Al Ly-α pumping by setting the VJS spectrometer to look at a different (2p-5d) iron transitions in the proper photopumping geometry. However analysis of the results to date is not conclusive.

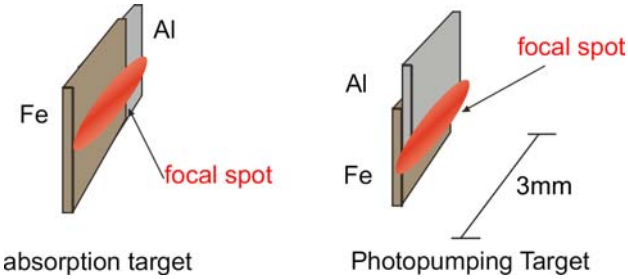

Figure 3. Schematic of the target geometries used.

In Figures 4 and 5 one can see comparative lineouts of the spectrum obtained with a pure Aluminium target and with the one observed by an Al-Fe target with the same experimental conditions. A significant decrease in the Al Ly-α emission can be seen in the lower frequency side of the spectrum.

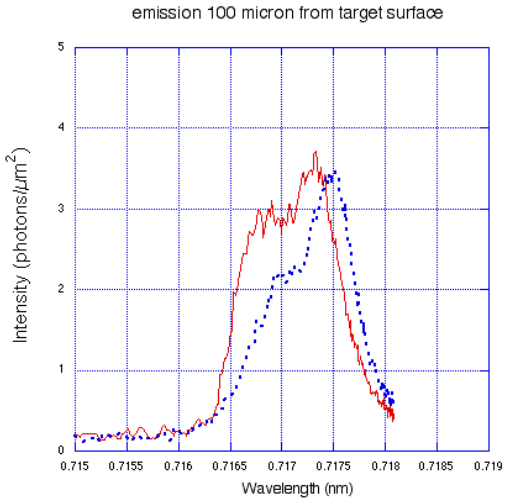

Figure 4. Comparative lineouts of the spectra obtained in the absorption geometry at 100μm from the target surface. Solid line: 0.2mm of Aluminium behind 1 mm of Iron. Dotted line: 0.2mm of Aluminium.

We are attempting to model this phenomenon with a full 3D radiation transfer post-processor to MED103 that takes into account the characteristics of the VJS spectrometer. Simpler 1D simulations made prior to this experiment predicted that absorption of the iron line would occur.

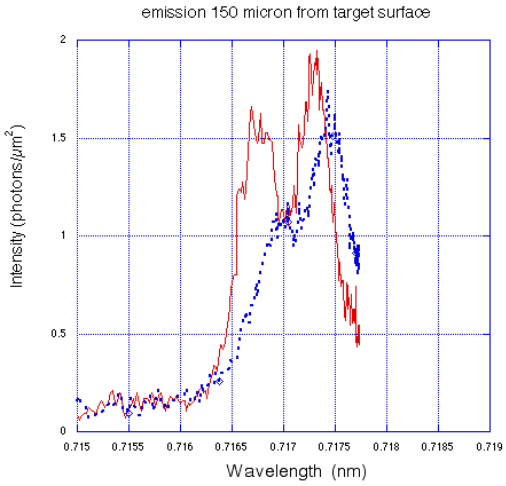

Figure 5. Lineouts of the spectra obtained in the absorption geometry:at 150μm from the target surface. Solid line: 0.2mm of Aluminium behind 1 mm of Iron. Dotted line: 0.2mm of Aluminium.

Conclusions

In the context of a photo-pumped X-ray laser experiment we have observed absorption of the Aluminium XIII Ly-α emission by the 2s-5p transition in a Fe XXIV plasma. This result should allow us to modify our models and better understand the radiation transfer and atomic physics of the photopumping mechanism.

References

1. A. V. Vinogradov *et. al*
Sov. J. Quant. Elect., 5, No.1 July 1975 pp 59

2. Joseph Nilsen,
Applied Optics, 31, No. 24 pp 4957 (1992)

3. Y. T. Lee *et. al.*
JQSRT, 43, No 4 pp 335-345 (1990)

4. I. R. Almiev, S. J. Rose, J.S. Wark
JQSRT, 71 pp 129-138 (2001)

5. O. Renner *et. al.*
Rev. Sci. Instrum, 68 (6) pp 2393 (1997)

X-ray Laser Thomson Scattering

F Y Khattak, D Riley, R Keenan, S Topping, A M McEvoy, J Angulo, C L S Lewis

School of Mathematics and Physics, Queen's University of Belfast, University Road, Belfast, BT7 INN, N. Ireland, UK

M Notley, D Neely

Central Laser Facility, CLRC Rutherford Appleton Laboratory, Chilton, Didcot, Oxon, OX11 0QX, UK

Main contact email address: *F. Khattak@qub.ac.uk*

Introduction

Thomson scattering is capable, in principle, of characterising a range of plasma parameters without perturbing the plasma significantly. In this technique photons of energy less than the rest mass energy of electrons are scattered from electrons and detected as a spectrally resolved signal. It has long been used as a diagnostic for the measurement of plasma temperature in θ-pinch and tokamak devices[1-5]. However, because of the relatively fast temporal evolution and the small scale-length, the technique has limited application in the context of laser-produced plasmas[6-10]. Moreover, the reported studies have so far been limited to maximum densities of ~10^{20} cm^{-3} by using 4ω of Nd:glass laser (263nm). Recently it has been proposed to extend this technique to the regime of very high-density plasmas using x-rays and x-ray lasers[11-12]. We report here on an experiment carried out at the Rutherford Appleton Laboratory using Vulcan in an attempt to extend Thomson scattering to the high density regime using a Ne-like Ni x-ray laser (231Å, 50ps duration, 3mJ). This, in principle, has the potential to probe plasma well above the solid density. Therefore, independent measurements of density and temperature can be made in a plasma regime where the other established diagnostic techniques are not applicable.

The theory of Thomson scattering has been extensively reviewed[1-3]. A basic theoretical background with the relevant formulation is presented here. In this technique, plasma is illuminated by monochromatic radiation and the spectrum of light scattered from the plasma is measured. The incident radiation of wave vector $\mathbf{k}_o$ is scattered from a plasma wave vector $\mathbf{k}$ and collected at angle θ with respect to the incident wave vector. Assuming that the magnitude of the incident wave vector does not change during the scattering process, then the scattered wave vector $\mathbf{k}_s$ can be worked out from the following wave-vector geometry as:

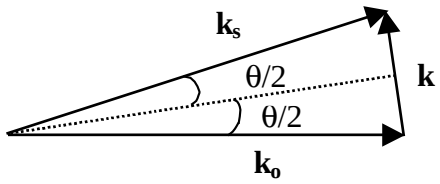

$$|\mathbf{k}| \approx 2|\mathbf{k_o}| sin\left(\frac{\theta}{2}\right), \text{ with } |\mathbf{k}_o| = \frac{2\pi}{\lambda_o}$$

$$\mathbf{k} = \mathbf{k_s} - \mathbf{k_o}$$

The scattered signal on the detector is integrated over a volume determined by the overlap between the focal volume of the collecting optics of the detector and focusing optics of the probe beam. The spectral distribution of the scattered signal is a function of the parameter α defined as: $\alpha = \frac{1}{|k|\lambda_D}$

Here $\lambda_D = (kT_e/4\pi n_e e^2)^{1/2}$ is the Debye length in the plasma with n_e, and T_e being the electron density and temperature respectively. Using the scattering parameter, plasmas are generally categorized into three main domains. In the limit where $\alpha << 1$, scattering occurs from oscillations of wavelength much less than the Debye length. The scattered spectrum in this limit is contributed mainly by the unshielded electrons and thus has a Gaussian distribution in wavelength space that reflects the thermal distribution of the electrons. In the domain near $\alpha = 1$, the scattered spectrum has a flat-topped distribution with distinct shoulders appearing on each wing. In the case of $\alpha > 1$, the contribution comes from oscillations of wavelength longer than the Debye length. This is called the *collective domain.* In this domain, the scattered spectrum has two distinct features. The maximum part of the scattered energy goes in to the central feature having width of the order of ion sound speed in the plasma. This feature is referred to as the ion feature. The other, electron feature, develops into two prominent satellites shifted by the Bohm-Gross frequency ω_{BG} from the main. In principle, all the three domains can be accessed using spectrometers at different angles (θ = 90° & 162° in our case) by probing the plasma with the x-ray laser pulses.

Experimental Arrangement

The general experimental arrangement is sketched in Figure 1.

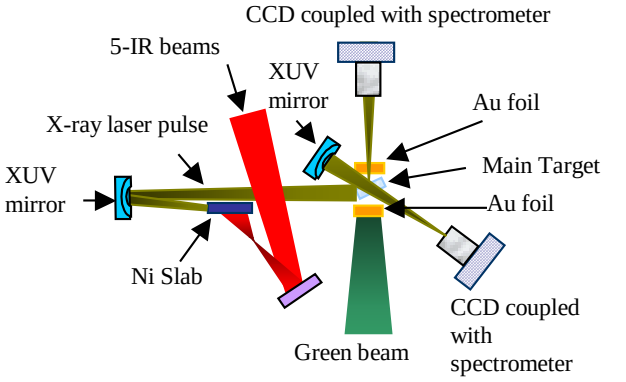

Figure 1. A schematic of the experiment showing the radiative-heating configuration. For clarity only one of the green beams is shown.

These experiments were performed with the Vulcan high power laser facility at the Rutherford Appleton Laboratory. Five of the main six beams were accessed as IR (λ= 1.053μm) and a pulse length of 80ps FWHM duration. The backlighter beams are used frequency doubled to a wavelength of 527nm and having a pulse width of 550ps FWHM duration. The Ne-like Ni x-ray laser pulses are produced by focussing five of the main six beams on a Ni slab target in a line focus configuration.

The long line-focus produced by overlapping foci of the 5 beams on the slab target was x-ray-imaged onto a CCD through crossed slits. One such image is shown in Figure 2a. The x-ray laser beam is imaged onto the scattering plasma with a magnification of x2 using a multi-layered XUV mirror. Pointing of the x-ray laser is done by imaging the x-ray laser onto a cross-wire in the target plane and relaying the image onto a CCD using another similar multi-layered mirror. Figure 2b shows an image of the x-ray laser beam. The intensity of the x-ray laser at the plane of the scattering target is ~ 10^{10} W/cm^2.

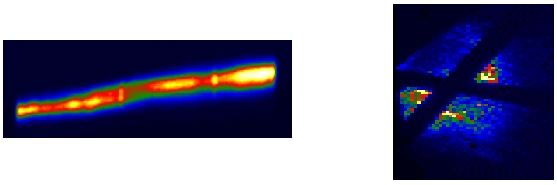

(a) (b)

Figure 2. (a) Cross-slit x-ray image of the line focus (b) X-ray laser imaged onto a cross-wire.

The scattering plasma is generated using two different configurations, radiative-heating and direct heating. In the radiative-heating case, the two backlighter beams are focused onto two foils (0.1μm thick gold coated onto 0.9μm mylar) one each on the two opposite sides of the 3μm thick, 0.5mm square scattering target. The focal spot and the energy of the beams are varied to change the irradiance on the Au foil. The x-rays produced from the gold foils are used to irradiate the CH foil and generate uniform density plasma. The distance between the two foils is varied between 6mm and 10mm. In the second case, the main CH target is directly irradiated from opposite sides with two beams each having intensity of $5x10^{12}$ - $8x10^{13}$ W/cm^2 on the target. The plane of the main target makes a 45^o angle with the horizontal as well as vertical in order to help reduce the absorption of the scattered signal.

The scattered signal is imaged onto CCDs with the aid of two flat-field imaging spectrometers at 90^o, and 162^o with a spectral resolution of ~ 10^{-4}. The imaging mirror of a 28^o spectrometer is replaced with a multi-layered mirror placed inside the chamber on the opposite side of the target to have a spectrometer at 162^o. The CCD on the 90^o spectrometer is replaced with a streak camera to resolve the scattered signal from the plasma emission and to avoid saturation of the detectors.

Discussion

Because of the very small Thomson cross-section ($6.65x10^{-25}$ cm^2 for free electrons), it requires a reasonably high-energy probe beam to detect a signal above the noise level. That is, one should have a signal to noise level greater than 1. The noise level can be estimated from the continuum plasma emission. Figure 3 shows the threshold of laser intensity required for the probe beam to have signal to noise level of the Thomson signal detected at the two spectrometers. It can be seen that by decreasing the time-bandwidth of the detector, the intensity of the probe required at the target also reduces. In case of the 10μs detector bandwidth, the threshold is very close to the intensity of the x-ray laser available on target (~10^{10} W/cm^2). It is, therefore, required to replace the time integrated CCD with a time resolved detector (an x-ray streak camera, for example) to resolve the scattered signal from the self-emission. Our calculations and simulations, to appear in a later publication, indicate that the plasma can be probed at a time when there is less emission as well as transparent to the x-ray laser. This could be tried in future with the use of a time resolved detector instead of a time integrated CCD. Although the experiment was not successful in the sense of getting scattered spectrum, enough is learnt to make it worth trying next time.

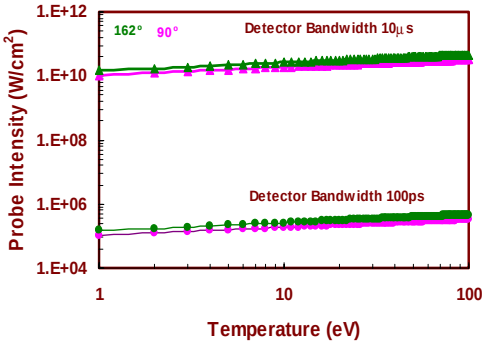

Figure 3. Threshold of the x-ray laser to overcome the background noise level for two different detector-bandwidths.

References

1. E.E. Salpeter, Phys. Rev. 120, 1528 (1960)
2. D.E. Evans and J. Katzenstein, Rep. Prog. Phys. 32, 207 (1969)
3. J. Sheffield, Plasma Scattering of Electromagnetic Radiation, Academic Press, New York (1975)
4. S.A. Ramsden and W. E. R. Davies, Phys. Rev. Lett. 16, 303 (1966)
5. N. C. LuhmanJr. And W. A. Peebles, in , Laser Handbook, edited by M. Bass and M. L. Stitch, North-Holland, Amsterdam, 5, 455 (1985)
6. B. La Fontaine *et al.*, Phys. Plasmas 1, 2329, (1994)
7. S. H. Glenzer *et al.*, Phys. Rev. Lett., 82, 97, (1999)
8. S. H. Glenzer *et al.*, Phys. Plasmas 6, 2117, (1999)
9. Kano and K. Nakatani, Rev. Sci. Instrum., 71, 2716, 2000
10. J. Hawreliak *et al.*, J. Quant. Spectosc. Radiat. Transfer 71, 383 (2001)
11. O. L. Landen *et al.*, J. Quant. Spectosc. Radiat. Transfer 71, 465 (2001)
12. H. A. Baldis *et al.*, J. Phys. IV, France 11 Pr2-469, (2001)

Measurement of the duration of X-ray lasing pumped by Vulcan CPA

Y Abou-Ali, M Edwards, G J Tallents

Department of Physics, University of York, Heslington, York, YO10 5DD, UK

R Keenan, CLS Lewis, S Topping

School of Mathematics and Physics, Queens University of Belfast, Belfast, BT7 INN, UK

O Guilbaud, A Klisnick, D Ros

Laboratoroire de Spectroscopie Atomique et Ionique,Université Paris-Sud,91405 Orsay, France

R Clarke, D Neely, M Notley

Central Laser Facility, CLRC Rutherford Appleton Laboratory, Chilton, Didcot, Oxon, OX11 0QX, UK

Main contact email address: *yaa100@york.ac.uk*

Introduction

The measurement of the pulse duration of X-ray laser output is important for potential applications and to help understand the gain and propagation conditions in the gain media. In this article, we report the measurements of the X-ray laser pulse durations for Ni-like silver and Ne-like nickel using a new X-ray streak camera with 700 fs temporal resolution and we obtain an estimate of the duration of the X-ray laser gain by temporally resolving the spectrally integrated resonance line emission from states near in energy to the upper lasing level.

Experiment

Figure 1 shows the geometry of the experimental set-up inside the target chamber and the position of the diagnostics.

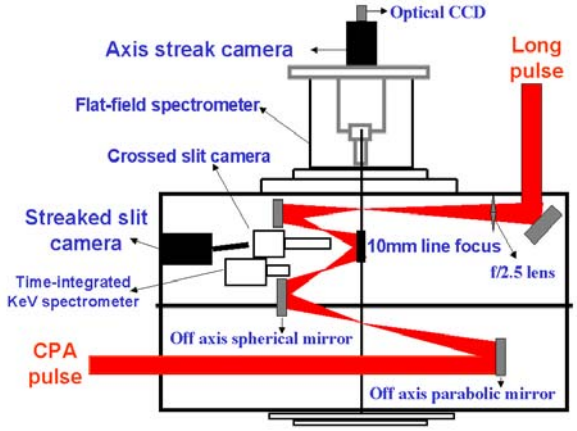

Figure 1. Experimental set-up and diagnostic positions.

X-ray lasing was produced in Ni-like silver at 13.9 nm and Ne-like nickel at 23.1 nm by irradiating solid silver or nickel slab target with two beams of wavelength 1.06 μm from the Vulcan glass laser. For Ne-like nickel, a pre-plasma was formed with a background pulse of duration 280 ps and peak irradiance 2×10^{13} Wcm^{-2}. The main pulse irradiance is enhanced by chirp pulse amplification (CPA) to give a pulse duration of 1.2 ps and peak irradiance 7×10^{15} Wcm^{-2}. So as not to over-ionise the plasmas, the laser energy for Ni-like silver experiments was reduced to give irradiances of approximately 5×10^{12} Wcm^{-2} and 2×10^{15} Wcm^{-2} for the background and main pulse respectively.

The background pulse was produced from a component of the uncompressed main pulse and hence arrived on target without random jitter relative to the main pulse. The main pulse was focused by a parabola and a spherical mirror onto the target to produce a line focus of length 12 mm and width 100 μm. The line focusing for the background pulse was obtained using an f / 2.5 focal lens and spherical mirror to generate a line focus of length 16 mm and width 100 μm (see Figure 1). The peak-to-peak separation of the two pulses was controlled by varying the optical path length of the long pulse via a timing slide within the target area. For results reported in this article, we used a delay between pulses of 200 ps (for Ni-like silver) or 300 ps (for Ne-like nickel). Since the duration of gain, ~ 10- 20 ps for Ni-like ions and 30-40 ps for Ne-like ions, is comparable or shorter than the X-ray propagation time along the whole length of the plasma (33 ps/cm), it is necessary to incorporate travelling wave pumping to ensure that the X-ray pulse and the gain onset coincide[1]. A combination of three effects was used to implement an optimum travelling wave (TW) velocity at the speed of light c:

i). there is an intrinsic travelling wave velocity of 2.5c produced by the off-axis focusing geometry.

ii). an additional 300 lines/mm grating was employed before the compression gratings to reduce the laser pulsefront velocity to close to c along the line focus.

iii). for fine tuning of the pulsefront velocity, a technique of slightly tilting the second pulse compressor grating was employed[2].

The X-ray laser output was recorded using a flat field grating spectrometer with a 1200 lines/mm, aperiodically ruled grating, coupled either with an X-ray CCD or with the Axis Photonique streak camera[3] equipped with a KI photocathode. The spectrometer was initially operated with a CCD detection system for each target material to check the position of the X-ray laser beam. The streak camera was subsequently positioned with a vertical entrance aperture at the position of peak X-ray laser output recorded by the CCD camera.

The streak camera was triggered using an Austin switch irradiated by a component of the chirped laser pulse separately compressed using a grating pair. This minimised jitter between the main laser pulse on target and the streak trigger. We endeavoured to operate the streak camera below saturation by using appropriate filters (e.g. 0.2 – 1.2 μm plastic CH) to attenuate the x-ray beam so that space charge effects in the streak tube due to the production of too many photo-electrons did not degrade the temporal resolution. The temporal resolution with a KI photocathode is estimated at 700 fs. Combining this resolution quadratically with temporal smearing due to the spectrometer gives a total instrument temporal resolution of 1.1 ps. For some shots the output signal from the streak camera was amplified by a standard 50/40 Kentech image intensifier and recorded by a butt-coupled optical CCD detector.

Another simple streaked slit diagnostic was developed to record resonance line emission from states near in energy to the upper lasing levels. A Kentech streak camera was used with an imaging slit, enabling acquisition of space-and time-resolved images of the plasma in the KeV photon energy range. The camera was coupled to an arm angled at 82.5^{o} to the line focus with a vertical slit. Angling the arm prevented any unconverted photons passing through the camera tube and hitting the

phosphor screen. The vertical imaging slit was placed at a distance of 43 cm from the target and the camera entrance horizontal timing slit was 24 cm away from the vertical slit giving an imaging slit magnification of 0.56. The vertical slit width was 270 μm to give spatial resolution of ~ 0.7 mm along the line focus length. The streak camera was equipped with a gold photocathode and a 500 μm wide slit which sets a time resolution of ~ 6 ps. A filter of 2.4 μm thick aluminum was employed so that emission in the 0.8 – 2.1 nm wavelength range was recorded with the diagnostic. The emission is dominated by resonance line emission for both Ni-like silver (resonance emission in the range 1.7 to 2.2 nm) and Ne-like nickel (resonance emission in the range 1 to 1.4 nm).

A CCD x-ray crossed-slit camera using two orthogonal slits with different magnification along the target length and width monitored the line focus plasma uniformity and overlap of the laser pulse. A KAP crystal spectrometer with space resolving slit measured the time integrated resonance line emission of Ne-like nickel with a spatial resolution along the plasma line of 300 μm.

Results

The temporal variation of the Ni-like silver output at 13.9 nm as recorded with the streaked spectrometer using an image intensifier is shown in Figure 2. The output shows a sharp rise with a slow fall in output as is expected from modelling studies[4]. The X-ray laser pulse duration (full-width at half-maximum FWHM) was measured as 3.7 ± 0.5 ps by fitting the lasing output with the predictions of a simple model developed by Strati and Tallents[5]. When not employing an image intensifier we measured a silver output with an approximately Gaussian shape, but again with 3 ps pulse duration.

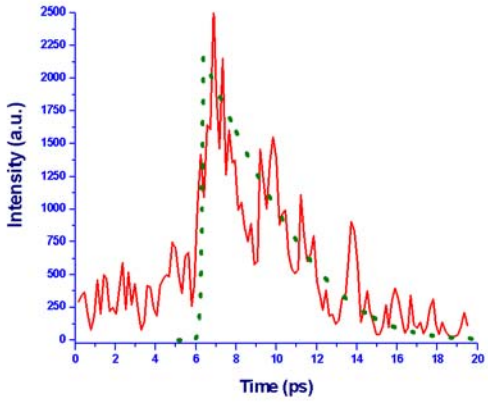

Figure 2. The temporal variation of X-ray lasing at 13.9 nm for Ni-like silver. An image intensifier was used with the streak camera. A 10 mm long silver target was irradiated with peak irradiance of 3.1×10^{12} Wcm^{-2} in the 280 ps background pulse and 1.2×10^{15} Wcm^{-2} in the 1.2 ps main pulse with peak-to-peak separation of 200 ps. The output was filtered with 1.2 μm plastic (CH). The FWHM X-ray laser duration was measured to be 3.7 ps. A model fit for $R = 10^{-6}$, peak small signal gain of 23 cm^{-1} and a gain duration of 22 ps is shown as a thick broken line.

The temporal variation of the Ne-like nickel output at 23.1 nm as recorded with the streaked spectrometer using an image intensifier is shown in Figure 3. It is likely that the observed double humped temporal profile for Ne-like nickel output at 23.1 nm arises because of saturation effects in the streak camera. The X-ray laser pulse duration (full-width at half-maximum FWHM) was measured as 10.7 ± 1 ps by fitting the lasing output with the predictions of a simple model[5]. A pulse duration of 3.5± 0.5 ps (full width at half maximum) was observed for the Ni-like silver line at 16.1 nm. This 16.1 nm line is probably largely pumped by resonant 3d → 4f photo-absorption[6].

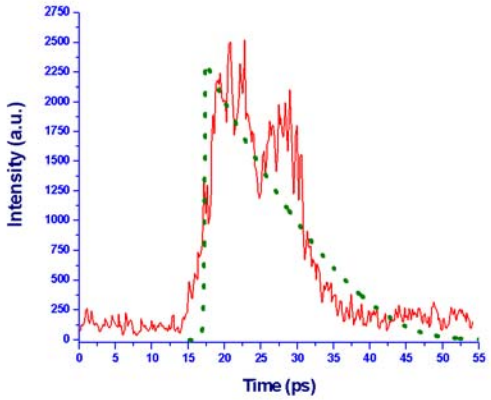

Figure 3. The temporal variation of X-ray lasing at 23.1 nm for Ne-like nickel. An image intensifier was used with the streak camera. A 6 mm long nickel target was irradiated with peak irradiance 6×10^{12} Wcm^{-2} in the 280 ps background pulse and 5×10^{15} Wcm^{-2} in the 1.2 ps main pulse with peak-to-peak separation of 300 ps. The output was filtered by 0.2 μm plastic (CH). The FWHM x-ray laser duration was measured to be 10.7 ps. A model fit for $R = 10^{-6}$, peak small signal gain of 60 cm^{-1}, and a gain duration of 35 ps, is shown as a thick broken line.

A sample streaked slit output showing spatial resolution of 0.7 mm along the target length and temporal resolution of 6 ps is given in Figure 4. Emission from the pre-plasma followed by the emission associated with the 1.2 ps main pulse is clearly apparent. This known time delay between the pulses has been used to calibrate the streaked slit camera streak speed. The main pulse emission occurs at times determined by the travelling wave irradiation.

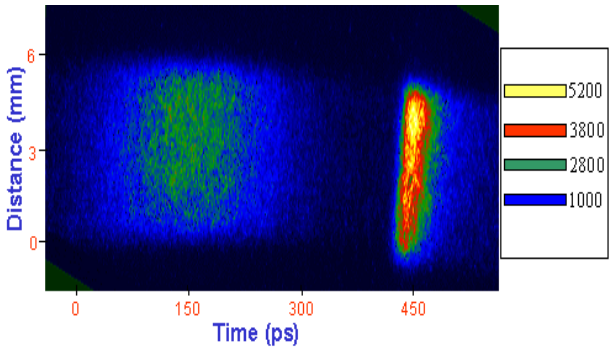

Figure 4. Streaked slit camera image showing the plasma emission filtered by a 2.4 μm aluminum filter from the background and main laser pulses incident onto a nickel target. The relative intensity scale is also shown.

The emission associated with the short pulse laser has measured fwhm duration of 22 ± 2 ps for silver and 35 ± 3 ps for nickel targets. We may expect the duration of this emission to be an upper bound on the gain duration.

Assuming that the leading edge of the main pulse emission corresponds to the time of laser light reaching the target, we measured the travelling wave velocity at the leading edge of the main pulse to be 0.95± 0.05c (Figure 5). This measurement is in agreement with measurements made using an optical streak camera viewing scattered laser light from the line focus during the setting-up of the travelling wave grating.

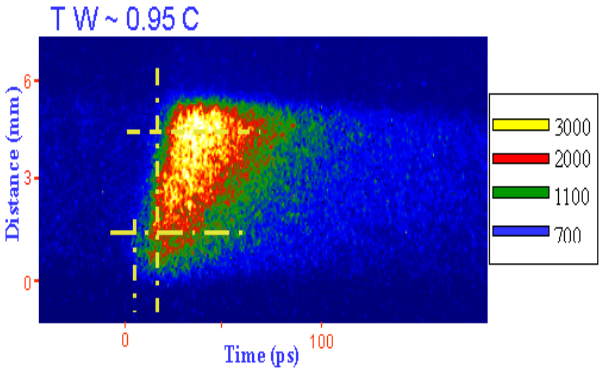

Figure 5. Emission at the leading edge of the main pulse emission recorded by the streaked slit camera can be used to measure the travelling wave excitation velocity (≈ 0.95 c). The relative intensity scale is also shown.

The spectrum recorded with the crystal spectrometer for the nickel target is shown in Figure 6. Time and spectrally resolved nickel spectra recorded over the 0.95 – 1.45 nm spectral range show that Ne-like emission is more intense than the F-like and continuum emission. The spectral lines have been identified following Boiko *et al*[7].

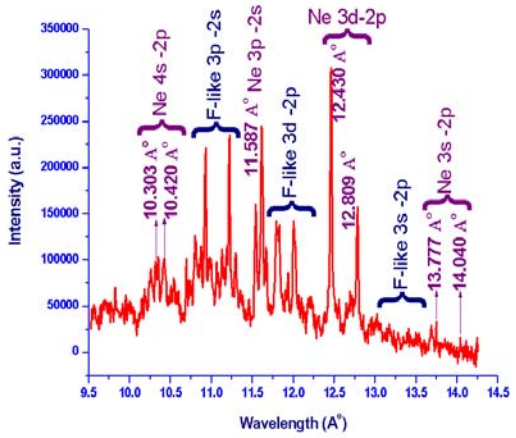

Figure 6. Time integrated Ne- and F-like nickel spectrum recorded with the crystal spectrometer.

The variation of emission along the target length as measured by the crossed-slit camera, crystal spectrometer and the emission integrated in time from the streaked-slit camera are shown for the same shot in Figure 7.

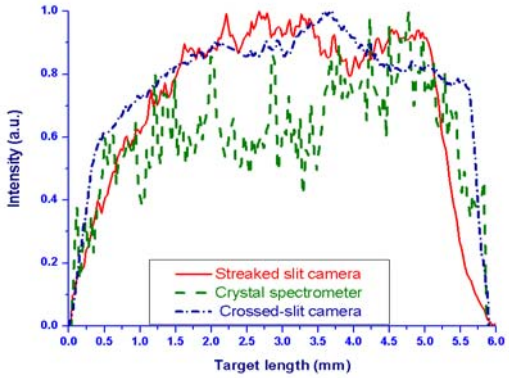

Figure 7. The variation along the target length as measured by three diagnostics. The nickel target was measured before the shot to have a length of 5.9 mm.

Conclusion

Measurements of the duration of X-ray lasing pumped with ~ ps pulses from the Vulcan optical laser have been obtained. We have measured X-ray laser pulse durations for Ni-like silver at 13.9 nm with a total time resolution of 1.1 ps. For Ni-like silver, the X-ray laser output has a steep rise followed by an approximately exponential temporal decay with full width at half maximum (fwhm) of 3.7 ps. For Ne-like nickel lasing at 23.1 nm, the measured duration of lasing is ≈10.7 ps (fwhm). An estimate of the duration of the X-ray laser gain has been obtained by temporally resolving the spectrally integrated resonance line emission from states near in energy to the upper lasing level. For Ni-like silver, this time of emission is ≈ 22 ps (fwhm), while for Ne-like nickel we measure ≈ 35 ps (fwhm).

References

1. G J Tallents, App. Of High Field and Short Wavelength Sources VIII OSA Tech. Digest Series 7, 47 (1997); M.P. Kalachnikov *et al*., Phys. Rev. A, 57 (6) 4778 (1998); Lewis CLS, SPIE 3776 (1999).
2. J.C. Chanteloup *et al*., J. Opt. Soc. Am. B 17, 151 (2000); A. Klisnick *et al*., J. Opt. Soc. Am. B 17, 1093 (2000).
3. Axis-Photonique Inc., Varennes, Canada.
4. L Casperson and A Yariv 1971 Phys. Rev. Lett. 26, 293.
5. F Strati and G J Tallents 2001 Phys. Rev. A, 64, 013807.
6. J Kuba *et al* 2000 Phys. Rev. A 62, 043808.
7. V A Boiko, A Y Faenov and S A Pikuz 1978 J. Quant. Spect. Radiat. Trans. 19, 11.

Development of X-ray lasers for applications

R Keenan, S Hubert, C L S Lewis, S J Topping

Department of Pure and Applied Physics, Queen's University Belfast, Belfast, BT7 1NN

M Notley, D Neely

Central Laser Facility, CLRC Rutherford Appleton Laboratory, Chilton, Didcot, Oxon, OX11 0QX, UK

Main contact email address: *r.keenan@qub.ac.uk*

Introduction

This report describes the further development of the five beam setup for pumping X-ray lasers (XRLs) at Vulcan. The initial work was carried out on the Sm XRL[1)] at 73 Å and the pump configuration has been extended to the Ne-like Ge and Ni XRLs at 196 and 231 Å respectively. This is now the routine configuration with the 'long', 100 ps, pump beams. These XRLs are mainly being developed with a view to applications such as Non-linear optics and Thomson scattering with XRLs. The optimisation of the target retraction for the Ge XRL was carried out for the radiography program with the length scan carried out at a later date. The Ni XRL at 231 Å was initially developed and characterised for the Non-linear optics work[2)]. The further characterisation of the source properties, presented as imaging work here, has been carried out as its use extends to other applications such as Thomson scattering[3)] and an XRL interferometer[4)].

Experimental Setup

The use of a prepulse has improved the brightness of X-Ray Lasers to the point where they can be used in applications. However, for target lengths beyond ~15 mm, into saturation mode, a double target arrangement had to be used, the alignment of which was critical. The lower density gradient and larger gain region produced with the prepulse technique had reduced refraction to the point where single long targets could be used. Five beams of Vulcan could be used to irradiate a single target, typically 25 mm long, which is much easier to align. The 25 mm long target provides a saturated XRL but still allows good uniformity at an intensity of $5x10^{13}$ W/cm^2. This five beam technique has provided saturated XRL outputs from Sm[1)] and the Ge and Ni XRLs discussed below.

For all the experiments the targets were irradiated by 5 beams of the Vulcan Nd:glass laser at 1.05 µm. Line foci 100 µm wide and 20 mm long were generated using a lens and off axis spherical mirror[5)]. These were displaced axially to produce uniform illumination and timed along the target so that each beam was incident on target centre at the same time. The beams were configured as shown in Figure 1(a) with one beam on axis, two at ±30^o and two at ±60^o. The beams were displaced along the axis as shown in Figure 1(b) with each beam delayed according to its position and positioned to provide maximum symmetry about the axis. The target base was mounted on a Sony magnascale so the target could be accurately retracted a distance d (see Figure 1(a)). This target retraction of a few 10s of µms allowed the beams arriving at an angle to heat the same region of the preformed plasma. Instead of creating two gain regions at the top and bottom, the target retraction should allow all beams creating the conditions for gain to arrive at the same small area of pre-plasma on axis. Without the retraction the beams at +30^o and +60^o (and conversely those at -30^o and -60^o) could create a separate gain region above (and below) the axis.

Five beams, 80 ps duration with 40 J per beam, were distributed along a 25 mm x 100 µm line focus giving an on-target intensity of up to $5x10^{13}$ W/cm^2. A prepulse with variable delay was generated in the laser area by splitting the oscillator pulse into two before the preamplifiers of Vulcan. For the Ge optimisation, carried out during radiography experiments[6)], the central, on-axis beam, was extended so that it could illuminate the entire target and be used as the prepulse energy source. The Ne-like Ni x-ray laser at 231 Å was characterised fully in the 5 beam setup for a four wave sum difference mixing (FWSDM) experiment[2)]. This XRL is now used as a source and as such has been further characterised through the imaging described below.

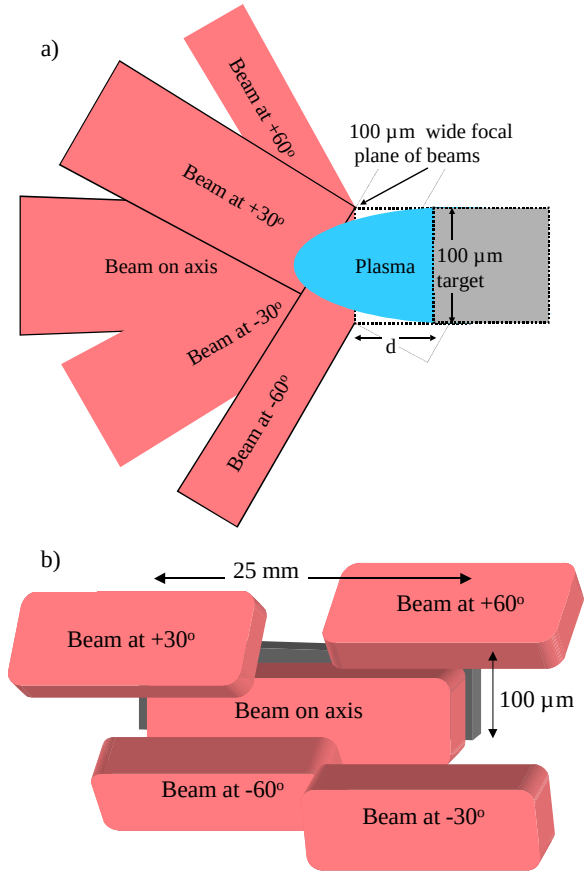

Figure 1. Sketch of five beam irradiation of a single target 100 µm wide x 25 mm long (a) side view showing how target retraction, d, allows the 5 beams to heat the same region of preplasma and (b) front view showing displacement of beams along the axis.

The main diagnostic for the XRL was a time integrated, angle resolving, axial grazing incidence flat-field spectrometer (FFS) with a 1200 lines mm^{-1} aperiodic ruled grating, coupled to a back-thinned CCD with 24 µm pixels. A crossed slits camera and a KAP crystal spectrometer monitored the uniformity and ionisation balance along the target.

The XRL was imaged at high magnification using Mo/Si multilayer X-ray mirrors onto a 13 µm pixel CCD with a resolution better than 5 µm. The setup for imaging the Ni XRL with two spherical mirrors at x40 total magnification (x2 from XRM1 and x20 from XRM2) is shown in Figure 2.

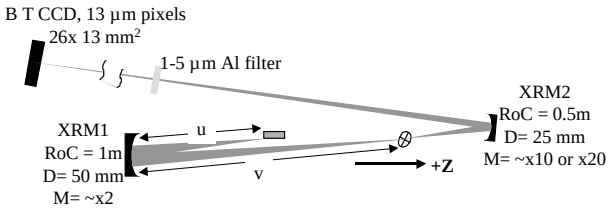

Figure 2. Imaging the XRL at high mag using two spherical multilayer X-ray mirrors (XRM).

For the absolute numbers presented below, a knowledge and best estimate of the detection parameters is required. The FFS measures the angular divergence but makes no measure of the vertical divergence as this is in the dispersion direction. This is taken account of by estimating the vertical as 3 times the horizontal divergence, as can be seen from the imaging shots, and combining this with the collection angle of the spectrometer. A best estimate of the grating reflectivity is made at 5%. The transmission of the Al filter is taken from Henke[7]. The final assumption is the conversion efficiency of the CCD from photons to counts which is taken to be 2 photons/count for a 196 Å photon for the specific detector used here. The counts on the CCD are integrated in the horizontal direction and across the spectral width of the laser line, a background is subtracted, and the assumptions described above used to get the total number of photons and hence the total output at the XRL wavelength. For the imaging case the total output is more readily obtained as the reflectivity of the mirrors has been calibrated.

Results

Ne-like Ge XRL at 196 Å

Initial optimisation of the target retraction was carried out using the flat-field spectrometer as the main diagnostic. This scan, shown in Figure 3, demonstrates the positive effect of retracting the target with a retraction of between 70-100 µm producing the brightest output. However no knowledge of how the vertical divergence is changing can be gained from the FFS and only through the imaging discussed below is the retraction truly optimised.

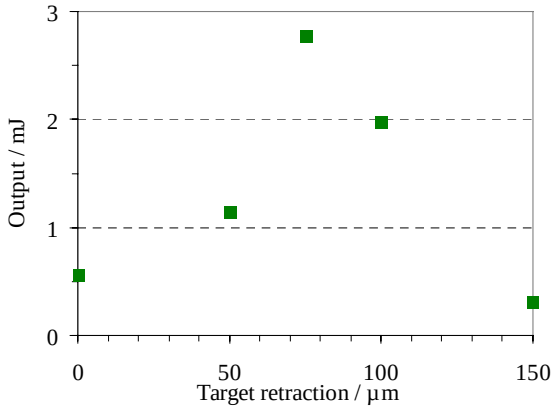

Figure 3. Optimisation of target retraction on FFS for Ge.

Images are shown in Figure 4 of the XRL 3 cm from the exit point taken at x18 magnification. With a target retraction of 70 µm, from the FFS optimisation, there is a double lobed structure but at 90 µm the output is optimised. It can clearly be seen that target retraction is important, not only to achieve maximum brightness, but also the large, relatively uniform area needed particularly for radiography.

The obvious double lobed structure for a retraction of 70 µm is from the beams above and below axis creating separate gain regions. Only when the target is retracted 90 µm do all the beams heat the same region, though still creating an XRL much larger in the vertical direction. This beam shape is highly reproducible as Figure 4c) shows with many shots taken at this retraction. The optimised target retraction depends mainly on the configuration of the prepulse, where the objective is creation of a single quasi-homogeneous gain region.

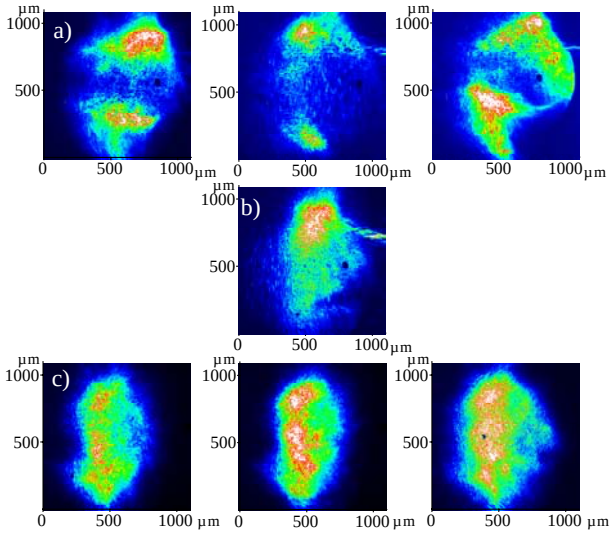

Figure 4. Optimisation of target retraction through imaging the Ge XRL 3 cm from the exit point showing (a) 70 (b) 80 and (c) 90 µm.

Ne-like Ni XRL at 231 Å

The Ni XRL has already been characterized[2]. Further work was carried out here with the setup shown in Figure 2. Images were taken at the lower magnification (x10 from XRM) at various distances, z, from best focus of XRM1 by moving XRM2 too.

The images in Figure 5 show the spot size decreasing as we get to best focus with similar images at –10 and –20 cm showing it increasing again. At the plane corresponding to ~5 cm from the exit point, we have a beam with a FWHM of 380x800 µm and a similar shape to the Ge images, i.e. at vertical divergence 2-3 times the horizontal divergence.

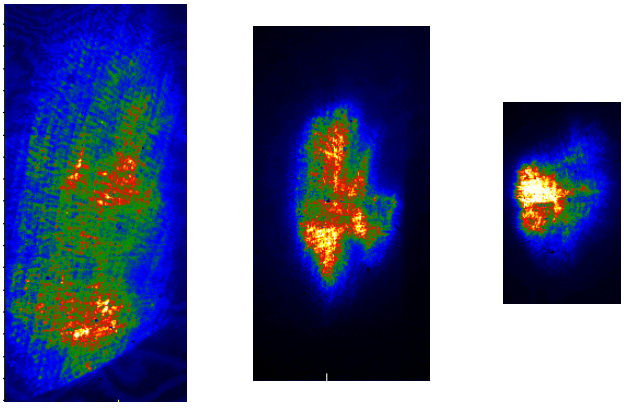

Figure 5. Images taken at +20, +10 and 0 cm from best focus.

The graph in Figure 6 shows the FWHM in both the horizontal and vertical directions as we go through best focus of XRM1. In the plane of best focus of XRM1 the spot size is ~300 µm. Given the magnification of this mirror is x2 this corresponds to an exit point size of ~150 µm. The FWHM size shown for +20 cm is an underestimate as the beam is overfilling the CCD at this point.

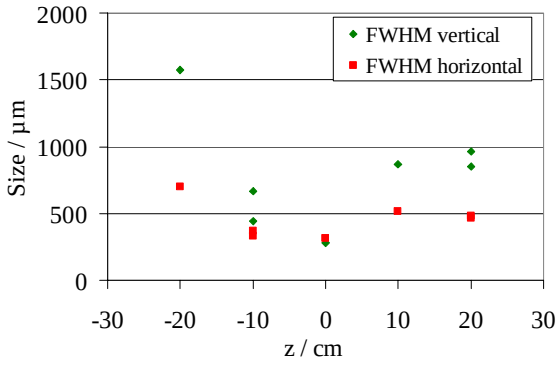

Figure 6. FWHM size of beam at various points through focus of XRM1.

Images were also taken at various distances z for different target retractions. The target retraction for Ni was optimised at best focus and at a total magnification of x40. A retraction of 100 µm gave the highest output in an exit point FWHM of 180x180 µm. Figure 7 shows the total output from the images for various target retraction.

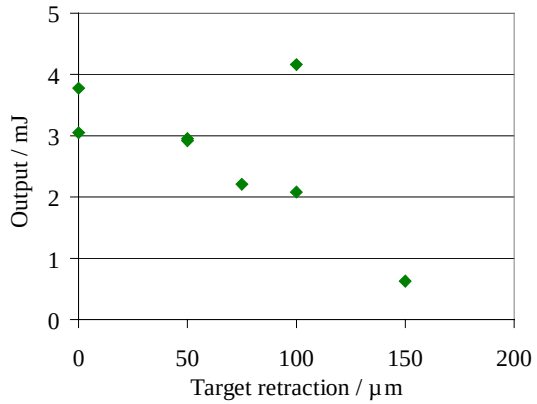

Figure 7. Optimisation of target retraction through imaging the exit point of the Ni XRL.

The reproducibility of the source was also verified at various retractions and positions through focus. Figure 8 shows two shots taken at 75 µm retraction and best focus, with an on target energy of 180 ± 2 J both producing a 3 mJ output in an exit point FWHM of ~150x150 µm.

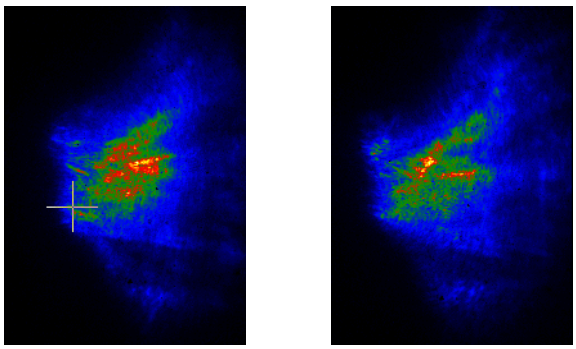

Figure 8. Shot to shot reproducibility of exit point.

Conclusions

The five beam setup has now been optimised such that a highly reproducible output of ~3 mJ is obtained for both the Ne-like Ge and Ni XRL at 196 and 231 Å respectively. Target retraction has been optimised through imaging allowing production of a well-defined source suitable for applications.

References

1. R Keenan *et al.* Central Laser Facility Annual Report 1998/99, RAL-TR-1999-062, 56, (1999)

2. S J Topping, R. Keenan, *et al.* J. Phys. IV France, 11, 487, (2001)

3. D Riley *et al* "Potential for Thomson Scatter with an X-ray laser" Submitted to IEEE (2002)

4. S J Topping, R. Keenan, *et al.* Central Laser Facility Annual Report 2001/2002, RAL-TR-2002-013, 53, (2002)

5. I N Ross, J Boon, R Corbett, A Damerell, P Gottfeldt, C Hooker, M H Key, G Kiehn, C L S Lewis, O Willi Applied Optics, 26, 1584, (1987)

6. E Wolfrum *et al.* Central Laser Facility Annual Report 1998/99, RAL-TR-1999-062, 43, (1999)

7. B L Henke, E M Gullickson, J C Davis At. Data Nucl. Data Tables, 54, 181, (1993)

Soft X-ray interferometry with a transmission grating

S J Topping, C L S Lewis, R Keenan, A M McEvoy

School of Mathematics and Physics, Queens University of Belfast, Belfast, BT7 1NN, UK

M Notley, D Neely

Central Laser Facility, CLRC Rutherford Appleton Laboratory, Chilton, Didcot, Oxon, OX11 0QX, UK

Main contact email address: *s.j.topping@qub.ac.uk*

Introduction

Interferometry measurements of the Ne-like Ni X-ray laser (XRL) at 23.1 nm had previously shown a degree of coherence was present in the beam[1]. A Lloyds mirror was used to split the XRL beam and create an overlap region, which was imaged at high magnification to a CCD camera. A new XUV interferometer has been designed based on a transmission grating (TG) and a set of Hoya plates to improve the fringe visibility measurements. Knowledge of the coherence properties of the XRL beam is important for applications such as in non-linear optics[2].

Transmission Gratings

The transmission gratings consist of a 1.4 x 1.4 mm silicon nitride substrate, 50 nm thick onto which, a gold resist grating is deposited with a periodicity of 1000 lines/mm. The substrate is suspended across a 5 x 5 mm silicon frame to allow safe handling of the TGs[3]. A 2000 lines/mm grating was also available.

At Queens University the TGs were characterized to estimate the transmission efficiency into the diffracted orders. A laser-produced plasma is formed by focusing pulses of a frequency doubled Q-switched Nd:YAG laser onto a solid lead cylinder located inside a vacuum chamber. The laser operates at 10 Hz with a pulse length of 7 ns and pulse energies up to 500 mJ. With a focal spot diameter of ~ 50 μm the resulting intensity on the lead target is of the order of ~ 10^{12} W/cm^2.

An X-ray mirror (XRM) with a reflectivity of ~ 20% and a narrow bandpass of ~ 30 Å centred around 23.1 nm is used to image the plasma and focus it onto the TG at ~ x2 magnification. The transmission grating introduces diffraction into the reflected and focused beam producing positive and negative diffracted orders and a straight through beam. A CCD camera with an Aluminium filter in place is then used to examine the diffracted beams, see Figure 1.

The 1000 and 2000 lines/mm TGs had similar characteristics showing 4% transmission into the straight through and 3% transmission into 1st order.

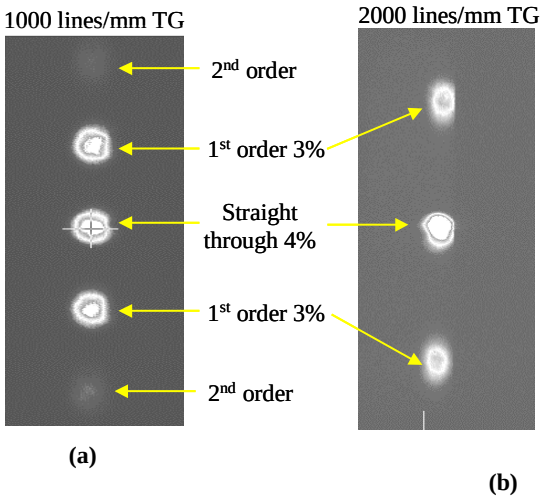

Figure 1. Straight through and diffracted orders from (a) 1000 lines/mm TG and (b) 2000 lines/mm TG.

The incident intensity was calculated with the focused beam directly onto the CCD and without the TG in place. The results showed good shot to shot reproducibility.

Experiment

The Ne-like Ni XRL is created from a plasma column produced from 5 beams at 1.054 μm in a line focus set-up. The beams are first focused to a point (surrogate focus) using a series of f/2.5 lenses. A set of spherical mirrors is then used to image the surrogate focus to the target plane. The spherical mirrors operate off axis and as a result a large astigmatism is introduced into the beams producing two line foci. One focus is a line, which is set within the plane of incidence and the beams are overlapped along the axis to create a uniform line focus, see Figure 2.

The beams have a pulse duration of 80 ps with an average energy of ~ 40 J per beam and when distributed across a 100 μm x 25 mm line focus gave an on target intensity of the order of ~ 10^{13} W/cm^2. A 10% pre-pulse was set 2 ns ahead of

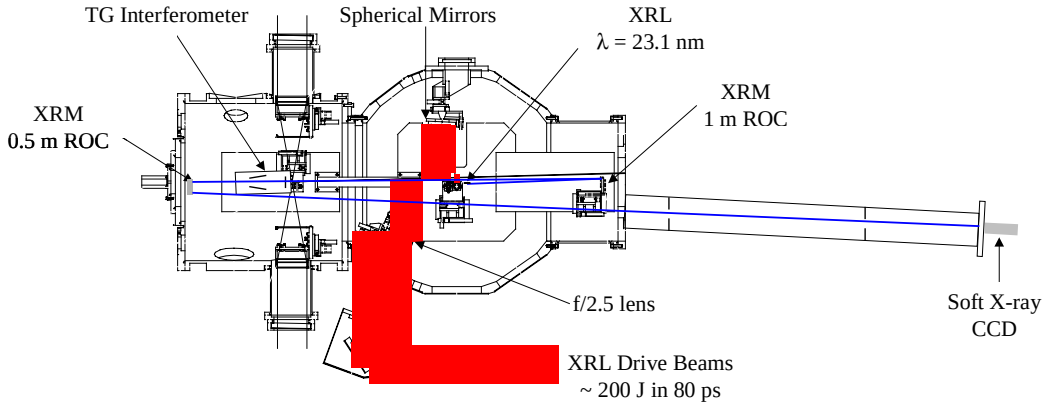

Figure 2. Experimental set-up of XRL Interferometer.

the main drive beams and the solid Ni slab target retracted 100 μm off axis to maximize the XRL output.

The illumination uniformity and ionisation balance were monitored on a shot to shot basis using a crossed slit camera and Bragg spectrometer. The images showed reasonably good uniformity along the line focus and indicated our Ni plasma was in the desired Ne-like state. The Ne-like Ni XRL was driven into saturation for a 25 mm long target.

The output was monitored with an on axis grazing incidence flat-field spectrometer with a 1200 lines/mm aperiodic ruled grating and a soft X-ray CCD. The XRL was found to have a maximum output of ~ 5 mJ, a FWHM divergence of ~ 10 mrad and a refraction angle of ~ 8 mrad which is consistent with previous results[4].

The XRL beam is focused onto a cross-wire on the interferometer at ~x2 magnification with a 1m ROC XRM. The TG is set a fixed distance of 2 cm from the focused XRL beam. The TG then produces positive and negative diffracted orders and a straight through beam. The straight through beam is blocked and the diffracted orders are overlapped using Hoya plates at grazing incidence angles, see Figure 3. The overlapped region containing fringes is then imaged using a 0.5m ROC XRM and relayed to the CCD with an overall magnification of ~ x20. By changing the angle of the Hoya plates it was possible to vary the fringe spacing in the overlap region.

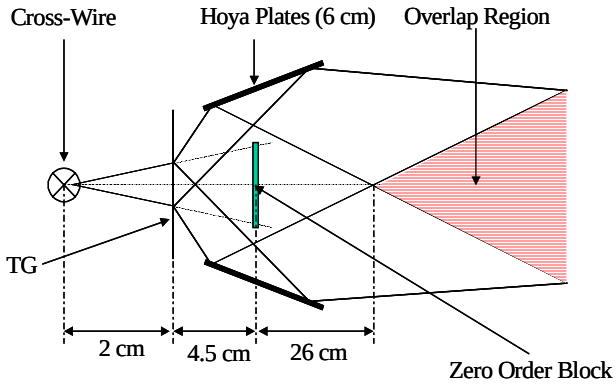

Figure 3. XUV Transmission Grating Interferometer.

The XRMs had a reflectivity of ~ 20% and a narrow bandpass of ~ 30 Å centred around 23.1 nm. A series of baffles were used to reduce the amount of scattered light in the imaging system and obtain a clean signal with low background. The pointing of the XRL beam onto the cross-wire was checked using a visible diode laser coupled to an optical fibre, the output of which was placed at the XRL exit point. The 1000 and 2000 lines/mm TGs introduce 23.1 mrad and 46.2 mrad diffraction respectively into the 1st order XRL beamlets.

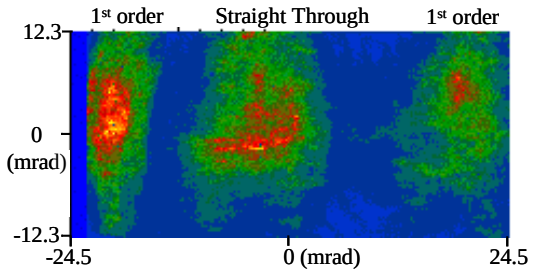

Figure 4. Straight through and 1st order of the Ne-like Ni XRL beam through 1000 lines/mm TG.

To test the transmission of the XRL beam through the TG the Hoya plates and zero order block were removed. The second relay XRM was moved to image a plane 5 cm from the 1000 lines/mm TG to look at the diffracted orders and the straight through at x10 magnification, see Figure 4. The estimated transmission efficiency with respect to an incident XRL beam with an output of 3 mJ, showed 1% into the straight through and 1% into 1st order.

For the interferometry shots an aperture ~ (1 x 1 mm) was placed in front of the XRM to sample a section of the XRL beam. The 2000 lines/mm TG was used, the zero order block was positioned and the Hoya plates were set to 20.7 mrad which corresponds to a fringe spacing of ~ 4 - 5 μm in the overlap region. The overlap region was then imaged, at ~ 40 cm from the TG with the 0.5m ROC XRM at ~ x12 magnification. Figure 5 shows an expanded image of the overlap region where we would expect to see fringes of ~ 50 μm. Analysis of the image showed that no fringes were present.

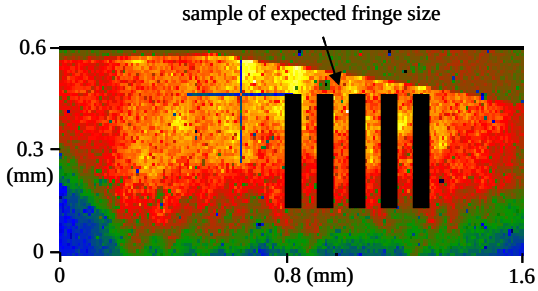

Figure 5. Overlap region imaged at x12 magnification.

Conclusions

This is a preliminary attempt to develop a novel interferometer for plasma density diagnostics. Characterisation of the TGs showed sufficient transmission of the XRL beam for the interferometer to work. Further progress will be reported at a later date.

References

1. S.J. Topping, R. Keenan, *et al*, J. Phys. IV France 11, 487 (2001)

2. S.J. Topping, R. Keenan, *et al*, Central Laser Facility Annual Report 1999-2000, RAL-TR-2000-034, 56 (2000)

3. P. Anastasi, Fabrication Services & Technology, England

Uniform plasma production from thin foils

R A D Grundy, C Courtois, R G Evans, N C Woolsey

Department of Physics, University of York, Heslington, York. YO10 5DD, UK

P Helander, K G McClements, R O Dendy

EURATOM/UKAEA Fusion Association, Culham Science Centre, Abingdon, Oxfordshire OX14 3DB, UK

J L Collier, R Heathcote, A Johnson, M M Notley, P A Norreys

Central Laser Facility, CLRC Rutherford Appleton Laboratory, Chilton, Didcot, Oxon, OX11 0QX, UK

Main contact email address: *radg100@york.ac.uk*

Introduction

Recent high power laser experiments have explored the possibility of studying collisionless shock processes relevant to supernova remnants in the laboratory.[1,2] These experiments required the production of large area, 1-dimensional, low-density plasmas with physical characteristics matched to those believed typical of a Supernova Remnant (SNR).[1,3] A convenient method of producing such a plasma was through laser explosion of thin plastic foils. However, the resulting plasmas were found to have density non-uniformities that impaired the data quality. Experimental data indicated that two significant causes for these non-uniformities were initial foil quality and the laser focal spot intensity profile. The initial foil quality was improved through target preparation procedures, and remains an area of study. Two-dimensional hydrodynamic simulations of the foil-laser interaction show that the resulting plasma density uniformity is sensitive to the initial laser intensity profile.[4] Furthermore, imprinted laser intensity variations will persist as density non-uniformities for several hundred ps. This is due to the supersonic nature of the plasma expansion.[5]

The pattern of laser intensity non-uniformity will in general vary in space and time, and indeed many smoothing techniques are based on the rapid motion of imposed high spatial frequency intensity structures and rely on lateral thermal conduction between the critical surface and ablation front for smoothing. Examples are random phase plates[6] (RPP), phase zone plates[7] (PZP), induced spatial incoherence[8], and smoothing by spectral dispersion[9]. Any laser imprint may be interpreted in terms of Equation (1) where a fractional change in ablation pressure Δp, due to a fractional change in intensity ΔI with spatial irregularities of scale length L is smoothed by a factor n.[10] The critical surface and ablation front are initially in contact and the separation, D, will increase in time until a steady separation is achieved.

$$\frac{\Delta p}{p} = n\frac{\Delta I}{I} \rightarrow n = \exp\left[\frac{-4\pi D}{L}\right] \qquad (1)$$

This separation represents the smoothing region; intensity fluctuation scales below this separation will be smoothed by lateral transport. Consequently smoothing is ineffective during the initial period of laser irradiation.

An alternative smoothing approach is to move the critical surface from the ablation front *before* laser irradiation, for example using a radiatively heated low-density foam buffered target.[11] Unfortunately, none of these smoothing methods is suited to the ablation of thin foil targets and in particular to applications where the plasma expansion should be uniform and the leading edge of the plasma, in this case, or the rear surface is of interest.

Improving the uniformity of the exploding plasma demands uniform target illumination during the initial phase of the laser interaction. Here we describe a smoothing technique, where a low energy prepulse is spatially smoothed immediately before the foil target. Following separation of the critical surface from the ablation front the foil is irradiated with the (non-uniform) high-energy beams.

Experiment

The experiment was conducted in Target Area East of the Vulcan Nd:Glass laser. The target geometry consisted of two 100 nm thick foils mounted on copper holders, separated by 1 mm and placed face parallel, see Figure 1. The foils are produced by thermal evaporation onto glass slides. Individual 2 mm square sections of foil were floated off the glass in a water bath and attached by surface tension to photo-fabricated 50 μm thick copper holders. The foil holders are 2 mm by 7 mm strips with a 1.2 mm diameter hole centred 1 mm above the bottom end over which the foil sits. This is identical to the type of mount used in our previous experiments[1], where the size is dictated by the Helmholtz coil target arrangement.

On some experiments a 75 μm diameter pinhole was mounted 20 mm before the right hand foil and aligned along the central axis of the foil. This pinhole spatially filtered the prepulse.

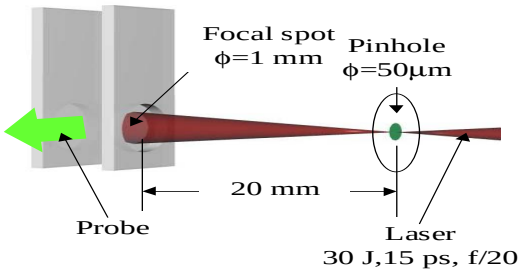

Figure 1. Target geometry showing the parallel foils and foil holders, the pinhole placement and prepulse and probe beam configuration.

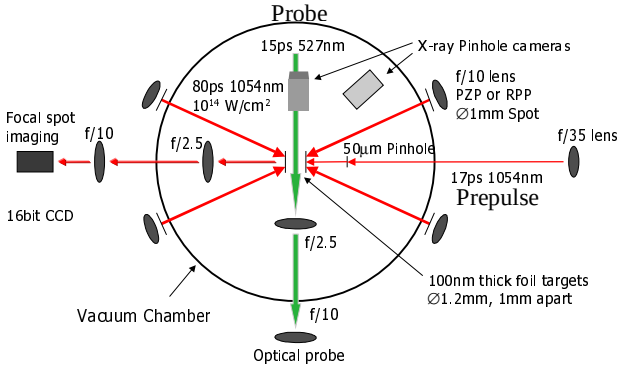

Figure 2. Experimental set up showing the beam configuration and diagnostics arrangement.

The Vulcan set up is shown in Figure 2 and consists of the main beams, a probe and a prepulse. All the beams were seeded by the same Nd:YLF oscillator to eliminate timing jitter, this oscillator delivered a 1.053 μm, 80 ps FWHM pulse with 2 nm bandwidth. The main beams, used in radial geometry, were focused through f/10 lenses and PZP or RPP to produce a 1 mm

diameter focal spot on each foil with an average irradiance of ~10^{14} W.cm^{-2}. The prepulse and probe beams were both compressed in air using grating pairs.

A prepulse was used on some experimental shots to preform a plasma on the right hand foil. The beam with FWHM of 17±5 ps, was focused with an f/35 achromatic lens onto the pinhole as shown in Figure 1. This irradiates the right hand foil with a spatially smooth beam at an average irradiance of 10^{13} W.cm^{-2}. The timing of the beams was arranged such that the prepulse could arrive between 100ps and 0 *before* the main drive beams. The long focal length optic enabled the use of a relatively large pinhole, diameter 75 μm, and minimised pinhole closure during the laser pulse.

The probe, with pulse length of 15±5 ps FWHM, was frequency doubled and *delayed* relative to the main beams by 0 and 1ns, and used to image the plasmas. The probe gave near diffraction limited imaging over a 3 mm^2 area at a magnification of x3.5 in a plane centred on the two foils. This was achieved using a 108 mm diameter f/2.5 doublet with spacing of 10.4 mm to collect the beam 284 mm from the target. The focus of the lens was contained under vacuum before entering a 108 mm diameter aspheric f/10 lens 1700 mm from the target. This produced an image 966.9 mm behind the f/10 lens with a 10 μm resolution.

Electron density structures were recorded using a dark field Schlieren[12] diagnostic array. The probe beam is split into three equal intensity channels using a combination of 30/70 and 50/50 beam splitters. These channels formed schlieren images using circular stops of diameter 1.1 mm, 1.6 mm, and 2.1 mm. These correspond to a sensitivity to deflections due to uniform electron density gradients in a 1 mm thick plasma of 2.2 x 10^{18}, 3.2 x 10^{18} , and 4.2 x 10^{18} cm^{-3}.mm^{-1} respectively. The degree of deflection is a path integral though the cylindrical plasma, which needs to be considered for a more accurate interpretation of the data[12]. The images were recorded on Teli CS3910 8 bit CCDs with 7 μm square pixels.

The focal spot on the left foil in Figures 1 and 2 was imaged with an optical system similar to that used with the probe. In this case the image was recorded onto a 16-bit CCD. CCD based pinhole cameras imaged X-ray emission from the right-hand foil at 37.5° to the foil surface normal and the collision of the two foils.

Results

Time integrated focal spot profiles are shown in Figure 3. The cross-section was averaged over a 50 μm wide strip through the centre of the spot. This profile, peaked at the centre, was typical of PZP and RPP focusing of two beams on the left-hand foil.

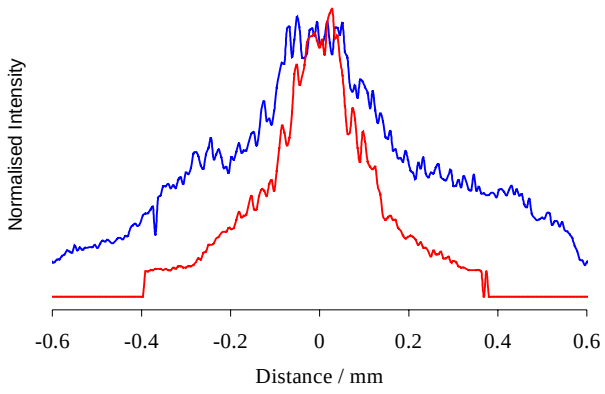

Figure 3. Focal spot profiles created using two main beams with PZPs (blue) and RPPs (red) defocused by 5mm.

The central peak feature is believed to result from flaws in the PZP manufacture and moving the focus of both beams back by 2 mm to 5 mm reduced the intensity of this peak as shown in Figure 3. Measured focal spots indicate high spatial frequency structures with a peak-peak separation of between 16 to 20 μm.

The effect of the PZP and RPP (at 5 mm defocus) is clear in Figure 4. These images are composites of three different schlieren measurements. Each separate schlieren channel is assigned a primary colour and the resulting image provides a contour map of areas of electron density gradient perpendicular to the probe propagation in the plasma.

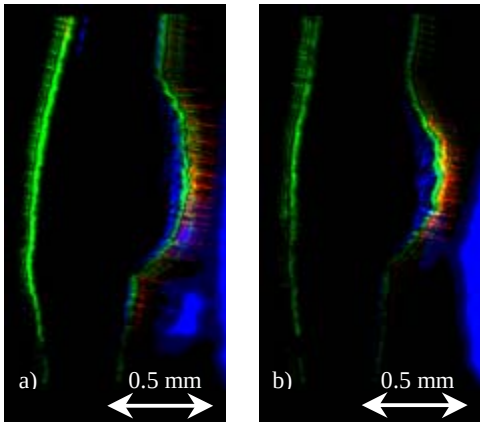

Figure 4. Schlieren image of the left CH foils taken 500 ps after irradiation with ~85 J. a) shows focusing with PZP, and b) focusing with RPP. The laser approaches from the left of the images. The blue, green and red images were recorded with 1.1mm, 1.6mm, 2.1mm diameter circular stops that correspond to electron density gradients above 2.2x10^{18} cm^{-3}.mm^{-1}, 3.2x10^{18} cm^{-3}.mm^{-1} and 4.2x10^{18} cm^{-3}.mm^{-1} respectively.

Both images show two vertical features corresponding to the front (laser irradiated) and back surfaces of the plasma as the left and right hand features respectively. The shape of the schlieren features is indicative of the envelope of the focus. The schlieren images also show filament structures with a spacing of 9 to 10 μm. As the schlieren image shows both the rising and falling slope of any electron density feature the scale of these filaments is 20 μm, a scale to the structure observed in Figure 3.

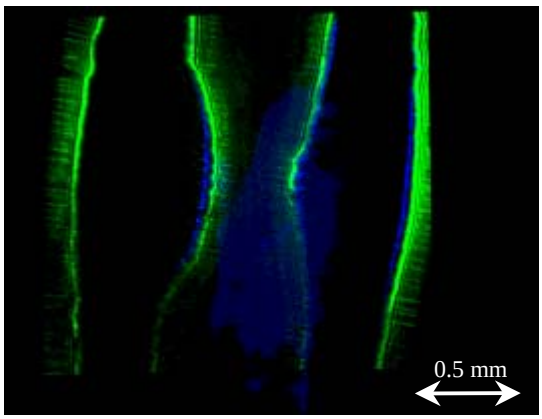

Figure 5. Schlieren images of two colliding CH plasmas, recorded 500 ps after irradiation with PZP focussed beams and ~90 J on each foil. Laser beams approach from the left and right of the image. The blue and green images were recorded with 1.1mm and 1.6mm diameter circular stops, which correspond to electron density gradients of at least 2.2 x 10^{18} cm^{-3}.mm^{-1} and 3.2 x 10^{18} cm^{-3}.mm^{-1} respectively.

The interaction of two CH plasmas 500 ps after laser irradiation is shown in Figure 5. This composite image clearly illustrates the effect of the central intensity spike due to the PZP, particularly on the right-hand foil. At this time the leading edges of the plasmas, in the centre of Figure 5, are expected to have interpenetrated by ~200 μm. Again horizontal electron density structure is observed, and is believed to be due to laser imprint.

The influence of a smoothed prepulse is shown in Figures 6; here schlieren images are taken 350 ps following the explosion of the right hand foil (see Figure 2). A 1.1mm diameter stop is used so gradients above 2.2 x 10^{18} $cm^{-3}.mm^{-1}$ are observed.

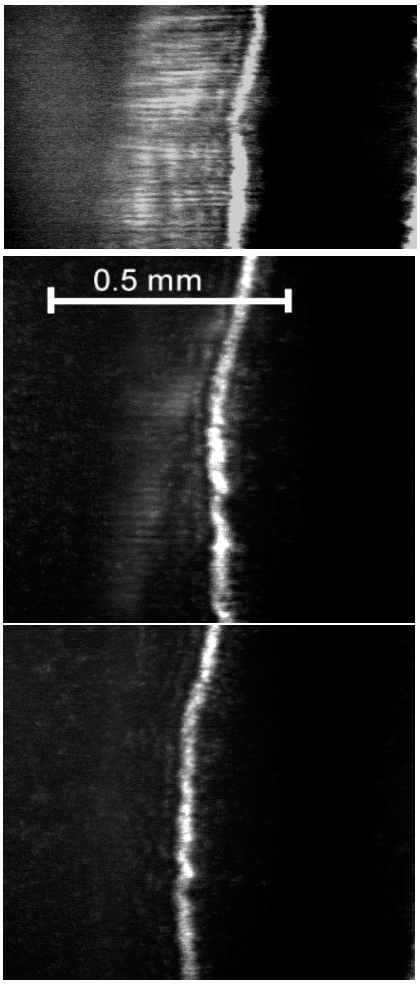

Figure 6. The effect of a smoothed prepulse on a CH foil is illustrated by three experiments. The rear surface of the foil is shown. The schlieren image in a) is recorded with no pre-pulse, in b) and c) the prepulse heats the foil from the right in 60ps, and 80ps *before* the drive beams respectively. The images were recorded 350ps after foil irradiation with the main beams using a 1.1mm diameter stop.

With no prepulse, Figure 6a, density filaments are clearly observed, and these structures are observed at all times. The horizontal filaments observed on the rear, non-irradiated, face of the foil are due to laser imprinting. Figures 6b, and 6c show a reduction in filamentation; in both cases this results from the smoothed prepulse that irradiated the foil target *before* the main PZP focused beams. Significant smoothing was observed in a narrow timing window. Prepulse timing is critical to obtain smoothing and optimum exploding foil performance. An optimum centre-to-centre prepulse to main beam delay was 80 ps.

This timing window occurs because the prepulse must arrive before the main pulse, see Figure 7, and a critical surface should form and detach before the main pulse irradiation. Further, the main pulse must irradiate the target before the plasma density falls below critical.

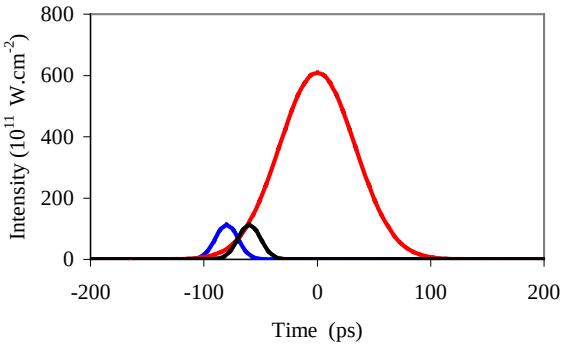

Figure 7. The curves illustrate the importance of relative timing between the prepulse and the main beams. In red is the main pulse with FHWM of 80 ps, and the prepulse (FWHM of 17 ps) 60ps early in black, and 80ps early in blue. 80 ps was the optimum timing.

Conclusion

RPP and PZP focusing techniques are often used to form large area focal spots and plasmas. However, these methods produce high spatial frequency intensity non-uniformities, which induce pressure modulations across the target that can drive electron density filaments. These filaments persist in supersonic exploding plasmas used here and impair experimental data. Here we described a successful method of laser smoothing using a pinhole to spatially filter a short duration prepulse to preform a plasma. This improved plasma uniformity sufficiently that filamentation was not detectable by our diagnostics with 10 μm spatial resolution and above 2.2 x 10^{18} $cm^{-3}.mm^{-1}$.

References

1. Woolsey NC, Ali YA, Evans RG, Grundy RAD, *et al*. Physics of Plasmas, 8, 5, 2439-2445, (2001)
2. Woolsey NC *et al*. CLF Annual Report 1999-2000, RAL-TR-2000-034, 42 (2000)
3. Woolsey NC *et al*. CLF Annual Report 1999-2000, RAL-TR-2000-034, 59 (2000)
4. Evans RG and Woolsey NC CLF Annual Report 1999-2000, RAL-TR-2000-034, 77 (2000)
5. Helander P, *et al*. CLF Annual Report 2000-2001, RAL-TR-2001-030, 58 (2001)
6. Y Kato, *et al.* Phys Rev Lett 53, 11, 1057 (1984)
7. R H Lehmberg, A J Schmitt, S E Bodner J Appl Phys 62, 7, 2680 (1987)
8. S Skupsky, *et al.* J Appl Phys 66, 8, 3456 (1989)
9. A. R. Jones. J Appl Phys D, 2, 1789--1791 (1969)
10. Manheimer WM, Colombant DG and Gardner JH Phys Fluids, 25, 1644 (1982)
11. Hoarty D, Iwase A, Meyer C, Edwards J, and Willi O Phys. Rev Lett. 78, 3322 (1997)
12. Grundy RAD, *et al.* CLF Annual Report 2001-2002, RAL-TR-2002-013, 58 (2002)

Ray tracing analysis of the interaction of opposing exploding foils

R A D Grundy, N C Woolsey

Department of Physics, University of York, Heslington, York. YO10 5DD

Main contact email address: *radg100@york.ac.uk*

Optical probing of counter-propagating thin foil plasmas has been used to form Schlieren images of two counter-propagating exploding foils for the study of plasma behaviour during interaction.[1)] The initial analysis of the data has been qualitative, and limited by the three dimensional nature of the plasma. We describe a computational approach for interpretation of the Schlieren images. This requires modelling the propagation of the optical probe through calculated plasma density profiles.[2,3)]

The experiment uses Vulcan to explode two 100 nm thick CH plastic foils, placed face parallel and separated by 1 mm (shown in Figure 1). Each foil is irradiated with an 80 ps pulse at approximately 10^{14} W.cm^{-2} over a 1mm diameter focal spot to ensure near 1-dimension expansion up to the interact point. Typical predicted electron densities, assuming collisionless interaction 500 ps after irradiating the foils, are between 10^{18} and 10^{19} cm^{-3}. These densities are ideal for optical probing and Schlieren images are a useful method for obtaining information on electron density gradients. The Schlieren probe is aligned perpendicular to the target surface normal (*x*-axis, Figure 1) and has a pulse length of 80 ps, and wavelength 527 nm.

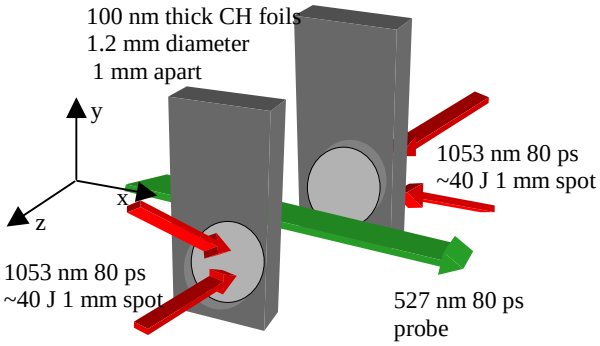

Figure 1. The experimental target configuration and probe propagation direction.

Schlieren imaging is a technique that is sensitive to refractive index change, and as such is a useful diagnostic of shock structures where rapid changes in electron density and thus refractive index are expected. For a plasma the refractive index, η, is related to the electron density n_e by

$$\eta(x,y,z) = \sqrt{1 - \frac{n_e(x,y,z)}{n_c}} \qquad (1)$$

Here n_c is the critical density at the probe laser wavelength. In our experiments we use dark field Schlieren imaging to record regions of high refractive index change, and the diagnostic is sensitive to refractive index change perpendicular to the probe propagation direction (*z*-axis in Figure 1). This makes possible the measurement of spatially resolved electron density gradients resulting from the interaction of the plasmas. Dark field Schlieren images are achieved by placing a stop at the focal point of the Schlieren lens. Light that is refracted in a region of refractive index (electron density) gradient will not focus at the stop; light passing the stop is then collected with a second lens to form an image onto a CCD detector. This is illustrated in Figure 2. By adjusting the diameter, *r*, of the stop for a fixed focal length, f_s, Schlieren lens light rays with angular deviation below θ are excluded.

$$-\theta < \arctan\left(\frac{r}{f_s}\right) < \theta \qquad (2)$$

The angular deviation depends on the electron density gradient dn_e/dz and propagation distance.

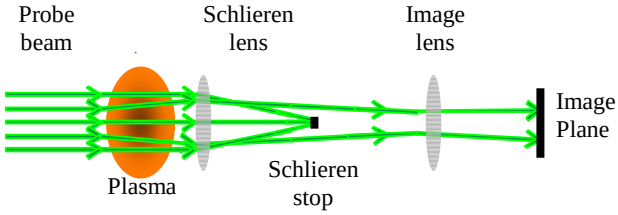

Figure 2. Schematic of dark field Schlieren diagnostic. The Schlieren lens focuses the probe onto a stop; light refracted around the stop is collected at the imaging lens onto a detector.

Experimental Schlieren data is reproduced in Figure 3. This image was recorded 500 ps after exploding the two foils with an 80 ps duration probe beam, with an f/10 optic and circular stop diameter of 1.2 mm. This corresponds to electron density gradients exceeding ~2.4x10^{18} cm^{-3}.mm^{-1}. In the image the original position of the two foils and the foil holders (50 µm thick copper mounts) are shown as two vertical white lines.

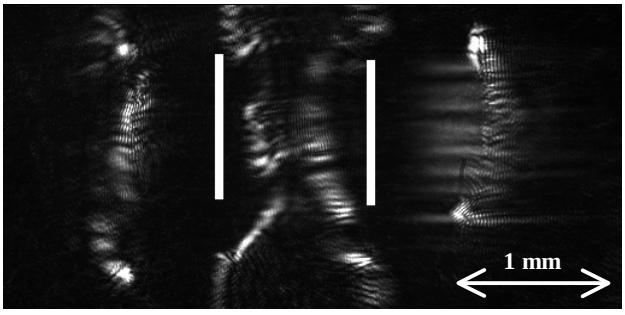

Figure 3. A Schlieren image of two exploding plasmas taken 500 ps after irradiation ~70 J on each foil. The vertical white lines indicate the initial position of the foils.

The four vertical features correspond to areas of high electron density gradient. The two features on the left side of Figure 3 correspond to the expanding regions of the left-hand foil, exploded with lasers approaching from the left. The two features to the right are the right-hand foil, exploded with lasers approaching from the right. At 500 ps the leading edges of the two plasmas are predicted to have interpenetrated by approximately 200 µm (central region in Figure 3). Imposed over these vertical features are horizontal filaments. These are believed to result from a combination of initial target structure, laser imprinting due to beam intensity non-uniformity,[5)] and the imaging system. It is interesting to note the horizontal density filaments persist for more than 1 ns. This is indicative of supersonic expansion.[6,7)]

The variation in peak density along the *z*-axis is modelled using Med103. Simulated n_e are shown in Figure 4. These simulations assumed 80ps FWHM Gaussian laser pulse with peak intensity

of 10^{14} W.cm^{-2}, and 100 nm thick CH plastic foils. Med103 is a fluid model and cannot model collisionless interactions nor magnetic fields. Simply adding the n_e from two plasmas can approximate the interpenetration of two non-interacting, non-magnetised counter-streaming plasmas. This is the approach used in Figure 4 where the solid lines represent the summed results and the dotted lines the Med103 simulations of single foils. The evolutions of the approximated electron density profile at 300 ps, 400 ps, and 500 ps after the peak of the laser pulse are shown. The derivative dn_e/dz can give some indication of the electron gradients that may be expected, and may be compared with experimental data.

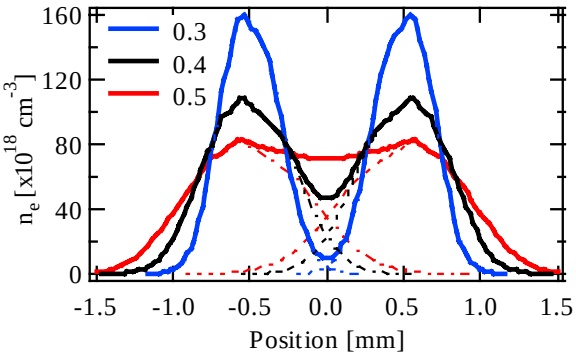

Figure 4. Med103 electron density profiles at 0.3, 0.4, and 0.5 ns following the explosion of the foils placed at ±0.5 mm. The dotted curves show the simulations and solid curves the sum.

However, a more quantitative interpretation requires further analysis that considers the radial symmetry of the plasmas (in the *xy*-plane). The probe beam will be refracted along the path through the plasma in the *y*-axis (due to dn_e/dy) and the *z*-axis. The information along the *z*-axis is of most interest. This is a problem that can be addressed using a ray-tracing approach.

As a probe beam propagates through a plasma of varying electron density the path of the ray is deviated according to the local refractive index η shown in equation (1). Under the assumption of geometric optics (i.e. the refractive index change is small compared to the wavelength of light) the propagation path of any given ray can be modelled [3] according to:-

$$\frac{\partial^2 r}{\partial \tau^2} = -\frac{1}{2} A\lambda^2 \frac{\partial n_e}{\partial x}\hat{x} \qquad (3)$$

Where A is a constant, r is the position of the ray and x is the direction of the local density gradient. Equation (3) is solved for a large ensemble of rays using an iterative leap-frog routine. The computer model was benchmarked against analytic results[4] obtained for beam propagation in a spherically symmetric density profile using a distance of closest approach method. The model was found to be both stable and accurate.

The computer model assumes an axial density profile similar to Figure 4. The effect of a finite laser spot size was approximated by a top-hat function, on the assumption that phase zone plates formed the focal spot and plasma expansion does not exceed the focal spot diameter, therefore approximately 1-dimensional.

The plasma is divided in a series of zones and a uniform array of rays (typical 10^6 rays) propagated across this cylindrically symmetric plasma. The angular deviation for a ray is calculated during each iteration. On completion of the ray trace calculation, the predicted Schlieren image is then reconstructed by; a) removing rays with deflection angles below those in the inequality (2), and b) projecting the remaining rays back to the mid-point of the simulated plasma. This is equivalent to modelling a perfect optical imaging system. The imaged rays are binned to represent the effect of the experimental CCD detector.

A ray tracing result for interpenetrating 100 nm thick CH plasmas with an initial separation of 1 mm and a delay of 500 ps is shown in Figure 5. This ray tracing result is compared and overlaid on the data shown in Figure 3. There is no temporal averaging to account for the 80 ps probe duration.

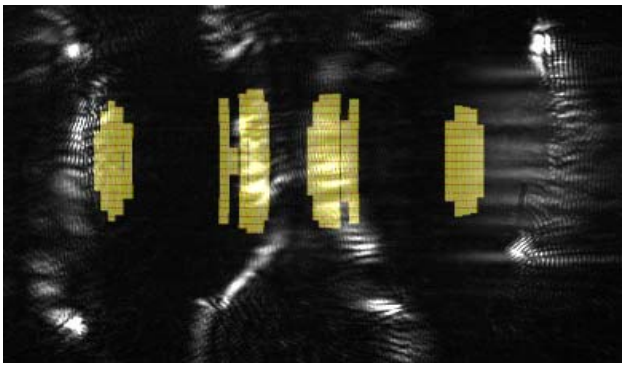

Figure 5. Comparison of a simulated Schlieren image in yellow with the experimental result taken from Figure 3.

Figure 5 clearly illustrates the correlation between the experimental data and the ray tracing results. The position and shape of the central two features, which are of most interest, is correctly predicted. The positions of these features from the laser-irradiated surfaces of the two foils are not as accurately matched.

We note the vertical modulation of intensity in the experimental data, particularly over a broad area of the right hand foil. These features in low-density plasma highlight plasma filamentation. This filamentation is attributed to the initial target foil quality, and imprinting by the drive laser beams.[5] These simulations do not model the affect of target nor laser intensity non-uniformities and are not expected to reproduce such features.

Schlieren images of colliding plasmas described here are three-dimensional in nature. The data may be approximately interpreted using 1-dimension hydrodynamic simulations and comparing the calculated electron density gradients. Comparison with experiment has been problematic and has led to the development of a procedure based on ray tracing though a cylindrically symmetric plasma. The simulated results broadly reproduce experimental data, under the assumption of non-interacting counter-streaming plasma flow; the model will be used to interpret future experimental data. These simulation results have enabled the design of a higher resolution, both spatial and temporal, Schlieren diagnostic for use in future experiments[5].

References

1. Woolsey NC, Ali YA, Evans RG, Grundy RAD, *et al*. Physics of Plasmas, 8, 5, 2439-2445, (2001)
2. Noll R, Claus R, Weikl B and Herziger G Applied Optics, 25, 5, 769-774, (1986)
3. Decker GW, Deutsch R, Kies W and Rybach J Applied Optics, 24, 6, 823-828, (1985)
4. G Pert Plasma Physics, 25, 4, 387-419, (1983)
5. Grundy RAD, *et al.* CLF Annual Report 2001-2002, RAL-TR-2002-013, 55, (2002)
6. Evans RG and Woolsey NC CLF Annual Report 1999-2000, RAL-TR-2000-034, 77 (2000)
7. Helander P, *et al*. CLF Annual Report 2000-2001, RAL-TR-2001-030, 58 (2001)

Stimulated Synchrotron Radiation from Ultra-intense, Circularly Polarized Laser Light in Plasma

L J Hill, H C Barr

Physics Department, University of York, Heslington, York, YO10 5HZ

Main contact email address: *hcb1@york.ac.uk*

Introduction

Electrons in the field of a circularly polarized laser pulse travel in circles with constant speed and radius. At ultrahigh intensities individual electrons achieve relativistic speeds and give rise to synchrotron emission into harmonics of the laser driver up to some maximum cut-off[1]. In plasma, electron density fluctuations are necessary to generate net synchrotron radiation; this arises from the anharmonic oscillation of electrons across a density gradient. If these harmonics are phase matched with plasma waves then growth can be seen via a mechanism similar to stimulated Raman scattering (SRS). At ultrahigh intensities the process becomes parametrically unstable; hence stimulated harmonic generation (SHG) occurs. Growth can be seen for all harmonics up to a predicted cut-off, after which growth decays exponentially with harmonic number. At intensities of 10^{21} Wcm^{-2} for a 1μm laser we see harmonic emission with wavelengths well into the hard x-ray region.

A simplified, but general dispersion relationship for the parametric instability of ultra-intense, circularly polarized, laser light in plasma of arbitrary density was presented in an earlier report[2]. The resulting difference equation, much simpler in form than previous work[3], reproduces familiar results and expressions for Raman growth rates and stimulated harmonic generation.

The following work describes analysis where the difference equation may be solved in underdense plasma by transforming into a more tractable form involving Bessel function summations. This low-density analysis links our dispersion relation to other separate but related studies in the field[4]. Expressions are derived for the growth rates of the generated harmonics for all scattering angles. The dependence on harmonic number and emission angle is the same as that governing the synchrotron radiation emitted into harmonics from an electron in arbitrary circular motion.

The Difference Equation

The main result of our previous report was the difference equation:

$$\sum_{n=-2}^{n=2} \alpha_n(\omega, \mathbf{k})\,\Phi(\omega + n, \mathbf{k} + n\mathbf{k}_0) = 0$$

where, letting $\omega_n = \omega + n$, $k_n = k + nk_0$ and $s = k_\perp v_0$,

$$\alpha_0(\omega,\mathbf{k}) = \frac{\Delta(\omega,\mathbf{k})}{D(\omega,\mathbf{k})} + \left(\frac{v_0^2\omega_{pr}^2}{2} + \frac{s^2}{4}\right)\left(\frac{1}{D(\omega_{+1},\mathbf{k}_{+1})} + \frac{1}{D(\omega_{-1},\mathbf{k}_{-1})}\right)$$

$$\alpha_{\pm1}(\omega,\mathbf{k}) = -\frac{s}{2}\left(\frac{\omega}{D(\omega,\mathbf{k})} + \frac{\omega_{\pm1}}{D(\omega_{\pm1},\mathbf{k}_{\pm1})}\right)$$

$$\alpha_{\pm2}(\omega,\mathbf{k}) = \frac{s^2}{4D(\omega_{\pm1},\mathbf{k}_{\pm1})}$$

$D(\omega,\mathbf{k})$ and $\Delta(\omega,\mathbf{k})$ are the familiar dispersion relations for light waves and electron plasma waves. Here v_0 is the electron oscillation velocity, which is directly related to the strength of the laser via the intensity parameter a_0 (the normalized peak vector potential $e\mathbf{A}_0/m_0c^2$), by $v_0 = a_0/\gamma_a$ ($\gamma_a = (1+a_0^2)^{1/2}$ is the relativistic mass increase of the electrons in the field of the laser). The laser modifies the plasma frequency such that $\omega_{pr}^2 = \omega_p^2/\gamma_a$. Times are normalized to the inverse of the laser driver frequency, ω_0^{-1}, velocities to c and lengths to c/ω_0..

This is a 4th order linear difference equation for a scalar unknown Φ with scalar coefficients. When expressed in matrix form the coefficients form the elements of an infinite symmetric penta-diagonal matrix. Solutions to the system are found by numerical root finding methods from which growing solutions can easily be extracted. Figure 1 shows contour plots of normalized growth rates (Γ/ω_0) in the (k_x , $k_\perp$) plane for underdense plasma. These figures show for fixed $\omega_{pr}^2 = 0.1$ the emergence of harmonic generation with increasing intensity and are consistent with previous studies[3].

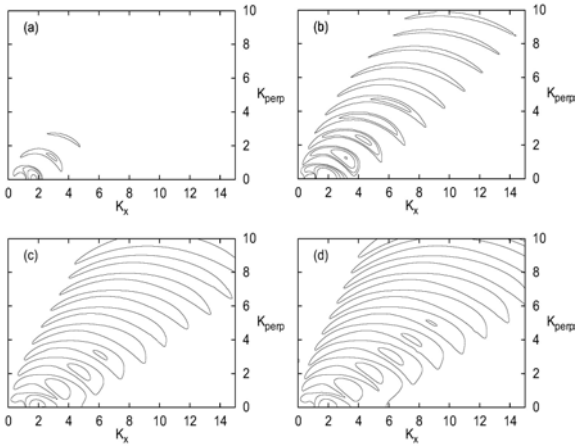

Figure 1. Normalized growth rates for $\sqrt{2}a_0$ = 1, 2, 5 and 10 (a, b, c and d). For a) and b) contours start at a minimum of 0.05 and increment by 0.05. For c) and d) contours start at 0.1 and increment by 0.1.

Rarefied Plasma Dispersion Relation

We begin by expressing the difference equation in the form of a pair of coupled second order difference equations, which can be solved in terms of Bessel functions of the first kind. In effect we have converted the penta-diagonal form with simple elements into a dense matrix form involving Bessel functions. However, for the case of 'rarefied' plasma ($\omega_{pr}^2 << 1$) headway can be made although this can still correspond to quite high densities in ultra-intense situations. We arrive at a general dispersion relation for low density plasma, subject only to $|\Omega| << 1$:

$$1 + \frac{\omega_{pr}^2 D_0}{\Omega^2}\sum \frac{F_l}{D_l} = 0$$

with the mode frequency, $\omega_n = N\omega_0 + \Omega$ and

$$F_l = \frac{v_0^2}{2}\left(J_{l+1}^2(s) - J_{l-1}^2(s)\right) - J_l^2(s) \quad \textit{and} \quad D_n = D(\omega_n, \mathbf{k}_n)$$

Restricting attention to stimulated harmonic generation, we assume that a single harmonic is resonant, $D_N \approx 0$ for a given harmonic number N. Isolating this resonant denominator we have:-

$$\left(\Omega^2 + \omega_{pr}^2 D_0 \sum_{l \neq N} \frac{F_l}{D_l}\right) D_N = -\omega_{pr}^2 D_0 F_N$$

F_N then reduces to

$$F_N = v_0^2 \left(J'_N(s)\right)^2 + \cot^2\theta_N \left(J_N(s)\right)^2$$

where $s = Nv_0 \sin\theta_N$ in the low density limit. θ_N is the emission angle relative to the laser propagation direction.

Non-relativistic intensities

In the low intensity limit, $s << 1$, further reduction of this equation is possible. Growth rates for simple three wave interactions can be calculated assuming phase matching such that both Δ and $D_N \approx 0$ are simultaneously resonant.

$$\Gamma_N = (N\omega_{pr})^{\frac{1}{2}} \frac{(Nv_0/2)^N}{N!} \sin\left(\frac{\theta_N}{2}\right) \sin^{N-1}\theta_N \left(1+\cos^2\theta_N\right)^{\frac{1}{2}}$$

This expression for the growth rate applies to SRS ($N=1$) and SHG ($N>1$) except for forwards SRS which is a four-wave interaction. For high harmonics this growth rate peaks close to exact side scattering. Using Stirling's formula the growth rate is

$$\Gamma_N \approx \frac{1}{2}\left(\frac{\omega_{pr}}{\pi}\right)^{\frac{1}{2}} \left(\frac{ev_0}{2}\right)^N$$

We see from these expressions the dominance of stimulated Raman scattering over harmonic emission in the weakly coupled limit.

Relativistic intensities

In the strongly coupled 'Compton' regime where $|\Omega| >> \omega_{pr}$, the Ω^2 term dominates in the left hand side of the equation. We can write $D_N = (N+\Omega)^2 - \omega_{pr}^2 - k_N^2 \approx 2N(\Omega - \delta k)$ where δk is a mismatch factor. Optimum growth arises when this mismatch is zero so that

$$\Omega^3 = -\frac{\omega_{pr}^2 D_0}{2N} F_N$$

For the low frequency fluctuation $D_0 \approx -k^2 \approx -4N^2 \sin^2(\theta_N/2)$, so that the growth rate is

$$\Gamma_N = \frac{\sqrt{3}}{2}\left|2N\omega_{pr}^2 \sin^2\left(\frac{\theta_N}{2}\right) F_N\right|^{\frac{1}{3}}$$

This is exactly the expression obtained by Sakharov & Kirsanov[4]. Assuming $N >>1$, $\theta_N = \pi/2$ and considering relativistic laser intensities so that the normalized electron velocity, $v_0 \rightarrow 1$, gives $s = N$ and $F_N \approx [J'_N(N)]^2 \approx 0.17N^{-4/3}$. This decrease of the growth rate with harmonic number is countered by the increase in the wavenumber of the low frequency fluctuation k, so that:

$$\Gamma_N = \frac{\sqrt{3}}{2}\omega_{pr}^{2/3}\left[NJ'_N(N)^2\right]^{1/3} \approx 0.48\omega_{pr}^{2/3}N^{-1/9}$$

Then for high harmonics at relativistic intensities, the growth rate falls off with N at a slow rate until $N = N_{max} = 3\gamma_a^3$. This is the same dependence that appears for stimulated backscattered harmonic generation from linearly polarized pulses[5]. For a linearly polarized laser, only odd harmonics exist in the back-scattered ($\theta_N = \pi$) direction[5], whereas for circular polarization F_N shows only the fundamental is non-zero in the back-scattered direction but both odd and even harmonics can exist at off axis angles.

The form of F_N from the low-density dispersion relation recovers exactly the same dependence on harmonic number and emission angle that is obtained for the synchrotron radiation from a single electron in circular orbit. This dependence emerges generally for rarefied plasma densities without making assumptions either about far field or about coherent or incoherent scattering.

An electron in circular orbit at relativistic speed emits a narrow pencil of light in the direction of motion contained within a range of angles $\delta\theta \sim 1/\gamma_a$. Viewed from a particular direction ($\mathbf{k}_N$), this is observed only for a short time and hence contains a broad range of frequencies up to $\omega \sim 3\gamma_a^3\omega_0$. Since the motion is periodic this is at the discrete set of harmonic frequencies $\omega_N = N\omega_0$. If the lifetime of the radiation is finite for, say, an ultra-intense, ultra-short pulse this will give width to the harmonic lines. For example a pulse of duration 500*fs* implies a line width of $\delta\omega/\omega_0 \approx 0.001$. The power radiated into a solid angle $d\Omega$ at the N^{th} harmonic is proportional to F_N:-

$$\frac{dP_N}{d\Omega} = \frac{e^2}{2\pi c}\omega_0^2 N^2 F_N$$

The two terms in F_N relate to radiation polarizations both in and out of the plane of the electron orbit and are of comparable magnitudes except for the $\cos\theta_N$ dependence.

For high harmonic numbers $N >> 1$, asymptotic forms for F_N are available. These show strong emission for harmonic numbers N and angles $\theta_N = \pi/2 + \delta\theta$ satisfying

$$\frac{N}{3}\left(\gamma_a^{-2} + \delta\theta^2\right)^{2/3} < 1$$

When $\delta\theta = 0$ the maximum harmonic number is $N_{max} = 3\gamma_a^3$.

Conclusions

Following on from our previous report we have presented some results of growth rates calculated from the difference equation. These results and others are in agreement with previous results from other studies given in the references.

For rarefied plasma we have linked our work to that of Sakharov & Kirsanov. Indeed the exact same expressions have been derived. Upon testing the assumptions made by the aforementioned authors we conclude that the rarefied plasma assumptions given are valid for densities of $\omega_{pr}^2 \leq 10^{-3}$. In this regime, growth rates directly from the difference equation agree with those calculated from the Bessel function formula given above to within a relative error of 10%. At higher intensities the difference equation must be used to obtain correct growth rates.

The expression for rarefied plasma growth rates at relativistic laser intensities is seen to recover the exact same dependencies as the well-known result obtained for the synchrotron radiation from a single electron in circular orbit.

References

1. J. D. Jackson
   Classical Electrodynamics, 2nd ed. (Wiley, New York, 1975), Chap 14.
2. H. C. Barr and L. J. Hill
   CLF Annual Report 2000-2001, RAL-TR-2001-030, 59 (2001)
3. B. Quesnel, P. Mora J. C. Adam, S. Guérin, A. Héron and A. Laval
   Phys. Rev. Lett. 78 2132 (1997)
4. A. S. Sakharov and V. I. Kirsanov
   Phys. Plasmas. 4 3382 (1997)
5. P. Sprangle and E. Esarey
   Phys. Rev. Lett. 67 15 2021 (1991)

Double ionization processes in the R-matrix Floquet approach

H W van der Hart, L Feng

Department of Applied Mathematics and Theoretical Physics, Queen's University Belfast, Belfast BT7 1NN

Main contact email address: *h.vanderhart@am.qub.ac.uk*

Introduction

The theoretical description of atoms and ions in strong laser fields is of essential importance to understand the atomic response to the laser field in detail. One of the topics that has received great attention over the last decade is the relative importance of double and single ionization. This ratio is of interest in two different types of laser fields: low frequency and high intensity, as well as high frequency and 'low' intensity.

Many theoretical methods have focused on double versus single ionization for atoms subjected to a high-intensity low-frequency laser field. Walker *et al*[1] demonstrated that double ionization was significantly more pronounced in the atomic response than could be expected from a single-active-electron picture. These experiments provided the impetus for many theoretical approaches to describe the non-perturbative behaviour of two-electron systems in intense laser fields[2-5].

Recent developments in the generation of high-intensity X-ray laser sources[6] have recently stimulated interest in the theoretical description of double ionization processes at high frequencies. At these frequencies only a few photons are required to eject two electrons from the atom. However, such photons may not only ionize the atom; they may also be sufficiently energetic to ionize singly charged ions. At these photon energies, the competition between sequential and non-sequential double ionization probes the influence of electronic interactions on the atomic behaviour.

Several different types of methods exist for the description of atoms in strong laser fields. In a time-dependent approach, one solves the Schrödinger equation for an atom subjected to a *short* intense laser pulse directly. In a time-independent approach, one uses the Floquet-Fourier Ansatz to transform the time-dependent Schrödinger equation into a time-independent one.

The time-independent R-matrix Floquet approach[5] is best suited when the number of photons absorbed is relatively small. As a consequence of the Fourier-Floquet Ansatz, the atomic wavefunction must be determined for each net number of photons absorbed or emitted. In order to keep the calculations feasible, it is necessary to restrict the total net number of photons absorbed or emitted.

The R-matrix Floquet approach has presently only been applied to investigate single ionization processes. In order to describe double ionization processes within the R-matrix Floquet approach, we have combined R-matrix Floquet theory with B-spline basis sets for the description of the two-electron continuum. B-spline basis sets were introduced for atomic physics calculations about 15 years ago[7]. Since B-spline basis sets allow continuum effects to be included in a straightforward manner, they are now widely used in theoretical atomic physics[8].

We have chosen to study He for our initial calculations on double photoionization within the R-matrix Floquet approach, since He is the simplest two-electron atom. A schematic diagram of the He energy levels is given in Figure 1, where we have highlighted the energy levels that we are particularly interested in: the $1s^2$ ground state, and the lowest doubly excited state $2s^2$. These states are chosen because of the large amount of experimental and theoretical data available for the $1s^2$ state, and because the competition between autoionization and photoionization for doubly-excited states is important for the dynamics of atoms in strong laser fields.

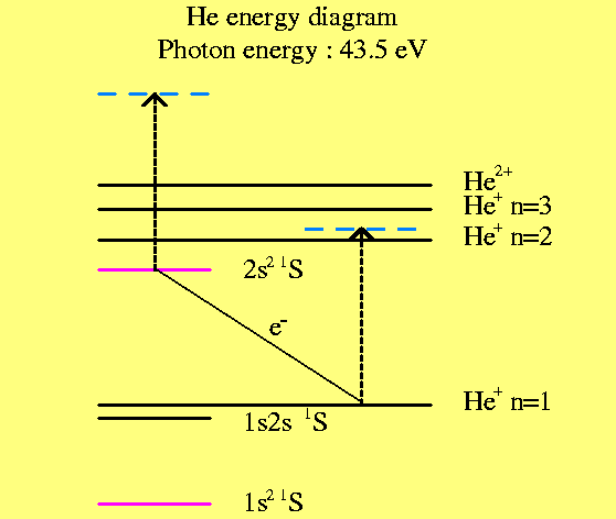

Figure 1. Schematic energy diagram of He. Our focus is on double and single photoionization of He initially in the $1s^2$ and $2s^2$ states. Two distinct photoabsorption pathways for the $2s^2$ state are indicated.

Double photoionization using B-spline basis sets

We have first established that B-spline basis sets are well suited for the description of the double continuum by examining the relation between double and single photoionization of He in the $1s^2$ ground state within perturbation theory. This process has been studied extensively over the last decade, since this process measures the importance of electron interactions within atoms. The photon is absorbed by a single electron; a many-electron response thus indicates energy transfer from one electron to the other.

In order to describe the two-electron continuum, we describe it in terms of products of B-spline basis functions. B-splines are piecewise polynomials with maximum smoothness. They are highly suited to describe smooth functions, such as atomic wave functions. Although B-splines are non-orthogonal functions, their limited extent means that each B-spline has a non-zero overlap with a small number of other spline functions. This means that the matrix calculations generally involve banded matrices.

Results for the ratio between single and double ionization of ground-state He[9] are shown in Figure 2, and are compared to other theoretical and experimental data[10,11]. The agreement with the converged close-coupling calculations[10] is highly satisfactory. The differences close to threshold are due to the present method having difficulty in describing outgoing electrons with identical energy. These differences can in principle be reduced by enlarging the box size. The agreement with experiment[11] is also quite good with a difference of less than 5% above a photon energy of 120 eV.

Combining B-spline basis sets and R-matrix Floquet theory

After demonstrating the appropriateness of the B-spline basis set for describing the two-electron continuum, we have integrated the B-spline basis sets into R-matrix Floquet theory. We thus describe the full motion of the two electrons in each Floquet block. The main changes involve the determination of the Floquet R-matrix and the data input routines.

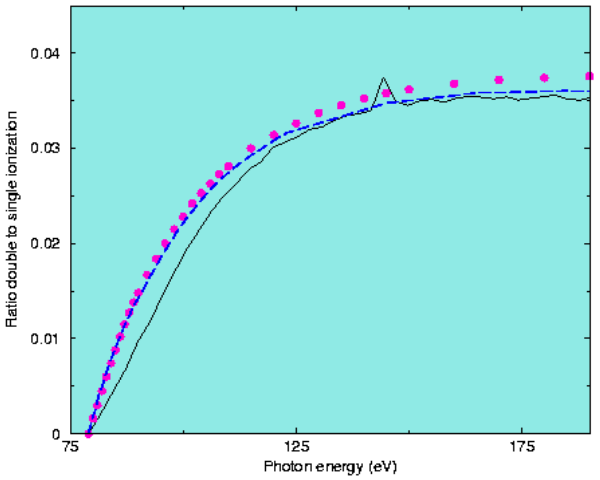

Figure 2. Ratio between double and single photoionization for ground-state He. Results using the B-spline basis (solid black line) are compared to experimental results[11] (purple circles) and other theoretical results[10] (dashed blue line).

Firstly, we have investigated single photoionization from the ground state of He within this approach. The results obtained using the new code are in excellent agreement with the previous results. It should be emphasized that the R-matrix Floquet approach employs a more sophisticated approach to describing the asymptotic wave functions than the previous calculations, and that minor differences between the two sets of results would not be unexpected. However, the agreement gives us confidence in the accuracy of the approach.

One of the problems of the R-matrix Floquet approach for double ionization is the computational requirement. A proper description of the double continuum requires an extensive basis set. In the R-matrix Floquet approach, we need to multiply this basis set by the number of Floquet blocks included in the calculation. In order to keep the calculation manageable on a 2Gb PC, we have only included the minimum number of Floquet blocks, namely 2.

Despite the limitation to 2 Floquet blocks, there are still new physical processes that can be investigated using this approach: the competition between double and single ionization when the initial state is a doubly excited state. In this case, as shown in Figure 1, several pathways involving the absorption of a photon lead to ionization. Firstly, direct photoabsorption can lead to single as well as double photoionization of $2s^2$. Secondly, the $2s^2$ state may autoionize to the 1s state of He^+ with the emission of an electron. Following autoionization, the 1s state of He^+ may absorb a photon, possibly exciting the 2p state of He^+.

Figure 3 shows the ratio for double to single photoionization for the $2s^2$ state of He embedded in a laser field with an intensity of $5x10^{11}$ W/cm^2 as obtained by the R-matrix Floquet approach with B-spline basis sets[12]. The results are compared to experimental results for double photoionization of Be[13], and He[11]. Since the two valence electrons of the Be ground state are in $2s^2$, the theoretical results and the experimental results for Be are expected to be similar. The similarity with the He results is more surprising, although electron-electron effects are expected to be strong for both types of states.

Figure 3 shows that the ratio between double and single photoionization is very similar for the He $2s^2$ state and the Be $1s^22s^2$ state with a relative difference of about 20%. The main difference with the He results can be seen around a final-state energy of 0.72 a.u. At this particular final-state energy, the 1s – 2p transition in He^+ becomes resonant, so that the dominant photoabsorption process is autoionization of $2s^2$ followed by excitation of the residual He^+ ion to the 2p state. Since reaching this final state requires absorption of one photon, the ratio between double and single ionization, involving the absorption of a single photon, decreases rapidly at a final-state energy of 0.6 a.u. This decrease is absent in the He results since the ground state of He cannot autoionize.

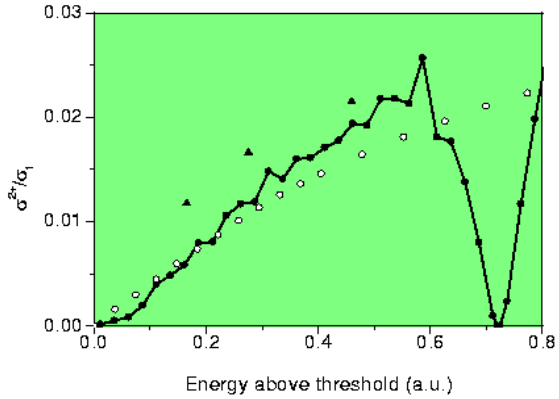

Figure 3. Ratio between double and single ionization involving photoabsorption. Present results for the $2s^2$ state of He (solid line, filled circles) are compared to experimental results for Be (filled triangles) and ground-state He (open circles).

Conclusions

We have extended the R-matrix Floquet approach to enable the study of double ionization of atoms embedded in strong laser fields. This has been achieved by combining R-matrix-Floquet theory and B-spline basis sets. The accuracy of the approach is verified by examining the ratio between single and double photoionization of ground-state He. We have determined the branching ratios for several photoabsorption processes that can lead to either single or double ionization. We have demonstrated that the ratio between double and single photoionization may be crucially dependent on the presence of resonances for the singly ionized target.

References

1. B Walker, B Sheehy, L F DiMauro, P Agostini, K J Schafer and K C Kulander, Phys. Rev. Lett. 73, 1227 (1994).
2. J S Parker, L R Moore, K J Meharg, D Dundas and K T Taylor, J. Phys. B 34, L69 (2001).
3. J B Watson, A Sanpera, D G Lappas, P L Knight and K Burnett, Phys. Rev. Lett. 78, 1884 (1997).
4. P G Burke, P Francken and C J Joachain, J. Phys. B 24, 761 (1991).
5. J Zhang and P Lambropoulos, Phys. Rev. Lett. 77, 2186 (1996).
6. J Andruszkow *et al*, Phys. Rev. Lett. 85, 3825 (2000).
7. W R Johnson and J Sapirstein, Phys. Rev. Lett. 57, 1126 (1986).
8. H Bachau, E Cormier, P Decleva, J E Hansen and F Martín, Rep. Prog. Phys. 64, 1815 (2001).
9. H W van der Hart and L Feng, J. Phys. B 34, L601 (2001).
10. A S Kheifets and I Bray, Phys. Rev. A 54, R995 (1996).
11. J A R Samson, W C Stolte, Z-X He, J N Cutler, Y Lu and R J Bartlett, Phys. Rev. A 57, 1906 (1998).
12. L Feng and H W van der Hart, submitted for publication.
13. R Wehlitz and S B Whitfield, J. Phys. B 34, L719 (2001).

Non-Hermitian Floquet Dynamics of Argon Atoms

M Plummer, C J Noble

CLRC Daresbury Laboratory, Daresbury, Warrington, Cheshire, WA4 4AD

Main contact email address: *c.j.noble@rdl.ac.uk*

Floquet theory simplifies the solution of the time-dependent Schrödinger equation for an atom in a strong laser field by assuming the laser intensity varies slowly with time. The resulting quasi time-independent Schrödinger equation may be solved accurately using R-matrix theory even for multielectron atoms and ions. Numerical solutions of the corresponding time-dependent Schrödinger equation have so far been limited either to one or two active electrons or to simplified target descriptions. In those cases where both Floquet and numerical solutions are available, the two are found to agree provided the laser pulse varies slowly over the cycle time of the laser.

Using R-matrix-Floquet theory we have studied the multiphoton ionization rate for argon atoms in a KrF laser field. The calculations predict resonance effects in the ionization rate for laser intensities in the range 10^{12} - 10^{14} W/cm^2. The resonant processes are manifested as strongly avoided crossings of the calculated Floquet quasi-energies. We have also shown that these field-atom resonances strongly influence the corresponding harmonic generation rates. The calculations for Ar atoms in a 248 nm laser field show strong enhancements of the 3, 5 and 7-th harmonics at relatively low laser intensities. These enhancements are expected to be experimentally observable. Similar calculations to investigate multiphoton ionization and harmonic generation by Neon atoms are continuing.

Floquet Dynamics

Floquet dynamics techniques provide a framework for considering shorter pulses where the usual Floquet approach would be invalid. In particular they allow the transfer of flux between the field-dressed states to be followed as the intensity of the laser pulse sweeps through the region of quasi-energy avoided crossings. In effect the Floquet states provide a basis in which to expand solutions of the time-dependent Schrödinger equation.

A non-Hermitian Floquet theory of this type has been tested by Day *et al* (2000) [2] against numerical solutions of the time-dependent Schrödinger equation for hydrogen atoms in a strong short laser pulse. It is assumed that the time evolution of the expansion coefficients of the time-dependent states is slow compared to the time-dependence of the Floquet state itself. The latter time-dependence may then be removed using the orthogonality properties of the Floquet states. Day *et al* obtained good agreement between the Floquet dynamics and full numerical solutions.

We have extended the Floquet dynamics method to treat multielectron atoms using R-matrix-Floquet states. In this initial study we have not taken full account of wave functions which extend beyond the R-matrix sphere. As a consequence errors are introduced into the results for the higher lying Floquet states in the regions near strongly avoided quasi-energy crossings. Numerical studies have been carried out to check the procedures introduced to minimize these effects. In future work these long-range effects will be taken fully into account. Floquet dynamics calculations have been carried out to study how multiphoton ionization of Ar atoms depends on the shape of the laser pulse.

The results in Figure 1, below, show Floquet state probabilities for a seven Floquet state calculation of Argon in a 248 nm sin^2 laser pulse with peak intensity 1.1 x 10^{14} W/cm^2. The states correspond to the quasi-energies described previously [3] . At the beginning and end of the pulse the Floquet states are field-free atomic states. Significant population of the excited states is observed. By controlling the pulse shape the Floquet state population can be controlled. These numerical experiments may serve as a guide to experiment.

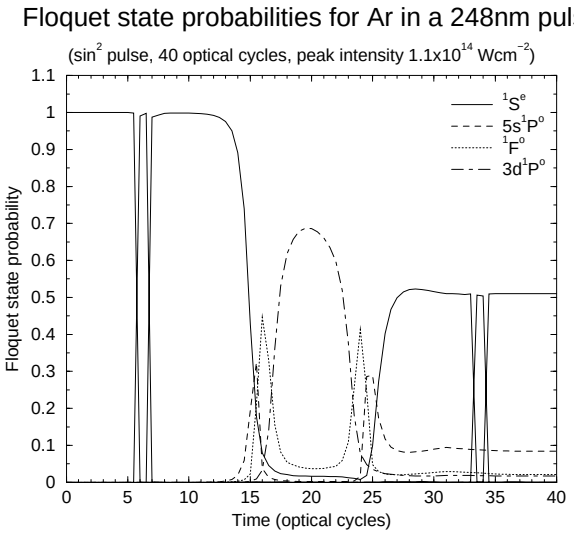

Figure 1. Floquet state probabilities during a 248nm pulse.

We have extended these experiments to study coherent control of field-free atomic state populations via asymmetric pulse shapes. The results will be published shortly.

The probability of populating a particular state at the end of the laser pulse is shown in Figure 2. Laser pulses with lengths up to 40 optical cycles have been considered. In each case the pulse is taken to have a sin^2 amplitude and the fraction of the pulse length over which the intensity is increasing is varied. This fraction is indicated in the legend for each of the curves in the figure. It is clear that the population of a state at the end of the pulse may be significantly altered depending on the pulse shape. For example, it is seen that the population of the 3d^{1}P^0 state is enhanced by a sharply rising pulse with a slow decay and is reduced for a slowly rising pulse.

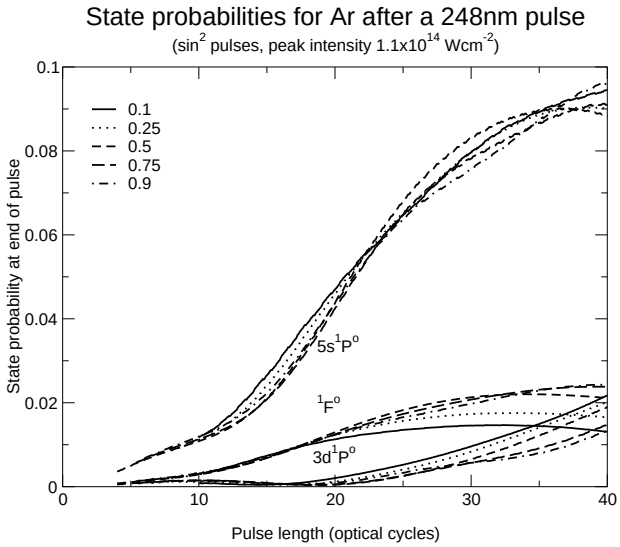

Figure 2. State probabilities after a 248 nm pulse.

Future work

Various improvements to our implementation of the Floquet dynamics approach are being developed and will be used in more general studies of the multiphoton ionization of the inert gases. This work will involve the use of large-scale parallel calculations.

Future work will concentrate on developing methods for obtaining numerical solutions to the time-dependent Schrödinger equation for multielectron atoms. Techniques such as time-dependent R-matrix theory will be investigated. It is expected that these new techniques will provide insight on multiphoton processes involving very short (attosecond) laser pulses and pulse intensities above 10^{15} W/cm^2.

References

1. M Plummer and C J Noble, J.Phys.B:At.Mol.Opt.Phys. 35 L51 (2002)
2. H C Day, B Piraux and R M Potvliege, Phys. Rev. Phys. A 61 031402 (2000).
3. M Plummer and C J Noble, J.Phys.B:At.Mol.Opt.Phys. 33 L807 (2000)

Simulations of Ponderomotively Generated Magnetic Fields

R G Evans

Physics Department, University of York, York, YO10 5DD

Main contact email address: *r.g.evans@physics.org*

Introduction

Magnetic fields can be generated in initially unmagnetised laser produced plasmas by a variety of effects which have their common origin in Faraday's equation $\partial\mathbf{B}/\partial t$ = curl **E**. The electric field is obtained from a general Ohm's law[1] and magnetic field generation occurs due to non-parallel density and temperature gradients, due to the ponderomotive light pressure and due to currents and instabilities in the plasma.

The equation for the evolution of magnetic field approximates to

$$\frac{\partial \mathbf{B}}{\partial t} = \frac{c^2}{4\pi\sigma}\nabla^2\mathbf{B} + \mathrm{curl}(\mathbf{v}\times\mathbf{B}) + \frac{c}{e}\mathrm{curl}\left(\frac{1}{n_e}\nabla p_e\right) \qquad (1)$$

where p_e includes the electron pressure and the ponderomotive pressure. Magnetic fields of some tens of MGauss are observed[2] at irradiances of 10^{14} - 10^{15} Wcm^{-2} due to the density and temperature gradients but fields of Gigagauss magnitude are predicted to occur[3], and have recently been measured[4] at irradiances around 10^{19}Wcm^{-2} due to the gradient of ponderomotive pressure.

Geometric Effects on the Magnetic Field Distribution

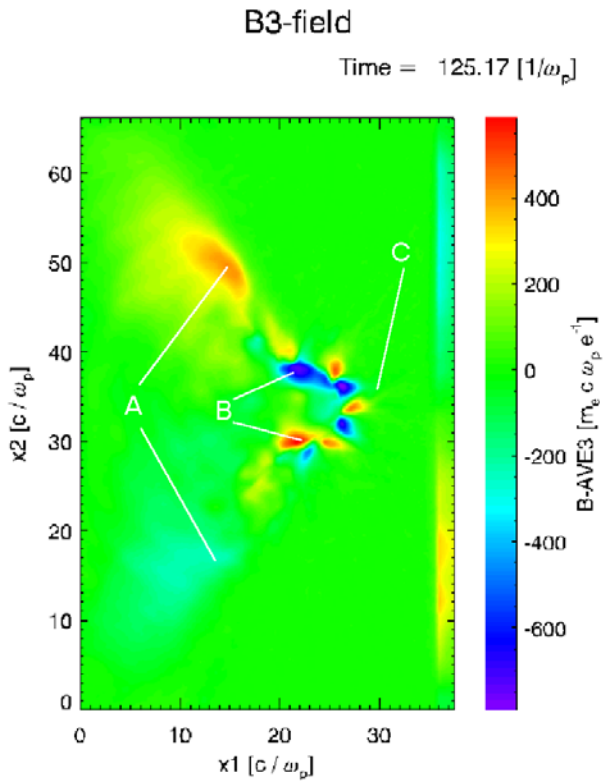

Figure 1. Osiris simulation of the quasi DC magnetic fields generated by a laser at normal incidence.

The original simulations of ponderomotively generated magnetic fields[5,6] considered lasers at normal incidence and the generated magnetic fields are toroidal around the laser focal spot. For comparison with the later simulations Figure 1 shows a simulation using the 2-1/2D PIC code OSIRIS[7] for an incident irradiance of 10^{19} Wcm^{-2} on a plasma with a linear density ramp increasing to $15n_c$. The features A, B, C label respectively the magnetic fields generated by the density and temperature gradients (at low density), by the ponderomotive force (around critical density) and by the Weibel instability (small features within the focal spot). Obviously in the normal incidence case the magnetic fields are of equal magnitude and opposite polarity either side of the focal spot.

The experimental measurements of GGauss magnetic fields by Tatarakis et al[4] used a laser incident at 45 degrees and this makes a surprisingly major difference to the magnetic field geometry, Figure 2. Equation 1 contains diffusion and advection terms as well as the source term and in the high temperature plasma the magnetic field is efficiently advected away from the source region by the electron flow.

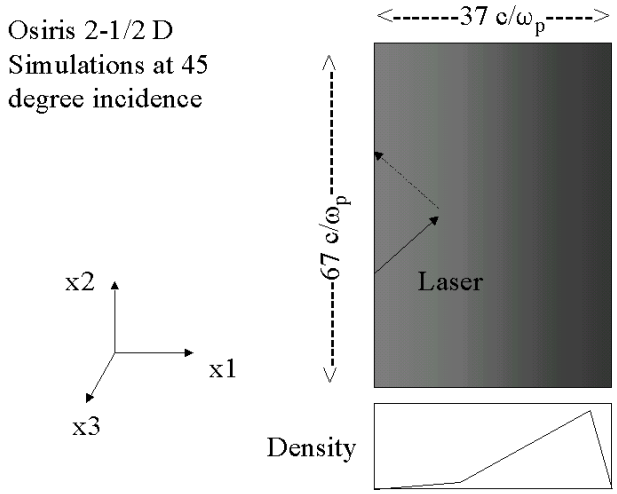

Figure 2. Schematic of the 45 degree simulation geometry.

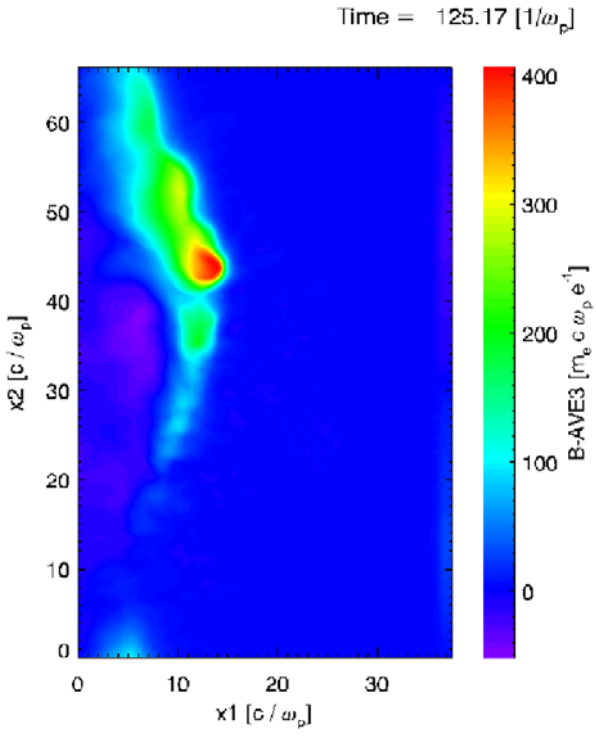

Figure 3. Osiris simulation of the quasi-DC magnetic field at 45 degree incidence.

The difference from Figure 1 is striking, Figure 3. The gradient of ponderomotive pressure now has components into and away from the target and the field generated on the low density side is rapidly advected away by the electron expansion while the field on the high density side is largely confined. The result is that the positive polarity field on the high density side is intense and compact while the negative polarity field on the low density side is weak and diffuse. The total flux is the same for both polarities except where the field is advected out of the simulation box.

The simulations of the quasi-DC magnetic field are very robust against changes in the density gradient, maximum density and laser polarisation which together change the DC magnetic field by no more than 20%. The magnetic field rises only a little more slowly than the laser rise time of 20 fs in the simulation and then the peak magnetic field stays fairly constant although its position moves as laser 'hole-boring' proceeds.

Intensity Scaling and Comparison with Experiment

Figure 4 shows the peak DC magnetic field in the Osiris simulations together with the experimental measurements of Tatarakis et al[4] and the scaling with the ponderomotive potential as would be expected from Sudan's analytical model[3]. Agreement with experiment is excellent although the experimental data shows signs of having a weaker dependence on irradiance. The agreement with Sudan's model is also good but the simulations fall increasingly below the model at irradiances above 10^{20}Wcm^{-2} where plasma motion due to hole boring becomes more rapid.

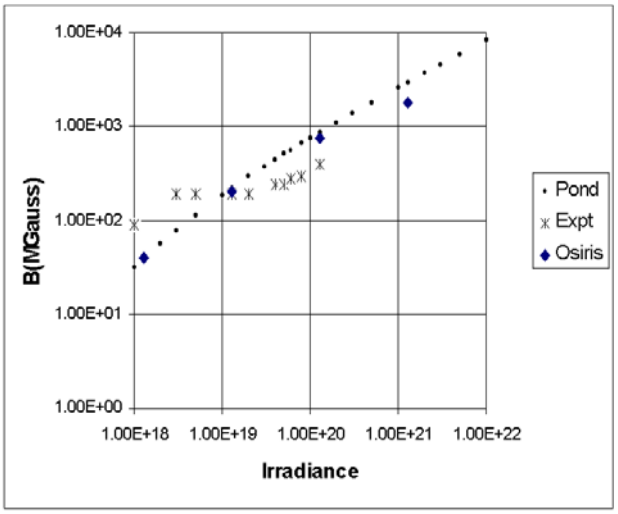

Figure 4. Intensity dependence of the DC magnetic field from the simulations and from experimental measurements.

Associated Plasma Density and Electric Fields

The technique for measuring magnetic fields in Reference[4] is through the effects on the propagation of laser harmonic light. Given the likelihood of producing GGauss magnetic fields at irradiances over 10^{21}Wcm^{-2} it is interesting to speculate as to whether these regions of highly magnetised plasma could be observed in X-ray emission so as to measure the effect of the huge fields on the bound energy levels. From the Osiris simulations it is possible to assign electron and ion densities to the region of magnetised plasma by calculating the densities on the high and low density sides of the magnetic field maximum where the field has fallen to half the peak value. Figure 5 shows these densities as a function of irradiance.

The density of the magnetised plasma increases from a fraction of critical density at 10^{18}Wcm^{-2} to over 10 times critical density at 10^{21}Wcm^{-2}. At the higher densities a plasma of a few microns in size will be readily detectable in its X-ray emission even though the duration of the magnetised phase may be less than 1 ps. Figure 5 also shows that the electron and ion densities are not equal and so the non-neutral plasma must also have an associated DC electric field. Osiris can also calculate the quasi DC electric field and this turns out to be remarkably large as shown in Figure 6 at an irradiance of 10^{20}Wcm^{-2}. The peak value of the electric field is around 2×10^{11}Vcm^{-1} and in spectroscopic terms this electric field will dominate the magnetic field in its effect on the energies of bound electrons.

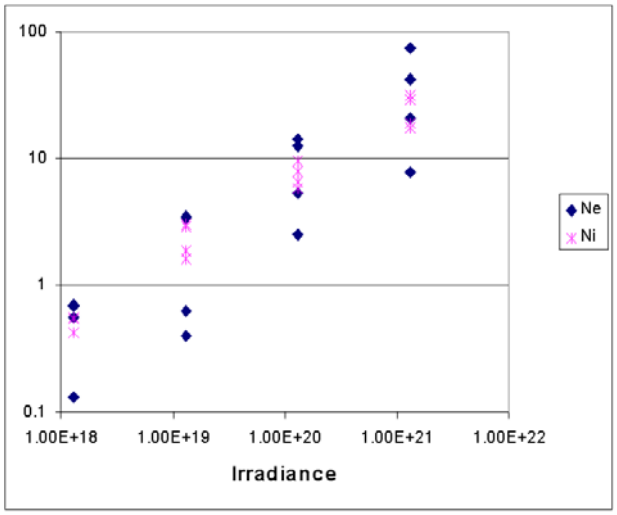

Figure 5. Plasma density associated with the magnetic fields.

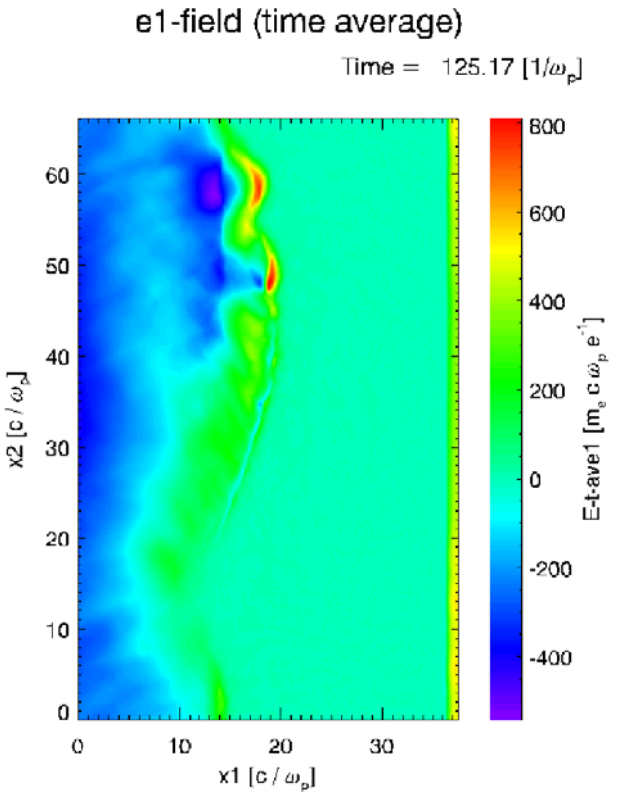

Figure 6. Quasi DC electric fields in the Osiris simulations.

Since Faraday's Law suggests that the time derivative of **B** depends on curl **E**, it might seem reasonable that the electric field would decay to zero faster than the magnetic field once the laser drive is turned off. This has also been investigated using Osiris with some very short laser pulses of 60fs duration but the results (Figure 7) show that the electric field persists after the laser pulse and its ratio to the magnetic field stays remarkably

constant. This is probably due to the fact that after the initial inductive generation of the **B** field it is subsequently supported by large quasi-DC plasma currents which are seen in the Osiris simulations and the resulting **j** x **B** force maintains the steep density profile and the charge separation electric field.

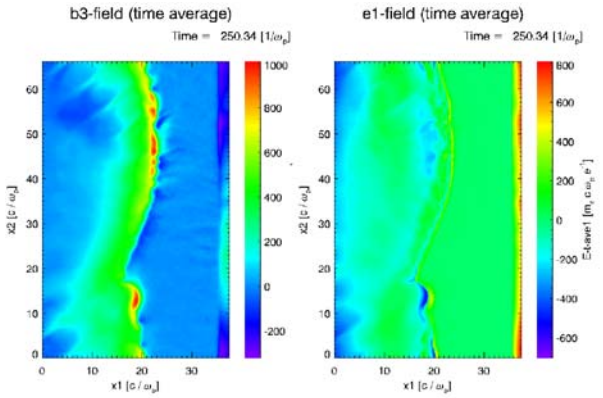

Figure 7. DC Magnetic and electric fields after the laser pulse.

Other Irradiation Geometries

Given the remarkable differences between normal incidence of the laser and 45 degree incidence and also motivated by the idea that X-ray spectroscopy of the magnetic field region would be most interesting, some other simple irradiation geometries have been simulated.

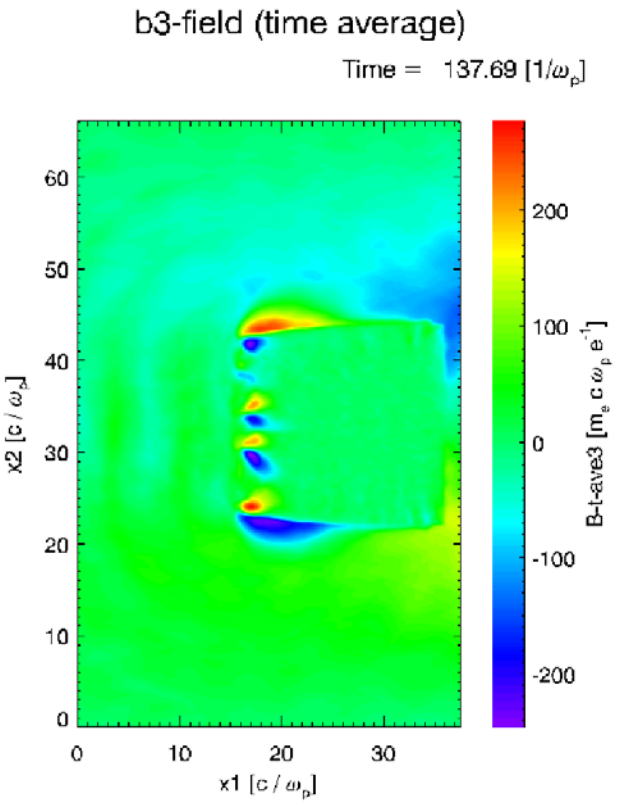

Figure 8. Simulation of a disk target extending from 22 c/ω_p to 44 c/ω_p in the transverse x2 direction.

Since normal incidence and its associated 'hole boring' result in the magnetic fields being generated somewhat 'inside' the initial target surface and by analogy the 45 degree 'hole boring' results in a constant movement of the magnetic field region, two interesting geometries designed for ease of diagnostic access and predictability of the region of maximum field are a small disk target, comparable to the laser spot radius and a small hole of similar size in a foil target.

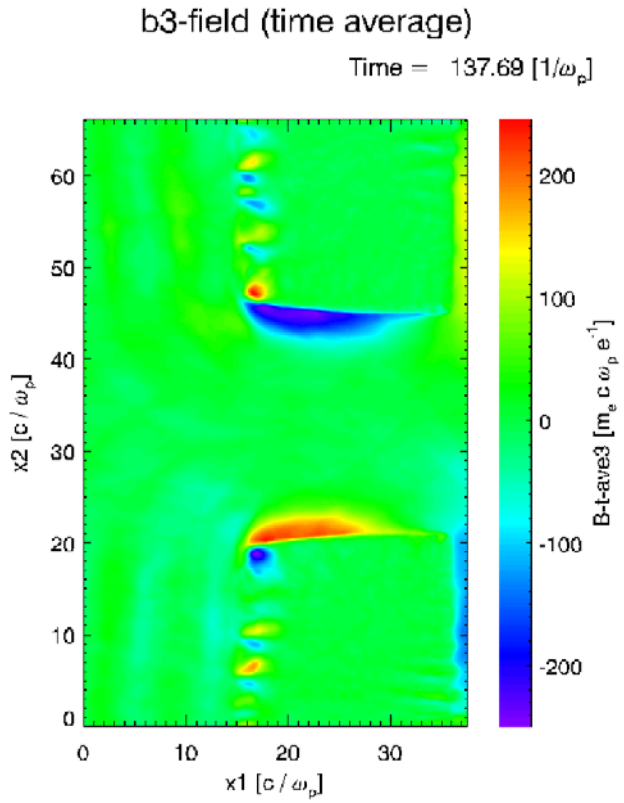

Figure 9. Simulation of a slab target with a hole extending from x2 = $22c/\omega_p$ to x2 = $44c/\omega_p$.

Osiris simulations of these two geometries are shown in Figure 8 and Figure 9. The magnetic field exists as expected on the outside of the disk target and on the inside of the hole in the foil. The 'hole' target produces somewhat higher magnetic fields since the plasma expansion into the hole is a converging flow compared with the free expansion on the outside of the disk and the flux losses due to advection of the field are less. Either target offers a simple alignment geometry for X-ray spectroscopy but the peak fields are slightly lower than for the illumination of 'solid' targets.

References

1. M G Haines
Can J Phys 64, 912 (1986) and references therein

2. J A Stamper and B H Ripin
Phys Rev Lett 34, 138 (1975)

3. R Sudan
Phys Rev Lett 70, 3075 (1993)

4. M Tatarakis, A Gopal, I Watts, F N Beg, A E Dangor, K Krushelnick, U Wagner, P A Norreys, E L Clark, M Zepf and R G Evans
Phys Plasma 9, 5, 2244 (2002)

5. S C Wilks, W L Kruer, M Tabak and A B Langdon
Phys Rev Lett 69, 1383 (1992)

6. B F Lasinski, A B Langdon, S P Hatchett, M H Key and M Tabak
Phys Plasmas 6, 2041 (1999)

7. R G Hemker,
PhD Thesis UCLA 2000

Birefringence in Unmagnetized Relativistic Plasmas

J Moore

Mechanical Engineering Department, Imperial College of Science and Technology, London SW7 2BX

R G Evans

Physics Department, University of York, York, YO10 5DD

Main contact email address: *r.g.evans@physics.org*

Introduction

Optical birefringence in magnetised plasmas is well known and is described by the Faraday effect for propagation along the magnetic vector and the Cotton-Mouton effect for propagation perpendicular to **B**. The birefringence and its associated cutoff frequencies have been used recently[1] for the measurement of Gigagauss magnetic fields in laser produced plasmas at irradiances around 10^{20}Wcm^{-2}.

What is not often appreciated is that in relativistic plasmas, even in the absence of a magnetic field, the velocity dependence of the relativistic mass and the distinction between the longitudinal and transverse masses of the electron can cause birefringence in some special cases when the electron distribution function is not isotropic.

Dielectric Tensor and the Dispersion Relation

In the absence of collisions the starting point is the relativistic Vlasov equation[2]:

$$\frac{\partial f}{\partial t}+\frac{c}{\gamma}\mathbf{p}\cdot\nabla f+\frac{e}{mc}(\mathbf{E}+\frac{\mu_0 c}{\gamma}\mathbf{p}\times\mathbf{H})\cdot\nabla_p f=0$$

where p is the momentum in units of mc and m is the electron rest mass. Labelling the coordinate axes 1,2,3 and considering a wave propagating in the 1 direction ie **k** = (k,0,0), the plasma dielectric function χ may be obtained by linearising the relativistic Vlasov equation to obtain,

$$\chi=\mathbf{I}-\frac{\omega_p^2}{\omega^2}\mathbf{K}$$

where the components of the tensor K are given by

$$K_{11}=\frac{a^2}{c^2}\int\frac{\gamma^2-p_1^2}{\gamma(p_1-\gamma a/c)^2}f^0 d^3\mathbf{p}$$

$$K_{1i}=K_{i1}=\frac{a}{c}\int\frac{p_i(\gamma-p_1 a/c)}{\gamma(p_1-\gamma a/c)^2}f^0 d^3\mathbf{p}$$

$$K_{ij}=(1-\frac{a^2}{c^2})\int\frac{p_i p_j}{\gamma(p_1-\gamma a/c)^2}f^0 d^3\mathbf{p}+\delta_{ij}\int\frac{f^0}{\gamma}d^3\mathbf{p}$$

a = ω/k is the phase velocity of the wave, f^0 is the unperturbed distribution function and i=2,3 in the second equation and i=2,3; j=2,3 in the third equation..

The dispersion relation is obtained from the dielectric tensor χ by requiring that

$$\chi_{11}E_1+\chi_{12}E_2+\chi_{13}E_3=0$$

$$\chi_{21}E_1+(\chi_{22}-n^2)E_2+\chi_{23}E_3=0$$

$$\chi_{31}E_1+\chi_{32}E_2+(\chi_{33}-n^2)E_3=0$$

where n = c/a is the refractive index for the wave.

Using the above expression for χ in terms of the tensor **K** we obtain the determinant

$$\begin{vmatrix}\omega^2-\omega_p^2K_{11} & -\omega_p^2K_{12} & -\omega_p^2K_{13}\\ -\omega_p^2K_{21} & \omega^2-\omega_p^2K_{22}-k_2c^2 & -\omega_p^2K_{23}\\ -\omega_p^2K_{31} & -\omega_p^2K_{32} & \omega^2-\omega_p^2K_{33}-k^2c^2\end{vmatrix}=0$$

The element in the upper left-hand corner of the determinant is contributed by the longitudinal mode, and the other two diagonal elements are contributed by the transverse modes for 2-polarisation and 3-polarisation respectively. The off diagonal elements, when non-zero, couple the various modes together.

For any momentum distribution for which

$$f^0(\mathbf{p})=f^0(p_1,|p_2|,|p_3|)$$

examination of the integrals for K_{ij} shows that

$$K_{1i}=K_{i1}=K_{ij}\,|_{i\neq j}=0 \quad (i=2,3;\ j=2,3)$$

so the dielectric tensor and the determinant in the dispersion relation become diagonal and the three modes uncouple. However the integrals K_{22} and K_{33} may still be different and the plasma will be birefringent with principal planes in the 2 and 3 axes.

The integrals for K_{ij} will in general have poles at $p_1 = \gamma a/c$ which will give rise to Landau damping but if we confine ourselves to the fast electromagnetic modes with phase velocity greater than c then the Landau damping will be absent.

Two Electron-Stream Plasma

As a simple example of a relativistic distribution that gives rise to strong birefringence consider a plasma composed of two counter-propagating electron streams:

$$f^0(p_1,p_2,p_3)=\frac{1}{2}\delta(p_1)\delta(p_3)\big(\delta(p_2-p_0)+\delta(p_2+p_0)\big)$$

This makes K_{ij} diagonal and directions 2 and 3 are the principal polarisation axes.

The refractive indices for the two transverse modes are:

$$n_2^2=1-\frac{\Omega_p^2}{\omega^2+\beta^2\Omega_p^2} \quad \text{and}$$

$$n_3^2=1-\frac{\Omega_p^2}{\omega^2}$$

where $\Omega_p^2 = \omega_p^2/\gamma$ and β,γ are the Lorentz factors associated with the momentum p_0.

The cut off frequencies from the above refractive indices are simply $\omega_2^2 = \omega_p^2/\gamma^3$ and $\omega_3^2 = \omega_p^2/\gamma$, i.e. they are determined respectively by the longitudinal and transverse masses γ^3m and γm.

The expressions for the two refractive indices show that for the non-relativistic case ($\beta << 1$), $n_2 \cong n_3$ and for the strongly relativistic case ($\gamma >> 1$), $n_2 \cong n_3 \cong 1$. The degree of birefringence is maximised for moderately relativistic cases and Figure 1 shows the dispersion in both transverse polarisations for the case $p_0 = 1.37$ which maximises the birefringence at $\omega/\omega_p = 2.0$ i.e. the quarter critical density in the non-relativistic limit. The ratio n_2/n_3 in this case is only 1.00873 and we see that for moderately under-dense plasmas the relativistically induced birefringence is always small. The birefringence can be very large for frequencies close to or below the non-relativistic cut off frequency, i.e. the plasma frequency.

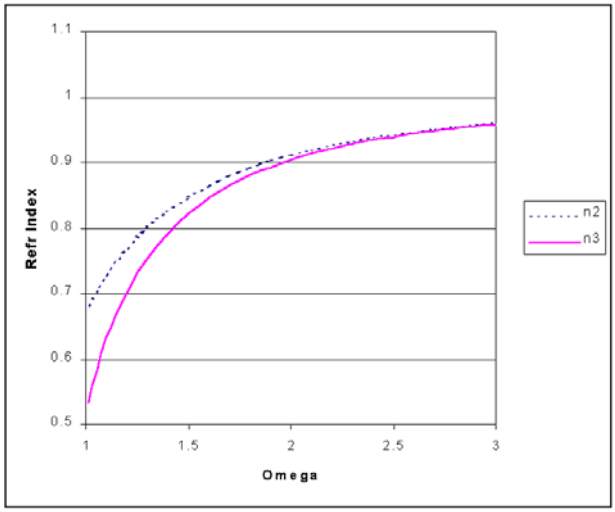

Figure 1. The refractive indices for each polarisation in the case of a two stream electron distribution function. The abscissa 'omega' is the ratio of the wave frequency ω to the non-relativistic plasma frequency ω_p.

Relevance to Harmonic 'Cut Off' Measurements

The recent observations of Ggauss magnetic fields in laser produced plasmas have observed that the harmonics of the laser light have their polarisation rotated by an amount that increases with irradiance and decreases with the order of the harmonic. In extreme cases one polarisation of the harmonic is suppressed, which is attributed to the cut off of the X-wave in the Cotton Mouton effect.

The relativistic effects described here will in principle complicate the interpretation of the polarisation data since these laser plasmas are known have very large populations of moderately relativistic electrons ($\gamma \sim 5$). However we believe that the relativistic effects are small since the major populations of laser accelerated electrons are in the direction of the laser **E** vector and in the direction of propagation **k** (due to **v** x **B** acceleration). This means that the principal axes of the polarisation ellipse are in the directions of the laser **E** and **B** fields and, since the harmonics are believed to be produced with the same polarisation as the laser, they are created in one of the principal planes and not subject to any rotation.

Also the modification of the refractive index due to relativistic effects always reduces the cut off frequencies below the normal plasma frequency and so will not cause any harmonics to be suppressed. On the contrary the relativistic effects reduce the effects of the magnetic fields since the Larmor frequency is reduced by the increasing electron mass so the true magnetic fields may well be even greater than those inferred using non-relativistic expressions for the Cotton-Mouton effect.

Experimental Observation of the Relativistic Birefringence

The model example of a two stream distribution function shows that for electromagnetic waves significantly above the non-relativistic plasma frequency the birefringence is maximised by having electron energies which are only moderately relativistic implying that the laser intensity required is modest by the standards of modern CPA lasers. Larger degrees of birefringence occur if the plasma is probed with waves at or below the normal plasma frequency but, in a real experiment, using lower frequency waves raises the difficulty of 'end effects' in a non-uniform plasma column, and probing the birefringence with light above the plasma frequency makes for a cleaner experiment.

A laser plasma experiment designed to maximise the observeability of the relativistic birefringence would require the plasma to have a large fraction of moderately relativistic electrons and for the distribution function to be anisotropic. This suggests the use of a low density plasma where the main laser can penetrate a long plasma column and all plasma electrons will be subject to the relativistic quiver motion of the main laser which produces motion only in the plane of **E** and **k**. The time for electron collisions to isotropise this motion is orders of magnitude longer than the typical laser pulse duration of 1ps. A coaxial and parallel propagating probe beam of different frequency from the main laser and polarised at 45^0 will then have its plane of polarisation rotated in traversing the plasma column.

Based on the simple two stream model of birefringence, the optimal intensity for the main beam will be around $3 \times 10^{18} Wcm^{-2}$ to give the optimal $p_0 = 1.37$ as described above and a plasma column length of 100μm at quarter critical density is required to resolve the less than 1% difference in refractive indices for the two polarisations.

The 100μm Rayleigh length is easily achieved at this modest intensity and the plasma requirements are within the capabilities of gas-jet targets. A sub-picosecond probe beam at a wavelength not simply related to the main laser is technically possible but not currently available. The timing of the probe laser and discrimination of the probe beam from the vastly more intense main laser will be among the main experimental challenges.

References

1. M Tatarakis, A Gopal, I Watts, F N Beg, A E Dangor, K Krushelnick, U Wagner, P A Norreys, E L Clark, M Zepf and R G Evans
Phys Plasma 9, 5, 2244 (2002)

2. B Kursonoglu
Nuclear Fusion 1, 213 (1961)

A Binary Collision Model for the PIC Code 'OSIRIS'

R G Evans

Physics Department, University of York, YO10 5DD

Main contact email address: *r.g.evans@physics.org*

Introduction

Traditionally the Particle in Cell (PIC) method is used to model plasmas at fairly low densities, around the laser critical density, where binary electron-electron and electron-ion collisions are insignificant. At the critical density for a 1μm glass laser and an electron temperature of 3keV the electron-ion collision time is 3ps, longer than most of the laser pulses of current interest. However for some of the applications of high intensity laser plasma interactions for instance the Fast Ignition concept, it is necessary to understand the interaction of laser generated fast electron streams with plasma at greater than solid density and in this case the collisional effects become important.

The interpolation algorithms used in the PIC method mean that each particle interacts with an average electric and magnetic field calculated from the values on the neighbouring grid points. Interactions between particles within the same computational cell are essentially smoothed away. Since calculating the forces between all possible pairs of particles would double count the long range interactions and would also be prohibitively expensive in computational terms, our binary collision model for OSIRIS calculates pairwise collisions only for particles in the same cell.

Implementation

In the normal PIC algorithm there is no requirement for particles in the same cell to have any defined relationship in computer storage and any initial ordering is quickly lost as the plasma evolves. OSIRIS already contains an option to sort the particles of each species at regular intervals to regain the storage adjacency of neighbouring particles since this makes for efficient use of the memory cache in almost all modern microprocessor architectures.

Our collision algorithm relies on the particles being newly sorted with the indexing arrays saved for re-use after the sort is complete. Two pointers, one for the electrons and one for the ions are advanced so that each points to the same cell (some cells may be empty of one or both species). For each pair of particles a Lorentz transformation is made into the centre of mass frame and a Monte Carlo calculation using the classical Rutherford scattering cross section gives a scattering angle. The particles' velocities are rotated in the centre of mass frame so that both momentum and energy are conserved and then Lorentz transformed back into the simulation frame.

Electron-electron and electron-ion collisions use the same algorithm but with an additional factor of Z to reflect the electron-ion cross section. The factor Z is arbitrary in that it does not relate to any of the usual simulation parameters but may represent the degree of ionisation of dense target material.

Since both electron-electron and electron-ion collisions are included, the model relaxes the electron distribution to a Maxwellian, couples electron and ion 'temperatures' and approximates all of the usual plasma collisional effects (resistivity, magnetic diffusion, Hall, Righi-Leduc, Nernst and Seebeck coefficients).

For improved computational speed the scattering angle is chosen from a predefined set of values of equally spaced log-likelihood. This means that all transcendental functions are pre-calculated and the scattering 'kernel' consists of simple and fast algebraic calculations.

Illustrative Calculation

As pointed out above the effect of binary collisions is of greatest effect only in very dense plasma and to illustrate the effect of collisions a model calculation has been performed where the laser is incident on a plasma at $50n_c$ but the collision term has been enhanced to mimic a density of $500n_c$.

Figure 1 shows the electron longitudinal phase space at a time of $94\omega_p^{-1}$ in the collisionless calculation. The laser accelerates many electrons in the forward direction and a 'beam' (indicated by feature 'A') of 1 MeV electrons is evident together with a spread of other energies. When the enhanced collision term is included as in Figure 2 the general slowing down of the forward going electrons is clear, the 'beam' is absent and the plasma at a distance $35c/\omega_p$ is showing the development of a Maxwellian distribution due to the heating from the beam electrons.

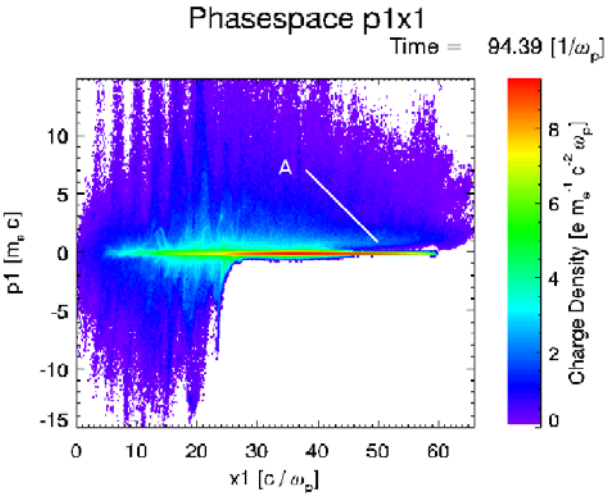

Figure 1. Electron longitudinal phase space in the collisionless calculation.

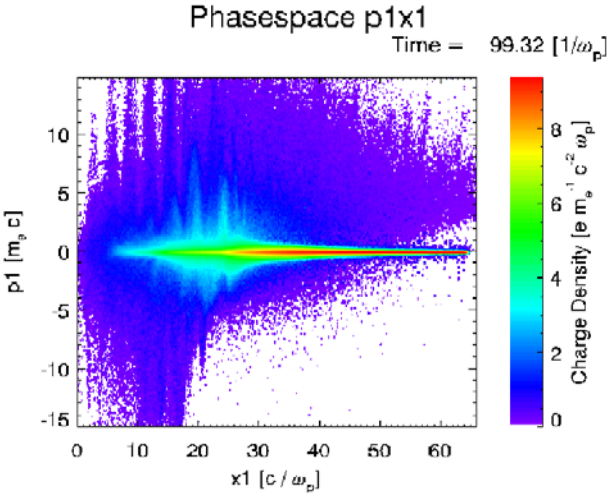

Figure 2. Electron longitudinal phase space in the calculation with an enhanced collision rate.

References

1. R G Hemker, PhD Thesis UCLA 2000

High-order wave-mixing by molecular ions in intense, ultrashort laser pulses

D Dundas, J F McCann, K T Taylor

Dept of Applied Mathematics and Theoretical Physics, Queen's University Belfast, Belfast BT7 1NN

Main contact email address: *j.f.mccann@qub.ac.uk*

Introduction

Intense laser heating of molecules results in extremely fast electron ejection, superheated ion fragments and high frequency secondary radiation. Even in simple diatomic molecules the complexity of the system of interacting ions, electrons and photons leads to a rich variety of processes[1]. The high-quality facilities at the Central Laser Facility have been used in recent years to characterize the variety and propensity of these processes in diatoms, in particular by developing diagnostics of the processes through measurements of the ion fragment charges and energies[2-4]. However, detailed measurements on the response of the hydrogen molecule and molecular ion[2-4] have only recently become available. Importantly, these systems are accessible to first-principles many-body theory and thus direct comparisons can be made. This report presents theoretical simulations for high-order wave-mixing processes, harmonic generation and multiphoton ionization for the hydrogen molecular ion in ultrashort pulses.

Harmonic generation and multiphoton ionization

In this paper we simulate dissociative ionization and high-order wave mixing by direct numerical solution of the time-dependent Schrödinger equation using grid methods [5]. For optical pulses much shorter than the rotational period of the molecule, the molecular axis orientation can be considered as fixed during the interaction time. Ultrashort pulse interaction is effectively sudden on the rotational relaxation timescale and only ultrafast vibrations and electronic motions are excited. For parallel electronic transitions the resulting 2+1+1 dimensional linear PDE can be solved directly on a parallel computer. For our calculations we used the SGI-Origin2000 and Cray-T3E computers at CSAR (Manchester) for this task. An example of the electronic orbital dynamics is shown in Figure 1. Here we fix the nuclear motion at equilibrium separation, and the electronic probability density is plotted in cylindrical polar coordinates, ρ and z, at three instants during the pulse. The light is polarized along the z-axis taken as the internuclear axis. The results shown correspond to an established theoretical benchmark angular frequency ω =0.2 au, that is λ=228nm, with peak intensity 6×10^{14} W cm^{-2}. The first frame represents the unperturbed ground state orbital, the second frame the orbital after 3 optical cycles, and the third frame the highly diffuse orbital after 9 cycles. This figure simply serves as an illustration of the highly distorted and fragmented nature of the electronic wavefunction under such intense external forces. The transfer of energy from the laser is most clearly seen in the ionization and molecular fragmentation. However it also manifests itself through the generation of high-order harmonic generation. We have found that the efficiency of this process, and the profile of the spectrum, is strongly dependent on the nuclear motion. Clearly moving nuclei will change the shape of the potential well and thus modify the entire electronic spectrum. Furthermore, the break up of the nuclear wavepacket creates a diffuse scattering centre that affects the electron-ion collisions. In Figure 2 we present results for harmonic generation for a 20 cycle pulse at λ=228nm, and peak intensity 6×10^{14} W cm^{-2} where the nuclear motion is anchored at the equilibrium bond length. The spectrum is a conventional series of odd-order harmonics that steadily and rapidly decrease in intensity with increasing order. On the other hand, allowing for dissociation and ionization gives a much different picture of the radiative scattering. In Figure 3, we see the presence of strong even- and odd-order harmonics. The molecular expansion allows inversion symmetry breaking and the production of even order peaks. This in turn results from a strong localization of the molecular orbital in polarized atomic states which are symmetry mixtures. The process occurs over femtosecond timescales as the dissociation proceeds. We also note that the intensity of harmonic generation is enhanced by this dynamical effect in the higher order peaks, for example the 10th harmonic. In physical terms the diffusion of the nuclear wavepacket provides an extended site for the electron-nucleus rescattering leading to enhancement of this process.

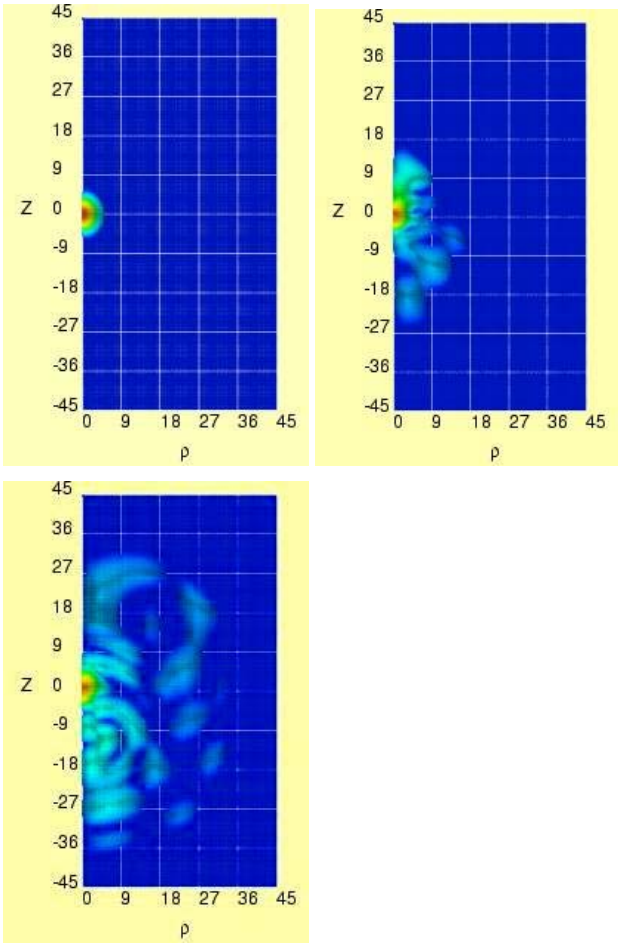

Figure 1. Evolution of the electronic orbital density for the hydrogen molecular ion in an intense laser field. Three snapshots of the motion are taken after 0, 3 and 9 optical cycles, respectively reading from left to right, and top to bottom. The red regions indicate high electron density, and the scales are in atomic units.

Wave-mixing

In Figure 4 we present results for high-order wave mixing processes at very high intensity in the hydrogen molecular ion. The simulations are for fixed nuclei at equilibrium separation and we consider mixing between a source of linearly polarized light at λ=750nm and its second harmonic (λ=375nm). The fragments from two-colour strong-field ionization and dissociation of hydrogen using a Ti:Sapphire λ=780nm and its second harmonic, have been studied by the group at Imperial College[5]. In our calculations, the spectral density of emitted radiation shows high-order wave-mixing and harmonic generation. The data corresponds to simulations for a pulse of

40 cycles. The emission spectrum is greatly extended and contains sharp lines with a low plateau extending to the 30th harmonic. The extended plateau for low-frequency light is consistent with the conversion of large amplitude free-electron recollisions. The emission signal is quite sensitive to the relative phase of the fields. Since the field amplitudes are comparable, the colour interference fringes in time have strong constructive interference will enhance field-ionization of the molecule. Figure 4 shows results for a zero phase difference between the fundamental and its second harmonic. For a phase difference of π (results not shown) we find the plateau extends to the 35th harmonic. Given the variety of parameters of relative phase and intensity, this problem requires further investigation to determine general properties of the system before including nuclear dynamics. The effect of nuclear motion for high-freqency light is very significant as we have shown in Figure 3. Moreover, typical timescales of Ti;Sapphire pulses of 100 fs mean that rotational effects are no longer negligible. Another highly significant factor found in experiments is the relative polarizations of the colours [6]. The effects of molecular axis and polarization orientation require higher dimensional simulations, and this is an effect we intend to investigate in the near future.

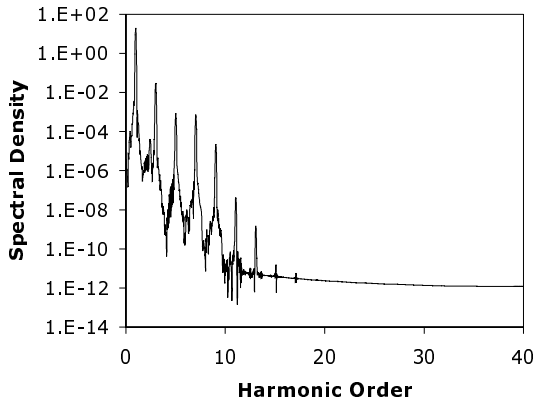

Figure 2. Power spectral density for harmonic generation with the nuclei fixed at the equilibrium separation. Photon angular frequency ω =0.2 au, with peak intensity $6x10^{14}$ W cm^{-2}.

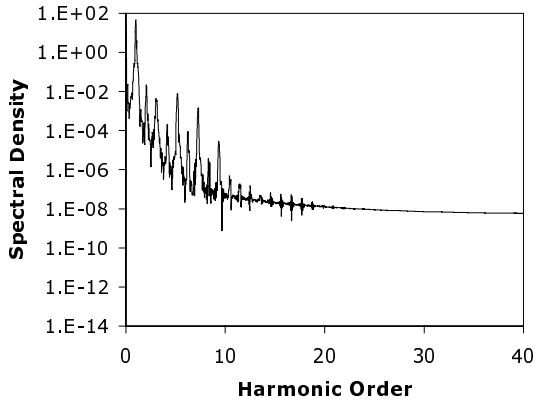

Figure 3. Power spectral density for harmonic generation with quantal nuclear motion. Photon angular frequency ω =0.2 au, with peak intensity $6x10^{14}$ W cm^{-2}.

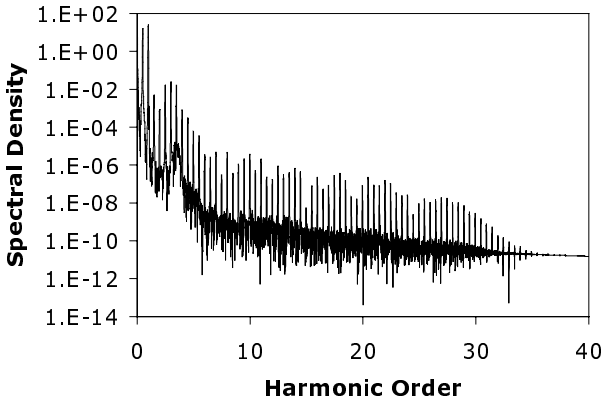

Figure 4. Spectral density of emitted radiation showing high-order wave-mixing and harmonic generation from the hydrogen molecular ion for wavelengths λ=750nm and λ=375nm both at peak intensity $3 x10^{14}$ W cm^{-2}. The harmonic order is in terms of the longer wavelength.

Conclusions

Simulations of the dynamics of the hydrogen molecular ion subjected to intense ultrashort laser pulses were studied including the vibrational nuclear motion quantally and without making the Born-Oppenheimer approximation. Results for one-colour and two-colour high-order harmonic generation and wave mixing were obtained. We find the dissociation process greatly amplifies high-order harmonic generation and creates new even-order frequencies. High-order wave-mixing is highly sensitive to relative phase and highly efficient. It remains to be seen how the effects of quantum nuclear dynamics will modify this spectrum.

References

1. J H Posthumus *et al.*
Molecules and clusters in intense laser fields (C.U.P. 2001)

2. J H Sanderson, R V Thomas, W A Bryan, W R Newell, A J Langley and P F Taday
J. Phys. B: At. Mol. Opt. Phys. 31, L599 (1998).

3. I D Williams, P McKenna *et al.*
J. Phys. B: At. Mol. Opt. Phys. 33 2743 (2000)

4. Frasinski LJ, Plumridge J, Posthumus JH
Phys. Rev. Lett. 86 2541 (2001)

5. D Dundas
Phys. Rev. A 65, 023408 (2002)

6. Y L Shao, D J Fraser, M H R Hutchinson, J Larsson, J P Marangos and J W G Tisch
J. Mod. Opt. 43, 1063 (1996)

Atomic data for Ni-like Gd XXXVII

K M Aggarwal, F P Keenan

Department of Pure & Applied Physics, Queen's University, Belfast BT7 1NN, UK

P H Norrington

Dept. of Applied Maths & Theoretical Physics, Queen's University, Belfast BT7 1NN, UK

G J Pert

Department of Physics, University of York, Heslington, York, YO19 5DD, UK

S J Rose

AWE plc, Aldermaston, Reading RG7 4PR, UK

Main contact email address: *K.Aggarwal@qub.ac.uk*

Introduction

Recently we have reported[1,2] results for collision strengths (Ω) and effective collision strengths (Υ) for resonance transitions in Ni-like Gd XXXVII. For calculating wavefunctions, we employed the GRASP code of Dyall et al[3] and for the computations of Ω we adopted the recent DARC program of Norrington and Grant[5]. While calculating the values of Υ, which are very simply related to the excitation and de-excitation rate coefficients, we included the contribution of resonances, which had a pronounced effect on many transitions, as demonstrated in our recent work[2]. For some of the transitions, the values of Υ were enhanced by an order of magnitude even at temperatures ~10^6 K. On the other hand, the earlier available corresponding results of Hagelstein[4] were found to be overestimated, by up to a factor of four for some of the transitions, because he performed his calculations of Ω only at energies above thresholds. Therefore, our recently reported results of Ω and Υ are the most accurate available today. However, such results have so far been completed and reported for the resonance transitions only, whereas data for other transitions are also required in the modelling of laser plasmas. The corresponding calculations for these transitions are still in progress, but in this short report we present our results of Ω for transitions from the lowest five levels of the $(1s^22s^22p^6)$ $3s^23p^23d^{10}$ and $3s^23p^63d^94s$ configurations to higher levels of the $3s^23p^63d^94p$, $3s^23p^63d^94d$ and $3s^23p^63d^94f$ configurations of Gd XXXVII. The results of Ω are reported at 4 representative energies of 200, 400, 600 and 800 Ry. We hope these results will be helpful in modelling calculations. The values of Υ for these transitions are not yet available, but results for Ω for all transitions and in a wider range of energy can be obtained on request from the first author.

Calculation Details

For the computations of energy levels and radiative rates, we have included the lowest 107 fine-structure levels arising from the $(1s^22s^22p^6)$ $3s^23p^23d^{10}$, $3s^23p^63d^94\ell$, $3s^23p^53d^{10}4\ell$ and $3s^3p^63d^{10}4\ell$ configurations. The specific list of these energy levels has already been reported[1]. However, the corresponding calculations for Ω are restricted to the lowest 59 levels because of computational limitations. CI has been included among the above listed configurations, and the option of EAL (extended average level), in which the weighted trace of a Hamiltonian is minimised, is chosen in the GRASP code. The calculations fully include the relativistic effects, and are in the *jj* coupling scheme. Further details of the calculations can be found in our earlier publication[1].

Collision strengths have been computed in a wide energy range below 800 Ry. A large range of partial waves ($J \leq 40.5$) has been included in order to obtain converged results for Ω. However, this range is not sufficient for the convergence of Ω in allowed transitions. Therefore, a top-up based on the sum rules has also been included. Results of Ω for resonance transitions at 4 representative energies of 200, 400, 600 and 800 Ry have already been presented, compared, and discussed by Aggarwal et al[1]. In this report we present similar results in Table 1 for transitions from the lowest 5 levels to higher excited levels. No other results are available in the literature for comparisons, but the accuracy of our calculations has already been discussed in earlier publications[1,2]. A complete set of results for both Ω and Υ for all transitions among the lowest 59 levels of Gd XXXVII will soon be available.

References

1. K. M. Aggarwal, P. H. Norrington, K. L. Bell, F. P. Keenan, G. J. Pert, and S. J. Rose, J.Phys. B 32 5067 (1999)
2. K. M. Aggarwal, F. P. Keenan, P. H. Norrington, G.J. Pert, and S. J. Rose, J.Phys. B 35 L127 (2002)
3. K. G. Dyall, I. P. Grant, C. T. Johnson, F. A. Parpia and E. P. Plummer, Comput. Phys. Commun. 55 425 (1989)
4. P. L. Hagelstein, Phys. Rev. A 34 874 (1986)
5. P. H. Norrington and I. P. Grant, Comput. Phys. Commun. - in preperation (2002)

Table 1. Collision strengths (Ω) for transitions from the lowest 5 levels of the ($1s^2 2s^2 2p^6$) $3s^2 3p^2 3d^{10}$ and $3s^2 3p^6 3d^9 4s$ configurations to higher levels of the $3s^2 3p^6 3d^9 4p$, $3s^2 3p^6 3d^9 4d$ and $3s^2 3p^6 3d^9 4f$ configurations of Gd XXXVII. (a-$b \equiv a \times 10^{-b}$).

Transition	Energy (Ry)				Transition	Energy (Ry)			
I - J	200	400	600	800	I - J	200	400	600	800
1 - 2	4.453-4	1.793-4	9.393-5	5.689-5	2 - 15	1.443-5	8.226-6	7.748-6	8.036-6
1 - 3	2.792-3	3.331-3	3.645-3	3.860-3	2 - 16	1.091-3	1.328-3	1.550-3	1.780-3
1 - 4	1.983-4	7.876-5	4.115-5	2.493-5	2 - 17	2.931-3	3.638-3	4.228-3	4.864-3
1 - 5	1.935-3	2.266-3	2.476-3	2.625-3	2 - 18	6.530-2	6.934-2	7.290-2	7.815-2
1 - 6	5.095-4	1.945-4	9.899-5	5.960-5	2 - 19	5.481-2	5.737-2	6.027-2	6.472-2
1 - 7	1.185-3	1.104-3	1.111-3	1.129-3	2 - 20	1.001-1	1.065-1	1.120-1	1.201-1
1 - 8	3.617-4	1.335-4	6.798-5	4.094-5	2 - 21	1.036-1	1.100-1	1.157-1	1.241-1
1 - 9	3.930-3	6.460-3	8.270-3	9.695-3	2 - 22	6.361-4	1.837-4	9.328-5	6.210-5
1 - 10	6.343-4	2.396-4	1.239-4	7.526-5	2 - 23	2.394-1	2.574-1	2.719-1	2.916-1
1 - 11	3.804-4	1.377-4	6.852-5	4.072-5	2 - 24	4.854-2	5.137-2	5.391-2	5.763-2
1 - 12	8.589-3	1.494-2	1.946-2	2.302-2	2 - 25	1.129-2	1.140-2	1.184-2	1.260-2
1 - 13	7.180-4	6.776-4	6.914-4	7.089-4	2 - 26	1.371-1	1.470-1	1.548-1	1.659-1
1 - 14	1.530-4	5.934-5	3.065-5	1.864-5	2 - 27	1.298-4	3.639-5	1.675-5	9.564-6
1 - 15	1.152-3	1.721-3	2.193-3	2.582-3	2 - 28	3.348-4	3.561-4	3.724-4	3.936-4
1 - 16	1.059-3	9.985-4	1.011-3	1.031-3	2 - 29	7.388-6	2.584-6	1.623-6	1.109-6
1 - 17	2.327-4	7.862-5	3.731-5	2.136-5	2 - 30	6.531-5	6.640-5	6.896-5	7.321-5
1 - 18	1.027-3	4.013-4	2.153-4	1.348-4	2 - 31	3.133-4	3.347-4	3.500-4	3.705-4
1 - 19	1.190-3	7.861-4	7.263-4	7.244-4	2 - 32	2.686-4	2.871-4	3.019-4	3.255-4
1 - 20	1.190-3	8.702-4	8.333-4	8.421-4	2 - 33	1.581-5	1.199-5	1.032-5	1.043-5
1 - 21	6.413-4	1.988-4	9.140-5	5.101-5	2 - 34	1.190-4	1.252-4	1.447-4	1.373-4
1 - 22	7.481-4	2.844-4	1.541-4	9.904-5	2 - 35	9.246-5	2.691-5	1.266-5	7.305-6
1 - 23	1.298-3	4.370-4	2.144-4	1.250-4	2 - 36	5.802-1	7.198-1	8.160-1	8.955-1
1 - 24	8.545-4	2.812-4	1.351-4	7.827-5	2 - 37	2.926-3	1.755-3	1.453-3	1.359-3
1 - 25	3.777-3	4.650-3	5.213-3	5.605-3	2 - 38	2.661-3	2.824-3	2.941-3	3.021-3
1 - 26	7.135-4	3.689-4	3.135-4	3.059-4	2 - 39	7.881-3	8.375-3	8.733-3	9.196-3
1 - 27	3.732-3	3.761-3	3.800-3	3.831-3	2 - 40	1.278-2	1.368-2	1.436-2	1.516-2
1 - 28	6.571-4	2.435-4	1.291-4	8.134-5	2 - 41	7.378-3	6.666-3	6.771-3	7.106-3
1 - 29	7.649-4	2.551-4	1.236-4	7.168-5	2 - 42	3.413-2	3.639-2	3.793-2	3.893-2
1 - 30	2.429-3	2.988-3	3.359-3	3.618-3	2 - 43	2.035-3	1.575-3	1.536-3	1.581-3
1 - 31	6.929-4	2.519-4	1.291-4	7.808-5	2 - 44	1.787-2	1.896-2	1.980-2	2.086-2
1 - 32	1.110-3	6.964-4	6.335-4	6.294-4	2 - 45	1.770-2	1.847-2	1.921-2	2.025-2
1 - 33	1.519-3	1.407-3	1.470-3	1.542-3	2 - 46	6.813-3	6.418-3	6.555-3	6.859-3
1 - 34	5.870-4	1.746-4	7.771-5	4.240-5	2 - 47	2.254-2	2.369-2	2.472-2	2.606-2
1 - 35	6.217-2	6.448-2	6.558-2	6.631-2	2 - 48	1.405-3	6.159-4	4.759-4	4.455-4
1 - 36	3.537-4	1.218-4	6.123-5	3.746-5	2 - 49	5.715-4	3.040-4	2.596-4	2.523-4
1 - 37	6.767-3	1.266-2	1.711-2	2.066-2	2 - 50	1.500-4	1.693-4	1.834-4	1.971-4
1 - 38	5.757-4	1.962-4	9.625-5	5.600-5	2 - 51	1.822-5	1.471-5	1.481-5	1.564-5
1 - 39	2.281-3	1.883-3	1.951-3	2.080-3	2 - 52	6.296-6	7.428-6	7.065-6	7.537-6
1 - 40	1.607-3	5.088-4	2.393-4	1.367-4	2 - 53	8.464-5	1.014-4	9.209-5	9.693-5
1 - 41	1.030-3	6.800-4	6.783-4	7.114-4	2 - 54	4.105-6	4.446-6	3.959-6	4.153-6
1 - 42	1.458-3	4.260-4	1.945-4	1.101-4	2 - 55	1.777-5	2.056-5	1.892-5	2.059-5
1 - 43	8.849-4	2.471-4	1.084-4	5.966-5	2 - 56	4.293-5	5.356-5	5.671-5	6.183-5
1 - 44	1.053-3	3.594-4	2.165-4	1.687-4	2 - 57	7.243-4	5.403-4	4.738-4	4.497-4
1 - 45	7.531-4	1.978-4	8.488-5	4.567-5	2 - 58	3.231-4	1.896-4	1.437-4	1.250-4
1 - 46	9.976-4	2.777-4	1.233-4	6.814-5	2 - 59	1.294-4	3.601-5	1.878-5	1.311-5
1 - 47	5.576-4	2.507-4	2.267-4	2.336-4	3 - 4	1.009-2	6.600-3	5.955-3	6.100-3
1 - 48	3.998-3	4.708-3	5.070-3	5.286-3	3 - 5	6.827-3	4.406-3	4.130-3	4.348-3
1 - 49	6.701-2	1.086-1	1.320-1	1.488-1	3 - 6	4.044-1	5.343-1	5.458-1	5.650-1
1 - 50	1.631-3	5.183-4	2.445-4	1.400-4	3 - 7	1.942-0	2.568-0	2.614-0	2.712-0
1 - 51	9.128-4	2.609-4	1.177-4	6.600-5	3 - 8	2.425-2	3.078-2	3.739-2	4.447-2
1 - 52	8.182-4	2.301-4	1.015-4	5.578-5	3 - 9	3.706-2	4.713-2	5.690-2	6.770-2
1 - 53	8.871-4	5.820-4	5.857-4	6.174-4	3 - 10	1.356-3	4.038-4	1.936-4	1.148-4
1 - 54	6.650-4	2.330-4	1.505-4	1.242-4	3 - 11	1.652-0	2.087-0	2.497-0	2.931-0
1 - 55	3.371-3	3.844-3	4.116-3	4.288-3	3 - 12	1.121-0	1.416-0	1.688-0	1.986-0
1 - 56	6.438-4	1.592-4	6.544-5	3.440-5	3 - 13	1.168-0	1.477-0	1.773-0	2.077-0
1 - 57	2.676-4	1.064-4	5.797-5	3.659-5	3 - 14	7.957-6	2.247-6	1.143-6	6.696-7
1 - 58	2.413-3	3.121-3	3.540-3	3.825-3	3 - 15	8.760-3	1.094-2	1.279-2	1.474-2
1 - 59	2.256-1	3.353-1	4.146-1	4.770-1	3 - 16	2.799-3	3.517-3	4.151-3	4.782-3
2 - 3	1.348-2	8.089-3	6.850-3	6.497-3	3 - 17	1.113-4	1.254-4	1.444-4	1.653-4
2 - 4	4.979-3	3.046-3	2.775-3	2.844-3	3 - 18	4.577-4	1.420-4	7.545-5	5.166-5
2 - 5	1.741-2	1.086-2	9.569-3	9.644-3	3 - 19	1.423-1	1.519-1	1.602-1	1.721-1
2 - 6	1.943-0	2.563-0	2.681-0	2.769-0	3 - 20	1.026-2	1.038-2	1.081-2	1.155-2
2 - 7	1.390-0	1.830-0	1.897-0	1.964-0	3 - 21	4.686-2	4.947-2	5.199-2	5.576-2
2 - 8	2.157-3	2.724-3	3.117-3	3.218-3	3 - 22	6.514-2	6.985-2	7.351-2	7.863-2
2 - 9	3.209-5	9.818-6	5.467-6	4.199-6	3 - 23	1.624-3	4.590-4	2.370-4	1.279-4
2 - 10	3.621-0	4.591-0	5.529-0	6.487-0	3 - 24	1.036-1	1.111-1	1.170-1	1.252-1
2 - 11	3.131-1	3.945-1	4.701-1	5.547-1	3 - 25	9.828-2	1.055-1	1.110-1	1.187-1
2 - 12	6.178-4	1.861-4	9.094-5	5.525-5	3 - 26	5.372-2	5.716-2	6.015-2	6.431-2
2 - 13	1.607-0	2.027-0	2.420-0	2.838-0	3 - 27	1.437-2	1.546-2	1.624-2	1.730-2
2 - 14	5.630-6	4.159-6	4.557-6	4.483-6	3 - 28	7.777-6	4.182-6	3.511-6	3.424-6

Transition	Energy (Ry)				Transition	Energy (Ry)			
I - J	200	400	600	800	I - J	200	400	600	800
3 - 29	2.329-4	2.456-4	2.568-4	2.729-4	4 - 44	1.938-6	2.267-6	2.423-6	2.364-6
3 - 30	2.746-5	2.557-5	2.596-5	2.715-5	4 - 45	8.929-5	1.016-4	1.062-4	1.170-4
3 - 31	1.850-4	1.950-4	2.028-4	2.142-4	4 - 46	2.115-5	2.316-5	2.423-5	2.719-5
3 - 32	1.772-4	1.894-4	1.988-4	2.119-4	4 - 47	4.936-6	1.100-6	5.032-7	3.751-7
3 - 33	1.419-4	1.487-4	1.568-4	1.684-4	4 - 48	1.989-5	1.933-5	2.042-5	2.266-5
3 - 34	6.452-5	6.643-5	7.175-5	7.915-5	4 - 49	8.091-5	2.712-5	1.730-5	1.415-5
3 - 35	7.410-3	8.084-3	8.479-3	8.949-3	4 - 50	4.744-3	4.870-3	5.046-3	5.310-3
3 - 36	4.997-2	6.020-2	6.790-2	7.407-2	4 - 51	1.793-2	1.918-2	2.001-2	2.056-2
3 - 37	3.626-1	4.505-1	5.110-1	5.598-1	4 - 52	8.624-3	9.208-3	9.616-3	1.014-2
3 - 38	1.177-4	3.018-5	1.347-5	7.792-6	4 - 53	1.169-3	3.078-4	1.773-4	7.589-5
3 - 39	9.182-4	7.930-4	8.299-4	8.846-4	4 - 54	1.700-2	1.837-2	1.923-2	2.029-2
3 - 40	1.867-3	1.602-3	1.603-3	1.665-3	4 - 55	1.226-3	7.418-4	6.776-4	6.865-4
3 - 41	2.272-2	2.425-2	2.542-2	2.621-2	4 - 56	5.826-3	5.727-3	5.895-3	6.029-3
3 - 42	1.501-3	3.949-4	2.090-4	9.683-5	4 - 57	8.686-5	9.086-5	9.371-5	9.675-5
3 - 43	1.160-2	1.247-2	1.306-2	1.378-2	4 - 58	4.736-5	3.167-5	2.701-5	2.557-5
3 - 44	1.067-3	4.922-4	3.943-4	3.748-4	4 - 59	5.649-4	4.575-4	4.791-4	5.105-4
3 - 45	6.390-3	6.227-3	6.429-3	6.790-3	5 - 6	3.716-3	4.420-3	4.533-3	4.683-3
3 - 46	1.737-2	1.854-2	1.937-2	2.045-2	5 - 7	5.741-4	6.805-4	7.008-4	7.254-4
3 - 47	6.706-3	6.429-3	6.566-3	6.709-3	5 - 8	1.106-0	1.464-0	1.514-0	1.567-0
3 - 48	1.748-2	1.885-2	1.971-2	2.079-2	5 - 9	1.190-0	1.565-0	1.658-0	1.713-0
3 - 49	6.132-3	6.609-3	6.904-3	7.266-3	5 - 10	3.439-5	1.037-5	6.513-6	5.706-6
3 - 50	4.024-5	4.176-5	4.584-5	4.999-5	5 - 11	1.564-2	2.010-2	2.218-2	2.297-2
3 - 51	4.702-5	4.584-5	4.762-5	5.042-5	5 - 12	2.156-2	2.770-2	3.053-2	3.155-2
3 - 52	2.738-5	3.221-5	3.057-5	3.229-5	5 - 13	4.385-3	5.645-3	6.462-3	6.708-3
3 - 53	2.567-5	2.239-5	2.208-5	2.222-5	5 - 14	2.386-4	7.197-5	3.328-5	1.982-5
3 - 54	1.975-5	2.265-5	2.689-5	2.642-5	5 - 15	1.614-1	2.035-1	2.428-1	2.861-1
3 - 55	4.261-5	5.665-5	5.394-5	5.887-5	5 - 16	2.807-0	3.560-0	4.282-0	5.027-0
3 - 56	1.217-5	1.061-5	1.053-5	1.085-5	5 - 17	1.047-0	1.323-0	1.581-0	1.853-0
3 - 57	5.011-5	4.065-5	3.901-5	3.914-5	5 - 18	3.571-4	3.747-4	3.969-4	4.325-4
3 - 58	2.712-4	1.716-4	1.327-4	1.153-4	5 - 19	8.046-6	3.213-6	2.204-6	1.847-6
3 - 59	1.684-3	1.777-3	1.841-3	1.924-3	5 - 20	7.337-5	7.424-5	7.844-5	8.572-5
4 - 5	9.657-3	6.856-3	6.230-3	6.034-3	5 - 21	9.769-5	9.795-5	1.026-4	1.110-4
4 - 6	6.165-4	7.139-4	7.331-4	7.582-4	5 - 22	5.440-6	1.985-6	1.134-6	8.439-7
4 - 7	1.850-5	5.068-6	2.857-6	2.387-6	5 - 23	6.374-6	3.012-6	2.242-6	2.081-6
4 - 8	1.248-0	1.648-0	1.703-0	1.764-0	5 - 24	7.347-5	6.977-5	7.197-5	7.721-5
4 - 9	1.716-1	2.249-1	2.366-1	2.448-1	5 - 25	1.786-4	1.839-4	1.927-4	2.077-4
4 - 10	8.331-6	2.677-6	1.763-6	1.438-6	5 - 26	6.262-4	6.674-4	7.062-4	7.631-4
4 - 11	1.576-2	2.028-2	2.228-2	2.310-2	5 - 27	7.876-3	8.341-3	8.772-3	9.414-3
4 - 12	2.499-2	3.214-2	3.654-2	3.783-2	5 - 28	6.380-2	6.785-2	7.132-2	7.640-2
4 - 13	9.302-6	3.500-6	2.612-6	2.560-6	5 - 29	5.055-2	5.300-2	5.563-2	5.966-2
4 - 14	3.992-1	5.053-1	6.049-1	7.120-1	5 - 30	7.697-2	8.174-2	8.587-2	9.195-2
4 - 15	1.015-0	1.283-0	1.533-0	1.798-0	5 - 31	2.014-3	1.644-3	1.621-3	1.695-3
4 - 16	9.778-4	2.906-4	1.395-4	8.332-5	5 - 32	1.941-1	2.087-1	2.200-1	2.356-1
4 - 17	9.281-1	1.174-0	1.406-0	1.645-0	5 - 33	3.228-2	3.400-2	3.561-2	3.802-2
4 - 18	1.275-4	1.323-4	1.402-4	1.529-4	5 - 34	1.008-1	1.079-1	1.135-1	1.214-1
4 - 19	4.598-6	2.041-6	1.315-6	1.122-6	5 - 35	1.414-2	1.520-2	1.592-2	1.688-2
4 - 20	2.613-5	2.663-5	2.816-5	3.057-5	5 - 36	6.423-2	7.705-2	8.685-2	9.484-2
4 - 21	3.579-4	3.795-4	4.018-4	4.346-4	5 - 37	1.179-2	1.371-2	1.529-2	1.664-2
4 - 22	2.032-4	2.156-4	2.299-4	2.501-4	5 - 38	2.281-7	8.144-8	5.432-8	3.153-8
4 - 23	2.604-6	9.009-7	6.124-7	5.739-7	5 - 39	1.285-4	1.442-4	1.550-4	1.663-4
4 - 24	1.276-4	1.320-4	1.392-4	1.505-4	5 - 40	8.639-5	8.706-5	9.111-5	9.703-5
4 - 25	1.215-4	1.263-4	1.329-4	1.428-4	5 - 41	6.769-6	4.725-6	2.660-6	2.176-6
4 - 26	3.261-6	2.071-6	1.063-6	9.813-7	5 - 42	3.921-6	1.288-6	7.352-7	8.326-7
4 - 27	5.110-5	1.412-5	6.406-6	3.623-6	5 - 43	3.812-5	4.642-5	5.508-5	6.347-5
4 - 28	1.792-3	1.588-3	1.599-3	1.683-3	5 - 44	3.983-5	4.835-5	5.687-5	6.546-5
4 - 29	1.025-1	1.095-1	1.153-1	1.236-1	5 - 45	1.145-5	6.050-6	6.174-6	5.045-6
4 - 30	3.021-2	3.194-2	3.351-2	3.584-2	5 - 46	7.292-6	4.672-6	2.565-6	2.149-6
4 - 31	6.382-2	6.858-2	7.212-2	7.709-2	5 - 47	1.445-4	1.534-4	1.535-4	1.659-4
4 - 32	1.225-3	3.408-4	1.594-4	9.462-5	5 - 48	5.849-5	6.900-5	8.250-5	8.318-5
4 - 33	7.670-2	8.245-2	8.672-2	9.266-2	5 - 49	1.639-3	1.759-3	1.853-3	1.965-3
4 - 34	4.874-2	5.211-2	5.478-2	5.850-2	5 - 50	9.062-3	9.378-3	9.741-3	1.026-2
4 - 35	9.113-5	2.595-5	1.198-5	6.821-6	5 - 51	6.655-3	6.032-3	6.104-3	6.370-3
4 - 36	1.030-2	1.191-2	1.331-2	1.445-2	5 - 52	4.928-3	4.725-3	4.856-3	5.119-3
4 - 37	3.824-2	4.630-2	5.227-2	5.707-2	5 - 53	2.863-2	3.049-2	3.197-2	3.305-2
4 - 38	7.725-6	9.559-6	1.108-5	1.211-5	5 - 54	1.723-3	8.580-4	7.186-4	6.978-4
4 - 39	9.116-6	6.609-6	6.449-6	7.009-6	5 - 55	1.767-2	1.868-2	1.952-2	2.063-2
4 - 40	1.043-4	1.130-4	1.192-4	1.277-4	5 - 56	1.820-2	1.905-2	1.987-2	2.097-2
4 - 41	2.931-6	7.757-7	5.027-7	3.111-7	5 - 57	1.215-4	1.110-4	1.085-4	1.094-4
4 - 42	3.653-7	3.343-7	3.589-7	4.031-7	5 - 58	5.968-5	3.058-5	2.134-5	1.770-5
4 - 43	4.095-5	4.785-5	5.238-5	5.665-5	5 - 59	7.133-3	7.665-3	8.055-3	8.505-3

Multiple Ionisation Suppression of Ar^+ Ions in an Intense Laser Field

T R J Goodworth, S L Stebbings, W R Newell

Department of Physics & Astronomy, University College London, Gower Street, London, WC1E 6BT, UK

J B Greenwood, I M G Johnston, I D Williams

Department of Physics, Queen's University Belfast, Belfast, BT7 1NN, UK

A J Langley, E J Divall, C J Hooker

Central Laser Facility, CLRC Rutherford Appleton Laboratory, Chilton, Didcot, Oxon, OX11 0QX, UK

Main contact email address: *w.r.newell@ucl.ac.uk*

Introduction

It is well understood, both theoretically and experimentally that, when exposed to high intensity, ultrafast laser pulses, multiple ionisation of atoms is substantially enhanced by non-sequential processes near the threshold intensity for ionisation[1]. Currently, the model which best describes these non-sequential effects is the recollision model[2,3]. Under this interpretation, the primary electron tunnel ionises through the finite potential barrier formed by the interaction of the laser electric field with the atomic potential. The liberated electron is then accelerated in the laser field and, depending on the initial phase, can return to the singly charged ion core with collision energies up to $3.17U_P$, where U_P is the classical ponderomotive energy in the field[1]. Thus, secondary ionisation of the target proceeds through interaction between the returning electron and the ionic core. Most recently, the effects of Coulomb focusing on the recolliding electron have also been considered[4], whereby the electron trajectory in the laser field is electrostatically channeled towards the ionic core, further enhancing the probability of non-sequential events. Experimentally, these non-sequential events have been observed through large reductions in ionisation rates near threshold for circularly polarized fields, and more recently from the momentum distribution of the recoil ions[5] as well as coincidence measurements between ions and ejected electrons[6]. Suppression of non-sequential ionisation has also been observed when the target is exposed to very short laser pulses of just a few optical cycles[7]. Currently all experimental investigations have concentrated on neutral atomic targets, in particular the rare gases, but it is important to investigate a wide range of targets in order to test the validity of the current theory. In light of this, we report on the first direct investigation of intense field ionisation of a positive atomic ion.

Experimental Configuration

Our ion beam apparatus has been used previously to provide unambiguous insight into the fragment dynamics of the H_2^+ molecular ion, and is described in detail elsewhere[8]. Ar^+ ions are produced in an oscillating electron type discharge source and momentum selected by a bending magnet to produce a well collimated 1 kV ion beam. In addition to groundstate ions, our ions source also generates low lying excited states, permitting strong field ionisation studies from the ensemble of Ar^+ metastable states lying between 16 and 19 eV.

60 fs laser pulses at a wavelength of 790 nm from the Astra Ti:Sapphire laser are focused using *f*/25 optics to produce a focal spot of 16 μm diameter which intersects the ion beam perpendicularly in the interaction region. The focusing lens is mounted on a computer driven, precision translation stage, which could be driven a distance of 25 mm parallel to the laser beam axis (z-axis), with respect to the optimum focusing position. In this way lower laser intensities were accessed with increased interaction volumes, thus enhancing the sensitivity of the instrument. Post interaction, ions were deflected into a 45 degree parallel plate analyser, such that the ionised products could be detected in an off-axis channel electron multiplier, while the primary Ar^+ beam was collected in a well-baffled Faraday cup.

Results and Discussion

Figure 1 shows ion yields for both (i) Ar^{2+} and (ii) Ar^{3+} resulting from ionisation of Ar^+ at a laser intensity close to the limit of the Ar^{3+} non-sequential regime. Ions were extracted

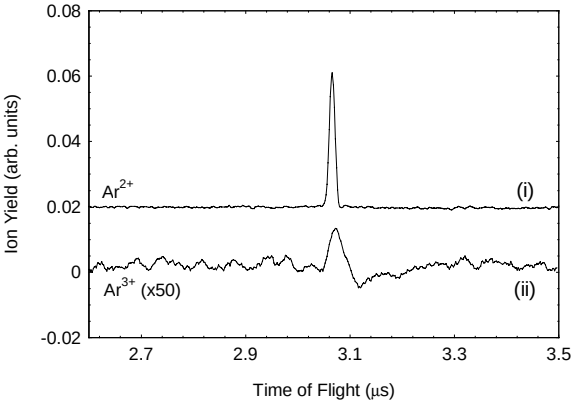

Figure 1. Strong field ionisation of an Ar^+ beam with the parallel plate analyser tuned for maximum transmission of (i) Ar^{2+} and (ii) Ar^{3+} (50 times vertical scaling).

through a 0.9 mm slit, thus restricting detection to the very centre of the focal volume. Following correction for these individual interaction volumes, the Ar^{3+}/Ar^{2+} production ratio was found to be just 0.007 ± 0.002 for the ion target. Under equivalent conditions, a neutral Ar target afforded a ratio of 0.038 ± 0.002. Thus at this intensity Ar^{3+} production is strongly suppressed when Ar^+ rather than neutral Ar provides the initial target.

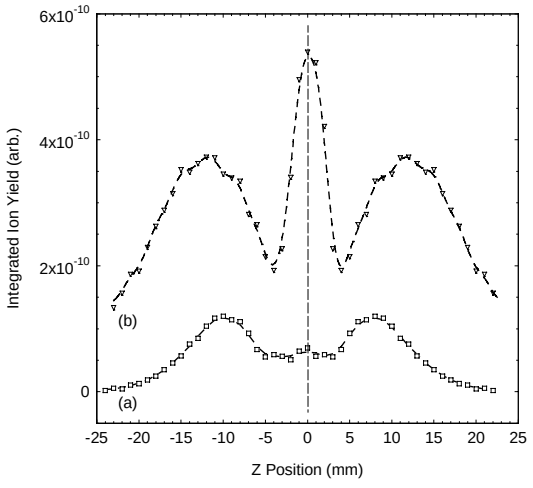

Figure 2. Ar^{2+} ion yield from Ar^+ as a function of focal detuning along the z-axis, perpendicular to the ion beam, for laser intensities (a) 10^{16} Wcm^{-2}, and (b) 5×10^{15} Wcm^{-2}.

Figure 2 shows the Ar^{2+} signal obtained from strong field ionisation of the primary ion beam, at a peak intensity of 10^{16} Wcm^{-2}, as a function of focal detuning with respect to $z = 0$. Each point represents the integral under the Ar^{2+} peak in the corresponding time of flight spectrum. The central narrow peak is due to sequential ionisation of groundstate Ar^{+}. Conversely, the broad peaks at large z (i.e. lower intensity) depict ionisation of metastable components with lower ionisation potentials (9 – 11 eV) than the Ar^{+} groundstate (27.6 eV). These peaks also highlight the expected profile resulting from the interplay of increasing interaction volume with decreasing intensity as the lens moves away from zero[9]. For this interpretation to be valid, the $z = 0$ groundstate peak must disappear rapidly in comparison to the metastable peaks as the laser intensity decreases. This is clearly confirmed by Figure 2b, in which the laser intensity was decreased by a factor of two. The slight decrease in the z position of the ionised metastable peaks as the intensity is reduced is a result of the change in the intensity dependent confocal volume.

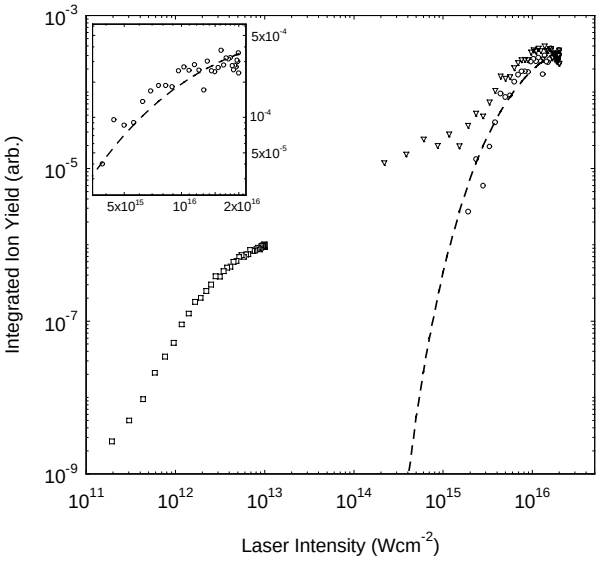

Figure 3. Ar^{2+} ion yields from an Ar^{+} target as a function of laser intensity. Low intensity data (squares) taken at a focal detuning of z = 12, high intensity data (triangles) taken on focus. Circles show the metastable subtracted component, representing Ar^{2+} production from groundstate Ar^{+}. The dashed curve illustrates an ADK fit, with an expanded view shown in the inset.

In order to quantify this intensity dependent behavior, both the groundstate Ar^{2+} peaks at $z = 0$ and the metastable ($z = 12$) peak were monitored as a function of laser intensity. Figure 3 shows these intensity dependent Ar^{2+} ion yields following volume normalisation. The low intensity curve (10^{11} - 10^{13} Wcm^{-2}) was obtained at a focal detuning of $z = 12$, whereas the higher intensity curve (10^{14} - 10^{16} Wcm^{-2}) was obtained with the lens positioned upon focus. As expected from intensity arguments, the lower curve arises purely from the ensemble of metastable states. Conversely, the high intensity curve arises from ionisation of both groundstate and metastable Ar^{+} ions; in essence a mixed beam. The component of the high intensity Ar^{2+} curve lying below 10^{14} Wcm^{-2} has a slope of 0.5, indicative of the onset of saturated ionisation from Ar^{+} metastables in the diffraction rings surrounding the Airy disk[10].

Quasiclassical tunneling (ADK) theory[11] has been employed to calculate the ionisation rate of groundstate Ar^{+} for the computed interaction volume. As shown in Figure 3, a direct fit to the high intensity Ar^{2+} curve has been obtained following subtraction of the estimated metastable contribution. The value of the effective principle quantum number (n* = 1.44) used in this fit is in good agreement with the accepted value of n* = 1.4, thus confirming the interpretation of our intensity plot.

The problem of multiple ionisation of rare gas atoms has also been studied theoretically by Becker and Faisal using intense-field *S*-matrix techniques[12]. In such cases, integrating over the experimental volume and normalising to the saturation intensity provides good agreement with a large number of experimental investigations. In particular, theory has been confirmed for the neutral Ar target by comparison to the benchmark work of Larochelle *et al*[13]. Whilst differences in pulse length and interaction volume forbid a direct comparison, it is still beneficial to compare the current work to that of Becker and Faisal for both the neutral Ar target and the Ar^{+} ion. Close to the upper limit of the non-sequential intensity regime, theoretical calculations provide an Ar^{3+}/Ar^{2+} ratio of 0.04, from an Ar target, and 0.03 from the ionic target. However under identical conditions, ADK predictions for purely sequential ionisation give a ratio of 0.01, much closer to the present work at 0.007. Thus, although dominant in the case of the neutral target, non-sequential Ar^{3+} production processes appear to be absent in the case of the ion target. These results confirm that the removal of an electron prior to interaction with the laser pulse comprehensively suppresses non-sequential mechanisms, leaving only the sequential ionisation contribution. This work[14] has also shown that the initial charge state of the target plays an important role in determining the mechanisms for multiple ionisation, in contradiction to previous predictions.

Study of this novel system has opened up experimental studies of multiple ionisation in a strong laser field, which to date have been limited to a small range of neutral atoms, to the use of positive ions for direct study. In this initial study we have shown that there are dramatic differences between the strong field ionisation of neutral and singly charged Ar, demonstrating the need for further experimental and theoretical work for positive ion targets.

References

1. See for example: M Protopapas, C H Keitel and P L Knight, Rep. Prog. Phys. 60, 389 (1997)
   L F DiMauro and P Agostini, Adv. At. Mol. Opt. Phys. 35, 79 (1995)
2. P B Corkum, Phys. Rev. Lett. 71, 1994 (1993)
3. H van der Hart, J. Phys. B. 33, L699 (2000)
4. G L Yudin and M Y Ivanov, Phys. Rev. A. 63, 033404 (2001)
5. R Moshammer *et al*, Phys. Rev. Lett. 84, 447 (2000)
6. R Lafon *et al*, Phys. Rev. Lett. 86, 2762 (2001)
7. V R Bhardwaj *et al*, Phys. Rev. Lett. 86, 3522 (2001)
8. I D Williams *et al*, J. Phys. B. 33, 2743 (2000)
9. P Hansch , M A Walker and L D van Woerkom, Phys. Rev. A. 54, 4 (1996)
10. L Zhang, L J Frasinski and K Codling, J. Phys. B. 27, 3427 (1994)
11. M V Ammosov, N B Delone and V P Krainov, Zh. Eskp. Teor. Fiz. 91, 2008 (1986)
12. A Becker and F H M Faisal, J. Phys. B. 32, L335 (1999)
13. S Larochelle, A Talebpour and S L Chin, J. Phys. B. 31, 2101 (1998)
14. J B Greenwood *et al*, Phys. Rev. Lett. 88, 233001 (2002)

Characterisation of the Astra Laser in Proton Acceleration Experiments

P McKenna, K W D Ledingham*, I Spencer, T McCanny, R P Singhal

Department of Physics and Astronomy, University of Glasgow, Glasgow G12 8QQ, UK
** also at AWE plc, Aldermaston, Reading RG7 4PR, UK*

A J Langley, P S Foster, C Ziener, E J Divall, C J Hooker, D Neely, P A Norreys, R J Clarke

Central Laser Facility, CLRC Rutherford Appleton Laboratory, Chilton, Didcot, Oxon, OX11 0QX, UK

K Krushelnick

Blackett Laboratory, Imperial College, Prince Consort Road, London SW7 2BZ, UK

E L Clark

AWE plc, Aldermaston, Reading RG7 4PR, UK

Main contact email address: *p.mckenna@physics.gla.ac.uk*

Introduction

The acceleration of beams of protons using ultra-high intensity lasers has been widely studied in the past few years (for a recent review see Mendonça *et al.* 2001).[1)] In particular proton acceleration from solid targets with thicknesses greater than the wavelength of the incident laser light has received a great deal of interest, partially because the proton energies measured are higher than with gas, cluster or thin solid targets [1)]. Most of this work was performed on large-scale, single-shot laser systems, although it is envisaged that smaller-scale higher repetition rate lasers providing multi-terawatt pulses at intensities above 10^{18} Wcm^{-2} will provide the basis for further systematic study.

To begin to look seriously at designing dedicated laser systems to accelerate ions for various applications, the question of the optimum laser pulse conditions needs to be addressed. This is only possible via careful and full characterisation of the various pulse parameters in laser-based acceleration experiments. In this article we present a study of proton acceleration using well-characterised pulses from the Astra laser system. Proton energy distributions as a function of laser intensity are presented.

Laser Pulse Characterisation

The Astra multi-terawatt laser was employed in this study. Langley *et al* (2000) [2)] provide a detailed description of the laser system. Here we present measurements made to characterise the laser pulse parameters for the present study.

Pulse Duration

A single-shot autocorrelator was used to measure the pulse duration at the output of the compressor. To avoid stretching the pulse to be measured, all reflective optics (apart from a pellicle beam splitter) were used to deliver pulses to the 250 μm thick doubling crystal used in the autocorrelator. Figure 1 shows a typical measurement of a compressed pulse obtained during the present study. A Gaussian fit to the trace is also shown. The mean value of 5 measurements determined the pulse duration (full width at half maximum (FWHM)) to be 60 fs. At the exit of the compressor the laser pulses were linearly polarised with the ***E***-vector vertical.

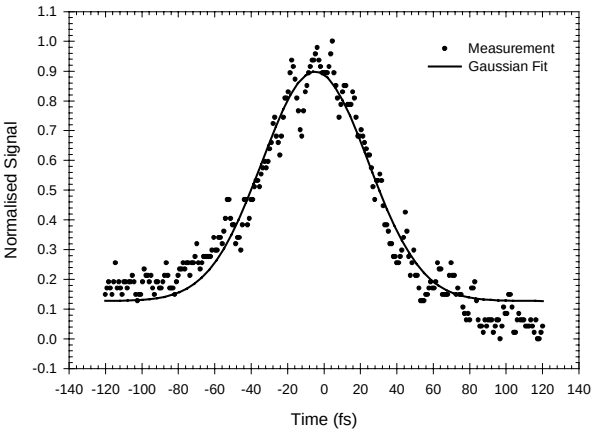

Figure 1. Autocorrelation measurement of a compressed pulse.

Contrast Ratio and Pre-Pulse Activity

In experiments involving short-pulse laser illumination of solid targets, prepulse activity pre-heats the target, causing it to ionise before the arrival of the main pulse. The level and timing of ionising prepulse and amplified spontaneous emission (ASE) defines the plasma expansion and density scale length during the interaction with the main modelocked pulse. Wharton *et al* (2001) [4)] demonstrated that even non-ionising pre-pulses with intensities of the order of 10^9 Wcm^{-2} can substantially alter high-intensity laser-solid interactions.

Whereas it is impossible to completely eliminate prepulse activity, it is important to keep it to a minimum. To help achieve this the Astra laser contains three KD*P Pockels cells (EM510. Leysop Ltd.), which have a manufacturer's specified optical rise-time of 0.25 ns. Two are placed within the first, 10-pass Ti-S amplifier stage and the third is placed between the first and second amplifiers. Each Pockels cell is placed between two crossed, Glan-Taylor polarising elements. The Pockels cells serve three roles within the laser. Firstly, they act as a pulse picker at a repetition rate of 10 Hz, secondly they serve to minimise the energy of pre-pulses on target and thirdly they reduce the amplification of spontaneous emission (ASE).

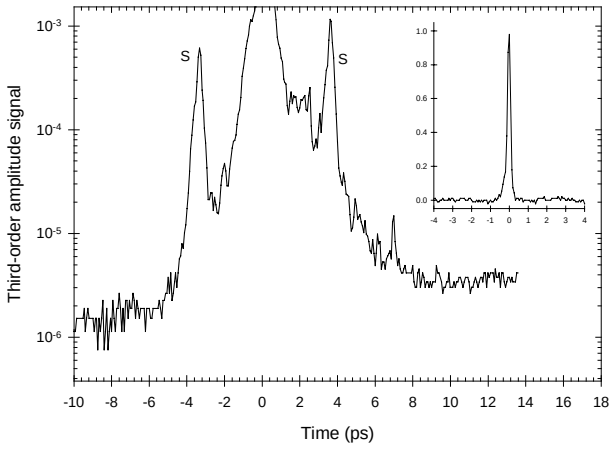

Figure 2. Third-Order Amplitude Diagnostic (TOAD) trace of the output pulse. The main logarithmic plot shows the trace obtained at maximum sensitivity. The satellite peaks S are due to reflections in the TOAD. The inset shows the corresponding trace obtained at low sensitivity and provides a calibration of the magnitude of the main trace.

The pulse-picking role is necessary because, as mentioned above, the femtosecond laser oscillator operates with an output repetition rate of 76 MHz and provides a train of pulses spaced 13 ns apart. The Ti-S amplifiers, however, are pumped at a repetition rate of 10 Hz, and gain is present within each amplifier crystal for several microseconds. The Pockels cells therefore serve to pick pulses for amplification whilst discriminating against the amplification of all other pulses in the train. Photo-diode measurements of the laser pulse showed that the best ratio between the energy of the preceding pulse (13 ns prior to the main amplified pulse) and the energy of the main pulse is 5 x 10^{-8}. Lastly the two Pockels cells placed within the first amplifier are particularly important for removing unwanted ASE. The amplified pulses make 5 passes through the TiS crystal and are then passed through the Pockels cell pair before being injected back into the amplifier for a further five passes. The first amplifier has an overall gain of 10^6 and the Pockels cells are very effective at removing the amplification of spontaneous emission.

To characterise the prepulse and ASE activity in the present study a third-order amplitude diagnostic (TOAD) measurement was carried out on the compressed pulses. The main purpose of a TOAD measurement is to highlight the intensity distribution in the wings of the main pulse. The main logarithmic trace in Figure 2 was obtained with the TOAD operated at its maximum sensitivity. At 10 ps before the main pulse, the background is at the 10^{-6} level or better since this represents the sensitivity limit of the TOAD. The background level rises to 10^{-5} at 4 ps and 10^{-4} at 1.5 ps before the arrival of the main pulse. The two satellite peaks (S) are caused by reflections in the tripling crystal of the autocorrelator (This was established by changing the crystal to one of different thickness and observing a change in the delay between the two peaks.) These reflections produce a weak post pulse for both the red (790 nm) and blue (395 nm) pulses which, when cross-correlated with the main red and blue pulses, result in two satellite peaks – one (apparently) before and the other after the central peak.

The linear plot in the inset of Figure 2 was obtained with the TOAD operated at low sensitivity by attenuating the energy of the input pulses. The low sensitivity scan serves to calibrate the magnitude of the high sensitivity data. It also demonstrates the instrument response of the TOAD which at ~200 fs is more than adequate for the measurement of contrast over the required tens of picoseconds time-window.

The Astra multi-terawatt laser is capable of delivering focused intensities above 10^{19} Wcm^{-2} on target. The distribution on the rising edge of the pulses as indicated by the TOAD measurement represents an intensity of 10^{14} Wcm^{-2}, 4 ps before the peak of the pulse, rising to 10^{15} Wcm^{-2} at about 1 ps. Assuming the plasma produced expands thermally at 10^7 cms^{-1}, a plasma scale length of the order of 0.4 μm is estimated.

Focused Intensity

An f/3, 15.1 cm focal length off-axis, parabolic mirror was used to focus the beam onto target. Due to the quantity of debris that can be generated in high-repetition rate laser-solid interactions it was necessary to shield the gold coating on this optic with a transparent plastic pellicle. The pellicle is 10 μm thick and therefore has a low B-integral and does not affect the overall focus quality.

To determine the size and quality of the laser focal spot a microscope objective was used to image it onto a CCD camera. The spatial resolution of the system has been calibrated to measure the focal spot size. The beam energy was attenuated to facilitate this measurement. Figure 3 shows a typical image, where best focus corresponded to a FWHM spot size of 2.5 μm, which is almost diffraction limited. 41% of the total energy on target was determined to be contained within FWHM of this spot. The maximum energy on target was 225 mJ, as determined with a calorimeter positioned in the beam path just in front of the focusing optic. Using these maximum pulse parameters the focused intensity within FWHM of the main focal spot is calculated to be (3.0 ± 1.8) x 10^{19} Wcm^{-2}.

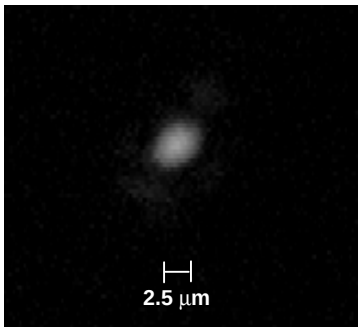

Figure 3. Focal spot image obtained with a CCD camera.

To calibrate the intensity experimentally, a Time-of-Flight (ToF) spectrometer has been developed to measure ion production within the laser focus. The intensity is determined by comparing the measured stages of ionisation of a target gas with predictions of an atomic ionisation model. This technique is widely used in the study of Atomic and Molecular Physics/Chemistry in laser fields of the order of 10^{16} Wcm^{-2}. It works particularly well when the observed ToF spectra can be statistically averaged over a number of laser shots and is therefore suitable in the present study with a laser repetition rate of up to 10 Hz at a reduced pulse energy. The technique is detailed in a separate article in this report (C. Ziener *et al*)[6]. The intensity determined by measuring the ion yields in this way was found to be in good agreement to within a factor of 1.5 with the calculated intensity.

Proton Diagnostics

Measurements of the proton energy spectra were carried out using a 'Thomson parabola' spectrometer with CR-39 plastic nuclear track detector, as shown schematically in Figure 4. CR-39 can be used to detect protons with energies above 100 keV.

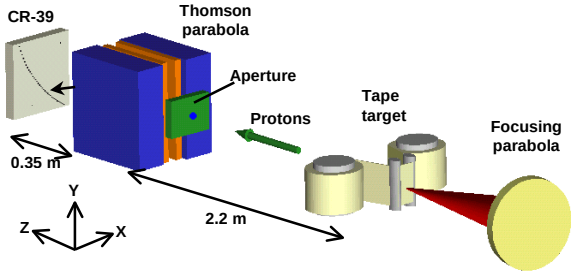

Figure 4. Schematic of proton diagnostic set-up.

The spectrometer was located along the target normal direction (and therefore the laser axis) at a distance of 2.2 m behind the target. A 1 mm aperture was positioned to subtend a solid angle of 0.1 μsr. Between the two poles of the spectrometer, parallel electric and magnetic fields were established in opposite directions along the X-axis of Figure 4. For a positively charged ion this resulted in an electric force in the +X direction and a magnetic force in a downward direction along the Y-axis. In this way ions entering through the defining aperture experienced a parabolic deflection between the poles according to their velocity. Although ions of different charge-to-mass ratio (q/m) are separated into distinct parabolas, only protons were detected in the present study.

The characteristic proton parabolas were imprinted on pieces of CR-39 located at a distance of 35 cm behind the spectrometer. As protons come to rest, the energy they deposit causes

structural damage to the plastic material. After etching the plastic in NaOH solution for several hours, a series of small pits visible under a microscope provides the signature of the ions. A spectrum is unfolded by sampling the number of pits in various energy bins along the parabola. Figure 5 shows an example of a piece of CR-39 illustrating some of the parabolas obtained in the present study. The sharpness of the trace depends on the acceptance angle of the instrument and hence the aperture size. The traces all result from protons, but produced under varying experimental conditions. The measurements were made with the same target (25 μm thick aluminium), but trace (A) was obtained at an intensity of 7.4 x 10^{18} Wcm^{-2}, with (B) and (C) resulting from measurements at 6.2 x 10^{18} Wcm^{-2} and 5.2 x 10^{18} Wcm^{-2} respectively. The parabolas were separated by changing the electric field strength in the spectrometer between measurements. Fields of strength 3 $kVcm^{-1}$, 2 $kVcm^{-1}$ and 1 $kVcm^{-1}$ were used for traces (A), (B) and (C) respectively. The magnetic field was held constant at a value of 0.1 T as determined by the fixed position of the permanent magnetic pole pieces. The result was a change in deflection along the X-axis for each measurement and therefore a change in the resulting parabola. In this way various parameter scans could be made with a single piece of CR-39. This avoided the need to recycle the vacuum conditions to change the detector frequently and thus made full advantage of the high repetition rate of the laser and the moving target mechanisms. Trace (D) in Figure 5 was made at a laser intensity of 7.4 x 10^{18} Wcm^{-2} (as with (A)), but with the electric field turned off. This line trace highlights the magnetic deflection in the downward direction along the Y-axis. A measurement of this nature was routinely made after each parameter scan and at the initial parameter condition to check reproducibility in the unfolded spectrum.

Additional pieces of CR-39 with up to 8 steps of mylar filter were positioned at various angles from target normal in the main target chamber. The filters had thickness up to 20 μm, which provided a proton spectrum of cut-off energies up to 1 MeV. These were used to provide measurements on the directionality and angular spread of the proton beams.

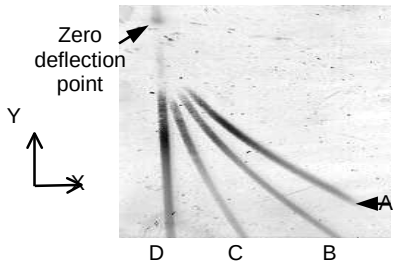

Figure 5. Proton parabolas imprinted on CR-39. The measurements were made with 25 μm Al target. The laser intensity was A,D: 7.4×10^{18} Wcm^{-2}; B: 6.2×10^{18} Wcm^{-2} and C: 5.2×10^{18} Wcm^{-2}. The electric field within the spectrometer was maintained at A: 3 kV/cm; B: 2 kV/cm; C: 1 kV/cm and D: no electric field.

Experimental Results

Proton measurements as a function of focused laser intensity for low energy (< 200 mJ) pulses are presented here. Figure 6 shows proton energy distributions measured behind a 25 μm Al target, irradiated at normal incidence with laser intensities between 5.2 x 10^{18} Wcm^{-2} and 7.4 x 10^{18} Wcm^{-2}. The overall shape of the spectra are quite similar and in good overall agreement with the results of Maksimchuk *et al* (2000) [5] for a 1.8 μm Al target at intensities up to 3 x 10^{18} Wcm^{-2}. Maksimchuk [5] presents maximum proton energy of about 1.5 MeV to 2.0 MeV for a 25 μm Al target at a laser intensity of 1.5 x 10^{18} Wcm^{-2}. The maximum proton energies in the present results for the same target thickness are lower, increasing from about 0.4 MeV to 0.8 MeV over the intensity range studied. Measurements were also made with copper target foils, which yielded maximum proton energies similar to the aluminium target.

In Figure 7 a similar set of measurements is presented for a 23 μm mylar target for intensities between 5.8 x 10^{18} Wcm^{-2} and 8.2 x 10^{18} Wcm^{-2}. As with the aluminium target, the maximum energy to which protons are accelerated is observed to scale with intensity. However, the maximum proton energies are higher for the mylar target than for the metal targets. This is contrary to the results of Maksimchuk [5] who observed no significant difference in the maximum energy of protons for different materials.

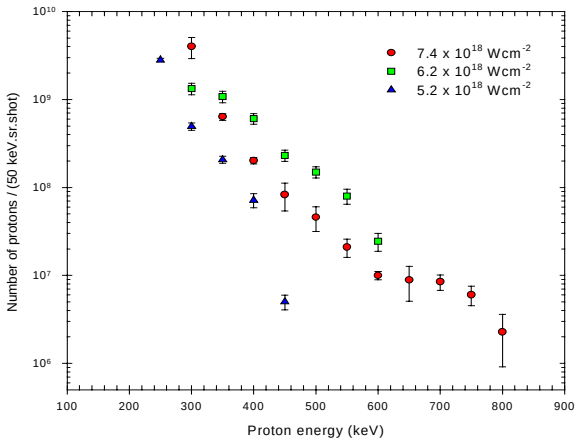

Figure 6. Scaling of the energy distribution of protons with laser intensity on a 25 μm Al target.

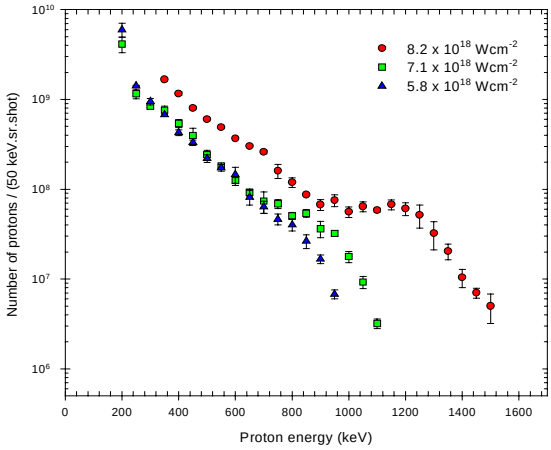

Figure 7. Scaling of the energy distribution of protons with laser intensity on a 23 μm mylar target.

Conclusions

The importance of good pulse characterisation in multi-terawatt laser-solid interactions is highlighted. The design and development of a dedicated laser system for proton acceleration will benefit from systematic studies of this nature using well characterised laser parameters.

References

1. J. T. Mendonça, J. R. Davies, and M. Eloy, Meas. Sci. Tech. 12, 1801 (2001).
2. J. Langley et al., Central Laser Facility Annual Report 1999/2000, RAL-TR-2000-034, 196 (2000).
3. D. Strickland and G. Mourou, Opt. Comm. 56, 219 (1985).
4. K. B. Wharton *et al*., Phys. Rev E 64, 025401(R) (2001).
5. A. Maksimchuk *et al*., Phys. Rev. Lett. 84, 4108 (2000).
6. C Ziener et al., Central Laser Facility Annual Report 2001/2002, RAL-TR-2002-013, 192 (2002).

Novel Target Drive Mechanisms for High Repetition Rate Laser-Solid Interaction Experiments

P McKenna, K W D Ledingham*, I Spencer, T McCanny, R P Singhal

Department of Physics and Astronomy, University of Glasgow, Glasgow G12 8QQ, UK
**also AWE plc, Aldermaston, Reading RG7 4PR, UK*

M Harman, P Hatton, D Neville, P Brummitt, P S Foster, A J Langley, D Neely, E J Divall, C J Hooker, R J Clarke, R M Allott

Central Laser Facility, CLRC Rutherford Appleton Laboratory, Chilton, Didcot, Oxon, OX11 0QX, UK

Main contact email address: *p.mckenna@physics.gla.ac.uk*

Introduction

When a laser pulse with peak intensity of the order of 10^{19} Wcm^{-2} interacts with a thin solid target (of the order of 10 μm) the target material breaks down resulting in a characteristic hole centred on the laser focal point. Each laser pulse must therefore be focused onto fresh target material. The use of a laser with the repetition rate of a few Hz such as Astra demands the adoption of a mechanical system to advance the target material in synchronisation with the laser pulse train. This facilitates a large number of laser shots to be taken before the vacuum conditions in the interaction chamber are recycled to replace the target. More importantly, integrating over many shots improves the systematics and quantity of data obtained. Two target mount arrangements were developed for use in the present study to accommodate Cu, Al and mylar targets with thickness between 0.2 μm and 125 μm.

Target drive system designs

Figure 1 shows a double-reel set up employed for 10 mm wide tape targets. This mounting system was used with both plastic and metal tapes with thickness above 10 μm. A computer-controlled stepper motor facilitated motion of the reels in either direction with the target tape moving across two support rods, each a few mm to either side of the laser focus. The drive was designed to operate at a velocity that ensured the tape remained under tension, and therefore flat, but not deformed. Experience showed that tapes thinner than 10 μm could not be used for this reason. Typically nearly 200 laser shots were taken on a 2 m long tape. In this way, measurements could be carried out for extended periods facilitating various parameter scans. Target tapes were loaded on spare reels in advance to ensure rapid target changeover.

A second target mount mechanism, shown in Figure 2, involved sandwiching thin target foils (< 10 μm) between two halves of a circular wheel. A stepper motor was used to rotate the wheel, to advance each target to the laser focus. Although only 24 shots could be taken between each changeover, several targets of differing material and thickness could be mounted on a single wheel.

Experiment and Results

The target drives described were used in a proton acceleration experiment. The experiment involved the use of a Thomson Parabola spectrometer with CR39 detectors, to measure the flux and energy of the protons emitted from the laser-solid interaction.

To experimentally establish if the target mount mechanisms of Figures 1 and 2 had any influence on the interaction process, the same target material was irradiated using both arrangements and the reproducibility of the energy distribution of protons emitted was checked. Figure 3 shows the corresponding spectra measured at the back of the 36 μm mylar targets irradiated at normal incidence. A total of 50 laser shots were made on the moving tape target and a maximum of 24 shots on the wheel-mounted target. The averaged laser intensities were 7.2 x 10^{18} Wcm^{-2} and 7.5 x 10^{18} Wcm^{-2} respectively. The data

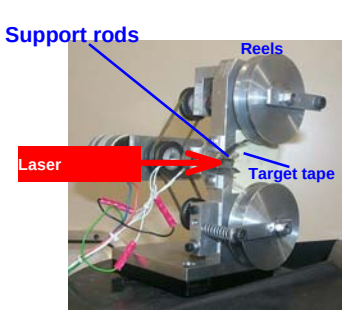

Figure 1. Double reel arrangement for tape targets.

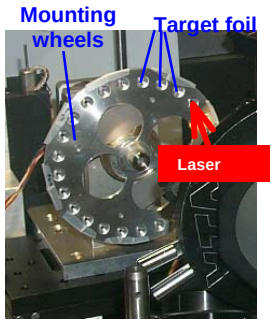

Figure 2. Wheel arrangement for thin target foils.

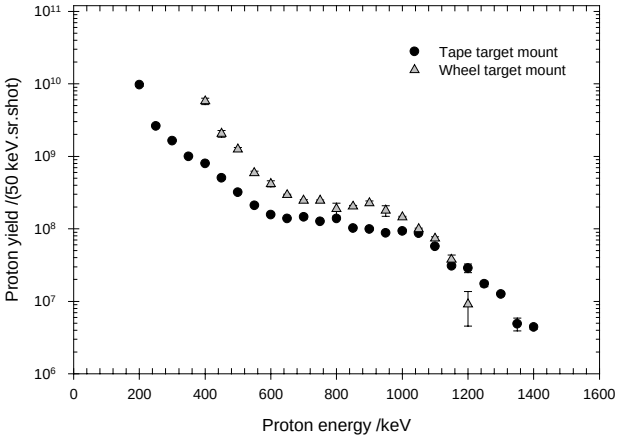

Figure 3. Energy distribution of protons as measured with a 36 μm mylar target mounted in both the 'tape-target' and 'wheel-target' mounts.

have been normalised to present the number of protons observed per shot (in 1 steradian and within a 50 keV energy bin). Both spectra have a characteristic plateau over a similar energy range. The highest energy points represent a cutoff, above which no protons were detected. There is a small difference of about 200 keV in comparing the maximum energies observed, but otherwise the spectra are quite similar.

Conclusions

Target systems have been designed to realise the full potential of a high-repetition rate laser system, specifically Astra in this study, for high-intensity experiments. Specifically, the novel target designs were used very successfully in proton production experiments, making it possible to integrate over many shots. These targets coupled with the 2 Hz repetition rate of the laser provided a large quantity of systematic and reproducible measurements, and made it possible to resolve the optimum conditions for a range of target conditions for proton acceleration.

Table-Top Proton Acceleration Using Astra

I Spencer, K W D Ledingham*, P McKenna, T McCanny, R P Singhal

Department of Physics and Astronomy, University of Glasgow, Glasgow G12 8QQ, UK
** also at AWE plc, Aldermaston, Reading RG7 4PR, UK*

K Krushelnick

Blackett Laboratory, Imperial College, Prince Consort Road, London SW7 8QQ, UK

E L Clark

AWE plc, Aldermaston, Reading RG7 4PR, UK

P A Norreys, R J Clarke, P S Foster, D Neely, A J Langley, E J Divall, C J Hooker

Central Laser Facility, CLRC Rutherford Appleton Laboratory, Chilton, Didcot, Oxon, OX11 0QX, UK

J R Davies

GoLP, Instituto Superior Técnico, 1049-001 Lisboa, Portugal

Main contact email address: *i.spencer@physics.gla.ac.uk*

Introduction

Advances in laser technology such as chirped pulse amplification (CPA) [1,2] have led to the construction of multi-terawatt and recently petawatt laser systems and proposed techniques such as optical parametric chirped pulse amplification (OPCPA) [3] promise to continue to extend these boundaries for the foreseeable future. Exciting new fields of research have developed in laser-matter interactions as a result of this technology. At intensities above about 10^{18} Wcm^{-2} relativistic plasmas are created as electrons quiver in the laser field with energies equivalent to their rest mass. Beams of electrons and protons are accelerated and sources of neutrons, high fluxes of X-rays and high energy γ-rays are created. Notable achievements including the laser induced fission of ^{238}U [4,5], the production of nuclear isotopes [6,7] and the measurement of the highest magnetic fields ever produced in a laboratory [8] have ensured that this continues to be an exciting area of research with many potential beneficiaries.

The generation of large numbers of fast ions in ultra high intensity laser-matter interactions, e.g. [9,10], in particular promises to find wide ranging applications including ion injectors for heavy ion accelerators [11], fast ion based fast ignitor schemes [12-14] and proton radiography [15]. In addition the authors have previously reported using laser-accelerated beams of protons with a mean energy of 2 MeV and peak proton energy of 37 MeV to induce (p,n) and (p,α) nuclear reactions [16,17]. This resulted in the production of the short-lived positron emitting isotopes ^{11}C and ^{13}N, which are used in positron emission tomography (PET), a non-invasive medical imaging technique. Laser produced protons may also find applications in proton oncology for the treatment of tumors of the eye.

Much of the 'proof-of-principle' experimentation has involved large-scale, 'single-shot', picosecond pulsed lasers. However, due to inherently large costs and low repetition rates it is unlikely that such laser systems will provide the quantity and range of data needed to fully elucidate the processes involved. The extension of these studies to smaller, but higher repetition rate lasers, maintaining focused intensities above 10^{18} Wcm^{-2} is required to realise the development and application of the new techniques. Laser systems providing multi-terawatt pulses at a repetition rate of a few Hz have been developed at a number of laboratories world-wide. These lasers facilitate the systematic experimentation required to optimise the conditions of ion acceleration and provide a fuller understanding of the physics involved. This is required for the design of dedicated laser systems for the applications outlined.

Studies on proton acceleration at the University of Michigan have involved a laser system with a repetition rate of 1 shot per 10 minutes [18] providing 1 J, 400 fs pulses focused to an intensity of 3×10^{18} Wcm^{-2} on thin-foil targets. Fast protons with energy up to 1.5 MeV were generated [19]. In another experiment, the same group accelerated deuterons at 6×10^{18} Wcm^{-2}, and produced small quantities of ^{11}C via (d,n) reactions in boron [20].

Developments in 'tabletop' laser technology seek to produce shorter pulse durations for a given pulse energy, thereby increasing the intensity. Due to the shorter heating time the interaction of short pulses of tens of fs with thin-foil targets could be expected to significantly change the interaction process and hence the physics of the ion acceleration. To fully understand what influence this new generation of short pulse lasers will have on the acceleration of ions and to test their feasibility for applications, it is important for experiments to be carried out in this unexplored regime.

Very recent results from MacKinnon *et al.* [21] using a 100 fs laser pulse and intensity >10^{20} Wcm^{-2} incident on aluminium targets showed that proton energies as high as 24 MeV were obtained from 3 μm targets, and this energy decreased to 6.5 MeV when 100 μm targets were used. Higher proton energies in thin targets were attributed to re-circulation of electrons in these targets, i.e. electrons being reflected at each of the target-vacuum boundaries and making multiple crossings of the target.

This report describes results of proton production using the Astra laser with pulse durations of tens of fs (60 fs) and energies below 200 mJ. The optimum target material and thickness for proton production has been characterised for this laser system.

Experimental

The experiment used the high-power beam-line of the Astra Ti: sapphire laser facility [22] at the Rutherford Appleton Laboratory, UK, operated in the CPA [1,2] mode. The system delivered pulses on target at normal incidence at a rate of 1 Hz with a wavelength centred at 790 nm within an evacuated vacuum chamber held at a modest vacuum of around 10^{-5} Torr. The beam was focused onto target using an F3 off-axis parabolic mirror. A full description of the characterisation of

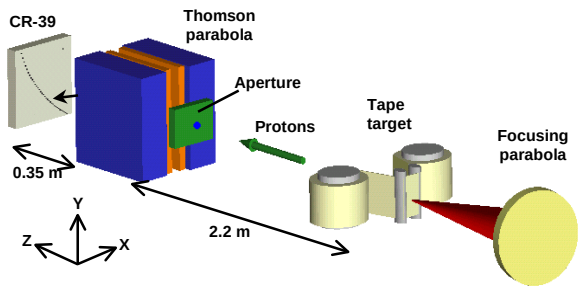

Figure 1. Experimental arrangement for proton measurements.

the various laser parameters is the subject of another publication [23]. Briefly, the system delivered pulses on target of 200 mJ and duration 60 fs. The contrast ratio was measured to be $1:10^{-6}$ or better at 10 ps before the main pulse, rising to $1:10^{-5}$ at 4 ps and 10^{-4} at 1.5 ps [23]. The maximum intensity on target was calculated to be 7×10^{18} Wcm^{-2}, and corroborated by measurements of multiple ionisation stages of argon [23].

Measurements of ion emission were made using a Thomson Parabola spectrometer [24-26] backed with CR39. The experimental set-up is shown in Figure 1. CR39 is a plastic nuclear track detector which is sensitive to ions greater than 100 keV / nucleon, and insensitive to X-rays and electrons. Each ion incident on the CR39 is recorded as a single pit, and since their energy can be calculated by the extent they are deflected in the spectrometer, spectral information i.e. numbers and energy can be obtained. Data were accumulated over 24 or 50 shots for every target.

Another experimental arrangement involved positioning CR39 detectors close to the rear of the target in order to make spatially integrated measurements of proton emission. Results of this study are described in the next section.

Results

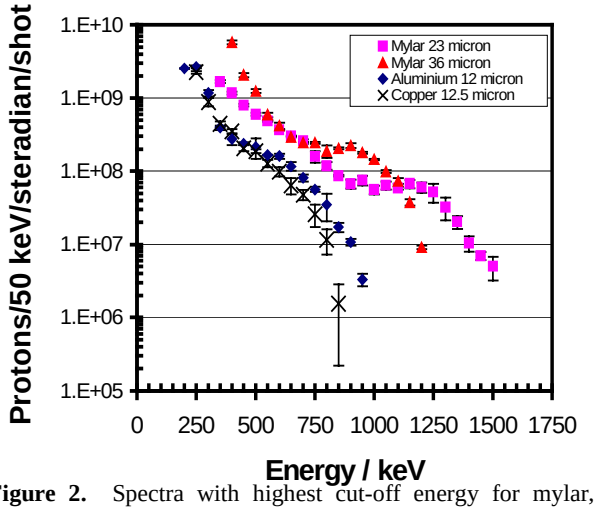

Figure 2. Spectra with highest cut-off energy for mylar, aluminium and copper targets. The highest energy point shown on each spectrum is the cut-off energy.

The experimental set-up described above was used to measure the energy spectrum of protons emitted from targets of mylar, aluminium and copper targets of various thickness. The spectra obtained for each material with the highest cut-off energies are shown in Figure 2. The highest energy shown on each spectrum represents the cut-off energy. The optimum thicknesses were between 23 and 36 μm for mylar and ~12-13 μm for both aluminium and copper, and the maximum proton energy obtained was 1.5 MeV with a mean energy of 250 keV, using a 23 μm thick mylar target. The metal targets gave lower maximum energies, 950 keV for Al, and 850 keV for Cu. It is instructive to plot the maximum proton energies as a function of target thickness, and this is shown in Figure 3 for mylar, aluminium and copper targets. Figure 3 shows clearly that low proton energies are obtained for thin targets, reaching an optimum (which is ~3 times as thick for mylar compared with aluminium and copper) and an eventual decrease in energy for thicknesses greater than the optimum.

Figure 4 shows the total proton flux ≥400 keV for the targets used. For the metals, this number was an order of magnitude lower than that of mylar. This is consistent with results obtained on the Petawatt at LLNL which operated at the higher

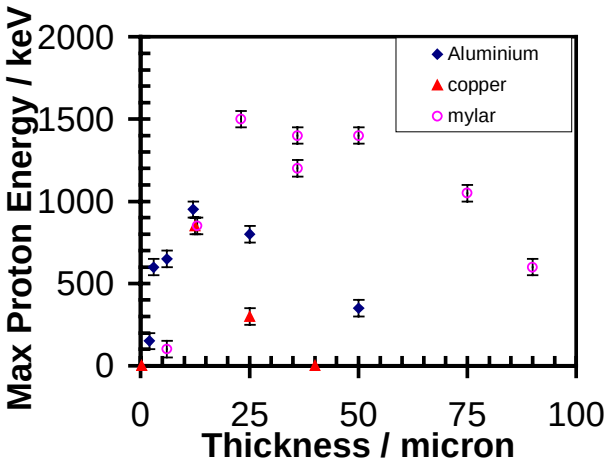

Figure 3. Maximum proton energies measured as a function of target thickness for mylar copper and aluminium. The highest energies were produced with mylar targets, and the optimum thickness for mylar is ~3× thicker than that of the metals.

energy of 500 J and longer pulse length of 500 fs [10]. It shows that surface contaminants are not the only source of protons.

Spatially integrated measurements were made for a number of mylar, aluminium and copper targets by positioning CR39 close behind the target. The protons were emitted in a cone of half angle 22° and the distribution was isotropic. No "ring" or "disc" structure [9,27] was observed in contradiction to measurements in higher energy, longer pulse experiments. This may be characteristic of the 60 fs pulse duration and 200 mJ pulse energy used in the present experiment.

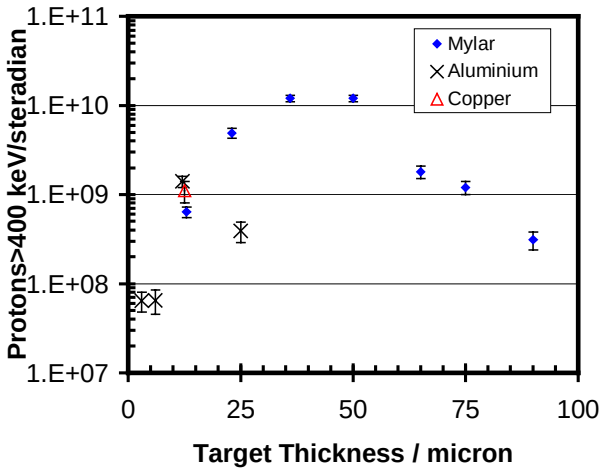

Figure 4. Number of protons ≥400 keV as a function of target thickness for mylar, aluminium and copper.

Discussion

The results presented for both plastic and metal targets show almost no proton emission from targets of thickness similar to the laser wavelength, then an increasing maximum energy up to an optimum thickness, then this energy falls off for increasing thickness. It is believed that the acceleration mechanisms for targets of thickness similar to the laser wavelength are very different from that of thicker targets [28]. The decrease in maximum proton energy after the optimum might be explained by collisional energy loss in the target. Interestingly, in the case of mylar, the optimum thickness appears to be $2c\tau$ where c is the speed of light and τ is the laser pulse length.

MacKinnon *et al.* [21] observed the highest proton energies from thin targets of the order of the laser wavelength, then a sharp decrease going to thicker targets up to ~10 μm, then a slower

decrease for targets up to 100 μm. High proton energies observed for thin targets was attributed to increased recycling of electrons in the target (reflections between front and rear surfaces) for the thinnest targets of the order of the laser wavelength, which was verified via PIC simulations.

This is in contradiction to the present results, but may be explained in terms of pre-pulse activity. The contrast ratio of the laser used in MacKinnon *et al.* was of the order 10^{10} which would give a pre-pulse intensity of 10^{10} Wcm^{-2}. This would not affect the target surface significantly prior to the arrival of the main pulse. In the present experiment, the contrast ratio was 10^{6} at 10 ps before the main pulse, and increased after this. A pre-pulse intensity of 7×10^{12} Wcm^{-2} would certainly ionise the front target surface and generate a plasma in front of the target prior to the arrival of the main pulse. Pre-plasma formation on the front surface effectively increases the target thickness and would lead to less than perfect electron reflection. For targets of the order of the laser wavelength pre-plasma formation on the rear would also be expected, which has been shown to perturb proton emission from the rear [29,30]. It is possible that a higher contrast ratio in the present experiment would have produced higher energy protons for the thinnest targets used, and this will be investigated in future experiments. In fact, MacKinnon *et al.* stated that the proton signal was sometimes lost for thin targets, and this was attributed to an increase in pre-pulse activity since the pre-pulse proved difficult to control.

By comparing the results found here with those of Maksimchuk *et al.*, [19], several similarities are observed. Firstly, the proton energies obtained are very similar, including a maximum energy of 1.5 MeV. Also, the spectral shapes show a striking resemblance, with a flattening off of the spectrum prior to a sharp cut-off in both cases. Interestingly, even though the results obtained are extremely similar, the difference in laser parameters between the present case and that of Maksimchuk *et al.* is as follows: the pulse length is a factor of seven shorter, the pulse energy a factor of five lower and the intensity here is a factor of two higher.

When comparing aluminium, the maximum proton energy obtained here was 800 keV compared to 1.5 MeV in [19], even though the intensity herein was a factor of two higher. It appears that the reduced pulse length affects the acceleration mechanisms and leads to lower proton energies for similar intensities. The much lower pulse energy may also affect the acceleration mechanisms, although it is believed that this should only affect the electron and subsequently proton flux. In the present case, the conversion efficiency from the laser to protons has been estimated to be 0.7 %. This is encouraging for the future of table-top laser based proton acceleration, and further details of the implications of this finding can be found in [23].

Maksimchuk *et al.*[19] saw also a dependence of pre-pulse intensity with the proton energies observed, and found a maximum. In this experiment, the pre-pulse arrived ~50 ps before the main pulse, and the optimum pre-pulse intensity was found at 10^{15} Wcm^{-2}. However, MacKinnon *et al.*[21] found optimum conditions by minimising the pre-pulse intensity and using thin targets of ~3 μm. The pre-pulse obviously plays a vital role in fast proton production, and this factor must be investigated further in future experiments.

The ponderomotive potential U_p for $I=6\times10^{18}$ Wcm^{-2} and $\lambda=0.8$ μm is 486 keV. The temperature of the hottest proton spectrum obtained in this study is 208 keV, over a factor of 2 lower. However, if the dominant absorption mechanism into fast electrons is ponderomotive $\mathbf{j}\times\mathbf{B}$ heating, then maximum proton energies of around 500 keV would be expected [28]. Proton energies 3 times higher than this have been measured. It is obvious that other proton acceleration mechanisms are at work, and that the pulse duration and contrast ratio of the laser plays an important role in proton production.

Conclusions

A study of proton emission from a table-top 1 Hz laser system operating at 60 fs, 200 mJ and 7×10^{18} Wcm^{-2} interacting with solid targets has been made. The proton energies obtained have been investigated for various target materials and thicknesses. Optimum conditions have been found and the highest energy of 1.5 MeV was obtained with mylar targets. It is obvious that the laser pulse duration and contrast ratio play important roles in the characteristics of proton acceleration, in terms of energies obtained and the spatial distribution. A large quantity of systematic and reproducible measurements was made to resolve the optimum targets for proton acceleration, which was made possible by the 1 Hz repetition rate of the laser. The results herein look promising in terms of table-top high-repetition rate laser proton acceleration and applications in terms of conversion efficiency to protons and the energies obtained.

References

1. D. Strickland and G. Mourou, Opt. Comm. 56, 219 (1985).
2. M. D. Perry and G. Mourou, Science 264, 917 (1994).
3. I. N. Ross *et al.*, Las. Part. Beams. 17, 331 (1999).
4. K. W. D. Ledingham *et al.*, Phys. Rev. Lett. 84, 899 (2000).
5. T. E. Cowan *et al.*, Phys. Rev. Lett. 84, 903 (2000).
6. T. W. Phillips *et al.*, Rev. Sci. Inst. 70, 1213 (1999).
7. K. W. D. Ledingham and P. A. Norreys, Contemp. Phys 40, 367 (1999).
8. M. Tatarakis *et al.*, Nature 415, 280 (2002).
9. E. L. Clark *et al.*, Phys. Rev. Lett. 84, 670 (2000).
10. R. A. Snavely *et al.*, Phys. Rev. Lett. 85, 2945 (2000).
11. K. Krushelnick *et al.*, IEEE Trans. Plas. Sci. 28, 1184 (2000).
12. M. Tabak *et al.*, Phys. Plasmas. 1, 1626 (1994).
13. M. Roth *et al.*, Phys. Rev. Lett. 86, 436 (2001).
14. R. Kodama *et al.*, Nature 412, 798 (2001).
15. M. Borghesi *et al.*, Plasma. Phys. Control. Fusion 43, A267 (2001).
16. M. I. K. Santala *et al.*, Appl. Phys. Lett. 78, 19 (2001).
17. I. Spencer *et al.*, Nucl. Inst. Meth. B 183, 449 (2001).
18. N. Saleh *et al.*, Rev. Sci. Inst. 71, 2305 (2000).
19. A. Maksimchuk *et al.*, Phys. Rev. Lett. 84, 4108 (2000).
20. K. Nemoto *et al.*, Appl. Phys. Lett. 78, 595 (2001).
21. A. J. Mackinnon *et al.*, Phys. Rev. Lett. 88, 215006 (2002).
22. A. J. Langley *et al.*, Central Laser Facility Annual Report 1999/2000, RAL-TR-2000-034, 196 (2000).
23. P. McKenna *et al.*, submitted to Rev. Sci. Inst. (2002).
24. M. R. Wehr, J. A. Richards Jr, and T. W. Adair III, *Physics of the Atom*, (Addison-Wesley Publishing Company, 1983).
25. K. Krushelnick *et al.*, Phys. Rev. Lett. 83, 737 (1999).
26. E. L. Clark *et al.*, Phys. Rev. Lett. 85, 1654 (2000).
27. Y. Murakami *et al.*, Phys. Plasmas. 8, 4138 (2001).
28. J. T. Mendonça, J. R. Davies, and M. Eloy, Meas. Sci. Tech. 12, 1801 (2001).
29. A. J. Mackinnon *et al.*, Phys. Rev. Lett. 86, 1769 (2001).
30. 30. M. Roth *et al.*, Nucl. Inst. Meth. A. 464, 201 (2001).

VUV/ Soft X-ray Emission from Laser-Preplasma Interactions with Picosecond and Femtosecond Pulses

J T Costello, J S Hirsch, E T Kennedy, J-P Mosnier, A Murphy, A Neogi
National Centre for Plasma Science and Technology, School of Physical Sciences, Dublin City University, Glasnevin, Dublin 9, Ireland

P Dunne, D Kilbane, G O'Sullivan
Department of Physics, University College Dublin, Dublin 4, Ireland

C L S Lewis, S Topping
Department of Pure and Applied Physics, Queen's University of Belfast, Belfast BT7 1NN, Northern Ireland, UK

R Clarke, E Divall, P Foster, C Hooker, A Langley, D Neely
Central Laser Facility, CLRC Rutherford Appleton Laboratory, Chilton, Didcot, Oxon, OX11 0QX, UK

Main contact email address: *jtc@physics.dcu.ie*

Introduction

Laser produced plasmas, formed when a high peak power laser pulse is focused onto a sample (usually *in vacuo*) are well known to be intense sources of deep UV to x-ray radiation. Such laser plasma light sources (LPLS) have many applications in UV to x-ray microscopy, lithography and analytical spectroscopy. The exact nature of the formation, expansion and radiation emitted from the plasma depends on many factors such as the laser pulse width, laser wavelength, target structure, etc. There is currently much interest in the generation of vacuum-UV (VUV) to x-ray radiation from ultrashort (100 fsec – 100 psec) laser produced plasmas[1]. At the ultrashort end of the time scale the goal is to produce an intense subpicosecond x-ray probe. Given the short lifetime of the inner shell hole state, the production of Kα radiation by collisions with rapidly heated plasma electrons has gained much currency and proven to be a promising mechanism. Yields of up to 10^{10} photons/sr for 3d elements look possible [2]. However, such a probe is going to be of relatively narrow bandwidth which limits its applicability to e.g., spectroscopic measurements. On the other hand, although longer pulse laser plasmas are capable of producing broadband extreme-UV continuum emission the shortest pulses to date have been on the 100 ps timescale for plasmas heated by 7 ps UV pulses [3].

Motivation

The present study is motivated by a desire to explore the divide between the interaction of short (150 ps) and ultrashort (80 fs) pulses with long pulse (ns) pre-plasmas with a view to reaching a compromise source delivering broad spectral range and short duration. Traditionally LPLS experiments have concentrated on direct laser-solid (usually metal) interactions. However, for some years now a number of studies on the effects of high power laser interaction with a pre-plasma have been undertaken. Almost universally, they have demonstrated an increase flux (mainly in the EUV) emitted compared to direct laser target interaction [4]. The increase in EUV flux is largely attributed to an increase in the plasma scale length and concomitant laser light absorption efficiency and emitting volume enhancement. Many such experiments worked with a pre-pulse, optically split from the main beam. However, in most cases the pre-plasma was formed by the (unwanted) amplified spontaneous emission (ASE) from the short pulse laser amplifier and hence not in any properly controlled fashion. Experiments on interaction of ultrashort pulses with electro-optically synchronised nanosecond laser generated plasmas could provide well defined experimental conditions for controlled exploration of the interaction and its modelling. One specific advantage of long pulse pre-plasmas is that they tend to be more homogeneous thereby reducing refraction of the main pulse out of the plasma and improving coupling efficiency.

Experiments

Pre-plasmas were formed by focusing the 8 ns output pulse from a Continuum Surelite laser onto flat slabs of Cu to irradiances in the range 10^{10} – 10^{11} W.cm^{-2} via a simple f/10 plano-convex lens. They were subsequently heated by either 150 ps or 80 fs pulses carrying up to 400 mJ and 200 mJ respectively. The laser systems were electro-optically synchronised permitting positive or negative time delays of up to 1000s ns with a jitter of < 500 ps. Pulse to pulse delays and jitter were measured on fast photodiodes coupled to a LeCroy 9362C, 100 ps/ point, 3 Ghz bandwidth oscilloscope. The overlap of focal spots on the Cu slab target was checked using a CCD camera with a high magnification objective. Following image capture and analysis, precision laser focusing optic drives permitted alignment of each laser's focal spot to better than 10 μm. For the 150 ps + 8 ns dual laser plasma experiments, VUV spectra were recorded on a 1m normal incidence vacuum spectrometer (Acton Research VM521) equipped with a 1200 grooves/mm grating. The spectrometer was operated with an entrance slit width of 50 μm, yielding a resolution of ca. 1000 at 50 nm. Readout was via a back illuminated CCD (Andor, 256 x 1024 array with 26x 26 μm^2 pixels). In the case of the 80 fs + 8ns dual laser plasma experiments x-ray emission was recorded on a KAP flat crystal spectrometer equipped with front illuminated Andor CCD readout. The entrance aperture included a thin (thickness 5 μm) Mylar filter/window for soft radiation rejection. The ultrashort pulse was focused by a paraboloid to a spot size of ~ 5 μm diameter (potential irradiance of up to 10^{19} W.cm^{-2}).

Results - VUV Experiments

In Figure 1 we show a comparison between a sum of individual ps + ns spectra and a synchronised dual ps/ns plasma spectrum where a significant gain in flux is observed for the latter case.

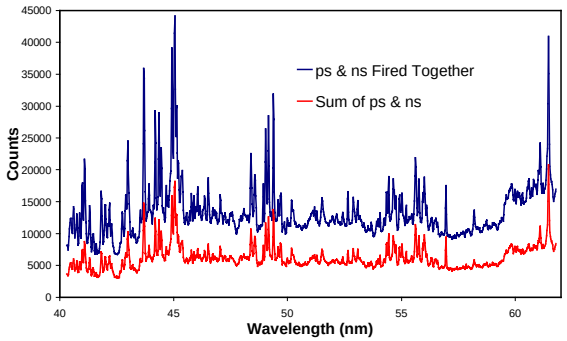

Figure 1. Comparison between synchronised and summed ps/ns laser generated plasma spectra.

The delay between the (ns) pre-plasma and the main picosecond beam was 20 ns. The focal spot size was ~ 250 μm in each case. The spectral distributions for both traces are very similar indicating almost identical plasma conditions. This is largely true at all time delays as is evident from Figure 2 where we show a 3D plot illustrating the time history of the VUV spectra.

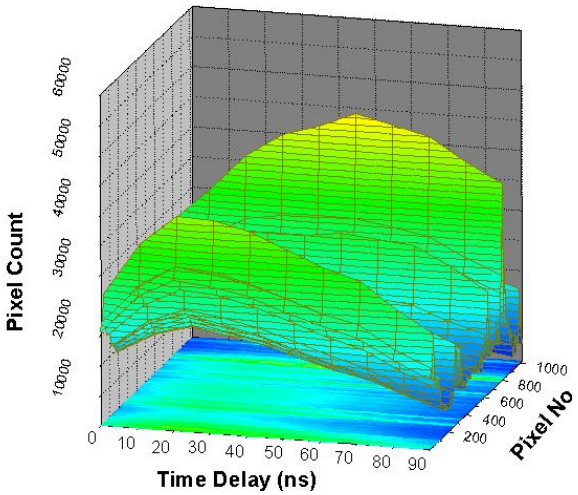

Figure 2. VUV spectral distribution as a function of inter-laser time delay.

Since the spectrometer is set to gather all light even from an extended plasma source the conclusion is that the emitting volume must simply be larger in the synchronised case. This is not unexpected since the pre-plasma provides a longer scale length thereby increasing the volume of pumped plasma and efficiency of collisional absorption and hence the emitting size/ brightness. Time resolved VUV imaging and space/time resolved spectroscopic experiments are planned to confirm this hypothesis. Further experiments on the effect of pre-plasma conditions (known to affect the plasma scale length[5]) are planned. Analysis of the spectra is ongoing in order to clarify the ionization balance.

In Figure 3 we summarise the time history of the VUV flux gain where a peak value of 3.5 at an inter-laser pulse delay of 10 ns is evident indicating an optimum value in the heated volume at this time delay.

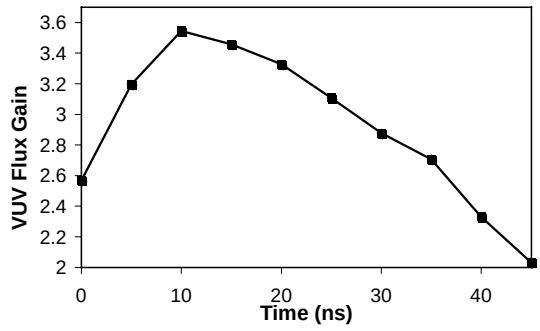

Figure 3. VUV flux gain as a function of interlaser time delay.

Results – Soft X-ray Experiments

For the experiments with the synchronised fs/ns laser generated plasmas we opted to look in the soft x-ray range (7–11 Angstroms) where the Ne-like and neighbouring ion stages of Cu predominantly emit. Up to 200mJ/ 80 fs pulses from Astra were focused to a spot size of diameter ca. 6 μm while the ns pulses were focused to a 50 μm diameter spot and overlapped on target. Peak on target irradiances approached 10^{19} W.cm^{-2} and a few times 10^{12} W.cm^{-2} respectively. A weak spectrum was obtainable using an 800 mJ/8ns pulse only at an irradiance of ~ 5 x 10^{12} W.cm^{-2} and an estimated plasma temperature of ~500 eV. In direct target interaction the emission from the femtosecond generated plasmas was predominantly hard x-ray in nature and tended to swamp the CCD even at 'low' power (~50 mJ/pulse). A strong component of fluorescence x-rays is also likely as high energy electrons impinged on the spectrometer entrance window. Attempts to reduce it with a fixed B-field on the entrance aperture failed. Hence the CCD essentially recorded direct and fluorescent x-ray emission within its sensitivity range (1 – 10 keV but can extend even higher with reduced sensitivity). In a sense the system is a total x-ray (relative) flux detector and we use the output in a far from rigorous but indicative manner to follow trends in the total x-ray signal.

Briefly we observed a largely linear dependence of detected x-ray flux with pulse energy in the 10 – 200 mJ range in the case of the interaction of the 80 fs pulse directly with the Cu slab. Inspection of Figure 3 in Reference [6] shows a similar trend in integrated x-ray emission above 30 keV (although a 3/2 power law dependence is mentioned by the authors).

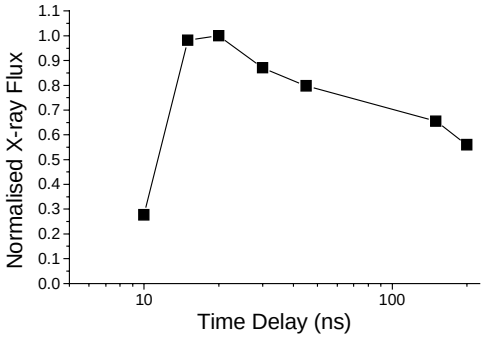

Figure 4. Scaling of (relative) X-ray signal with delay between pre (ns) and main (fs) pulses.

In the case of a pre-plasma the total x-ray signal displayed a strong dependence on time delay between pre-plasma emission and the ultra-intense pulse (Figure 4). The x-ray signal peaks at an inter-plasma delay of 20 ns or so.

The (normalised) x-ray signal for plasmas generated with the 80 fs pulse only is 0.45 and a similar value is obtained for the twin synchronised plasma experiments where both laser peaks are overlapped (0 ns – point not shown). Murnane et al. [7] have already alluded to the fact that a pre-plasma is likely to be a necessary condition for efficient hard x-ray (HXR) generation. The above result would seem to indicate that not only is this so but there is a clear dependence on pre-plasma conditions and hence a comprehensive hard photon and particle spectroscopy experiment is warranted. It also pointed out in [7] that the HXR pulse duration are not yet known.

References

1. G Kulcsar *et al.* Phys.Rev.Lett 84, 5149 (2000)
2. Ch Reich, P Gibbon, I Uschmann & E Forster, Phys.Rev.Lett 84, 4846 (2000)
3. Meighan *et al.*, J.Phys.B:At.Mol.Opt.Phys 33, 1159 (2000)
4. U Teubner, G Kuhnle and F P Schafer, Appl.Phys.B 54, 493 (1992)
5. J A Cobble *et al.*, J.Appl.Phys 69, 3369 (1991)
6. Kmetec *et al.*, Phys.Rev.Lett 68, 1527 (2000)
7. Murnane *et al,* Appl.Phys.B 58, 261 (1994)

Lasers for Science Facility Programme

1) Chemistry

2) Biology

3) Physics

Time-resolved infrared absorption study of 4-dimethylaminobenzonitrile (DMABN) in acetonitrile and methanol

C Ma, W M Kwok, D Phillips

Department of Chemistry, Imperial College, Exhibition Road, London SW7 2AY, UK

M W George, D C Grills

School of Chemistry, University of Nottingham, University Park, Nottingham NG7 2RD, UK

A W Parker, M Towrie, P Matousek

Central Laser Facility, CLRC Rutherford Appleton Laboratory, Chilton, Didcot, Oxon, OX11 0QX, UK

W T Toner

Department of Physics, Clarendon Laboratory, Parks Road, Oxford, OX1 3PU, UK

Main contact email address: *c.ma@ic.ac.uk*

Introduction

The dual fluorescence of 4-dimethylaminobenzonitrile (DMABN), observed only in polar solvents results from a forward charge transfer reaction from a locally excited state (LE) to an intramolecular charge transfer state (ICT) stabilised by solvent polarity, followed by equilibration of the populations in the two states[1]. Recent work has concentrated on issues of intramolecular structure[2-5] and polar solvation properties have been adequate to describe the behaviour in aprotic solvents[6]. However, the results in protic solvents are complex and seemingly contradictory when analysed in that way[6]. Although specific solute-solvent and solute-solute interactions have been discussed[7], there is no generally accepted explanation. Other cases of dual fluorescence present similar problems of reduced quantum yield and increased fluorescence red-shift and bandwidth in protic solvents[8]. Hydrogen bonding has been inferred, but direct evidence has been lacking.

The time-resolved infrared (TRIR) absorption spectra presented here demonstrate the formation of a hydrogen-bonded ICT state (HICT) of photoexcited DMABN in methanol (MeOH), through the development of the C≡N absorption band from a singlet into a doublet, which does not occur in acetonitrile (MeCN) solution. This is the first direct observation of hydrogen-bonding in an excited state. The data show the growth of HICT from ICT and the establishment of a dynamic equilibrium between their populations. This can account for the confusing fluorescence results. A mechanism of this kind has not been proposed before, to our knowledge. We believe it is applicable to other dual fluorescence molecules.

Experimental Arrangements

Measurements were made using the Picosecond Infrared Absorption and Transient Excitation (PIRATE) system[9]. Samples at room temperature were excited at 1 kHz repetition rate by a 267 nm pump beam (0.2 ps, 5 μJ/pulse in 200 μm diameter), produced by frequency-tripling a fraction of the 800 nm regenerative amplifier output. Triple-recrystallised DMABN at 5 mM concentration in spectroscopic grade solvents was circulated to ensure fresh material was exposed on every shot. The femtosecond signal and idler outputs of an optical parametric amplifier (OPA), pumped by the remaining 800 nm beam, were mixed in silver gallium sulphide ($AgGaS_2$) to give a broadband IR beam. Absorption spectra were obtained as described elsewhere[9].

Results

Figure 1 shows spectra of DMABN in acetonitrile (a) and methanol (b), recorded at pump-probe delays from 2 to 3000 ps after excitation. Figure 2 gives the time dependence of band areas. The 2065 to 2235 cm^{-1} spectral region shown covers the C≡N bands of the ground, LE and ICT states at 2219, 2180 and 2095 cm^{-1}, respectively[2,3,5,10]. The LE band is seen in Raman but not TRIR experiments[5,10].

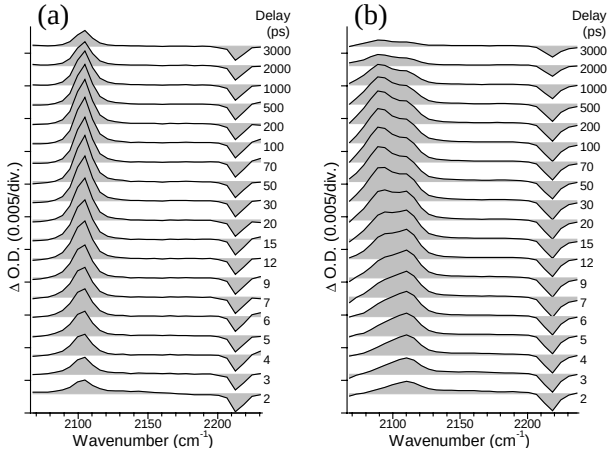

Figure 1. Time-resolved infrared spectra of DMABN obtained at different pump-probe time delays in acetonitrile (a) and methanol (b) with excitation at 267 nm.

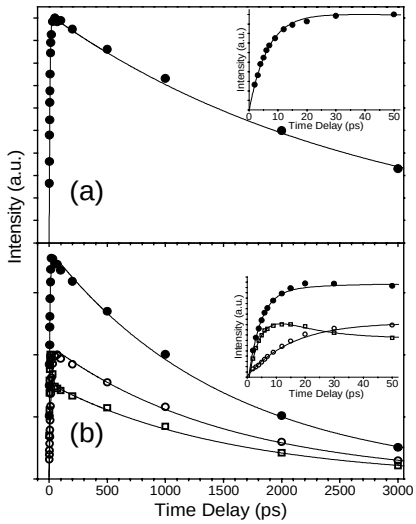

Figure 2. (a) Temporal change of infrared absorption of the ICT state C≡N (filled circles) of DMABN in acetonitrile. (b) Temporal change of infrared absorption of C≡N band of the total (filled circles), the ICT (open squares) and HICT states (open circles) of DMABN in methanol. Solid lines are fitting results (see text). The insert gives detail of the early time dynamics.

In acetonitrile, the ICT state C≡N absorption at 2104 cm^{-1} and ground state depletion bleach at 2213 cm^{-1} are clearly seen in Figure 1. The bleach recovers by no more than 10% in 3 ns. Time-constants for the non-radiative reaction LE↔ICT plus

decay (lines in Figure 2(a)), are 6.4 ps (equilibration) and 2.7 ns (decay). Using 0.030 for the quantum yield, rates for fluorescence, internal conversion to the ground state (IC) and intersystem crossing (ISC) are found to be 1.1 x 10^7, 2.6 x 10^7 and 3.4 x 10^8 s^{-1}. We have observed similar TRIR kinetics in THF and triacetin, but with different time constants. Our results agree with many fluorescence studies indicating prompt formation of LE and fast equilibration of LE/ICT populations, with rates and ratio varying with solvent.

The results are very different in methanol (Figures 1(b) and 2(b)). As the C≡N infrared absorption grows, the band can be resolved into components at 2091 and 2109 cm^{-1}, reaching constant relative intensities by ~50 ps. The total intensity has 5.5 ps and 1.6 ns time-constants for growth and decay and the doublet structure develops with a 13 ps time-constant (lines in Figure 2(b)) but is not resolvable at the earliest times. The component widths are significantly broader than the ground state bleach indicating that some faster processes or inhomogeneous effects are also involved. Qualitatively similar results were obtained in ethanol and butanol. The ground state bleach recovers with a 5 ns time constant. The much more rapid bleach recovery in methanol when compared to acetonitrile indicates a strongly enhanced internal conversion (IC) rate to the ground state. This is consistent with the large deuteration effect on DMABN fluorescence in alcohol solvents[7)].

The doublet structure is clearly due to an interaction that occurs in protic MeOH after charge separation, but not aprotic MeCN. We attribute it to hydrogen-bonding in the ICT state. Since the weak solvent dependence of DMABN ground state vibrational spectra indicates no bonding, we conclude that charge separation is a necessary precursor. The high negative charge density on the cyano electron acceptor region of ICT state DMABN would be expected to facilitate bonding at this site in the presence of a proton donor alcohol, the electron acceptor group in turn becoming a proton acceptor. The 13 ps doublet development timescale agrees with the 10-15 ps for the hydrogen bonding of ground state N-methylacetamide in MeOH[11)], and we note that the 20 cm^{-1} shift of C=O in that case is comparable with the 18 cm^{-1} C≡N shift we observe, and the resolution of the components is similar. Since hydrogen-bonding is highly sensitive to solute-solvent orientation and distance, one would expect the rate for this intermolecular interaction to reflect specific solvent reorganisation timescales, and it is significant that the ~18 ps forward reaction time-constant one can deduce from the results above lies close to the 15.8 ps for solvent-solvent bond breaking and R-OH rotation in methanol[12)].

We therefore interpret the data in terms of two charge-transfer states, ICT and HICT. The dynamics may be complex, as may be reflected in the bandwidths of the doublet components relative to the bleach, but we have used a simple decomposition of the doublet into two superposed components of equal width to make an approximate assessment of the properties of the two ICT states. The kinetics are well described by sequential non-radiative transitions leading to equilibrium populations: LE↔ICT↔HICT, followed by decay (lines in Figure 2(b)), though a small amount of direct LE↔HICT cannot be excluded. Since the total C≡N intensity is in the same ratio to the ground state bleach in both solvents and the downshift of the C≡N component at 2109 cm^{-1} in MeOH from the ground state bleach is the same as that of singlet in MeCN, it is taken to belong to a "free" ICT state similar to that formed in MeCN.

Since the three excited states, LE, ICT and HICT, co-exist, our results imply that the fluorescence in protic solvent is a superposition of three overlapping bands: the fluorescence is triple, not dual. We believe that the presence of a hydrogen-bonding interaction accounts for the abnormal further red-shifting and broadening of the red fluorescence in protic relative to aprotic solvents, and that much of the confusion in the literature arises from treating both protic and aprotic cases in terms of a simple dual fluorescence model.

We conclude that the data demonstrate the existence of two charge transfer states of photoexcited DMABN in methanol, ICT and HICT, where HICT is hydrogen-bonded. ICT is populated from the locally excited state and a dynamic equilibrium between the populations of the two charge transfer states is established on a 13 ps timescale. The internal conversion rate of the HICT state is very much larger than that of ICT and is mainly responsible for the reduced quantum yield in MeOH. A three-state mechanism for dual fluorescence molecules in protic solvents has not been proposed before. It can account for the main anomalies in fluorescence spectra. The results lead to a substantially better understanding of the long-term controversial dual fluorescence phenomenon. It also illustrates the power of the high resolution, high sensitivity TRIR technique employed and the ability to follow the formation of excited state bonding in real time.

References

1. E Lippert, W Rettig, V Bonacic-Koutecky, F Heisel, J A Miehe
   Adv. Chem. Phys., 68 1, (1987)
2. W M Kwok, C Ma, P Matousek, A W Parker, D Phillips, W T Toner, M Towrie, S Umapathy
   J. Phys. Chem. A., 105 984, (2001)
3. M Hashimoto, H Hamaguchi
   J. Phys. Chem., 99 7875, (1995)
4. H Okamoto
   J. Phys. Chem. A, 104 4182, (2000)
5. C Chudoba, A Kummrow, J Dreyer, J Stenger, E T J Nibbering, T Elsaesser, K A Zachariasse
   Chem. Phys. Lett., 309 357, (1999)
6. P Changenet, P Plaza, M M Martin, Y H. Meyer
   J. Phys. Chem. A, 101 8186, (1997), and references therein
7. R J Visser, C A G O Varma, J Konijnenberg, P Bergwerf
   J. Chem. Soc., Faraday Trans. II, 79 347, **(**1983)
8. T Okada, M Uesugi, G Kohler, K Rechthaler, K Rotkiewicz, W Rettig, G Grabner
   Chem. Phys., 241 327, (1999**)**
9. M Towrie, D C Grills, J Dyer, J A Weinstein, P Matousek, R Barton, P D Bailey, N Subramaniam, W M Kwok, C Ma, D Phillips, A W Parker, M W George
   Appl. Spectrosc., submitted
10. C Ma, W M Kwok, P Matousek, A W Parker, D Phillips, W T Toner, M Towrie
    J. Phys. Chem. A, 106 3294, (2002)
11. S Woutersen, Y Mu, G Stock, P Hamm
    Chem. Phys., 266 137, (2001)
12. M L Horng, J A Gardecki, A Papazyan, M Maroncelli
    J. Phys. Chem., 99 17311, (1995)

Time-resolved resonance Raman and transient absorption study of locally excited states of 4-aminobenzonitrile (ABN) and 4-dimethylaminobenzonitrile (DMABN)

C Ma, W M Kwok, D Phillips

Department of Chemistry, Imperial College, Exhibition Road, London SW7 2AY, UK

A W Parker, M Towrie, P Matousek

Central Laser Facility, CLRC Rutherford Appleton Laboratory, Chilton, Didcot, Oxon, OX11 0QX, UK

W T Toner

Department of Physics, Clarendon Laboratory, Parks Road, Oxford, OX1 3PU, UK

Main contact email address: *c.ma@ic.ac.uk*

Introduction

DMABN undergoes an intramolecular charge transfer (ICT) reaction from a locally excited (LE) excited state to an ICT state in polar solvents, and often used as a model compound. The structure of the LE state has been investigated by rotationally resolved electronic spectroscopy in the gas phase[1,2] and picosecond time-resolved resonance Raman (ps-TR^3)[3] and time-resolved infrared (TRIR)[4] spectroscopy in solution. Conflicting results have been presented. Some gas phase studies suggest the LE state has a 22^o or 30^o twist between the planes of the amino group and phenyl ring[1] but a planar LE structure is suggested by others, for example, the super-cooled molecular jet study of Salgado et al[2]. Solution phase studies are in agreement with planar structure but the key ν(ph-N) mode was not identified. Theoretical studies are also in conflict. Ab initio RCIS work by Scholes et al[5] and Lommatzsch et al[6] supports the twisted conformation, but calculations using CASSCF, and some other semi-empirical methods, with and without solvent effects, lend support to a planar geometry[6,7]. Recently, the possibility of a slightly wagged LE conformation has also been suggested[7].

In contrast to DMABN, ABN does not undergo the intramolecular charge transfer (ICT) reaction in either the gas or solution phase and only normal fluorescence can be observed, even in polar solvents. The absence of the ICT fluorescence in ABN has been attributed to an increased energy gap between the two lowest excited states and a low amino group donor strength[8]. It has often been taken as a model for the LE state of DMABN. From gas phase rotationally resolved excitation spectroscopy studies, pyramidal or planar structure has been suggested[6]. Based on a comparison of the experimental TRIR spectrum with CASSCF calculations, Chudoba et al and Dreyer et al proposed a conformation with a pyramidal amino group[7]. However, this view contradicts theoretical work predicting a planar structure for the S_1 state of ABN[6].

To clarify and establish the structural and electronic properties of the LE states of DMABN and ABN, we obtained ps Kerr gate TR^3 (ps-K-TR^3) spectra over the 800 - 2400 cm^{-1} range. Spectra of methyl-deuterated DMABN (DMABN-d_6) were used to help assign modes related to the dimethylamino group. To find suitable TR^3 probe wavelengths for the TR^3 experiments and also to help identify the intermediate species probed, the transient absorption (TA) of ABN and DMABN was measured. In order to relate the experimental observations to excited state structure, equilibrium geometries and vibrational frequencies were calculated by the ab initio RCIS method.

Experimental Arrangements

Time-resolved experiments were carried out using a system based on optical parametric amplifiers. Transient absorbance spectra were measured under "magic angle" conditions using the arrangement described in Reference 3 with a pump wavelength of 267 nm. The ps-K-TR^3 spectra of the LE states of ABN and DMABN were obtained using the methods described in References 3 and 9, with pump and probe wavelengths of 267 and 460 nm, respectively. TR^3 spectra of the LE state of DMABN and DMABN-d_6 were obtained with 267/600 nm pump/probe wavelengths. Each spectrum shown is the sum of 3 individual background-subtracted spectra with accumulation times typically of 2000 seconds. The spectra were not corrected for variations in spectral throughput and detector efficiency.

Acetonitrile Raman bands were used to calibrate the spectra with an estimated accuracy in absolute frequency of +/- 10 cm^{-1}. Sample concentrations were 1-5 x 10^{-3} mol dm^{-3}. UV absorption measurements before and after sample use revealed no degradation.

Results

Transient absorption spectra of ABN and DMABN in hexane and acetonitrile, excited at 267 nm, are shown in Figure 1. The fine structure is due to uncorrected instrumental effects. The ABN spectra (Figure 1a) resemble the spectrum of DMABN in non-polar hexane (Figure 1b) and change little with time. There is no significant solvent dependence for ABN, in contrast to the well-known behaviour of DMABN, where there is no ICT reaction in non-polar solvent but an isobestic point at ~455 nm indicates the picosecond timescale transfer from LE to ICT in acetonitrile[10]. These observations are in good agreement with the scenario that LE states of similar properties are formed in ABN in either polar or non-polar solvent.

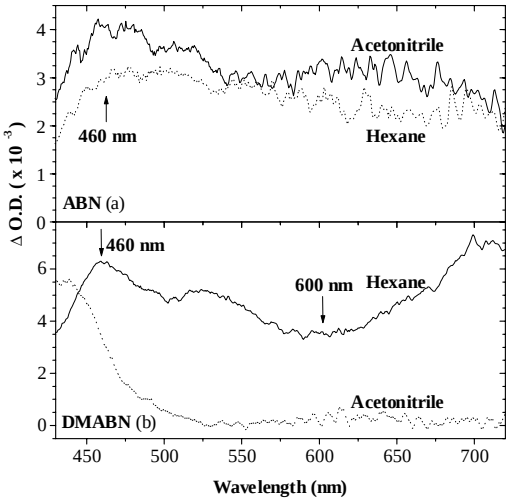

Figure 1. Transient absorption spectra of ABN (a) and DMABN (b) in hexane and acetonitrile with excitation at 267 nm, at 50 ps delay time.

The ps-K-TR^3 experiments were carried out for ABN and DMABN with pump and probe wavelengths 267 and 460 nm, respectively, and ps-TR^3 measurements of DMABN and DMABN-d_6 were made at 600 nm probe wavelength where the Kerr gate was not required. The probe wavelengths used are indicated by arrows in Figure 1. The pump wavelength falls into the lowest absorption band of ABN and DMABN. The spectra obtained are shown in Figure 2.

Assignment	LE state							S_0 state		
	ABN			DMABN		DMABN-d_6		ABN	DMABN	DMABN-d_6
	Experiment	cc-pVZD	6-31G(d)	Experiment	6-31G(d)	Experiment	6-31G(d)	Experiment	Experiment[a]	Experiment[a]
C≡N	2172 (1.0)	2288	2299	2176 (1.0)	2294	2178 (1.0)	2294	2211	2210	2210
19a (ring CC streching)	1481 (1.5)	1437	1446	1467 (1.4)	1477	1454 (3.2)	1466	1518	1523	1515
δ_{Me} (methyl deformation)				1416 (1.1)	1420		1122		1414	1134
ν(ph-N)	1367 (0.4)	1295	1297	1357 (0.6)	1357	1351 (2.4)	1360	1314	1370	1375
3(ring CH bending)	1289 (0.2)*	1272	1288	1325 (0.3)*	1308	1285 (0.2)*	1309	1299	1306	1306
ν(ph-CN), 9a (ring CH bending)	1189 (0.6)	1141	1143	1168 (1.5)	1154	1166 (1.5)	1166	1209	1227	1227
9a (ring CH bending), ν(ph-CN)	1135 (0.6)	1109	1124	1113 (1.0)	1136	1102 (2.0)	1142	1174	1180	1178

Table 1. Observed and calculated Raman band frequencies and their assignment for the LE states of ABN, DMABN and DMABN-d_6. Observed ground state frequencies are included for comparison. [a]Reference 11. *Weak features of uncertain assignment.

The DMABN spectrum at 600 nm probe wavelength (c) is very similar to that previously obtained in cyclohexane using a 615 nm probe[3]. The spectrum of DMABN-d_6 in non-polar solvent (d) has not been reported previously. Bands appearing between ~1000 and 1600 cm^{-1} are not well resolved in the 460 nm DMABN spectrum (b), but the C≡N stretch at 2180 cm^{-1} is clearly seen and we note that it is absent in polar solvents at 400 nm probe wavelength but has been observed at 2095 cm^{-1} using 330 nm probe wavelength at 50 ps delay. Interference effects may occur in resonance Raman scattering when the absorption bands of electronic states overlap, as is likely to be the case here. There may also be mode mixing. In the absence of Raman excitation profiles, band intensities therefore give only a qualitative indication of molecular properties and no definite conclusions can be drawn, but we take the data to indicate that S_n states of similar character are resonant with LE at both 460 and 600 nm (or there is a single very broad state in this region). The spectrum of ABN in methanol at 460 nm probe wavelength (a) closely resembles the 600 nm spectrum of DMABN in hexane (c), indicating that both molecules have LE and S_n states of similar character and ABN does not form the ICT state in polar solvent.

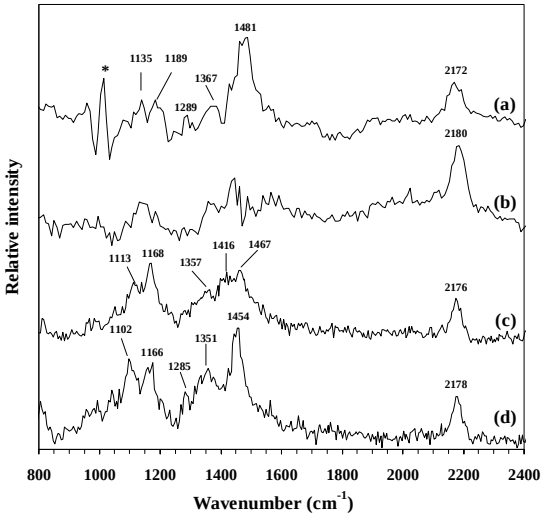

Figure 2. Picosecond Kerr-gated time-resolved resonance Raman spectra of ABN in methanol (a) and DMABN in hexane (b) with 267 nm pump and 460 nm probe wavelength at 50 ps delay time. Picosecond time-resolved resonance Raman spectra of DMABN (c) and DMABN-d_6 (d) in cyclohexane with 267 nm pump and 600 nm probe wavelength at 50 ps delay time. *indicates improper solvent band subtraction.

Band positions and relative intensities obtained using unconstrained Lorentzian fits are summarized in Table 1. Tentative assignments, RCIS calculated frequencies[12] and frequencies of the corresponding bands in the ground states are included in the table for comparison. The assignments are based on DMABN/DMABN-d_6 isotopic shifts and the RCIS frequency calculations.

It is important to note that all the spectra in Figure 2 show the C≡N stretch at ~2180 cm^{-1}, corresponding to the same ~30 cm^{-1} downshift for ABN and DMABN relative to the ground state. This indicates a decrease of the C≡N bonding order and can be interpreted as being due to a similar degree of partial localisation of transferred charge on the cyano anti-bonding orbital in the LE states of both molecules.

Most of the recorded bands in the LE states of both ABN and DMABN were observed at frequencies shifted from ground state values. Besides the C≡N stretch, for example, the ABN mode dominated by Wilson 19a has ~37 cm^{-1} downshift while the band dominated by ν(ph-N) up shifts by ~53 cm^{-1} from the ground to LE state. We note that these frequency shifts observed using TR^3 in this and our previous work are not seen in the TRIR experiments[4].

We conclude that the experimental fluorescence, transient absorption and TR^3 spectra of the LE states of ABN and DMABN are very similar, indicating similar electronic and vibrational properties. Based on general agreement between the experimental and calculated frequencies, a planar structure has been suggested for the LE state of both the molecules.

References

1. O Kajimoto, H Yokoyama, Y Ooshima, Y Endo Chem. Phys. Lett., 179 455, (1991)
2. F P Salgado, J Herbich, A G M Kunst, R P Rettschnick J. Phys. Chem. A, 103 3184, (1999)
3. W M Kwok, C Ma, D Phillips, P Matousek, A W Parker, M Towrie, J. Phys. Chem. A, 104 4188, (2000)
4. C Chudoba, A Kummrow, J Dreyer, J Stenger, E T J Nibbering, T Elsaesser, K A Zachariasse Chem. Phys. Lett., 309 357, (1999)
5. G D Scholes, D Phillips, I R Gould Chem. Phys. Lett., 266 521, (1997)
6. U Lommatzsch, B Brutschy, Chem. Phys., 234 35, (1998)
7. J Dreyer, A Kummrow, J. Am. Chem. Soc., 122 2577, (2000)
8. K A Zachariasse, Chem. Phys. Lett., 320 8, (2000)
9. W M Kwok, C Ma, P Matousek, A W Parker, D Phillips, W T Toner, M Towrie, S Umapathy, J. Phys. Chem. A, 105 984, (2001)
10. C Ma, W M Kwok, D Phillips, P Matousek, A W Parker, M Towrie, W T Toner , CLF RAL. Ann. Rep., 107, (1999-2000)
11. W M Kwok, I Gould, C Ma, M Puranik, S Umapathy, P Matousek, A W Parker, D Phillips, W T Toner, M Towrie Phys. Chem.Chem. Phys., 3 2424, (2001)
12. C Ma, W M Kwok, P Matousek, A W Parker, D Phillips, W T Toner, M Towrie, J. Phys. Chem., 106 3294, (2002)

Picosecond Time-resolved Infrared Spectroscopy in Supercritical Fluids

X-Z Sun, D C Grills, O S Jina, K Stanley, M W George

School of Chemistry, University of Nottingham, University Park, Nottingham, NG7 2RD, UK

P Matousek, M Towrie, A W Parker

Central Laser Facility, CLRC Rutherford Appleton Laboratory, Chilton, Didcot, Oxon, OX11 0QX, UK

Main contact email address: *Mike.George@nottingham.ac.uk*

Introduction

Research into supercritical fluids (SCFs) has grown dramatically in recent years. This is in part due to the promise they hold as environmentally friendly alternatives to the toxic organic solvents commonly used in industry. Any substance whose pressure and temperature exceed their critical values (p_c and T_c respectively) is called a supercritical fluid[1]. These fluids are a curious hybrid of gases and liquids and their physical properties are generally intermediate between the two. Furthermore, near the critical point their physical properties (e.g. density, viscosity, dielectric constant etc.) become highly tuneable with small changes in pressure and temperature. This means that the solvating power of an SCF can be controlled, allowing the desired reaction rate and selectivity of a chemical process to be achieved, with the added advantage that removal of the solvent is simply a matter of releasing the pressure and returning to the gaseous state.

It is of vital importance that we fully understand chemical reactivity and reaction mechanisms in SCFs, together with fundamental processes such as vibrational relaxation and solvation, since these are often very different than in conventional solvents. Pump-probe time-resolved spectroscopy is an excellent technique for such studies since it allows the kinetics of fast processes to be measured directly on timescales down to femtoseconds.

Time-resolved spectroscopy in SCFs has largely been limited to UV/visible transient absorption and fluorescence. However, vibrational spectroscopy such as time-resolved infrared (TRIR) spectroscopy offers advantages over these techniques since it allows the direct structural characterisation of transient species[2]. UV pumped TRIR on the nanosecond and longer timescale has previously been applied to supercritical fluid samples[2]. Also, on the picosecond timescale IR pumped TRIR spectroscopy has been perfomed in SCFs[3]. However, UV pumped TRIR in SCFs on the ps/fs timescale has not been reported, largely due to limitations in the physical and optical properties of cell window materials.

Spectroscopic studies in SCFs require an optical cell that is capable of withstanding the high pressures involved. Furthermore, the windows must be optically transparent to all the beams used in the experiment. For TRIR this means that the windows must be transparent throughout the UV/visible and infrared regions. High pressure cells have previously been used for nanosecond TRIR in SCFs and these employed thick (ca. 10 mm) CaF_2 windows[2], which were capable of withstanding pressures in excess of 5000 psi and which were completely transparent from the UV to IR. Unfortunately, the fs/ps UV pulses used in ultrafast TRIR spectroscopy would generate undesirable non-linear effects such as filamentation and white-light continuum generation in the thick CaF_2 windows and therefore these cells are unsuitable for sub-nanosecond TRIR. In order to prevent non-linear effects the windows must be below a critical thickness, determined from the parameters of the optical pulses and window material. For flash photolysis experiments in the UV/visible region this is not such a problem since optical materials exist (e.g. sapphire or diamond) that are suitably transparent and strong enough to withstand high-pressures at low thickness. For TRIR the choice of optical material is more limited.

In this paper we describe the design and construction of a new optical cell for ps/fs TRIR spectroscopy in SCFs and high-pressure liquids. Using the recently developed PIRATE facility we have performed preliminary ps-TRIR experiments, examining the vibrational relaxation dynamics of short lived reactive intermediates generated by the photolysis of $Cr(CO)_6$ in supercritical fluid solution.

Experimental

The PIRATE facility for broadband ps-TRIR spectroscopy has previously been described in detail[4]. Briefly, the system employs broadband (ca. 150 cm^{-1}) 150 fs IR pulses to probe the sample. These are dispersed over 64-element linear IR array detectors and processed in real time at the 1 kHz repetition rate of the laser system.

The design of the new high-pressure cell is shown in Figure 1. The cell was required to safely withstand pressures and temperatures up to 5000 psi and ca. 50 °C respectively and have a small internal volume. For these reasons it was constructed from thick walled 316 stainless steel. Furthermore, it had to incorporate two optical windows that are transparent throughout the UV/visible and mid-IR and which can withstand the maximum working pressure whilst being thin enough to prevent non-linear optical effects with the fs UV pulses.

The most suitable window material in terms of optical transparency and mechanical strength was MgF_2. Although its transmitting range (ca. 83300 – 1300 cm^{-1}) is slightly narrower than that of the related CaF_2, it is stronger, with an apparent elastic limit of 7200 psi compared with 5300 psi for CaF_2. In order to estimate an upper limit for the thickness of the MgF_2 windows, below which non-linear optical effects would be avoided, we made use of the B integral concept. The B integral is useful for predicting the onset of self-phase modulation and self-focusing of ultrashort laser pulses in optical windows. A value of ≤ 1 is considered low enough to prevent these effects. The equation is given below,

$$B = \frac{2\pi n_2}{\lambda} \int_0^L I(z).dz$$

where n_2 is the non-linear refractive index of the window material, λ the laser wavelength, I(z) the intensity of the laser pulse and L the interaction length. Using typical parameters of the PIRATE laser system it was found that a maximum MgF_2 thickness of 2 mm would give a B integral of 1.

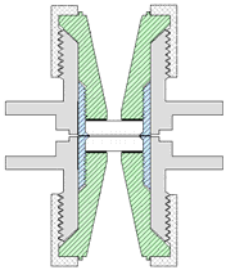

Figure 1. Cross-section of the new high-pressure ps-TRIR cell.

In order to calculate the dimensions of the windows and window apertures, required to safely withstand a working pressure of 5000 psi, standard window pressure formulae were used. These suggested that with 2 mm thick circular MgF_2 windows with a diameter of 6 mm, a safe window aperture would be 2 mm. The high-pressure cell is connected, by means of 1/16" o.d. stainless steel tubing, into a high-pressure recirculating flow system containing the solution under study and a conventional high-pressure cell[2] for online FTIR monitoring.

Results and Discussion

We have demonstrated the potential of the supercritical ps-TRIR apparatus by performing a series of experiments in supercritical and high-pressure liquid solutions, monitoring changes in the ν(CO) absorptions of a transition metal carbonyl complex following UV excitation. The ν(CO) bands of metal carbonyls are intense and narrow and provide an excellent probe of the electronic and structural environment around the metal centre.

Vibrational Relaxation Dynamics of Transition Metal Carbonyls

The redistribution and dissipation of excess energy in vibrationally excited molecules has long been the subject of intense study and is a key factor governing chemical reactivity. Transition metal carbonyl complexes offer an interesting opportunity to study vibrational relaxation since the frequencies of the ν(CO) vibrations are virtually isolated from other molecular vibrations and solvent modes. This lack of coupling often leads to relaxation lifetimes that are 1 or 2 orders of magnitude longer than those of typical molecular vibrations.

Heilweil and co-workers have previously used broadband ps-TRIR to measure the vibrational relaxation of $M(CO)_5$(hexane) transients (M = Cr, Mo or W) in hexane solution[5]. These alkane complexes were generated by the photoejection of a CO molecule from a $M(CO)_6$ precursor and the subsequent rapid solvation of $M(CO)_5$ by a solvent molecule. Relaxation lifetimes of the ν(CO) modes (from the v=1 to v=0 levels) were found to be ca. 160 ps. Fayer has previously measured the relaxation dynamics of $W(CO)_6$ in a series of supercritical fluids using IR pump-IR probe TRIR on the ps timescale[3] and has found that in noble gases the relaxation lifetime is significantly extended to ca. 1 ns. The tunability of SCFs permits a study of the effect of reaction environment on vibrational energy relaxation. Our aim was to use ps-TRIR to investigate the relaxation dynamics of the 'hot' solvated intermediates, $Cr(CO)_5$(L) generated by UV excitation of $Cr(CO)_6$ in a range of SCFs and SCFs doped with hexane.

Figure 2 shows a series of ps-TRIR spectra obtained after the 267 nm excitation of $Cr(CO)_6$ in supercritical Xe (scXe) (1250 psi, 25 °C) doped with CO (60 psi). CO was added to the solution to make it photoreversible, thus preventing rapid decomposition of $Cr(CO)_6$ during the experiment. An instantaneous bleaching of the parent T_{1u} ν(CO) band is observed together with the generation of an extremely broad absorption centred around 1945 cm^{-1}. This new band is assigned to the overlapping absorptions of the photogenerated $Cr(CO)_5(Xe)$ complex in a series of high-lying vibrational levels. This narrows and slightly blue shifts over the next ca. 20 ps into four overlapping bands, assigned to the low frequency a_1 and e ν(CO) modes of $Cr(CO)_5(Xe)$ in the v=1 (1950 and 1916 cm^{-1}) and v=0 (1964 and 1937 cm^{-1}) vibrational energy levels. Rapid narrowing and blue shifting of ν(CO) absorption features in $M(CO)_5$(hexane) (M = Cr, Mo, W) complexes have previously been observed and were attributed to the vibrational relaxation of low frequency modes coupled to the CO stretches[5]. For the remainder of the experiment, up to 1 ns, the v=1 bands decay as the v=0 bands increase in intensity, forming two well-resolved a_1 and e absorptions. It should be noted that the high frequency a_1 mode of $Cr(CO)_5(Xe)$, which is expected to appear at ca. 2090 cm^{-1}, is extremely weak in the IR and was not monitored in these experiments.

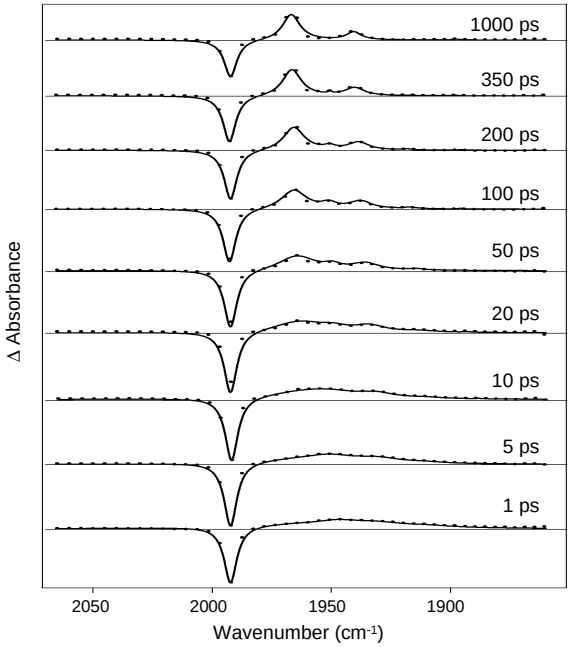

Figure 2. ps-TRIR spectra shown at selected time delays between 1 and 1000 ps following 267 nm excitation of $Cr(CO)_6$ in scXe (1250 psi, 25 °C) in the presence of CO (60 psi).

In order to measure the rate of v=1→0 vibrational relaxation of $Cr(CO)_5(Xe)$, kinetic traces were constructed by plotting the absorbances of the v=1 and v=0 a_1 bands of $Cr(CO)_5(Xe)$ versus time delay. These produced a decay and a growth respectively, which both fitted to a single exponential function to give a vibrational relaxation lifetime under these conditions of 110 ± 20 ps. These experiments were repeated in scAr, liquid CO_2 and scAr doped with hexane. The results of these studies suggest that under the conditions of our experiments, the dominating relaxation pathway is that of vibration-vibration resonance energy transfer between $Cr(CO)_5$(L) and free CO or liquid CO_2. This is because the high frequency a_1 mode of $Cr(CO)_5$(L), at ca. 2090 cm^{-1}, is completely overlapped with the extremely intense IR bands of CO and CO_2. Future experiments in the absence of added CO will be used to probe this mechanism.

Conclusions

We have demonstrated UV pumped TRIR spectroscopy in SCFs on the picosecond time scale and have shown the potential of these experiments to monitor vibrational relaxation processes.

References

1. T Clifford
Fundamentals of Supercritical Fluids
Oxford University Press, Oxford (1999)

2. M W George, M Poliakoff and J J Turner
Analyst, 119 551, (1994)

3. D J Myers, M Shigeiwa, M D Fayer and B J Cherayil
J. Phys. Chem., 104 2402, (2000)

4. M Towrie, P D Bailey, R Barton, P Matousek,
A W Parker, M W George and D C Grills
CLF Annual Report 2000/2001, RAL-TR-2001-030, 165, (2001)

5. T P Dougherty and E J Heilweil
Chem. Phys. Lett., 227 19, (1994)

Photo-induced metal-metal bond splitting of Os carbonyl clusters

F W Vergeer, F Hartl, D J Stufkens

Institute of Molecular Chemistry, Universiteit van Amsterdam, Nieuwe Achtergracht 166, 1018 WV Amsterdam, The Netherlands

P Matousek, M Towrie

Central Laser Facility, CLRC Rutherford Appleton Laboratory, Chilton, Didcot, Oxon, OX110QX, UK

Main contact email address: *stufkens@science.uva.nl*

Introduction

Transition metal carbonyl clusters are of interest because of their potential application as a catalyst or catalyst precursor. The photoactivation of such clusters may lead to novel reaction types, since it either avoids undesired fragmentation or activates clusters that are thermally stable. From these clusters the photoreactivity of $[M_3(CO)_{12}]$ (M= Ru, Os) has been studied in most detail. Photoactivation of $[Ru_3(CO)_{12}]$ results in the formation of a short-lived primary photoproduct that was quite recently identified at RAL with picosecond time-resolved IR (ps-TRIR) as a CO-bridged isomer of this cluster[1]. In contrast to this, nanosecond time-resolved IR (ns-TRIR) spectra of the substituted cluster $[Os_3(CO)_{10}$(1,3-cyclohexadiene)] showed that in this case the photoproduct contains two CO bridges instead of one[2]. In order to determine whether these two bridges are formed in a stepwise fashion or in a single concerted process, the mechanism of their formation was studied at RAL with ps-TRIR spectroscopy. A second type of substituted clusters viz. $[Os_3(CO)_{10}(\alpha$-diimine)] undergoes instead splitting of an Os-Os bond without CO bridge formation. In apolar media biradicals are formed, in coordinating solvents, these clusters produce zwitterions[3]. Although it was established that at least part of the zwitterions are formed out of the biradicals in the microsecond time domain, a second, much faster, process of zwitterion formation directly from the excited state by heterolytic splitting of an Os-Os bond could not be excluded. Supporting evidence for the occurrence of this latter reaction was presented by the picosecond transient absorption (ps-TA) spectra, which showed biexponential decay of the excited state, indicating the formation of both biradicals and zwitterions[4]. The zwitterions were proposed to be formed from a solvated excited state (exciplex). In order to confirm the occurrence of this heterolytic splitting, which has never been observed before, we have studied at RAL the ps-TRIR spectra of a representative cluster $[Os_3(CO)_{10}(^i$Pr-AcPy)] (^{i}Pr-AcPy = 2-acetylpyridine-*N*-isopropylimine) (Figure 1).

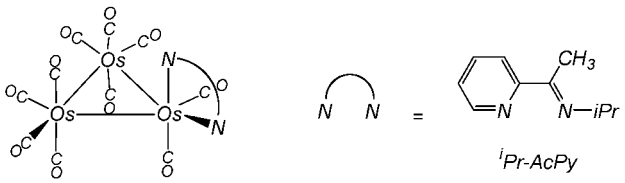

Figure 1. Schematic structure of the cluster $[Os_3(CO)_{10}(^i$Pr-AcPy) and the α-diimine ligand used in this study.

Results and Discussion

CO-bridge formation in $[Os_3(CO)_{10}$(1,3-cyclohexadiene)]

The ps-TRIR spectra of $[Os_3(CO)_{10}$(1,3-cyclohexadiene)] were recorded in heptane at several pump-probe delays between 0 and 500 ps after 400 nm excitation. Representative difference IR spectra in the CO-bridge region 1900-1750 cm^{-1} are shown in Figure 2. At early time delays (< 5 ps) a single, broad $\nu(\mu$-CO) band appears around 1815 cm^{-1} that reaches its maximum intensity after ca. 3 ps. Two new bands then show up, one at 1801 cm^{-1}, first observed as a shoulder of the 1815 cm^{-1} band, the other at 1857 cm^{-1}. Both bands increase in intensity at the expense of the 1815 cm^{-1} band. At t_d = 20 ps the initial $\nu(\mu$-CO) band has completely disappeared and the two new bands have reached their maximum intensity. They do not change any more up to 500 ps and their position and intensity closely resemble those of the bands observed on the ns time scale[2]. According to these IR spectral changes, the primary photoproduct has one CO bridge just as the primary photoproduct of $[Ru_3(CO)_{12}]$[1]. It is, however, much shorter lived than the latter species having a lifetime of 56.6ps [1] as it is completely converted into the product with two CO bridges after 20 ps. Most latter species regenerate the parent cluster, but a small part decomposes into fragments.

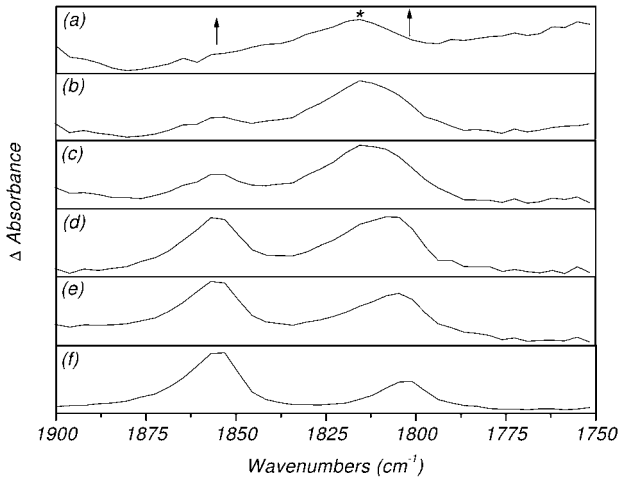

Figure 2. TRIR difference spectra of $[Os_3(CO)_{10}$(1,3-cyclohexadiene)] in heptane between 1900-1750 cm^{-1} at: (a) 1.5 ps, (b) 2.5 ps, (c) 3 ps, (d) 5 ps, (e) 7 ps and (f) 20 ps after 400 nm (150 fs FWHM, 5 μJ per pulse) excitation.

These processes are schematically depicted in Scheme 1. Excitation gives rise to metal-metal bond splitting, followed by a shift of a terminal CO ligand at Os2 to a bridging position between Os2 and Os3. The electron deficiency at Os2 is then compensated by a shift of a terminal CO ligand at Os1 to a bridging position between Os1 and Os2.

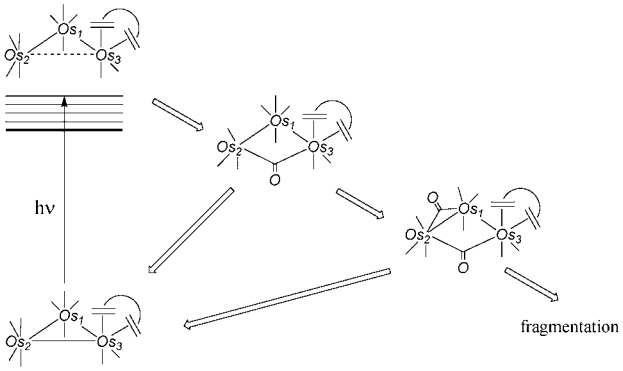

Scheme 1. Schematic representation of the primary events taking place after the photoexcitation of $[Os_3(CO)_{10}$(1,3-cyclohexadiene)].

Zwitterion formation from the excited state of $[Os_3(CO)_{10}(^{i}Pr\text{-}AcPy)]$

The ps-TA spectra of this complex in MeCN show biexponential decay of the excited state, which was tentatively ascribed to biradical formation from the excited state and zwitterion formation from the solvated excited state (exciplex)[4]. The ps-TRIR spectra of the cluster in MeCN were recorded at several pump-probe delays between 0 and 500 ps after excitation at 500 nm. The first spectra are very similar to those obtained in 2-ClBu and display instantaneous bleaching of the parent ν(CO) bands together with transient absorptions belonging to the cluster in its excited state (Figure 3). At longer time delays (up to 100 ps) the excited state ν(CO) bands decay and weak bands arise, which, in agreement with the spectrum of the cluster in 2-ClBu, are assigned to the biradical. The wavenumbers in MeCN are somewhat smaller than in 2-ClBu due to the coordination of solvent molecules to the open site at the $\{Os(CO)_2(^{i}Pr\text{-}AcPy)\}$ moiety of the cluster. However, unlike in 2-ClBu, the biradicals are not the only product. This is evident from a comparison of the difference IR absorption spectra (a) and (b) in Figure 3, recorded in 2-ClBu and MeCN, respectively. Spectrum (b) recorded 100 ps after the laser pulse shows two extra bands at 1971 and 1873 cm^{-1} (indicated with an arrow) not present in the 2-ClBu spectrum. These two bands also show up in the rapid scan FTIR spectra of this cluster in MeCN on the time scale of seconds (Figure 3c) when the biradicals have disappeared and only the long-lived zwitterions are present in solution.

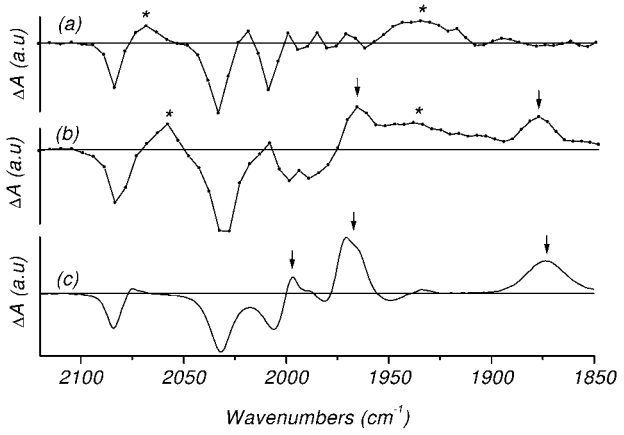

Figure 3. Difference IR spectra of $[Os_3(CO)_{10}(^{i}Pr\text{-}AcPy)]$ (a) in 2-ClBu at t_d = 500 ps after 500 nm excitation; (b) in MeCN at t_d = 100 ps after 500 nm excitation; (c) in MeCN at t_d = 2.5 s after 532 nm excitation.

Thus, the ps-TRIR spectra prove that zwitterions are formed directly after excitation, most probably from a solvated excited state by heterolytic splitting of an Os-Os bond. To our knowledge this is the first evidence that a metal-metal bond is split heterolytically in the excited state, albeit under the influence of a coordinating solvent. Previous ns-TA and TRIR spectra had already shown that in MeCN or in the presence of alkenes, zwitterions are also formed out of the biradicals in the microsecond time domain[3,4]. These two ways of zwitterion formation are schematically depicted in Scheme 2.

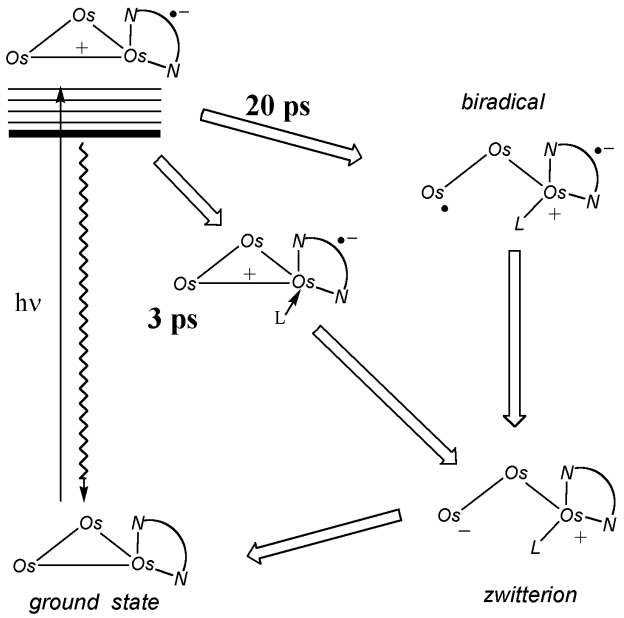

Scheme 2. Schematic representation of the primary photoprocesses of $[Os_3(CO)_{10}(^{i}Pr\text{-}AcPy)]$ in MeCN (= L), together with their lifetimes.

Acknowledgements

We acknowledge the financial support from the Council for Chemical Sciences of the Netherlands Organization for Scientific Research (NWO-CW, project no. 348-032; FWV and FH) and from the European Union (LSF ref. no. USEV13C2/01)

References

1. F W Vergeer, F Hartl, P Matousek, D J Stufkens and M Towrie
Chem. Commun., 1220, (2002)

2. M J Bakker, F W Vergeer, F Hartl, O S Jina, X-Z Sun and M W George
Inorg. Chim. Acta, 300-302 597, (2000)

3. F W Vergeer, M J Bakker, C J Kleverlaan, F Hartl and D J Stufkens
Coord. Chem. Rev., in press.

4. F W Vergeer, C J Kleverlaan and D J Stufkens
Inorg. Chim. Acta, 327 126, (2002)

Early Excited-State Dynamics of Re Complexes with a Photoisomerising Styrylpyridine Ligand

M Busby, A Vlček, Jr.

Department of Chemistry, Queen Mary, University of London, Mile End Road, London E1 4NS, UK

Main contact email address: *A Vleck@qmul.ac.uk*

Introduction

Photochemical *trans-cis* isomerisation of a C=C or N=N bond is a much studied problem that is relevant to chemical manipulation of optical information (vision) and to molecular devices. For example, supramolecules containing these isomerisable bonds can change their shape and physical properties on irradiation, acting as switches. Generally, it is understood that *trans-cis* isomerisation is ultrafast (≤200 fs) and involves ππ* excited states. Several time-resolved absorption (TA) and resonance Raman (TR^3) studies have been performed on simple model molecules such as stilbene or even large functional molecules like rhodopsine. The isomerisation mechanism and underlying excited-state dynamics are expected to change profoundly when an isomerising molecule is coordinated to a metal atom, whose presence will both introduce new excited states and modify the behaviour of ππ* excited states of the organic ligand. The most important new excited states are the metal-to-ligand charge transfer (MLCT) states which involve transfer of electron density either to the isomerising ligand or to another ancillary ligand present in the coordination sphere.

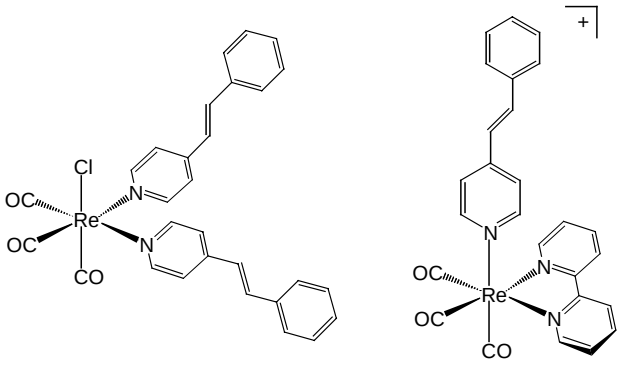

Figure 1. Schematic structures of $[Re(Cl)(stpy)_2(CO)_3]$ (left) and $[Re(stpy)(CO)_3(bpy)]^+$ (right).

In this report, we describe our recent investigations of the nature and dynamics of excited states of two molecules: $[Re(Cl)(stpy)_2(CO)_3]$ and $[Re(stpy)(CO)_3(bpy)]^+$, where stpy is the isomerisable styrylpyridine ligand, Figure 1. Besides the stpy-localized intraligand (IL) ππ* excited states, both complexes can have Re→stpy MLCT excited states. In addition, a low-lying Re→bpy MLCT excited state is expected for the latter complex.

Time-resolved visible absorption spectrum of $[Re(Cl)(stpy)_2(CO)_3]$ (Figure 2a) shows a strong absorption at wavelengths shorter than 530 nm with a long tail extending into the red spectral region. The signal is fully developed within the instrument time-resolution, ≤400 fs. The absorption at short wavelengths decays with a biexponential kinetics: ca. 1 and 11 ps, leaving a residual long-lived weak absorption over the whole spectral region investigated. Kerr-gate time-resolved emission spectrum (Figure 3a) exhibits a broad signal at 450 nm, that decays with a lifetime of ca. 1.6 ps, which is (within the experimental accuracy) identical to the short component of the TA decay. This observation shows that the initial transient observed in TA is an excited state and not a photochemical intermediate. The TR^3 spectrum (Figure 4a) shows peaks at ca. 1020 (w), 1225(m), 1325 (w) and 1511 (s) cm^{-1} that are developed within the instrument time resolution and decay with an 11 ps lifetime. The spectral pattern indicates that the 11 ps transient is a stpy-localized ππ* IL excited state. The time-resolved IR spectrum (Figure 5a) of $[Re(Cl)(stpy)_2(CO)_3]$ measured at 1 ps after excitation shows two broad bands at ca 1960 and 2062 cm^{-1} that disappear within the next picosecond, concomitantly with the emission decay and the fast component of the TA decay. These two bands are shifted upwards from the ground-state IR bands, indicating that they belong to a Re→stpy MLCT excited state. The 1 ps spectrum also contains a broad band with an apparent maximum at 2016 cm^{-1} that is shifted slightly downwards from the ground state band at 2024 cm^{-1}. Therefore, it is assigned to a ππ* IL excited state, called IL(a). Over the next picosecond, this band rises in intensity and sharpens to form a maximum at 2014 cm^{-1}. TRIR spectra reveal that this IL(a) state converts into another ππ* state, IL(b), with a 12 ps time-constant, concomitantly with the TA and TR^3 decay. This is manifested by the decay of the 2014 cm^{-1} maximum and formation of another maximum at 2018 cm^{-1}, accompanied by band narrowing. The bleached ground-state bands at 1886 and 1920 cm^{-1} also decay with a 12 ps lifetime while weak bands at approximately 1902 and 1926 cm^{-1} grow in. (Analysis of the 1850 - 1950 cm^{-1} spectral region is complicated due to a strong overlap of the bands belonging to the ground-state and photoproduced transient).

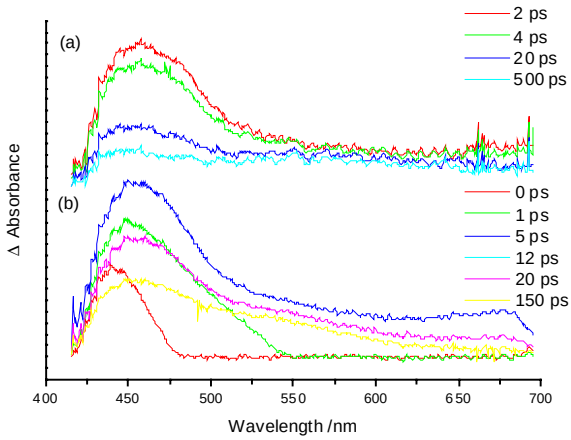

Figure 2. Time-resolved visible absorption spectrum, measured after excitation at 400nm (a): $[Re(Cl)(stpy)_2(CO)_3]$ in dichloromethane (b): $[Re(stpy)(CO)_3(bpy)]^+$ in acetonitrile.

The TA spectrum of $[Re(stpy)(CO)_3(bpy)]^+$ (Figure 2b) evolves with distinctly different dynamics than that of $[Re(Cl)(stpy)_2(CO)_3]$. The TA grows with a rise-time of 2 ps rise, followed by a 15 ps decay to leave a weak, long-lived residual absorption. The TA rise is concomitant with a decay (3.7 ps) of emission at 440 nm, (Figure 3b) showing that the TA rise is due to conversion of a weakly absorbing excited state either to another excited state or a photochemical intermediate. Accordingly with this dynamics, TR^3 shows an approximately 2 ps followed by a ca. 20 ps decay. The TR^3 spectrum of $[Re(stpy)(CO)_3(bpy)]^+$ (Figure 4b) (1020 (w), 1225 (w), 1350 (w) and 1539 (s) cm^{-1}) is very similar to that of $[Re(Cl)(stpy)_2(CO)_3]$, showing that the secondarily populated excited state of $[Re(stpy)(CO)_3(bpy)]^+$ has a ππ*(stpy) IL

character. No Raman bands due to bpy or $bpy^{\bullet-}$ chromophore were observed. TRIR spectra (Figure 5b) reveal the presence of two MLCT states that decay with 1 and 6 ps lifetime to form a ππ* IL(a) state (2030 cm^{-1}) which undergoes further conversion (τ = 15 ps) to the IL(b) state (2036 cm^{-1}). The transients with the 1 and 6 ps lifetimes are tentatively attributed to Re→stpy and Re→bpy MLCT states, respectively, because of the upward shift of the IR bands from their ground-state wavenumbers. The IR spectra of both IL states are very similar to those observed for $[Re(Cl)(stpy)_2(CO)_3]$ and they feature a small downward shift of the highest A_1^2 ν(CO) IR band from its ground-state wavenumber.

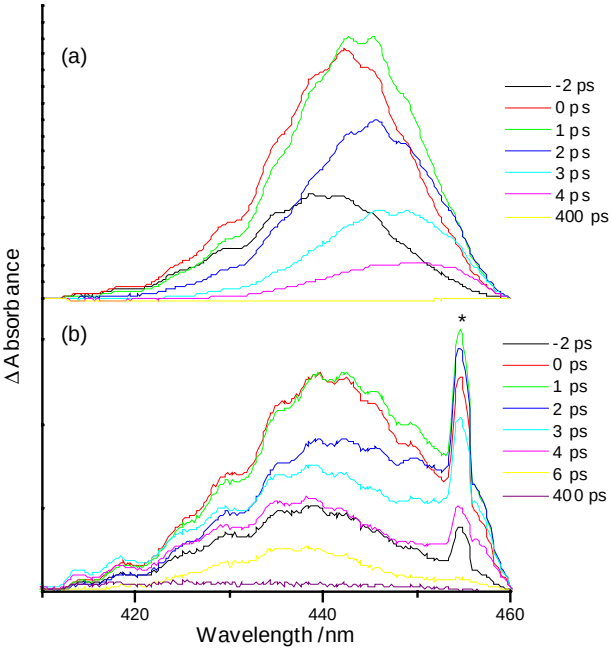

Figure 3. Kerr-gate time-resolved emission spectrum, measured after excitation at 400nm (a): $[Re(Cl)(stpy)_2(CO)_3]$ in dichloromethane (b): $[Re(stpy)(CO)_3(bpy)]^+$ in acetonitrile. (* indicates a solvent band).

Discussion

The excited-state dynamics of $[Re(Cl)(stpy)_2(CO)_3]$ and $[Re(stpy)(CO)_3(bpy)]^+$ complexes containing isomerising styrylpyridine ligand are summarised in Scheme 1. It follows that optical excitation at 400 nm always populates MLCT states which eventually evolve into ππ* IL states. The main difference between the two complexes originates in the occurrence of the Re→bpy MLCT state for $[Re(stpy)(CO)_3(bpy)]^+$. This state is an intermediate of the population of IL states. Formation of the Re→bpy MLCT state is manifested by the rise of the TA and TR^3 signals. For both complexes, we have observed a conversion of the initially populated IL(a) state into the IL(b) state that occurs with 11 and 15 ps lifetimes for $[Re(Cl)(stpy)_2(CO)_3]$ and $[Re(stpy)(CO)_3(bpy)]^+$, respectively. The very nature of this process and the difference between the two states is not yet completely clear. It is possible that they differ in the orientation of the stpy ligand plane with respect to the Re-CO and, in the latter complex, also Re-N bonds. The IL dynamics would then correspond to a conformational change.

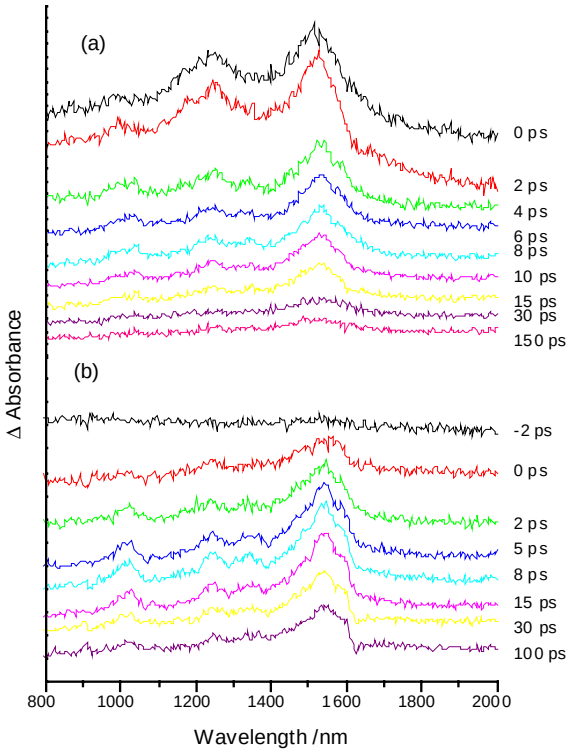

Figure 4. Kerr-gate time-resolved resonance Raman spectrum, measured after excitation at 400nm and probing at 475 nm.
(a): $[Re(Cl)(stpy)_2(CO)_3]$ in dichloromethane
(b): $[Re(stpy)(CO)_3(bpy)]^+$ in acetonitrile.

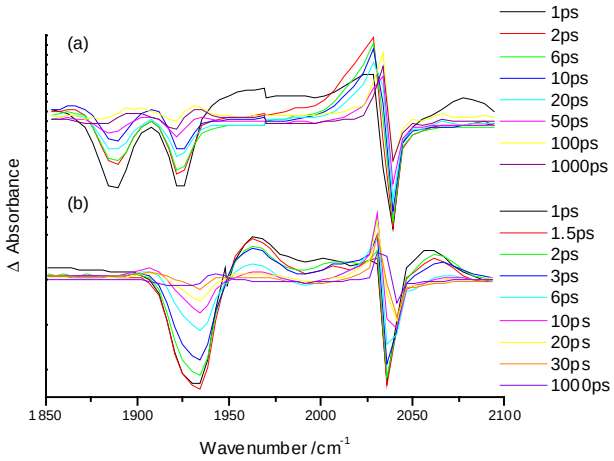

Figure 5. Time-resolved infra red spectrum, measured after excitation at 400nm (a): $[Re(Cl)(stpy)_2(CO)_3]$ in dichloromethane (b): $[Re(stpy)(CO)_3(bpy)]^+$ in acetonitrile.

This study has also demonstrated the great power of combining several time-resolved experiments to reveal complex photochemical dynamics. Herein, we have employed visible and IR absorption, Kerr-gate TR^3 and Kerr-gate emission spectroscopies, that are uniquely available at the Ultrafast Spectroscopy Laboratory at RAL.

Acknowledgments

Pavel Matousek and Mike Towrie (RAL) are thanked gratefully for their highly qualified help with all the ultrafast experiments. Financial support from EPSRC is appreciated.

Kerr gated resonance Raman study of tetracyclines and their complexes with divalent metal ions

S Schneider, G Brehm, M Schmitt, C Leypold, M Reiher

Institut für Physikalische und Theoretische Chemie, Friedrich-Alexander-Universität Erlangen-Nürnberg, D-91058 Erlangen, Germany

P Matousek, M Towrie

Central Laser Facility, CLRC Rutherford Appleton Laboratory, Chilton, Didcot, Oxon, OX11 0QX, UK

Main contact email address: *schneider@chemie.uni-erlangen.de*

Introduction

During the last fifty years, Tetracycline and several of its derivatives (see Scheme 1) have been successfully employed as antibiotics. Due to their extensive and sometimes improper application, most bacteria have developed various resistance mechanisms. One of these relies on the synthesis of a so-called antiporter protein, TetA, which is located in the cell membrane and eliminates the tetracyclines from the cell via an active transport. The protein synthesis is regulated on the transcription level by the repressor protein TetR. In the absence of antibiotics, TetR is bound to the operator DNA (TetO), thereby preventing transcription of the genes which encode TetR and TetA. In the presence of minute amounts of antibiotics, these are, before they can harm the cell by binding to the ribosomes, incorporated in the two binding pockets of dimer TetR, thereby inducing allosteric changes which result in a dissociation of TetR from the DNA. (For a review on all aspects related to tetracyclines, Reference 1 is recommended).

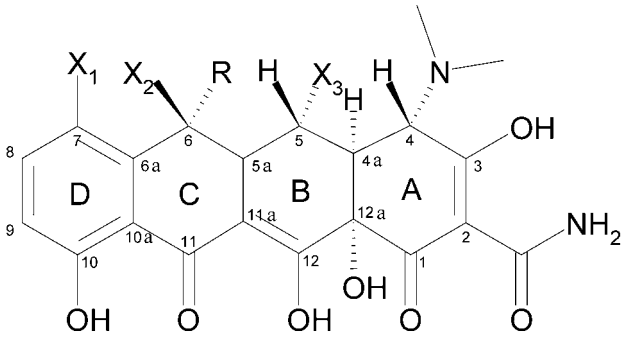

	X_1	X_2	R	X_3
Tetracycline	H	OH	CH_3	H
Minocycline	$N(Me)_2$	H	H	H
Oxicycline	H	OH	CH_3	OH
Doxicycline	H	H	CH_3	OH
Methacycline	H	$(CH_2)/2$	$(CH_2)/2$	H

Scheme 1. Chemical structures of investigated compounds.

An aspect of major importance in understanding the pharmaco-kinetical properties of drugs and the mechanism of their action is that of acid-base equilibria. An orally administered drug will most likely change its protonation state during its passage through the acidic stomach and the alkaline intestinal tract. This change influences its solubility in an aqueous environment, its permeability through membranes and its binding constant to the receptor site. In the case of tetracyclines, the situation is made more complicated by two additional facts: (i) Most pharmacologically active derivatives contain three functional groups which can be subject to protonation – deprotonation equilibria. Furthermore, it is generally believed that the fully protonated species (tcH_3^+ in Scheme 2) adopts a geometry different from that of the completely deprotonated species ($tc^=$); (ii) It is well-established that tetracyclines bind to many proteins preferentially, if not exclusively, as complexes with metal ions. In body fluids, the predominant divalent metal ions are Mg^{++} and Ca^{++}. Therefore, most of the investigations concentrated on the effect of these two ions. The conclusions concerning the site of metal ion binding appear very often to be contradictory. It could, however, be that the experimental conditions (pH, concentrations, etc.) were not similar enough to justify a direct comparison of the published results.

$$tcH_3^+ \rightleftharpoons tcH_2^\circ + H^+ \rightleftharpoons tcH^- + 2H^+ \rightleftharpoons tc^= + 3H^+$$

Scheme 2. Deprotonation scheme of tetracyclines.

In view of the medical importance of the described dependencies e. g. for the bioavailability of these drugs in blood plasma, we decided to apply resonance-enhanced Raman spectroscopy to collect further information about similarities and differences in drug behaviour under well-defined conditions. Since vibrational spectra only yield indirect information about the molecular geometry, extensive quantum chemical model calculations are necessary to deduce more detailed conclusions. Nevertheless, a phenomenological interpretation already yields useful information.

Materials and Methods

Tetracyclines and solvents were used as supplied by the manufacturers. For preparation of samples, the compounds were dissolved in H_2O (D_2O). In order to assure complete protonation (deuteration), 1 n HCl (DCl) was added until pH2 (pD2) was reached. Alternatively, 0.1 n NaOH (NaOD) was added until the solution showed pH 11 (pD 11). Stock solutions of $MgCl_2$, $CaCl_2$ and $EuCl_3$, respectively, in H_2O (D_2O) were then added to the alkaline solutions of the tetracyclines until the ratio tetracycline : metal ion approached unity. Depending on concentration and kind of tetracycline and nature of the metal ion, the formed complexes stayed in solution or precipitated. In the latter case, acid was added until the precipitation dissolved again (the corresponding pH (pD) is reported with the results).

For monitoring the (time-resolved) resonance Raman spectra (λ_{pr} = 400 nm) the newly developed technique using a fast Kerr gate for fluorescence rejection was applied[2]. Alternatively, UV-pulses (λ_{ex} = 280 nm) were employed which matched a higher transition of the ring BCD chromophore and the first transition of the ring A chromophore[3].

Concentration of the tetracyclines was chosen such that the absorbance at 400 nm was as close as possible to 2/mm (limitation by solubility).

Results and Discussion

Tetracyclines comprise two different π-electronic systems (chromophores), a smaller one located on ring A, and a larger one located on rings BCD (see Scheme 1). Since the NIR-FT Raman spectra of tetracyclines contain, like the IR spectra, a large number of closely lying bands, an assignment to calculated normal coordinates is impossible without further information. Such information can be provided via the

resonance enhancement. If the excitation wavelength is chosen in resonance with the first absorption band (λ_{ex} ~ 400 nm), then modes located on the BCD-chromophore should dominate the spectrum. If, on the other hand, the excitation wavelength matches the absorption of the A-chromophore (λ_{ex} ~ 288 nm), then the modes located on the A-chromophore should be observed. Consequently, in Figure 1, the Raman spectra of Tetracycline in acidified H_2O and D_2O, respectively, are shown with three different excitation wavelengths employed.

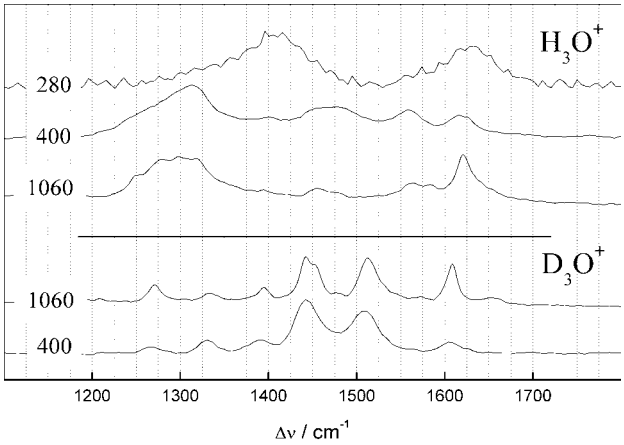

Figure 1. Comparison of Raman spectra of Tetracycline in acidified H_2O / D_2O recorded with excitation wavelengths (in nm) given in the plot.

It is immediately obvious that nearly all of the more intense NIR-Raman bands observed in the spectral region 1100< ṽ/cm < 1700 are connected with the BCD-chromophore. Only the bands around 1410 and 1620 cm^{-1} (H_3^+O) are due to the A-chromophore. Because essentially no band (position) is conserved upon switching to the deuterated system, one can conclude that the corresponding normal coordinates must contain a significant fraction of O-H/O-D local modes (intramolecular deuterium isotope effect) or movement of C=O groups which are hydrogen-bonded to the solvent. Normal mode calculations employing the crystal structure of Tetracycline hydrochloride confirm these conclusions.

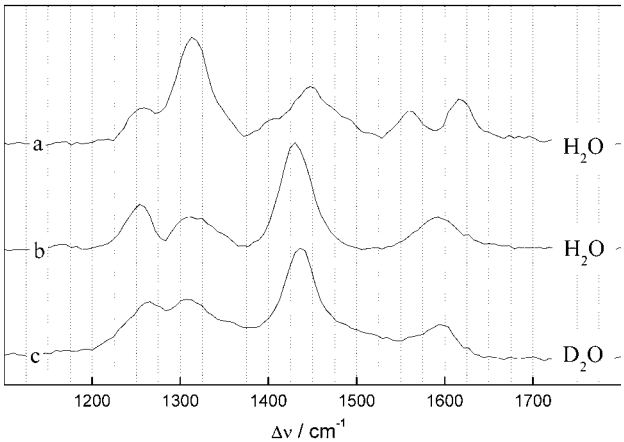

Figure 2. Raman spectra of Tetracycline in H_2O at pH 7.5 (trace a), at pH 11 (trace b) and D_2O at pD 11 (trace c).

In alkaline solution, where the tetracyclines are completely deprotonated, the differences in vibrational spectra due to the involved OH/OD vibrations should disappear and only distinctions because of interaction with the solvent should persist. The resonance Raman spectra recorded in alkaline solution (Figure 2) are nearly in perfect agreement with this expectation and provide further evidence that the bands observed in acidic solutions are related to OH/OD movement, as do most of the bands seen in the spectrum recorded at pH 7.5 (trace a in Figure 2).

The products of metal ion complexation are most unique with respect to the degree of protonation, if one works at high pH, where the dianion $tc^{=}$ predominates in the metal ion free solution. As can be seen in Figure 3, significant changes are produced in the resonance Raman spectra, these being different for Mg^{2+}, on one hand, and Ca^{2+} and Eu^{3+}, on the other hand. Even without a detailed analysis, one can conclude that the complexation pattern must be different for the two groups of metal ions. In the past, it was argued that, because of similar size, Eu^{3+} should exhibit the same complexation behaviour as Ca^{2+}. The Raman spectra seem to confirm this assumption.

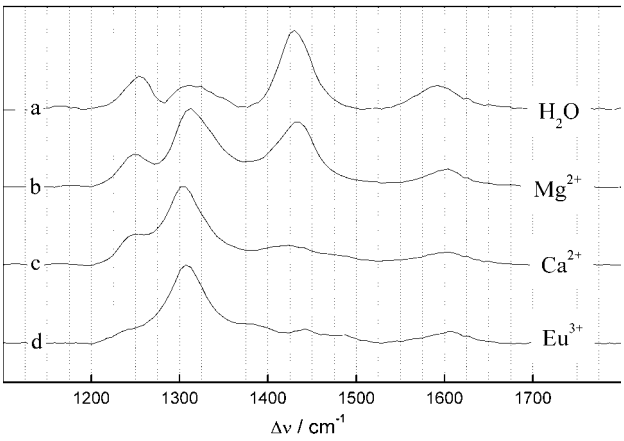

Figure 3. Effect of metal ion complexation on resonance Raman spectra of Tetracycline in H_2O (pH 11): a) without metal ions, b) with Mg^{2+}, c) with Ca^{2+} and d) with Eu^{3+} (pH 7.5).

The conclusions drawn from the diverse Raman spectra of Tetracycline also hold for the derivatives investigated as can be seen in Figures 4 and 5. Doxicycline can be considered the closest analogue to Tetracycline since it differs only by a shift of an OH group from C6 to C5. Consequently, the Raman spectra match very well. In Minocycline, the π-electronic system of the BCD-chromophore is slightly perturbed by the electron donating $N(Me)_2$ group and the substitution pattern of phenyl ring D is changed. Therefore, larger changes in relative intensities of the Raman bands can be rationalized. In Methacycline, an additional double bond is introduced which affects the spectral distribution severely. Noteworthy is that the two predominant bands observed in D_2O (pD 2) around 1442 and 1506 cm^{-1}, respectively, appear to be fairly conserved in all derivatives except Minocycline. Quantum-chemical calculations using the BP86/RI/TZvP harmonic force field predict that these modes comprise mainly motion of the OD groups at C10 and C12 (Figure 6).

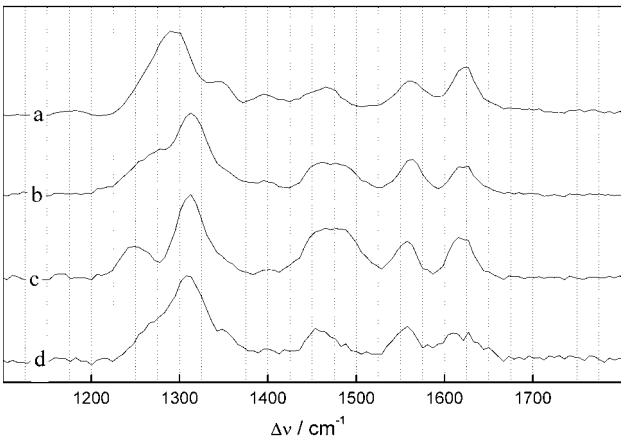

Figure 4. Resonance Raman spectra of derivatives in H_2O (pH2): a) Minocycline, b) Oxicycline, c) Doxicycline, d) Methacycline.

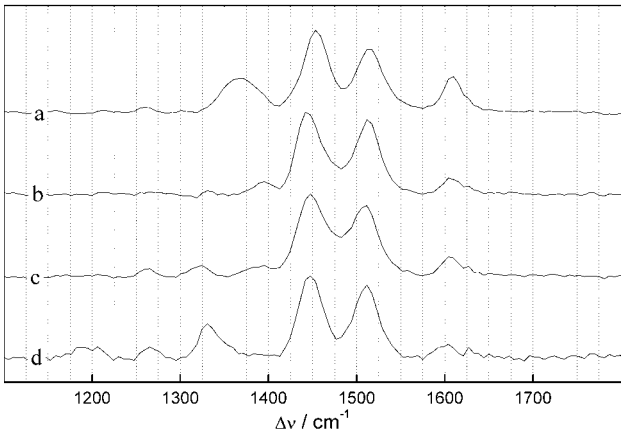

Figure 5. Resonance Raman spectra of derivatives in D_2O (pD2): a) Minocycline, b) Oxicycline, c) Doxicycline, d) Methacycline.

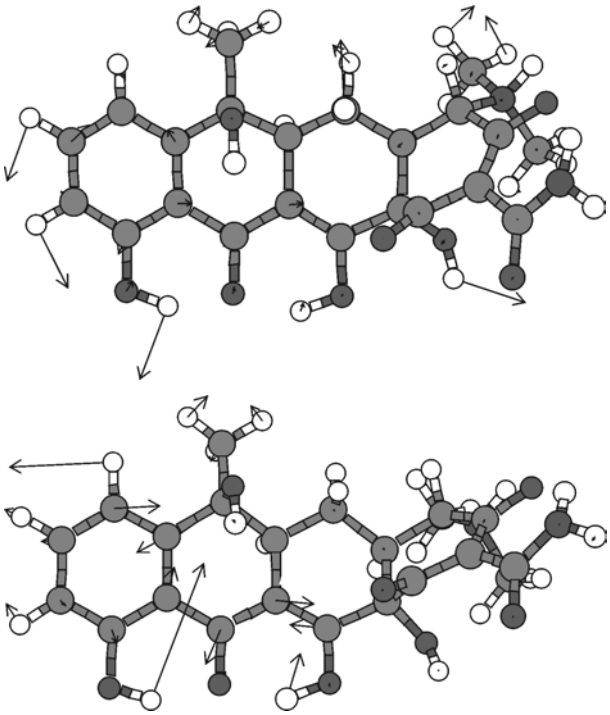

Figure 6. Calculated normal coordinates of deuterated Tetracycline assigned to the Raman bands seen at 1442 cm^{-1} (top) and 1506 cm^{-1} (bottom).

In view of the above, it is not surprising that the Raman spectra of the corresponding Mg^{2+}-complexes recorded at pH 11 (not shown) also resemble each other very closely thus giving evidence that the complexation pattern is the same in all derivatives investigated. Furthermore, the changes provide evidence against the suggestion that complexation could occur at a functional group of the A-chromophore and support O10 – O11 as the chelation site for Mg^{2+}. The band observed around 1430 cm^{-1} in both alkaline H_2O and D_2O is, according to the normal mode calculations, connected with the hydroxide group at C12a. That its intensity is reduced upon complexation with Ca^{2+}, but not upon complexation with Mg^{2+}, is, in our opinion, strong evidence for complexation of Ca^{2+} to O12 – OH12a at high pH.[3)]

Summary and Conclusion

The attainable concentration of the tetracycline derivatives investigated is high enough to record, due to the resonance enhancement obtained with 400 nm excitation, Raman spectra with high S/N. Most of the intense bands are related to the BCD-chromophore with high contribution of the OH/OD local modes. The changes in band position upon metal ion complexation confirm the suggestion that the complexation site is at the BCD- rather than at the A-chromophore.

Acknowledgements

Financial support by Deutsche Forschungsgemeinschaft (SFB 583) and Fonds der Chemischen Industrie is gratefully acknowledged. We appreciate a grant by the European Union TMR Large Scale Facility Access Programme. We also thank HOVIONE for donation of samples (Minocycline and Methacycline).

References

1. Tetracyclines in Biology, Chemistry and Medicine edited by M. Nelson, W. Hillen and R.A. Greenwald, (2001) Birkhäuser Verlag, Switzerland

2. P Matousek, M Towrie, A W Parker J. Raman Spectrosc. 33, 238 (2002)

3. M O Schmitt, S Schneider PhysChemComm 9 (2000)

Picosecond time-resolved fluorescence of Tetracycline and its complexes with Mg^{++} or Ca^{++}

S Schneider, G Brehm, M Schmitt, C Leypold

Institut für Physikalische und Theoretische Chemie, Friedrich-Alexander-Universität Erlangen-Nürnberg, D-91058 Erlangen, Germany

P Matousek, M Towrie

Central Laser Facility, CLRC Rutherford Appleton Laboratory, Chilton, Didcot, Oxon, OX11 0QX, UK

Main contact email address: *schneider@chemie.uni-erlangen.de*

Introduction

Since the discovery of the antibiotic action of Tetracycline in 1947, a large number of derivatives has been synthesized and successfully applied. In recent years, the use of many of them has been reduced due to the fact that numerous bacteria developed efficient resistance mechanisms. Consequently, a major effort is presently put into the investigation of the various bacterial strategies. One of them relies on the active transport by a membrane-located antiporter protein, TetA, whose synthesis is down-regulated by the so called TetR protein[1)]. In the absence of tetracyclines, the latter is bound to the DNA. If tetracyclines penetrate into the bacterial cell, they are, as complexes with already present Mg^{++} or Ca^{++}, bound by TetR. As a consequence of effector binding, allosteric changes are induced in the binding domain of TetR causing dissociation of TetR from the DNA and thereby allowing the transcription of the genes encoding TetR and TetA.

The binding constants of various tetracyclines in a specific mutant of one of the 8 different naturally occurring classes of TetR proteins can vary by 10 orders of magnitude. If the antibiotic action of a certain derivative has to be evaluated, one must determine separately whether this compound is bound and, if yes, whether the dissociation is induced effectively.

One common procedure to determine binding constants is by means of fluorescence titration. This technique works generally both for the determination of complexation constants between tetracyclines and the chosen metal ions and the binding of the tetracycline / metal ion complex in the homodimeric TetR protein. The main reason for the effectiveness of fluorescence titration is the phenomenological observation that the fluorescence yield of the tetracycline / metal ion complexes is higher than that of metal free tetracyclines and that incorporation into the binding pocket is accompanied by another significant increase in fluorescence yield. The reasons for such a behaviour are by no means understood and, to the best of our knowledge, not even the pH-dependence of the fluorescence kinetics of metal free tetracyclines nor that of its metal ion complexes.

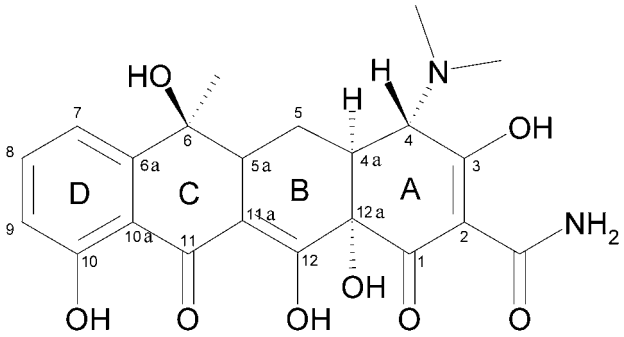

Scheme 1. Chemical structure of Tetracycline.

Tetracycline (see Scheme 1 for structure) must be considered as a three protic acid. In water, the first deprotonation step ($pK_{a1} \approx 3.3$) involves the proton at O3, the second ($pK_{a2} \approx 7.7$) the proton bound to the diketone moiety involving O11 and O12 and the third one ($pK_{a3} \approx 9.5$) the proton at the dimethylamino group bound to C4[2)]. In view of the well-known effect of intra- and intermolecular hydrogen bonding on the rate of radiationless processes, one immediately suspects that the excited state lifetimes of the four species: fully protonated form, tcH_3^+, the neutral form, tcH_2^0, the monoanion, tcH^-, and the dianion, $tc^=$, should show the following ordering:

$$\tau\,(tcH_3^+) \leq \tau\,(tcH_2^0) < \tau\,(tcH^-) \leq \tau\,(tc^=)$$

This proposed ordering of lifetimes could be modified due to the conformational change, which, according to evidence from CD spectroscopy, should occur when going from acidic to basic solution or by formation of specific intermolecular hydrogen bonds.

Because of the importance of metal ion complexation for binding the effector in the TetR protein, numerous studies have been performed to elucidate their association constants and the site of complexation. Based on the results of different spectroscopic techniques, one can conclude that at pH around 7, both Mg^{++} and Ca^{++} bind to O10 and O11. This agrees also with the binding pattern of the $[7Cl\text{-tetracycline-Mg}]^+$ complex embedded in TetR(D). At higher pH, the binding pattern is different for Ca^{++} and Mg^{++} [2)].

The aim of the research described in this contribution was twofold: (i) We wanted to establish a set of excited state lifetimes for a series of tetracycline derivatives, which are used in antibacterial and / or new non-antibacterial applications as solid basis for the interpretation of fluorescence experiments engaging these compounds under different experimental conditions, and (ii) we wanted to find an explanation for the variation of excited state lifetimes with environment.

Materials and Methods

Tetracyclines and solvents were used as supplied by the manufacturers. Concentration of the solutes was chosen such that optical density at the excitation wavelength ($\lambda_{ex} \sim 266$ nm) was about 2/mm.

For monitoring the time-resolved emission spectra, the experimental set-up developed for recording of Kerr gated Raman spectra was employed[3)]. Since the sample is flowed in an open jet, one must consider quenching by oxygen as an unwanted side effect. Keeping in mind the solubility of oxygen in water, one can say that the decay times of the short-lived species should not be falsified. The lifetimes of the long-lived species can, however, appear with significantly reduced values.

Results and Discussion

Whereas the red absorption band, which is due solely to the BCD chromophore (see Scheme 1 and Figure 1), shows a pronounced wavelength shift upon changing pH, absorbance is less dependent on pH at the chosen excitation wavelength ($\lambda_{ex} = 266$ nm). Accordingly, one finds a variation of the steady state emission maximum with pH. The calculated Stokes shift appears unusually large indicating either a significant reorganisation of the solute's geometry and / or a large change in solute – solvent interaction. To exploit the latter point, H_2O, D_2O and H_2O/MeOH mixtures were applied as solvents.

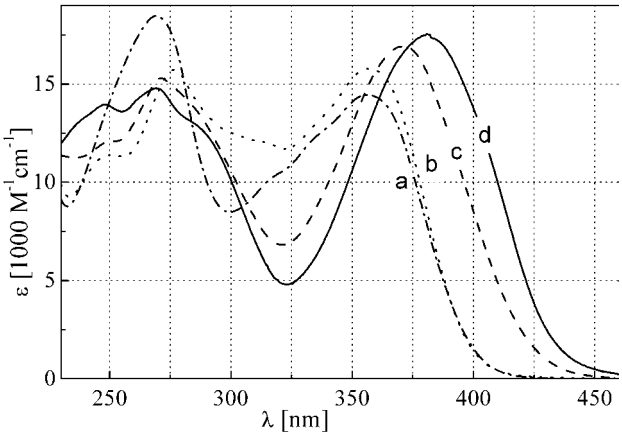

Figure 1. Calculated absorption spectra of Tetracycline in different states of protonation in H_2O: tcH_3^+ (a), tcH_2^0 (b), tcH^- (c) and tc^{2-} (d).

In Figure 2, the time evolution of the (spectrally not corrected) fluorescence of tcH_3^+ in H_2O is shown. It is immediately evident that there are at least three different contributions: (i) an extremely fast decaying component between 400 and 500 nm, (ii) a fast decaying component and (iii) a longer-lived one in the range 500 to 700 nm. The steady state emission spectrum is in accord with the time-resolved spectra because it shows the maximum around 600 nm, but in addition a second, weaker band around 450 nm.

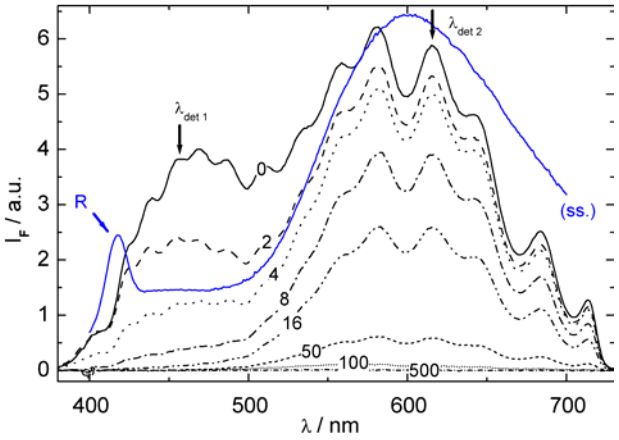

Figure 2. Time-resolved fluorescence spectra (λ_{ex} = 266 nm) of fully protonated Tetracycline, tcH_3^+, in H_2O. Time delays Δt are: 0, 2, 4, 8, 16, 100 and 500 ps. For comparison, the steady state emission spectrum (ss.) for λ_{ex} = 365 nm is also shown (R denotes the Raman band of water).

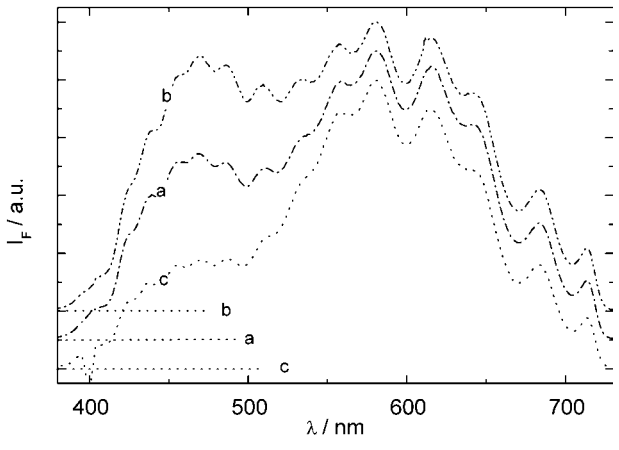

Figure 3. Initial spectral distribution (Δt = 0) observed for Tetracycline in acidic H_2O (a), D_2O (b) and H_2O/MeOH (c).

The time evolution of the fluorescence spectra in D_2O and H_2O/MeOH is qualitatively similar. However, the relative contribution of the extremely fast decaying component is larger in D_2O and smaller in H_2O/MeOH (Figure 3). Noteworthy is that the spectral distribution above about 550 nm is solvent independent.

The choice of the solvent has also a significant influence on the fluorescence-decay kinetics as shown in Figure 4. In deuterated solvent - which implies partial deuteration of the solute - the decay times become larger (τ_2 = 70 ps (D_2O) versus τ_2 = 25 ps (H_2O)). This can be taken as evidence that intra- and intermolecular hydrogen bonding is an essential factor in the radiationless decay of the excited state. In H_2O/MeOH, the ultrafast decaying component is too weak for a reliable lifetime determination; the medium decay time is even longer than in the case of D_2O ($\tau_2 \approx$ 90 ps). This again is in accord with expectation since MeOH should establish weaker intermolecular hydrogen bonds.

Furthermore, one finds that the spectral distribution of neither the “blue” nor of the “red” fluorescence seems to change in the time range 0 – 25 ps. This means that whatever mechanism is causing the large Stokes shift, it must occur on a (sub-) picosecond time scale.

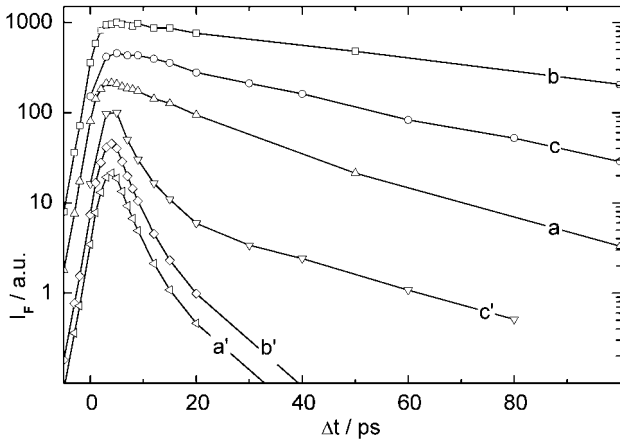

Figure 4. Normalized fluorescence decay of Tetracycline in acidic H_2O (a), D_2O (b) and H_2O/MeOH (c) monitored around 450 nm (a′, b′, c′) and 620 nm, respectively (a, b, c) (see also arrows in Figure 2).

Around pH 5, Tetracycline should exist in H_2O preferentially in its zwitterionic form ($tcH^{\pm}$). In accordance with the results of steady state measurements, the spectral distribution of the major component with medium decay time ($\tau_2 \approx$ 40 ps) exhibits only a small hypsochromic shift versus the acidic solution (Figure 5, trace a). This can be rationalized because deprotonation at O3 should have only a minor effect on the (photophysical) properties of the BCD chromophore. Interestingly enough, one finds again a “blue” component with very short lifetime (giving rise to a shoulder in the steady state fluorescence spectra).

At pH above about 10, the dianion $tc^{=}$, which lacks the proton at O12, is the predominant form in H_2O. Therefore, it is not surprising that now the steady state fluorescence spectrum is shifted hypsochromically by about 70 nm (Figure 5, trace c). The time-resolved spectra appear to decay uniformly across the whole spectral region, although not mono-exponentially (Figure 6). The relative amount of the longer-lived component is larger at pH11 than at pH8.5 thus explaining why the total fluorescence intensity increases significantly at high pH. Since the initial spectral distribution is, however, nearly equal at pH11 and pH 8.5, the emission spectra of the monoanion tcH^- must resemble closely that of the dianion $tc^{=}$. This conclusion can again be rationalized in view of the small interaction between

the BCD chromophore and a proton at the dimethylamino group bound to C4.

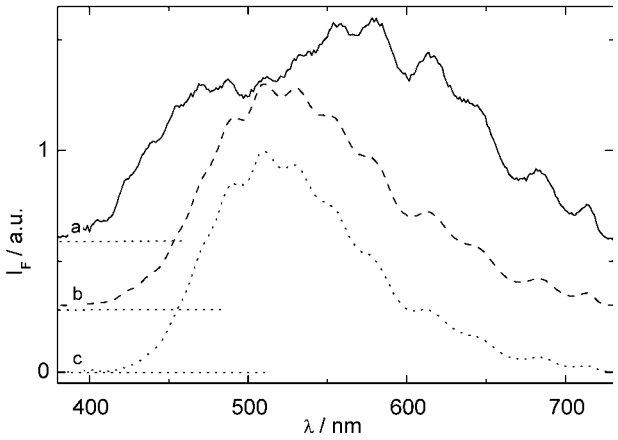

Figure 5. Initial spectral distribution (Δt = 0) observed for Tetracycline in H_2O at pH = 5.2 (a), 8.5 (b) and 11 (c), respectively.

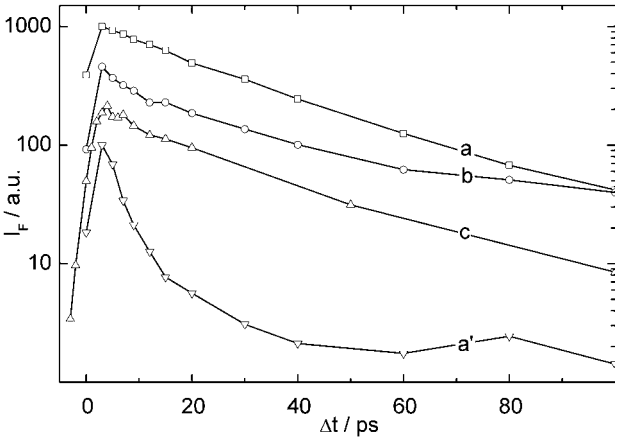

Figure 6. Normalized fluorescence decay of Tetracycline in H_2O at pH = 5.2 (a and a' (λ_{obs} = 450 nm)), 8.5 (b) and 11 (c) monitored around the fluorescence maximum.

Complexation of the Tetracycline dianion by Mg^{++} and Ca^{++}, respectively, results in fluorescence spectra with essentially the same spectral distribution at Δt = 0. As in the previously discussed examples, we find an extremely fast decaying component of low amplitude in the wavelength range $400 < \lambda/nm < 500$. In case of Mg^{++}-complexes, the decay of the predominant component with maximum around 530 nm appears non-monoexponential, the shorter decay time being around 150 ps, the longer around 500 ps. In case of the Ca^{++}-complexes, the latter decay time equals about 320 ps. It should be noted in passing that the steady state fluorescence intensity of the tetracycline-Mg^{++}-complexes was found to increase if acetonitrile is added to the aqueous solution thereby providing an alternative hint to the importance of hydrogen bonding for fast radiationless deactivation [4].

The time-resolved fluorescence spectra of the solutions of the derivatives investigated, namely Doxicycline, Minocycline and Methacycline, follow the same pattern as described for Tetracycline. One can, therefore, conclude that the intriguing features observed in the fluorescence decay are determined by the conserved part, especially the intramolecular hydrogen bonding of the hydroxyl groups attached at C10 to C12a and the intermolecular hydrogen bonding involving O11. Morimoto et al[5], for example, proposed that in case of 2-piperidinoanthrachinone, whether the formed solvated state is emissive or non-emissive depends on the direction of the interacting OH-group of the solvent (in plane or out of plane).

Summary and Conclusion

The pronounced deuterium isotope effect and the influence of solvent hydrogen bonding capability on spectral distribution and decay characteristics of the fluorescence provide clear evidence that both intra- and intermolecular hydrogen bonding are predominant factors in determining the rate of radiationless deactivation. The short-lived blue fluorescence should originate from a specially solvated, i. e. hydrogen bonded form whereby the lifetime-determining interaction is hardly influenced by protonation / deprotonation or metal ion chelation. The formation of this heavily quenched species must be prevented by imbedding the tetracyclines into the TetR binding pocket thus giving rise to an overall increase in fluorescence yield. The second class of emitting species, which exhibits an unusually large Stokes shift, must be formed from the primarily excited Franck-Condon state within less than a few picoseconds. We assume that the related (relaxation) processes involve not only deprotonation.

One can also suspect that the decay law is more complex than just biexponential thereby reflecting the fact that there exists a large heterogeneity with respect to solvation and extent of hydrogen bonding. Quantum-chemical calculations for Tetracycline are very sensitive to the number and location of included water molecules and thereby provide evidence for the occurrence of strong solvent effects.

Acknowledgements

Financial support by Deutsche Forschungsgemeinschaft (SFB 583) and Fonds der Chemischen Industrie is gratefully acknowledged. We appreciate a grant by the European Union TMR Large Scale Facility Access Programme. We also thank HOVIONE for donation of samples (Minocycline and Methacycline).

References

1. W Hinrichs, C Kisker, M Düvel, A Müller, K Tovar, W Hillen, W Sänger
Science 264, 418 (1994)

2. M O Schmitt, S Schneider
PhysChemComm, 9 (2000)

3. P Matousek, M Towrie, A W Parker
J. Raman Spectrosc. 33, 238 (2002)

4. M Kunz
PhD Thesis, Univ. Erlangen (2000)

5. A Morimoto. T Yatsuhashi, T Shimada, S Kumazaki, K Yoshihara, H Inoue
J. Phys. Chem. A 105, 8840 (2001)

Picosecond TR^3 Studies of Complexes with DNA-Intercalating and Related Ligands: Some New Investigations of Fe(II) Spin Crossover Complexes and of Ru(II) Polypyridyl Species

C Brady, C G Coates, J J McGarvey, K L Ronayne

School of Chemistry, The Queens University of Belfast, Belfast, BT9 5AG, UK

W R Browne[+], J G Vos

National Centre for Sensors Research, Dublin City University, Dublin 9, Ireland. ([+]Presently at School of Chemistry, QUB)

P Matousek, M Towrie, A W Parker

Central Laser Facility, CLRC Rutherford Appleton Laboratory, Chilton, Didcot, Oxon, OX11 0QX, UK

Main contact email address: *j.mcgarvey@qub.ac.uk*

Picosecond TR^3 Studies of Fe(II) Spin Crossover Complexes

Previous reports from the Queens group have concentrated on spectroscopic investigations of ruthenium and rhenium complexes containing the DNA-intercalating dipyridophenazine (dppz) ligand (Figure 1). Recently, investigation of $[Ru(phen)_2qdppz]^{2+}$ (where qdppz is dipyridophenazine with a fused anthraquinone unit) has been undertaken to investigate the photoinduced electron transfer in this compound and how this might influence the light-switch properties compared to the parent $[Ru(phen)_2dppz]^{2+}$. Closer study of these paradigm dppz complexes is continuing with TRIR studies planned to complement the TR^3 investigation.

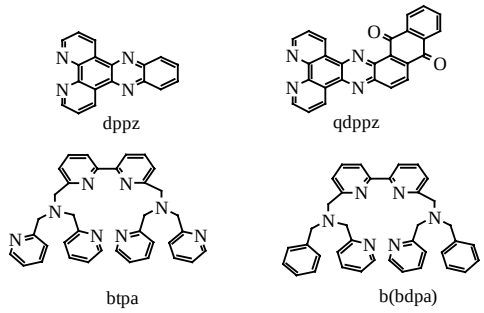

Figure 1. Ligand structures.

Recent investigations have involved the study of $[Fe(dppz)_2(NCS)_2]$ (**1**) with the same intercalating dppz ligand. This complex belongs to the family of spin crossover (SCO) species. These are complexes of first row transition metals with d^4-d^7 electron configuration which can be switched between low-spin (LS) and high-spin (HS) electronic states by temperature, pressure or irradiation. The presence of the dppz ligand in this complex should encourage intercalation with the DNA strand which may perturb the spin equilibrium.

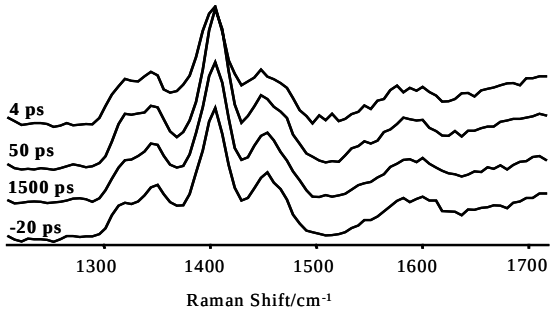

Figure 2. ps-TR^3 spectra of (**1**) in deuteriated methanol at 390 nm pump and probe at various time delays.

ps TR^3 studies of $[Fe(dppz)_2(NCS)_2]$ in deuteriated methanol carried out at 390 nm pump and probe are shown in Figure 2. Spectral subtractions have been used to provide evidence of an early time process with a relaxation time of < 50 ps.

Preliminary TR^3 experiments have also been performed on another Fe(II) spin crossover complex, $[Fe(btpa)](PF_6)_2$(**2**).

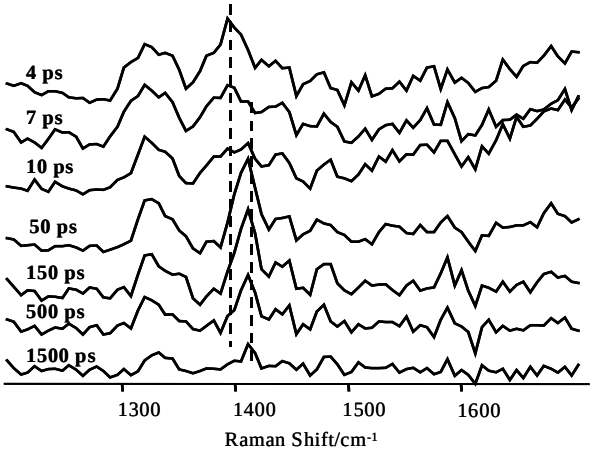

Figure 3. Series of spectra generated through subtraction of the spectrum at –20 ps.

(Figure 1) Comprehensive TR^3 studies on the nanosecond timescale were carried out in Belfast and showed subtle shifts in the ligand modes, indicating structural perturbation of the ligand due to the changing electronic character of the metal from LS to HS. Kinetics plots obtained from the nanosecond spectra showed biphasic relaxation which is in good agreement with the plots obtained from temperature-dependent flash photolysis measurements.[1)] Studies on the analogous $[Fe(b(bdpa))](PF_6)_2$ complex (**3**) where the pyridyl arms are replaced by benzyl groups showed single exponential relaxation on a similar timescale to the fast relaxation in $[Fe(btpa)](PF_6)_2$. This process is assigned to the HS-LS relaxation and occurs within the timescale previously reported for Fe(II) spin crossover complexes. The slower process occurs over 1500 ns and has been attributed to a coupling of the HS-LS relaxation with a rearrangement of the pendent pyridyl arms.

The ps-TR^3 spectra recorded with 390 nm probe wavelength in order to provide resonance enhancement with the bipyridyl modes are shown in Figure 4 below. Due to the resolution of the bands recorded on the picosecond timescale, the subtle shifts are not apparent. However there are changes in overall intensity as well as relative intensity. As Figure 4 shows, the complex and the solvent show opposite effects which confirm that the changes are structural (vibrational) as opposed to electronic (transient absorption). Kinetics plots derived from the picosecond studies reveal a biphasic decay, with an early process which is complete in ~20 ps and a slower process which extends beyond the 1500 ps limit of the TR^3 experiments.

Picosecond transient absorption measurements (ps-TA) suggest early time states with stronger transient absorption than the 'final' high spin state. The ps-TA measurements revealed similar dynamics to the TR^3 data.

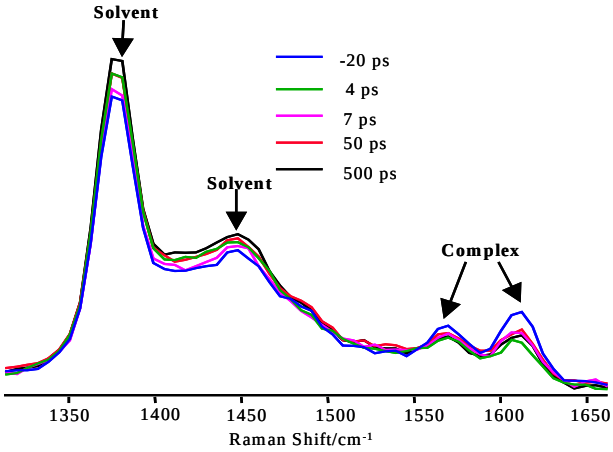

Figure 4. ps-TR^3 of (**2**) in acetonitrile at 390 nm pump and probe at various time delays.

The analogous $[Fe(b(bdpa))](PF_6)_2$ complex which demonstrated single exponential relaxation in the nanosecond experiments also showed biphasic decay in the picosecond studies. This eliminates contribution from the rearrangement of the pendent pyridyl arms to this early process.

This initial fast process is not unique to this family of spin crossover complexes. As mentioned earlier, $[Fe(dppz)_2(NCS)_2]$ also revealed a process with a relaxation time of <50 ps. Whether this is attributable to population of the HS ($^5T_2$) state from the MLCT state is uncertain. The studies carried out so far at the CLF on these SCO systems provide significant parallels with recent picosecond TA studies reported from a US Laboratory[2)] and will be the subject of further study.

Picosecond Spectroscopy to Probe Initial States of Ru Polypyridyl Complexes

With regard to application of these complexes as sensitisers in solar cell devices, interest in the early photophysical processes has increased dramatically in recent years. This interest arises from the proposal that direct injection of electrons from those states is a competitive process to intersystem crossing to the lowest ^{3}MLCT manifold. Improving the quantum efficiency of electron transfer to semiconductors and thereby improving conversion efficiency is desirable, as is a better understanding of these short lived states. The timescale of injection of an electron into nanocrystalline TiO_2 has been estimated at less than 1 ps, with some estimates as low as 25 fs. It has been suggested that fast electron transfer from states energetically higher than the lowest ^{3}MLCT excited states not only increases the efficiency of the sensitisers but also precludes deactivation by potentially photoreactive ^{3}MC states.

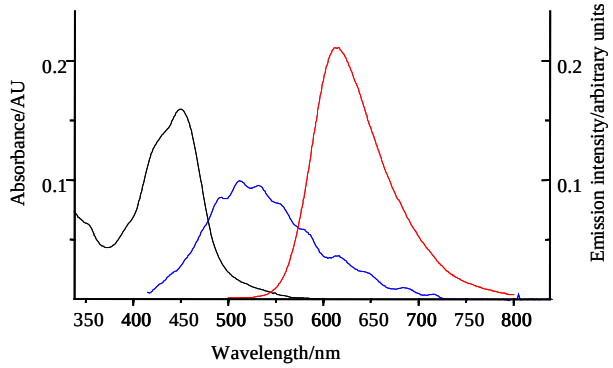

Figure 5. Absorption spectrum (black), steady state emission (red) of $[Ru(bpy)_3]^{2+}$ and emission spectrum at 2 ps after laser excitation in water at 298 K. (spectral intensity is adjusted for clarity).

We have carried out ultrafast studies on a range of Ru polypyridyl complexes, including triazole-based systems. However, some of the most fundamentally significant results have arisen from studies with $[Ru(bpy)_3]^{2+}$. For $[Ru(bpy)_3]^{2+}$ the efficiency of ISC from ^{1}MLCT states and the lowest ^{3}MLCT states is almost universally taken to be unity. We have used, picosecond time resolved luminescence spectroscopy to study the early time processes which occur subsequent to excitation of $[Ru(bpy)_3]^{2+}$.

The emission spectrum recorded from time resolved luminescence studies 2 ps after excitation together with the steady state absorption and emission (^{3}MLCT) spectra for the complex are shown in Figure 5. The emission at 520 nm rapidly decays to the long lived ^{3}MLCT emission. The decay is less than 3 ps and shows no change in emission λ_{max} during the course of its decay. (The decay is below the limit of resolution of the ps systems).

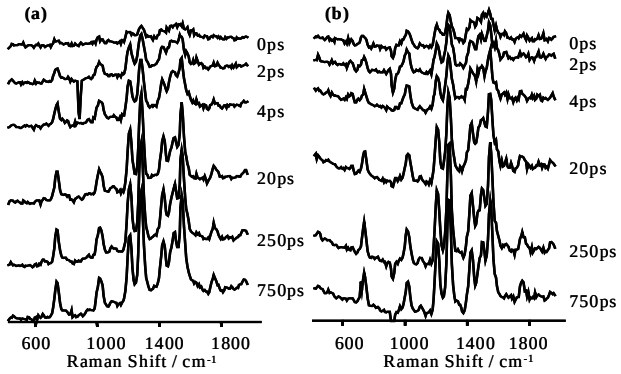

Figure 6. Pure excited state spectra of $Ru(bpy)_3$ (ground state subtracted, not normalised). Pump = 400 nm; probe = 350 nm (a) in water and (b) in acetonitrile.

ps-TR^3 spectra of $Ru(bpy)_3$ in water and acetonitrile were also recorded. The pure excited state spectra are displayed in Figure 6. A kinetic plot derived from these subtractions is shown in Figure 7. Although there is evidence of an early process in both solvents, there are subtle differences between them. These findings are under further investigation.

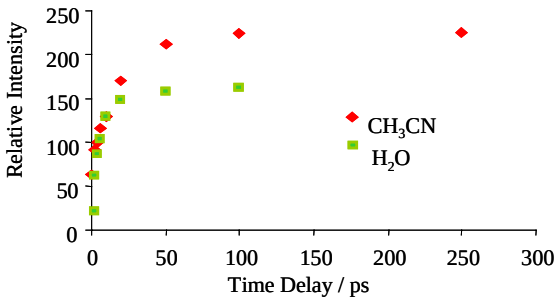

Figure 7. Kinetics derived from pure excited state spectra in Figure 6. Intensity of 1288 cm^{-1} band plotted against time.

Acknowledgements

We thank EPSRC (Grant GR/M45696) for access to USL.

References

1. S Schenker, P C Stein, J A Wolny, C Brady, J J McGarvey, H Toftlund and A Hauser
Inorg. Chem., 40, 134, (2001)

2. J E Monat and J K McCusker
J. Am. Chem. Soc., 122, 4092, (2000)

Nanosecond Time-Resolved Resonance Raman Spectroscopy of Functional (diimine)Re(CO)$_3$(L) Complexes

J D Lewis, J N Moore

Department of Chemistry, The University of York, Heslington, York, YO10 5DD, UK

I P Clark

Central Laser Facility, CLRC Rutherford Appleton Laboratory, Chilton, Didcot, Oxon, OX11 OQX, UK

Main contact email address: *jnm2@york.ac.uk*

Introduction

The metal-to-ligand charge-transfer (MLCT) excited states of (NN)Re^{I}(CO)$_3$L complexes (where NN = diimine, and L = Cl, Br, etc.) have been well characterized. The dπ(Re) $\rightarrow$ π*(NN) transition creates an MLCT state, (NN•–)Re^{II}(CO)$_3$L, which has a lifetime typically on the order of 50-150 ns dependent on the identity of the NN and L ligands.[1] Complexes in which L is an electron donor can undergo intramolecular electron transfer in the MLCT state, from L to Re^{II}, to create a ligand-to-ligand charge-transfer (LLCT) excited state, (bpy•–)Re^{I}(CO)$_3$L•+, which cannot be accessed directly by photon absorption (Scheme 1).

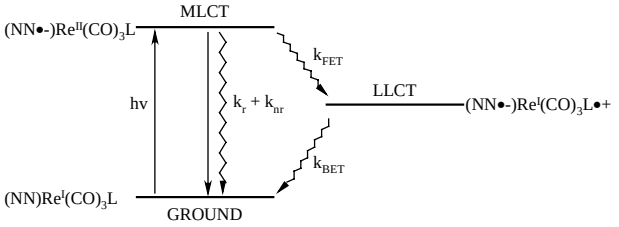

Scheme 1.

Systems such as these, which create charge-separated excited states, have potential applications as optical probes and switches, and as light-harvesting subunits in supramolecular assemblies. Previous studies of the MLCT states of this type of complex have generally involved time-resolved UV/vis absorption and emission and, in some cases, time-resolved infrared[2] and resonance Raman spectroscopy.[3] The LLCT states of complexes which undergo photophysics according to Scheme 1 have been studied directly in a few cases, using time-resolved UV/vis absorption (TRVIS) spectroscopy, but only a very limited number of time-resolved vibrational studies of these LLCT states have been reported.[3]

We have synthesised the (NN)Re(CO)$_3$L complex **1** and model compounds **2**-**4** (Scheme 2).[4] The azacrown ether of **1** selectively binds alkali and alkaline earth metal cations, and the complex acts as an ion-selective optical probe. Using ultrafast and nanosecond TRVIS spectroscopy, we have shown that excitation transfers electron density away from the azacrown nitrogen atom in the MLCT state, lowering the association constant for ion binding and ejecting a cation from the azacrown in bound complexes **1**-M^{n+}. After ejection of the cation, ultrafast relaxation to the LLCT state occurs according to Scheme 1, placing a positive charge at the azacrown nitrogen atom and effectively blocking geminate recombination. The LLCT state decays to the ground state on the nanosecond timescale, and the thermal equilibrium is ultimately restored as cation rebinding occurs from solution. Thus, **1**-M^{n+} undergoes a photo-controlled ion release and recapture cycle. Very few organometallic ion switches such as this have been reported.

Initial studies at RAL have involved investigations of **1** and its models **2**-**4** using nanosecond time-resolved resonance Raman (TR^3) spectroscopy: the aim of the experiments was to record TR^3 spectra of the excited states in the photo-controlled ion-release cycle.

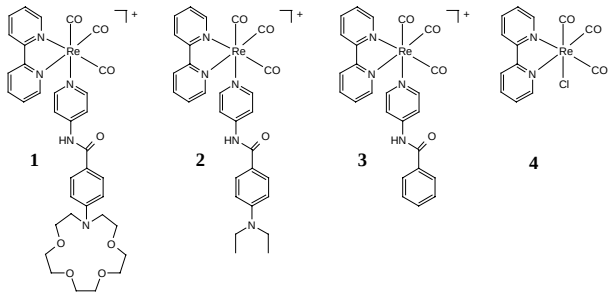

Scheme 2.

Results and discussion

The ground-state MLCT absorption bands of **1**-**4** occur at 350-400 nm. All of the complexes have MLCT excited-state TRVIS spectra with (bpy•–)-localised bands at 370 nm. Complexes **1** and **2**, where L includes a dialkylamino electron-donor group, undergo sub-nanosecond electron transfer to create LLCT states which have TRVIS spectra with both a (bpy•–)-localised band at 370 nm and a (R_2N•+)-localised band at 500 nm.[5]

Single-colour pulsed-laser experiments using 385 nm as both pump and probe wavelengths enabled both ground- and excited-state resonance Raman bands of **1**-**4** to be observed. Ground-state bands were identified by comparison with cw resonance Raman spectra recorded in York. Excited-state bands were identified by their increase in relative intensity with an increase in pulsed-laser energy.

The ground-state Raman bands of model compounds **3** and **4** (Figure 1a) are assigned to bpy modes and one ν(CO) mode.[6] The excited-state bands of **3** and **4** (Figure 1c) are assigned to bpy•– modes of the MLCT state, as reported in the literature.[6]

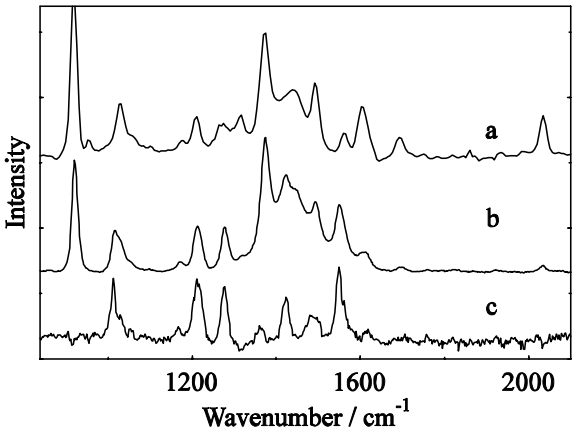

Figure 1. Resonance Raman spectra of 3 recorded with (a) 350.6 nm cw excitation; (b) 385 nm pulsed excitation with (c) a difference spectrum showing MLCT excited-state bands of **3.**

The ground-state Raman bands of functionalised complexes **1** and **2** (Figure 2a) are much stronger that those of the model compounds recorded under comparable conditions, and they are

assigned to modes of the functionalised ligand L because of their strong enhancement in resonance with an intense L-centred band at ca. 350 nm in the ground-state absorption spectra. The excited-state Raman bands of **1** and **2** (Figure 2b) are assigned to bpy•– modes and one ν(CO) mode at 2010 cm^{-1}, arising from resonance with the (bpy•–)-localised TRVIS band at 370 nm. The excited-state bpy•– bands of **1** and **2** are observed to be shifted by up to 20 cm^{-1} from the equivalent excited-state bands of **3** and **4** (Figure 1c). These shifts indicate that the bonding within the bpy•– ligand is different, and they are consistent with the observation of an LLCT state spectrum from **1** and **2** because the change from Re^{II} to Re^{I} on going from MLCT to LLCT states would be expected to result in stronger backbonding into the bpy ligand π* orbitals and a consequent shift in band positions. In addition, the ν(CO) bands of **1** and **2** show a downshift of ca. 20 cm^{-1} on going from ground to excited states. This is also consistent with the observation of an LLCT state spectrum because the significant change at the rhenium centre between ground and LLCT states is reduction of the bpy ligand, which would be expected to result in stronger backbonding into the CO ligand π* orbitals.

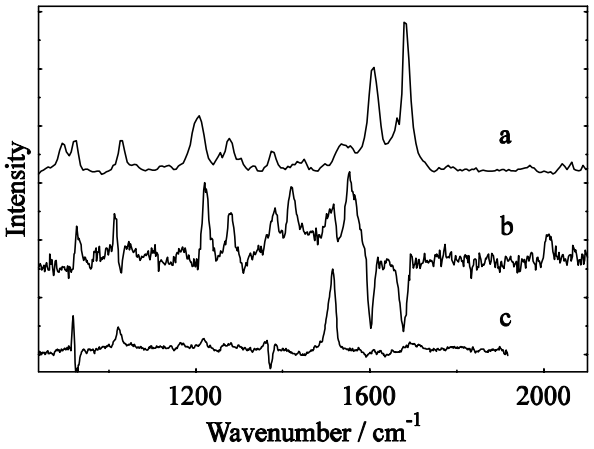

Figure 2. (a) Resonance Raman spectrum of 1 recorded with 350.6 nm cw excitation. (b) Difference spectrum obtained from 385 nm single-colour pulsed-laser excitation of 1, showing LLCT excited-state bands. (c) TR^3 spectrum of the LLCT state of **1** recorded with 355 nm pump and 500 nm probe pulses at 8 ns delay time.

A two-colour experiment using 355 nm as the pump wavelength and 500 nm as the probe wavelength enabled time-resolved resonance Raman spectra of the LLCT states of **1** and **2** to be obtained. Variation of the delay time gave a kinetic profile for the TR^3 bands that matched the TRVIS kinetics for the decay of the LLCT state, confirming the assignment. The probe wavelength of 500 nm resulted in a different LLCT spectrum (Figure 2c) from that obtained at 385 nm (Figure 2b) because of resonance with the (R_2N•+)-localised TRVIS band rather than with that of the (bpy•–)-localised TRVIS band. The Raman bands observed with a probe wavelength of 500 nm are assigned to modes of the ligand L associated with the (R_2N•+) chromophore: these include those associated with the nitrogen-centred radical cation but may extend onto the rest of the ligand; calculations to aid with assignments are in progress.

Single-colour pulsed-laser experiments at 385 nm yielded a complicated pattern of Raman bands for cation-bound complexes **1**-M^{n+}, where M^{n+} = Li^+, Na^+, Ca^{2+} or Ba^{2+} (Figure 3a,b). This pattern may be attributed to the observation of bands assigned to both MLCT and LLCT states, and is consistent with an increase in the MLCT state lifetime that is known to occur when a cation is bound to complex **1**: both MLCT and LLCT states are present during a single nanosecond pump and probe pulse.

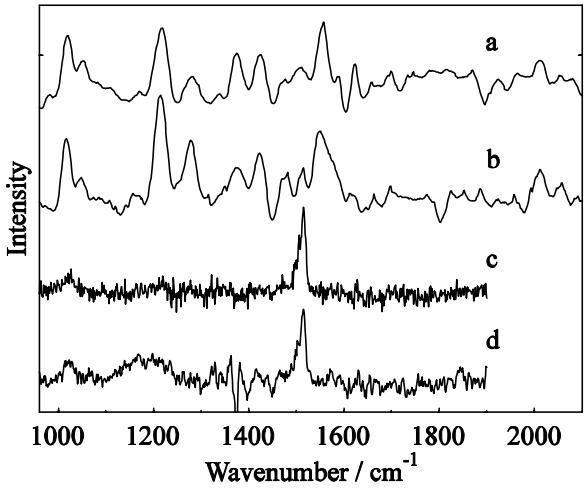

Figure 3. Difference spectra obtained from 385 nm single-colour pulsed-laser excitation of (a) 1-Na^+ and (b) 1-Ba^{2+}, showing MLCT and LLCT excited-state bands. TR^3 spectra from (c) 1-Na^+ and (d) 1-Ba^{2+}, recorded with 355 nm pump and 500 nm probe pulses at 8 ns delay time and assigned to the LLCT state of **1**.

Two-colour experiments on **1**-M^{n+}, pumping at 355 nm and probing at 500 nm, resulted in Raman spectra (Figure 3c,d) which closely resembled the spectrum obtained from two-colour experiments on **1** in the absence of bound cations (Figure 2c), and thus may be assigned to the LLCT state of **1**. The observation of a TR^3 spectrum of the LLCT state from a sample of **1**-M^{n+} provides further proof that the cation is released following excitation: electrochemical measurements indicate that electron transfer to form the LLCT state cannot occur while the cation remains bound.[4)] Moreover, variation of the delay time gave kinetic profiles for the LLCT state TR^3 bands that varied with cation, and matched the respective TRVIS kinetics for the decay of the LLCT state formed on excitation of **1**-M^{n+}.

Conclusions

We have studied a series of (bpy)$Re(CO)_3L$ complexes using nanosecond time-resolved resonance Raman spectroscopy, and we have obtained Raman spectra of MLCT and LLCT excited states. A probe wavelength of 385 nm, in resonance with a (bpy•–)-localised absorption band, enables Raman bands assigned to bpy•– modes to be observed from both MLCT and LLCT states, with bands positions that are different between these two states. A probe wavelength of 500 nm, in resonance with a (R_2N•+)-localised absorption band, enables Raman bands assigned to the functionalised ligand L to be observed from the LLCT state. The observation of a characteristic TR^3 spectrum of the LLCT state of **1** indicates that cation ejection occurs on excitation of the metal-bound complex **1**-M^{n+}.

References

1. K Kalyanasundaram
J. Chem. Soc. Faraday Trans. 2, 82 2401, (1986)

2. M W George and J J Turner
Coord. Chem. Rev., 117 201, (1998)

3. J R Schoonover, C A Bignozzi and T J Meyer
Coord. Chem. Rev., 165 239, (1997)

4. K S Schanze and D B MacQueen
J. Am. Chem. Soc., 113 6108, (1991)

5. M Forster and R E Hester
J. Chem. Soc. Faraday Trans. 2, 77 1535, (1981)

6. W K Smothers and M S Wrighton
J. Am. Chem. Soc., 105 1067, (1983)

Photosensitization of Singlet Oxygen by Oxazole Yellow

E Tuite, F Dickinson

Department of Chemistry, Bedson Building, University of Newcastle, Newcastle upon Tyne, NE1 7RU, UK

I P Clark

Central Laser Facility, CLRC Rutherford Appleton Laboratory, Chilton, Didcot, Oxon, OX11 0QX, UK

Main contact email address: *e.m.tuite@ncl.c.uk*

Introduction

Asymmetric cyanine dyes were developed in the early '90s as highly sensitive fluorescent probes for DNA. However, in single molecule imaging studies it became clear that the dyes photonick the DNA backbone. Subsequent mechanistic studies demonstrated an unusually high double strand break yield[1]. The involvement of various reactive oxygen species, including singlet oxygen, in photosensitized DNA damage, as well as in photobleaching of the free and bound dyes was implicated by indirect scavenger studies and ESR spin trapping[2].

Our primary aim in these investigations was to confirm and quantify, by direct detection of its luminescence, the generation of $^1O_2$ by the excited states of YO-Pro-1 (**1**), YOYO-1 (**2**) and unmodified Oxazole Yellow (YO, **3**), both free in solution and when bound to DNA at different nucleotide/dye ratios (P/D). The dyes intercalate at P/D > 4, and beyond saturation also bind externally, either as monomers or stacked dimers.

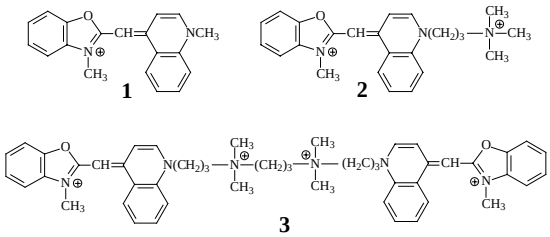

1 **2**

3

Experimental

The dyes were from Molecular Probes as solutions in DMSO, which was rigorously removed for these experiments. Emission was detected at 1270 nm at which energy only $^1O_2$ should emit. Excitation was at 489 nm (Coumarin 102 in MeOH pumped by an XeCl excimer laser at 308 nm) with pulse width ~14 ns and energy ~1 mJ. Detection was at 90° with a liquid N_2-cooled North Coast EO-817P fitted with a 1270 nm interference filter (30 nm FWHM). Typically, 32 traces were averaged. Solutions were prepared in D_2O with free dyes in pure solvent and dyes bound to $[poly(dA\text{-}dT)]_2$, $[poly(dG\text{-}dC)]_2$, or calf thymus (CT) DNA in D_2O buffered with 50 mM phosphate (pH 6.9). Samples were excited in quartz tubes (4 mm i.d.).

Results and Discussion

	ϕ_Δ (%)	k_q (M^{-1} s^{-1})
YO	1.7	2×10^7
YO-Pro-1	0.6	1×10^9
YOYO-1	2.4	6×10^6

Table 1. $^1O_2$ quantum yields and dye quenching constants.

Excitation of the YO dyes (~300 μM) at 489 nm produced luminescence at 1270 nm that decayed with a lifetime (~40 μs) substantially longer than the fluorescence of the dyes (~2 ns), although shorter than expected for $^1O_2$ in D_2O. Rose Bengal (RB) sensitization under the same conditions gave the expected lifetime of 62 ns. Therefore, YO dyes do produce $^1O_2$ but also appear to quench it. Scavenging experiments had implicated singlet oxygen in the photobleaching of YOYO-1 but radicals in the photobleaching of YO-Pro-1[2]. However, we found that $^1O_2$ is generated by both YO-Pro-1 and YOYO-1, although the quantum yield of $^1O_2$ production (Φ_Δ, estimated with respect to that of RB) is notably higher for the dimer (Table 1). These results suggest that YO-Pro-1 undergoes electron transfer with $^1O_2$ it has produced to generate superoxide which dismutates to hydroxyl radicals (in a Fenton cycle) that subsequently destroy the dye. In contrast, YOYO is apparently directly decomposed by a chemical reaction with the singlet oxygen it generates.

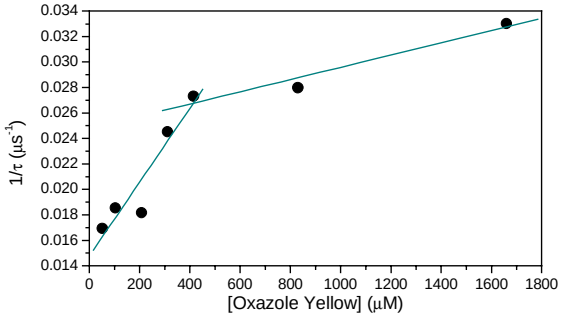

Figure 1. Quenching of the $^1O_2$ luminescence decay by YO.

The quenching of $^1O_2$ by the dyes was further investigated by measuring the luminescence as a function of YO concentration (Figure 1). Whilst the signal intensity increased with increasing dye concentration, the lifetime became shorter. Extrapolation of the decay rate to zero dye concentration gave a lifetime of 68 μs. Quenching was confirmed by independent observation of a reduced lifetime of RB-sensitized $^1O_2$ in the presence of YO-Pro-1 and YOYO (Table 1), similar to the effect of azide.

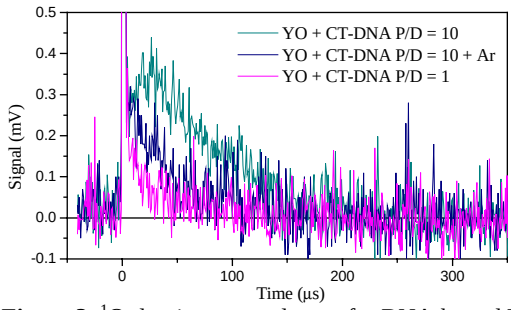

Figure 2. $^1O_2$ luminescence decays for DNA-bound YO.

Scavenger studies had also implicated $^1O_2$ in the highly efficient photocleavage caused by externally bound dye (P/D<4), whilst radicals were implicated in the low efficiency cleavage by intercalated dye. However, once again, singlet oxygen luminescence was detected under all conditions (Figure 2) for all dyes. Argon bubbling reduced the luminescence intensity, as expected. The shorter lifetime at P/D=1 is likely due to quenching by dye rather than DNA.

Clearly, excited state YO dyes can produce singlet oxygen both when free in solution and when bound to DNA. The nature and behaviour of the dye excited state (presumably the lowest triplet) involved remain to be clarified however.

References

1. B Akerman, E Tuite, Nucl. Acids Res., 24 1080, (1996).

2. C Kanony, B Akerman and E Tuite, J. Am. Chem. Soc., 123 7985, (2001).

Picosecond Studies of Ruthenium and Rhenium dipyridophenazine complexes in solution and when bound to polynucleotides

J M Kelly[a], C M Creely[b], M M Feeney[a], S Hudson[a], W J Blau[b]

[a]Department of Chemistry and [b]Department of Physics, University of Dublin, Trinity College, Dublin 2, Ireland

B Elias, A Kirsch-De Mesmaeker

Departement de Chimie Organique Physique, Universite Libre de Bruxelles, Brussels B-1050, Belgium

P Matousek, M Towrie, A W Parker

Central Laser Facility, CLRC Rutherford Appleton Laboratory, Chilton, Didcot, Oxon, OX11 0QX, UK

Main contact email address: *jmkelly@tcd.ie*

Introduction

Metal polypyridyl complexes are finding extensive uses both as photophysical probes and as photochemical reagents.[1)] For applications with DNA, dipyridophenazine (dppz) complexes have attracted special attention as the dppz ligand can intercalate between the base pairs of the polynucleotide. In particular $[Ru(phen)_2(dppz)]^{2+}$ (phen = 1,10-phenanthroline) has been studied in detail as the complex, which is essentially non-luminescent in water, becomes emissive when bound to DNA.[2)] The reasons for this behaviour have been elucidated by picosecond spectroscopy.[3)]

Another group of ruthenium complexes, which show interesting behaviour with DNA, are complexes such as $[Ru(TAP)_2(L)]^{2+}$, (TAP = 1,4,5,8-tetraazaphenanthrene; L = bpy, phen, TAP), because the electron accepting ability of the TAP ligand makes the excited states capable of oxidising guanine.

$$[Ru(TAP)_2(L)]^{2+*} + G \longrightarrow [Ru(TAP)_2(L)]^{+} + G^{\cdot+} \quad (1)$$

The initial electron transfer can lead to enhanced yield of strand breaks and to adduct formation.[4)] While direct evidence for electron transfer has been obtained with guanosine monophosphate,[5)] the process in DNA is too fast to measure using nanosecond methods and must occur on a picosecond time scale. A further disadvantage of complexes such as $[Ru(TAP)_2(phen)]^{2+}$ is that their mode of binding is uncertain. For this reason we have chosen to carry out a picosecond study of $[Ru(TAP)_2(dppz)]^{2+}$, which is expected to intercalate into DNA in a fashion similar to that of $[Ru(phen)_2(dppz)]^{2+}$, yet have an oxidizing power comparable to $[Ru(TAP)_2(phen)]^{2+}$.

To elucidate the specific interactions of the excited states of the complexes with DNA it is desirable to work with defined sequence DNA. As a first step we compare the transient absorption (TA) spectroscopy of the metal complexes when bound to the double-stranded synthetic polynucleotides $[poly(dG\text{-}dC)]_2$ and $[poly(dA\text{-}dT)]_2$. These experiments need to be carried out with small sample volumes (< 300 μL) and this was achieved by using a well-stirred solution in a $(5\ mm)^2$ quartz cuvette. Sample decomposition during the course of the experiment was found to be negligible.

$[Ru(TAP)_2(dppz)]^{2+}$ The absorption spectrum of the complex in aqueous buffer is shown in Figure 1. The complex shows a strong absorption in the region 400-500 nm, as expected for MLCT transitions. Interestingly the strong bands corresponding to the dppz (π-π*) intraligand transitions found for each of $[Ru(phen)_2(dppz)]^{2+}$, *fac*-$[(dppz)Re(CO)_3(py)]^{+}$ and the free ligand in the region 350 - 400 nm are not readily visible with this complex. The picosecond processes of the complex $[Ru(TAP)_2(dppz)]^{2+}$ in aqueous buffer and when intercalated into polynucleotides have been studied following transient absorption changes after excitation with a 400 fs pulse of 400 nm light. At this wavelength it is probable that the molecule will be excited partly to a dppz-localised (π-π*) excited state and partly to its MLCT states.

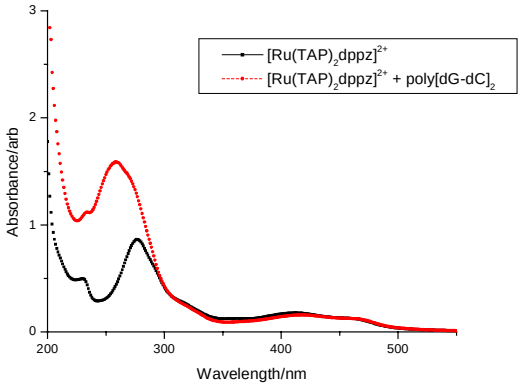

Figure 1. UV/visible absorption spectra of $[Ru(TAP)_2(dppz)]^{2+}$ (8×10^{-6} M) in (a) 10 mM phosphate buffer and (b) with the addition of $[poly(dG\text{-}dC)]_2$ (1.6×10^{-4} M nucleotide).

The transient spectra in aqueous buffer were recorded at intervals between 4 and 1500 ps after excitation. It was observed that there were substantial spectroscopic changes occurring only over the first 100 ps. Figure 2 shows the spectra at 4 ps, 100 ps and 1000 ps. The nature of this fast process (lifetime 43 ± 4 ps) is uncertain but it could involve conversion from an initially formed IL (π-π*) state to the lowest-lying MLCT excited state. The latter is very long-lived (1090 ns) and has been shown by transient resonance Raman spectroscopy (TR^3) to correspond to an excited state where the electron is located on one of the TAP ligands.[6)]

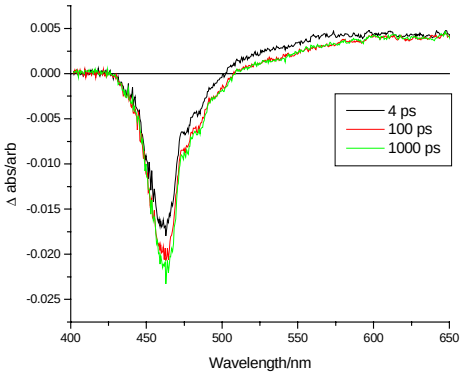

Figure 2. Transient absorption spectra observed at 4,100 and 1000 ps following laser excitation (400 fs; 400 nm) of $[Ru(TAP)_2(dppz)]^{2+}$ (8×10^{-5} M) in 10 mM phosphate buffer.

In the presence of $[poly(dA\text{-}dT)]_2$ a similar rapid partial decay of the absorption at ca. 520 nm is noted (lifetime 36 ± 8 ps).

By contrast, in the presence of $[poly(dG\text{-}dC)]_2$ a strong *increase* in absorption in this wavelength region is observed with a lifetime of 480 ± 40 ps. (Figure 3) This is consistent with the formation of $[Ru(TAP)_2(dppz)]^+$ through electron transfer from the guanine to the excited state. Similar results are obtained when the complex is intercalated into calf thymus DNA (GC content 42%) although the magnitude of the "grow-in" of the absorption is less.[6] The back electron transfer reaction is too slow to be measured with this equipment, proceeding with a lifetime greater than 1 ns.

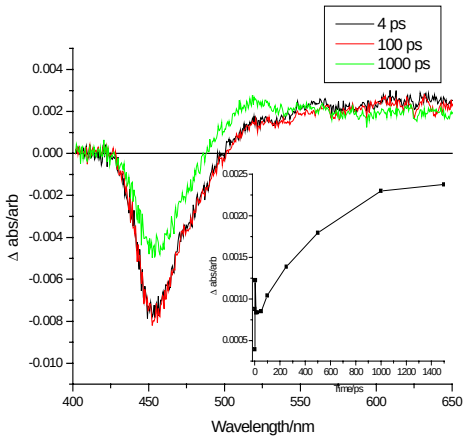

Figure 3. a) Transient absorption spectra observed at 4,100 and 1000 ps following laser excitation (400 fs; 400 nm) of $[Ru(TAP)_2(dppz)]^{2+}$ (8 x 10^{-5} M) in 10 mM phosphate buffer in the presence of $[poly(dG\text{-}dC)]_2$ (1.6 x 10^{-3} M nucleotide). Inset: Growth of absorption at 510 nm over 4 - 1000 ps.

The driving force for reaction (1) can be estimated knowing the reduction potential for the excited state $E^o([Ru(TAP)_2(dppz)]^{2+*}/[Ru(TAP)_2(dppz)]^+)$ (1.42 V) (vs NHE) [7] and the oxidation potential of guanine. However the value for the latter is still contentious. A value of ca. 1.33 V [8a] had been determined for guanosine. More recently the value for guanosine has been redetermined as 1.58 V [8b] and a value of 1.53 V for $[poly(dG\text{-}dC)]_2$ has been found to give a good fit for the electron transfer reactions of thionine and various polynucleotides.[9] It is clear therefore that reaction (1) is at best only weakly exergonic and the slowness of the back reaction is consistent with the predictions of Marcus theory.

***fac*-$[(R_2dppz)Re(CO)_3(py)]^+$**

(R = F, H, Me; py = pyridine). These complexes, which are expected to intercalate into DNA,[10] are attractive as DNA probes as they possess strong IR absorptions due to the CO stretch vibrations. Transient IR should be an effective means of determining the nature of the excited state {it is known that for similar dppz complexes the triplet dppz (π- π^*) and MLCT states lie close in energy[10]} and of identifying the species formed in redox reactions. As a preliminary to picosecond infrared transient absorption (PIRATE) measurements, we have carried out UV/vis TA studies. The derivatives have been selected as we anticipate that both the oxidising power and nature of the lowest excited state can be controlled by the electron-withdrawing or electron-donating properties of the substituent on the dppz ligand.

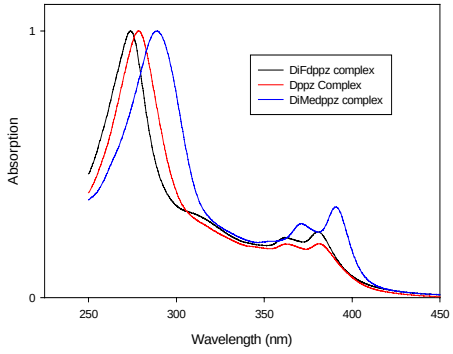

Figure 4. UV/visible absorption Spectra of *fac*-$[(R_2dppz)Re(CO)_3(py)]^+$, (R = F, H, Me) (1.7 x 10^{-4} M; 1.5 x 10^{-4} M and 1.7 x 10^{-4} M resp.) in acetonitrile solution.

The 350 – 400 nm section of the UV/Visible spectrum (Figure 4) of each of the compounds is dominated by the dppz (π-π^*) intraligand band, although a weaker MLCT transition also occurs in this wavelength range.

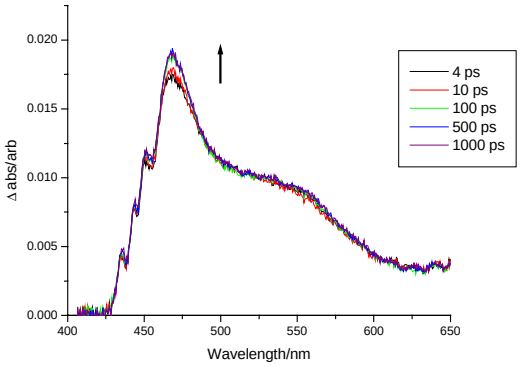

Figure 5. Transient absorption spectra observed at various delays following laser excitation (400 fs; 400 nm) of *fac*-$[(dppz)Re(CO)_3(py)]^+$ in acetonitrile solution.

Figure 5 shows the transient spectra observed after the laser excitation at 400 nm. At 4 ps a broad absorption with a maximum at 470 nm and a shoulder at ca. 540 nm is evident. An increase in intensity (ca. 5 %) at the maximum is then observed over the first 100 ps, with only very small changes occurring elsewhere. At 1000 ps the final spectrum is essentially identical to that reported by Schanze and coworkers[10] for *fac*-$[(dppz)Re(CO)_3(4\text{-}Mepy)]^+$ and is assigned to the ^{3}IL π-π*(dppz) excited state. The nature of the process occurring in the first 100 ps is still uncertain. Possibilities include (i) the conversion of an initially formed MLCT state to the π-π*(dppz) or (ii) the conversion from singlet to triplet state. It is interesting that PIRATE studies with this complex show vibrational cooling within its CO vibrations over this time range.[11] To further elucidate this phenomenon we have also studied the transient spectra of the free dppz ligand (Figure 6).

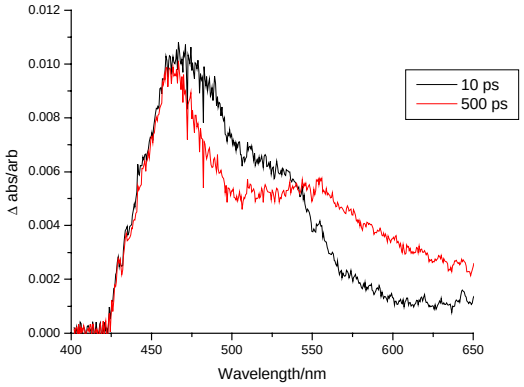

Figure 6. Transient absorption spectra observed at 10 and 500 ps following laser excitation (400 fs; 400 nm) of dppz in acetonitrile solution.

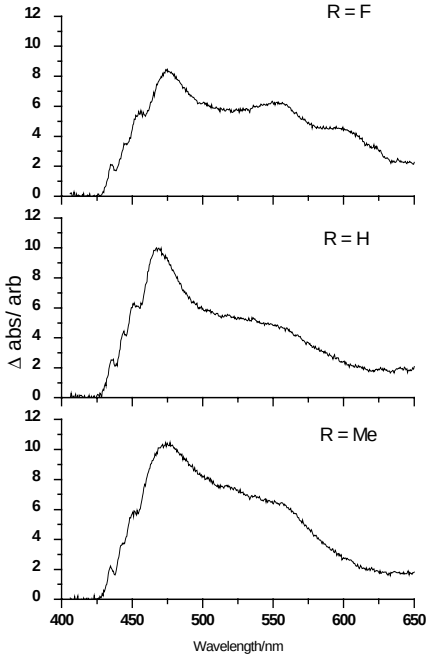

Figure 7. Transient absorption spectra observed 1000 ps following laser excitation (400 fs; 400 nm) of *fac*- $[(R_2dppz)Re(CO)_3(py)]^+$ (R = F, H, Me) in acetonitrile solution.

The initially formed species shows a broad maximum at 470 nm and a shoulder at ca. 530nm. This species converts (lifetime 63 ± 12 ps) to another, which possesses a narrower band at 460 nm and a better resolved peak at 550 nm. It is probable that these species are the singlet and triplet excited states of the heteroaromatic compound. While these spectra are both reasonably similar to those of that observed for *fac*-$[(dppz)Re(CO)_3(py)]^+$, it appears unlikely that the spectroscopic changes noted within the first 30 ps of excitation of the rhenium complex are due to singlet to triplet conversion.

Changing the electron density in the dppz ring might be expected to affect the relative energies of the MLCT and IL $\pi\rightarrow\pi^*$(dppz) excited states. As shown in Figure 7, while the spectrum of the *fac*-$[(Me_2dppz)Re(CO)_3(py)]^+$ is similar to that of the parent complex (the features being somewhat broader) the spectrum of the *fac*-$[(F_2dppz)Re(CO)_3(py)]^+$ shows a new feature at longer wavelengths. This might be due to the electron-withdrawing fluorine substituent causing a stabilisation of the MLCT state of the complex and PIRATE experiments are planned to verify this.

Finally we have studied the effect of solvent polarity and DNA binding on the TA spectra of *fac*-$[(dppz)Re(CO)_3(py)]^+$. It will be observed that change of the solvent from acetonitrile to water causes a significant red shift of the band maximum. There is only a very small decrease in intensity over 1000 ps. By contrast when the complex is bound to $[poly(dG\text{-}dC)]_2$ there is a substantial decrease in absorption over the first 100 ps. It may be speculated that this change is due to electron transfer from the guanine but if this is the case then the spectra of both the excited state and the reduced complex must be similar. It is hoped that this matter may be resolved by PIRATE measurements.

Summary

These UV/vis transient absorption experiments have revealed a rich range of photophysical properties and photochemical reactivity for these dppz complexes. A full elucidation will require the tools of transient vibrational spectroscopy. Our preliminary data have shown that it is possible to make both transient resonance Raman (TR^3) and PIRATE measurements

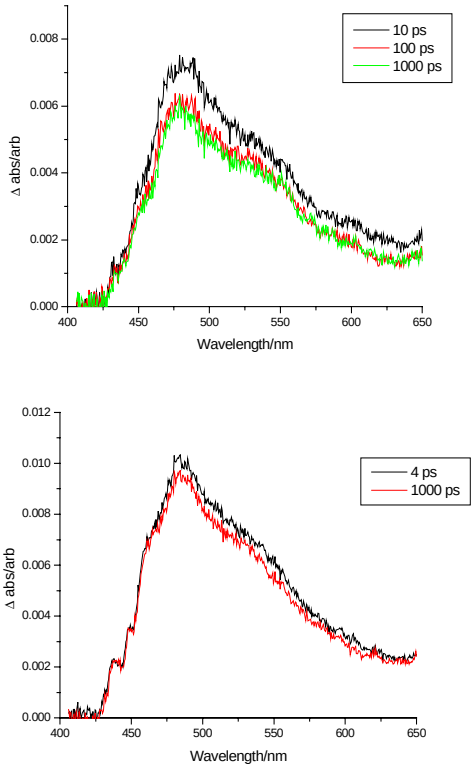

Figure 8. Transient absorption spectra observed at various delays after laser excitation (400 fs; 400 nm) of $[(dppz)Re(CO)_3(py)]^+$ (1.7×10^{-4} M) in (a) 10 mM phosphate buffer and (b) in the presence of $[poly(dG\text{-}dC)]_2$ (3.4×10^{-3} M nucleotide).

with the small quantities of solutions available. However in the case of TR^3 experiments our procedures will have to be refined, so as to prevent photo-degradation of the sample at the high laser pulse intensities necessary.

Acknowledgements

We greatly appreciate the close and ongoing collaboration with the teams of Dr. M. W. George (University of Nottingham) and Professor J.J. McGarvey (Queen's University Belfast). We thank the EUTMR programme (FMRX-CT98-0226) and HEA (PRTLI) for support.

References

1. C. Moucheron, A. Kirsch-De Mesmaeker and J.M. Kelly; Structure and Bonding 92 163-216, (1998)

2. (a)A.E. Friedman, J.C. Chambron, J.P. Sauvage, N.J. Turro, and J.K. Barton, J. Am. Chem. Soc. 112 4969,(1990) (b)C.H. Hiort, P. Lincoln and B. Norden; J. Am. Chem. Soc. 115 3448, (1993)

3. (a)E.J.C. Olson, D. Hu, A. Hoermann, A.M. Jonkman, M.R. Arkin, E.D.A. Stemp, J.K. Barton and P.F. Barbara, J. Am. Chem. Soc. 119 11458, (1997) (b)B. Onfelt, P. Lincoln, B. Norden, J.P. Baskin and A.H. Zewail, Proc. Natl. Acad. Sci. 97, 5708-5713, (2000) (c)C.G. Coates, J. Olofsson, M. Coletti, J.J. McGarvey, B. Onfelt, P. Lincoln, B. Norden, E. Tuite, P. Matousek, and A.W. Parker, J. Phys. Chem. 105 12653-12664, (2001)

4. L. Jaquet, R.J.H. Davies, A. Kirsch-De Mesmaeker and J.M. Kelly, J. Am. Chem. Soc. 119 11763-11768, (1997)

5. J.P. Lecomte, A. Kirsch-De Mesmaeker, M.M. Feeney and J.M. Kelly, Inorg. Chem, 34 6481-6491, (1995)

6. C.G. Coates, P. Callaghan, J.J. McGarvey, J.M. Kelly, L. Jacquet and A. Kirsch-De Mesmaeker, J. Mol. Struct. 598 15-25, (2001)

7. Ortmans, Ph.D. thesis, Universite Libre de Bruxelles, 1996

8. (a) S.V. Jovanovic and M.G. Simic, J. Phys. Chem. 90 974-978, (1986)
(b) S. Steenken and S.V. Jovanovich, J. Am. Chem. Soc. 119 617-618, (1997)

9. G.D. Reid, D.J. Whittaker, M.A. Day, D.A. Turton, V. Kayser, J.M. Kelly and G. S. Beddard, J. Am. Chem. Soc. 124 5518-5527, (2001)

10. H.D. Stoeffler, N.B. Thornton, S.L. Temkin and K.S. Schanze, J. Am. Chem. Soc. 117 7119-7128, (1995)

11. M.W. George, personal communication.

Infrared Ion Dip and Ultraviolet Spectroscopy of 4-Phenyl Imidazole, its Tautomer, 5-Phenyl Imidazole, and its Multiply Hydrated Clusters

F O Talbot, L C Snoek, N A Macleod, P Butz, J P Simons

Physical and Theoretical Chemistry Laboratory, South Parks Road, Oxford OX1 3QZ, UK

R T Kroemer

Molecular Modelling & Design, Discovery Research Oncology, Pharmacia, Viale Pasteur 10, 20114 Nerviano (MI) Italy

Main contact email address: *jpsimons@physchem.ox.ac.uk*

Introduction

In the amino acid, histidine, the presence of both >NH and >N: sites in the imidazole ring allows it to function both as a donor and an acceptor in a hydrogen-bonded environment. Its combined operation as an acceptor (from the hydroxyl group of a serine residue) and a donor (to the carboxylate ion in an aspartate residue) in the hydrogen-bonded triad sites is thought to play a crucial role in promoting the enzyme's catalytic activity[1]. To study the incidence and mechanism of proton transfer along water chains, a logical strategy for experimentalists, proposed by Leutwyler[2], includes three components: "the construction of a molecular 'scaffold' with defined proton injection and extraction sites (into and out of the water chain); a triggering event (typically photon absorption); and detection of the result of proton transfer (into or through the H-bonded chain)." Two recent studies of the electronic spectra of jet-cooled 4-phenyl imidazole (4PI), its singly hydrated complex, and its tautomer, 5-phenyl imidazole (5PI), conducted at intermediate[3] and high[4] resolution, represent the first step in this sequence. Using the LSF loan laser system to record their spectroscopic signatures, we came to the conclusion that 4PI is planar in its ground electronic state (S_0) but its tautomer, 5PI, is twisted about the inter-ring axis by 27°; in the S_1 state both tautomers become planar. Proton transfer between the two nitrogen sites would result in tautomeric inter-conversion between the 4- and 5-PI clusters.

Results

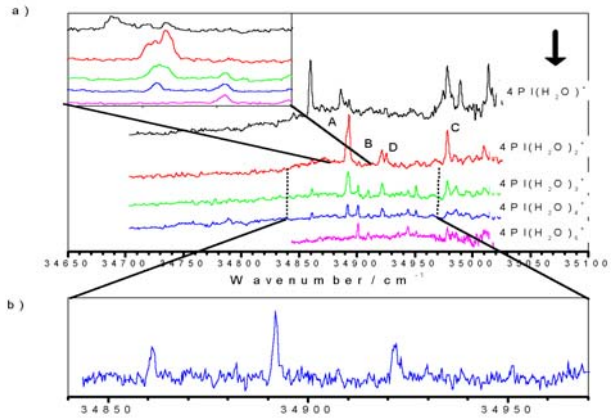

Figure 1. (a) One-colour-R2PI spectra recorded in the 4PI.$(H2O)_{n=1..4}$ mass channels, in the 34600-35100 cm^{-1} region. The arrow indicates the position of the monomer's band origin. (b) R2PI spectrum of the 4PI.(H2O)4 cluster, obtained by subtracting the spectrum recorded in the n=5 channel from that in the n=4 mass channel.

R2PI spectra of the hydrated clusters of 4PI, recorded in the mass channels, 4PI.$(H_2O)_{n=0-4}^+$, are shown in Figure 1. They display series of resolved vibronic bands in the region 34600-35100 cm^{-1} (~200 cm^{-1} to the red of the monomer's spectrum), associated with the $S_1 \leftarrow S_0$ transition. Many bands appear in more than one mass channel, reflecting the incidence of extensive cluster ion fragmentation. In order to establish their individual assignments unambiguously, their IR ion-dip spectra were recorded in all mass channels. Bands due to 4PI$(H_2O)_2$, 4PI$(H_2O)_3$, and 4PI$(H_2O)_4$ clusters all appear in the 4PI$(H_2O)_2^+$ mass channel and are labelled "A...D" in Figure 1.

4PI. The IR-UV ion dip spectra of the monomers of 4PI and 5PI display a single intense band associated with the ν(NH) stretching vibration, lying at 3514 cm^{-1} (4PI) and 3506 cm^{-1} (5PI) respectively, close to the liquid phase value[5] of ~3500 cm^{-1} (see Figure 2).

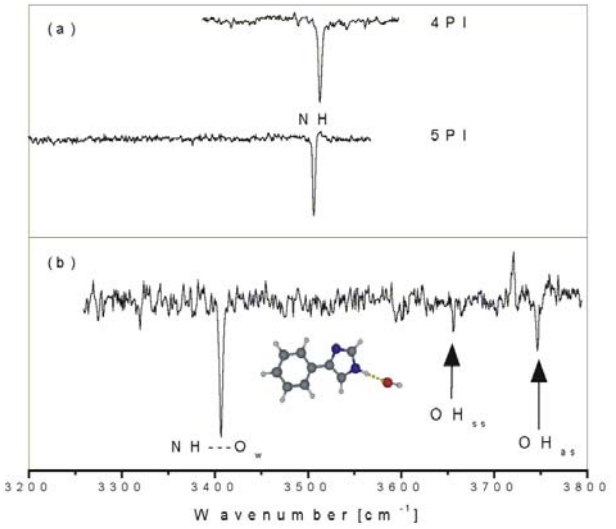

Figure 2. IR ion dip spectra of (a) 4PI and 5PI and (b) 4PI.(H2O).

4PI(H$_2$O). Only one mono-hydrated cluster (origin band at 34865 cm^{-1}) could be identified in the UV 'hole-burned' MS-R2PI spectrum recorded in the ion channel associated with 4PI$(H_2O)^+$. The corresponding IR ion dip spectrum (shown in Figure 2-b)) displays the 'free', symmetric and anti-symmetric stretches of the water molecule, lying at 3656 and 3747 cm^{-1}, respectively. The ν(NH) stretching band at 3409 cm^{-1}, is displaced by 104 cm^{-1} to the red of the monomer frequency. Such a shift clearly indicates an NH→O_{water} hydrogen bond, with the water molecule acting as an acceptor at the >NH site of the imidazole ring.

4PI(H$_2$O)$_2$. Only one band (band D at 34925 cm^{-1}) was associated with the doubly hydrated cluster. This was confirmed by its IR ion-dip spectrum (recorded in the 4PI$(H_2O)^+$ mass channel to minimise contamination from higher clusters) shown in Figure 3-a). The band at 3596 cm^{-1} is typical for an OH →π hydrogen bond. This clearly identifies the conformer as W2B' (shown in the Figure), which is the only structure showing a band in this region (at 3623 cm^{-1}). The NH frequency of the imidazole is now at 3317 cm^{-1}, further shifted to the red due to cooperativity in the NH →OH →OH →π daisy chain of H-bonds.

4PI(H$_2$O)$_3$. Two bands in the R2PI spectra (labelled A and C in Figure 1) were associated with the n=3 cluster. Band A is actually a composite band with three components at 34890, 34891 and 34893 cm^{-1} (see inset in Figure 1-a)). The central band (34891 cm^{-1}) appears in the n=2, 3 and 4 mass channels

and is associated with the n=4 cluster. The other two, which both generate the same IR spectrum, whether monitored in the n=2 or n=3 cluster ion channel, are associated with an n=3 cluster. The IR spectrum (see Figure 3-b)) recorded when monitoring the third band at 34893 cm^{-1}, clearly indicates its association with an n=3 cluster. The spectra recorded when monitoring band C were identical to those shown in Figure 3-b) and are not presented.

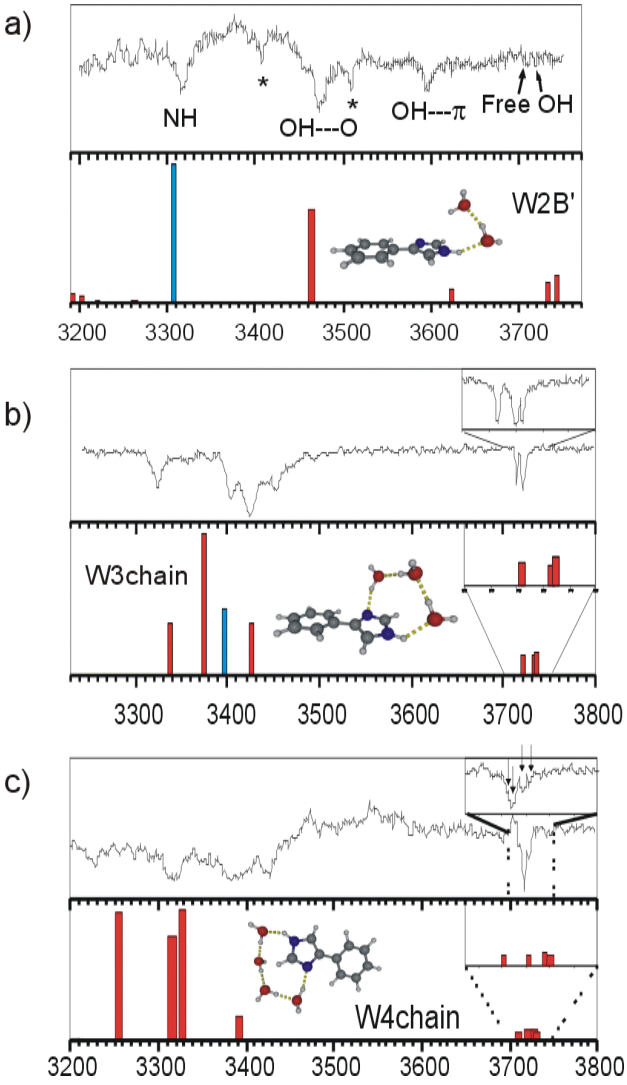

Figure 3. IR ion dip spectra of multiply hydrated clusters of 4PI.

As shown in Figure 3-b), the predicted frequencies of the most stable conformer (W3chain) give a very good match with the experimental band positions. A scan at higher resolution in the "free-OH" region clearly identifies three bands, confirming the assignment to the most stable conformer, "W3chain".

4PI(H_2O)$_4$. The UV R2PI spectrum of the n=4 cluster shows a progression of four bands reflecting the excitation of a low frequency mode, with a frequency ~30 cm^{-1}. This spectrum was obtained following subtraction of the n=5 spectrum from the one recorded in the n=4 channel and is shown as an inset in Figure 1. The IR ion-dip spectrum of 4PI(H_2O)$_4$, recorded when monitoring the most intense band of the progression (band A's central component at 34891 cm^{-1}), is shown in Figure 3-c); an identical spectrum was also recorded on the band at 34922 cm^{-1}. Four features appear in the 3400 cm^{-1} region, at 3226, 3317, 3387 and 3424 cm^{-1}, in good agreement with the ab initio calculations for conformer W4chain (the most stable calculated conformer) shown in Figure 3-c).

Conclusion

Clusters of 4-phenylimidazole with up to four water molecules have been investigated under supersonic expansion conditions. Their separately resolved IR/UV ion dip spectra, coupled with the results of ab initio calculations, have provided sufficient information to allow their individual structural assignment. In each case, the water molecules bind primarily to the NH site of the imidazole ring. The clusters with n≥2 form linear water chains, in which the proton donating terminus bridges either to the π-electron system (n=2) or to the >N: atom site (n=3,4) on the imidazole ring. Structures in which water molecules are *separately* bound at the >NH and >N: sites to provide a "donor-imidazole-acceptor" unit are not generated; the only way to form such a structure appears to be through a "water wire" bridge, benefiting from cooperative effects in the chain of hydrogen bonds. However, the resolved UV and IR spectra of the chain clusters (n=2...4) remain discrete, and provide no evidence of proton transfer either in the excited or in the ground electronic state of the clusters.

References

1. T.E.Creighton, Proteins, Structures and Molecular Properties, 2nd. Edition, W.H.Freeman and Company, New York, Ch. 9,(1997)
2. S.Coussan, M.Meuwly and S.Leutwyler, J.Chem.Phys., 114, 3524, (2001)
3. M.R. Hockridge, E.G. Robertson, J.P. Simons, Chem. Phys. Letters, 302, 538, (1999)
4. M.R. Hockridge, E.G. Robertson, J.P. Simons, D.R. Borst, T.M. Korter, D.W. Pratt, Chem. Phys. Letters, 334, 31, (2001)
5. H. Wolff, E. Wolff, Spectrochim. Acta, ,27A, 2109, (1971)

Towards an understanding of multiply hydrated tryptophan clusters in the gas phase

L C Snoek, N A Macleod, F O Talbot, P Butz, J P Simons

Physical and Theoretical Chemistry Laboratory, South Parks Road, Oxford OX1 3QZ, UK

R T Kroemer

Molecular Modelling & Design, Discovery Research Oncology, Pharmacia, Viale Pasteur 10, 20114 Nerviano (MI) Italy

Main contact email address: *jpsimons@physchem.ox.ac.uk*

Introduction

The preferred structures of amino acids, isolated in the gas phase, always appear to be neutral, *i.e.*, non *zwitter-ionic*. Even for the most basic isolated amino acid, arginine, which offers a strongly proton accepting guanidine side chain, both infrared[1)] and high level, *ab initio* computational data[2)] point to its preferred neutral structure(s).

In the condensed phase the situation is quite different: *zwitter-ionic* structures can be stabilised in ionic solids such as KBr, and in aqueous solutions over a wide range of pH. Comparisons between computational modelling and experimental vibrational, and circular diochroism (VCD) spectra (of L-alanine) suggest the operation of specific local interactions between *explicit* water molecules and the dissolved *zwitter-ions*, as well as with the more remote solvent environment[3)]. The optimised *ab initio* modelled structures of L-alanine also suggest a conformational reorganisation of the hydrated amino acid.

Experimental investigations of isolated, hydrated amino acid clusters are sparse. Peteanu and Levy[4)] reported in 1988, a resonant two photon ionisation (R2PI) spectrum associated with tryptophan-water cluster(s) generated in a free jet expansion, together with a corresponding time of flight mass spectrum which showed cluster ion signals in the Trp·$W_{1,2}^+$ and possibly, but very weakly, in the Trp·W_3^+ mass channels. Interpretation of the R2PI spectrum, which was recorded in the Trp·W_1^+ mass channel, was restricted by the multiplicity of potential binding sites and side chain conformations; with hindsight, the appearance of Trp·$W_{n>1}^+$ cluster ions, together with the possibility of extensive cluster ion fragmentation, might also cloud its assignment to singly hydrated cluster(s) only. A laser induced fluorescence (LIF) spectrum attributed to (singly) hydrated tryptophan clusters was also reported in the following year[5)].

The enormous advances in *ab initio* computational methods since Peteanu and Levy's pioneering work, together with recent success in assigning the low-lying conformational structures of phenylalanine[6)] and tryptophan[7)] in the gas phase, have set the scene for a new investigation of *neutral* (*i.e.*, non 'cationised') amino acid hydrate clusters, which can address the difficult issue of their structural assignment. Where are the preferred water binding sites in the singly and/or multiply hydrated clusters? What are their preferred amino acid side chain conformations and how do they depend upon the level of hydration? Can *zwitter-ionic* structures be stabilised in the gas phase, solely by hydration and can they be accessed under supersonic expansion conditions, and identified?

Methodology

The strategies employed to address these questions combine thermal evaporation, and also laser desorption of the amino acid into an expanding pulsed supersonic jet of moist argon, with mass-selected R2PI and ultraviolet hole-burning spectroscopy, infrared ion dip (RIDIR) spectroscopy, and crucially, the results of *ab initio* computation. The strategies are powerful and well established and although they have been severely tested by the present exploration, they have allowed a start to be made on answering at least some of the questions listed above and raised some interesting new ones.

Results and discussion

The results of an extended series of *ab initio* structural calculations for singly, doubly and triply hydrated clusters of tryptophan, exploring in particular their dependence on the method of calculation and on the size and composition of the basis sets employed, are presented elsewhere[8)].

The MS-R2PI spectrum of tryptophan and its hydrated clusters, generated through thermal evaporation into the pulsed argon expansion and recorded in the Trp·W_1^+ mass channel, is shown in Figure 1(a), together with a series of ultraviolet hole-burn spectra recorded in (b) the Trp^+ and (c) Trp·W_1^+ channels.

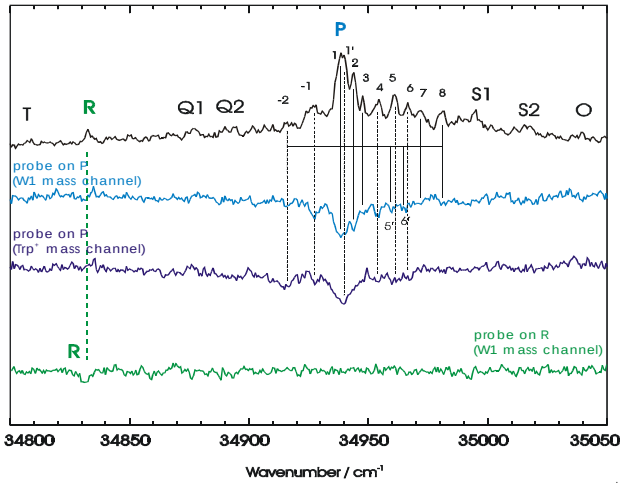

Figure 1. (a) R2PI spectrum of tryptophan in the Trp·$(H_2O)_1^+$ mass channel; UV-UV holeburn spectra of feature P in: (b) the Trp·$(H_2O)_1^+$ mass channel, and (c) the Trp^+ mass channel. (d) UV-UV holeburn spectrum of feature R in the Trp·$(H_2O)_1^+$ mass channel.

When the principal banded system P, which appears strongly in the R2PI spectrum (a), is compared with the hole-burn spectrum associated with the most intense feature labelled P1, the two band progressions do not quite coincide. System P appears to be a blend of *two* overlapping electronic band systems. When the hole-burn spectrum of band P1 is recorded in the Trp^+ monomer channel (c), the banded system is replaced by a broad feature, on the grounds of its infrared spectrum[8)] a previously unnoticed, resonant monomer conformer. None of the weaker features, T,Q,R,S, etc., is associated with system P, and can therefore be assigned to different carriers (e.g. band R in Figure 1(d)).

The infrared spectrum recorded in the Trp·W_1^+ mass channel, with the probe (ionisation) laser centred on peak P1, is shown in Figure 2 (black, central trace). It is a surprisingly rich spectrum, containing far more features than could be accommodated by an assignment to a single, singly hydrated tryptophan cluster:

1. at least two 'free' OH stretch modes around 3710-20 cm^{-1},
2. two weakly bound OH modes, around 3640-60 cm^{-1},
3. NH_{indole} at 3422 cm^{-1},and NH_{as} modes around 3400 cm^{-1},
4. strongly bound OH modes, associated with the broad bands around 3340, 3170 and 3070 cm^{-1}.

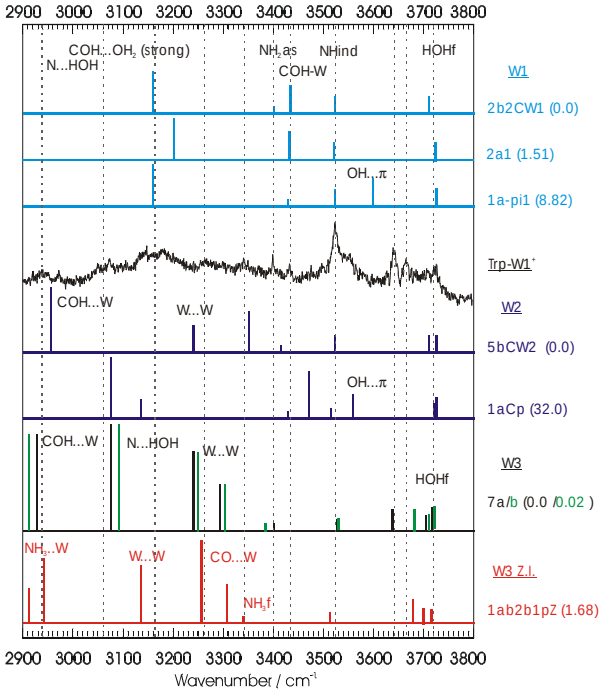

Figure 2. Central trace: IR-UV ion depletion spectrum recorded with the UV probe on band P in the Trp·$(H_2O)_1^+$ mass channel. In light blue, top: calculated IR-frequencies for the three lowest lying *singly hydrated* Trp structures. Dark blue: idem for the two most stable *doubly hydrated* Trp clusters. Bottom two traces: IR-frequencies of the three most stable *triply hydrated* Trp clusters (see Figure 3).

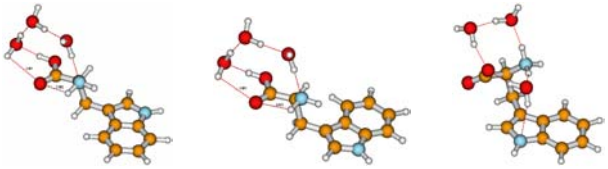

7b (0.0) **7a** (0.02) **1aZ** (1.68)

Figure 3. Geometries of the three most stable conformers of tryptophan·$(H_2O)_3$, optimized at the B3LYP/6-31+G(d) level of theory, with relative energies (MP2/6-311+G(d,p)) in kJ/mol.

How do the infrared frequencies observed in the Trp·W_1^+ cluster ion channel compare with those predicted *ab initio*? A careful analysis does not favour their assignment to either single or double hydrates, but does support their assignment to a pair of near-degenerate, *triply hydrated clusters*, in which the extended alanyl group accommodates a water trimer, that bridges both the C- and N-termini, and the (*syn*)carboxylic acid group itself. *The most stable monomer side group conformation predicted by theory –and supported by experiment– is altered by hydration.*

Laser ablation: a remarkable observation

Figure 4 shows the TOF mass spectra recorded (a) under thermal evaporation conditions on the R2PI band 'P', and in the continuum region near peak R under thermal (b), and under laser desorption conditions (c). While spectra (a) and (b) each show a comparable distribution of cluster population (Trp^+> Trp·W_1^+>Trp·W_2^+), the only hydrated cluster ion signal appearing during laser desorption (c) is in the Trp·W_3^+ channel. The appearance of a single, Trp·W_3^+ peak is remarkable, since it implies a uniquely stable cluster ion, either formed directly or through efficient fragmentation of larger clusters. This recalls a similar 'bottleneck' in the rate of fragmentation of Val·Li^+·W_3 clusters heated by black body infrared absorption, reported by Jockush *et al.*[9], which they associated with the generation of a stabilised *zwitterionic* amino acid structure. Perhaps the unique Trp·W_3^+ signal recorded under laser desorption conditions might also be associated with the generation of *zwitterionic* tryptophan clusters, which 'normally' remain inaccessible under the less energetic collision conditions associated with thermal evaporation. Encouraged by this observation and by the results of the *ab initio* computation, further infrared experiments are planned, to explore their possible association with triply hydrated *zwitterionic* structures, stabilised by hydration in the gas phase.

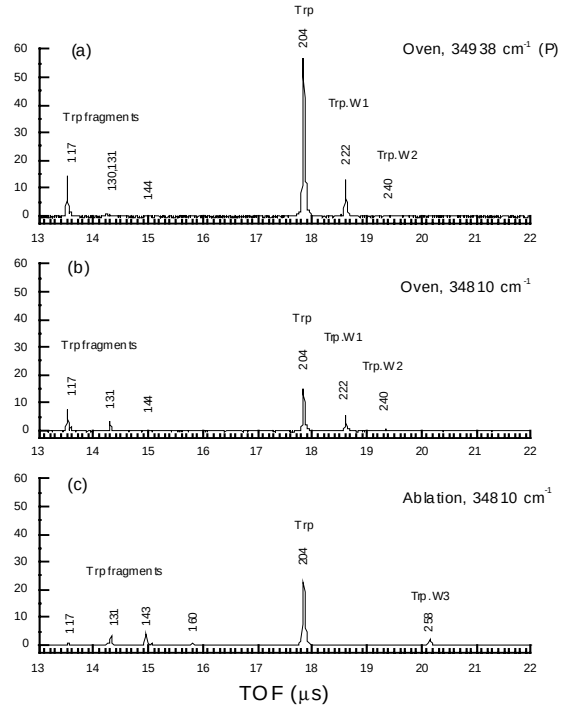

Figure 4. R2PI-TOF mass spectra recorded using (a) the oven at 200 °C and at the P band, (b) the same, but at 34810 cm^{-1}, (c) using laser desorption and the same wavelength as under (b).

Acknowledgements

We wish to thank the EPSRC for grant support (NAM) and a CASE studentship (GlaxoSmithKline: PB), the Dutch Ramsay Memorial Fellowship Trust (LCS) and the Leverhulme Trust for postdoctoral support (LCS, FOT). We also thank the Lasers for Science Facility at the Rutherford Appleton Laboratory for the loan of a YAG/dye laser combination.

References

1. C.J. Chapo, J.B. Paul, R.A. Provencal, K. Roth and R.J. Saykally, J.Amer.Chem.Soc., 120, 12956, (1998)
2. P. Skurski, M. Gutowski, R. Barrios and J. Simons, Chem.Phys.Lett., 327,143, (2001)
3. E. Tajkhorshid, K.J. Jalkanen and S. Suhai, J.Phys.Chem. B, 102, 5899, (1998)
4. L.A. Peteanu and D.H. Levy, J.Phys.Chem., 92, 6554, (1988)
5. C.K. Teh, J. Sipior and M. Sulkes, J.Phys.Chem., 93, 5393, (1989)
6. L.C. Snoek, E.G.Robertson, R.T. Kroemer and J.P. Simons, Chem.Phys.Lett., 321, 49, (2000)
7. L.C. Snoek, R.T. Kroemer, M.R. Hockridge and J.P. Simons, PCCP, 3, 1819. (2001)
8. L.C. Snoek, R.T. Kroemer and J.P. Simons, PCCP, 4, 2130, (2002)
9. R.A. Jockush, A.S. Lemoff and E.R. Williams, J.Phys.Chem. A, 105, 10929, (2001)

Rate Coefficients for the Transfer of OH($X^2\Pi_{3/2}$, v = 1, j) between Λ-Doublet and Rotational Levels in Collisions with He, Ar, N_2 and HNO_3

K M Hickson, C M Sadowski, I W M Smith

School of Chemical Sciences, The University of Birmingham, Edgbaston, Birmingham B15 2TT, UK

Main contact email address: *i.w.m.smith@bham.ac.uk*

Introduction

The dynamics of collisions involving diatomic free radicals with both S, the total spin quantum number, and Λ, the projection of the orbital angular momentum, greater than one are of great fundamental interest. As well as transfer between rotational levels, collisions can bring about changes in fine structure states (i.e. with different values of Ω) and between the Λ-doublets that are associated with each rotational level (j).

Because of its ease of handling and favourable spectroscopy, NO($X^2\Pi$) serves as a paradigm for such radicals and its collisional behaviour has been widely studied in both molecular beam and double resonance experiments, not least through experiments in our laboratory[1]. The hydroxyl radical, which is immensely important in a number of environments, especially the Earth's atmosphere, also has an $X^2\Pi$ electronic ground state but its collisional behaviour has received less attention. Unlike NO, OH radicals must be prepared *in situ*; here, we use photolysis of HNO_3 at 266nm. Although the $X^2\Pi$ states of OH and NO are similar in some respects, they also differ in several important ways: (i) the fine structure states of OH are inverted with Ω = $^3/_2$ below Ω = ½, (ii) the rotational levels in OH are much more widely spaced, on account of its much lower moment of inertia, and (iii) the Λ-doublet levels in OH are also more widely spaced. In addition to fundamental interest, it is important to understand the collisional behaviour of OH($X^2\Pi$) in regard to observations of OH in high rovibrational levels in the high atmosphere[2], and because of the OH astronomical maser for which the population inversion is apparently created in collisions[3].

Using an infrared-ultraviolet double resonance method, we have examined the transfer of OH($X^2\Pi$) radicals between rotational levels (j) and between the Λ-doublet levels (e/f) associated with individual rotational levels, in collisions with He, Ar, N_2 and HNO_3. These experiments employed three lasers: a frequency-quadrupled Nd:YAG laser to produce OH radicals by photolysis of HNO_3 at 266 nm; a difference-frequency mixing Continuum laser system from the RAL Laser Loan Pool to generate pulsed tuneable IR and promote some fraction of the OH radicals to a selected level in $X^2\Pi_{3/2}$, v = 1, and a frequency-doubled excimer-pumped dye laser to observe the fate of the excited sub-set of molecules by laser-induced fluorescence (LIF) in the $A^2\Sigma^+$–$X^2\Pi$(1,1) band. We report rate coefficients: (a) for transfer between the Λ-doublet levels associated with j = 3.5 and 6.5, and (b) for total transfer out of the rotational levels j = 1.5 and 3.5 — 8.5.

Experimental Method and Analysis

The principle of the IR-UV double resonance method is well-known.[1] Here, we largely report the results of *kinetic*, as distinct from *spectroscopic*, experiments. In these, the frequency of the tuneable UV probe laser is fixed and the LIF signal is recorded as the time delay between the pump and the probe laser is systematically varied. Such experiments yield information about the evolution of populations in the level being probed. The symmetry properties of the levels in the $A^2\Sigma^+$and $X^2\Pi$ states of OH are such that information about populations in *e* Λ-doublet levels of OH($X^2\Pi_{3/2}$, v = 1, j) is obtained by setting the frequency of the probe laser to coincide with an R- or P-branch, whilst measurements on Q-branch lines provides information about populations in *f* levels.

To obtain information about transfer between the Λ-doublet levels of j = 3.5 and 6.5, two traces of LIF signals *versus* time were recorded in quick succession. In each experiment, population in same Λ-doublet level was observed. However, the frequency of the pump laser was changed first to promote OH directly to the Λ-doublet level being observed and then to the other Λ-doublet level. It is straightforward to show that the variation of the *ratio* of signals with time then only depends on k_Λ^{1st}, the pseudo-first-order rate coefficient for transfer between the Λ-doublets. On the other hand, the *sum* of the populations depends only on k_{RET}^{1st}, the pseudo-first-order rate coefficient for removal of OH from this particular rotational level. In order to derive second-order rate coefficients (k_Λ^M and k_{RET}^M) for these processes, it was necessary to perform many experiments both on samples of pure HNO_3 and on mixtures of HNO_3 in another gas, He, Ar or N_2.

Results and Discussion

Derived values of the second-order rate coefficients, k_Λ^M, for transfer between the Λ-doublets associated with j = 3.5 and 6.5 in OH($X^2\Pi_{3/2}$, v = 1) are listed in Table 1.

	k_Λ / 10^{-10} cm^3 molecule^{-1} s^{-1}			
j	HNO_3	N_2	Ar	He
3.5	(24 ± 3)	(2.1 ± 0.3)	(0.5 ± 0.2)	—
6.5	(7.5 ± 0.9)	(1.1 ± 0.3)	(0.3 ± 0.1)	(0.1 ± 0.1)

Table 1. Rate coefficients (k_Λ / 10^{-10} cm^3 molecule^{-1} s^{-1}) for the transfer of OH radicals between Λ-doublets levels in the j = 3.5 and 6.5 rotational levels of the ($X^2\Pi_{3/2}$, v = 1) vibronic state.

The values of k_Λ^M depend strongly on collision partner and quite strongly on j. The large values of $k_\Lambda^{HNO_3}$ presumably reflect the large dipole-dipole forces between these collision partners. The larger values of k_Λ^M found for j = 3.5 compared with those for 6.5 probably reflect the changing degree of electron alignment associated with different Λ-doublets as j changes.

As already explained, for j = 3.5 and j = 6.5, it was possible to obtain values of k_{RET}^{1st} by plotting the sum of the two sets of LIF data *versus* time. For other levels, we fitted the signals from the Λ-doublet levels that were directly populated by absorption of radiation from the pump laser to an expression involving the sum of two exponentials. This procedure was tested by fitting the data for j = 3.5 and j = 6.5 both ways and found to be satisfactory. In Figure 1, we show the rate coefficients k_{RET}^M obtained for all four of the collision partners as a function of j, the initial rotational quantum number.

The difference between collision partners, i.e. $k_{RET}^{HNO_3} >> k_{RET}^{N_2} > k_{RET}^{Ar} \approx k_{RET}^{He}$ is not unexpected, in view of the strong dipole-dipole forces between OH and HNO_3, and results for NO with the other three collision partners. As with collisions of NO with He, Ar and N_2, the rate coefficients for total removal from a given rotational level is found to decrease as the rotational quantum number increases. It is likely that this is associated with the increasing energy gap between neighbouring levels as j increases. The data for rotational relaxation of lower j levels in collisions with He are in good

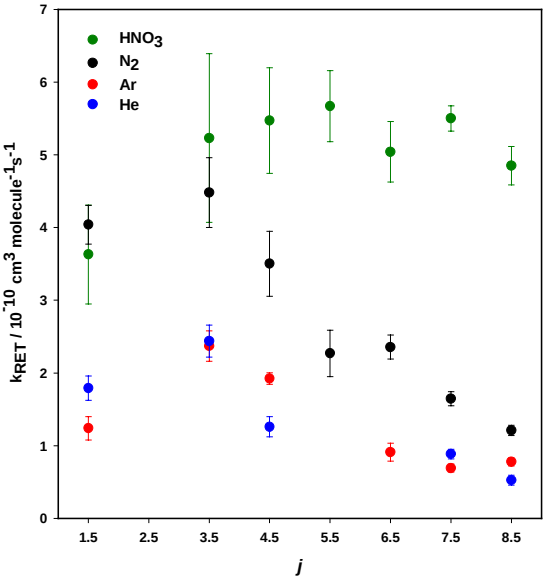

Figure 1. Second - order rate coefficients (k_{RET} / 10^{-10} cm^3 molecule^{-1} s^{-1}) for total transfer of OH($X^2\Pi_{3/2}$, v = 1, j) to other rotational levels

agreement with the *ab initio* calculations of Esposti et al[4]. In particular, the increase in k_{RET}^{Ar} and k_{RET}^{He} from j = 1.5 to 3.5 is reproduced and is presumably, in part, due to the fact that all transfers from j = 1.5 are necessarily endothermic.

Summary and Prognosis

The research reported here has added substantially to our knowledge of the collisional behaviour of OH($X^2\Pi$). It has led to two papers, one accepted for publication[5], one in the final stages of preparation[6]. The data on transfer between pairs of Λ-doublets associated with the same rotational level are the first of their kind and should stimulate further theoretical work. The results on rotational energy transfer constitute the most extensive data set yet for transfer from rotational levels in OH($X^2\Pi$).

Nevertheless, despite our successes, our measurements on collisions involving OH can be said to have only scratched the surface of what might, and indeed should, be done. Only lack of time has prevented us from measuring state-to-state rate coefficients, including in the definition of both initial and final states the Λ-doublet, as well as the rotational, level. Theory[4] suggests that there should be a strong dependence of state-to-state rate coefficients for rotational energy transfer on Λ-doublet level and this prediction needs to be checked by experiment. A second extension of the present work would be to obtain data on still higher j levels by decreasing the time delay between the pulses from the photolysis and pump lasers, in a manner similar to that used in experiments on NO in levels up to j = 40.5. Finally, it would be of great interest to extend our measurements to very low temperatures, just as we did for NO.[1(e)] Besides fundamental interest, such measurements should have great relevance to the mechanism of the OH astronomical maser.

At present, work is in progress on the behaviour of state-selected CN($X^2\Sigma^+$, v = 2, N) radicals in collisions with N_2 and C_2H_2. In N_2, collisions can only lead to rotational energy transfer and we find rate coefficients for total collisional loss that fall steeply from N = 0 to N = 57. With C_2H_2, collisions can lead to reaction or rotational energy transfer. By comparing the rate coefficients for *total* removal with the sum of state-to-state rate coefficients for rotational energy transfer, we expect to be able to obtain rate coefficients for reaction of CN in specific rotational levels with C_2H_2. Measurements on CN($X^2\Sigma^+$, v = 2, N = 0) have demonstrated that this approach is possible. We expect to report exciting and unique results on this system in the next CLF Annual Report.

References

1. M. J. Frost, M. Islam and I. W. M. Smith Can. J. Chem., 1994, 72, 606 (b) M. Islam, I. W. M. Smith and J. W. Wiebrecht J. Phys. Chem., 1994, 98, 9285 (c) M. Islam, I. W. M. Smith and J. W. WiebrechtJ. Chem. Phys., 1995, 103, 9676 (d) P. L.James, I. R. Sims and I. W. M. Smith Chem. Phys. Lett., 1997, 272,412 (e) P. L. James, I. R. Sims, I. W. M. Smith, M. H. Alexanderand M. Yang J. Chem. Phys., 1998, 109, 3882 (f) M. Islam, I. W.M. Smith and M. H. Alexander Chem. Phys. Lett., 1999, 305, 311(g) M. Islam, I. W. M. Smith and M. H. Alexander Phys. Chem. Chem. Phys., 2000, 2, 473

2. K. W. Holtzclaw, B. L. Upschulte, G. E. Caledonia, J. F. Croni, B. D. Green, S. J. Lipson, W. A. M. Blumberg and J. A. Dodd J. Geophys. Res. 1997, 102A, 4521

3. (a) M. J. Reid and J. M. Moran Ann. Rev. Astron. Astrophys., 1981, 19, 231
(b) M. Elitzur Rev. Mod. Phys., 1982, 54, 1225
(c) J. J. ter Meulin Molecules in Astrophysics: Probes and Processes, IAU Sympos. 178, ed. E. F. van Dishoeck, (Kluwer, Dordrecht, 1997) p. 241

4. A. D. Esposti, A. Berning and H.-J. Werner J. Chem. Phys., 1995, 103, 2067

5. K. M. Hickson, C. M. Sadowski and I. W. M. Smith J. Phys. Chem A, 2002, in press.

6. K. M. Hickson, C. M. Sadowski and I. W. M. Smith Phys. Chem Chem. Phys., 2002, in preparation.

Reaction of O(^{3}P) with vibrationally excited methane

H Kelso, F Ausfelder, D A Henderson, K G McKendrick

Department of Chemistry, Heriot-Watt University, Edinburgh, EH14 4AS

Main contact email address: *k.g.mckendrick@hw.ac.uk*

Introduction

A key aim in the field of chemical reaction dynamics is to establish the critical motions of individual atoms and groups during a chemical process. The specific objective of this study was to advance such knowledge for the reaction

$$O(^3P) + CH_4 \rightarrow OH + CH_3 \qquad (1)$$

by investigating the effects of *selectively vibrationally exciting the CH_4 reactant.*

Reaction (1) is the parent member of the important general category of hydrogen abstraction by ground state oxygen, O(^{3}P), from a saturated hydrocarbon. These reactions are of considerable practical importance in the combustion of hydrocarbon fuels. Consequently, they have been subjected to numerous conventional kinetic measurements. They exhibit significant activation barriers, with a magnitude that scales as expected with the enthalpy of reaction. This in turn depends on the type of C-H bond attacked.

These energetic factors have important consequences for the investigation of the dynamics of the reactions. They have small reaction cross-sections and require relatively high collision energies for vibrational ground state reactants. Early, ground-breaking dynamical work by Andresen and Luntz[1)] was based on microwave-discharge generation of O(^{3}P). They examined a series of representative primary, secondary and tertiary hydrocarbons, but, significantly, not the parent compound, CH_4. Its behaviour was not established experimentally until the development of laser-photolytic methods for O(^{3}P) production.[2,3)] The existing experimental work has recently been reviewed in some detail.[4)] The most characteristic feature of the reactions is the very low level of rotational energy release. This has been interpreted as a tight constraint to collinearity during a direct abstraction reaction in which the incoming O(^{3}P) atom interacts with only one H-C bond.

Theoretical interest in the dynamics of these reactions, and in particular the parent reaction (1), dates to a similar period to the first experimental work. The early *ab initio* calculations confirmed the collinear saddle point geometry inferred experimentally[5)] . There has been a substantial revitalisation of theoretical interest in these systems recently. This has been driven not only by the obvious increases in available computational power but also by development of refined approximate algorithms for multidimensional quantum scattering calculations.[6,7)] Of particular relevance to this study is the clear prediction of substantial and specific enhancement of reactivity due to vibrational excitation of the CH_4. Testing these predictions was the aim of the current work.

To provide a method of validating our experimental approach, and to allow any enhancement of reactivity for reaction (1) to be calibrated in a relative fashion, we have also carried out parallel measurements on the closely related system

$$O(^3P) + HCl \rightarrow OH + Cl \qquad (2)$$

Reaction (2) is known experimentally to be substantially enhanced by IR overtone excitation of HCl(v=2),[8)] reproduced in extensive supporting *ab initio* work.

Experimental

The experimental method was based on three independent pulsed laser sources, and is indicated schematically in Figure 1. A fixed wavelength, relatively high power Nd:YAG photolysis laser was used to generate O(^{3}P) by photolysing NO_2 at either 266 or 355 nm. Tunable IR pulses were generated by difference frequency mixing the fundamental output of a second Nd:YAG laser and the dye laser which it pumped [system provided from the LSF Loan Pool]. This radiation state-selectively vibrationally excited the molecular reactant CH_4 or HCl. IR pulse energies were typically around 1 mJ at ~3,000 cm^{-1} and 4 mJ at ~6,000 cm^{-1}. A final Nd:YAG pumped dye laser system provided the tunable UV pulses which were used to detect any OH produced in the reaction by laser-induced fluorescence (LIF) on the well-known A-X bands around 300 nm.

The gases were confined in a custom-built stainless steel vacuum chamber. Originally, we had intended to introduce a mixture of the NO_2 precursor and CH_4 or HCl reactant through a pulsed molecular beam valve. This would have had advantages of higher instantaneous number density and of rotationally cooling the molecular reactant. This would increase the efficiency of the vibrational pumping process by reducing the spread of population over rotational levels of the vibrational ground state. However, in practice we discovered during the course of this work that photolysis of jet-cooled NO_2 was an efficient source of electronically excited O(^{1}D), presumably due to the high N_2O_4 concentrations present. The O(^{1}D) produces characteristically highly rotationally excited OH from the reaction with CH_4, masking any desired products from the much less efficient O(^{3}P) reactions. Therefore, we reverted to introducing the gases as bulk mixtures at pressures typically in the range 100-500 mTorr. It was then important to establish that the path through which the IR pump radiation passed before

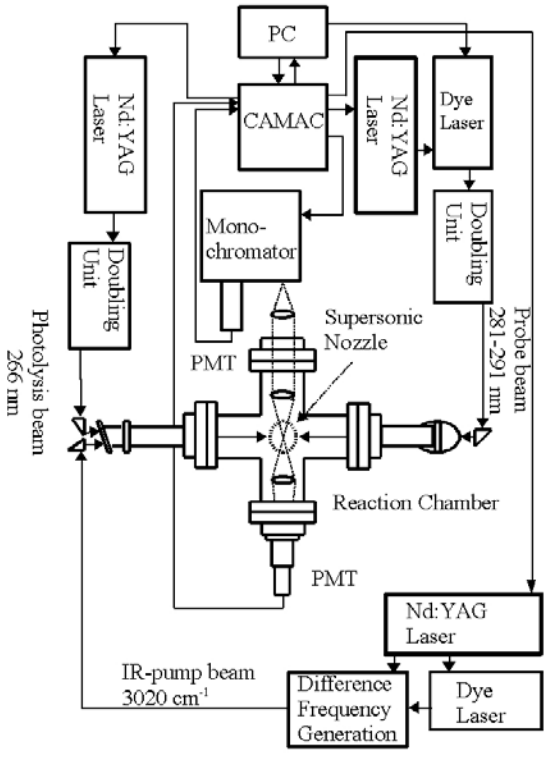

Figure 1. Schematic of experimental apparatus.

reaching the observation zone in the centre of the chamber was not optically dense. This was verified by placing an optoacoustic cell, containing either CH_4 or HCl buffered by a moderate pressure of Ar, in the exit beam path (not shown in Figure 1). The optoacoustic signal was reduced by less than 25%, due to the presence of the gas in the reaction chamber, even for the strongest transitions. The optoacoustic cell also provided a very useful method of ensuring that the IR laser remained tuned exactly in resonance with the molecular transition of interest during the primary measurements of IR enhancement of OH production.

The OH LIF signals were detected by a photomultiplier tube and captured by an electronic data collection system. This allowed active control of the firing of the three lasers, providing in particular a method of shotwise subtraction of signals with the IR laser effectively either on or off.

Results

$O(^3P) + CH_4$

The initial series of experiments involved pumping the CH_4 ν_3 fundamental stretch in the region of 3,000 cm^{-1}. The IR laser was tuned to the strongest feature in the Q-branch bandhead.[9] NO_2 was photolysed at 266 nm to provide relatively translationally hot $O(^3P)$ atoms.[3] Typical total pressures were up to 500 mTorr, made up of equal amounts of NO_2 and CH_4. OH LIF excitation spectra were recorded at a variety of delays between photolysis and probe lasers between 100 ns and 20 µs, with the IR pump laser firing simultaneously with the photolysis laser on alternate shots.

Representative LIF spectra for OH(v'=0) are shown in Figure 2. The photolysis + pump to probe delay was in this case 500 ns. The upper trace is the OH A-X(1,0) excitation spectrum with the IR laser firing simultaneously with the photolysis laser. The middle trace is the result without the IR pump laser. The lower trace shows the subtraction of the two on the same vertical scale, and should reveal any enhancement due to vibrational

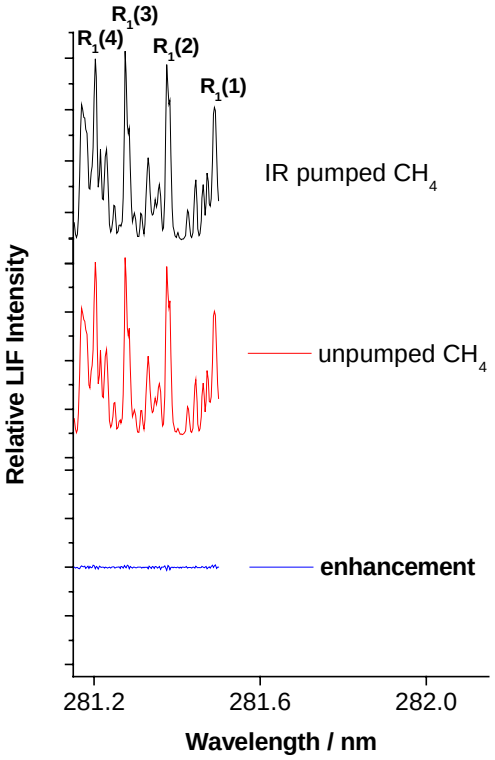

Figure 2. OH(1,0) LIF excitation spectra from the reaction $O(^3P) + CH_4$. IR pumping of ν_3 stretch Q-head at 3,108 cm^{-1}. NO_2 photolysis at 266 nm. Photolysis + pump to probe delay of 500 ns. Pressure 500 mTorr.

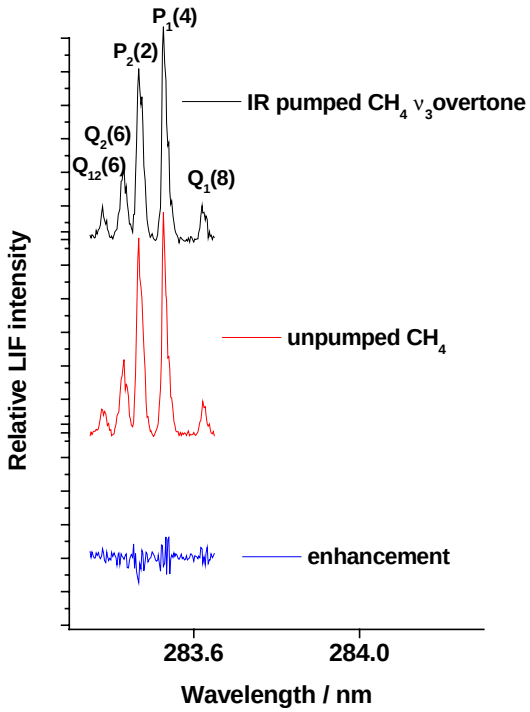

Figure 3. OH(1,0) LIF excitation spectra from $O(^3P) + CH_4$. IR pumping of ν_3 overtone feature at 6,000 cm^{-1}. NO_2 photolysis at 355 nm. Delay of 5 µs. Pressure 500 mTorr.

excitation of the CH_4. As is obvious, there is no discernible increase in OH(v'=0) production within the excellent signal-to-noise ratio.

A similar lack of enhanced OH(v'=1) production was observed when pumping the CH_4 ν_3 fundamental, above a much smaller baseline because reaction of vibrational ground state CH_4 produces very little OH(v'=1).[2,3] More limited measurements made in the vicinity of the combination band at 4,300 cm^{-1} also failed to reveal a positive enhancement.

A more comprehensive set of measurements was made for pumping the strongest feature in the region of the ν_3 overtone around 6,000 cm^{-1}. This was examined more extensively because it provides the closest comparison with HCl overtone pumping (see below). The NO_2 photolysis wavelength was increased to 355 nm to match the conditions under which an enhancement for the O + HCl reaction was known to have been observed previously.[8] Corresponding LIF excitation spectra for OH(v'=0) production for CH_4 ν_3 overtone region pumping are shown in Figure 3. A longer photolysis + pump to probe delay of 5 µs has been selected in this case to illustrate the signal-to-noise level that can be achieved for increased reaction times, at the expense of observing near nascent rotational distributions. However, once again there is no significant increase in OH production due to IR pumping. A similar lack of a clear effect was found for OH(v'=1).

$O(^3P) + HCl$

In marked contrast to all the results above for CH_4, we were readily able to detect substantial enhancement of OH production through overtone pumping of HCl around 5,700 cm^{-1}. As an example, the growth of the OH(v'=0) signal as a function of probe delay following simultaneous photolysis + pump is illustrated in Figure 4. This shows the expected build up with time characteristic of a bimolecular process, and also the rotational relaxation towards a thermalised rotational distribution from the hotter nascent distribution at shorter delays. The subtraction process of the un-pumped from the pumped reaction for OH(v'=1) at fixed delay of 5 µs is shown in

Figure 5. Unlike the corresponding CH_4 results in Figures 1-3, the enhanced signal due to IR pumping is unmistakable and easily outweighs that present from the unpumped reaction.

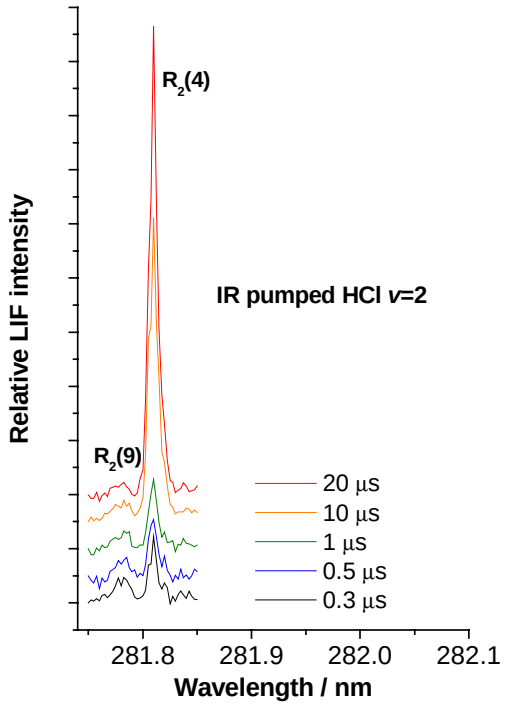

Figure 4. OH(1,0) LIF excitation spectra as a function of photolysis + IR pump to probe delay for the reaction $O(^3P)$ + HCl. $H^{35}Cl$ pumped on R(3) of overtone at 5,720 cm^{-1}. NO_2 photolysis at 355 nm. Pressure 500 mTorr.

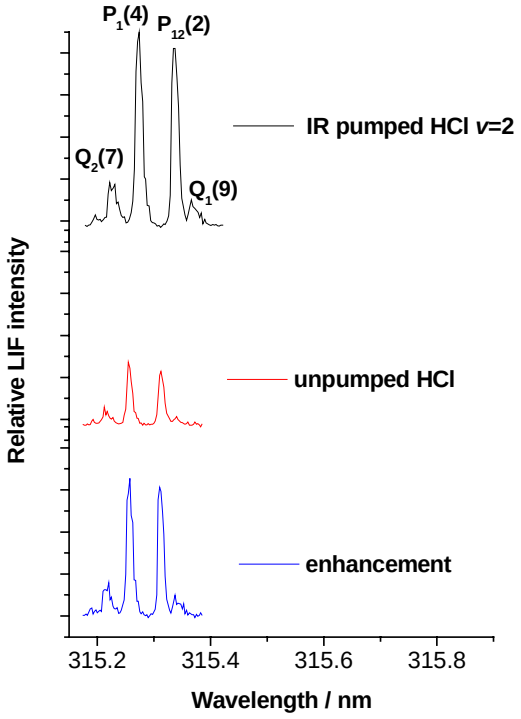

Figure 5. OH(1,1) LIF excitation spectra from reaction $O(^3P)$ + HCl. $H^{35}Cl$ pumped on R(3) of overtone at 5,720 cm^{-1}. Photolysis + pump to probe delay 5 µs. NO_2 photolysis at 355 nm. Pressure 300 mTorr.

Discussion

Our principal observation is that IR pumping of CH_4 does not produce any enhanced OH production from the $O(^3P)$ + CH_4 reaction above the level of our limiting signal-to-noise. This is the case for pumping either the ν_3 fundamental stretch at 3,000 cm^{-1}, the strongest feature in the overtone region around 6,000 cm^{-1}, or, less fully investigated, the combination band near 4,300 cm^{-1}. Production of both OH(v'=0) and (v'=1) were investigated and are equally unaffected.

This behaviour is in marked contrast to $O(^3P)$ + HCl, where we readily observe that overtone pumping of HCl(v'=2) produces substantially increased production of both OH(v'=0) and (v'=1), in line with previous independent observations.[8] This will allow us to make a direct relative comparison between the reactivity of CH_4 and HCl containing similar amounts of vibrational energy. One factor which clearly favours the observation of an effect for $O(^3P)$ + HCl is the approximately order of magnitude stronger IR absorption for the HCl overtone than for the CH_4 $\nu_3$overtone.[9] We will take this into account in a future quantitative analysis of the relative reactivities of the pumped molecules.

We will also compare this qualitatively surprising result with the quantitative predictions of reduced-dimensional quantum scattering calculations.[6,7] This requires the predicted excitation functions to be averaged over the experimental collisional energy distributions. The fraction of the sample excited by the IR pump laser must also be estimated from the known absorption strengths and the experimental pulse energies.

When fully analysed these results will provide the first experimental information on the effects of vibrational excitation for this important elementary reaction and provide a new test of the current understanding of its mechanism.

References

1. P. Andresen and A. C. Luntz, J. Chem. Phys., 72, 5842, (1980).

2. G. M. Sweeney, A. Watson, K. G. McKendrick, J. Chem. Phys., 106, 9172, (1997).

3. F. Ausfelder, H. Kelso and K. G. McKendrick, Phys. Chem. Chem. Phys., 4, 473, (2002).

4. F. Ausfelder and K. G. McKendrick, Prog. React. Kinet. Mech., 25, 299, (2000).

5. S. P. Walch and T. H. Dunning, Jr., J. Chem. Phys., 72, 3221, (1980).

6. D. C. Clary, Phys. Chem. Chem. Phys., 1, 1173, (1999); J. Palma and D. C. Clary, J. Chem. Phys., 112, 1859, (2000); J. Palma and D. C. Clary, Phys. Chem. Chem. Phys., 2, 4105; J. Palma and D. C. Clary, J. Chem. Phys., 115, 2188, (2001).

7. H.-G. Yu and G. Nyman, J. Chem. Phys., 112, 238, (2000).

8. D. J. Rakestraw, K. G. McKendrick and R. N. Zare, J. Chem. Phys., 87, 7341, (1987); R. Zhang, W. J. van der Zande, M. J. Bronikowski and R. N. Zare, J. Chem. Phys., 94, 2704, (1991).

9. HITRAN96, L. S. Rothman et al., JQRST, 60, 665, (1998).

Molecular Young's slits: Interference effects in the UV photodissociation of hydrogen peroxide

A J Alexander

Department of Chemistry, University of Edinburgh, West Mains Road, Edinburgh, EH9 3JJ

Main contact email address: *andrew.alexander@ed.ac.uk*

Introduction

The directional properties of angular momentum have been widely used as a means to understanding the processes that occur when molecules dissociate or are ionised[1]. More recently there has been a surge of interest in measurements of interference between angular momentum states arising from multiple pathways in molecular photodissociation[2]. However, most experimental studies to-date have been limited to measurements of coherent alignment or orientation of atomic photofragments.

The present work demonstrates the first measurement of electronic orientation of a diatomic fragment OH($^2\Pi$) resulting from the ultraviolet photolysis of H_2O_2 at wavelengths 330 to 370 nm. The results show a strong coherent orientation of OH fragments, resulting from dissociation via multiple electronic states.

Experimental setup

60% w/v aqueous hydrogen peroxide was gently distilled under vacuum and stored in a glass bulb. The vapour was constantly flowed through a PTFE coated stainless steel reaction cell at a constant pressure below 100 mTorr.

The second harmonic (532 nm) output from a Surelite Continuum III-10 YAG laser was used to pump two dye lasers. Tunable photolysis radiation in the range 330 – 370 nm was obtained from the doubled output of a Continuum ND6000 dye laser. The probe radiation was obtained from a Sirah dye laser (GS-R-2400), which was doubled to approximately 308 nm.

Both laser pulses were circularly polarised using zero-order quartz quarter waveplates. The polarisation of the probe pulse was flipped between left (LCP) or right (RCP) circularly polarised light on a shot-to-shot basis by synchronizing the laser to the stress cycle of a fused-silica photoeleastic modulator (Hinds PEM-90D). The probe pulse was temporally delayed (~10 ns) from the photolysis pulse, and the pulses were spatially overlapped at the centre of the reaction cell. Following absorption of the photolysis radiation, the H_2O_2 molecules dissociate, and the resulting OH radicals are detected by the probe pulse, using (1+1) laser-induced fluorescence (LIF), collecting the fluorescence without polarisation analysis.

Doppler lineshapes D(ν) were obtained by scanning the probe laser wavelength over individual rotational lines in the (0,0) band of the A–X electronic transition. Composite sum and difference profiles $D_{iso}(\nu) = D_{LCP}(\nu) + D_{RCP}(\nu)$ (independent of product orientation), and $D_{aniso}(\nu) = D_{LCP}(\nu) - D_{RCP}(\nu)$ (depends only on product orientation) were fitted by Monte Carlo simulations to obtain the degree of orientation of the OH molecules.

Results

The photodissociation of H_2O_2 at around 350 nm is known to proceed via at least two electronic states of different symmetry: these are believed to be the $\tilde{A}\,^1$A(perpendicular ⊥) and the $\tilde{B}\,^1$B(parallel ||) states[3]. The distribution of directions of the OH molecule products in the laboratory frame can be parameterised by the so-called beta parameter (β):

with $D(\theta)$ the angular distribution of the velocity vector of the products in the laboratory frame, and P_2 the second Legendre polynomial:

$$D(\theta) = 1 + \beta P_2(\cos\theta) \qquad (1)$$

The limits of β = +2 and –1 indicate || and ⊥ transitions respectively. Figure 1 shows that at ~250 nm the dissociation is mostly via the $\tilde{A}$ state, with an increasing contribution from the $\tilde{B}$ state at longer wavelengths. As can be seen from Figure 1, the β for dissociation of Cl_2 are very similar to those of H_2O_2, suggesting that the molecules are very similar electronically, and this is borne out by the orientation results below.

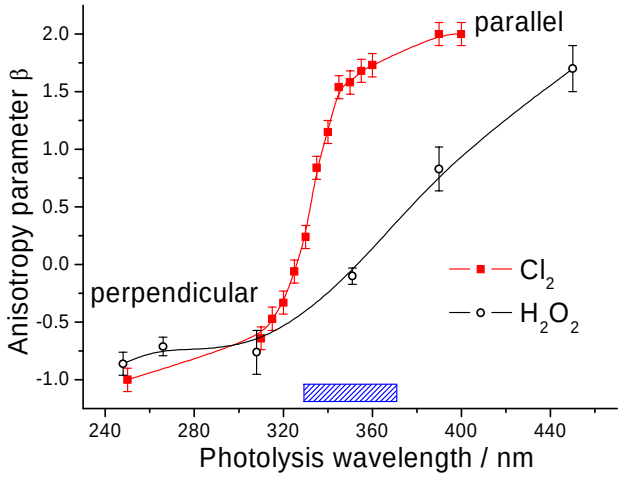

Figure 1. Anisotropy parameter (β) for H_2O_2 and Cl_2 as taken from References 3 and 4. The shaded bar indicates the wavelength range of the present study.

Composite profiles $D_{aniso}(\nu)$ show that the OH molecules are oriented in the laboratory frame. The orientation of the angular momentum of the OH molecules in the laboratory frame (A_{10}) can be written in terms of molecule frame orientation parameter $a_{1Q}(p)$:

$$A_{10}(\theta,\phi) = (1+\beta)a_{10}(\perp)\cos^2\theta + \tfrac{1}{2}a_{11+}(\|,\perp)\sin^2\theta \qquad (2)$$

In Equation 2, the $a_{10}(\perp)$ represents an incoherent orientation parameter that arises solely from dissociation via the $\tilde{A}$ (⊥) state, and $a_{11+}(\|,\perp)$ represents coherent orientation that results from interference between || and ⊥ transitions. By using Equation 2 to model the $D_{aniso}(\nu)$ composite profiles, we can determine the coherent molecule frame contributions to the total orientation.

The contribution due to the coherent $a_{11+}(\|,\perp)$ measured for the J = 0.5 state of OH, using the $^PQ_{12}(N = 1)$ rotational line in the OH LIF spectrum is shown in Figure 2. The coherent orientation is nearly zero at 330 nm and increases at longer wavelengths. The trend closely follows the results for β shown in Figure 1. If the observed $a_{11+}(\|,\perp)$ results from interference between multiple states, we would expect the following relationship to hold:

$$a_{11+}(\|,\perp) \propto \sqrt{(1+\beta)(2-\beta)}\cos\Delta\phi \qquad (3)$$

where $\Delta\phi$ is the phase difference between the radial parts of the outgoing rotational wavefunctions. In essence, what we measure is akin to a Young's slit experiment, where the two pathways involve two different electronic states of the molecule. Equation 3 shows that we would expect $a_{11+}(\|,\perp)$ to go to zero when β is purely ‖ or purely ⊥, and the amplitude can be maximal when we have an equal mixture of ‖ and ⊥ transitions (β = 0.5). The trend for H_2O_2 shown in Figure 2 is in good qualitative agreement with Equation 3.

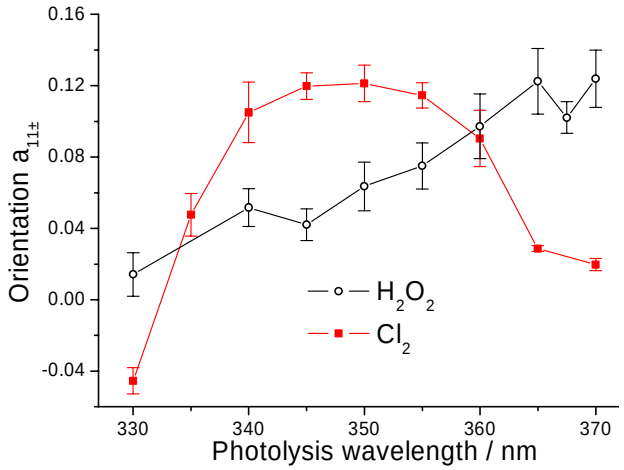

Figure 2. Coherent orientation moment $a_{11+}(\|,\perp)$ for OH(J=0.5) and $a_{11-}(\|,\perp)$ for Cl(J = 0.5).

The most remarkable observation, however, is that the results are very similar to previous measurements of the orientation of Cl($^2P_{1/2}$) atoms in the same wavelength region[5]. The results are shown for comparison in Figure 2. The orientation parameter plotted for Cl atoms is the $a_{11-}(\|,\perp) \propto \sqrt{(1+\beta)(2-\beta)}\sin\Delta\phi$, which is dependent on the sine of the phase difference, rather than the cosine. Also, in comparing the plots in Figure 2, one must take account of the differences in the β parameters for each molecule: these are displaced with respect to wavelength, as shown in Figure 1.

The β parameter and orientation results for H_2O_2 and Cl_2, and indeed for HOCl (not shown here) are all very similar. We would expect that a much greater degree of averaging over product pathways would be required to model the H_2O_2 results due to the increased number of atoms. In spite of the implicit averaging involved, the coherent electronic orientation of OH($^2\Pi$) was measured. These effects are more general than previously explored, and not limited to atomic products of simple diatomic species, as might first have been expected.

Acknowledgements

I wish to thank the Royal Society for a University Research Fellowship, and Mark Brouard (Oxford Univeristy) and Petros Rakitzis (FORTH IESL) for helpful discussions. The loan of a dye laser system from the Lasers for Science Facility of the Rutherford Appleton Laboratory is gratefully acknowledged.

References

1. H Sato, Chem. Rev., 101 2687, (2001)
2. A J Alexander and R N Zare, Acc. Chem. Res., 33 199, (2000)
3. M Brouard, M T Martinez, C J Milne, J P Simons, Chem. Phys. Lett., 165 423 (1990)
4. P C Samartzis, B L G Bakker, T P Rakitzis, D H Parker, T N Kitsopoulos, J. Chem. Phys., 110 5201 (1999)
5. Z H Kim, A J Alexander, T P Rakitzis, S A Kandel, R N Zare, Faraday Discuss., 113 27 (1999)

Picosecond Time-resolved Photoelectron Spectroscopy as a Probe of Intramolecular Dynamics in para-Fluorotoluene

J A Davies, K L Reid

School of Chemistry, University of Nottingham, Nottingham, NG7 2RD, UK

M Towrie, P Matousek

Central Laser Facility, CLRC Rutherford Appleton Laboratory, Chilton, Didcot, Oxon, OX11 0QX, UK

Main contact email address: *Katharine.Reid@nott.ac.uk*

Introduction

Intramolecular vibrational energy redistribution (IVR) remains a dynamical process that is poorly understood in most systems. IVR following the preparation of excited electronic states has commonly been studied by dispersed fluorescence which may or may not be time-resolved. Photoionization of the excited molecule followed by the measurement of a photoelectron spectrum provides some advantages over the fluorescence method. Firstly, laser excitation followed by laser photoionization is a pump-probe technique thus allowing easy control of the timing of the two steps. Secondly, molecules can be photoionized from any state, but do not necessarily fluoresce from any state. The photoelectron spectrum provides information on the ion internal states formed which in turn reflect the internal states populated in the prepared electronic state; in this sense the photoelectron spectrum is analogous to the dispersed fluorescence spectrum. If picosecond pulses are used then the pump and probe are of the appropriate timescale to monitor IVR processes, and the vibrational structure of the ion is resolvable in the photoelectron spectrum. This latter point is critical in the interpretation of the dynamics.

Para-fluorotoluene (pFT) in its first excited electronic state S_1 is an example of a molecule which appears to show anomalous IVR lifetimes when compared with the very similar molecule para-difluorobenzene (pDFB)[1)]. Whereas S_1 pDFB with an excitation energy of ~2000 cm^{-1} has an IVR lifetime of 350 ps, S_1 pFT with the same excitation energy has an IVR lifetime of 3.5 ps. It has been shown that this effect cannot be attributed simply to the increase in density of states that occurs due to the extra degrees of freedom in pFT, and the torsional motion of the methyl group on pFT has been specifically held responsible for this observation[1,2)]. Although there have been a number of experiments performed[3,4)], and models proposed[5)], there has been no systematic study of how the populations of the vibrational states in S_1 evolve as a function of time which is the key to understanding the mechanism of the energy redistribution.

In this work we prepared S_1 pFT with a picosecond laser pulse and ~1200 cm^{-1} of internal excitation, and probed with a second picosecond laser pulse which ionized the excited molecule. The resulting photoelectron spectrum was measured as a function of pump-probe time delay.

Experimental

Para-fluorotoluene (Aldrich, 99%) was seeded in He and introduced via a pulsed nozzle and skimmer into one end of a doubly mu-metal shielded drift tube creating a molecular beam with a rotational temperature of ~30 K. The beam was photoionized with co-propagating laser beams (pump and probe) perpendicular to the axes of the drift tube and the molecular beam propagation direction. A triple microchannel plate electron detector (Photek) was mounted at the other end of the drift tube to detect photoelectrons ejected along its axis. Precautions were taken to reduce electric fields to an absolute minimum by coating the inside of the drift tube with colloidal graphite. The operating pressure in the chamber was around 3×10^{-6} Torr, thus providing a collision-free environment.

A 1 kHz titanium sapphire regenerative amplifier (Spectra-Physics, Spitfire) was configured for the chirped pulse amplification of picosecond pulses. The output was frequency tripled to give ~1 ps pulses at ~262.5 nm. The 262.5 nm beam was split into two parts one of which, acting as the probe, was sent down a computer controlled optical delay line. Both pump and probe beams were loosely focused and had pulse energies of around 2-3 μJ in the interaction region, and beam diameters of around 100 μm as determined by a CCD camera with a microscope objective. These conditions ensured that there was no saturation of either the excitation or the ionization step. The flight times of photoelectrons were recorded with a time-to-digital converter (TDC, LeCroy 2277), and the timings of the initial laser pulse and nozzle opening were controlled by a Stanford gate and delay generator.

In the experimental runs photoelectron spectra were recorded with pump alone, probe alone and pump plus probe at each time delay. In addition, photoelectron yield experiments were performed in which the total number of photoelectrons produced was measured as a function of time delay. Eight different time delays were studied; 0, 2, 5, 10, 30, 60, 100 and 1000 ps. In each case the final spectrum is the pump plus probe spectrum from which the pump only and probe only spectra have been subtracted.

Results and Discussion

The photoelectron spectrum measured with a 0 ps delay between the pump and probe pulses is shown in Figure 1 both in its original form (as a function of photoelectron time-of-flight) and as it appears when plotted as a function of ion internal energy, using the known ionization potential of pFT[6)].

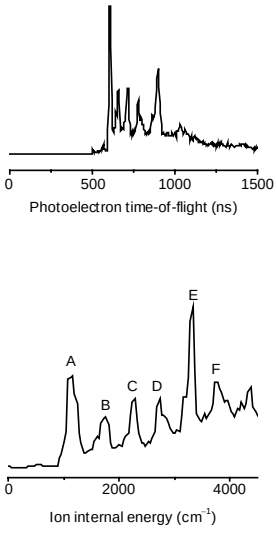

Figure 1. Photoelectron spectrum of S_1 pFT prepared with ~1200 cm^{-1} of internal energy. The ionization pulse is overlapped with the pump pulse.

This photoelectron spectrum has never been recorded before to our knowledge, and neither are the ion vibrational frequencies known so that only a provisional assignment could be made. This was done partly by analogy with pDFB[7], and with the known excitation and dispersed fluorescence spectra of pFT[3,8], and partly by assuming that the first small peak in Figure 1 is due to 0^0 in the ion; work is in progress to analyse photoelectron spectra following the excitation of other levels in S_1 with nanosecond laser pulses to confirm this assignment[9]. The provisional assignment appears in Table 1[10]. The ion vibrational frequencies are compared with the corresponding frequencies of the same modes in S_1[8]. There are discrepancies in the literature over the numbering of the vibrational modes. We have followed strict Mulliken notation[11] in which ν_8 is the C-CH_3 stretch (ν_6 in Reference 12) and is the prepared mode in S_1 at the experimental wavelength, and ν_{13} is a ring bend (ν_{11} in Reference 12). The important point to note is that there is good resolution of ion vibrational states in this spectrum; this would not have been the case had the experiment been performed with femtosecond pulses as is common for time-resolved photoelectron spectroscopy[13].

Peak	Position (cm^{-1})	Assignment	S_1 [8] (cm^{-1})
A	1151	8^1	1194
B	1756	?	
C	2280	8^2	2388
D	2723	$8^2 13^1$	2796
E	3328	8^3	3582
F	3732	$8^3 13^1$	3990

Table 1. Provisional assignment of peaks appearing in the photoelectron spectrum in Figure 1.

Figure 2 shows photoelectron spectra for three time delays. It is clear that the vibrational structure deteriorates as the time delay increases, as has also been observed in reported dispersed fluorescence spectra[1,3]. This loss of structure is caused by IVR and the data shown in Figure 2 is of sufficient quality for us to quantify the timescale of the redistribution process and follow the behaviour of the populations of individual ion vibrational states which in turn reflect populations in S_1. We are currently working on this quantitative analysis of the dynamics, and on modelling the redistribution process[10].

Conclusions

We have demonstrated that picosecond time-resolved photoelectron spectroscopy is a powerful tool with which to study intramolecular dynamics. We have measured the first photoelectron spectra of S_1 para-fluorotoluene and shown that they evolve dramatically over a 100 ps timescale. Quantitative analysis of the dynamical behaviour of S_1 pFT is in progress and will be published in due course.

Acknowledgements

We would like to thank Paul Hockett for his assistance in the assignment of the photoelectron spectrum.

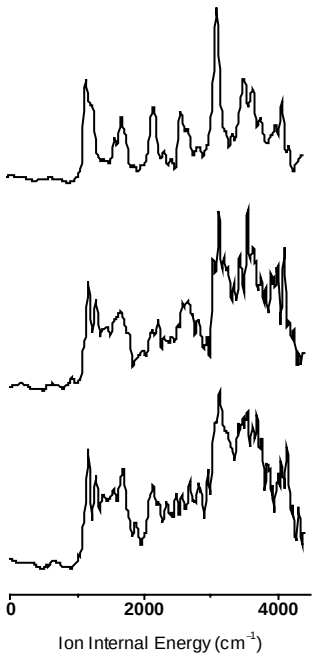

Figure 2. Photoelectron spectra as a function of ion internal energy as in Figure 1 but for three excitation-ionization time delays; 5 ps (top), 30 ps (middle) and 60 ps (bottom).

References

1. C S Parmenter and B M Stone, J. Chem. Phys. 84, 4710 (1986)
2. See, for example, D R Borst and D W Pratt, J. Chem. Phys. 113, 3658 (2000); Q Ju, C S Parmenter, T A Stone and Z Q Zhao, Is. J. Chem. 37, 379 (1997)
3. See, for example, D B Moss and C S Parmenter, J. Chem. Phys. 98, 6897 (1993)
4. J S Baskin, T S Rose and A H Zewail, J. Chem. Phys. 88, 1458 (1988)
5. See, for example, P J Timbers, C S Parmenter and D B Moss, J. Chem. Phys. 100, 1028 (1994); C C Martens and W P Reinhardt, J. Chem. Phys. 93, 5621 (1990)
6. K Takazawa, M Fujii and M Ito, J. Chem. Phys. 99, 3205 (1993)
7. E Sekreta, K S Viswanathan and J P Reilly, J. Chem. Phys. 90, 5349 (1989)
8. K Okuyama, N Mikami and M Ito, J. Phys. Chem. 89, 5617 (1985)
9. S Bellm, P Whiteside, P Hockett and K L Reid, in preparation
10. J A Davies, P Hockett, K L Reid, M Towrie and P Matousek, in preparation
11. R S Mulliken, J. Chem. Phys. 23, 1997 (1955); C G Hickman, J R Gascooke and W D Lawrance, J. Chem. Phys. 104, 4887 (1996)
12. A A Jarzecki, E R Davidson, Q Ju and C S Parmenter, Int. J. Quant. Chem. 72, 249 (1999)
13. See, for example, D R Cyr and C C Hayden, J. Chem. Phys. 104, 771 (1996)

REMPI-LIF studies of simple ion-molecule reactions

M J Frost, C R J Sharpe

Department of Chemistry, Heriot-Watt University, Riccarton, Edinburgh, EH14 4AS

Main contact email address: *M.J.Frost@hw.ac.uk*

Introduction

Molecular ions are important species in a range of environments including weakly-ionised plasmas which encompass most electrical discharges, technological plasmas and the terrestrial and other planetary ionospheres. The modelling of ion concentrations and optical emissions from these environments requires a detailed knowledge of the kinetics of individual participating chemical reactions. In recent work,[1] we have reported the use of a technique by which ions are formed by Resonance Enhanced Multiphoton Ionisation (REMPI) and probed by Laser Induced Fluorescence (LIF) to measure the kinetics of reactions involving the N_2^+ ion. In those studies, we ionised N_2 molecules *via* the a $^1\Pi_g$ electronic state and probed LIF in the B $^2\Sigma_u^+$ - X $^2\Sigma_g^+$ electronic band of N_2^+. Using this scheme, the ionisation step is rather inefficient whereas the LIF detection is facile. We therefore wished to investigate the opposite case where the ionisation step is relatively facile and the LIF detection rather more demanding. With these factors in mind, it was proposed to study the NO^+ ion. This ion is important in weakly-ionised plasmas and is often regarded as a 'terminal' ion owing to the low ionisation potential of NO. However, the scarcity of optical studies on the ion led Albritton *et al.*[2] to conclude 'the NO^+ ion has only grudgingly given up information about its structure'. For the proposed experiments, NO was to be ionised in the A $^2\Sigma^+$, v'=0 - X $^2\Pi$, v''=0 electronic band. This ionisation is known to produce NO^+ ions almost exclusively in the lowest vibrational state.[3-5] It was envisaged that NO^+ ions would then be probed in the $A^1\Pi$– X $^1\Sigma^+$ electronic band by two photon LIF. It was recognised that these would be challenging experiments since we were unaware of any previous reports of the application of this technique to the NO^+ ion.

Experimental

The experimental approach employed has been described in detail in a previous publication.[1] For these experiments, nitric oxide was ionised using the unfocused output of a frequency-doubled Nd:YAG pumped dye laser operating at ~226 nm. The NO^+ ions so formed were to be probed by a second frequency-doubled Nd:YAG pumped dye laser (from the EPSRC Laser Loan pool) operating with a fundamental output in the 505-525 nm range. LIF was detected through a lithium fluoride window using a solar blind photomultiplier tube (Hamamatsu R1081) which has minimal sensitivity at wavelengths above 230 nm.

Results

Although we had previously recorded ionisation spectra for NO in the A $^2\Sigma^+$ - X $^2\Pi$ electronic band, we encountered unforeseen problems in achieving this during the initial stages of the loan period. In order to monitor excitation in this band we chose either to record ion signals with a parallel plate electrode system or detect LIF using a photomultiplier tube. For the latter, we could use either single or two photon excitation. However, neither of these schemes resulted in the predicted spectra. The main source of the problem was that, whilst intense spectral features were observed using excitation at 220 nm (or 440 nm in the case of two photon LIF), spectra recorded at wavelengths ~226 nm did not produce spectra which were immediately recognisable as arising from NO (i.e. no discernible bandheads). As examples, Figure 1a shows a single photon LIF spectrum recorded at wavelengths ~226nm and Figure 1b shows a two photon LIF spectrum recorded at wavelengths ~440 nm. The reason for these problems required extensive investigative work. When working with NO, purity is always of some concern and, owing to the large absorption cross-sections for transitions in the A $^2\Sigma^+$, v'=0 - X $^2\Pi$, v''=0 band, the optical density of samples requires careful consideration.

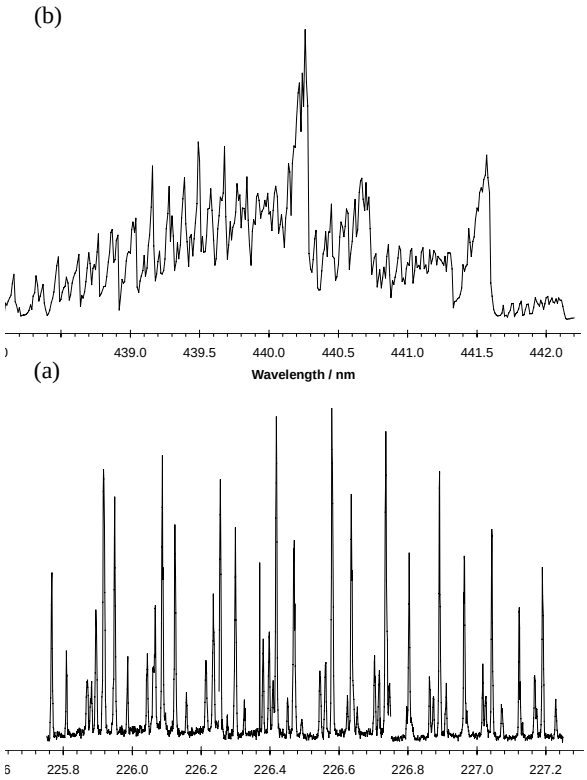

Figure 1. Single photon (a) and two photon (b) LIF spectra of NO.

However, neither of these proved to be the source of our problems. Instead, it was found that the excitation laser fundamental output was shifted from the expected value by ~16 nm. Whilst this would have been rather more obvious with other molecules, we were initially (mistakenly) drawn to the conclusion that we were recording spectra in the NO $B^2\Pi$- X $^2\Pi$ band. In fact, the spectrum of Figure 1b represents transitions in the A $^2\Sigma^+$, v'=0 - X $^2\Pi$, v''=0 band whilst those in Figure 1a at a recorded wavelength of ~226 nm arise from high rotational lines of the A $^2\Sigma^+$, v'=0 - X $^2\Pi$, v''=1 at an actual wavelength of ~234 nm.

Once this problem was rectified, we were able to record and assign NO spectra with confidence. We embarked upon our target experiments by incorporating the second frequency-doubled dye laser system to probe NO^+. Figure 2 shows a sample spectrum recorded at a pressure of 100 mTorr and delay of 1μs between the ionisation and probe lasers. The discontinuities in Figure 2 (highlighted with asterisks) mark positions where the ionisation laser was blocked during the scan. Further investigation showed that the recorded spectra were reliant upon the wavelength of the ionisation laser being coincident with a transition in the A $^2\Sigma^+$ - X $^2\Pi$ electronic band. The spectral coverage of Figure 2 is in the region of the A $^1\Pi$, v'=3 - X $^1\Sigma^+$, v''=0 vibronic band of NO^+. It is immediately obvious from Figure 2 that only broad (LIF) spectral features were observed. This was rather puzzling since far narrower

spectral features were expected. One consideration was whether excitation *via* the W $^1\Delta$ state may have been leading to spectral complications but this seemed unlikely. Broad spectral features were also observed in the regions ~263 and ~252 nm; the positions for the A $^1\Pi$, v'=2 - X $^1\Sigma^+$, v"=0 and A $^1\Pi$, v'=4 - X $^1\Sigma^+$, v"=0 vibronic bands, respectively. Again, after extensive investigations we were led to conclude that the loan laser was operating in a 'broadband' mode although it should be noted that the output bandwidth was sufficiently narrow to provide efficient frequency-doubling.

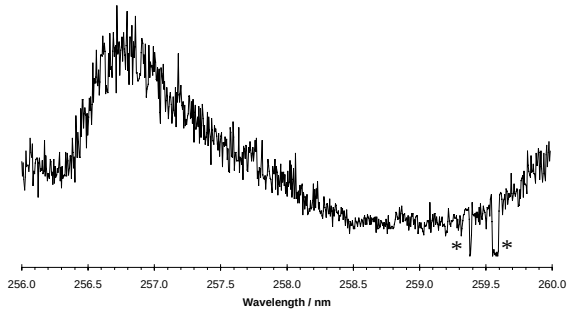

Figure 2 . LIF spectrum recorded in the region of the NO^+ A $^1\Pi$, v'=3 - X $^1\Sigma^+$, v"=0 band. (Asterisks denote positions at which the excitation laser was blocked).

Following a service visit, the problem with the laser was rectified and the experiments repeated. This time, narrow spectral features were observed as shown in Figure 3. Again, these features required the pump laser to be on-resonance with a transition in the A $^2\Sigma^+$, v'=0 - X $^2\Pi$, v"=0 electronic band of NO.

Of particular note was the spectral congestion observed with no clearly-identifiable bandhead as expected in the NO^+ spectrum. Further, these spectral features were evident without focusing of the LIF probe laser. We therefore concluded that these features did not arise from NO^+. We believe that these features arise from states populated following collisional relaxation of the intermediate A $^2\Sigma^+$, v'=0 state. There are a number of important points to note in this regard. First, the frequency of the second laser is such that the detected levels lie below the a $^4\Pi$ state of NO. Given the combination of pump and probe frequencies and knowing the ionisation potential of NO, leads us to conclude that the probed levels must correspond to the removal of at least (E/hc =) 8300 cm^{-1} from excited molecules. Therefore these levels lie below v=19 of the NO X-state. However, the observed transitions cannot be reliably assigned using the LIFBASE spectral simulation programme[6] . An additional point to note is that these spectral features have a range of fluorescence lifetimes ranging from 10 ns or less, to hundreds of microseconds (see Figure 3). Whilst attempts were made to discriminate against these spectral features and enhance any NO^+ LIF through use of focused radiation and short delay times between ionisation and probe lasers, these were unsuccessful during the very limited time remaining in the loan period.

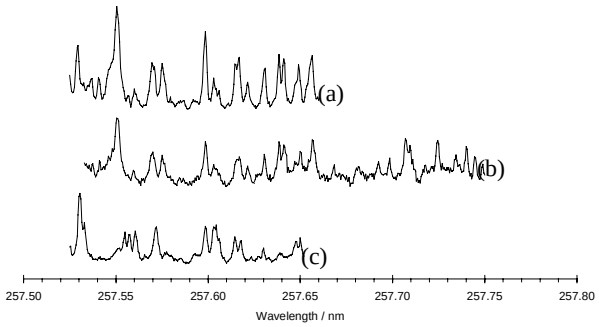

Figure 3 . LIF spectra recorded following A $^2\Sigma^+$, v'=0 - X $^2\Pi$, v"=0 excitation at 100 mTorr pressure of NO and with a delay of 1μs between the excitation and LIF probe lasers. Spectra (a) and (b) were recorded with unfocused and focused LIF probe beam radiation, respectively, and fluorescence integrated in a 200 ns interval with no delay. Spectrum (c) was recorded with unfocused LIF probe beam radiation and fluorescence integrated over a 130 ns gate, delayed by 70 ns from the LIF probe beam.

Conclusion

We have had a rather frustrating loan period and encountered a number of problems which have ranged pretty much from the sublime to the ridiculous. Unfortunately, this left us with only a short time to address the goal of this work. Our attempts to study the NO^+ ion by a REMPI-LIF technique have been unsuccessful owing to unexpected, intense fluorescence signals from states populated in the collisional relaxation of the intermediate state used in the REMPI scheme. It is not unreasonable to believe that a suitable production and detection scheme for the study of NO^+ is possible but time constraints did not allow an exploration of these.

References

1. M.J. Frost and C.R.J. Sharpe.,
Phys. Chem. Chem. Phys., 3, 4536, (2001)

2. D.L. Albritton, A.L. Schmeltekopf and R.N. Zare
J. Chem. Phys., 71, 3271, (1979)

3. J.C. Miller and R.N. Compton,
J. Chem. Phys., 84, 675, (1986)

4. K.S. Viswanathan, E. Sekreta and J.P. Reilly,
J. Phys. Chem., 90, 5658, (1986)

5. D.C. Jacobs, R.J. Madix and R.N. Zare,
J. Chem. Phys., 85, 5469, (1986)

6. J. Luque and D.R. Crosley,
"LIFBASE : Database and Spectral Simulation Programme (Version 1.5)"
SRI International Report MP99-009 (1999)

Time-resolved imaging with lanthanide complexes

R J Aarons, B P Burton-Pye, S Faulkner

Department of Chemistry, University of Manchester, Oxford Road, Manchester, M13 9PL

S W Botchway, A W Parker, S Topley

Central Laser Facility, CLRC Rutherford Appleton Laboratory, Chilton, Didcot, Oxon, OX11 0QX, UK

A Beeby

Department of Chemistry, University of Durham, South Road, Durham, DH1 3LE

J S Snaith, A Ashraf, J Notta

School of Chemical Sciences, University of Birmingham, Edgbaston, Birmingham, B15 2TT

Main contact email address: *Stephen.Faulkner@man.ac.uk*

Luminescent lanthanide ions have long (μs to ms) luminescence lifetimes. This provides an easy means of differentiating luminescence arising from lanthanide complexes from fluorescence arising from organic molecules. This is particularly useful when designing optical probes for microscopy of living systems, where it is necessary to distinguish between signals arising from the probe and those arising from background autofluorescence.

We have previously shown that lanthanide ions can be used in time gated imaging microscopy, and that lifetime maps can be derived from calculating the luminescence decay rate constant for each pixel in an image.[1)] Our current interests in this area centre on the application of these techniques.

Lanthanide complexes designed to recognize cells

Tuftsin is a bioactive tetrapeptide internalized by macrophages; it has been considered a suitable targeting vector for such cell types,[2)] particularly as macrophages are found in high concentrations around tumour cells and in areas of inflammation. We have been investigating the attachment of this peptide sequence to lanthanide complexes with a view to providing 'smart' imaging agents.

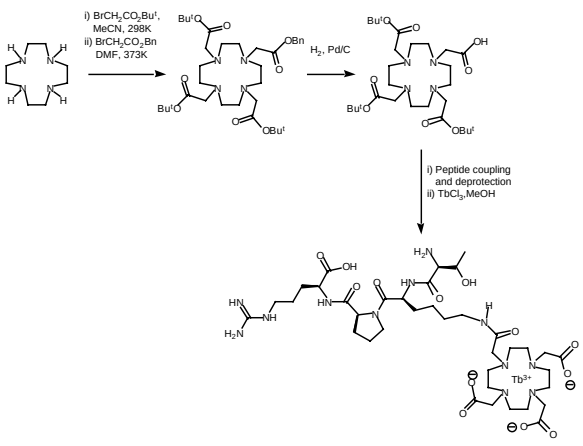

Scheme 1. Synthesis of a tuftsin conjugate.

A simple tuftsin conjugate (**1**) was prepared by coupling of a DOTA derivative (**2**) to a protected tuftsin moiety via the lysine side chain as shown in Scheme 1, followed by subsequent deprotection and complexation with Tb^{3+}. The luminescence properties of the complex were characterized in solution in H_2O and D_2O, and the luminescence lifetimes (1.71 ms and 2.58 ms respectively) were used to establish the inner sphere hydration number (0.7).[3)] In all respects these corresponded to values expected for an eight-coordinate terbium complex with a single coordinated water molecule, with principal emission maxima at 480, 545 and 590 nm.

Initial imaging experiments were carried out on silica particles, following laser excitation by the third harmonic of a neodymium:YAG laser (355nm). Time resolved images were obtained by using a time gated image intensifier interposed between the microscope optics and the image intensifier, and synchronized with the laser pulse. Images of a typical particle and a corresponding lifetime map are shown in Figure 1.

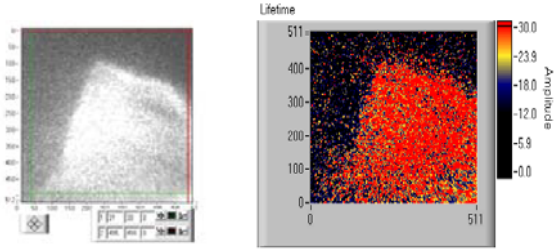

Figure 1. Visible image (left) and lifetime image of a silica particle labelled with the tuftsinconjugate.

Studies on macrophage-like leukaemia cell lines were not so successful. Active uptake of tuftsin conjugates has been reported,[2)] but we could see no evidence for internalization of the macrophage complex in this case. There may be a number of reasons for this: for instance, the highly polar complex may be too close to the peptide, resulting in perturbation of the uptake pathway. Further studies are ongoing, and are concentrating on variation of the point of attachment of the complex, and on the influence of incorporating spacer groups into the conjugate. We are also investigating the use of cell-surface receptor antagonists, which do not need to be internalized by the cell before selective imaging becomes possible.

Parallel addressing of lanthanide complexes

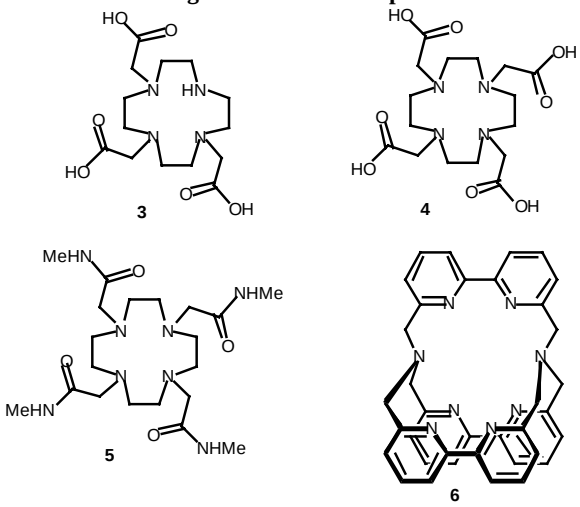

Luminescent lanthanides have sharp, quasi-atomic, emission lines: this makes it possible to address more than one lanthanide

complex at once. Such parallel addressing is potentially important in speeding up the drug discovery process, since it offers the potential of carrying out several assays simultaneously.[4] It also offers potential for encoding applications in the security industry, since lanthanide complexes can be used to form an alphabet based on the wavelengths of their luminescence and the associated luminescence lifetime.

With a view to demonstrating the potential of parallel addressing in imaging applications, we carried out a study on a range of lanthanide complexes using the experimental set-up described above. A series of particles were doped with a range of lanthanide complexes (e.g. Ln.**3**-**6**), and time-gated images and lifetime maps were obtained for mixtures of the particles.[5] Figure 2 shows a white light image obtained for a mixture of Tb.**3** and Tb.**4**, which have different luminescence lifetimes. Lifetime mapping allows the particles to be identified without difficulty.

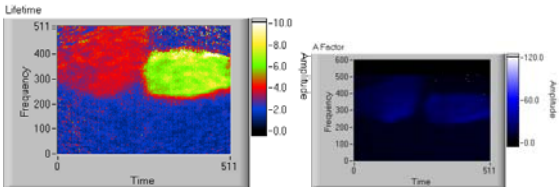

Figure 2. Visible image and lifetime map of silica particles labelled with Tb.3 (right hand particle) and Tb.4 (left hand particle).

Similarly, interference filters can be used to separate the signals from different lanthanide ions. For instance, Eu^{3+} has principal emission bands at 595, 620 and 690 nm, while those of Tb^{3+} are found at 480, 545 and 590 nm, with a weaker band around 620 nm. Thus interference filters can be used to view individual metals by concentrating on non-overlapping bands.

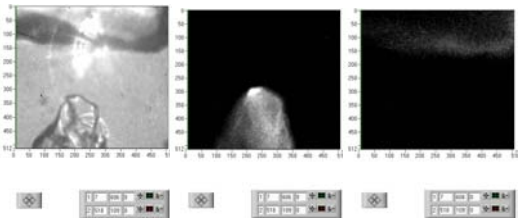

Figure 3. Images of silica particle labelled with Tb.5 and Eu.6: visible image (left), time-gated image using a 545nm interference filter (centre), time-gated image with a 700nm interference filter (right).

The images in Figure 3 show a pair of particles, one of which is labelled with Tb.**5** while the other is labelled with Eu.**6**. When a 545 ± 25nm interference filter is used, only the Tb.**5** labelled particle is visible, and it can be addressed alone. Similarly, when a 700±25 nm interference filter is used, only the particle labelled with Eu.6 is visible.

We are currently developing methods for linking chromophores such as these to a solid support, with a view to developing the technique further.

References

1. A Beeby, I M Clarkson, S Faulkner, S Botchway, D Parker and A W Parker
J. Photochem. Photobiol. B Biol, (2000), 57, 83.

2. A A Amascato
Ann. NY Acad. Sci. 1983, 419, 114

3. R J Aarons, A Ashraf, B P Burton-Pye, J Notta, J S Snaith and S Faulkner, manuscript in preparation

4. S Faulkner, D Parker and J A G Williams, Chapter 4 in 'Supramolecular Science, Where it is and where it is going', eds. R Ungaro and E Dalcanale, Kluwer, 1999.

5. R J Aarons, A Beeby, S W Botchway, B P Burton-Pye, A W Parker, S Topley and S Faulkner, manuscript in preparation.

Exposure of mammalian cells to soft x-rays: effects on gap junctional intercellular communication and its implications for the study of the radiation-induced 'bystander' effect

G O Edwards, R A Meldrum, C W Wharton, J K Chipman

School of Biosciences, The University of Birmingham, Edgbaston, Birmingham, B15 2TT

S W Botchway, G J Hirst, W Shaikh, A J Bodey, S Topley

Central Laser Facility, CLRC Rutherford Appleton Laboratory, Chilton, Didcot, Oxon, OX11 0QX, UK

Main contact email address: *G.O.Edwards.1@bham.ac.uk*

Introduction

As part of a larger study employing technologies developed at the CLF to study inter- and intra-cellular dynamics, we have been studying the effects of laser plasma generated soft x-rays on gap junctional intercellular communication (GJIC) in mammalian cells, and the associated 'bystander' effect. In summary, our data demonstrate that exposure of cells to soft x-rays significantly reduces GJIC in a dose dependent manner. Furthermore, through the development of advanced masking and micropositioning techniques, we have been able to demonstrate inhibition of GJIC in 'bystander' cells, which are not directly exposed but are in contact with target cells.

Gap Junctional Intercellular Communication

Gap junctions are organelles that form between mammalian cells, creating a pore that allows cytoplasmic continuity. The basic unit of a gap junction is the connexin protein and to date at least 14 mammalian connexins have been characterized. Connexins are comprised of four transmembrane domains, an intracellular loop, intracellular amino- and carboxy-termini, and two extracellular loops. Connexins join to form a hexamer known as a connexon: this is a hemichannel, that is, one half of a gap junction (Figure 1a). Connexons are transported to the

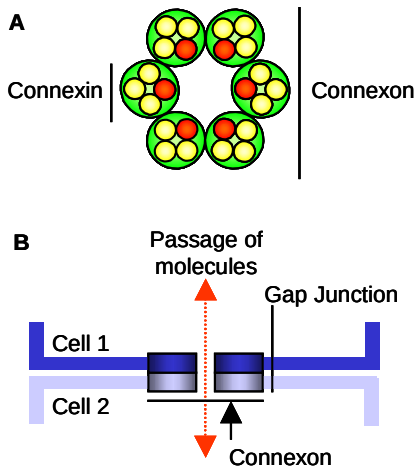

Figure 1. Structure of a gap junction. A: the connexon (hemichannel), formed from six connexins. B: A single junction, formed when hemichannels on adjacent cells dock.

cell membrane, where the extracellular loops dock with the extracellular loops of connexins on neighbouring cells to form a gap junction (Figure 1b). Once assembled, gap junctions allow the passage by diffusion of molecules of less than 1 kDa in size between cells. Since these molecules include cell messengers, gap junctions are important for control of cellular function across a population of contacting cells.

Rat liver epithelial cells, cell line WB-F344, provide an ideal subject for our studies as they form confluent monolayers of cells that readily communicate via connexin43 gap junctions. Initially it was planned to assess the effects of soft x-rays on GJIC by means of microinjection. However, the incidence of low frequency vibrations hindered our progress, as microinjection requires a very stable environment. Thus, an alternative approach was required: this took the form of the GapFRAP assay[1] (fluorescence redistribution after photobleaching via gap junctions). Cells were incubated with the fluorescent dye carboxyfluorescein diacetate (CFDA), following which they were washed in phosphate buffered saline (PBS) and placed in fresh culture medium. CFDA is taken up into cells, and converted into a fluorescent by-product that is membrane impermeable but able to pass from cell to cell via gap junctions. Dishes of cells were observed under the confocal microscope (BioRad MRC 500) and excited with the 488 nm line of an argon:ion laser, and an image, 'prebleach', was recorded. Using the zoom function on the confocal microscope, a single cell was selected, and five passes of the argon:ion laser, operating at full power (<1 mW at the microscope stage), bleached the dye in this cell. The microscope was returned to the previous configuration, and an image, 'postbleach', was captured. At four minutes post-bleaching a final image was captured, and the degree of redistribution of fluorescence into the photobleached cell was determined using the ScionImage computer program. Redistribution of fluorescence was clearly observed (Figure 2). When cells were incubated with the GJIC inhibitor 18αGlycyrrhetinic Acid, this redistribution of fluorescence was reduced to 30.6 ±4.5 %, which was shown to be significant ($P<0.001$).

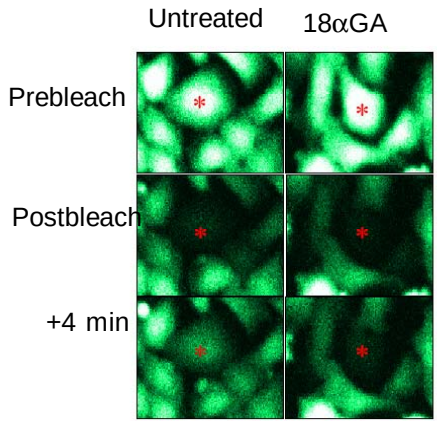

Figure 2. Images of untreated WB-F344 cells and cells treated with the gap junction blocker 18αGlycyrrhetinic Acid, demonstrating the GapFRAP technique Assessment of GJIC .

Gap junctions have been implicated in the spread of damage from cell to cell, and it has been suggested that cell-cell uncoupling by means of closing gap junctions could prevent the spread of such damaging molecules[2]. The spread of damage from exposed to unexposed cells has been termed the 'bystander' effect and is of great interest in radiobiology. It has been shown that when cells are exposed to low doses of α-particles, stress responses (micronucleus formation, p53 phosphorylation) are observed in more cells than predicted to have been exposed at the dose used (0.3 cGy)[3]. In the presence of a gap junction inhibitor (lindane), the number of cells showing stress responses was significantly reduced[3]. At higher

doses, death of unexposed cells in contact with exposed cells has been observed[4]. Such experiments are useful in that they can demonstrate that exposure to ionizing radiation results in stress responses in more cells than have been irradiated.

Exposure of cells to soft x-rays

The laser plasma generated x-ray source at the CLF produces Cu x-rays that are of sufficiently low energy and penetration (1.1 keV) to affect only the cells that are exposed. The production of such x-rays has been outlined elsewhere, but in summary, a high power pulsed UV laser is focused onto a moving copper target within a vacuum, thus generating a plasma[4]. X-rays are given off from the plasma at a rate of up to 3 Gy s^{-1}, and are passed through a 3 µm aluminium filter, which is opaque to UV. In order to collimate the x-ray source, 25 µm and 100 µm slits of length 3 mm were machined in a disk of stainless steel, 13 µm in thickness. Previous work has demonstrated that illumination through the 25 µm slit produces a sharp-edged pattern of irradiation 25 µm wide[4, 5].

Irradiation of discrete regions of cells was determined by exposure of a radiochromic material, Gaffchromic film, glued to the base of a cell culture dish. Culture dishes were constructed from 35 mm diameter glass rings fitted with 1 µm Hostaphan bases. Cells were cultured in a dish, and stained with a fluorescent dye. The dish was then placed onto the x-ray source, and exposed to 100 Gy soft x-rays. An image of the 100 µm slit was clearly visible on the Gaffchromic film (Figure 3a). The confocal was then used to capture an image of cells growing at the same position, and when the two images were combined it could be seen that the configuration of the equipment successfully allowed us to irradiate very distinct regions of cells (Figure 3b).

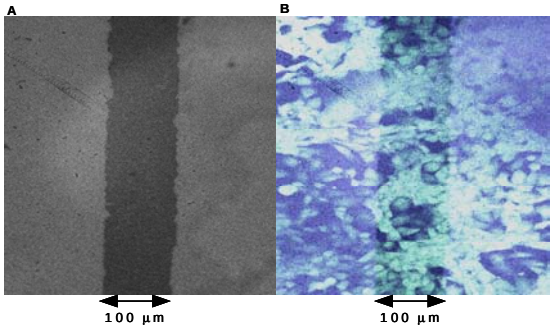

Figure 3. A: Image of soft x-rays collimated through 100 µm slit, developed using Gaffchromic film attached to the base of a cell growth chamber. B: Image of the same slit, superimposed with image of fluorescently labeled WB-F344 cells growing in the chamber the Gaffchromic film was attached to.

Effects of soft x-rays on GJIC

In order to determine the effects of soft x-rays on GJIC, cells were loaded with CFDA and exposed to doses of 1, 3 and 5 Gy soft x-rays. GapFRAP was carried out to determine the degree of communication that could be observed. Irradiation reduced communication in a dose-dependent manner (Figure 4). Exposure of cells to 1 Gy reduced communication to 82.8 ±7.1 % (P=0.057) of communication in untreated cells, 3 Gy to 54.5 ±5.5 % (P<0.01) and 5 Gy to 24.0 ±5.4 % (P<0.001).

To elucidate the mechanism behind this reduction in communication, a biochemical technique known as western blotting was carried out. Western blotting involves isolating proteins from a sample of cells, separating them by electrophoresis, transferring them to a membrane, and detecting specific proteins using specific antibodies.

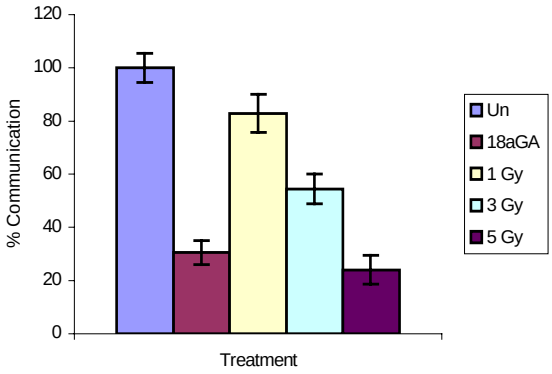

Figure 4. Graph representing % communication in directly exposed cells. Error bars represent standard error of the mean.

Gap junction closure involves the connexin becoming 'hyperphosphorylated', which can be detected by altered electrophoretic mobility as observed on a western blot. Entire dishes of WB-F344 cells were exposed to 5 Gy soft x-rays, and total protein was isolated. A 15 µg aliquot of this sample was analysed, along with samples of protein from untreated cells and cells that had been treated with the gap junction inhibitor TPA (previously demonstrated [6] to inhibit GJIC by means of hyperphosphorylation of connexin43). When compared to untreated cells, cells treated with TPA and cells exposed to 5 Gy soft x-rays showed hyperphosphorylation of connexin43 (data not shown).

Figure 5. Images of the micropositioners from the x-ray source and the stage of the confocal microscope, and (upside down) the cell growth chamber holder. Coloured circles indicate triangulation points for one position of irradiation.

Effects of soft x-rays on 'bystander' cells

Once the effect of soft x-rays on GJIC in directly illuminated cells had been assessed, it became desirable to assess the effects of soft x-rays on indirectly irradiated, 'bystander' cells. To do this, a highly precise relocation micropositioning system was developed, so that we could target cells that had been directly irradiated and distinguish them from cells that had not been directly irradiated and determine the spatial relationships between such areas. The x-ray source and the confocal stage were modified by the addition of a series of recesses, allowing a clamp that held the cell culture dish to be positioned by means of triangulation between three points (Figure 5). The stage on the confocal microscope was controlled by a computer running an 'in-house' computer program (programmed on LabVIEW™). Six regions of illumination were defined, detected on Gaffchromic film, and the confocal stage was

calibrated using this so that the computer could send the stage to an exact region of illumination. By doing this, it was possible to reposition the stage to investigate cells a known distance from the illuminated region.

GapFRAP was carried out on cells exposed to soft x-rays (1, 3 and 5 Gy) through the 100 μm slit. Samples were transferred to the confocal microscope, and the micropositioning system allowed us to initially locate the irradiated region of cells, and then move to a position approximately 100 μm (ca. 4-5 cells) away from this region, where cells were unirradiated. Results obtained (Figure 6) demonstrate inhibition of GJIC: 1 Gy reduced redistribution of fluorescence to 78.9 ±5.9 % ($P<0.05$), and 3 and 5 Gy reduced redistribution of fluorescence to 59.3 ±5.1 % ($P<0.01$) and 69.0 ±10.0 % ($P<0.01$), respectively. Thus, communication in bystander cells is reduced by exposure to soft x-rays. However, when we compare the redistribution of fluorescence in cells directly exposed to 5 Gy to bystander cells where target cells were exposed to 5 Gy, a large difference in communication was observed (24.0 ±5.4% compared to 69.0 ±10.0%).

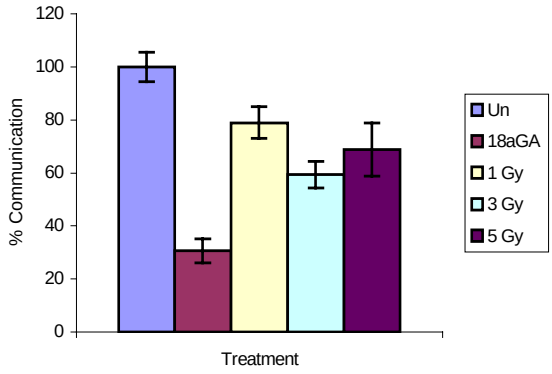

Figure 6. Graph representing % communication in bystander cells. Error bars represent standard error of the mean.

Conclusions

a. We have developed techniques to allow illumination of finely defined regions of a population of cells with soft x-rays.
b. Exposure of cells to soft x-rays reduces GJIC in a dose-dependent manner, which is associated with hyperphosphorylation of connexin43.
c. By employing an identical micropositioning system on the x-ray source and confocal microscope stage, and in combination with precise computer-control of the stage, we are able to select regions of cells that have not been directly irradiated for analysis.
d. This technological development has allowed us to begin to study the bystander effect with excellent spatial clarity, and we can demonstrate that soft x-rays have an inhibitory effect on GJIC in unexposed 'bystander' cells neighbouring irradiated cells.
e. Although very low doses of exposure may elicit stress responses in bystander cells, a slight increase in dose can inhibit GJIC and it can be postulated that this would prevent the spread of toxic molecules to bystander cells.

References

1. M L Cotrina, J H C Lin, A Alaves-Rodrigues, S Liu, J Li, H Azmi-Ghadimi, J Kang, CCG Naus and M Nedergaard Proc Natl Acad Sci USA 95, 15735 (1998)
2. C Peracchia, X G Wang and L L Peracchia Methods 20, 188 (2000)
3. EI Azzam, S M de Toledo and J B Little Proc Natl Acad Sci USA 98, 473 (2001)
4. R A Meldrum, G O Edwards, J K Chipman, C W Wharton, S W Botchway, G J Hirst and W Shaikh CLF Annual Report 2000/2001, RAL-TR-2001-030,117 (2001)
5. R A Meldrum, G O Edwards, J K Chipman, C W Wharton, S W Botchway, G J Hirst and W Shaikh International Congress Series 1236, 289 (2002)
6. P Ren, P P Mehta and RJ Ruch Carcinogenesis 19, 169 (1998)

Investigation of 'Hyperluminescence' produced by Multiphoton Excitation of 5-Hydroxytryptophan

R H Bisby, D Tobin

BioSciences Research Institute, University of Salford, Salford, M5 4WT

S Botchway, I Clark, A W Parker

Central Laser Facility,CLRC Rutherford Appleton Laboratory, Chilton, Didcot, Oxon., OX11 0QX, UK

Main contact email address: *r.h.bisby@salford.ac.uk*

Introduction

Investigations have been undertaken in an attempt to identify the species responsible for the unusual "hyperluminescence" of 5-hydroxyindoles. On intense illumination with near-infrared femtosecond laser pulses, hyperluminescence, with λ_{max} ca. 500 nm, from these compounds is observed at considerably longer wavelength than normal fluorescence (λ_{max} 340 nm) excited with one photon ultraviolet excitation [1,2]. Experiments have been undertaken in the Nanosecond Laboratory to study combined ultraviolet and visible excitation, whilst in the Confocal Microscope Laboratory the Ti:sapphire laser has been used to characterize the hyperluminescence arising from near infrared multiphoton excitation of 5-hydroxytryptophan.

The 5-hydroxyindole structure is of interest from a biochemical viewpoint because it is part of the serotonin (5-hydroxytryptamine, an important neurotransmitter) and because substitution of tryptophan by 5-hydroxytryptophan within specific proteins has been used to study their intracellular localization [3]. Near-infrared three-photon excitation of the ultraviolet fluorescence of serotonin has been used to image its distribution within live cells [4]. Differences in multiphoton excitation spectra allow some discrimination between the ultraviolet fluorescence of serotonin and background luminescence. Further opportunity to selectively observe serotonin and related molecules arises from the hyperluminescence emission maximum at 500 nm [1,2] which is at longer wavelength than the fluorescence emission of many cellular components. The overall process leading to hyperluminescence has been resolved into a four-photon step in which an unknown transient species is produced, followed by two-photon excitation of the intermediate [1].

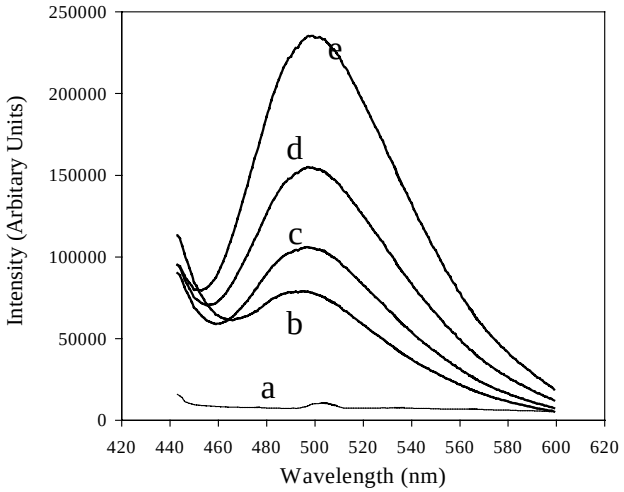

Figure 1. Emission spectra recorded on excitation of 5-hydroxytryptophan in neutral solution with nanosecond laser pulses – a) probe (430 nm) pulse only; b) pump pulse (308 nm) only. The remaining curves show spectra with both lasers and with the probe pulse delayed by c) 10 ns; d) 1 μs and e) 100 μs.

Results and Discussion

Figure 1 shows the luminescence observed on excitation of a neutral aqueous solution of 5-hydroxytryptophan with a nanosecond UV (308 nm) laser pulse, followed by probing with a 430 nm laser pulse to excite fluorescence from a photochemical product. The results show that maximum luminescence is observed when the probe laser pulse is delayed by between 10 and 100 μs. The intensity of the emission was quenched by about 20% in oxygen-saturated solution, compared with deaerated solutions.

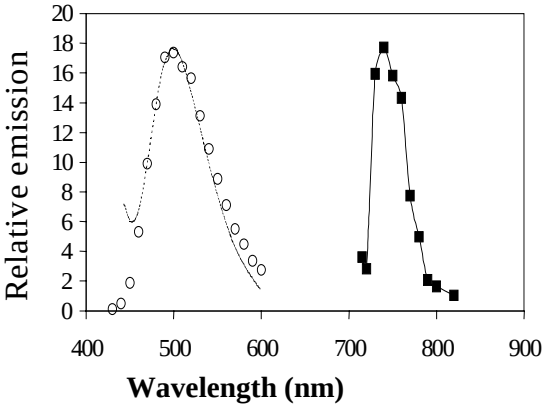

Figure 2. Multiphoton infrared excitation spectrum (■) and emission spectra from nanosecond experiment (dashed line) and from multiphotophotoninfrared excitation (O) for hyperluminescence from 5-hydroxytryptophan.

Figure 2 shows that the emission spectrum, with a maximum at 500 nm, measured with dual wavelength nanosecond laser excitation coincides almost exactly with that observed on multiphoton excitation employing a Ti:sapphire laser (120 fs, ca. 720-800 nm). The small discrepancy between the spectra may be a result of considerable correction factors applied to the data as a result of the very different spectral response of the detectors (photomultiplier and CCD array) used for the two measurements. The excitation spectrum of the hyperluminescence was also measured using the tunability of the Ti:sapphire laser. The results show an excitation peak at 740 nm. The power dependence at this wavelength has not yet been determined.

The identity of the species producing hyperluminescence is unknown, but one possibility that has been suggested is the 5-indoxyl radical produced by one-electron oxidation of 5-hydroxytryptophan through photoionisation [1]. This process is known to occur in alkali solution at 248 nm [5]. On laser flash photolysis (308 nm) of 5-hydroxytryptophan in neutral solution, we have observed formation of a species with an absorption spectrum, λ_{max} 410 nm, very similar to that of the 5-indoxyl radical [6]. However in the laser flash photolysis experiments this transient is only partially quenched by ascorbate. Complementary pulse radiolysis studies undertaken at the Free Radical Research Facility at the Daresbury Laboratory (FRRF@DL) confirm that the 5-indoxyl radical is completely reduced by ascorbate with a second order rate constant of ca.

10^8 dm^3 mol^{-1} s^{-1}. This indicates that two species are produced in the laser flash photolysis experiments. In the pump-probe experiments such as those in Figure 1, addition of ascorbate at concentrations of up to 4 mmol dm^{-3} has no significant effect on the 500 nm emission. Similarly ascorbate was found to be ineffective in quenching multiphoton near infrared-excited hyperluminescence of 5-hydroxytryptophan. It is therefore concluded that the 5-indoxyl radical cannot be the species responsible for hyperluminescence.

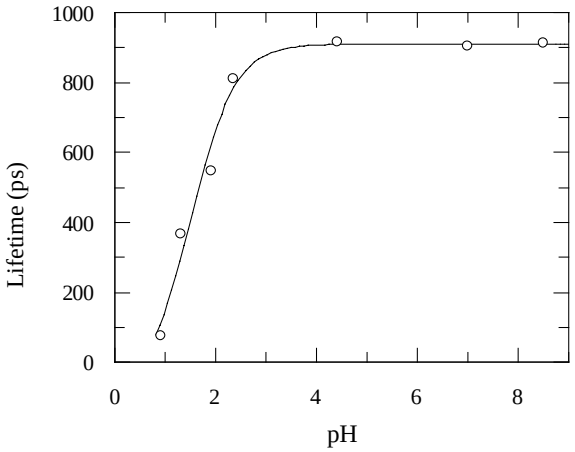

Figure 3. Effect of pH on the fluorescence lifetime of the hyperluminescence from 5-hydroxytryptophan on multiphoton near-infrared excitation.

The properties of the hyperluminescence on multiphoton excitation have been investigated in a number of solvents. In neutral aqueous (H_2O) solution the fluorescence shows a single exponential decay with a lifetime is 0.91 ns, close to a previously estimated value [2]. In D_2O the lifetime increases to 1.76 ns, showing a similar deuterium isotope effect to other indoles [7]. The fluorescence lifetime and intensity are unchanged between pH 5 and pH 9, but the lifetime is strongly quenched in acidic solutions, Figure 3. Figure 4 shows that in organic solvents the lifetime increases with decreasing polarity, reaching a value of 3.3 ns in ethanol (90%) / water (10%) v/v. However the intensity of hyperluminescence is considerably reduced in less polar solvents. This unusual relation between fluorescence lifetime and emission intensity is possibly explained by the two-step excitation of the hyperluminescence process. Whilst decreasing solvent polarity may increase fluorescence efficiency in the two photon excitation of fluorescence from the intermediate, it appears to considerably reduce the formation of the intermediate via the four photon step.

The results show that hyperluminescence of 5-hydroxytryptophan residues in proteins may be a novel probe with which to explore protein conformation and dynamics. Whilst hyperluminescence is unaffected by solution pH and ascorbate concentrations within the physiological range, it displays a fluorescence lifetime which is sensitive to solvent polarity. Further, when compared with one-photon excitation of normal fluorescence the multiphoton excitation of hyperluminescence may be a more sensitive probe of protein dynamics as a result of the anticipated increased anisotropy values demonstrated for a number of other probes on multiphoton excitation [8].

References

1. J.B.Shear, C.Xu and W.W.Webb, Photochem.Photobiol., 65, 931 (1997)
2. M.L.Gostkowski, T.E.Curey, E.Okerberg, T.J.Kang, D.V.Bout and J.B.Shear, Anal.Chem., 72, 3821 (1998)
3. S.W.Botchway, A.W.Parker, I.Barba and K.Brindle, Central Laser Facility Annual Report, 2000-2001, RAL-TR-2001-030: pp. 170-171.
4. S.Maiti, J.B.Shear, R.M.Williams, W.R.Zipfel and W.W.Webb, Science, 275, 530 (1997)
5. S.V.Jovanovic, S.Steenken and M.G.Simic, J.Phys.Chem., 94, 3583 (1990)
6. S.V.Jovanovic and M.G.Simic, Life Chem.Rep., 3, 124 (1985)
7. L.P.McMahon, W.J.Colcucci, M.L.McLaughlin and M.D.Barkley, J.Amer.Chem.Soc., 114, 8442 (1992)
8. D.J.S.Birch, Spectrochim. Acta A, 57, 2313 (2001)

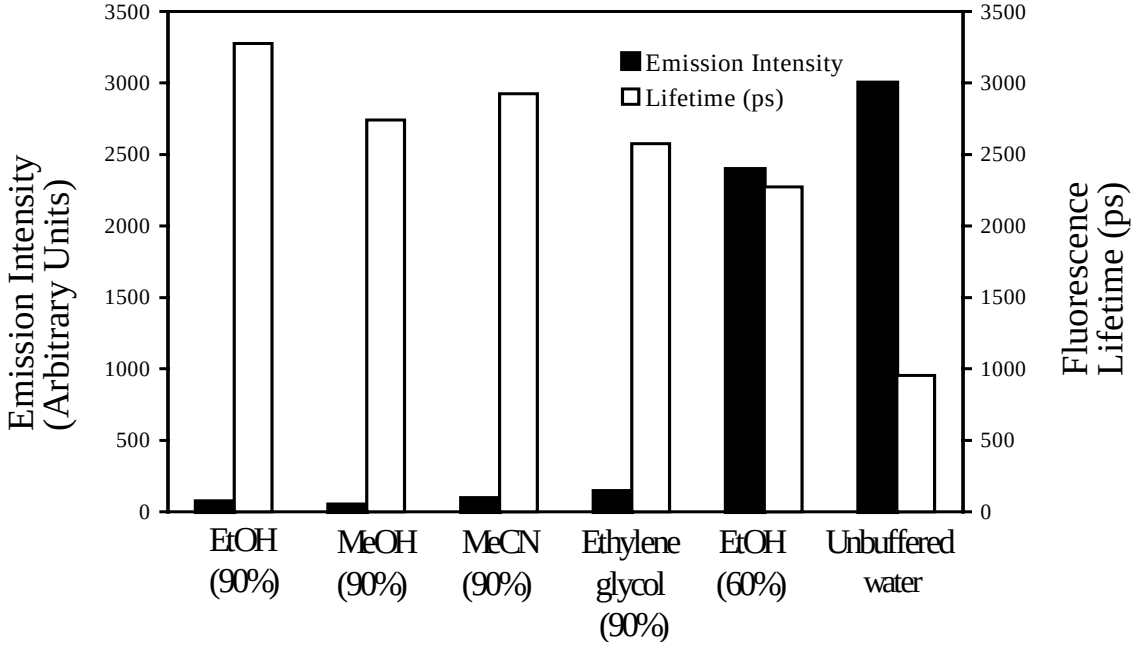

Figure 4. Effect of solvent on fluorescence lifetime of fluorescence at 500 nm from multiphoton excitation of 5-hydroxytryptophan at 740 nm.

Following Adenovirus Entry in Living Cells by Fluorescence Lifetime Microscopy

M L Martin-Fernandez, M J Tobin, S V Jones, G R Jones

Synchrotron Radiation Department, CLRC Daresbury Laboratory, Daresbury, Warrington, Cheshire, WA4 4AS

S W Botchway

Central Laser Facility, CLRC Rutherford Appleton Laboratory, Chilton, Didcot, Oxon, OX11 0QX, UK

Main contact email address: *m.l.martin@dl.ac.uk*

Introduction

Adenoviruses (Ads) are infectious virions of significant interest in gene therapy, mainly due to their many advantages as vectors for gene delivery. These advantages include very high titers, their ability to infect both dividing and quiescent cells of many types, and their availability as replication-deficient particles that can carry large DNA insets (for a review see Reference 1).

Ads are non-enveloped, double-stranded DNA viruses, about 90 nm in diameter, and are commonly sub-divided into serotypes based on their ability to induce specific neutralising antibodies[2]. For subgroup C Ads, which includes the most extensively studied serotypes 2 (Ad2) and 5 (Ad5), the primary receptor is the 46 kDa transmembrane Coxsackie-Adenovirus receptor (CAR)[4].

To deliver their genome into the cell nucleus Ads need to transverse three formidable cell barriers, the plasma, endosomal, and nuclear membranes, and in order to achieve this they must highjack the machinery that cells have developed for protein and nucleic acid trafficking. The first interaction of the fibre with the host-cell through CAR is followed by the interaction between the Ad's penton-base with cellular $\alpha v\beta 3$ and $\alpha v\beta 5$ vitronectin-binding integrins[5]. Then bound Ads are rapidly endocytosed into clathrin-coated vesicles via a process regulated by lipid kinases, actin-modulating small GTPases, and dynamin[5]. From endosomes the fibre-less Ad particles are somehow able to break the membrane of the surrounding endosome and escape into the cytosol via a poorly understood pH-dependent mechanism[5]. Once in the cytosol Ads use microtubules and microtubule-depending motors to be transported to the nuclear membrane, where they bind nuclear pore complexes and ultimately make use of the cell nucleus as a site for replication[6].

Understanding the mechanism by which internalised Ads escape from acidified endocytic vesicles is important to determine the strategy used by these viruses for efficient translocation of viral DNA, a key requirement for efficient Ad-mediated gene transfer[1]. To shed some light in this process we have carried out fluorescence lifetime imaging measurements on live Ad5 labelled with a pH-sensitive fluorescein tag as they enter CHO-CAR cells. These cells overexpress the CAR receptor to a level of a few hundred molecules per cell, and therefore have an increased sensitivity for the virus[7]. Here we present preliminary data obtained at the CLF showing the potential of the method to image pH-dependent viral trafficking process in cells.

Results

We have used 2-photon laser excitation and the confocal microscopy facilities at the CLF to determine the localisation of fluorescein-labelled Ad5 particles during entry in CHO-CAR cells (Figure 1) at the same time as we recorded the fluorescence decay profile of individual virus particles on a pixel-by-pixel basis. The fluorescence decay of the fluorescein probe is pH-sensitive, and can therefore report on the degree of acidification of the environment surrounding the internalised Ad5 particles. Figure 2 shows a fluorescence image of single Ad5 particles bound to the plasma membrane of CHO-CAR cells recorded using a CW Ar+ laser and the BioRAD confocal microscope facility at the CLF. We used these data to check the degree of Ad5 labelling in the samples and select a plane of focus.

A pulsed Ti:Sa laser was used in conjunction with a Becker & Hickel card (SPC-700 time-correlated single photon counting imaging Module) to collect the fluorescence decay of individual fluorescein-labelled virus particles for each pixel. Virus binding to cells is temperature-independent; consequently, by cooling the cells, the attachment step can be experimentally separated from penetration, which only occurs at temperatures above 37°C [5].

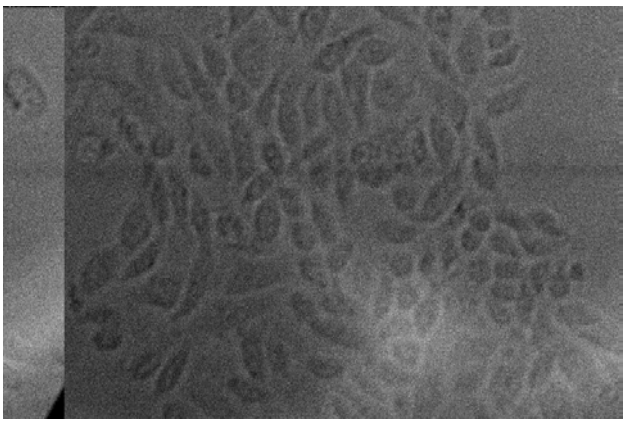

Figure 1. Transmission image of CHO-CAR cells before exposure to Ad5 particles. The cells are approximately 20 μm in diameter.

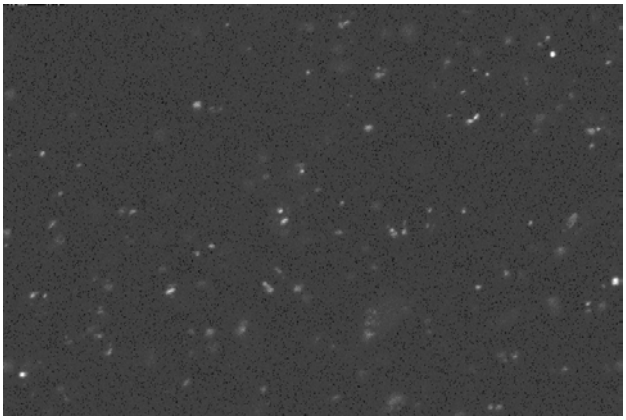

Figure 2. Fluorescence confocal image of fluorescein-labelled Ad5 particles bound to CHO-CAR cells at 4°C. The smaller spots show individual virus particles labelled with about 1000 fluorescein molecules.

Labelled Ad5 were also imaged using 2-photon pulsed excitation (Figure 3). The corresponding fluorescence lifetime image map showing the average lifetime of fluorescence decay data taken 10 minutes after raising the temperature to 37°C is shown in Figure 4.

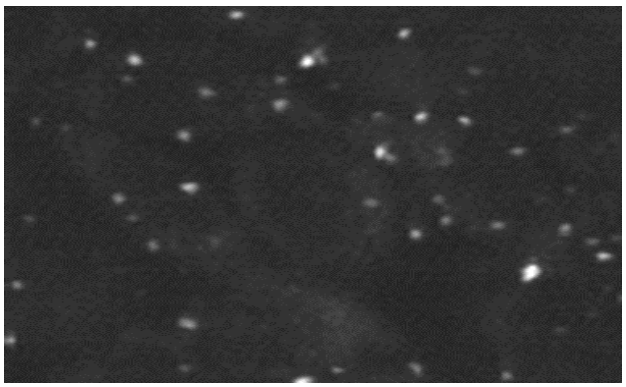

Figure 3. 2-photon fluorescence image of fluorescein-labeled Ad5 particles bound to CHO-CAR cells collected about ten minutes after raising the sample temperature from 4^{o}C to 37^{o}C.

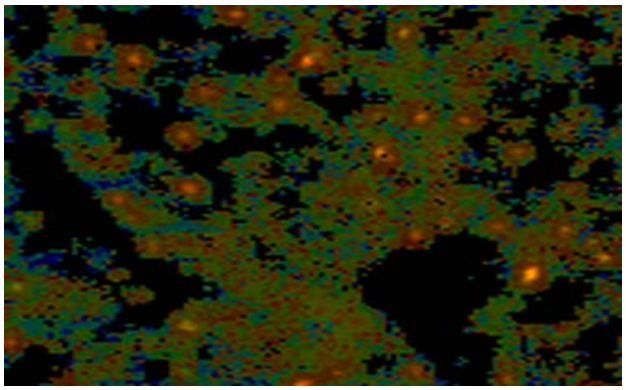

Figure 4. Fluorescence lifetime image map showing different degrees of environment acidification around internalised Ad5 particles. The colour coding indicates shorter fluorescence lifetime values (red = more acidic) and longer fluorescence lifetimes (blue).

Conclusions

The data presented in this report are the results of preliminary experiments using fluorescence lifetime imaging to follow Ad entry in live cells. This method has not been applied before in virology and much more work is required to obtain quantitative results. We are in the process of combining the method with time-lapse microscopy to be able to measure a series of fluorescence lifetime image maps on the same field of view from which the time course of acidification can be obtained. Despite being early days, the pioneer data obtained at the CLF clearly demonstrate the potential of fluorescence lifetime microscopy for the study of viral trafficking processes.

We thank the BBSRC for funding this work through grant C09632. We also thank the Instrumentation Department at CLRC for financing our access to the CLF facility. Thanks are also due to Dr. Gareth Derbyshire for his invaluable help to carry out these experiments.

References

1. W C Russell.J. Gen. Virol. DOI:10.1099/vir.0.17217-0 (2000)
2. U F Greber, M Willetts, P Webster, and A Helenius. Cell, 75:477-486 (1993).
3. H Liebermann , R Mental, U Baur, P Pring-Akerblom, R Dolling, S Modrow, and W Seidel. J. Virol. 72:9121-9130 (1998).
4. X Wang and J M Bergelson.J. Virol. 73(3) 2559-2562 (1999).
5. K Wang. T Guan, D A Cheresh, and G R Nemerow , M J. J Virol. 74(6) 2731-2739 (2000).
6. G R Whitaker, M Kann, and A Helenius. Ann. Rev. Cell Dev. Biol. 16:627-651(2000).
7. D McDonald, L. Stockwin, T Matzow, ME Blair Zajdel, and G E Blair. Gene Therapy 6:1512-1519 (1999).

Induction of localized UV photoproducts in cell nuclear DNA by 3-photon near infrared absorption

R A Meldrum, C W Wharton

School of Biosciences, University of Birmingham, Edgbaston, Birmingham , B15 2TT , UK

S W Botchway, G J Hirst, S Topley

Central Laser Facility, CLRC Rutherford Appleton Laboratory, Chilton, Didcot, Oxon, OX11 0QX, UK

Main contact email address: *r.meldrum@bham.ac.uk*

Introduction

Two-photon and three-photon excitation processes have recently generated interest because localization of the photonic interaction is possible within a femtolitre volume [1,2]. In biological studies, two and three photon phenomena have been applied mainly to imaging microscopy, where fluorescence excitation by multiphoton absorption can provide unique three-dimensional detail with sub-micron resolution. Near infrared (NIR) multiphoton microscopy is becoming the tool of choice for biological imaging as it allows non-destructive multiphoton fluorescence excitation in biological materials [3]. Localised induction of DNA damage is a major goal of cell biologists who study DNA repair dynamics, intra-cellular signaling processes and cell-cell communication.

In a programme which set out to apply multiphoton near infra-red and micro-UV irradiation methods to study a hotly disputed question about the dynamics of the DNA repair processes, we successfully used near diffraction limited 750 nm near infra-red laser radiation to induce sub-micron sized areas of DNA UV photoproducts in H1C1 (rat liver epithelial) cell nuclei.

Laser irradiation of cells

The original program was designed to address a vigorously disputed question concerning the extent of mobility of the repair proteins and/or the DNA in the removal of damaged sites. The central question is whether proteins which function in the more general replication, transcription as well as nucleotide excision repair processes are fixed at nuclear matrix sites [4], translocate along the DNA, or diffuse in three dimensional pathways [5] to find repair sites.

Recent findings from protein mobility experiments in living cells indicate that many kinds of nuclear factors move rapidly and exchange quickly with multiple targets, but some factors may reside in long term complexes [6].

Scientists are becoming increasingly aware that methodology can influence the nature or interpretation of the results obtained, thus techniques which can interrogate systems at the single molecular level and on sub-second time scale are necessary. For DNA repair studies the ultimate goal would be to study single repair sites as dense areas of DNA lesions would obscure the finer details of protein interactions. As a first step towards this, DNA damage must be induced in the cell in as small an area and quantity as possible.

The experimental set up is as illustrated below. A 750nm laser beam from a Spectra-Physics Tsunami titanium-sapphire laser, pulse length 120fs, was focused through an Olympus Planapo 40x objective with a focal length of 2mm and numerical aperture 0.85. Live cells growing on a glass coverslip were brought into focus under white light and positioned using a micro-manipulator stage so that the beam would center on a cell nucleus. The power output of the laser was attenuated with neutral density filters to give a final power density of 10mW at the stage. The peak power of the IR laser beam that induced UV photoproducts detected by immunostaining, was calculated to be ca. 190 GW/cm^2. DNA damage was induced and detected at a minimum laser power of 10mW when the dwell time at each pixel position (0.25μm^2) was 25ms. A dwell time of 50ms gave rise to more intense images (not shown). The laser beam was guided by a galvanometric scanning mirror moving at a rate of about 1kHz and was interfaced with computer software that defined a chosen pattern.

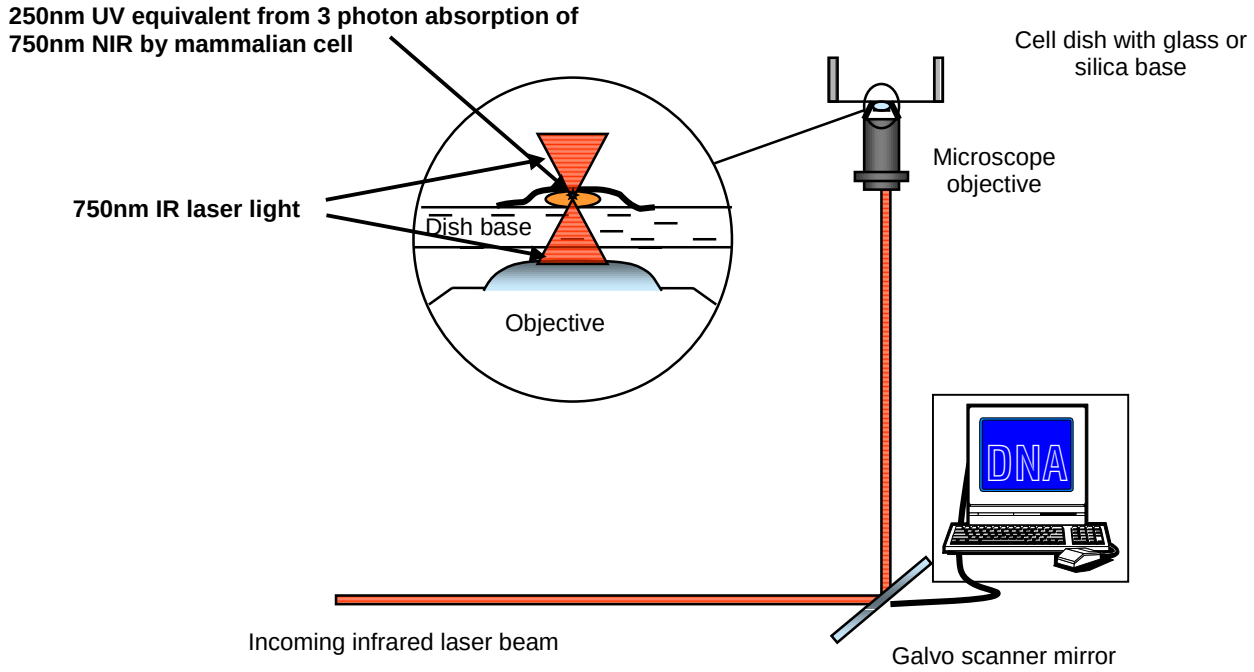

Figure 1. Experimental arrangement.

Induction of focused UV photoproducts in DNA by 3-photon near infra-red absorption.

The photoproducts induced in DNA by one-photon absorption around 260nm, the peak absorption of DNA, are cyclobutane pyrimidine dimers (CPDs) and 6-4 photoproducts. The image in Figure 2 demonstrates that triple infra-red (IR) photon absorption may be used to induce CPDs in cell nuclear DNA. The damage can also be generated in a precise and distinct pattern with nanometer three-dimensional resolution.

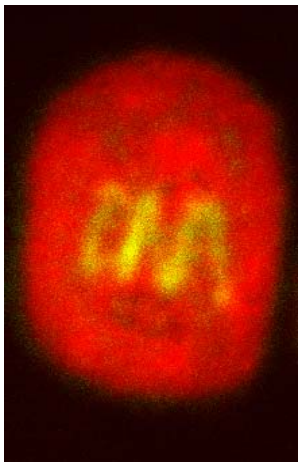

Figure 2. Triple Infra-red induced damage.

This image shows the letters DNA outlined by immunostained CPDs. The nuclei of the cells are visible as the DNA is counterstained red with propidium iodide. The cell cytoplasm is not visible. The minimum diameter of these nuclei is 10 microns. The pattern is made up of 200 pixel points, therefore damage induced in the range of one individual pixel will be confined to an area of less than 500nm. This indicates that the focused resolution obtained by 3-photon IR induction of CPDs is much higher than that obtained by one photon induction of CPDs in cell nuclei [7].

Collateral two-photon IR damage in cells

To be useful for DNA repair studies it is important that the induction of specific damage in the DNA by focused three-photon near infra-red laser irradiation does not create significant collateral damage by two and one photon process. Approximations of the volumes affected by single photon and multi-photon from 750nm laser excitation can be estimated by modeling. The models used so far are based on Gaussian beams focused using a microscope objective with numerical aperture of 1.2 with an arbitrary choice of beam size at the objective.

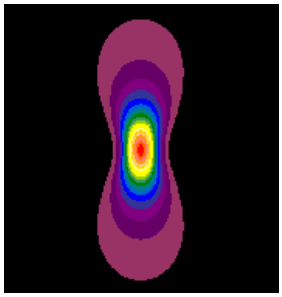

Figure 3. Affected volume of one-photon 750nm NIR intensities.

Figure 3 shows the calculated affected volume of one-photon 750nm intensities. This shows the axial direction (vertical) and equatorial (horizontal). The colours represent the intensity of the laser beam which is greatest at the centre (red) and decreases as outlined by the contours extending outward. Initial measurements (data not shown) made on the staining of the DNA damage by the fluorescent labeled antibody suggest that the minimum intensity from the beam that gives rise to the photoproducts is 50% (green/yellow contours). At 50% intensity contours the volume of the one-photon affected volume is 0.814μm in the axial direction and 0.366μm in the equatorial direction. The two-photon affected volume is √2 times smaller than one-photon affected volume, 0.524μm in the axial direction and 0.259μm in the equatorial direction. The volume affected by three-photon absorption is √3 times smaller than one-photon absorption, 0.415μm in the axial direction and 0.211μm in the equatorial direction.

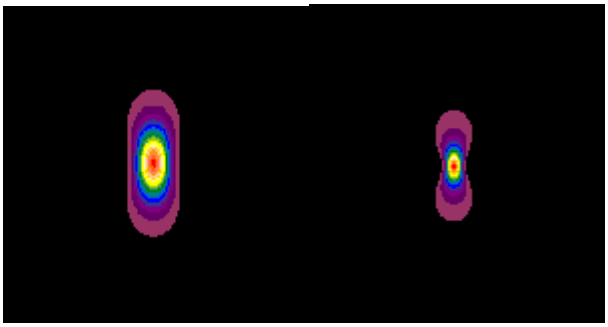

A **B**

Figure 4. Two-photon, 750nm affected volume (A) and three-photon 750nm affected volume (B).

It can be seen from Figures 3 and 4 that the shapes of the one and two and three-photon excitation profiles differ.

The calculations neglected phase aberrations caused by refractive index changes and intensity changes due to absorption that may be important in the case of 3-photon, 750nm absorption. Further work will be carried out to estimate more accurately the size of affected volumes and increase the resolution of the minimum spot size obtainable. It is estimated that we can increase the resolution of the minimum damage spot by a factor of ten. However, even at the present resolution no collateral radiation will spread outside the cell nucleus that is 10-20 μm in size.

Two-photon excitation from 750nm radiation will give rise to absorbance at 375nm. At this wavelength flavins and NADH are potential endogenous cellular absorbers. The major localization site of these co-enzymes is in the mitochondria that are situated in the cytoplasm. The techniques which we have described here will confine two-photon reactions in the cell nucleus, thus it is unlikely that significant absorption will occur at 375nm and collateral effects from this radiation will be minimal.

The maximum photon flux density from focused near infra-red laser irradiation that leads to optical breakdown in water is greater than 450 $GWcm^{-2}$ [8], considerably higher than the intensity of 190 $GWcm^{-2}$ used to induce DNA damage in our experiments. It is noteworthy that femtosecond laser microscopy of living cells has been performed for several minutes with a peak intensity of about 200 $GWcm^{-2}$ without impact on cellular reproduction or viability [3]. This suggests that the consequence of the radiation that the cells were exposed to in our experiments is confined to the DNA damage illustrated.

Repair of photoproducts induced by three-photon near infra-red absorption

Cells were irradiated using the pattern seen in Figure 2 and replaced in a CO_2 incubator at 37°C. Figure 5 shows the typical loss in intensity and definition of the staining of CPDs when the cells were incubated for one hour before staining.

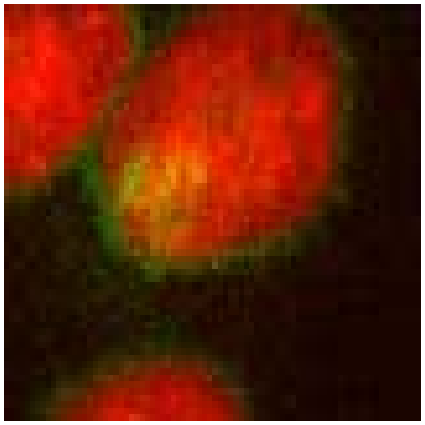

Figure 5. Loss of intensity of staining after incubation.

Since these cells were in the quiescent state of growth, the disappearance of lesions is most likely to represent repair of the lesions. Diffusion of the DNA could also cause loss in the definition of the pattern, but cells that had been irradiated with the same focused pattern showed even lighter staining in a localized region following 2 hours post-irradiation incubation (micrograph not shown). In quiescent cells, it is unlikely that diffusion of the DNA in time course could account for the apparent disappearance of the lesions. When a cell relocation system is used, detailed mapping of the lesions over a time course will be possible. If this is carried out on repair inhibited cells or repair deficient cells, the movement of lesions due to DNA diffusion will be distinguishable.

Focused damage patterns were also traced on the cell nucleus by focusing the near infra-red laser beam through a 100 x objective as well as the 40 x objective used to create the DNA damage illustrated above. As the 100 x objective was used with glycerine but the 40 x times was used dry, this demonstrates that the 3-photon NIR induced DNA photoproducts can be produced under variable conditions.

References

1. Kawata, S., Sun, H.B., Tanaka, T. & Takada, K. Finer features for functional microdevices- Micro-machines can be created with higher resolution using two-photon absorption. Nature 412, 697-698 (2001)
2. He, G.S., Markowicz, P.P., Lin, T.C., Prasad, P.N. Observation of stimulated emission by direct three-photon excitation. Nature 415: 767-770 (2002)
3. König, K. Multiphoton microscopy in the life sciences. Journal of Microscopy, 200, 83-104 (2000).
4. P.R.Cook. (1999) Molecular Biology – The organization of replication and transcription Science, 284, 1790-1795
5. N.P.Stanford, M.D.Szczelkun, J.F.Marko and S.E.Halford (2000) One and three-dimensional pathways for proteins to reach specific DNA sites. EMBO Journal, 19, 6546-6557
6. G.L.Hager, C.Elbi and M.Becker (2002) Protein dynamics in the nuclear compartment. Current Opinion in Genetics and Development, 12, 137-141
7. Volker, M., Mone, M. J., Karmakar, P., van Hoffen, A., Schul, W., Vermeulaen, W., Hoeijmakers, J. H. J., van Driel, R., van Zeeland, A. A., & Mullenders, L. H. F. Sequential assembly of the nucleotide excision repair factors in vivo. Molecular Cell 8, 213-224 (2001).
8. Hammer, D.X., Thomas, R.J., Noojin, G.D., Rockwell, B.A., Kennedy, P.K. and Roach, W.P. Experimental investigation of ultrashort pulse laser-induced breakdown thresholds in aqueous media. IEEE J. Quant. Electron. 62, 963-976 (1996)

Prepulse enhanced EUV yield from a xenon gas-jet laser produced plasma

G Kooijman, R de Bruijn, K Koshelev*, F Bijkerk

FOM Institute for Plasma Physics Rijnhuizen, P.O. Box 1207, 3430 BE Nieuwegein, the Netherlands
** also at ISAN, RAS, Troitsk, Russia*

W Shaikh, A J Bodey, G Hirst

Central Laser Facility, CLRC Rutherford Appleton Laboratory, Chilton, Didcot, Oxon, OX11 0QX, UK

Main contact email address: *bruijn@rijnh.nl*

Introduction

Laser produced plasmas (LPPs) based on either gaseous, cluster or liquid target material are prospective sources of Extreme Ultraviolet (EUV) radiation for future lithography applications. This is primarily because of their low debris production rate and convenient target material supply. However, the conversion efficiency (CE) of laser light into EUV radiation is low as compared to solid target LPPs. In general, gaseous targets, including cluster and liquid targets, are produced by sonic[1)] or supersonic[2)] expansion of gas through a pulsed or continuous nozzle. Most frequently xenon is used, firstly because the Xe spectrum contains high intensity broadband structures around 11 and 13-14 nm. Secondly, because of its noble gas nature, xenon will not deposit on surfaces at room temperature, and no contamination occurs. This is crucial for application in EUV lithography (EUVL). At the laser plasma and XUV optics group at FOM Rijnhuizen research is done on a laser plasma EUV source based on a pulsed supersonic xenon jet. In order to increase EUV yield several approaches have been investigated. Preshaping the target gas density distribution by applying a transparent buffer gas close to the target showed more than an order of magnitude increase in EUV yield[3)]. This report discusses experiments aimed at further increasing the EUV yield by application of a short intense laser prepulse to precondition the xenon target gas prior to the creation of the EUV emitting plasma by a main laser pulse.

Experimental set-up

The set-up used in the experiments is shown in Figure 1. A short (4 ps), high intensity (~10^{15} W/cm^2), low energy (10 mJ) 248 nm laser prepulse[4)] efficiently ionized the target material. Then, after a certain time delay, the preplasma was further heated by a main pulse of moderate intensity (Continuum 8000 frequency doubled Nd:YAG, 532 nm,6 ns,10^{13} W/cm^2, 350 mJ). The variable time delay between prepulse and main pulse was measured using a fast photodiode. After the preplasma was generated it further evolved, i.e. expanded, cooled, recombined, and set the target conditions, like electron density and temperature, for the subsequent main pulse.

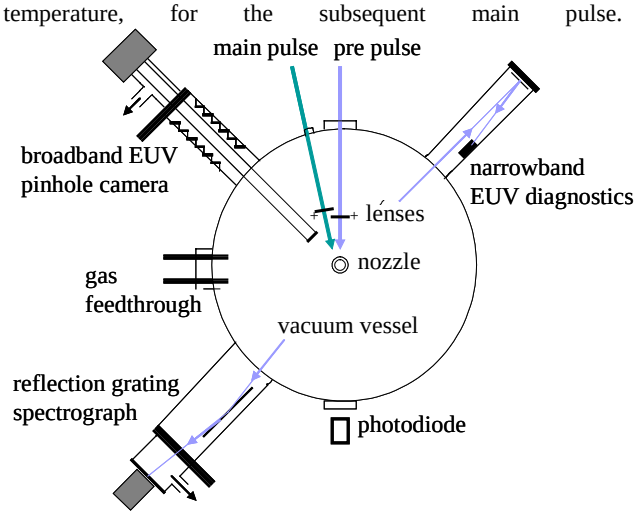

Figure 1. Experimental set-up.

Varying the time delay between the pulses therefore offered us the possibility of changing the target preconditioning for main pulse coupling, and consequently of optimizing EUV emission. Three different diagnostics were used to study emission from the plasma. A differentially pumped pinhole camera consisting of a 50 µm pinhole and a back thinned CCD (Reflex s.r.o.) filtered by 50 nm Si_3N_4/100 nm Nb imaged the broadband emission of the plasma (7-16 nm FWHM) with 10 times magnification. Narrowband EUV yield (13.5 nm, 0.4 nm FWHM bandwidth) was monitored by a diagnostic tool consisting of a calibrated curved Mo/Si multilayer mirror and a filtered junction diode (so-called Flying Circus[5-7)]). Spectrally resolved emission was imaged by a 1200 lines/mm reflection grating on a second differentially pumped back thinned CCD (Andor DH425-V). A 211 nm zirconium filter was used to select EUV wavelengths. The angle between the two laser beams was approximately 20°. Using a 10 µm pinhole, pictures of plasma generated on a solid slab target placed above the nozzle indicated that the focal spots of pre- and main pulse were ~10µm respectively ~30 µm in diameter and coincided within ~30 µm.

Results

Figure 2 shows both the EUV broadband yield, obtained by integrating the intensity of pinhole images, and the EUV narrowband yield at 13.5 nm versus time delay. All points are normalized to the yield measured when no prepulse was applied. The xenon backing pressure, i.e. the pressure in the reservoir behind the nozzle, was 10 bar. An increase in EUV yield at 13.5 nm yield is seen for delays up to 300 ns, while maximum increase is a factor 2.5 at 140 ns. The broadband yield increases between 30 ns and 200 ns delay when applying the prepulse. The maximum increase is a factor 1.8 at 160 ns delay. The broadband yield appears to decrease initially for delays shorter than 30 ns. For delays longer than 200 ns the broadband yield decreases with a maximum decrease of a factor 3 at 300 ns. Note that prepulse instabilities may account for the large deviation of some measuring points in Figure 2.

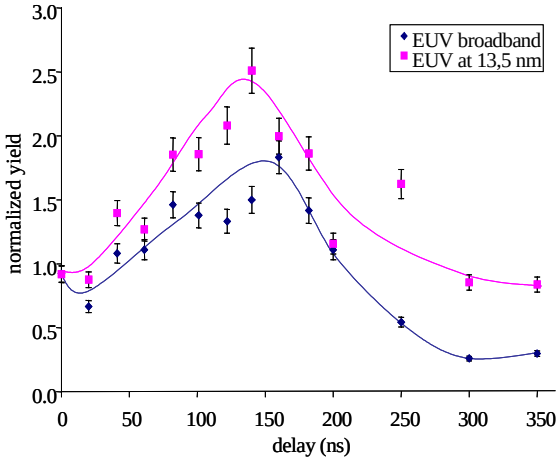

Figure 2. Normalized narrowband and broadband EUV yield versus prepulse-main pulse delay at 10 bar xenon backing pressure.

At higher backing pressures, thus higher initial target gas densities, a similar dependence of yield on delay was found. However the optimum delay, i.e. at maximum EUV yield increase, appeared to decrease with increasing backing pressure: at 15 bar an increase by a factor ~2.2 at 130 ns in narrowband- and a factor ~1.8 at 150 ns in broadband yield was found. At 20 bar the narrowband- and broadband yield had a maximum increase by a factor ~2.2 respectively ~1.5, both at 100 ns delay.

When applying the main pulse only, the measured narrowband- and broadband EUV yield were found to be independent on backing pressure within the error bars. Furthermore the size of the broadband EUV emitting part of the plasma did not change significantly for different backing pressures and delays. It amounted to 66 ± 6 μm perpendicular- and 130 ± 10 μm parallel to the laser beams (FWHM).

Pinhole images indicated that, above a certain time delay, the (centre) position of the plasma shifted in the direction of the incident laser beams. Figure 3 shows the displacement Δx_{plasma}, being the difference in the position of the plasma when a prepulse was applied and the position of the plasma without prepulse, versus delay for 10, 15 and 20 bar backing pressure. It can be seen that the threshold delay, above which the plasma position started to shift, decreases with increasing backing pressure: from 145 ± 5 ns to 120 ± 20 ns and 65 ± 15 ns for 10, 15 and 20 bar respectively. Remarkable is that, especially at 10 and 15 bar, the threshold delay appears to coincide with the optimal delay for EUV yield increase.

Spectrally resolved emission of a plasma generated without prepulse at 10 bar backing pressure is shown in Figure 4. Especially high emission around 10.8 nm and 11.1 nm can be seen. Due to technical problems no spectra of sufficient quality could be recorded at (other) comparable experimental conditions of Figure 2 and 3.

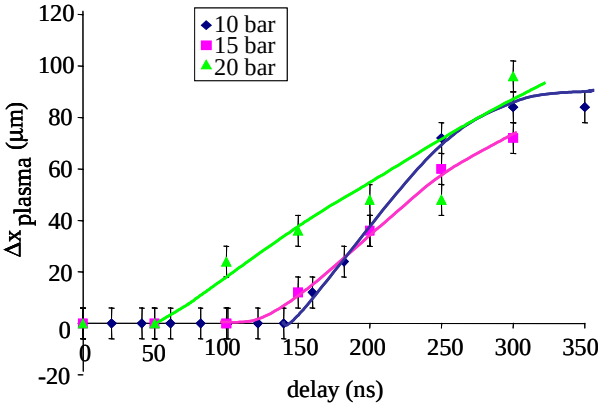

Figure 3. Shift in plasma position versus delay for three xenon backing pressures.

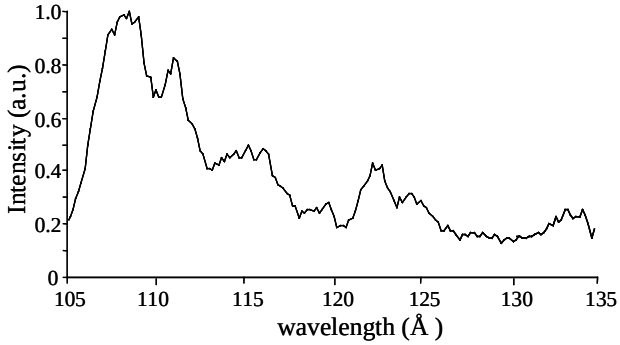

Figure 4. Xenon spectrum at 10 bar backing pressure without prepulse.

Discussion

The gain in narrowband- and broadband EUV, Figure 2, is tentatively explained by a change of the dominant xenon ionization stages with delay. Broadband EUV is known to be emitted by roughly Xe^{8+} to Xe^{12+} [8,9], while 13.5 nm radiation is mainly from Xe^{10+}. The Xe spectrum in Figure 4 suggests an 'overheated' plasma[10], with dominant ionization stages higher than Xe^{10+}, and consequently low EUV yield at 13.5 nm. However, some broadband emission can be present from e.g. Xe^{12+}. Application of the prepulse alters conditions for the main pulse such that it is less absorbed (density decreases due to preplasma expansion). This results in a colder plasma. The broadband EUV emitting ionization stages Xe^{8+} to Xe^{12+} then become relatively more populated, and an increase in broadband yield results. Since Xe^{10+} becomes more populated, the narrowband yield at 13.5 nm also increases.

At the optimum delay (~140 ns) the main ionization stages will be Xe^{8+} to Xe^{12+}, with Xe^{10+} being the highest populated stage. This explains the fact that optimum delay for both broadband- and narrowband yield was about the same. At longer delays the broadband yield decreases again, because the higher ionization stages Xe^{11+} and Xe^{12+} start to disappear. Xe^{10+} also becomes less populated resulting in a decrease in yield at 13.5 nm.

Eventually, at delays >200 ns, the plasma becomes so 'cold', that the broadband EUV emitting ionization stages are hardly populated at all, and a decrease in yield even compared to the non-prepulse case results. The narrowband yield is not (much) less than in the non-prepulse case for these long delays, because the population of Xe^{10+} may be comparable. Note that a reverse shift from lower to higher ionization stages, due to an increase in temperature (thus main pulse absorption) with delay, could in principle also explain the results. This is however less likely considering the 'overheated' nature of the spectrum taken for initial target conditions (no prepulse).

The relatively long delay in the order of 100 ns at which the effect of yield increase was observed is noteworthy. Numerical modeling to determine the preplasma parameters such as electron density and temperature on such a timescale is currently undertaken. Note that the velocity of xenon gas in the jet is estimated to be ~290 m/s (Mach number is 4.8), calculated at the nozzle's orifice, giving a gas displacement of ~29 μm in 100 ns. This may also have to be taken into account.

The shift of the plasma position as given in Figure 3 indicates that the main pulse interacted with expanding target material. The observed threshold delay may indicate a point where target material began to expand outside the initial boundaries of the gas jet, shifting the 'front' of the laser target interaction volume from the jet boundary towards the incoming main pulse laser beam. When assuming that the expansion induced by the prepulse started at the center of the jet, the (average) expansion velocity has to be in the order of 10^3 m/s, with the radius of the gas jet being 150 μm. The velocity with which the position of the plasma shifts above the threshold delays (thus the slope of the graphs in Figure 3) is of about the same magnitude. This velocity corresponds to a plasma temperature of ~2 eV for single ionized xenon, which is plausible because a few ns after the prepulse a low temperature, weakly ionized plasma is expected to remain due to expansion and recombination.

Conclusion

A short, intense, low energy prepulse was used to enhance EUV yield from a laser produced plasma generated on a supersonic xenon gas jet.

Yield increase was observed on a relatively large 100 ns delay timescale with a maximum of a factor ~2.5 at ~140 ns delay (for 10 bar backing pressure). Most probably, without a prepulse, an overheated plasma was generated by the main pulse. Prepulse application then resulted in less overheating by

decreasing the main laser pulse absorption. Spectral measurements (in a wider wavelength range) on plasmas generated by a comparable Nd:YAG laser are expected to provide verification on this in the near future.

Acknowledgements

This work is part of the research programme of the 'Stichting voor Fundamenteel Onderzoek der Materie (FOM)', which is financially supported by the 'Nederlandse organisatie voor Wetenschappelijk Onderzoek (NWO)'. The authors gratefully acknowledge financial support by the EU for providing access to the CLF and the EPSRC Engineering Instrument Pool.

References

1. X-ray emission from laser irradiated gas puff targets; H. Fiedorowicz *et al*.; Appl. Phys. Lett., 62 (22), pp. 1-3, 1993.
2. High-power extreme ultraviolet source based on gas jets; G. D. Kubiak *et al*.; SPIE 3331, 81-89, 1998.
3. Characterization of a novel double gas-jet laser plasma EUV source; R. de Bruijn *et al*.; SPIE 3997, p.157, 2000.
4. A plasma light source for the VUV spectral region; W. Shaikh; IEEE journal of quantum electronics, Vol.5, no.6, Nov/Dec 1999.
5. Flying Circus EUV source comparison, absolute yield, absolute yield fluctuations and contamination, R. Stuik *et al*.; Second SEMATECH Workshop on Extreme UV Lithography, San Francisco, International Sematech Vol. CD,http://www.sematech.org/public/news/conferences/euvl2000/documents/102_SRC14_stuik.PDF (2000).
6. Linearity of P-N junction photodiodes under pulsed irradiation; R. Stuik, F. Bijkerk; SPIE Vol. 4688, 2002.
7. Calibration of Flying Circus EUV diagnostics; R. Stuik, F. Bijkerk; Nuclear Instruments and Methods A, submitted 2002.
8. Analysis of the $4p^6 4d^8 4f$ and $4p^5 4d^{10}$ configurations ox Xe X and some highly excited levels of Xe VIII and Xe IX ions; S. S. Churilov, Y. N. Joshi; Physica Scripta, vol. 65, 40-45, 2002.
9. S.S. Churilov, private communication.
10. Highly ionized xenon spectra (95-260 Å) excited in TFR tokamak plasmas; C. Breton *et al*.; Physica Scripta, vol. 37, 33-37, 1988.

A New Approach to the Production of High Resolution X-ray Masks

J A Cairns, M R Davidson, G J Berry, A G Fitzgerald, J Thomson*

Division of Electronic Engineering and Physics, School of Engineering, University of Dundee, Dundee DD1 4HN, UK

**Division of Chemistry, School of Life Sciences, University of Dundee, Dundee DD1 4HN, UK*

W Shaikh, G Hirst, A J Bodey

Central Laser Facility, CLRC Rutherford Appleton Laboratory, Chilton, Didcot, Oxon, OX11 0QX, UK

Main contact email address: *j.a.cairns@dundee.ac.uk*

Background

The ability of optical lithography to transfer circuitry onto silicon chips has been central to the success of the microelectronics industry from its earliest beginnings. However as the features on such devices are predicted to shrink to tens of nanometres, one may have anticipated that optical lithography would be inherently incapable of meeting such demands. In fact this is not so. The 2001 edition of the International Technology Roadmap for Semiconductors predicts that optical lithography will continue to meet the requirements of the industry, even down to dimensions as narrow as 65nm. Admittedly, in order to do so, it is necessary to move to shorter wavelengths, first from 248nm to 193nm, and subsequently to 157nm, the latter generated by fluorine lasers. It should be noted that to achieve the production of circuitry with dimensions less than the wavelength of illumination it is necessary to use so-called *resolution enhancement techniques*, which include: *off-axis illumination, phase shift masking, and optical proximity correction*.

However, looking further ahead, it is generally accepted that the realisation of features with dimensions of less than 65nm will require a new type of lithography, usually referred to as next-generation lithography (NGL). Possible candidates for this include *extreme ultraviolet lithography* (EUV), *electron projection lithography* (EPL) and *proximity X-ray lithography* (PXL). One common feature of all of these is that they require substantially different masks, compared to those used in optical lithography. For example, EUV technology, operating in the 10-15nm wavelength region, requires a reflective mask, while both EPL and PXL require a thin membrane (typically 100nm silicon nitride) with a patterned metal layer on its surface.

The primary objective of this research programme is to demonstrate how such a patterned metal layer can be achieved. Conventional methods of producing metal patterns, such as by selective etching of continuous metal films or by electroless plating, are less than ideal when used in conjunction with thin fragile membranes. Therefore a new approach, involving the use of metal-containing organic compounds, was proposed.

The production of the X-ray masks

It was postulated that a potentially elegant method of producing X-ray masks would be to deposit a film of a suitable metal-containing organic compound on to the membrane, and then convert the film to metal in selected areas by the use of electron beam irradiation. Naturally this required that the metal-containing films had the capability of being deposited on to the membranes without causing damage to the latter. In addition, it was necessary to prove that subsequent electron beam irradiation of the films would yield high-resolution metallic patterns on the surface of the membrane; and that the non-irradiated regions of the film could subsequently be removed easily, without disturbing the metal patterns.

Taking these objectives in turn, a number of suitable compounds were identified, including cis-dichlorobis (triphenyl-phosphine) platinum(II), chlorotriphenyl phosphine gold(I) and chloro (1,5-cyclooctadiene) platinum(II). One of the attractions of these particular compounds was that they had the most useful property of being convertible into the vapour phase by sublimation, without undergoing decomposition in the process. This enabled them to be deposited as thin films (<1μm thick) by simple thermal evaporation in vacuo. The advantage of thermal evaporation over other methods of thin film deposition, such as spin-coating, is that the films can thereby be deposited on to a wide range of materials, including the fragile non-wettable substrates required to make X-ray masks.

Exposure to the electron beam was performed in a modified scanning electron microscope (JEOL T220). The positioning of the electron beam was controlled by the use of RAITH ELPHY Quantum Software. Following exposure, the non-irradiated material was removed simply by rinsing in acetone, followed by isopropyl alcohol. In this way it was demonstrated that high-resolution metal patterns could readily be achieved, as shown in Figure 1.

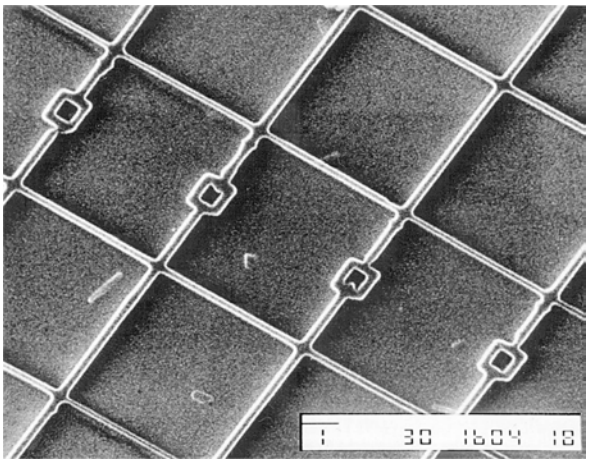

Figure 1. Example of high-resolution patterns obtained by electron beam irradiation of metal-containing organic films. Scale bar is 1 micron.

X-ray lithography

The next step in the programme was to demonstrate the applicability of these X-ray masks. For this purpose we used the soft X-ray source at the Central Laser Facility of the Rutherford Appleton Laboratory. This source generates a range of X-ray wavelengths by irradiating a target, in the form of a thin tape, with the focused output of a high power UV laser. In our programme carbon X-rays were used, generated from a Mylar tape. The X-ray mask was placed in close proximity to a silicon wafer, which had been coated with a layer of resist, in order to achieve a one-to-one transfer of the pattern between the mask and the resist layer. Incidentally, since it is impossible to focus X-rays, this type of proximity printing must inevitably be used. The result is that the dimensions of the features required on the circuitry are the same as those on the mask.

UV lithography

As mentioned above, the generation of X-rays at the Rutherford Appleton facility requires the use of an ultra-violet laser. In fact it is a pulsed laser, operating at 248nm. We had

observed that our films exhibited a strong absorption in this region of the spectrum, and so we exposed them directly to the laser source and found that they decomposed readily to metal.

This observation opens up a potentially attractive method of producing metal-rich patterns on surfaces, in essentially a one-step operation. Figure 2 shows a pattern transfer, achieved by passing the UV beam through a photomask in contact with one of the metal-containing films.

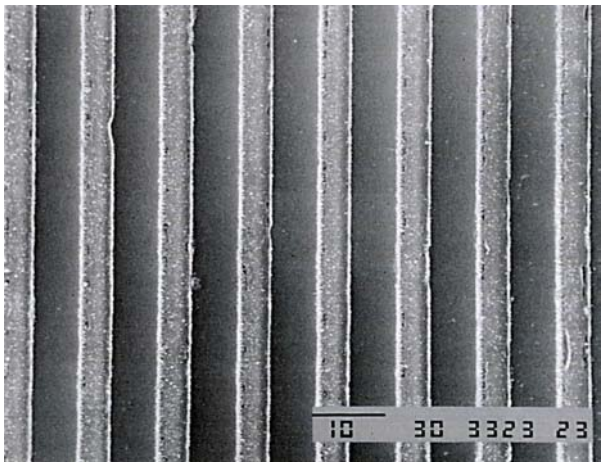

Figure 2. Example of platinum lines transferred by UV irradiation. Scale bar 10μm.

Several analytical techniques were used to investigate the nature of this process in more detail.[1-4] For example, X-ray photoelectron spectroscopy (Figure 3) confirmed the progressive transition of the film to a more metallic state under the influence of increasing UV irradiation, while the corresponding progressive decomposition of the organic components was monitored by the use of infrared spectroscopy (Figure 4).

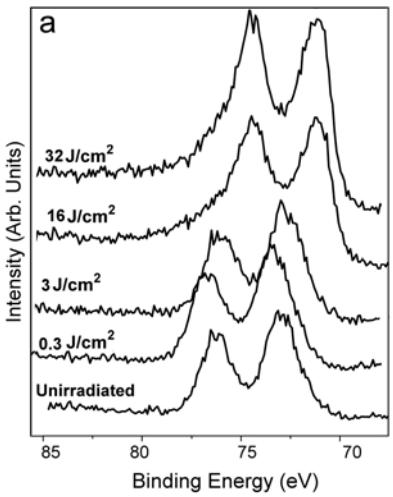

Figure 3. XPS analysis of UV irradiated films.

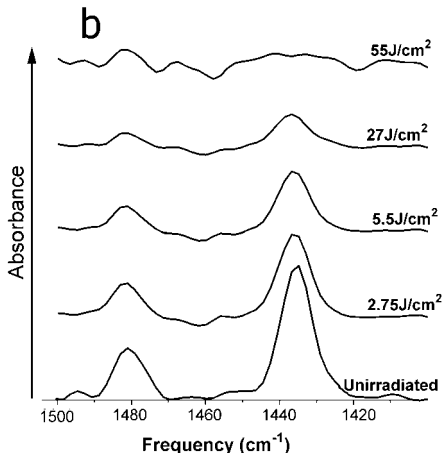

Figure 4. Infrared analysis results from UV irradiated organo platinum films.

Conclusions

It has been demonstrated that X-ray masks can be fabricated by the use of the metal-containing compounds described in this research study.

Furthermore, it has been shown that metal-rich features can be produced by direct UV irradiation of the same compounds.

Acknowledgements

This work was funded by EPSRC, Grant Number GR/M41223. The authors would also like to thank Dr A. Hourd, Compugraphics International Ltd., for the production of photomasks used in this work.

References

1. M R Davidson, G J Berry, Y Fan, J A Cairns and J Thomson, Institute of Physics Conference Series, 168, 215-218, 2001.
2. G J Berry, J A Cairns, M R Davidson, Y C Fan, A G Fitzgerald, A H Fzea, J Lobban, P McGivern, J Thomson and W Shaikh, Materials Research Symposium Proceedings, 624, 249-254, 2000.
3. G J Berry, J A Cairns, M R Davidson, Y C Fan, A G Fitzgerald, J Thomson, W Shaikh, Applied Surface Science, 162: 504-507, 2000
4. M R Davidson, Y Fan, G J Berry, J A Cairns, and A G Fitzgerald. Accepted for publication in Mikrochimica Acta.

Fibre Bragg grating fabrication using fluoride excimer laser for sensing and communication applications

T Sun, S Pal, J Mandal, K T V Grattan

School of Engineering, City University, Northampton Square, London EC1V 0HB, UK

Main contact email address: *t.sun@city.ac.uk*

Introduction

Fibre Bragg gratings (FBGs) in optical fibres have been demonstrated in a wide range of applications, such as for sensors [1,2], dispersion compensators, optical fibre filters and all-optical switching and routing [3]. Fibre Bragg grating sensors offer several properties which are unrivaled by comparison with their electrical or other fibre optical counterparts [4] and they have been widely used in structural and composite monitoring [5,6], and environmental analysis [7] under various conditions [8-10]. However, the thermal characterization of fibre Bragg gratings is essential for higher temperature sensing applications[11-13],for both increased reliability and to ensure an adequate operational lifetime for FBG-based optical components in wavelength division multiplexing (WDM) systems, for example. Recent work on material optimization reported by the University of Southampton has shown that tin-doped fibres are potential candidates for many grating-based applications in both the sensor and communication markets [14-16]. Several different types of FBGs have been reported (Type I, Type IIA or II), the difference relating to their fabrication conditions, as discussed in some detail by Othonos[17]. Arising from their different fabrication mechanisms, it is expected that they will also have different high temperature performance characteristics. A long-term thermal test on Type I FBGs written in B-Ge co-doped photosensitive fibres has been reported recently by the authors [18].

This report will focus on the maximization of the thermal capacity of FBGs created by varying the UV exposure time of the writing excimer laser (LSF - Lasers for Science Facility, Rutherford Appleton Laboratory, UK and a lower power, faster repetition rate Tuilaser), used to write gratings in different photosensitive materials.

The Fibre Bragg grating writing system

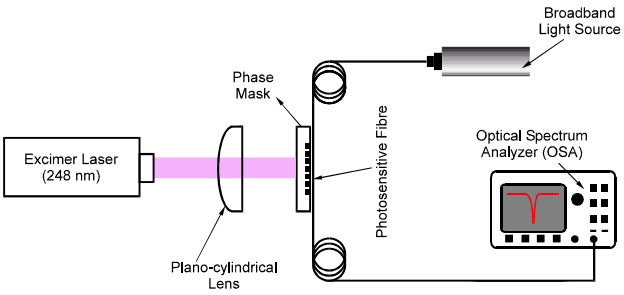

Figure 1. Fibre Bragg grating writing system using an excimer laser.

The setup to fabricate FBGs is shown in Figure 1, where the pulse power of the LSF excimer laser (LAMBDAPHYSIK COMPEX 205) centred at 248 nm was adjusted to 18 mJ and the repetition rate to 15 Hz (after the loan period, the above laser was replaced in the same set-up by a new BraggStar 500 supplied by Tuilaser AG). The plano-cylindrical lens was used to focus the laser beam from the excimer laser through the phase mask, a diffractive optical element, where a fringe pattern is produced by the interference of the plus and minus first order diffracted beams. The interference pattern photo-imprints a refractive index modulation in the core of a photosensitive optical fibre placed in close proximity to and immediately behind the phase mask. The photosensitive fibre is connected to a broadband source and an optical spectrum analyzer (OSA), which are used to monitor the effects on the fibre of the FBG writing process [17].

FBGs written in different types of photosensitive fibres

Two types of photosensitive fibres were used: (i) Ge-doped silica fibre (Redfern GF1) and (ii) B-Ge co-doped silica fibre (Fibercore Ltd). Figure 2 shows the Bragg wavelength and the refractive index modulation of the FBGs varying as a function of UV exposure time. The growth of the refractive index modulation stops when the Type I grating is being saturated, dropping to a very low level before increasing once again to form a Type IIA grating [19]. B-Ge co-doped fibre was found to be more sensitive to the fabrication of Type I, as well as to Type IIA gratings (taking less than 10 minutes for Type IIA with a laser energy of 12 mJ/pulse and a frequency of 200 Hz) compared to the Ge-doped fibre which requires more than 75 minutes to create the Type IIA grating, under the same conditions. When the photosensitive fibres were exposed to the UV beam from the excimer laser, the Bragg wavelength (λ_b) of the B-Ge co-doped fibre was seen to shift to the longer wavelength side even though it remained a Type I grating, but when it was over-exposed its center wavelength changed, moving to the shorter wavelength side, indicating the formation of a Type IIA grating. However, the shift of the Bragg wavelength (λ_b) of the Ge-doped fibre was always towards the longer wavelength side throughout the whole process. Both of these effects are shown in Figure 2. The opposing effect of the Boron and Germanium on the refractive index change may be one of the major factors causing the bi-directional shift of the Bragg wavelength (λ_b) of B-Ge co-doped fibres.

The process enabled the production of high reflectivity gratings which could readily be produced using the set-up described, fitting them for several specific applications. For example, such gratings are being used in a multiplexed Bragg grating based strain/temperature sensor system for structural integrity monitoring [20]. The next step in the study was to evaluate the high temperature performance of these gratings, given the interest in sensing strain and temperature in furnace linings from Corus Ltd. These techniques may require operation at temperatures up to 700°C, and it was important to test how well these gratings responded to that measurement challenge.

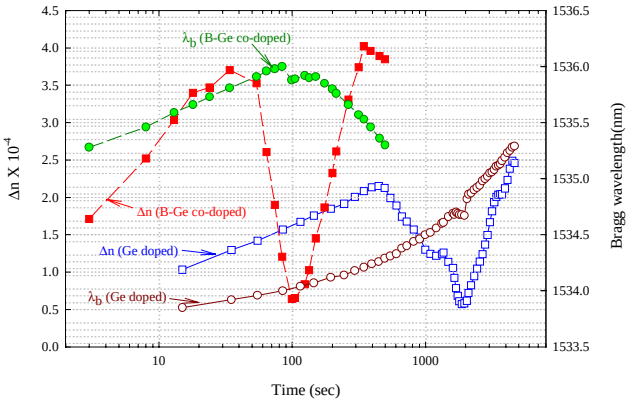

Figure 2. Variation of refractive index modulation and Bragg wavelength shift as a function of the UV exposure time.

Long-term thermal characteristics of various gratings

The four gratings fabricated above have been subjected to a series of long-term thermal exposure tests at 100°C, 200°C and then up to 750°C with a temperature increment of 50°C and their long term thermal decay process is shown in Figure 3. It was observed that up to 200°C, there was little change in reflectivity for all the gratings, but above this temperature, the decay first started for a Type I B-Ge co-doped FBG and soon a rapid decay occurred at ~ 300°C. Reaching a temperature of 350°C erased the grating completely within a few more hours. However, the B-Ge co-doped Type IIA grating remained almost unaffected up to ~ 400°C and only at 450°C could the rapid decay of the reflectivity be seen. This occurred until 500°C was reached, the temperature at which the grating was washed out completely. This confirms that Type IIA gratings can survive at temperatures higher by comparison with those for Type I gratings, even though the photosensitive materials used are the same.

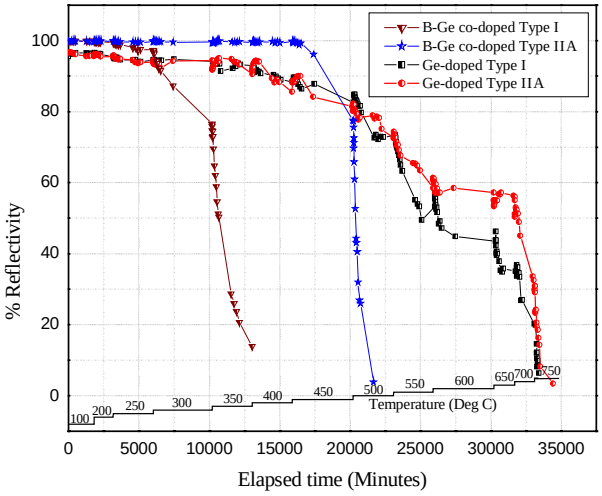

Figure 3. Decay of Ge-doped and B-Ge co-doped Type I and Type IIA gratings for long term thermal testing.

In addition, the work has shown that different photosensitive fibres have demonstrated different high temperature performance, which was also shown in Figure 3. The Ge-doped Type I and Type IIA FBGs are more able, by comparison to B-Ge co-doped FBGs, to sustain these high temperatures, where the Type I can withstand a temperature of 600°C with ~45% of reflectivity at an almost negligible decay rate. The demarcation point for the Type IIA is 650°C, with it retaining more than 55% of its reflectivity. Unlike the sudden decay of B-Ge co-doped FBGs at certain temperatures, the Ge-doped FBGs revealed a much slower rate of decay with each increment of 50°C during this study.

The Bragg wavelength shift with temperature has been widely used for temperature sensing or temperature compensation over a lower temperature range [19]. However, as shown in Figure 4, at each particular temperature the drift of the Bragg wavelength with elapsed time was observed for each grating, taking ~ 10 hours to stabilize. The rate of change is slightly different from one FBG to another. Figure 5 shows the Bragg wavelength shift with temperature after the stabilization has occurred (sampled 24 hours after each increment of temperature). The curves were almost linear but with slightly different slopes. The temperature sensitivities of the gratings were estimated by using a linear curve fitting of the data for each type of grating. The sensitivity for the B-Ge Type I grating showed 9.57 pm/ °C but for the Type IIA the dynamic range increased by 100°C, at the cost of a slightly lower value of sensitivity of 9.07 pm/ °C. The corresponding sensitivity values for the Ge-doped Types I and IIA FGBs were 12.80 pm/ °C and 12.35 pm/ °C respectively.

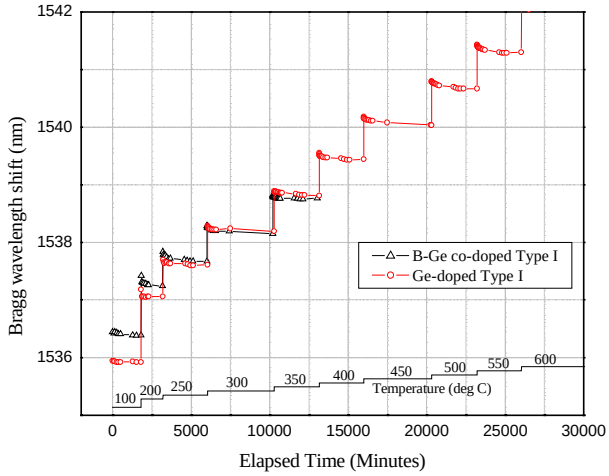

Figure 4. Bragg wavelength shift with elapsed time at each specific temperature.

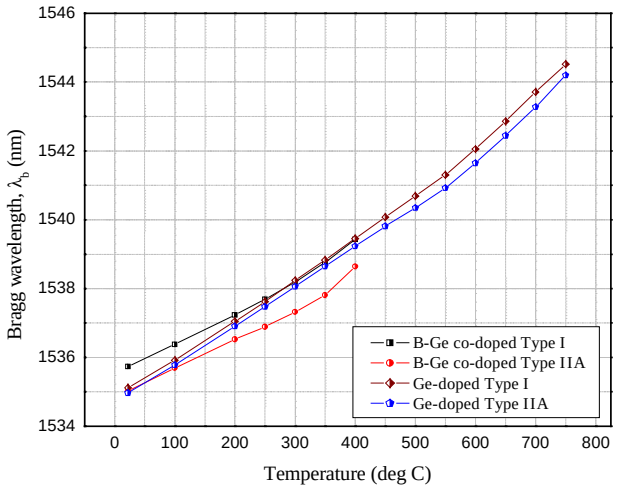

Figure 5. Bragg wavelength shift with temperature.

Conclusions

The above work has successfully demonstrated that FBGs can be tailored in such a way as to sustain high temperatures of up to 750°C, by writing Type IIA gratings on Ge-doped photosensitive fibres. Work is continuing and being carried out to optimize the photosensitive materials as well as the writing parameters, for example, finding the best conditions of UV exposure energy and exposure time, to maximize the thermal capacities of FBGs.

Acknowledgement

The authors would like to thank the staff of the Central Laser Facility for their assistance and support throughout the experiment. The experiment was supported by EPSRC through several schemes including the INTErSECT Faraday Partnership. The authors would also like to acknowledge the support from Commonwealth Scholarship Commission of ACU for one of us (SP) and the supply of the Redfern fibres for this experiment from Victoria University, Melbourne based on our long term collaboration between these two institutions.

References

1. A D Kersey, M A Davis, H J Patrick, M LeBlanc, K P Koo, C G Askins, M A Putnam and E J Friebele, J. Lightw. Technol., 15, 1442, (1997)

2. Y J Rao, Meas. Sci. Technol., 8, 355, (1997)

3. D Payne, EPSRC Laser Applications Theme Day, Manchester, (2002)

4. D Betz, L Staudigel, M N Trutzel, M Schmuecker, E Huelsmann, U Czernay, 15th Optical Fibre Sensors Conference, Technical Digest, 55, (2002)

5. R Willsch, W Ecke and H Bartelt, 15th Optical Fibre Sensors Conference, Technical Digest, 49, (2002)

6. E Udd, K Black, W Schulz, S Kreger and M Kunzler, D, Heider, 15th Optical Fibre Sensors Conference, Technical Digest, 59, (2002)

7. R Falciai, A G Mignani and A Vannini, Sensors and Actuators B – Chemical 74, 74, (2001)

8. A Fernandez, B Brichard, P Borgeermans, F Berghmans, M Decreton, P Megret, M Blondel and A Delchambre, 15th Optical Fibre Sensors Conference, Technical Digest, 63, (2002)

9. S W James and R P Tatam, 15th Optical Fibre Sensors Conference, Technical Digest, 87, (2002)

10. M Winz, K Stump and T K Plant, 15th Optical Fibre Sensors Conference, Technical Digest, 195, (2002)

11. J Canning, M Englund and K Sommer, Proceedings of the 14th International Conference on Optical Fiber Sensors, postdeadline paper, 1, (2000)

12. R J Schroeder, T Yamate and E Udd, Proceedings of SPIE, 3746, 42, (1999)

13. T Wavering, J Greene, S Meller, T Bailey, C Kozikowski, S Lenahan, K Murphy, M Camden, L Simmons, Proceedings of SPIE, 3538, 58, (1999)

14. G Brambilla, H J Booth, E K Illy, L Reekie, H Rutt and L Dong, Abstracts and Programme of In-fibre Bragg gratings and special fibres, The Institute of Physics, (2001)

15. G Brambilla, T P Newson and H Rutt, Abstracts and Programme of In-fibre Bragg gratings and special fibres, The Institute of Physics, (2001)

16. D Razafimahatratra, P Niay, M Douay, B Pumellec and I Riant, Applied Optics, 39, 1924, (2000)

17. A Othonos, Optical fibre sensor technology, advanced applications – Bragg gratings and distributed sensors (eds K T V Grattan and B T Meggitt), Kluwer Academic Publishers, 79, (2000)

18. T Sun, K T V Grattan, S A Wade, D I Forsyth and W M Sun, 1st International Symposium on Optical and Quantum Technology (invited paper), Bangkok, Thailand, November 2001, 24, (2001)

19. R Kashyap, Fiber Bragg Gratings, Academic Press, (1999)

20. Y M Gebremichael, B T Meggitt, W J O Boyle, W Li, K T V Grattan, L Boswell, B McKinley, K A Aarnes & L Kvenild, Proceedings of the 11th Conference on Sensors and their Applications XI, 3-6 September 2001, London, UK, 341, (2001).

Molecular Nanostructures Fabricated by Photolithographic Processes

S Sun, K S L Chong, G J Leggett

Department of Chemistry, UMIST, PO Box 88, Manchester M60 1QD

Now at: Department of Chemistry, University of Sheffield, Brook Hill, Sheffield S3 7HF

Main contact email address: *Graham.Leggett@shef.ac.uk*

Introduction

Self-assembled monolayers (SAMs) formed by the adsorption of alkanethiols, $HS(CH_2)_nX$, where X is an organic functional group, onto gold surfaces have attracted widespread interest as templates for the fabrication of molecular and biomolecular microstructures. Through variation in the adsorbate tail group X it is possible to generate a range of clean, well-defined organic surfaces. The use of substrates with reactive tail groups facilitates the immobilization of biological molecules (for example through the attachment of proteins via amide linkages to carboxylic acid groups). A number of methods have been reported for the preparation of micropatterned SAMs, the most widely used of which is microcontact printing (μCP)[1]. We have been exploring the possibility of using photolithographic methods to pattern SAMs. At the micron scale, these prove to be highly effective, yielding clean, well-defined patterns with good edge definition[2]. The basis of SAM photopatterning is the photochemical oxidation of the alkylthiolkate adsorption product to a weakly bound sulfonate on exposure to UV light in the presence of air[3]. Subsequent exposure of the sample to an ethanolic solution of a thiol with a contrasting terminal group functionality leads to displacement of the oxidation products and the formation of a chemical pattern[4].

Previously photopatterning has been thought of as being restricted to the micron scale, because of the well-known diffraction limit. However, we have explored a novel approach to nanofabrication using photochemistry by utilizing a frequency-doubled argon ion laser coupled to a near-field scanning optical microscope (NSOM). We term this approach scanning near-field photolithography (SNP)[5]. Using fused silica fibres, drawn to an apex with a diameter of only 50 nm, this configuration enables exposure of the sample in the near-field regime. The experimental configuration is shown in Figure 1. Using this approach we have been able to fabricate routinely features with dimensions on the order of a few tens of nm, representing a powerful and flexible new tool for the creation of molecular nanostructures.

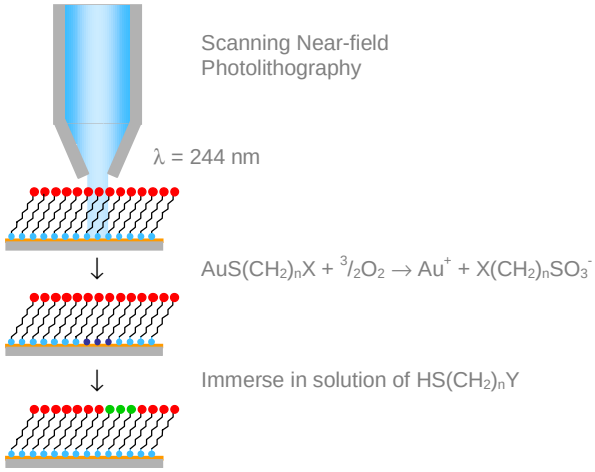

Figure 1. Schematic diagram showing the basic principles behind SNP.

Experimental

A Coherent Innova 300C FreD, from the Laser Loan Pool was coupled to a ThermoMicroscopes Aurora near-field scanning optical microscope (NSOM) using fused silica optical fibres (ThermoMicroscopes). SAMs were prepared by the adsorption of alkanethiols from 1 mmol solutions of the appropriate thiol in degassed ethanol. Lithography was carried out with the laser emitting at powers in the range 10 – 50 mW (prior to coupling to the optical fibre). Writing rates were 1 μm s^{-1}. After photo-oxidation, samples were immersed in 10 mmol dm^{-3} solutions of contrasting thiols for 10 min to displace oxidized material and create a pattern. Alternatively, wet etching was carried out by immersion of oxidized samples in a solution containing 0.001 mol dm^{-3} $K_4Fe(CN)_6$, 0.01 mol dm^{-3} $K_3Fe(CN)_6$, 0.1 mol dm^{-3} $Na_2S_2O_3$ and 1.0 mol dm^{-3} KOH.

Results

Figure 2 shows an AFM data for a sample that has been patterned by SNP. Three lines have been traced across a carboxylic acid terminated monolayer, and the sample immersed in a methyl terminated monolayer. The resulting pattern has been imaged in contact mode (topographical imaging) and the lateral force data acquired simultaneously. The topographical image shows no contrast because the two adsorbate molecules used here have identical alkyl chain lengths. However, the pattern may be clearly observed in the lateral force microscopy image. The cantilever used here was fabricated from silicon nitride, the outer surface of which is polar. The tip thus interacts most strongly with polar regions of the surface, but interacts weakly with non-polar regions. Consequently a higher friction force is measured for polar regions than for non-polar ones, leading to dark contrast on the methyl-terminated lines created by the nanofabrication process. A high resolution image (Figure 3) reveals that the line widths are less than 40 nm, even at the widest points.

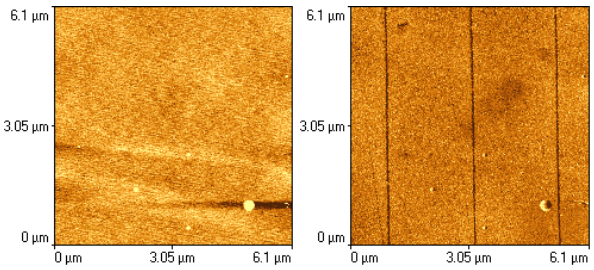

Figure 2. Left: AFM topographical image of a SAM patterned by SNP. Right: lateral force microscopy image acquired simultaneously, showing darker contrast on methyl terminated regions than on acid terminated ones.

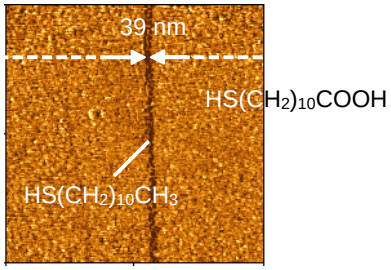

Figure 3. High resolution image showing a single line with a width of less than 40 nm.

Repetition of the patterning process in the reverse order (starting with a methyl terminated monolayer, writing lines and then immersing the sample in a solution of a contrasting thiol)

leads to patterned materials with the opposite contrast, but similar feature sizes (Figure 4).

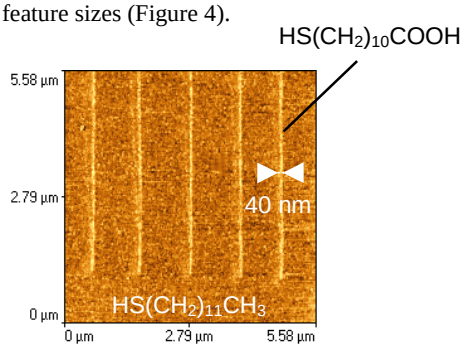

Figure 4. Lateral force microscopy image of a methyl terminated SAM into which 5 lines of carboxylic acid terminated adsorbates have been written.

Feature sizes of 40 nm were routinely achieved. However, on occasions, even smaller features were fabricated. The narrowest lines written to date were only 25 nm wide. This was a surprising observation, given that SEM revealed that the internal diameters of the SNOM figures used were approximately 40 nm. One would have expected that the feature sizes would be limited be the diameter of the aperture through which the SAMs were exposed to UV light. It seems that the feature sizes were dependent to some extent on the morphology of the underlying gold, and the connection between gold morphology and oxidation chemistry is currently under investigation.

The alkylsulfonates that result from the photo-oxidation of alkanethiolate adsorbates are susceptible to displacement by a wide variety of solution-phase reagents. If, following exposure to UV light, the sample is immersed in a solution of a ferri/ferrocyanide etchant, then the sulfonates will be displaced and the underlying gold dissolved[6]. Unoxidised thiols protect the substrate from erosion. Thus photopatterned SAMs may be used as masks for the selective etching of gold. The feasibility of using SNP in conjunction with such wet etching processes was explored. Figure 5 shows a sample that has been patterned in this way. Two lines have been oxidized in a monolayer of mercaptohexadecanoic acid. The sample has then been immersed in the ferri-ferrocyanide etch solution for 15 minutes. It can be seen that the gold has been removed from the oxidized regions, leading to the formation of two trenches that have widths very similar to those of the features created by SNP (50 nm) and which are 30 nm deep, indicating the complete removal of the gold film from those areas. This result illustrates that SNP offers potential for the fabrication of three-dimensional nanostructures, as well as chemical patterns, suggesting it may be a versatile tool for the construction of a wide range of nanoscale structures.

Conclusions

Using a UV laser coupled to a SNOM, we have demonstrated that it is possible to routinely fabricate structures in SAMs that are substantially smaller than the diffraction limit of $\lambda/2$. Routinely we have achieved linewidths of $\lambda/6$, and on occasions we have achieved $\lambda/10$. SNP facilitates not only the patterning of surface chemical structure, but also the creation of three-dimensional nanostructures by combination with suitable etching methods. Photochemical methods provide powerful and flexible routes to the immobilization of biological molecules at surfaces, and the data presented here demonstrate that these methods may now be utilized in the creation of biological nanostructures through the application of SNP. SNP thus appears to be a valuable new tool for use in nanofabrication and we expect it to find widespread utility in biological nanotechnology, molecular electronics and other fields where small-scale control of chemistry and structure is critical.

Acknowledgements

The authors are grateful to the Laser Loan Pool for three loans of a frequency doubled argon ion laser, and to EPSRC for financial support.

References

1. Y. Xia and G. M. Whitesides, Angew. Chem. Int. Ed. 37, 550 (1998).
2. E. Cooper and G. J. Leggett, Langmuir 15, 1024 (1999).
3. J. Huang and J. C. Hemminger, J. Am. Chem. Soc. 115, 3342 (1993); N. J. Brewer, R. E. Rawsterne, S. Kothari and G. J. Leggett, J. Am. Chem. Soc. 123, 4089 (2001).
4. M. J. Tarlov, D. R. F. Burgess and G. Gillen, J. Am. Chem. Soc. 115, 5305 (1993).
5. S. Sun, K. S. L. Chong and G. J. Leggett, J. Am. Chem. Soc. 124, 2414 (2002).
6. Y. Xia, X.-M. Zhao, E. Kim and G. M. Whitesides, Chem. Mater. 7, 2332 (1995).

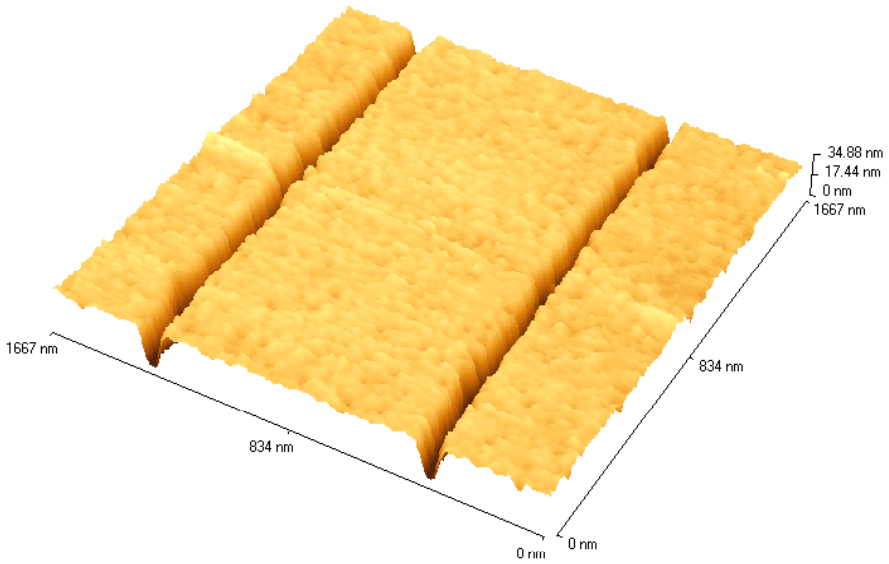

Figure 5. AFM topographical image showing a SAM of mercaptohexadecanoic acid, following the writing of two lines by SNP and immersion in a ferri/ferrocyanide etch solution.

Progress with the King's College Laboratory Scanning X-Ray Microscope

A G Michette, S J Pfauntsch, A K Powell, T Graf, D Losinski, C D McFaul

Department of Physics, King's College London, Strand, UK

G J Hirst, W Shaikh

Central Laser Facility, CLRC Rutherford Appleton Laboratory, Chilton, Didcot, Oxon, OX11 0QX, UK

Main contact email address: *Alan.Michette@kcl.ac.uk*

Introduction

Although the previous version of the laboratory x-ray microscope[1)] was successful in obtaining images of test specimens, its performance was compromised by several limitations. These included the following.

- The image acquisition time should, ideally, be limited by the repetition rate of the laser used to form the x-ray source plasma. However, the best scan rate that was achieved was ≈1 Hz; this was because the scanning was done by moving the tape target mechanism using stepper motors, and the large mass that had to be moved resulted in a long settling time.
- The alignment of the x-ray optical elements (zone plate and order-selecting aperture) was done using manually driven stages, resulting in a tedious and lengthy procedure.
- The x-ray beam was taken off in a horizontal direction, leading to vertical specimen mounting. This was a left-over from synchrotron based microscopes, and is clearly not ideal for hydrated specimens.
- The image resolution should have been ≈0.2 µm, with the major contribution coming from the demagnified source size. However, the best that was achieved was ≈0.4 µm, due to vibrations and (primarily) electrical noise in the detector[2)].

In order to overcome these limitations several potential improvements to the x-ray microscope are planned, and some of these have been tested as described below. Two which do not need further discussion here are the motorisation of all movable components and the minimisation of vibrations using an isolation table.

Beam Scanning

In order to overcome the limitation on scanning speed, source scanning will be replaced by beam scanning using galvanometer mirrors. This still moves the source point, keeping the specimen stationary as in the original concept of the scanned source microscope[1)], but a lot less mass needs to be moved. For a horizontal beam, when the tape surface is vertical, two orthogonal mirrors are used, each scanning at up to 800 Hz (for a vertical beam, this has to be modified slightly, as described below). The imaging time is thus determined by the laser repetition rate, as required. The full angular range of the mirrors is ±30°, but for a 20 µm field of view, which is typical in x-ray microscopy, the range is only ±1°. Over this range the rotations are essentially hysteresis free and so a "snake" scan pattern can be used, rather than raster scanning, eliminating fly-back time and thus allowing faster imaging. The noise on the rotations is ≈15 µrad which, allowing for demagnification by the zone plate, corresponds to a step of ≈8.5 nm on the specimen; this does not degrade the image resolution to any significant extent.

Horizontal Specimen Mounting

All synchrotron-based x-ray microscopes use horizontal x-ray beams and therefore vertical specimen mounting. This is because x-ray reflection through 90°, requiring a mirror to operate at 45° incidence angle, is extremely inefficient even using multilayer mirrors. However, with a laser-plasma source it is relatively simple to tilt the target surface to allow x-rays to be observed in the vertical direction. A modification to the previously used tape target drive has shown that this is feasible, without affecting the tape driving, and a new drive is now being designed to incorporate this.

Using a vertical beam does have one implication for the design of the scanning mechanism. Scanning the laser beam along the slope direction of the target surface would cause the beam to go out of focus, requiring a (slow) mechanical step to refocus it. The scan range would also be limited by the width of the tape. Since a mechanical step is needed in any case, the mirror scan is redundant, and so in this configuration the slow scan direction will be performed using a stepper motor to move the target and focusing lens together. The target drive will be made lighter than before, and a settling time τ of a few milliseconds should be achieved. For an $N\times N$ image this will only increase the imaging time by $N\tau$ ms, small compared to the total imaging time.

With a horizontal beam the x-ray microscope is at an angle of 45° to the incoming laser beam, so that the target surface is set at an angle of 22.5° to the beam. For a vertical beam the microscope axis is at 90° to the laser beam, which could result in a different distribution of spectral intensity. Spectra in the two directions, from a Mylar tape target, have therefore been taken with a transmission grating spectrometer[3)].

Unfortunately it was not possible to compare these directly, since a grating which had lasted over 130,000 laser shots in the horizontal direction broke almost immediately when the spectrometer was moved to the vertical direction. At first this was thought to be due to chance, but another grating and then a membrane also broke very quickly. This suggests that the debris is enhanced in the vertical direction, which could be due to the vertical polarisation of the laser beam or to the beam profile. Subsequent experiments, currently being analysed, have been carried out to characterise this. It should be noted that the debris will not be a problem for microscopy since the spectrometer grating was much closer (12 cm) to the source than the vacuum window prior to the zone plate (40 cm) for microscopy. It will still be important to minimise debris, however, for a high repetition rate source as the dust cloud which builds up around the source point has to be cleared before the next laser pulse since it causes the focused beam to expand. This leads to a

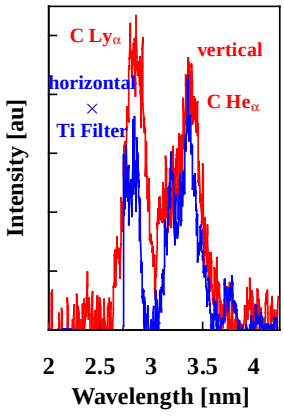

Figure 1. Comparison of vertical and horizontal spectra from a Mylar tape target.

larger source and possibly different emission characteristics and also absorbs the x-rays.

In order to overcome the vertical debris problem temporarily, a 1(±0.25) µm titanium foil was placed in front of the grating. As well as acting as a debris shield, this selectively transmits water-window x-rays. The spectrum obtained is compared with the horizontal spectrum convolved with the titanium transmission in Figure 1, and it can be seen that there are no major differences.

Criticality of Focusing

It has previously been noted[1)] that the x-ray emission, measured by the reference diode inside the target chamber, is constant over a range of about 300 µm, and to date the practice adopted to determine the best focus has been to use the centre of this range. However, since the depth of focus of the lens is only about ±10 µm, and also because of the de-focusing effect of the dust cloud, it is not certain that this was the best approach. A range of spectra, at –150 µm, 0 µm and +150 µm (+ meaning away from the target surface), from the nominal focus was therefore taken (Figure 2).

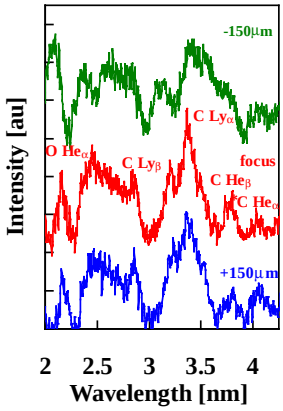

Figure 2. Comparison of Mylar spectra at different focal positions.

The spectra shown in Figure 2 were taken with 20 torr of helium in the target chamber, which effectively transmits all of the source emission. It is clear that the spectrum at nominal focus is sharper than the other two. The linewidths are instrumental, and the source sizes derived from them (Figure 3) indicate that the nominal focus was not in fact quite the best. Sectra filtered with 10 torr of N_2 and 1 µm of titanium (the latter being in the vertical direction) lead to the same conclusion. The source sizes at what these data indicate are the best foci are shown in Table 1; the different source sizes for the different filters are since different spectral lines were sampled.

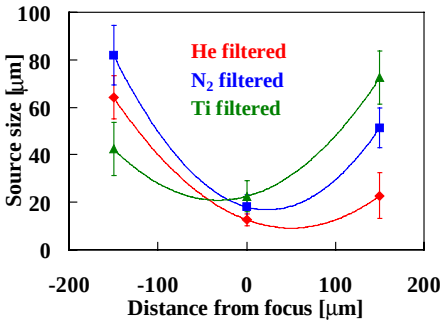

Figure 3. Source sizes derived from the spectra.

A New Detection Strategy

The main problem with previously used detectors was caused by noise generated by the laser system and by the plasma, which is coincident with the x-ray pulse. It is also non-random and so cannot be removed by integration. This is the limiting factor on image quality if the x-ray pulse is detected directly.

Filter	Spectral components	Source size [µm]
20 torr He	All	9^{+5}_{-4}
1 µm Ti	Water window	21^{+4}_{-7}
10 torr N_2	Mainly H-like C Ly$_\alpha$, some He-like C He$_\alpha$	17^{+6}_{-5}

Table 1. Measured source sizes at focus.

The solution is not to detect the x-rays directly. Instead, an x-ray sensitive phosphor (Gd_2O_2S:Pr) was coated onto a glass coverslip which was then placed in front of a light-sensitive diode. The decay time of the phosphor (several microseconds) is much longer than the noise pulse duration and so the diode can be gated to remove the noise. The signal can then be amplified and integrated. Initial tests, in which the phosphor coated diode was placed next to the reference diode inside the target chamber, show that the response is linear (Figure 4). In these measurements the phosphor coated diode had either a 2 µm titanium (2×1 µm, since the 1 µm foils have pinholes) or a silicon nitride (100 nm) / aluminium (45 nm) filter in front of it to act as a light and UV shield. The titanium filter was only about 1% transmissive in the water window but was larger than the active area of the diode (2×2 mm), while the other filter was about 50% transmissive but smaller (1×1 mm). Further tests are planned with a 2×2 mm silicon nitride (100 nm) / titanium (~0.5 µm) filter and with the diode placed outside the chamber to simulate the signal levels expected in the x-ray microscope.

The phosphor is about 15% efficient for soft x-rays and, of course, emits isotropically. The signal could therefore be enhanced by fitting the diode with a reflective cap (with a small hole for the x-rays), since the phosphor is transparent to its own radiation (which peaks at λ = 510 nm).

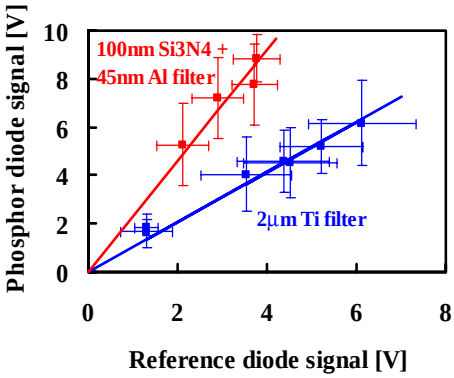

Figure 4. Comparison of the phosphor coated diode with the reference diode.

Conclusion

Significant advances have been made in the instrumentation for the laboratory scanning x-ray microscope which should shortly allow a performance evaluation of the whole system.

References

1. A G Michette *et al*, Central Laser Facility Annual Report 1998-1999, RAL-TR-1999-062, 151, (1999)
2. A G Michette *et al*, Central Laser Facility Annual Report, 1999-2000, RAL-TR-2000-024, 144, (2000)
3. A G Michette *et al*, Central Laser Facility Annual Report, 2000-2001, RAL-TR-2001-030, 123, (2001)

Terahertz generation at semiconductor surfaces

E H Linfield, A G Davies, M B Johnston, A Dowd

Semiconductor Physics Group, Cavendish Laboratory, Madingley Road, Cambridge CB3 0HE, UK

Main contact email address: *ehl10@cam.ac.uk*

Introduction

The terahertz (THz) frequency range, usually defined as 100GHz – 10THz, represents a significant portion of the electromagnetic spectrum (Figure 1), for which compact, solid-state, room temperature, sources are still not available.

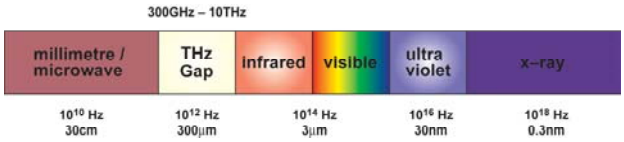

Figure 1. A schematic representation of the electromagnetic spectrum showing the THz region.

On the microwave side of the spectrum, it is difficult to fabricate electronic devices which operate at frequencies substantially above 100 GHz. On the optical side, interband diode lasers have long been designed for operation at visible and near-infrared frequencies. However, this concept, where light is generated by the radiative recombination of conduction band electrons with valence band holes, cannot be simply extended into the mid-infrared since suitable semiconductors are not available. Instead, research has used the quantum cascade (QC) concept in which inter-subband or inter-miniband transitions in layered semiconductor heterostructures are used to generate light in the mid-infrared. These unipolar injection lasers, have been demonstrated at room temperature up to 24 μm (12.5 THz). However, extending this concept to frequencies below 10THz is a considerable challenge: for example, free carrier absorption in semiconductors scales approximately as the wavelength squared requiring a large-gain active region, and the small energy (10–20 meV) of the optical transition necessitates very selective injection. Despite these issues, 4.4 THz QC lasers have been demonstrated (R Köhler *et al*, Nature 417, 156 (2002)), but at cryogenic temperatures.

Owing to the difficulties in fabricating solid-state THz sources, researchers have focused attention on all-optical techniques of producing THz radiation employing visible/near-infrared, femtosecond pulsed lasers. It is with these *coherent* THz systems that many of the exciting prototype experiments have been undertaken which have demonstrated the potential of THz radiation for imaging and spectroscopy in the biomedical sciences. In this report, we will focus on such systems. We will discuss how semiconductors structures can be used to convert ultra-short (~100 fs) near-infrared pulses into THz pulses, and then concentrate our discussion on the ultra-fast transport of electrons and holes at semiconductor surfaces.

Coherent THz Imaging and Spectroscopy Systems

A schematic representation of a THz time-domain spectroscopy system is shown in Figure 2. At the heart of this system is an ultra-short (~100 fs) visible/near-infrared laser, and, for the work described here, we made use of the Rutherford Appleton Laboratory loan pool femtosecond laser. Pulses from such a laser (typically centred at 780 nm) are directed onto a semiconductor THz generator which converts the incident pulses into THz pulses. The THz pulses are either emitted colinearly with the reflected incident pulses, or propagate through the semiconductor generator and emerge from the far side. The emitted THz radiation is collected and collimated by an off-axis parabolic mirror, and then focused by a second off-axis parabolic mirror onto the sample, which can be stepped across the beam to build up an image.

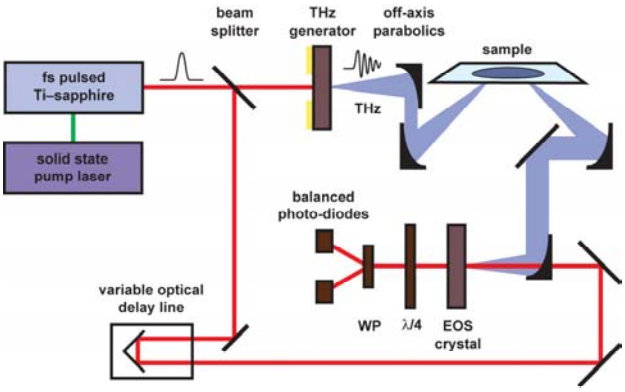

Figure 2. Schematic diagram of a THz spectroscopy system.

Coherent detection of the transmitted or reflected THz radiation can be achieved in a number of ways. Figure 2 shows a technique based on the ultrafast Pockels effect in which the THz beam is collected and focused onto an electro-optical sampling (EOS) detection crystal (for example, {110} ZnTe). The THz field induces an instantaneous birefringence in the electro-optic medium, which is readily probed with a second visible/near-infrared beam, initially split from the pump beam. The birefringence modulates the ellipticity of the probe beam, which is measured using a quarter waveplate, a Wollaston polarization (WP) splitting prism, and two balanced photodiodes. By placing an acousto-optic modulator in the pump beam (not shown), lock-in techniques can be used to measure the photodiode signal. Furthermore, by measuring this signal as a function of the time-delay between the arrival of the THz and probe pulses at the EOS crystal, the electric field of the THz pulse in the time domain can be obtained. A Fourier transform then gives the frequency spectrum of the radiation.

THz Semiconductor Sources

Semiconductor surfaces have been widely used in conjunction with femtosecond visible/near-infrared lasers as THz emitters, exploiting bulk electro-optic rectification (difference-frequency mixing) and ultrafast charge transport.

Bulk electro-optic rectification

In this mechanism, the second order non-linear susceptibility of a semiconductor is exploited for the generation of THz radiation. A time-dependent polarization is induced which is proportional to the intensity of the incident pulse. To date, this mechanism has been used to generate THz radiation in a number of semiconducting materials (e.g. GaAs, GaSe and ZnTe). However, the difficulty in achieving phase matching over a broad band of THz frequencies provides a fundamental limitation.

Ultra-fast charge transport

THz radiation can also be generated by the acceleration of photoexcited electron-hole pairs in semiconductor structures. Here an ultrafast visible/near-infrared pulse, of photon energy greater than the semiconductor band gap, creates electron-hole pairs close to the surface of the generation crystal. These can be accelerated by an appropriate electric field and the resulting changing dipole leads to generation of a THz pulse.

Typically, suitable surface fields are realised in two ways (Figure 3). First, a lateral antenna comprising two electrodes can be deposited onto a semiconductor surface. A large electric

field is applied between the electrodes which accelerates the photocarriers generated by the incident laser pulse focused between the electrodes.

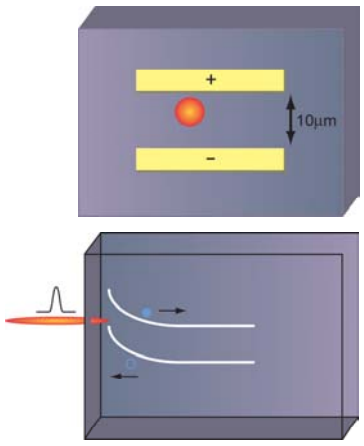

Figure 3. Schematic diagrams showing two THz emitters in which photoexcited carriers generated by a focused visible/near-infrared laser pulse are accelerated and radiate in an electric field. The field can be provided by a lateral antenna structure (upper) or the intrinsic semiconductor surface depletion/accumulation field (lower).

Second, ultrafast charge transport can be driven by both the intrinsic electric field perpendicular to the semiconductor surface and by differences in the electron and hole mobilities (photo-Dember effect). The emitted power and bandwidth for this generation mechanism depend critically upon the temperature and properties of the semiconductor crystal, as well as the energy, pulse width and flux of the incident laser pulse. Recently, there has been enormous interest in this mechanism, which forms the basis for our discussion here, following the demonstration that an external magnetic field can be used to enhance the emitted THz power by over an order of magnitude. We will explain fully the mechanism for this enhancement and discuss how it is being used as the basis for the design of new emitters.

Surface Field Generation

Our experimental work with the Rutherford Appleton Laboratory femtosecond laser has focused on THz radiation generated via ultrafast charge transport perpendicular to a semiconductor surface. (Optical rectification effects are negligible for the crystal orientations used here.)

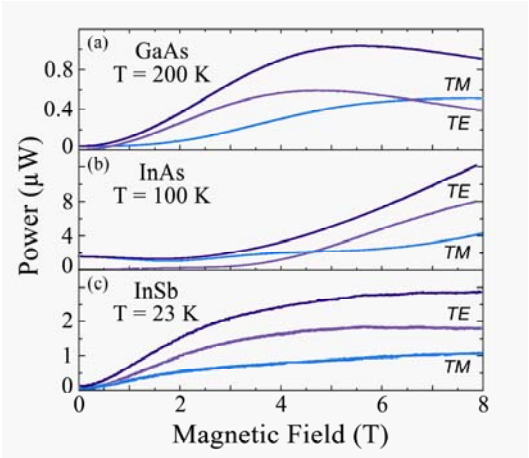

Figure 4. Emitted THz power as a function of applied magnetic field for bulk GaAs, InAs, and InSb. The *TE* and *TM* components of the radiation (labelled) are shown together with the total radiated power. The measurement temperature is chosen in each case to maximize the THz power. Wafer details are given in Reference 1.

Figure 4 shows the typical THz emission as a function of magnetic field for GaAs, InAs and InSb. The three semiconductor surfaces were excited at an angle of 45° to the surface normal by 2 nJ pulses of 1.6 eV photons from a mode-locked Ti-sapphire laser. The emitted THz radiation was collected parallel to the applied magnetic field and perpendicular to the incident beam as shown in Figure 5. Emission was measured both by an incoherent bolometeric detection scheme and also by coherent electro-optic sampling. As expected, the emitted THz radiation is completely *TM*-polarised in the absence of a magnetic field because the photocarriers accelerate perpendicular to the semiconductor surface. However, as the magnetic field is increased, a *TE* component is induced and the emitted THz radiation becomes elliptically polarized. Both *TE* and *TM* powers show enhancement in a magnetic field (Figure 4).

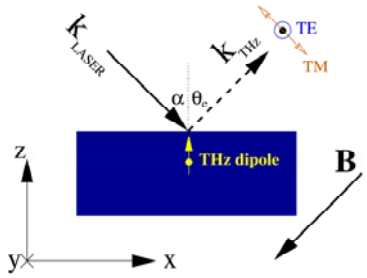

Figure 5. Schematic diagram of the experimental geometry.

The dependence of the *TM* and *TE*-polarised THz fields on the applied magnetic field, and the maximum emitted THz power, differs significantly between semiconductor surfaces. A nearly monotonic increase in both THz fields is seen in InAs, whilst peaks in the emission are observed in GaAs and InSb. This behaviour does not simply reflect the carrier concentrations or effective masses in these materials[1].

To understand the carrier dynamics following absorption of a visible/near-infrared pulse, and explain the enhancement of THz emission in magnetic field, we developed a three-dimensional semi-classical Monte-Carlo simulation[2,3]. Figure 6 shows the time derivatives of the ensemble average current perpendicular to the sample surface, $\partial \mathbf{j}_z/\partial t$, for GaAs and InAs. The THz internal field is proportional to $\partial \mathbf{j}_z/\partial t$, and has a peak value in *n*-type InAs which is four times that in *n*-type GaAs. This 16-fold power difference agrees well with experiment.

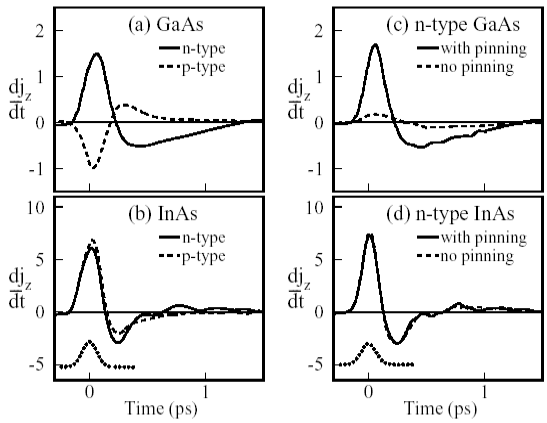

Figure 6. Time derivatives of the *z*-components of the simulated average current. Graphs (a) and (b) compare *n*-type (solid lines) and *p*-type (dashed lines) GaAs and InAs, respectively. Graphs (c) and (d) compare simulations with (solid lines), and without (dashed lines), Fermi level pinning in (c) *n*-type GaAs and (d) *n*-type InAs.

If the semiconductor surface energy bands lie within the bulk bandgap, Fermi level pinning and band-bending occur, leading to the formation of a surface depletion or accumulation region. The resulting electric field will separate photo-excited electrons and holes, forming a dipole perpendicular to the surface that can emit THz radiation. By changing from *n*-type to *p*-type doping, the field direction is reversed producing a change in dipole polarity and hence a change in sign of the THz transient.

A photo-Dember field can also occur at a semiconductor surface after photoexcitation. In a typical semiconductor, electrons have a larger diffusion coefficient than holes. After photo-excitation, the electron population diffuses more rapidly than the hole population but in the absence of a surface boundary, there is no net dipole field, since the centre of charge does not change. In the vicinity of the surface, however, reflection or capture causes the net electron and hole charge centres to move away from the surface. The greater diffusivity of the electrons produces a perpendicular dipole which leads to THz emission. Now, changing the semiconductor doping from *n*- to *p*-type has no effect on the sign of the emitted THz pulse.

These simulations reproduce the larger THz electric-field amplitudes (and hence powers) observed experimentally in InAs when compared with GaAs, and demonstrate that InAs is primarily a photo-Dember emitter while GaAs is primarily a surface field emitter.

In order to explain the dramatic enhancement of THz emission with magnetic field (Figure 4), We modeled the carrier dynamics for both InAs and GaAs in magnetic fields ranging from 0 to 8 T, and calculated the amplitude and three-dimensional orientation of the THz emitting dipole[2,3]. The coupling of the radiation out of the semiconductor is strongly affected by the dipole orientation with respect to the semiconductor surface.

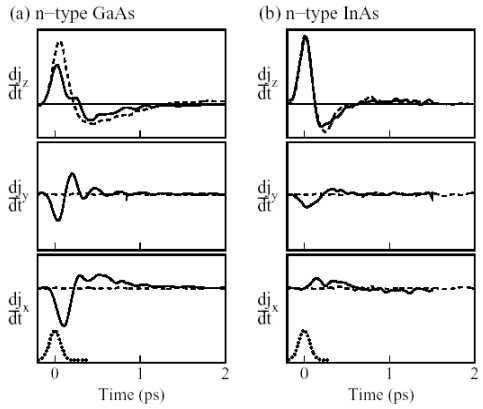

Figure 7. Three spatial components of the time derivative of average current density for *n*-type (a) GaAs and (b) InAs at B = 0 T (dashed lines) and B = 8 T (solid lines). The dotted curve represents the intensity profile of the exciting laser pulse. The vertical axis range in (b) is 4x that of (a).

Figures 7(a) and 7(b) show the simulated time derivatives of the current densities in *n*-type GaAs and *n*-type InAs, respectively, during and after photoexcitation. The dashed lines show the situation with no magnetic field present. In this case, the only net acceleration of carriers ($\partial\mathbf{j}/\partial t$) occurs in the z-direction since the only asymmetries in the system are the surface boundary and surface electric field, both of which are rotationally symmetric about the z-axis. The solid lines represent a simulation with a magnetic field of 8 T. Although there is little change to the strength of the dipole as the magnetic field is increased, the x and y components of $\partial\mathbf{j}/\partial t$ show that the Lorentz force produces a net acceleration of carriers in the x-y plane and rotates the THz dipole. This is much less pronounced in InAs compared with GaAs, because inter-valley scattering is a much more important electron scattering process in InAs than in GaAs. The large effective mass of electrons scattered into the *L* valleys then limits the rotation of the photogenerated dipole, and hence the relative magnitude of the lateral $\partial\mathbf{j}/\partial t$ components.

In order to be measured in free space, the THz radiation generated within the semiconductor of refractive index $n_i \sim 3.5$ must be transmitted into a medium of refractive index $n_e \sim 1.0$. It is clear that any radiation generated outside a cone of about $\theta_i < 17°$ (measured from the surface normal) will be totally internally reflected. Fresnel transmission coefficients were used to calculate the emission pattern resulting from radiation generated within this cone[2,3,4].

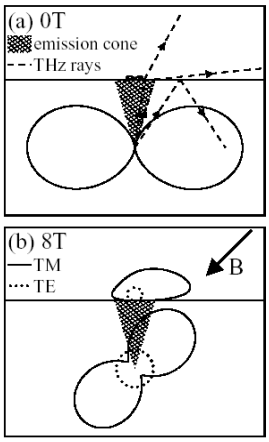

Figure 8. Calculated polar radiation patterns for GaAs at (a) B = 0 T and (b) B = 8 T. The horizontal lines represent the semiconductor surface. The 'bow tie' pattern below the surface shows the radiation within the semiconductor; the pattern above the surface shows the free-space emission. The vector B indicates the magnitude field direction.

Figure 8(a) shows the 'bow-tie' radiation pattern of the power produced inside the GaAs at B = 0 T, together with the radiation pattern emitted from GaAs into free space. The amount of radiation emitted is very low because of the small overlap between the (shaded) emission cone and the internal radiation pattern. Figure 8(b) shows the situation at B = 8 T. The internal radiation pattern shows the rotation of the *TM*-emitting THz dipole from being parallel to the z-axis to being approximately perpendicular to the magnetic-field vector. A *TE* component also emerges. In this case there is now considerable overlap between the internal radiation pattern and the emission cone, and hence the corresponding free-space radiation pattern is much larger. For InAs, there is only a small rotation of the THz dipole (not shown) and hence the enhancement of the free-space radiation is much less. The enhancement in total THz power emitted at $\theta_e = 45°$ between 0 and 8 T has been measured experimentally to be 35x for GaAs and 8x for InAs. Here, the calculated values are 15x and 4x, respectively. These results are in reasonable agreement considering the simplicity of the semi-classical simulation, and possible differences between the experimental and simulation parameters.

To confirm further our interpretation of the experimental results, we have calculated the expected radiation pattern from (100) InAs in the absence of an applied magnetic field as the angle of incident optical pulse and detected THz radiation are altered. Figure 9 shows the experimentally measured THz radiation patterns, as the incident laser pulse is progressively focused to a spot size of 80 μm. At this point the spot size is the same order as the wavelength of the emitted THz radiation, and hence the dipole acts as a point source, as assumed in the theoretical simulations.

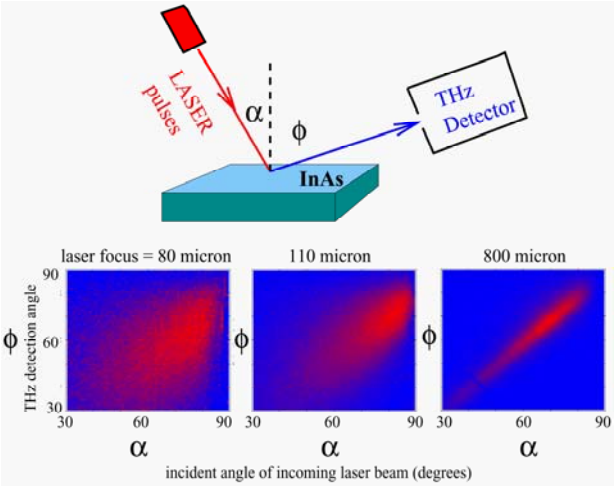

Figure 9. Schematic diagram and results for an experiment in which emitted THz radiation is measured as a function of the optical pulse incidence angle and the THz detection angle for bulk InAs at 300K. Results are shown for three different focusing conditions of the incident optical pulse. Red and blue represent high and low signals respectively.

From the 80 micron data, a polar plot of the experimental data is obtained, Figure 10, in which the incident optical pulse and detected THz radiation angles are altered concurrently to maintain a reflection geometry. Excellent agreement between theory and experiment is obtained[1)].

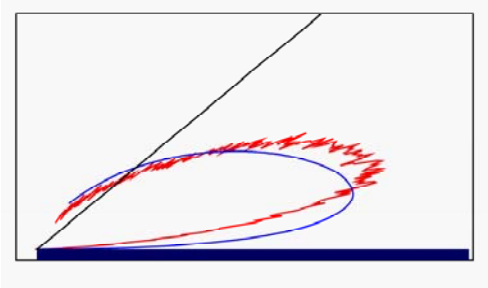

Figure 10. Calculated (blue) and measured (red) polar radiation patterns for InAs at B = 0 T. The line at 45° represents the detection direction used in the magnetic field studies (Figure 4).

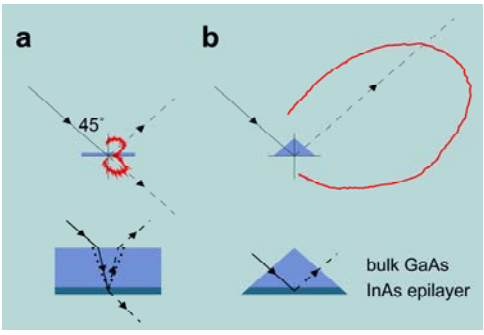

Figure 11. Polar radiation patterns from InAs on GaAs emitters excited with a 920nm femtosecond pulse. The incident radiation (being below the GaAs band gap) passes through the GaAs and excites a THz dipole in the InAs layer. The resulting THz emission is collected with much greater efficiency with a prism (b) rather than planar (a) geometry. This is seen in the experimentally measured radiation patterns (red).

Having obtained a good understanding of the THz generation mechanism in bulk semiconductors, and the origin of the observed enhancement in a magnetic field, we proceeded to design a new type of emitter based on a prism[4,5,6)] , Figure 11. Excitation was achieved using a 920nm optical pulse which would pass through the GaAs without adsorption, but was then adsorbed in the underlying InAs layer. Use of a prism geometry allows a far more effective coupling of the dipole radiation out of the THz emitter, and this is reflected by the measured polar radiation patterns given in Figure 11. This new technique has been both published and patented by the investigators. We have also investigated grating patterning the semiconductor surface as a means of improving the outcoupling of THz radiation[7,8)].

Conclusions

We have discussed THz radiation from semiconductor surfaces excited by ultra-fast optical pulses[9)]. Through a semiclassical Monte Carlo model, we have shown that the primary THz emission mechanism from InAs is based on the photo-Dember effect, whilst surface depletion fields dominate in GaAs[2,3)]. The effect of magnetic field on these systems has been calculated and the observed enhancement of THz power with magnetic field found to be predominantly caused by a reorientation of the THz dipole with respect to the surface dielectric boundary, rather than by an increase in the dipole strength[1)]. Once transmission through the semiconductor-air dielectric interface is considered, the experimentally observed enhancement in emission is reproduced. These results suggested that a magnetic field was not necessary to obtain an order-of-magnitude enhancement in THz power, and a similar enhancement was produced by modifying the dipole orientation with respect to the dielectric–air interface using a prism[4,5,6)].

Acknowledgements

AGD and EHL acknowledge the support of the Royal Society and Toshiba Research Europe Limited, respectively. This work was supported by EPSRC (UK), and we gratefully acknowledge the loan of a femtosecond laser system by the Rutherford Appleton Laboratory.

References

1. M B Johnston, A Corchia, A Dowd, E H Linfield, A G Davies, R McLaughlin, D D Arnone, and M Pepper, Physica E, 13 896, (2002)
2. M B Johnston, D M Whittaker, A Corchia, A G Davies, and E H Linfield, J. Appl. Phys. 91 2104, (2002)
3. M B Johnston, D M Whittaker, A Corchia, A G Davies, and E H Linfield. Phys. Rev. B 65 165301, (2002)
4. M B Johnston, D M Whittaker, A Dowd, A G Davies, E H Linfield, X Li, and D A Ritchie, in press (Optics Letters)
5. D M Whittaker, M B Johnston, A Corchia, A Dowd, A G Davies, and E H Linfield, to be published in the proceedings of ICPS (2002)
6. M B Johnston, D M Whittaker, A Dowd, A G Davies and E H Linfield, poster presentation at the Tenth IEEE International Conference on THz Electronics, and to be published in the IEEE proceedings.
7. A Dowd, M B Johnston, D M Whittaker, S Vijendran, A G Davies, and E H Linfield, to be published in the proceedings of ICPS (2002)
8. A Dowd, M B Johnston, D M Whittaker, A G Davies and E H Linfield, oral presentation at the Tenth IEEE International Conference on THz Electronics, and to be published in the IEEE proceedings.
9. A G Davies, E H Linfield and M B Johnston, to be published in J. Phys. Med. Biol.

Laser Processing of Thin Film Phosphors for Flat Screen Displays

W M Cranton, D Koutsogeorgis, S Liew, B Nassuna, R Ranson, C B Thomas

The Nottingham Trent University

Main contact email address: *wayne.cranton@ntu.ac.uk*

Introduction

The Displays Research Group at Nottingham Trent University has been working with the LSF since 1997 to investigate excimer laser processing of thin films suitable for use in flat screen display applications. Initial work, funded by the EPSRC, demonstrated the feasibility of using pulsed laser annealing to enhance the luminescence of thin film ZnS:Mn phosphors for use in miniature high intensity displays. Following this early work, the investigations have progressed to include thin film phosphors used in mid-size instrumentation display panels, with the result being the demonstration of a technique for phosphor processing that could be suitable for large volume manufacture. More recently, access to the NSL5 fluoride laser via the LSF Loan Pool has facilitated the investigation of laser processing for alternative wide band-gap thin film phosphors and cathodoluminescent phosphors. This report presents the initial results from the work performed at NTU using the Loan Pool NSL5 laser.

Background

In the field of emissive flat panel displays, thin film electroluminescence (TFEL) is a technology that has been a subject of commercial and scientific interest for over 4 decades. Display panels based on this technology have been utilised where ruggedness, reliability, high contrast, and high viewing angles are required; such as in medical, transport, and military applications. In a novel TFEL device configuration, reflected lateral emission from TFEL devices has been shown by research at Nottingham Trent University (NTU) to demonstrate the feasibility of high intensity luminous emission from fixed legend miniature displays [1]. These laterally emitting thin film electroluminescent (LETFEL) displays are intended for use in low cost see-through head mounted systems, where luminances in excess of 3000cdm^{-2} are required, but without the need for a full graphics display. Realisation of these high luminances relies upon optimising the internal light generation processes of TFEL devices by optimising the materials processing of the constituent thin films.

At the heart of these LETFEL, and indeed all inorganic emissive displays, is a light emitting layer composed of a wide band-gap polycrystalline phosphor. Phosphors under investigation at NTU include thin films of ZnS:Mn (3.68eV), SrS:Cu,Ag and SrS:Ce (4.4eV), and Y_2O_3:Eu (5.9eV). Each of these materials is of interest for TFEL display applications, although the primary research area for the Y_2O_3 based phosphor is for a light emitting thermographic sensor. In addition, thin films phosphors such as ZnS:Cu are under investigation for cathodoluminescent display applications - such as night vision and image intensifiers.

Prior Work with The LSF

Critical to the luminescent efficiency of a TFEL device is an annealing treatment, which allows for the effective incorporation of luminescent dopant ions within the host lattice (activation). Commercial TFEL devices are typically fabricated on glass substrates and are subjected to a post deposition anneal at 500ºC for ~ 1hr. Since 1997, EPSRC funded work at the LSF has demonstrated that pulsed laser annealing using a high energy flouride excimer laser is an effective means of activating the phosphor by achieving significantly higher temperatures localised to the phosphor thin film [2]. It is a combination of the higher processing temperatures attained and the localisation of the heat dissipation to within the phosphor layer that leads to a major enhancement in phosphor performance. This is due to the joint requirement for the phosphor layer to act as a light emitting material, and as the electron transport medium for luminescent excitation. High annealing temperatures are required to form an efficient phosphor, but the annealing process is detrimental to the electron emission process that provides the source of excitation. By localising the annealing effect to the light generating region, excimer laser processing has been demonstrated to be a viable means of spatially separating the optimisation of the light generating and electron emitting regions of a TFEL structure. Devices incorporating a ZnS:Mn thin film phosphor were subjected to 20ns pulses of KrF Excimer laser irradiation at 248nm. The optical systems used for beam delivery provided variable energy densities from 300-1500mJ/cm^2. At 248nm, the absorption coefficient of ZnS has been determined to be 3.33×10^5 cm^{-1} for crystalline ZnS and 3.15×10^5 cm^{-1} for polycrystalline ZnS:Mn thin films, hence the energy absorption is contained within ~ 300nm of the thin film surface. This initial work was undertaken at the x-ray laboratory of the LSF, with the help of Graeme Hirst and his team. Additional work on this system was used to demonstrate a potential scanning technique for larger area irradiation of ZnS:Mn based TFEL panels.

Colour Displays

ZnS:Mn is an efficient EL phosphor, but is limited to broad-band yellow emission - hence it is used in the commercially successful monochrome TFEL displays. Achieving full colour has historically been a problem for these displays, due to the inefficiency of the blue phosphors. However, with the loan of the NSL5 laser to NTU, we have recently demonstrated that the laser annealing technique is also suitable for this wide band-gap phosphor.

Experimental Technique

For the initial phase of the loan pool work, the phosphors investigated were ZnS:Mn (0.43%), and SrS:Cu,Ag (0.2%,0.4%). ZnS:Mn was investigated to ensure that the results obtained previously at the x-ray lab at RAL could confidently be repeated within the facility at NTU. The SrS:Cu,Ag phosphor is a potential blue emitting TFEL material. Phosphors were investigated for luminescence via photoluminescent (PL) excitation, electroluminescent (EL) excitation, and cathodoluminescent (CL) excitation as appropriate. The NSL5 laser (Lambda Physik LPX 205, 248nm/193nm 20ns) was installed within the clean-room facility at NTU and the optical arrangement was set up as described previously [2]. Samples of thin film phosphors were deposited by rf-magnetron sputtering and housed in a pressure cell during irradiation to minimise ablation. Various numbers of laser irradiations were used with the fluence varied from 0.3 to 1.5 J/cm^2, while the samples were in an overpressure of Ar (150 psi). For the PL measurements a UV laser (He-Cd, 326nm, 16mW) provided the excitation, an optical fibre collected the generated light and directed it to an Ocean Optics (S2000) spectrometer. The EL devices were characterised on a probe station located in a dark enclosure, driven by a sinusoidal wave at 5 kHz with a p-p voltage of 364Volts, and the generated light was collected by an optical fibre and fed to the spectrometer. Finally the CL was measured in a vacuum chamber with an electron beam at 6 kVolts and beam current 0.3mA with the generated light being collected and directed to the spectrometer via an optical fibre.

Results and Discussion.

Initial experimentation involved only single laser annealing pulses and the resulting PL and EL improvement for ZnS:Mn thin films is shown in Figure 1. Both curves, demonstrating improvement, show the same trend, requiring a minimum fluence of ~0.5 J/cm^2 (threshold fluence) to induce any luminescence improvement. This is further enhanced with increasing the fluence until ~1.2J/cm^2 when the improvement is saturated. These results are consistent with previous work, demonstrating the transferability of the technique between experimental systems. The previously reported modelling of the laser annealing process [3] suggests that with laser annealing the front surface of the phosphor reaches temperatures in excess of 2000ºC, for nanoseconds only, while the back surface, that forms the interface between the phosphor and the insulator, does not exceed ~500ºC. Hence, the interface states that act as donors of hot electrons are preserved, since the critical temperature is not exceeded. The knee observed at 1.2J/cm^2 is attributed to reduction of the phosphor thickness due to probable ablation [4]. Therefore a laser pulse of adequate fluence can achieve highly localised annealing of the phosphor film only.

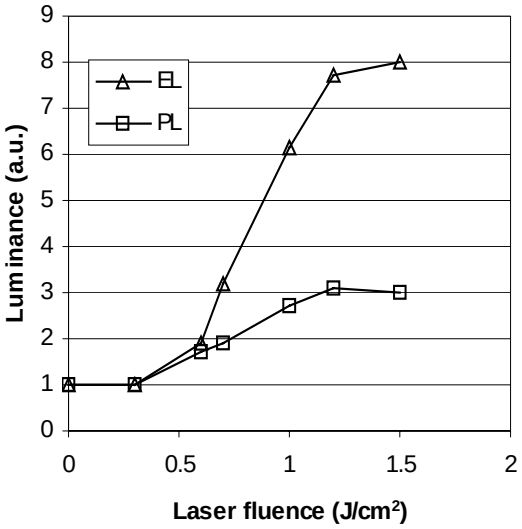

Figure 1. Photo-luminescence and electro-luminescence improvement for ZnS:Mn thin films with one laser annealing pulse. Both curves are normalised to the as-deposited film performance.

For the case of EL characterisation, multiple pulse irradiation experiments (Figure 2) show that one pulse is beneficial but not as significant as two pulses, which showed the best improvement at ~1.3J/cm^2. Three pulses have proven to be detrimental for EL, suggesting that two pulses induce a heat treatment that does not reach the back surface of the phosphor, unlike three pulses, which also probably causes excessive ablation. These results extend the information on the process that has been demonstrated to improve over thermal annealing, producing EL devices of higher luminance and better electrical characteristics.

Laser processing of SrS:Cu,Ag based TFEL devices was also successful - most critically as a viable annealing technique for rf-sputtered films of this phosphor, as compared to thermal and rapid thermal annealing which resulted in unusable films. Thin films were deposited and characterised initially for structural stability and also luminescence via photoluminescent excitation. With thermal annealing, at the temperatures reported as necessary for viable luminescence (up to 800°C [5]), crazing of the films prevented fabrication of EL devices. A detailed matrix of deposition and annealing parameters was investigated, varying the substrate temperature from 100°C to 400°C, and with annealing, both thermal and rapid thermal up to 800°C. The result of this study was that reliable films exhibiting luminescent behaviour were only achievable at low deposition temperatures, up to 200°C, and with no annealing. However for the TFEL devices produced from these films, the luminance was too weak to provide reliable measurements.

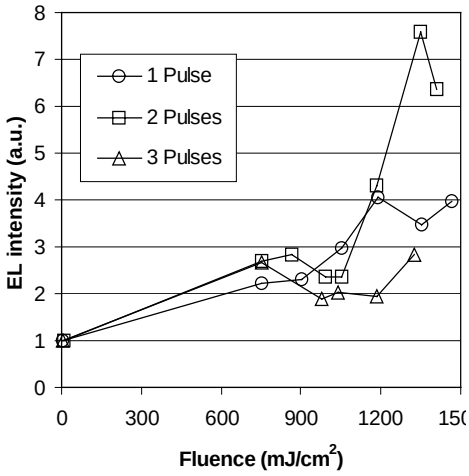

Figure 2. Electroluminescence improvement of ZnS:Mn based TFEL devices with one, two and three laser annealing pulses. Curves normalised to the as-deposited films.

For the laser annealing study, SrS:Cu,Ag thin films, grown at 200°C, onto 200nm thick layers of Y_2O_3, were exposed to 20ns pulsed irradiation at varying fluences using the KrF irradiation. Viable TFEL devices were obtained with single pulse irradiation fluences in the range of 0.4 –1.5 Jcm^{-2}. The effect of the higher fluence was to enhance the film crystallinity, as indicated by increased XRD intensity from the SrS (111) peak, which is consistent with the ZnS:Mn crystallinity enhancement demonstrated previously. Reproducible films for TFEL devices were obtained at the higher fluences, which were consequently used for the device fabrication used here. Figure 3 shows the blue/green emission spectrum of the EL devices fabricated using the laser processing technique.

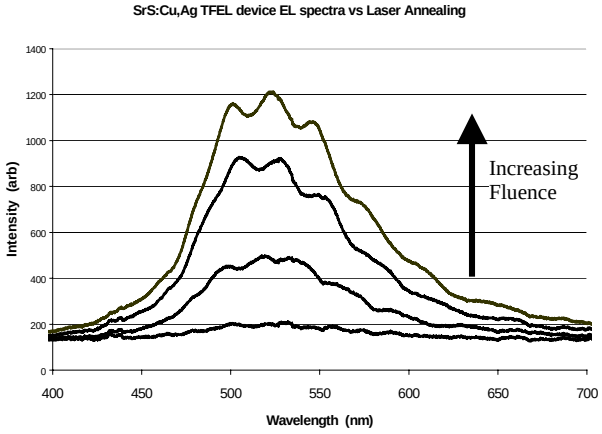

Figure 3. EL emission spectra as a function of laser annealing with 248 KrF irradiation for SrS:Cu,Ag TFEL devices driven at 640 V pk-Pk

Finally, laser processing of ZnS:Mn films on glass substrates for CL applications was investigated, with a similar result to the ZnS:Mn EL devices in that one pulse is again beneficial, while two or three show further improvement, although ablation effects dominate at higher fluences with three pulses. The results, shown in Figure 4 clearly demonstrate the enhancement

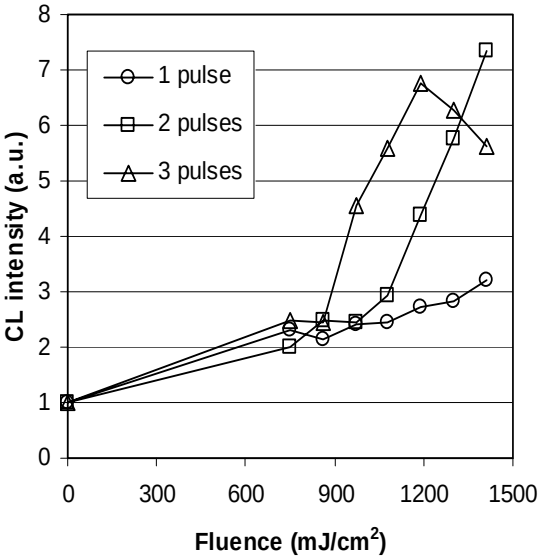

Figure 4. Cathodoluminescence improvement of ZnS:Mn thin films with one, two and three laser annealing pulses. Curves normalised to the as-deposited films.

in CL emission from these thin films as a result of the laser irradiation technique, hence highlighting the potential for application to a wide variety of flat screen display materials. Currently, films of ZnS:Cu phosphor are being investigated. This phosphor material is used as the CL screen in image intensifiers, and thin films are of interest for enhanced uniformity and reduced graininess in the final image which is a problem with powder based screens used. However, the luminous intensity from thin films has to date been insufficient for practical applications. Hence, the potential demonstrated here for luminescent enhancement via laser processing may help to solve this problem.

Additional work currently utilising the loan pool system is concerned with examining the use of the ArF 193nm emission for Y_2O_3 (5.9eV) based phosphors. Preliminary results are encouraging, once again highlighting the diverse potential of this materials processing technique.

References

1. C B Thomas, R Stevens, W M Cranton.; 1996 SID International Symposium. Digest of Technical Papers. First Edition. Soc. Inf. Display. 1996, pp.365-9.

2. D.C. Koutsogeorgis, E.A. Mastio, W.M. Cranton and C.B. Thomas. Thin Solid Films, 383, No. 1-2, Feb. 2001, pp. 31-33.

3. E.A. Mastio, W.M. Cranton, C.B. Thomas, E. Fogarassy, S. de Unamuno. Pulsed KrF laser annealing of RF sputtered ZnS:Mn thin films. Applied Surface Science, 138-139, Jan. 1999, pp. 35-39.

4. E.A. Mastio, E. Fogarassy, W.M. Cranton, C.B. Thomas. Ablation study on pulsed KrF laser annealed electroluminescent ZnS:Mn/Y2O3 multilayers deposited on Si. Applied Surface Science, 154-155, No. 1-4, Feb. 2000, pp. 35-39.

5. H.M. Menkara, W. Park, M.Chaichimansour, T.C. Jones, B.K. Wagner, C.J. Summers, and S.Sun; 4th Int. phosphor Conf. / 9th Int. Workshop on EL, Bend (Oregon) Extended Abstracts, p. 191 –194.

Femtosecond Non-Linear Laser Spectroscopy

R Devonshire, M Jinno

High Temperature Science Laboratories, Chemistry Department, Sheffield University, Sheffield S3 7HF, UK

Main contact email address: *r.devonshire@sheffield.ac.uk*

Introduction

The Loan Pool Verdi-Mira femtosecond laser system is being used in our laboratories to demonstrate the feasibility of novel diagnostic and materials characterisation techniques which, if successful, would have a significant impact on two of our major research programmes. Firstly, to support our work on the diagnostics and modelling of technologically important reactive gases and plasmas we are developing novel diagnostic techniques which exploit the precise, microscopic spatial extent of femtosecond laser pulses. Secondly, we are extending our use of non-linear Raman techniques to the fs pulse regime to both reveal the dynamical behaviour of the laser induced polarization and to revive, possibly, a somewhat dormant but potentially very important technique for materials characterization, namely hyper-Raman scattering.

Plasma Diagnostics

Our objective is to map precisely the temporal-spatial distributions of atomic species in plasmas in an electronically state-specific manner. In particular we are trying to obtain data on such states from the generally difficult to access plasma sheath regions near the plasma's boundaries. The experimental strategies being explored exploit the spatial transform of femtosecond laser pulses (100 fs ≡ 30 μm) to achieve high spatial resolution measurements of plasma species.

The laser system is unamplified and provides high repetition rate (> 70 MHz) tunable (fundamental is in near-ir region) pulses with average power of ≈ 1 W and ≈ 10 nm linewidth. Individual pulse energies are not adequate to operate a Kerr Gate and so a number of interesting plasma diagnostic techniques based, for example, on imaging of back scattered ballistic photons could not be explored during the loan period. Instead, emphasis was placed on exploring techniques in which small stationary regions of excitation are created inside the systems of interest using the colliding pulse geometries used in some autocorrelator designs. These small regions of excitation may be scanned systematically through plasmas to produce high spatial resolution 3-D maps of species or physical property distributions. The system's response could be measured, for example, via optogalvanic or fluorescence signals.

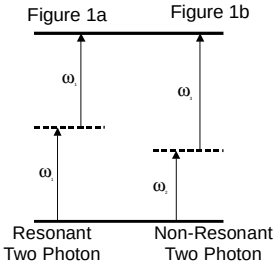

Figure 1. Resonant and Non-Resonant 2-photon excitation.

The principle of the technique was first evaluated using resonant two-photon excitation, Figure 1 (a) of dyes used in two-photon fluorescence microscopy using both single beam, single sided excitation (as used typically in this technique; simple focusing imparts some axial spatial resolution), and then the colliding (counter-propagating) pulse geometries of interest.

Resonant two photon excitation has the disadvantage, as seen readily in colliding pulse autocorrelators which image two-photon excited dye fluorescence, of showing a background track of excitation along the entire length of the path of the pulses. This track is, in effect, the two-photon excitation produced by the non-overlapping, but still two-photon resonant, pulses as they pass through the dye solution. The measurement becomes background-free if the two-photon excitation is made non-resonant, Figure 1 (b). The necessary beams can be created from the Loan Pool laser by using two angle tuned, narrow bandpass filters to spectrally separate two beams from the spectrally broad, 10 nm, 150 fs laser pulses from the oscillator; the first at a λ that is Δλ below that of the two-photon resonant peak, the second at a λ that is Δλ above the peak. The concept is illustrated below:

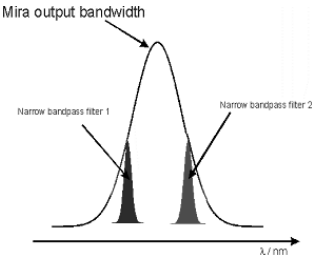

Figure 2. Laser Pulse Filtration.

As the two pulses are derived from the same Mira output pulse they are jitter free. The spectral narrowing lengthens the pulses in time but the consequent increased length of the overlap region of the counter-propagating pulses is still sufficiently small to be of diagnostic value. The peak powers are lowered which reduces the efficiency of non-linear excitation but the increased size of the overlap region compensates to some extent for this as more species of interest are present. A more flexible system to select λ of the individual pulses would give opportunities to exploit resonances with intermediate states.

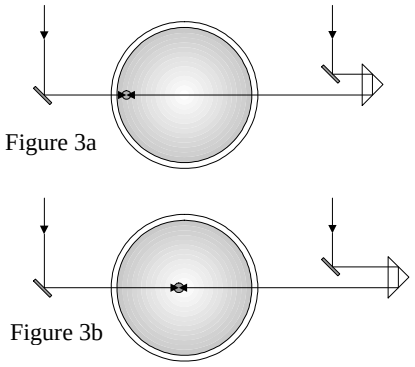

Figure 3. Experimental Configuration.

The configuration used in a colliding pulse diagnostic technique is represented in Figure 3. The collision region can be moved systematically along tracks through the system of interest using simple optical delay line techniques, e.g., the beam on the right hand side in Figure 3b has been delayed relative to the rhs beam in Figure 3a. Alternatively, and often more conveniently, the system itself may be moved through a fixed overlap region.

Plasma sheath regions are of considerable practical and theoretical interest and experimental techniques which can access these regions and retrieve data on species concentrations, etc., have high potential value. The optical track that is a diameter of a cylindrically symmetric plasma system (Figure 3; e.g., a lighting discharge) is of particular

experimental convenience and theoretical interest. The two-photon technique represented in Figure 3 has the potential to provide spatial profiles along such tracks for a much greater proportion of the track's length than is possible with currently used techniques. For example, present single beam, line of sight, techniques are unable to access near wall regions sensibly because of the strong refractive effects of the walls at large angles of incidence. Evanescent wave techniques are able to access these near wall regions but not so conveniently and practically as being investigated here.

As an example of the specific systems we are investigating the Grotrian diagram of mercury below shows a strategy for the non-resonant two-photon excitation of the 7 $^1S_0$ excited state from the ground state with detection via the 408 nm emission to the 6 $^3P_1$ resonance state. The work extends earlier studies where we achieved spatial resolution by focusing of a pump beam into a low pressure Hg discharge and detecting the excited states using the optogalvanic effect[1)].

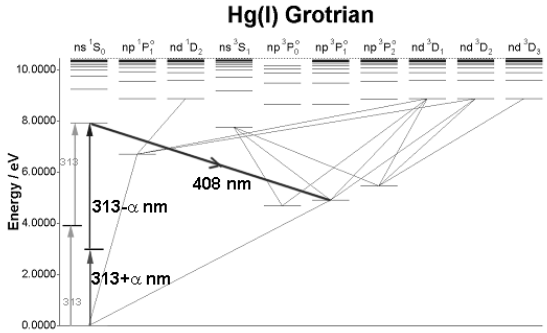

Figure 4. Grotrian Diagram for Mercury.

Non-linear Raman Techniques

Hyper-Raman Scattering: We are establishing a database of reference Raman spectra of materials of interest in light source science and technology (see www.shef.ac.uk/~htsl/raman/). The spectra are used to support studies of lamp chemistry [2)]. The spectra are measured using Raman microscopy because it is compatible with the length scales present in the reference samples and samples requiring analysis. Many materials of interest give featureless Raman spectra with this technique because of their crystal structures; for example, the alkali halides are compounds where dipole modes are forbidden in Raman. These modes can often be observed using the complementary technique of infrared absorption but this technique does not have the versatility and convenience of Raman microscopy. We are evaluating a new technique that will make it possible to obtain both Raman and "infrared" spectra from the same instrument. The concept is to adapt a conventional Raman microscope to accept an alternative laser excitation source that would excite hyper-Raman scattering; the detection system required being identical to that used by the "standard" laser source (typically a dc Argon ion laser). The combined instrument would uniquely be able to measure both Raman and infrared spectra. The pulse stream from the Verdi-Mira system is ideally suited to be such an excitation source. The pulses have the necessary peak power for non-linear excitation of Raman scattering and the laser-material interaction in the fs regime minimises sample damage.

To realise the instrument we are modifying a commercial 514 nm Raman microscope to accept either 514 nm (dc or fs) or 1028 nm fs laser excitation (N.B. the long wave optic set for the Mira is required). The fs laser excitation is being delivered to the sample using low transmission loss hollow optical fibres developed by a Japanese group[3)]. The vibrational modes seen in hyper-Raman using 1028 nm fs excitation will complement those seen in spontaneous Raman using 514 nm excitation and, in addition, make it possible to see "silent" modes.

When available the technique will be applied to a range of technologically important materials that are of interest to the group; these include metal halides, oxides of aluminium, silicon, titanium, etc., and doped silica glasses. It is expected that it significantly enhance the range of our analytical investigations. It could impact several other areas also.

Coherent anti-Stokes Raman Scattering (CARS): We have exploited the CARS technique for some time to provide spatially and temporally resolved spectra of species in reactive gases and plasmas[4)]. Computer simulation of the spectra leads to information on species identity, temperature, pressure and relative concentration. The spatial resolution when using a folded-BOXCARS configuration is typically 50 μm x 50 μm x 1 mm and the temporal resolution is defined by the few ns pulses from the Nd:YAG pump and dye lasers.

We are attempting to perform fs CARS measurements of plasmas using the basic Verdi-Mira system. The CARS pump and Stokes beams are derived from the 2nd harmonic and fundamental, respectively, of the Mira. This configuration gives access to Raman resonances in the range from approximately 9,000 cm^{-1} to 13, 000 cm^{-1} (N.B. requires both mid and long range optics sets to achieve this range). This is a region known from previous work in our laboratories to be rich with Raman resonances from species that are not well characterised and which are probably dication species. Our previous CARS work to investigate this region was restrained by the constant need to change dyes in the dye laser to achieve the full range of interest.

The peak powers of the "pump" and "Stokes" beams from the Mira are comparable to those achieved in typical Nd:YAG CARS systems but the repetition rate and overall mark-space ratio are considerably greater. A major aim of the work with the loan system is to demonstrate whether or not the advantages of the fs system over the Nd:YAG translate into a more efficient CARS signal recovery (N.B. a 200 MHz lock-in detection system is used in the fs CARS experiments). Aside from the potential for gains in signal recovery there is the important added dimension of operating CARS in the fs time-frequency domain and we anticipate new layers of information on the collision processes in operating plasmas[5, 6)].

References

1. M Duncan and R Devonshire, Chem. Phys. Lett., 187 545 (1991)
2. R J Forrest, R Devonshire, C V Varanasi and T R Brumleve, Appl. Spectrosc., 56 (2002)
3. Y Matsuura, *et al*, J. Appl. Phys., 91 887, (2002)
4. D S Payne, G J Wilson and R Devonshire, Chem. Phys. Lett., 332 58, (2000)
5. T Lang *et al*, J. Chem. Phys., 115 5418, (2001)
6. M Scmitt *et al*, Chem. Phys. Lett., 280 339 (1997)

Laser Science and Development

1) **Vulcan Petawatt**
2) **Vulcan**
3) **Astra**
4) **Lasers for Science Facility**
5) **Laser Optics and Laser Design**
6) **Instrumentation**

Vulcan Petawatt Upgrade Overview

C B Edwards

Central Laser Facility, CLRC Rutherford Appleton Laboratory, Chilton, Didcot, Oxon, OX11 0QX, UK

Main contact email address: *c.b.edwards@rl.ac.uk*

The project to upgrade the ultra-short pulse CPA beam of Vulcan to the Petawatt level began on 1st April, 1999. The upgrade, funded through an EPSRC Research Grant, will deliver an energy on target of 500J in a pulse of 500 fs duration giving a focused target irradiance in the 10^{21}W.cm^{-2} regime.

A summary of some of the main areas of activity in the year to the end of March 2002 is given below. Further details are described in articles following.

Laser oscillator and pre-amplifier

The compression of the amplified pulse to 500 fs at the output of the Vulcan system depends critically on the spectral bandwidth of the stretched pulse. While the oscillator produces pulses of extremely short duration, the gain profile of Vulcan's Nd:glass amplifiers imparts significant spectral narrowing, thereby reducing the bandwidth of the stretched pulse and limiting the pulse duration of the compressed pulse.

In order to minimize the gain narrowing effects, Optical Parametric Chirped Pulse Amplification (OPCPA) is being used at the front end of Vulcan. This technique, pioneered at the CLF, provides pre-amplification of the oscillator pulse up to the level of 20mJ with virtually no reduction of bandwidth. This reduces the energy gain required from the Nd:glass amplifiers and will enable the 500 fs specification for the upgrade to be met. A further important advantage of the OPCPA approach is that it operates at 10Hz, greatly simplifying alignment and pulse optimization.

Nova amplifier commissioning

The delivery of a 500J pulse to target has required substantial modifications and additions to the power conditioning and disc amplifier architecture. The first phase of this work was the replacement of the capacitor bank to provide additional drive for the CPA beamline. This work was completed in April 2001 as described in last year's Annual Report.

The second phase has been the installation and commissioning of three 208mm disc amplifiers, made available to the project by the U.S. Dept. of Energy following the closure of NOVA.

These amplifiers have been refurbished in the CLF clean rooms and modified to use the same large bore lamps as are fitted to the existing 150mm amplifiers. This improves efficiency, simplifies the pulse forming networks and reduces the number of spares that are required to underpin operations.

The three amplifiers have been installed and tested and a beam energy in excess of 750J has been obtained at the output, giving confidence that the upgrade energy specification will be met.

Compression chamber

The compression and target chambers were delivered to the RAL site in August 2001 and installed into the new Petawatt target area under the watchful eyes of many employees and visitors to the Chilton site!

The compression chamber was supplied as three separate tanks which were manoeuvered precisely into their correct positions and then welded to form a single vacuum vessel. Following commissioning of the vacuum system and an extensive cleaning programme, the large aperture optical mounts were installed and tested, followed by the installation of the beam delivery optics and compression gratings (see Figure 1).

Project Management

The project has been managed according to the CCLRC's Corporate Project Management procedures. The Project Management Committee, which oversees the project, is chaired by Dr A D Taylor, Deputy CE CCLRC, Director ISIS and includes Prof. J Wark and Dr D Riley (Vulcan user representatives), Ms. J Nicholson and Mr D Harman (EPSRC), Prof. MHR Hutchinson (Director, CLF) and Dr C B Edwards (Project Manager).

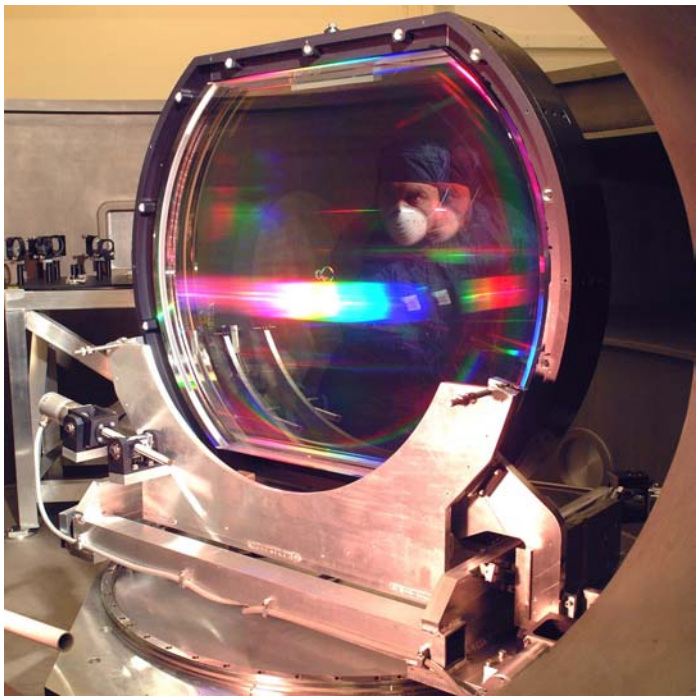

Figure 1. Petawatt Compression Grating.

Installation of the Compressor and Interaction Chambers and associated engineering hardware for the Vulcan Petawatt Upgrade

B E Wyborn, P A Brummitt, A J Frackiewicz, J A C Govans, B J Gray, S Hancock, P E Hatton, P Holligan, A R Jackson, W J Lester, Z A Miljus, D R Neville, D A Pepler, M R Pitts, C J Reason, J K Rodgers, D A Rodkiss, A G Ryder, G N Wiggins, R W W Wyatt

Central Laser Facility, CLRC Rutherford Appleton Laboratory, Chilton, Didcot, Oxon, OX11 0QX, UK

Main contact email address: *B.E.Wyborn@rl.ac.uk*

Introduction

Last year we reported on the design of the Vulcan Petawatt Compressor Chamber [1)] and Interaction Chamber [2)]. This article sets out the progress made on the construction of the vessels and their installation, together with associated engineering hardware, in the new target area.

Manufacture

The compressor chamber which holds the two large aperture gratings was fabricated [3)], from mild steel and subsequently nickel plated [4)], in three main parts: two cylindrical vessels that house the optics and a rectangular interconnecting section. Its volume is ~ 120 m^3 and it weighs ~ 70 tonnes.

The interaction chamber houses the final turning mirror, focusing parabola, target and experimental diagnostics. Weighing in at ~ 60 tonnes, the chamber was constructed [5)] from 100 mm thick steel plate and similarly nickel plated.

Installation

On the 20th August 2001 the compressor and interaction chambers were delivered to the Rutherford Appleton Laboratory. During the following day a large crane was used to unload the chambers which were then manoeuvred into position in the Petawatt target area. The following paragraphs and photos 1 - 6 describe this installation.

Following delivery, the north tank of the compression chamber was offloaded, brought inside the building and roughly positioned. The compressor tunnel section was then brought into the area and fully inserted into the north tank. Lastly the south tank was brought in and positioned. The tunnel section was then partially withdrawn from the north tank and inserted into the south tank. The chamber was aligned relative to the predetermined interaction point marked on the floor. Next the interaction chamber was transported into the building and positioned relative to the compression chamber and the interaction point.

Photo 1. The north tank of the compressor chamber being brought into the building.

Photo 2. The north tank of the compressor chamber being positioned inside the target area.

Photo 3. The interconnecting tunnel of the compressor vessel being brought into the building.

Photo 4. The interconnecting tunnel of the compressor chamber being positioned between the two tanks.

Photo 5. The interaction chamber being offloaded.

Photo 6. The interaction chamber being positioned in the target area.

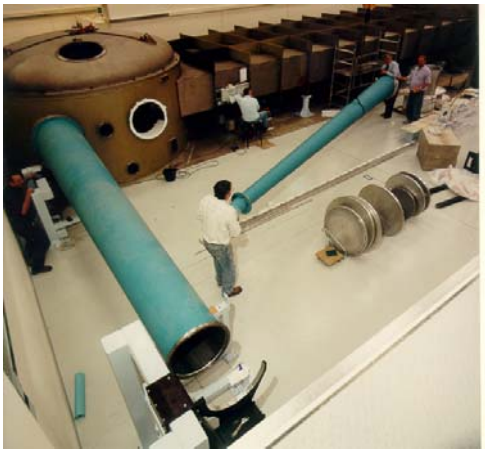

Photo 7. The vacuum spatial filter tubes being assembled.

Photo 8. The vacuum spatial filter completed.

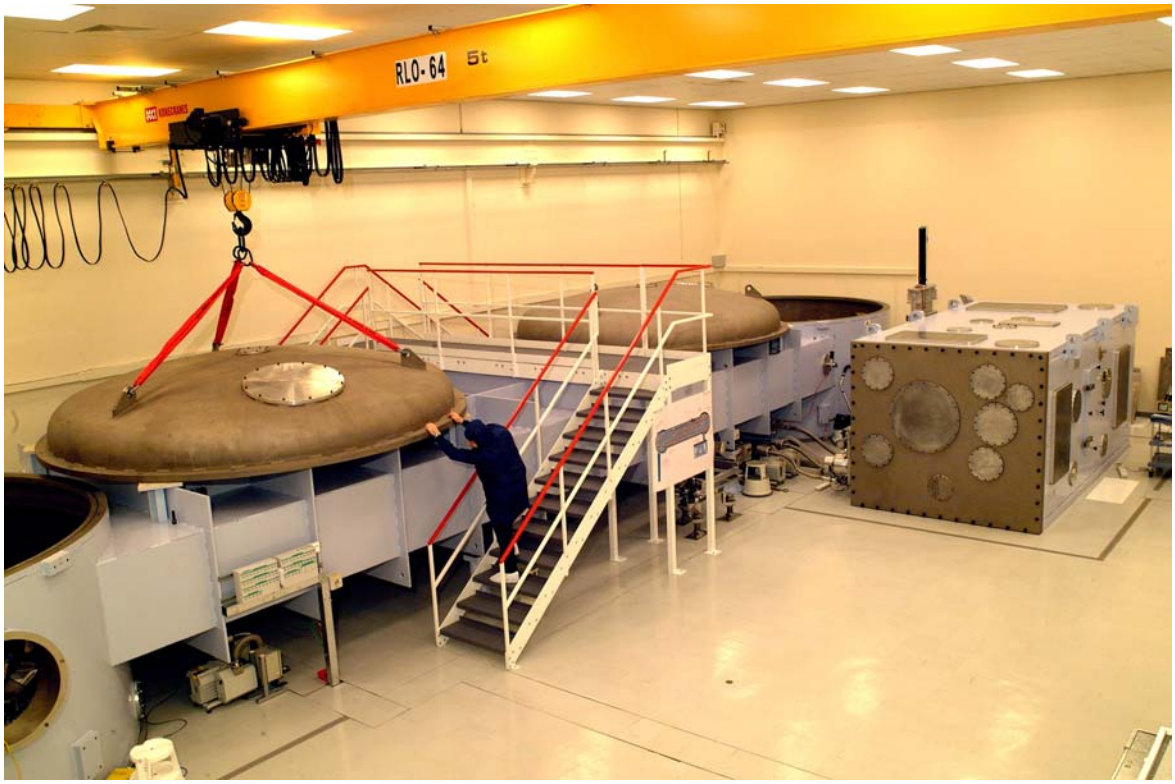

Photo 9. Compressor and Interaction Chambers installed with associated engineering hardware.

Once the chambers were in their final position the concrete floor was drilled and the chambers bolted down [6]. The three parts of the compressor chamber were welded together and leak tested. To complete the plating of the chambers, nickel was brush plated to the inner welds on the compressor chamber, the inside of the tunnel and the machined 'O' ring seal on the interaction chamber [7] . The outside of the compressor chamber was also painted.

In October 2001, the vacuum spatial filter tubes (VSF) and pinhole chamber were aligned to the compressor chamber and to the 208 amplifier chain already established in LA4 (see photos 7 & 8).

The chambers, VSF and interconnecting parts were very thoroughly cleaned and the vacuum and let up systems commissioned as described elsewhere [8]. The large gate valve and interconnecting pipe between the two chambers was carefully installed and leak tested.

In tandem to the work on the main components outlined above a lot of activity took place installing the various services needed i.e. interlocks, cooling water, nitrogen, computer network, control network, trigger/signal network, local power, intercoms, surveillance cameras, floor tiling and completion of concrete shielding walls.

The area was handed over to become a clean area for laser commissioning just prior to Christmas 2001 bar the stairway over the compressor chamber which was installed in January 2002 (see Photo 9).

Conclusions

With a lot of hard work by many people the building shell of August 2001 was converted into a clean area with all the infrastructure ready for optics installation and commissioning to carry on by Christmas 2001.

References

1. C N Danson, Central Laser Facility Annual Report 2000/2001, RAL-TR-2001-030, pg 148
2. C Ziener, Central Laser Facility Annual Report 2000/2001, RAL-TR-2001-030, pg 150
3. Metalcraft, Chatteris, Cambridge, PE16 6SA
4. NiTec, Chesterfield, Derbyshire, S41 9RX
5. Kvaerner Metals, Sheffield, S9 4EX
6. Btex, Newbury, Berkshire, RG145SH
7. SIFCO, Redditch, Worcs., B98 9HD
8. P A Brummitt, Central Laser Facility Annual Report 2001/2002, RAL-TR-2002-013, pg 168

Vacuum system commissioning for Vulcan Petawatt Interaction and Compression Chambers

P A Brummitt, D Rodkiss

Central Laser Facility, CLRC Rutherford Appleton Laboratory, Chilton, Didcot, Oxon, OX11 0QX, UK

Main contact email address: *P.A.Brummitt@rl.ac.uk*

Introduction

The vacuum system for the interaction and compression chambers was designed to allow evacuation of the chambers to be carried out within set performance goals and to maintain a clean environment within the chambers.

Chamber cleaning process

Once the chambers were installed it was essential that they were thoroughly cleaned before the vacuum system could be commissioned. The system was initially cleaned using a petroleum based cleaning agent. This was used to clean off the initial contamination from the inside of the chambers left over from when the chambers were manufactured. The chambers were cleaned several times using this method. Once it was felt that the initial dirt layers were removed from the chambers, they were then cleaned with Isopropyl Alcohol. This again was carried out several times until there was no residual dirt being removed when a swab was taken.

Vacuum pump installation

The vacuum pump installation was carried out in two parts. The roughing pumps were installed prior to installation of the chambers. This could be carried out due to their location within the plant room. Once the chambers had been installed and cleaned the rest of the vacuum system could be installed. The high vacuum pumping systems were installed first. The high vacuum pumps are sets of turbo molecular pump, a rotary vane backing pump and a high vacuum valve. The high vacuum pump sets required electrical and air services to be installed. There are three sets of high vacuum pumps in total, two on the interaction chamber and one on the compression chamber. Once the high vacuum systems were fully installed the connection of the roughing system could be completed. This was done through the connection of a 160mm-diameter pipeline from the plant room through to the two chambers.

Let up system installation

The majority of the let up system is located within a plant room. So, as with the vacuum roughing system, much of the installation of the let up system could be done prior to installation of the chambers. The system consists of two oil free air compressors, an air-drying unit, various levels of filtering and an air receiver. All of this is housed within the plant room. After installation of the chambers the let up system was connected to the chambers using 50mm diameter stainless steel pipeline. Due to the nature of the system and the cleanliness requirements, this pipeline system was supplied pre-cleaned and bagged ready for installation.

Vacuum system testing

Before any of the optical mounts or optics themselves could be installed inside the chambers a thorough test of the vacuum system was required. The testing had two important goals: to test the performance of the vacuum system; and to check how clean the system was. Initial testing was carried out using the vacuum system. These initial tests were used to provide information on how leak tight the chamber was, so that any leaks may be found and fixed. This was important because the chamber had to be below a certain pressure before carrying out cleanliness tests using a residual gas analyser. During the initial pump-down tests the chamber was tested for leaks using a Helium leak detector. On initial test there were some leaks which were found and fixed. Once the system had been pumped for the required time a pressure suitable for the residual gas analyser was reached. This equipment could then be utilized for the cleanliness tests.

Cleanliness tests

Due to the requirement for cleanliness inside the chambers, a residual gas analyser was used to provide important information on the state of the chamber. Tests were carried out after the initial pumping tests and the results analyzed. The data recorded was compared with data from existing Vulcan systems to give direct comparison with the current systems in use. The initial results were favorable, giving similar levels of cleanliness to the chamber in target area west. The chambers were cleaned thoroughly again after initial tests to try and improve on the current level of cleanliness. Following cleaning, further tests were carried out and final results were obtained showing that the new chambers now exceed the best levels of cleanliness of any of the other Vulcan vacuum systems. This was considered acceptable enough to proceed with the installation of the optics and mounts.

Performance tests

Once the system had been commissioned the performance of the vacuum pumping system could then be evaluated. The specification performance against true system performance for the interaction chamber is shown in Table 1 below and the measured performance of the vacuum system for the compression chamber is shown in Table 2.

Pressure	Specification	Performance
10^{-3} mbar	20 Minutes	16 Minutes
10^{-4} mbar	60 Minutes	60 Minutes

Table 1. Vacuum system performance for interaction chamber.

Pressure	Specification	Performance
10^{-3} mbar	2 Hours	2 Hours
10^{-4} mbar	24 Hours	24 Hours

Table 2. The measured performance of the compression chamber against the specification.

The results show that the specification has been fully met by the vacuum system.

Conclusion

The commissioning of the vacuum system has been completed to the required time-scale and fully meets the performance criteria set upon it. The system has been fully tested to allow the best possible vacuum environment for the optical components and laser to operate effectively.

References

1. Leybold Vacuum, Plough Lane, London, UK
2. Pfeiffer Vacuum, 2-4 Cromwell Business Centre, Newport Pagnell, UK

Petawatt Interaction and Compression Chamber Vacuum control

P Holligan, R W W Wyatt

Central Laser Facility, CLRC Rutherford Appleton Laboratory, Chilton, Didcot, Oxon, OX11 0QX, UK

Main contact email address: *P.Holligan@rl.ac.uk*

From the beginning of the Vulcan Petawatt upgrade project a conscious decision was made to move away from the practice of developing in house hardware driven from a PC, and to work with commercially available products intended for this type of operation.

The system has been designed to provide uncomplicated control of joint or independent chamber evacuation and let-up processes, using a 'Schneider Momentum Modular PLC' system. Control of the components involved, and their sequence of operation is initiated from a 'Magelis' user terminal that uses a colour graphics screen to provide monitoring of the system status. A high level of personnel safety is programmed into the control procedures, and components can be driven manually or through automatic control as required.

The PLC modules deployed consist of digital I/O units with relay outputs and analogue inputs. The digital I/O is used to operate solenoid valves and return the valve position status, whilst the relay outputs are used to engage the contactors that supply the vacuum pumps. An analogue signal is taken from the gauge controller which allows the chamber pressure to be displayed on the graphics screen. A schematic diagram is also displayed showing pump operation and valve position, with various pump down and let up options available to the operator.

Different stages of password protection are included to protect against misuse, and a Castell key safety lockout system has been installed to prevent pump and valve operation that could endanger personnel. Operator keys are also required to start the pumping process for both compressor and interaction chambers.

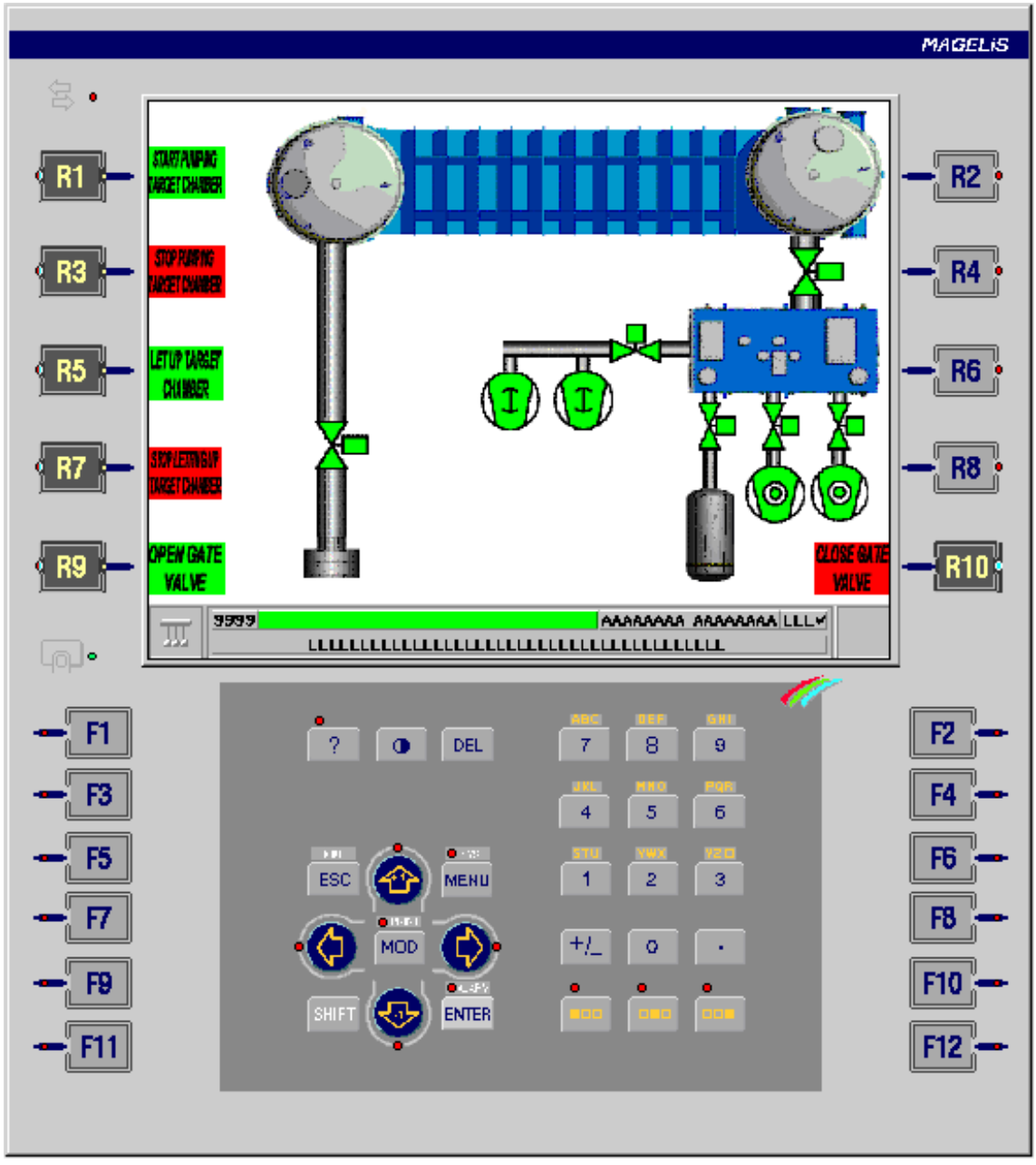

Figure 1. Magelis display showing schematic diagram of vacuum system.

Petawatt Mirror / Grating Mount Alignment Control System

P Holligan, RWW Wyatt, K Rogers, G Wiggins, M Dominey

Central Laser Facility, CLRC Rutherford Appleton Laboratory, Chilton, Didcot, Oxon, OX11 0QX, UK

Main contact email address: *P Holligan@rl.ac.uk*

The Petawatt upgrade presented an opportunity to introduce a new style of control and alignment hardware based on commercially available products to provide greater flexibility for future expansion, and reliable operation in the harsh environment that TAP is expected to present.

The Alignment control is split into two separate systems. These are the Compression Chamber Alignment System that controls all the large optics inside the chamber, and the Interaction Chamber Control System, which provides stepper motor control for the two large optical components, and dc motor control for the target mounts.

Both systems use a control PC linked via Ethernet to a number of Parker 6K8 motion controllers. The motion controllers generate the control signals that are sent to the relevant motor drive. The Compression Chamber Control System is run on a dedicated network to eliminate any unauthorised movement of optical components. The software which provides the user interface is written in LabVIEW, and allows the operator flexible control of all of the mounts inside the chamber. A separate stepper motor control rack also linked to the compression chamber has been installed to control mirror slides used to dump high energy before the beam reaches the diagnostic instrumentation.

The Interaction chamber control system consists of 10 Stepper motor drives that are used to control a Turning Mirror, and Parabolic lens mounts, whilst Target Mounts inside the chamber are controlled through a 48volt dc motor drive system. The control software is written in Visual Basic to provide a user interface for alignment purposes, and control signals regarding shot type etc., required by the main Vulcan control PC. A remote pad designed and built in house provides a remote user interface to the control software, allowing users to move stepper and dc motors whilst away from the control desk. The remote pad also displays the Sony Magnescale position feedback for the mount selected to aid alignment.

To protect against the expected EM noise generated during a high power shot, filters have been used on all mains and dc supplies, and ferrite beads attached to all susceptible cabling.

High quality shielded twisted pairs cable has been used on the Magnescale unit as ferrite beading interfered with the control signals.

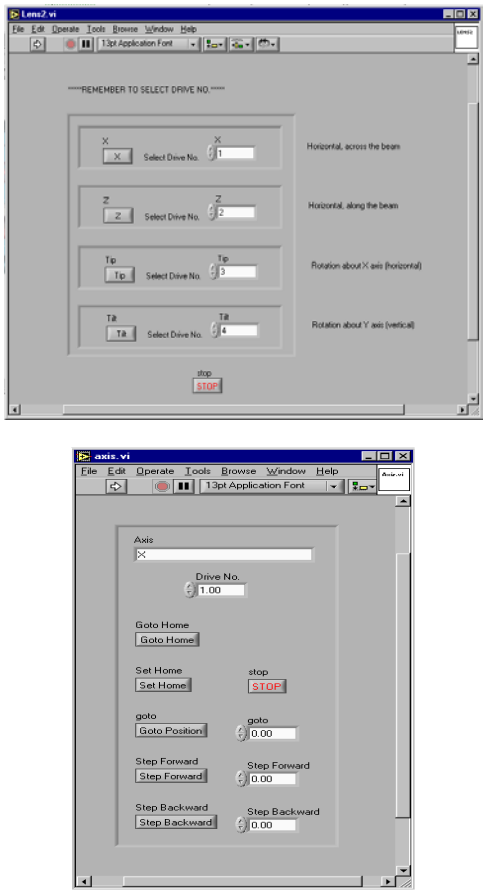

Figure 1. Specific mirror / grating mount control interface.

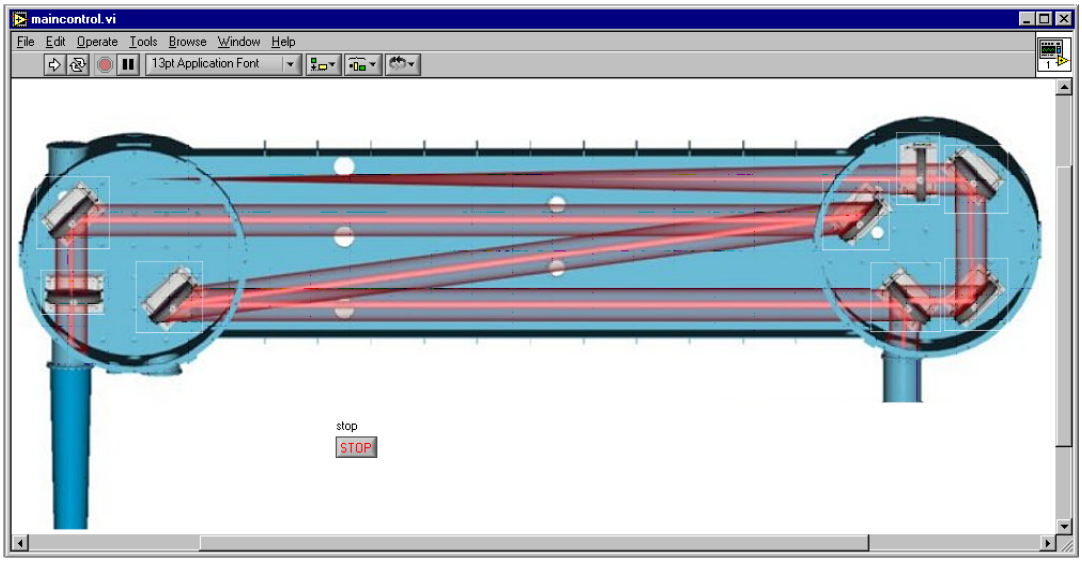

Figure 2. Main user interface page for compressor mirror / grating control.

Gain Measurements on the Petawatt 208 mm Amplifier Chain

D Pepler, C Danson, J Collier, C Edwards, S Hawkes, A Kidd, T Winstone, R Wyatt

Central Laser Facility, CLRC Rutherford Appleton Laboratory, Chilton, Didcot, Oxon, OX11 0QX, UK

Main contact email address: *D.A.Pepler@rl.ac.uk*

In order to achieve the 500 J in 500 fs necessary for the Petawatt Laser Facility a 208 mm diameter disc amplifier chain has been installed on the Vulcan Laser Facility. Previous measurements [1)] have been reported that were made on a single 208 amplifier but we now report on the performance of the three stage 208 amplifier chain.

The output from beam 8 of Vulcan was directed into the newly commissioned laser bay Laser Area Four (LA4), the use of which has been taken over from Target Area Two (TA2). The full beam size of beam 8 was slightly apodised to bring the beam diameter down to 180 mm which is the working beam diameter for the amplifiers. The normal disc amplifiers (108 mm diameter and 150 mm diameter) were used to produce a 25 J pulse (derived from a broadband, long-pulse oscillator) which was directed through the 208 mm amplifiers onto laser burn paper. This burn is shown in Figure 1 and shows a good overall beam uniformity with only one or two small diffraction centres indicating minor damage spots in the 208 mm amplifier chain.

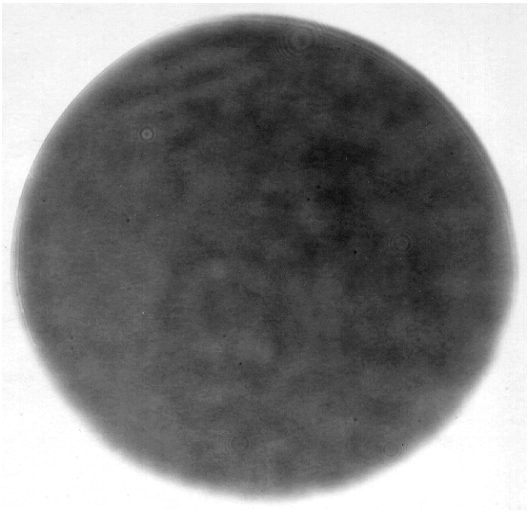

Figure 1. Laser burn taken in LA4 after propagating through the three stage 208 mm diameter amplifier chain. The burn is approximately 180 mm in diameter.

The small signal and saturated gain of the 208 mm amplifier chain were measured in a similar fashion to previous experiments. The beam was directed from the end of laser area three (LA3) through the 208 mm amplifier chain, (situated in LA4) with the resultant beam energy being measured by a whole-beam calorimeter. This was positioned further "downstream" in order to reduce the background energy reading that the firing of the flashlamps would otherwise have induced.

Figure 2 shows part of the 208 mm amplifier chain and final steering optics during commissioning. The right-hand wall shown in the photo was in fact a temporary structure and the full-beam laser calorimeter was positioned beyond these optics.

Figure 2. Photograph of LA4 during the commissioning phase, showing the last two 208 mm disc amplifiers and some of the turning mirrors. The final beam expansion optics are situated behind the temporary wall (at right).

To ascertain the small signal gain of the amplifiers, a range of energy shots (up to ~20 J input) were taken with the full beam, using either individual amplifiers or all three amplifiers together. This latter data is shown in Figure 3 at the lower-left end of the best-fit Franz Norvic saturated laser gain curve. The small signal gain taken from this curve is 8.27 (i.e. 2.02 per amplifier).

Because the calorimeter was unable to withstand more than ~ 200 J, to measure the saturated gain, further shots were initially taken with a smaller beam size. The beam was apodised to 76 mm diameter which from the shots subsequently taken gave equivalent energies of 72 J in and 440 J out i.e. a saturated gain for this level of drive, of 6.1.

In order to confirm the saturated gain using the full 180 mm beam diameter, further measurement was undertaken using an uncoated high-power laser window as a beam-splitter / sampler. The beam-splitter was placed at the output of the 208 amplifier chain at an angle of 13.5º which then reflected 7.1% of the beam into the calorimeter. The remainder of the pulse passed through the window onto burn paper (encapsulated in a plastic laminate to minimize the debris blow-off.) With this arrangement a shot was fired with 122 J in and 792 J obtained out of the three stage 208 amplifier chain. This data is shown in Figure 3 and shows excellent agreement with the lower energy measurements.

References

1. "Gain Measurements on a 208 mm Amplifier" D Pepler *et al*. CLF Annual Report 1999 / 2000. (RAL-TR-2000-034) p 187.

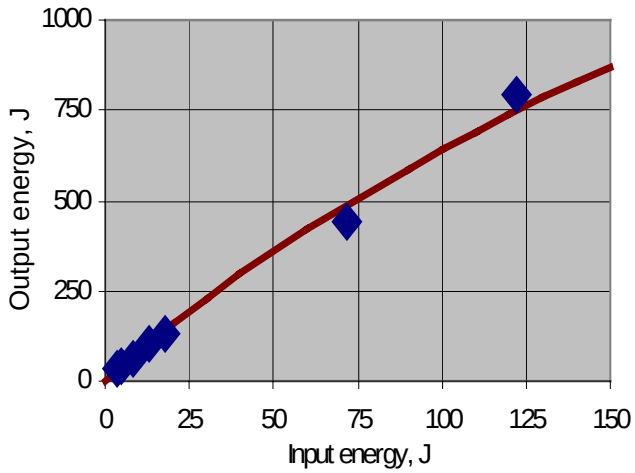

Figure 3. Graph showing the input energy to output energy gain curve for the three stage 208 mm amplifier chain. The solid line is a Franz Norvic gain curve that has been fitted to the data points.

Reconfiguration of the Vulcan Front End Systems

C Hernandez-Gomez, J Collier, J Smith

Central Laser Facility, CLRC Rutherford Appleton Laboratory, Chilton, Didcot, Oxon, OX11 0QX

Main contact email address: *C.Hernandez-Gomez@rl.ac.uk*

Introduction

A new front end for the Vulcan laser has been configured to accommodate the Vulcan Petawatt upgrade. The existing Oscillator Room has been extended by the addition of the adjacent room, which used to be the Vulcan Clean room. There were two main reasons to extend the room: to accommodate the new Petawatt stretcher and an oscillator and stretcher previously located in the laser area. The Petawatt stretcher will use a large optical table 3.75 m long by 1.5 m wide and could not be accommodated in the former oscillator room. The extension of the oscillator room has enabled the centralization of all the CPA Front End systems.

The pulse generation systems for the Chirped Pulse amplification (CPA) for Target Area West (TAW), East (TAE) and Petawatt (TAP), including a new Optical Parametric Chirped Pulse Amplification (OPCPA) preamplifier, are now located in the new Front End room.

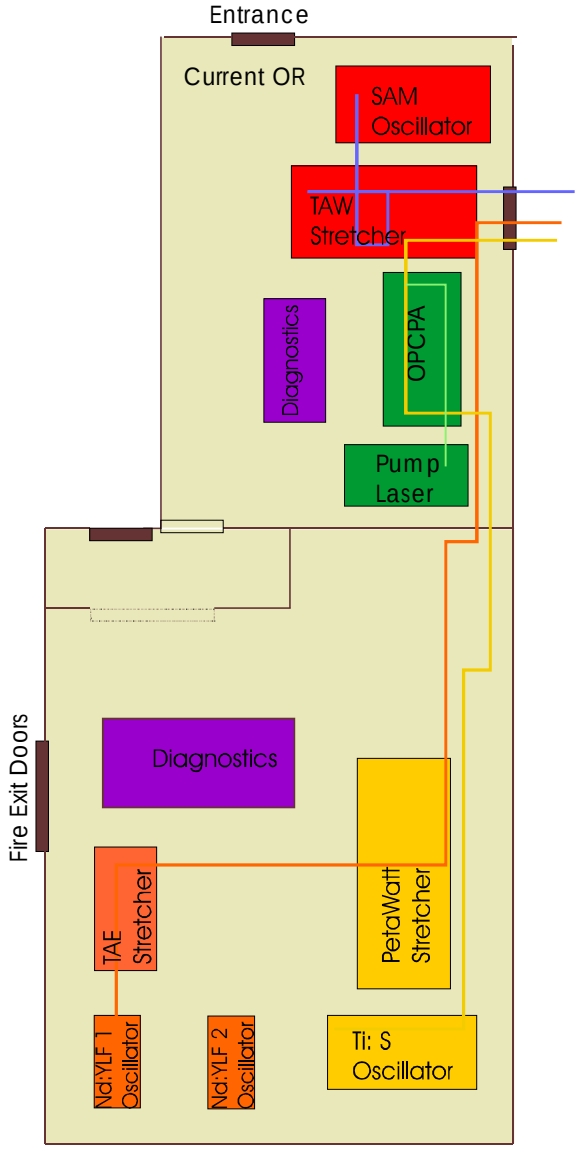

Figure 1. Schematic of the Front End.

This consists of 3 ultra short pulse oscillators, 3 stretchers and an OPCPA preamplifier and a Q-Switched 10 Hz pump laser. These systems are individually detailed below. A schematic of the Front End is shown in Figure 1. The organization of systems has been designed such that it allows the independent operation of all three areas.

TAW CPA configuration

The seed pulses for the TAW configuration are produced by a Time Bandwidth commercial oscillator. The GLX-100 is an oscillator with Nd: Glass as the active medium. It is mode locked by a state of the art device known as a semiconductor Saturable Absorber Mirror (SAM). The 80 MHz cavity produces 170 fs pulses at 1nJ per pulse. Each pulse is stretched using a double passed refractive confocal telescopic stretcher [1)] and injected into Vulcan. The telescope produces an effective grating separation of 3.5 m to match the compressor separation in TAW. The stretcher produces a group velocity dispersion of approximately 150 ps/nm [1)]. The SAM oscillator has 5 nm FWHM resulting in a 750 ps stretched pulse duration, which is subsequently gain narrowed in Vulcan to 350 ps.

TAE short pulse configuration

Target area East operations can require long pulse operations from 600 ps to 2 ns or short pulse operations at 80 ps. For the short pulse operations the oscillator used is YLF 1. This was the first oscillator used in Vulcan for CPA operations. It has been located in the extension to the oscillator room from inside the laser area. An in-house designed Nd:YLF Additive Pulse Modelocked system, it produces pulses of 1.8 ps duration at 1nJ per pulse [2)].A double passed stretcher stretches the pulse from 2.5ps to 80ps. This stretcher has also been relocated from the laser area to the new Front End room. This pulse is not usually compressed, however there is the capability to do so in TAE.

TAP CPA configuration

The seed pulses for the TAP configuration are produced by a Spectra Physics Tsunami oscillator. It is a commercial Kerr Lens Modelocked (KLM) oscillator using Ti:Sapphire as the active medium. It is pumped by the Millennia X, a commercial diode pumped Nd:Yag laser. This oscillator emits a train of 5nJ pulses 120fs long at a repetition rate of 80MHz. The Target Area Petawatt stretcher is a four pass Offner reflective Stretcher. The stretcher has become a Double Decker design [3)]. The 100fs pulse from the Ti:S oscillator is stretched to a pulse 4.8 ns long. In addition to the stretcher and oscillator there is a new front end preamplifier [4)] which will amplify the pulses up to energies at the mJ level. This OPCPA amplifier is pumped by the Nd:YAG Continuum laser: This customized commercial pump laser is a frequency doubled Nd:YAG laser which emits a train of 1J pulses with a wavelength of 532nm at a repetition rate of 10Hz .

References

1. J. Collier *et al*. CLF Annual Report 1996/97, RAL-TR-97-045, pg 188
2. Z. Chang *et al*. CLF Annual Report 1992, RAL-92-020, pg 94
3. J. Collier *et al*. CLF Annual Report 2001/2, RAL-TR-2002-013, pg 173
4. C. Hernandez-Gomez. CLF Annual Report 2001/2, RAL-TR-2002-013, pg 175

"Double Decker" Stretcher Design for the Petawatt Upgrade

J Collier, C Hernandez-Gomez

Central Laser Facility, Rutherford Appleton Laboratory, Chilton, Didcot, Oxon, OX11 0QX, UK

Main contact email address: *j.collier@rl.ac.uk*

Introduction

The CPA design[1)] for the Petawatt Upgrade of Vulcan specifies the use of 1480 line/mm gratings separated by some 13 m. At the compressor end this has been one of the primary drivers that has dictated the large scale of the compression chamber and indeed the actual size of the target area building itself. For optimum pulse compression it is imperative that at the front end of the system the stretcher is perfectly conjugate with the compressor. Duplicating therefore this large scale system on a "table top" at the front end in an aberration free way has been a significant challenge. This report details the final design of the stretcher system that has been developed to meet this challenge.

Design

The stretcher design is based on the use of an Offner triplet optical arrangement. On Offner triplet is a telescope that is formed using two con-focal equal positive lenses and one negative lens located at this common focus. The negative lens has half the focal length of either positive lens. This is in contrast to the conventional stretcher design, such as that employed for the TAW CPA system, that generally use a Newtonian telescope – a telescope formed from two con-focal equal positive lenses only. A comparative optical arrangement is shown in Figure 1.

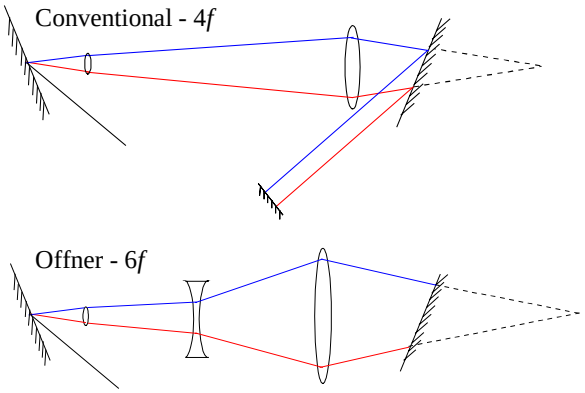

Figure 1. Conventional and Offner Triplet schemes.

There are a number of advantages in using a Offner system,. The first is that it forms a 6-*f* system in comparison to the 4-*f* Newtonian design. This enables a smaller scale design to be employed and this is of particular use in relation to the Petawatt system. Secondly, if the central negative lens is half the focal length of either positive lens then the system is intrinsically aberration free. This is very important because is allows the use of large aperture (for maximum bandwidth), short focal length (to fit on the "table top"), spherical optics (for low cost and ease of manufacture). It is possible to depart from the condition that the negative lens is half the focal length of the positive and even higher N-*f* systems are possible, but under these circumstances the aberration cancelling properties are no longer valid.

The implementation of the Offner system for the Petawatt upgrade is entirely reflective, utilising mirrors and not lenses. This is to mitigate against chromatic errors which would otherwise be significant. The Offner system employs a single negative mirror and a single common positive mirror. The design of the Offner system is shown in Figure 2. The system has been designed to have a maximum bandwidth transmission

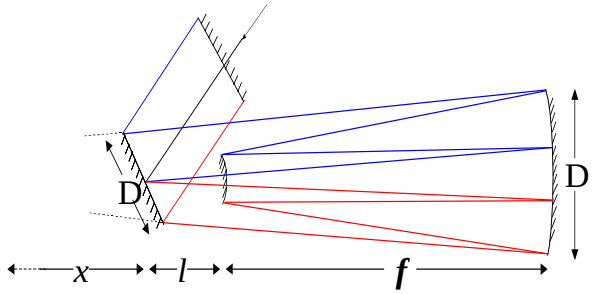

Figure 2. Reflective Offner scheme for the Petawatt upgrade f = 2250 mm, l = 625 mm, x = 3250 mm and D = 300 mm.

of 18 nm, some 4.5 times that design output bandwidth of Vulcan when using the OPCPA technology at the front end [2)].

A unique feature to the stretcher is the "double decker" nature of the design. The stretcher is designed using two identical double pass reflective Offner triplets described above that are located one above the other. They share a single common diffraction grating. This is shown in a side view in Figure 3.

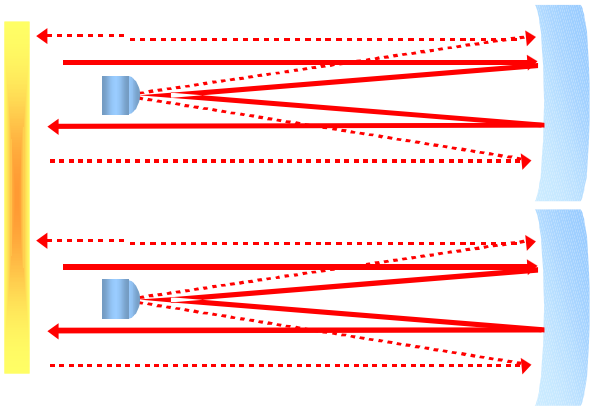

Figure 3. The "Double Decker" Design – two identical Offner systems sharing a common diffraction grating.

The incident beam first passes through one system and then the other. Using two Offner systems substantially reduces the size and cost of the optics involved. Furthermore using a single grating also has a marked impact on reducing costs, with it being by far the most expensive single component. However, a fundamental reason for using a double decker design is that it gives access to the beam after passing through the first of the two decks. At this point the beam has been stretched in time by half the amount required for the CPA design of the upgrade. The 18 nm bandwidth is dispersed to 2.7 ns. At this pulse length it is exactly compatible with the design of the OPCPA Front End amplifier. Thus following its passage through the first deck of the stretcher the pulse passes to the OPCPA system. Following amplification, the pulse is then returned to the second deck of the stretcher for final stretching.

Optical Specification

One of the drawbacks of using this reflective Offner design is that it places a very high specification requirement on the optics used. For each deck, the beam is twice spectrally dispersed at exactly the same location, in the far field, on the negative mirror. The specification on the surface quality of this mirror must therefore be high in order to avoid spatial surface errors being directly transferred into spectral phase errors. Similar

arguments apply to the common positive mirror. Great care has been taken to assess the effect in time of spatial surface errors on the optics. The optical specifications that have applied to the components are such that any residual surface errors will not introduce a temporal distortion that is outside that that arises through the 4.5 x bandwidth clip in the stretcher and the soft spectral apodization that is applied by propagation through the compressor. Details of these can be found in Reference 1. The details of the optical specification of the various components are listed in the table below. All components are protected gold coated.

Comp.	Size mm	Rad. mm	Surface p-v (at λ= 1μm)	Surface rms (at λ= 1μm)
Positive Mirror	305 x 60	4500	λ / 50	λ / 250
Negative Mirror	120 x 10	-2250	λ / 50	λ / 250
Retro	200 x 25	Inf	λ / 25	λ / 125
Grating	350 x 150	Inf	λ / 25	λ / 125

Table 1. Optical Component Specifications.

The stretcher is housed on a single 4.0 m x 1.5 m optical table. The path length through the double decker system is about 52 m during which the majority of its time is spent spatially spectrally dispersed. It is important therefore that the optical table and stretcher are environmentally enclosed to prevent air turbulence inducing spectral phase errors through air refractive index variations that would otherwise substantially affect the pulse compressibility. An artists impression of the completed system is shown in Figure 4 below.

Conclusion

A novel table top double decker stretcher system has been designed for the Petawatt upgrade that is conjugate with the compressor. The design enables a Stretch-Amplify-Stretch architecture to be implemented for the Petawatt upgrade by retaining compatibility with the OPCPA system. A key driver for the design has been to retain spectral phase purity and a sufficiently large bandwidth transmission that pulse fidelity and a high contrast is preserved upon compression.

References

1. J. Collier *et al*, "CPA Design Considerations for the Vulcan Petawatt Upgrade", CLF Annual Report 1999-2000, RAL-TR-2000-034, pg 174

2. C. Hernandez-Gomez *et al*, "Commissioning of the Vulcan OPCPA Pre-Amplifier" , CLF Annual Report 2001/2, RAL-TR-2002-013, pg 175

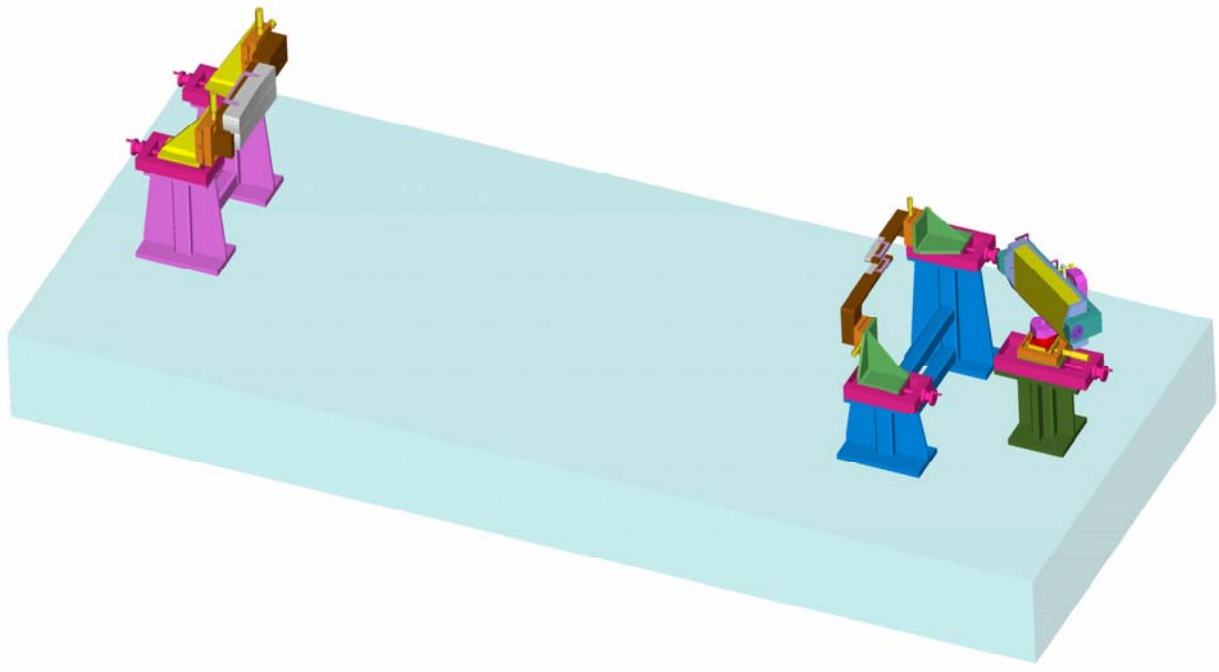

Figure 4. An artist's impression of the completed stretcher.

Commissioning of the Vulcan OPCPA preamplifier

C Hernandez-Gomez, J Collier, M Csatari, J Smith

Central Laser Facility, CLRC Rutherford Appleton Laboratory, Chilton, Didcot, Oxon, OX11 0QX

Main contact email address: *c.hernandez-gomez@rl.ac.uk*

Introduction

We describe the new Preamplifier for the Vulcan laser based on the Optical Parametric Chirped Pulse Amplification technique [1-2]. The preamplifier has been designed on the basis of results obtained with a test bed preamplifier [3] .

Description

The front end system is formed by an oscillator, a stretcher, the preamplifier and a pump laser. The seed is generated by a commercial Kerr mode-locked. oscillator with Ti:Sapphire as the active medium. This oscillator generates an 80 MHz pulse train of 5 nJ pulses. Each pulse is 120 fs long and has FWHM bandwidth of 15 nm centred at 1053 nm. A single pulse is selected for amplification and is stretched in time using one of the Vulcan stretchers. The amplifier is designed for a stretched seed pulse 2.4 ns long.

The OPCPA preamplifier is shown in Figure 1. The amplification of the seed is achieved in three single-pass stages. Stage one and two have been designed to be identical with a gain of 10^3. Stage three is used to saturate the process and has been designed with different parameters to give a gain of 10^2. The non linear medium used for the amplification is *ß - Barium Borate (*BBO) for all the stages. Each crystal is kept in an oven at 40^o C. The pump laser used is a custom-commercial Q-switched Nd:YAG. It is a Single Longitudinal Mode laser that generates a train of 1J pulses at 10Hz. The pulselength is 15 ns with a Gaussian shape and a wavelength of 532 nm. The output is split into two beams by using the combination of λ/ 2 waveplate and plate polariser. The beam transmitted through the thin polariser is used to pump stages one and two and the reflected beam is used to pump stage three.

The pump beam for stages one and two contains 400 mJ in a 9 mm diameter beam and is demagnified to 6 mm. The central 3 ns are sliced by a fast Pockel cell such that the pump pulse has an almost top hat temporal profile. Immediately after the slicing the beam is split by a 50/50 splitter to feed stages one and two. A polariser in each stage isolates the 3 ns vertically polarised pulse and then injects it into each stage. Each 3 ns pump pulse contains 40 mJ and is further demagnified by a factor of 4 prior to injection in the crystals. The maximum pump intensity is 400 MW/cm^2 . The near field of the pump pulse is an image relay of the near field of beam inside the pump laser to ensure a good spatial profile in each stage. The pump pulse that feeds stage three is image relayed from the laser by a one to one telescope. This beam is sliced by a second Pockel cell, such that the central 3ns pulse is injected via a thin poliser into stage three. This pump beam is then demagnified by a factor of 3.3. This 3ns pulse contains 100 mJ of energy with a maximum intensity of 200 MW/cm^2.

The seed is demagnified to a 0.5 mm diameter beam and is horizontally polarised. The pump and seed pulses are synchronised in time using an SRS delay unit. The seed is injected slightly non-collinear with respect to the pump into all three stages. The phase matching is achieved by angle tuning. The nearfield of the pump pulse is larger than the seed in stages one and two to compensate for the walk off. The amplified signal is image relayed to stage two with a one to one telescope, after amplification in stage one. The idler is disposed of by the use of a pinhole at the focus of the relay telescope making use of the non-collinear geometry. After stage two the amplified signal is expanded by a 3.2 magnification telescope prior to the injection into stage three and the idler is disposed of by a similar pinhole to stage one. In stage three the beam diameters of pump and seed are very similar. The idler is again disposed of by the use of a one to one telescope and pinhole.

Implementation with Vulcan

The OPCPA amplifier as a standalone system has been designed to deliver an output energy of 1 mJ/nm, and remains compatible with both Target Area West (TAW) and Target Area Petawatt (TAP) configurations.

The TAW configuration requires a stretched pulse 2.4ns long. This is achieved using a telescopic stretcher which is formed by a pair of 1740 l/mm diffraction gratings separated by a confocal telescope. The available bandwidth is 16nm.

The spectrum of the amplified seed and un-amplified seed spectra are shown in Figure 2. It shows all the bandwidth is amplified in the OPCPA amplifier.

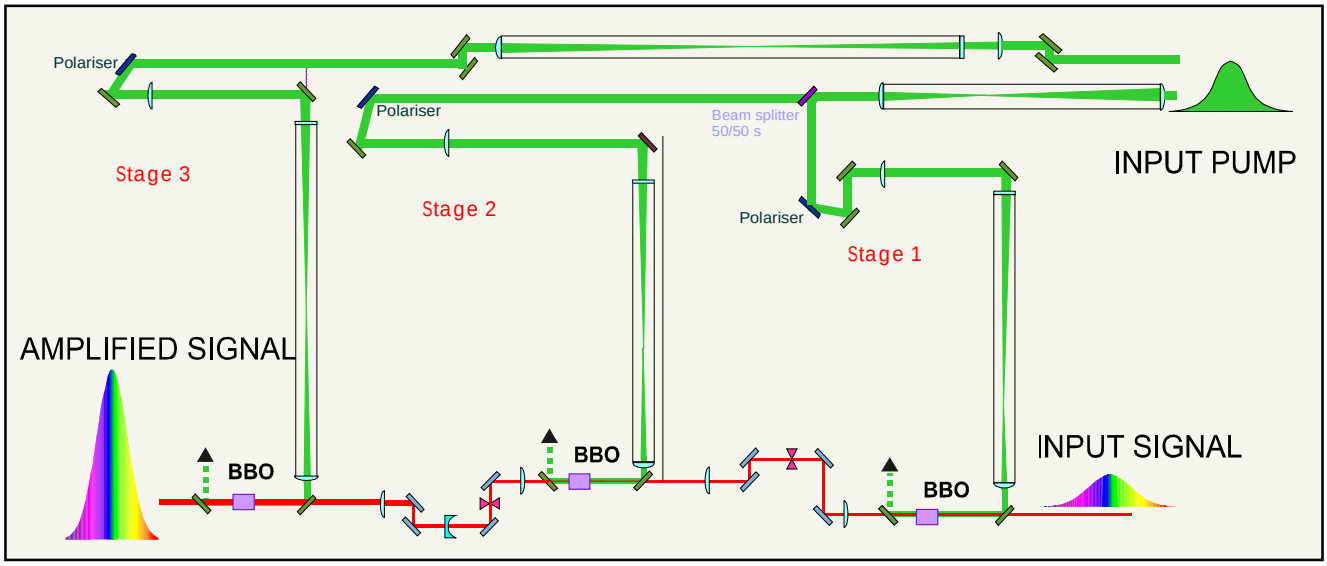

Figure 1. OPCPA Preamplifier layout.

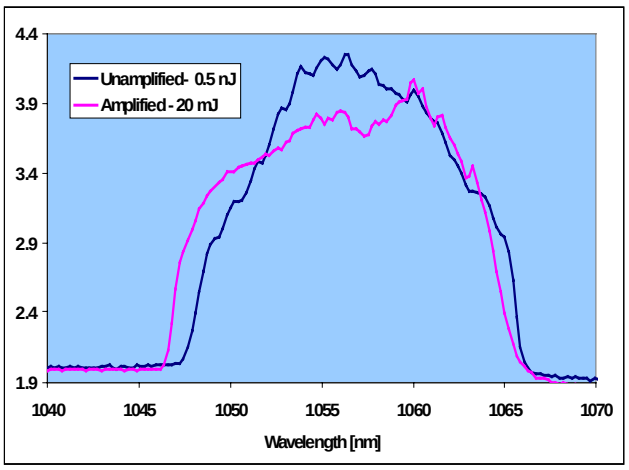

Figure 2. Spectra of the seed and amplified seed (vertical scale in arbitrary units).

The output energy from the OPCPA preamplifier needs to fulfil a 10% stability requirement for its use in Vulcan. Therefore stability measurements were carried out. Figure 3 shows the output over 2000 shots. The stability is within the $\pm$ 10%, required for Vulcan. Occasionally there is a drop in the energy. This low energy output is caused by the pump laser not being seeded to a single mode. The important feature is that there is never a high energy output, above the 10%. This could be catastrophic for Vulcan, as it could result in a high energy shot, above the maximum energies permitted.

The OPCPA preamplifier has subsequently been configured for PW operations. For the TAP configuration the stretched pulse is 4.8ns. This is to be achieved by using a four-pass Offner stretcher system, using a single 1480 l/mm grating with an effective separation of 13 m, operated at a 47^0 input angle. The stretched pulse will be 2.4 ns after the first double pass. Therefore at this pulse length it can be amplified by the OPCPA preamplifier and after amplification re-injected into the Petawatt stretcher for a second double pass to achieve the required 4.8ns pulse length. The bandwidth available will be 18nm.

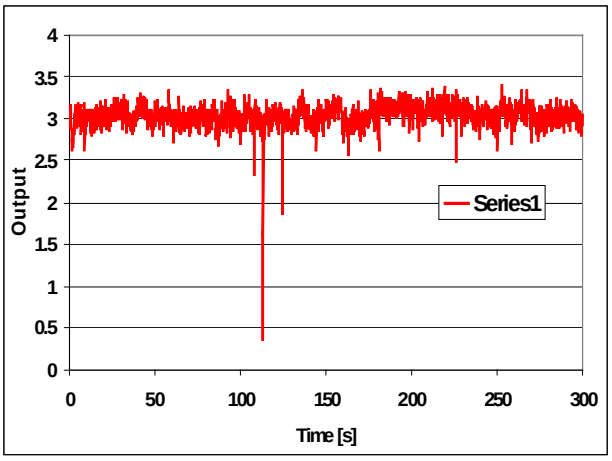

Figure 3. Stability measurements (vertical scale in arbitrary units).

However a temporary stretcher has been built for the initial commissioning of the Petawatt system, due to the long lead of the optics for the Offner stretcher. This telescopic stretcher is 9.3m long with an effective separation of 13m. It is a double pass system with a single grating and lens. There is a hard clip of the spectrum at the lens and folding mirror such that the bandwidth is limited to 7.4nm. These stretched pulses were then injected into the OPCPA amplifier for amplification and then injected into the Vulcan laser.

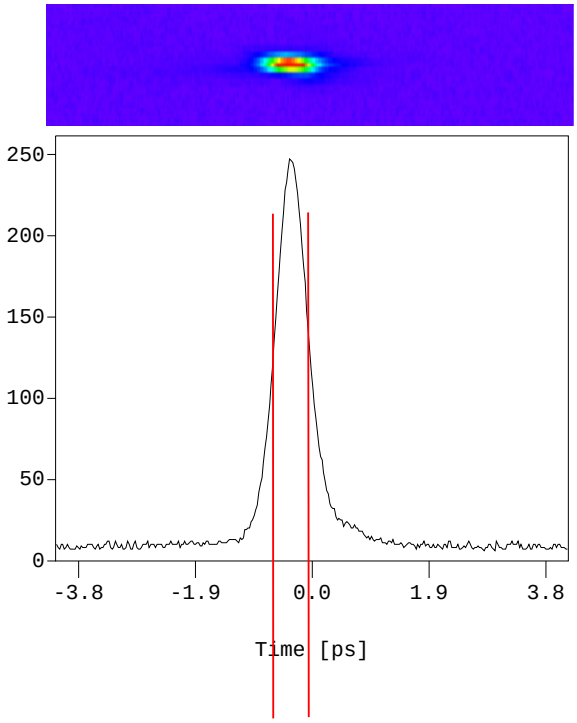

Duration 430 fs FWHM

Figure 4. OPCPA Vacuum compression (vertical scale in arbitrary units).

The beam is then injected into the rod and disk chain, bypassing the 9 mm rod amplifiers. Energy tests were carried out to demonstrate the compatibility of the OPCPA preamplifier with the Vulcan laser in the TAW and Petawatt configuration. The energy delivered using the OPCPA preamplifiers was 100 J on a full beam for TAW and 80 J on the apodised beam for Petawatt.

The stretched pulses amplified by OPCPA can propagate through the Vulcan laser without further amplification and compressed using the Petawatt compressor. An auto-correlation of these pulses is shown in Figure 4. The pulse was successfully compressed to 430 fs.

Conclusion

A new Front End preamplifier has been commissioned for the Vulcan laser system The beam amplified in the OPCPA preamplifier has played an important role in the alignment and commissioning of the Petawatt compressor.

References

1. Ross *et al*, Optics Communications, 144, (1997) 125
2. Dubietis *et al*, Optics Communications, 88, (1992) 437
3. Collier *et al*, Applied Optics, 38, No. 36, (1999) 7486

Radiation shielding for the interaction chamber in Target Area Petawatt

C Ziener, P E Hatton, P N M Wright, R J Clarke, C B Edwards, D Neely, D A Rodkiss, B E Wyborn

Central Laser Facility, CLRC Rutherford Appleton Laboratory, Chilton, Didcot, Oxon, OX11 0QX, UK

Main contact email address: *c.ziener@rl.ac.uk*

Introduction

If a super-intense laser interacts with a solid target, a substantial part of the laser energy can be converted into kinetic energy of electrons, protons and heavy ions. When these fast particles interact with matter, their kinetic energy is converted into x-rays, γ-rays and neutrons. It is necessary to build radiation shielding, so that no ionising radiation or neutrons can escape from the target area. This radiation shielding could interfere with the experimental geometry, so maximum flexibility was also a main objective for the shielding design.

Design of the radiation shielding

For experiments in Target Area Petawatt where up to 500 J on target at an intensity of 10^{21} W/cm^2 can be delivered, the γ-radiation dose produced during one laser shot is predicted to be up to 130 mSv @ 5m from the interaction point[1]. Assuming 300 shots per year, the total annual dose would be 39 Sv per year @ 5m from the target. The Maximum Permissible Annual Dose for a member of the public (MPAD) is 1mSv per year. Taking into account an additional factor of 2 for safety, the necessary attenuation factor provided by the radiation shielding is 8×10^4.

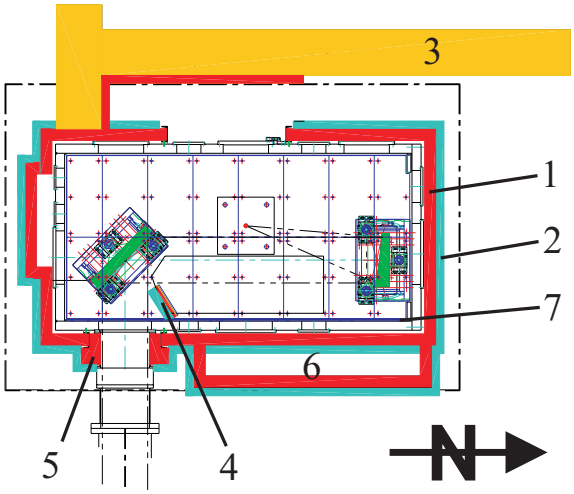

Figure 1. Layout of the interaction chamber with the radiation shielding: 1) lead, 2) high-density polyethylene, 3) concrete labyrinth, 4) Internal shielding, 5) Collimator around the entrance tube, 6) housing around the vacuum pumps, 7) Aluminium lining.

To achieve the attenuation, the radiation shielding of Target Area Petawatt consists of several elements as shown in Figure 1. The whole chamber is enclosed with 150 mm of lead as γ-ray shield and 100 mm of high density polyethylene for moderating and absorbing the neutrons produced. This first step ensures that the dose in the target area for a single high intensity shot on a solid target is below the MPAD. Safety measures are in place which ensure that it is impossible for people to be in the target area during a disk shot for laser safety and radiation safety reasons. The walls of the target area consist of 60 cm of concrete to attenuate the radiation further below the MPAD even for 300 high radiation yield shots per year.

To ensure the best possible flexibility it was decided to use lead bricks of 200×100×50mm^3 to build the γ-ray shielding around the interaction chamber. The lead walls are held in place by the plastic neutron shielding. On the roof, chevron shaped lead blocks have been used to reduce the possibility of radiation leakages even further. ISIS provided a significant quantity of lead to the CLF which reduced the shielding cost considerably. The total amount of lead provided by ISIS was about 55t and about 45t of new lead had to be purchased.

A number of ports necessary for experiments scheduled for the first year of operations were singled out. Steel frames are used to support the lead around these ports. All ports have to be covered (backfilled) with the same amount of lead and plastic as the whole interaction chamber. Labyrinths from Lead blocks will be used for the feedthrough ports. For the higher ports on the south and the north side of the chamber, special steel frames to hold the backfill will be used. It was necessary to build a complete housing for the vacuum pumps on the east side of the interaction chamber to ensure the integrity of the radiation shielding.

To shield the entrance tube of the interaction chamber, an internal shielding wall of 50mm of lead and 100mm of plastic will be installed. There will also be an external collimator built from lead bricks in a steel frame around the tube .

High density polyethylene sheets will be mounted outside the lead for neutron shielding. Since there is no concrete roof above the target area, borated high density polyethylene will be used for the roof of the interaction chamber. This ensures a sufficient neutron shielding and prevents any neutron sky-shine.

The entrance door of the interaction chamber is covered by a labyrinth built from concrete blocks with the dimensions 1830×610×610 mm^3. This will enable very quick access to the interaction chamber between laser shots. The concrete works as γ-shield as well as neutron shield. Because the thickness is not quite sufficient for full energy shots, the interior of the concrete labyrinth will be lined by 100 mm of lead bricks.

In all, the shielding will require about 100t of lead and 50t of concrete.

Commissioning of the radiation shielding

During the first experiment, a very careful commissioning of the complete radiation shielding will be done. The γ–ray as well as the neutron dose will be measured as a function of laser energy and intensity on target inside the chamber, outside the chamber in the target area and outside the target area. The dose produced on each shot will be measured during the whole experiment. The intensity will be increased slowly from 50 J (100 TW) to the full energy of 500 J. This will ensure that the results are directly comparable to previous dose measurements made in Target Area West.

During the experiment the level of activity for the targets used, the target mounts and the interior of the target chamber will also be measured.

Installation of the radiation shielding in TAP

Figure 2 shows the lead shielding of the west and the north wall almost completely installed. The I-beam on top of the lead on the north wall is bolted to the interaction chamber for stability reasons. All the frames around the ports are bolted to the chamber as well.

In Figure 3 the steel frame work and the lead for the shielding around the vacuum pumps are shown. A removable lid design enables quick access to all the ports for maintenance and in case of failures.

Figure 2. Lead shielding of the north and west walls of the interaction chamber. The two ports alongside the entrance door will be used as an optical port and a feedthrough port respectively. The lower port in the north wall is also a feedthrough port.

Figure 3. Lead housing for the vacuum system of the interaction chamber partially installed.

The whole interior of the interaction chamber has been lined with 20mm thick aluminium plates. This ensures, that a large portion of the particles are stopped in a low-Z material thus shifting the Bremsstrahlung spectrum to lower energies. This down-shifting of the γ-ray energies increases the efficiency of the external shielding. The Aluminium lining will also prevent the chamber walls (mostly iron) from becoming activated after several experiments. An additional advantage of this particular design of the Aluminium lining is the possibility to take out single plates and modify them, to enable the mounting of equipment and/or diagnostics.

Figure 4. The interior of the interaction chamber with almost all of the Aluminium plates in place.

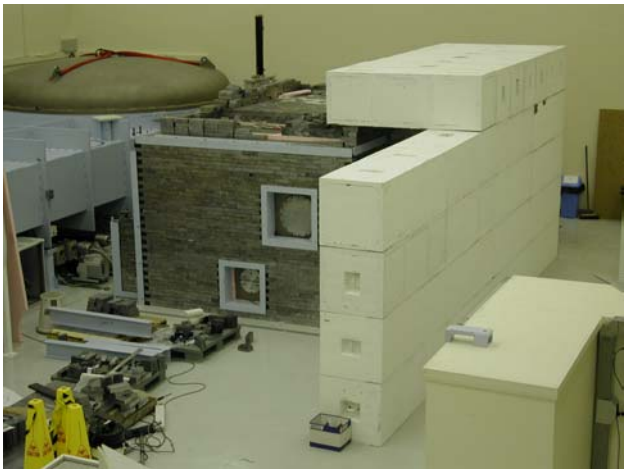

Figure 5. The concrete labyrinth for shielding the entrance of the interaction chamber.

The installation of the radiation shielding is a major engineering task but necessary for the safe operation of the new Target Area Petawatt.

A commissioning experiment run during August 2002 will verify the radiological safety of the shielding design and construction.

References

1. R. Allott, P. Wright, C.Danson, C. Edwards, D. Neely, P.Norreys, D. Rodkiss, B. Wyborn, Central Laser Facility Annual Report 1999-2000, RAL-TR-2000-034, pg 177

Laser area 4 beam delivery and diagnostics commissioning

S Hawkes, J Collier, S Hancock

Central Laser Facility, CLRC Rutherford Appleton Laboratory, Chilton, Didcot, Oxon, OX11 0QX, UK

Main contact email address: *S.J.Hawkes@rl.ac.uk*

Introduction

An integral part of the Vulcan Petawatt upgrade was the commissioning of a new laser area. This new area served several purposes: to increase the energy from 120J to 600J[1)]; provide beam delivery and local alignment lasers for Target Area Petawatt (TAP); forward going diagnostics for TAP operations; retro diagnostics for compressor commissioning and an adaptive optics wavefront sensor channel.

Beam delivery and local alignment lasers

Figure 1 shows the layout of laser area 4. For normal TAP operations the output of the 208mm-amplifier chain is injected in to the expanding Vacuum Spatial Filter (VSF) and compressor. The two mirrors used to propagate the beam are 99% reflective, generating two forward going diagnostic channels. The first comprises the adaptive optics sensor channel while the second generates the forward going near-field, far-field, calorimeter channel and a spare channel into which a spectrometer or radial shear interferometer [2)] can be installed.

The TAP local alignment laser is generated in LA4. This is injected into the TAP beam line using a slide mirror as indicated in Figure 1.

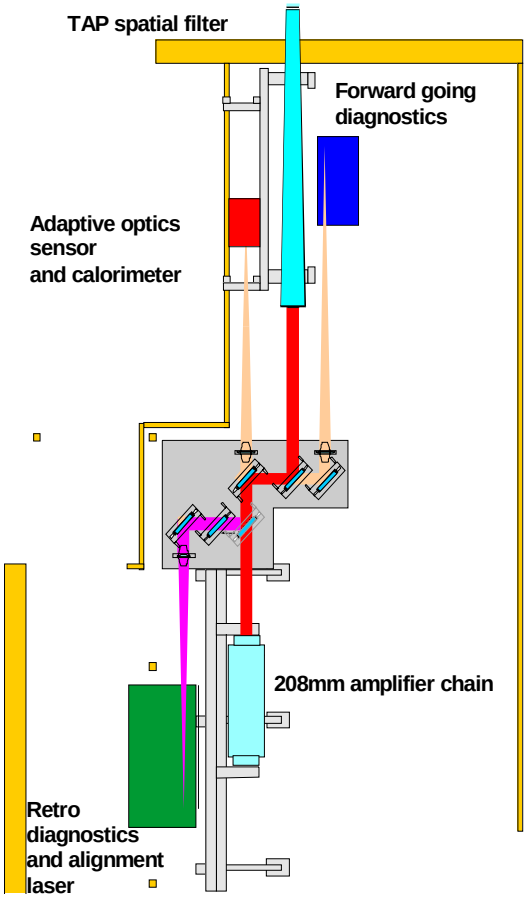

Figure 1. Laser area 4 schematic.

Forward going diagnostics

Figure 2 details the forward going diagnostics. A Fresnel reflection off the first optic in the diagnostics suite generates a far field channel, which has a magnification of 10X to increase sensitivity for pointing stability and monitoring encircled energy in the focal spot. The near field CCD camera images the output of the 208mm-amplifier chain. This is a useful diagnostic for monitoring clipping and diffraction on the beam which would cause damage to the diffraction gratings in the compressor. The final channel is a multifunctional channel and comprises a re-collimated 20mm beam, which can either be used for taking wavefront measurements with a radial shear interferometer, or spectral information with a spectrometer.

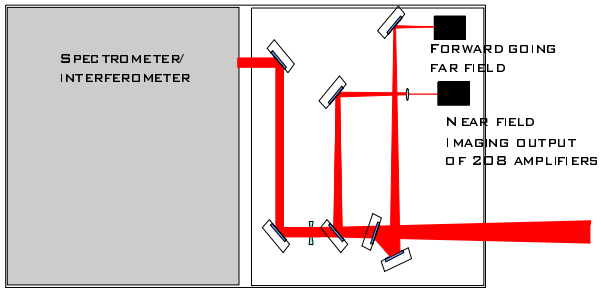

Figure 2. Forward going diagnostics.

Adaptive optics sensor channel and calorimetry

The adaptive optics sensor channel provides closed loop wavefront feedback for the adaptive optic [3)]. The leakage from the first mirror in LA4 is passed through a focus and re-collimated at the 10mm aperture. This is then passed through a micro lens array, which generates an array of focal spots at its 40mm focal length. These are then imaged on to a CCD camera. A shutter is used to protect the sensor channel when high-energy shots are delivered to TAP. The calorimeter for the 208mm amplifiers is also located here. A beam splitter and negative lens generate a 15mm collimated beam for the calorimeter.

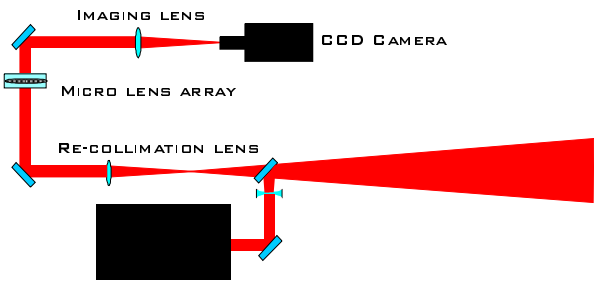

Figure 3. Adaptive optics sensor channel.

Retro diagnostics and Local alignment beam

Part of the compressor set up procedure requires an alignment beam to be propagated through the compressor, retro-reflected through the spatial filter and focused to a far-field. In order to set the parallelism of the gratings, the retro reflected far-field spots from the two wavelengths should be exactly on top of each other. For increased sensitivity in this procedure a third wavelength, 1064nm is also available. Figure 4 shows the dual wavelength laser and retro diagnostics. The two lasers have orthogonal polarisation and with the use of a cube polariser are co-linearly injected through a diffraction-limited pinhole. A 50% beam splitter is used to propagate the expanding beam from the dual wavelength laser to the collimating lens (as in Figure 1). This beam splitter in turn allows a retro-reflected beam from the compressor to be propagated through it and then

subsequently split several times to generate a number of diagnostics channels.

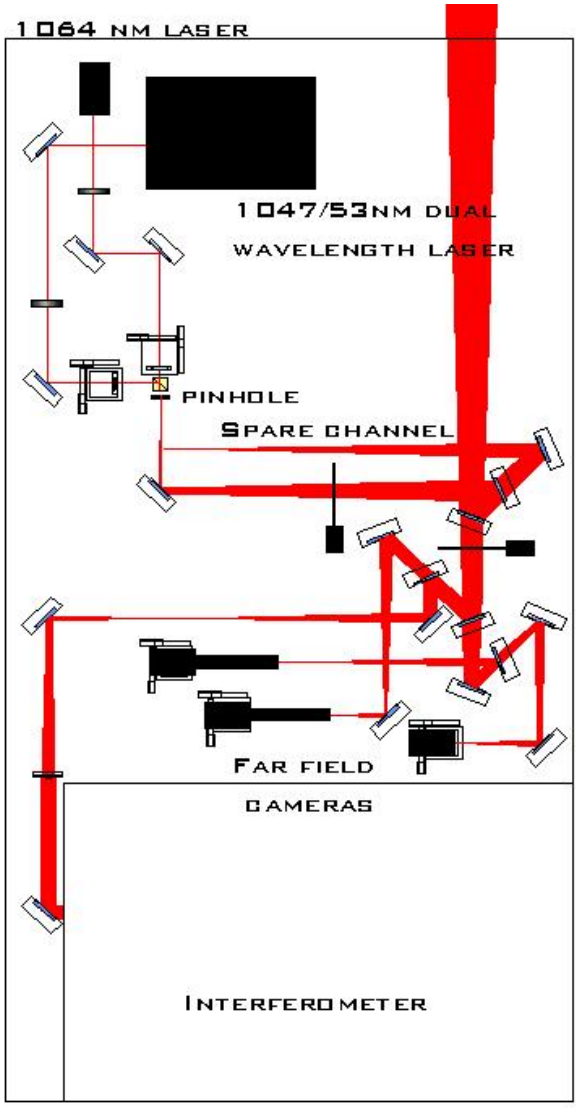

Figure 4. Retro diagnostics.

The diagnostics available for the return beam include: a wide-field far-field camera; a narrow-field, or magnified, far-field camera; a driven equivalent plane far-field camera and a radial shear interferometer. Two optics are used to split the return beam and turn it through 90^0. This is because a converging beam propagated through a beam splitter will impose a certain degree of astigmatism on the beam. However the amount of astigmatism generated is angle specific, and is significantly smaller when propagated through a beam splitter orientated at 22.5^0, than one at 45^0.

Results obtained using LA 4 diagnostics

The first significant result from the LA4 commissioning was the generation of a near diffraction limited beam. This will serve as both the TAP local alignment laser and the reference beam for the adaptive optics system. The 180mm beam generated showed some aberrations from the 350*260 beam delivery optics, but still showed a flatness of better than $1/5^{th}$ of a wave peak to valley. Presented in Figure 5 are the interferogram of the alignment beam and far-field obtained from the retro diagnostics.

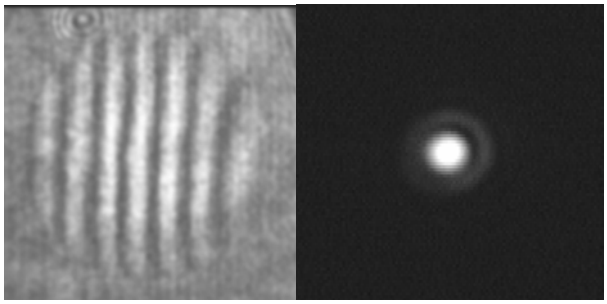

Figure 5. Inteferogram and far field of LA 4 laser.

Conclusions

The LA4 alignment beams, diagnostics, and beam delivery systems have been successfully used in the commissioning of the TAP spatial filter and compressor. This included setting the parallelism of the diffraction gratings to within the tolerances required to generate the short pulses required by the upgrade. The LA4 set up has also been successfully used in an IHP EU European access experiment studying adaptive optics as well as the trials for the CLF developed adaptive optics system.

References

1. Gain Measurements on the Petawatt 208 mm Amplifier Chain, D. Pepler *et al*, CLF Annual Report 2001/02, RAL-TR-2002-013, pg 171
2. A radial shear interferometer, C Hernandez-Gomez *et al*, CLF Annual Report 1997/98, RAL-TR-1998-080, pg 165
3. Adaptive optics trials on Vulcan, S. Hawkes *et al*, CLF Annual Report 2000/01, RAL-TR-2001-030, pg 153

Adaptive Optics for the Petawatt upgrade

J Collier, C Hooker, S Hawkes, C Edwards

Central Laser Facility, CLRC Rutherford Appleton Laboratory, Chilton, Didcot, Oxon, OX11 0QX, UK

C Haefner, K Braeur

Phelix, GSI, Planckstrasse 1, D-64291, Darmstadt, Germany

Main contact email address: *j.collier@rl.ac.uk*

Introduction

For optimum performance of the Petawatt upgrade, the dynamic correction of wavefront errors that arise from propagation through the optical chain of Vulcan is necessary. An adaptive optic development programme has therefore been in progress throughout the Petawatt upgrade. Previous reports have highlighted the specific technical details with regard to this programme [1-2)] and the reader is referred to these for additional information. This article reports on the final commissioning of the adaptive optics system on Vulcan for the Petawatt upgrade. The wavefront sensor was located in LA4 after the 208 mm amplifiers and the deformable mirror located mid chain in LA1.

Specification

The specification for closed loop operation of the adaptive optics system for use with Vulcan is for a cycle time faster than 1Hz, correction to 1.5 times the diffraction limit, and a high level of immunity to electrical noise. The relatively modest closed loop time arises from the type of errors that the system is required to compensate. These are principally those arising from static aberrations of the optics in the beamline and slowly varying distortions caused by the thermal gradients set up in the optics during the course of firing laser shots throughout the day. With a repetition frequency of three laser shots per hour at most, the need for faster loop times is not justified.

Vulcan already operates with a beam quality of approximately 3 times the diffraction limit, and reduction of a factor of 2 will give an increase in intensity on target of a factor of four. In addition, when considering the ultimate performance capability of the chirped pulse amplification (CPA) beamline, the wavefront quality determines the compressibility of the chirped pulse and influences the contrast ratio.

The effect of electrical pickup, transient magnetic fields, etc. is a very serious issue. The system must operate in a hostile electrical and magnetic environment. It is vital that the system does not exhibit failure modes which could cause catastrophic damage to the laser itself, by inducing beam focusing, for example, or causing wasted shots through undesirable changes in beam pointing or beam quality.

System Design

The wavefront sensors that were employed for the development of this system have been either a Hartman array (array of apertures) or an AZP Hartman array (array of Fresnel amplitude zone plates). This type of sensor actually measures wavefront gradient and has worked satisfactorily in previous trials. However, when deployed on Vulcan with sensing at a 200 mm aperture it was discovered that its performance was degraded, with an appreciable loss in signal to noise ratio. It was replaced by a Shack Hartman sensor (array of refractive lenses), which also measures gradient, and which operates on an appropriately de-magnified beam. This has been found to work significantly better. The Shack Hartman system produces an average of 2-3 times increase in spot centroid displacement. This array is a commercially available product, comprising a 40x40 micro-lens array with individual lens focal length of 40 mm. The lens pitch is 0.6 mm.

The deformable mirror used to effect wavefront correction is an in-house design based on a bi-morph piezo-electric architecture, the details of which are contained in the citations. The mirror has 61 electrodes and produces at each electrode a localised change to the radius of curvature of the beam proportional to an applied voltage.

A PC applies the appropriate control algorithm, as reported in the citations, coupling the sensor and the mirror. One point however to note about the control process is that it is modal in the way that it couples the sensor to the mirror. There is an external control over the number of modes that are present within the algorithm, which is important because the lower power modes (or higher spatial order modes) tend to be dominated by noise.

System Performance

The results presented below using the adaptive optic corrector include 3 datasets; ao15, ao25 and ao61. Each set refers to the maximum number of modes that is used in the correction algorithm. In the case of ao61, all the modes contribute to the correction. For ao25, only the 25 highest power modes are included and for ao15 only the highest 15.

Data set “169” corresponds to the replacement of the deformable mirror with a flat, static reflector while “ref” corresponds to a “perfect” beam that provides the reference wavefront for the system. A summary of the results is shown in the table below.

It is interesting to note that with the limited amount of data available at this time, there seems to be little difference between the p-v flatness of the wavefront between the best adaptive result, ao25, and the flat mirror. Indeed the non-optimised mode number results actually show an inferior wavefront compared with the static mirror. The second column of wavefront data was obtained from the raw data in the first column by removing all but the first 45 terms of the Zernike expansion of the wavefront in an attempt to filter out the effects of noise in the fringe pattern. Again, the same behaviour is observed.

File	Description	Phase r.m.s (waves)	Phase r.m.s (Z45 terms)	StrehlRatio (no filter)	StrehlRatio (after Zern. filter)	2nd moment (arb. units)
ref	Reference beam	0.091	0.088	0.725	0.74	44
169	169mm static mirror	0.134	0.132	0.434	0.481	72
AO15	Matrix truncated at 15 elements	0.189	0.135	0.497	0.514	62
AO25	Matrix truncated at 25 elements	0.133	0.128	0.477	0.51	52
AO63	Matrix not truncated	0.189	0.184	0.276	0.288	-

Strehl ratio analysis is shown in the 5th and 6th columns, firstly using the raw wavefront data and secondly using the Zernike filtered case. The ao15 result shows a small improvement over the static mirror. It is important to note that the Strehl ratio has been calculated from the wavefront data alone, and a uniform "top-hat" near field beam profile has been assumed.

The 2nd moment far field beam width measurement was made using the algorithms proposed by Giesen [3] and applied to the far field images shown in Figure 1. This method uses an iterative approach to determine the aperture within which the moment is calculated, to reduce the effects of noise at large distance from the centroid of the beam. First, the background is subtracted and the data is first windowed by eye, and the second moment, centred on the centroid of the distribution, calculated in both x and y propagation directions. The window is then resized horizontally and vertically to 3 times the value of the moment in the x and y axes. The moments are then re-calculated and the window re-sized as before. This process is repeated until the value of the 2nd moment converges.

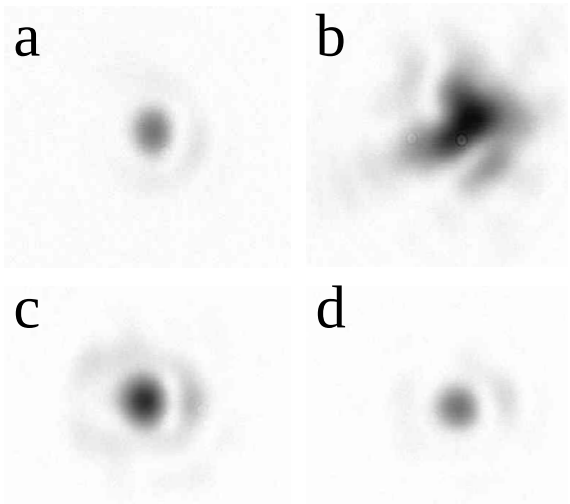

Figure 1. Far Field patterns under different configurations - a) reference beam, b) uncorrected beam "169", c) correction with 15 modes "ao15" and d) correction with 25 modes "ao25".

The results of the second moment analysis clearly show an improvement in the case of ao25 over the static mirror. The corresponding far field images are shown in Figure 1 above. It is clear from the measurement of the 2nd moment far field beam width, and also from the far field images shown above, that there is a clear improvement in the focal spot using the adaptive corrector compared with the static mirror. In the case of ao25, the focal spot quality approaches that of the reference beam.

Both ao15 and ao25 show a significant visual improvement in the far field, in agreement with the 2nd moment analysis. There is clear evidence of the first outer ring of the Airy pattern in both. It is not possible to differentiate between these two images visually due to the lower exposure of the ao25 image. The dynamic range of the measurement is also rather limited, with the peak of the ao25 image at approximately 6 bits above the noise level.

It can be seen from the table that the performance of the corrector system as diagnosed through far field images and the 2nd moment analysis gives a different result from that implied by the wavefront analysis. This will be the subject of further study outside the project.

Environmental effects

Environmental stability of the system was not tested extensively during the programme reported here but has been investigated previously. There is no evidence that the system is affected by the electrical environment in which it is required to operate. Both the sensor and actuator are located in close proximity (<2m) to the disc amplifiers and their associated pulsed power circuits. However, the earliest electrical activity prior to a shot occurs 2 ms in advance. Previous measurements have shown that it takes typically 25 ms for the deformable mirror to respond to a voltage stimulus. Thus, the observed insensitivity to shot noise is not surprising.

Summary

The latest version of the adaptive optics correction system has been tested on the Vulcan CPA beamline. The system was operated closed loop at 7Hz, using the Vulcan c.w. alignment beam as a source.

The far-field intensity distribution of the beam with the adaptive corrector in the line was significantly improved, as evidenced by far field imaging and 2nd moment width measurement.

In order to carry out final system tests with the Vulcan facility at full beam energy it will be necessary to install a fast shutter in order to protect the AO sensor and beam diagnostics from damage.

References

1. Central Laser Facility Annual Report 2000/2001, RAL-TR-2001-030, pgs 153, 175 & 177
2. Central Laser Facility Annual Report 1998/99, RAL-TR-1999-062, pg 199
3. Giesen, ISO/FDIS/11146 (to be published)

Beam splitter implementation for proton radiography

S Hawkes

Central Laser Facility, CLRC Rutherford Appleton Laboratory, Chilton, Didcot, Oxon,. OX11 0QX, UK

Main contact email address: *S.J.Hawkes@rl.ac.uk*

Introduction

Proton imaging is a diagnostic technique for the probing of dense plasmas, which is potentially capable of imaging the complex electric field structures around laser produced plasmas. This paper describes the configuration changes made to the Vulcan glass laser system in order to produce two temporally and spatially separated ultra high intensity pulses.

Laser Re-configuration

The ultra high intensity pulses are generated using the Chirped Pulse Amplification technique (CPA)[1)]. Figure 1 shows the schematic for generating the two temporally and spatially separated chirped pulses, which was installed in one of the Vulcan rod amplifier chains at the 25mm aperture point. Vulcan uses a single rod chain to drive two of its 8 beam lines. In this particular experiment target area East (TAE) and target area West (TAW) required both of these beams. As the twin pulse was only required by TAW the use of a cube poloriser and waveplate allowed the arrangement to be bypassed for TAE. This was interlocked along with beam dumps to prevent pre-pulses being generated when operating in the other mode.

The CPA beam was split using a square mirror, such that half the beam was reflected and the other half allowed to pass by. An apodiser strip was attached to the edge of the mirror in order to generate a “soft” edge to the split pulses and prevent damage in the Vulcan amplifier chain from diffraction. One CPA pulse was then propagated using two circular mirrors and re-injected into the Vulcan rod chain using a single square mirror. The other pulse was similarly propagated, but with two optics on a timing slide, this was then re-introduced into the rod chain past the side of the second square mirror. These two pulses were then amplified as per normal using the Vulcan rod and disc chain to around 50J per pulse.

Figure 2 shows the burn pattern formed at the end of the rod chain. The two 50J chirped pulses were then compressed to around 1.0 ps using the existing TAW single beam compressor with no modifications for the twin pulse configuration. The two pulses were focused onto target using two F3.5 parabolas in the TAW interaction chamber. The first CPA pulse was focused to a solid target while the second pulse was focused to an aluminium foil in order to produce a beam of protons. This then imaged the plasma formed using the first pulse, Figure 3.

Conclusions

The twin CPA configuration was used in a highly successful proton radiography experiment. This mode of operation has also been successfully used in a positron source experiment.

References

1. D Strickland, G Mourou, Opts. Comm. 56, 219-221 (1985)

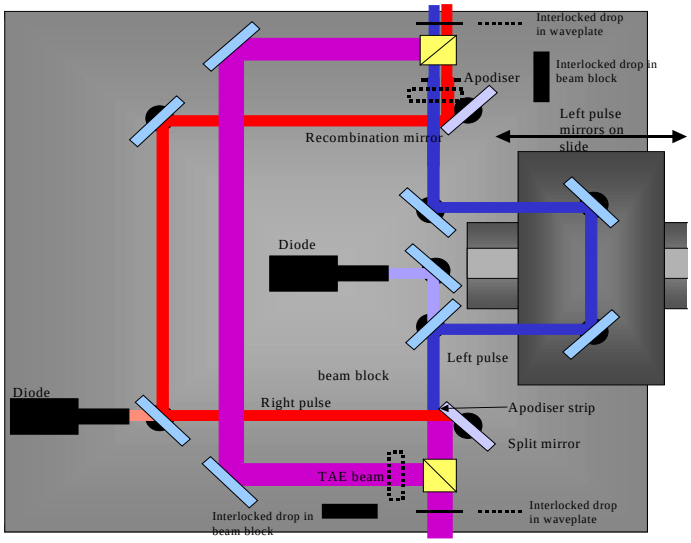

Figure 1. Schematic of the twin CPA pulse generator.

Figure 2. Rod chain burn.

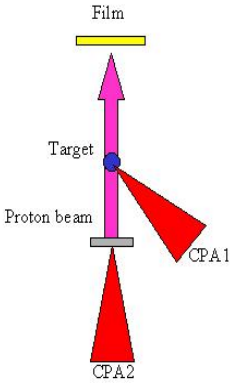

Figure 3. Target geometry.

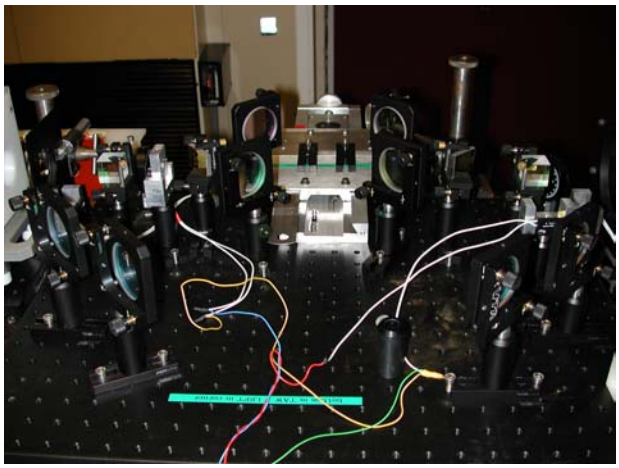

Figure 4. Twin CPA pulse generator.

Disc amplifier Flash Lamp Test Facility

R W W Wyatt, C Aldis, A Frackiewicz, D A Pepler, M Pitts, C Reason, R Wellstood

Central Laser Facility, CLRC Rutherford Appleton Laboratory, Chilton, Didcot, Oxon, OX11 0QX, UK

Main contact email address: *R.W.W.Wyatt@rl.ac.uk*

The assembly of Vulcan laser Disc Amplifiers is a precisely documented closely monitored process, by which the high performance and long term reliability of the amplifiers can best be assured. A part of the process involves the selection and test of the amplifier flash lamps, calling for close inspection of tube quality, and dynamic pulsed power tests. Dynamic tests are performed upon each occasion that it is necessary to handle lamps or lamp arrays, and possibly incur damage, or mechanical stress on the lamps. Therefore tests are carried out after the initial lamp quality inspection, and at two other significant points of amplifier construction.

The lamp test facility used until this time provided for adequate single lamp testing, but it contained obsolete technology and was technically difficult to support. It was considered that a more accurate simulation of the amplifier circuit could now be provided off line using the amplifier test facility if we were to design a suitable housing to contain two lamps coupled in series as they are in the amplifier circuits.

The amplifier test facility is equipped with full Camac control, circuit monitoring, and data acquisition through an Ethernet link to a PC as in Vulcan, and in principle dual lamp testing was considered to be possible if a suitable lamp housing could be provided. It also required an extension to the control software to provide for automated cycling, and close data monitoring to initiate shut down in the event of deviation from pre set limits.

A new lamp test housing was designed and constructed in house, using component parts manufactured in stainless steel off site. It has two isolated chambers to house the lamps, and these are top sealed with independent clip on lids that provide ease of access for lamp changes. Complete isolation of the lamps is essential in the event of the catastrophic failure of a lamp. The lamp mountings are a close replication of those used in amplifiers to simulate the mounting condition. They are constructed on a solid stainless steel base that is electrically isolated from the case, but electrically connected to the pulsed power return line, thereby providing a current return path in the event of catastrophic failure. This stray ground current, and the lamp current are monitored via current transformer networks mounted on the amplifier junction box, and connected to PC driven Camac based Transient Recorders. Ports for the exit of lamp leads are provided at each end of the housing, and a filtered cooling fan provides air flow along the lamps as in amplifiers. The unit is mounted on a trolley to provide mobility that will allow the lamps to be loaded and removed for storage in the adjacent amplifier assembly clean room. Simply plugging in to one channel of the appropriate source provides pulsed power, and the whole system is Castel Key interlocked for safe remote operation. Data from all tests is saved to disk, and hard copies are provided on completion of each test run.

The lamps are discharged twenty times at energy levels up to full power plus 10% after inspection, and again after installation into amplifier shells without the discs. In the fully assembled amplifier they are discharged ten times at full power.

The lifetime of the lamps is a function of the discharge energy, and the level at which they are nominally run on Vulcan will give a lifetime of at least 10^4 discharges. Each amplifier has eight lamps connected in series coupled pairs, to dissipate a maximum total energy of 200kJ.

The fully enhanced test facility has proved to be a great success. A replica of the on line system using state of the art technology throughout with a high degree of operational safety built in, it has effectively streamlined the whole amplifier construction and test process.

Figure 1. A flashlamp being loaded into the dual flashlamp tester by Andy Frackiewicz.

The Manufacture of Random Phase Plates and Phase Zone Plates

T Boland, D Pepler, T B Winstone, C Danson

Central Laser Facility, CLRC Rutherford Appleton Laboratory, Chilton, Didcot, Oxon, OX11 0QX, UK

Main contact email address: *C.Danson@rl.ac.uk*

Introduction

Vulcan has used Random Phase Plates (RPPs)[1)] and Phase Zone Plates (PZPs)[2)] for a considerable period of time as part of a suite of focal spot smoothing and manipulation techniques. During this period of time the manufacturing processes have altered due to availability issues with some of the original chemicals used. Here we present the current manufacturing process for the masks and the phase plates.

The new manufacturing method uses a visible photoresist to coat a quartz plate and a UV sensitive resist on a glass plate. Figure 1 below shows schematically how a design for either a RPP or PZP is transferred from an acetate template onto a quartz mask, and then from the quartz mask to the resist coated plate.

Mask Generation

The design of the mask is computer generated using the PostScript graphics language. The image of the mask is created on to an acetate sheet using a high resolution Linotronic laser printer that has a resolution of 2540dpi, having a smallest feature of 10 microns. The uncoated quartz plate is cleaned by drag wiping with acetone and the dust removed using a compressed air blower. Approximately 5ml of positive photoresist (Shipley S1813 SP-15)[3)] is applied to the central region of the plate, which is then spun at 1500rpm for 60 seconds. The plate is then placed in a preheated oven (115°C) and baked for 4 minutes.

When the plate has cooled it is ready to be exposed. The plate is placed resist side down onto the printed side of the acetate mask and exposed in a UV light box for 20 seconds as shown in Figure 2.

The plate is developed in Universal developer[3)] for 45 seconds, then rinsed with water for a further 45 seconds and left to dry in a fume cupboard.

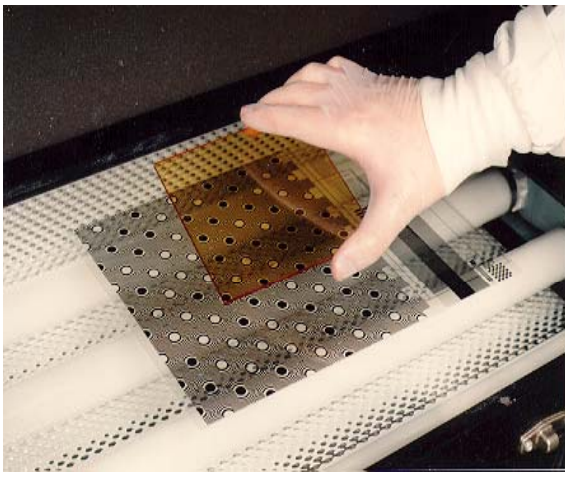

Figure 2. Exposure of optical mask.

Phase Plate Manufacture

The phase plate is made using a glass or quartz substrate and coating it with UV photo-resist. The thin film depositions on phase plates manufactured at RAL are produced using the Microlithographical Chemical Corporation's PMMA A11 positive radiation sensitive resist[3)] and thinned using a standard photo resist thinner.

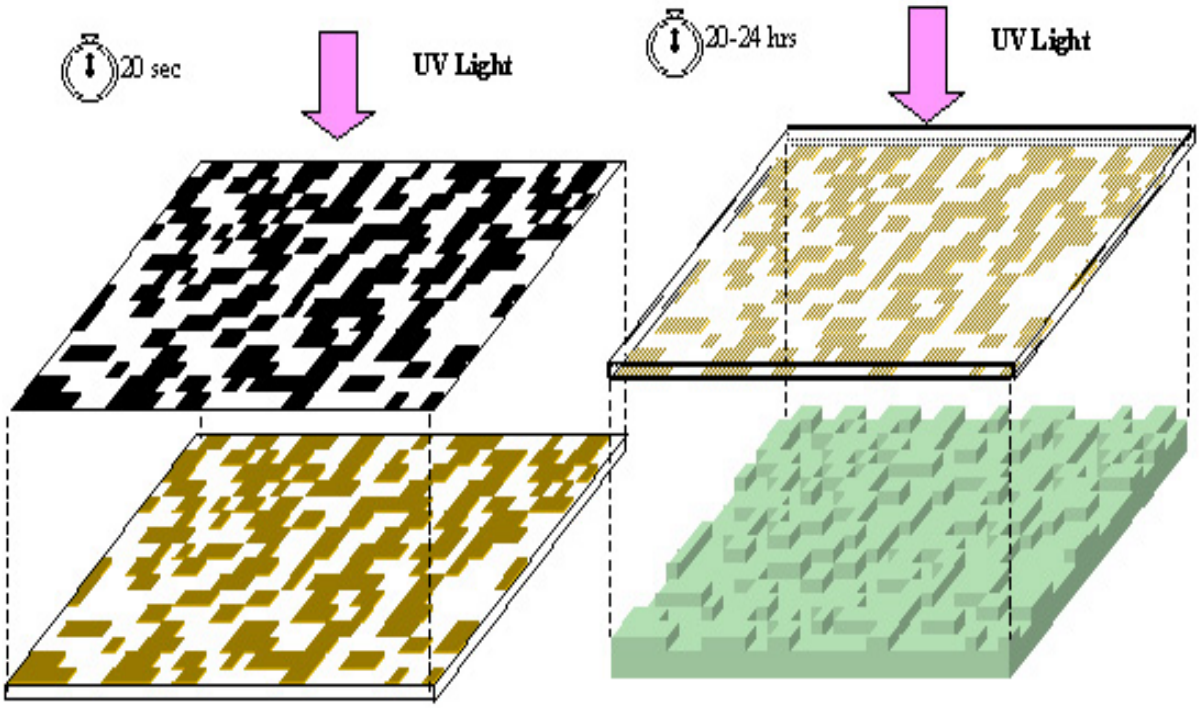

Figure 1. Showing how a pattern is transferred from acetate to quartz mask, then from the quartz mask to the glass plate.

The depth of the resist is of importance as it determines the operating wavelength of the plate. It can be determined by varying the spin speed and the dilution of the resist. The two main concentrations used are 60/40 and 50/50.

A number of test plates were spun using these concentrations at different spin speeds. The resist thicknesses were then measured using an interference microscope. The results are shown in Figure 3.

Generally phase plates used on Vulcan are manufactured for use at the principal and second harmonics (1053nm and 527nm). From the graph it is possible to optimize the spin speed and concentration to produce the required thickness. For instance: 600 rpm at 60/40 concentration for 1053nm, and 900 rpm at 50/50 concentration for 527nm. Intermediate thicknesses, e.g. for a plate to be used at 640nm, can be obtained by varying the concentration of PMMA to Thinner.

The plate is baked for 20 minutes in an oven, preheated to 160°C, then left to cool slowly to prevent the resist cracking.

For exposure the plate is placed resist side up and the mask is placed on top with resist side down so that the coated sides of mask and plate are in contact. The plate is then exposed beneath two mercury UV lamps, (253nm) positioned 10cm above the plates. Exposure time is twenty hours for green (527nm) plates and twenty-two hours for infrared (1053nm) plates.

Once the plate has been exposed it is developed in a mix of 50% Hexone (MIBK) and 50% Isopropyl Alcohol (IPA). The plate is developed for thirty seconds whilst being gently agitated then washed in 100% IPA for the same amount of time.

Discussion

There are several fabrication errors that affect the quality of the phase plate, and hence its operational performance. These lead to a central spike being evident in the far-field. For small errors it is possible to overcome this by placing the target slightly out of the focal plane to achieve a smooth profile.

The three most common errors, why they occur and how we test for them are:

- *The photoresist layer is not the correct thickness*. This occurs if the spin speed or resist concentration is not correct or even if the room temperature is different from that when the tests were carried out.
- *The 0 and π phase areas are not exactly the same.* This can be due to an incorrect mask design or an exposure problem during the manufacture. The mask is fully checked in advance through numerical analysis and the areas compared following manufacture.
- *The phase transitions do not have an exact edge definition*. This is usually due to the mask not being fully in contact with the UV resist and becomes evident when the resist thickness is checked in the interference microscope.

Accurate control of the production process and the use of fresh chemicals for all procedures can minimize these errors.

References

1. Y Kato, K Mima, N Miyanaga, S Arinaga, Y Kitagawa, M Nakatsuka and C Yamanaka, 'Random Phasing of high-power lasers for uniform target acceleration and plasma-instability supression,' Phys Rev Lett. 53, 1057-1060 (1984)
2. RM Stevenson, MJ Norman, TH Bett, DA Pepler, CN Danson and IN Ross, 'Binary Phase zone plate arrays for the generation of uniform focal profiles,' Opt. Lett. 19, 363-365 (1994)
3. Chestech Ltd, 79 Somers Road, Rugby. CV22 7DG.

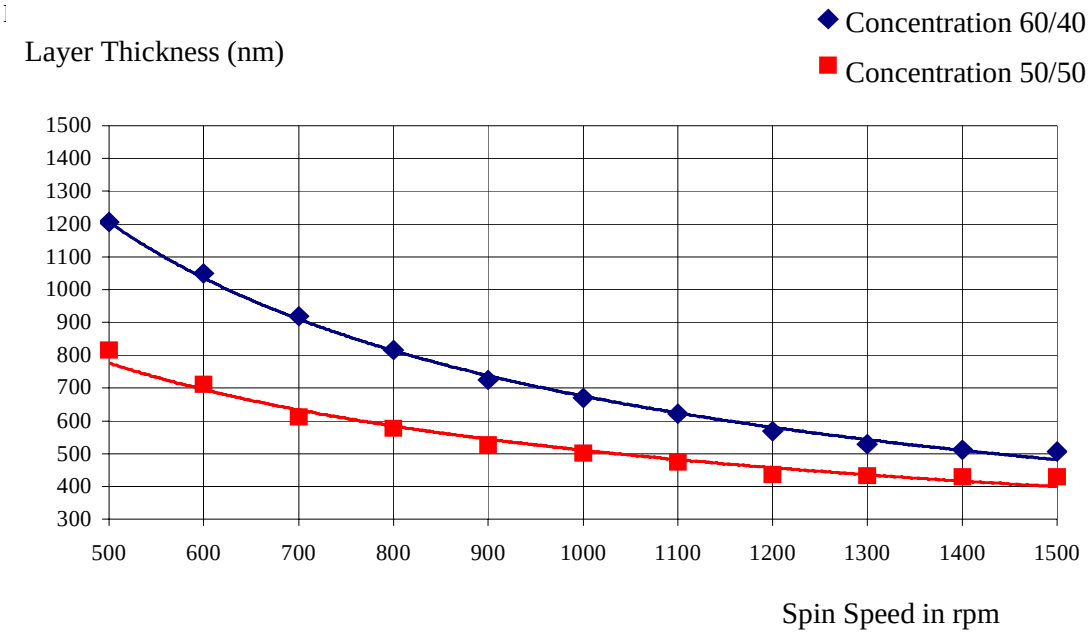

Figure 3. Results of spinning test plates as described above.

The New Target Area Drive System

E Divall, P Holligan

Central Laser Facility, CLRC Rutherford Appleton Laboratory, Chilton, Didcot, Oxon, OX11 0QX, UK

Main contact email address: *E.J.Divall@rl.ac.uk*

Introduction

Since the early laser experiments on Vulcan the target areas have used motorised mounts to position the mirrors, parabolas and targets. For the last 15 years, in its second generation, this has been done using a dedicated PC driving the motors via a custom crate/card system. Last year the Astra TA2 system became increasingly unreliable and was replaced by a new system based on more commercial hardware similar to that used in TAP.

Hardware

The new system is based around a commercial unit, the Parker 6K8. This unit is controllable via Ethernet and has 8 independent motor channels. Each channel has a separate drive box enabling it to drive either a stepper or DC motor. A typical experiment may typically use 1 or 2 stepper motors and 20 or more DC motors. To provide additional DC channels with minimal cost a multiplexing board was designed to switch each DC channel 8 ways. Some of the flexibility is lost through the multiplexing process since only certain combinations are permitted. However, many combinations are not required and this has not posed any problems. It should be noted that due to their complexity stepper channels cannot be multiplexed. In the Astra system, 2 of the 8 channels were designated for stepper drives and the remaining 6 channels were multiplexed. See Figure 1. This allows up to 48 DC motors to be driven and is sufficient for any foreseeable experiment.

Remote pad

A remote pad is currently used to control the drives from within the target area. In the early system this had 6 buttons which enabled forward and reverse motion in the X,Y and Z directions of the selected mount. An improved version which had an LCD display and more buttons had been built, tested and was in use in the Astra target area. These additions enabled the user to view current laser settings and remotely select the mount to be moved. Previously this had involved walking back to the control PC or having a second person. This pad was a useful addition to the system, but the push button menu was seen as too complicated. It was redesigned keeping the basic XYZ movement buttons, but with a much simpler rotating knob for mount selection, a faster update/response time and a larger 4 line display, Figure 1 (inset). The larger display was needed to show Magnascale (positional) readings for all 3 axes simultaneously. (NB. The pad was designed internally and uses a standard RS232 encoding/decoding chip to decode data for the LCD display and send back the button presses. This leads to a powerful pad with a simple RS232 interface. Unfortunately a similar device could not be found commercially.)

Software

The software was rewritten in Visual Basic for the Windows environment. It is a communications intensive program having to communicate with the remote pad and Sony Magnascales position sensor via the RS232 ports and the Parker drive controller via Ethernet. The Astra software also controls the Shot Control PC to request laser shots, move the waveplate attenuator and alter the shot rate. The main software screen is similar to the pad and gives control of the drive motors from the control room. It also shows the current laser settings, i.e. high or low power, attenuator position etc. Positional information from the Magnascale unit is shown on a second monitor via a dual head graphics card manufactured by Matrox. This display is also fed through to the target area. The software also has an internal editor to set which motors are connected to each channel / multiplexer setting. To prevent two or more channels being connected to the same motor an error checking routine highlights any clashes.

Installation

The majority of the hard/software was built/written and tested off-line and was hence in good shape for the switch-over from the old system. The new system had identical wiring on the output plugs which enabled the motors to be switched over and tested in minutes.

The system has now successfully been used for 1 Astra experiment and a software upgrade is planned to prepare it for use in the Petawatt target area of the Vulcan laser.

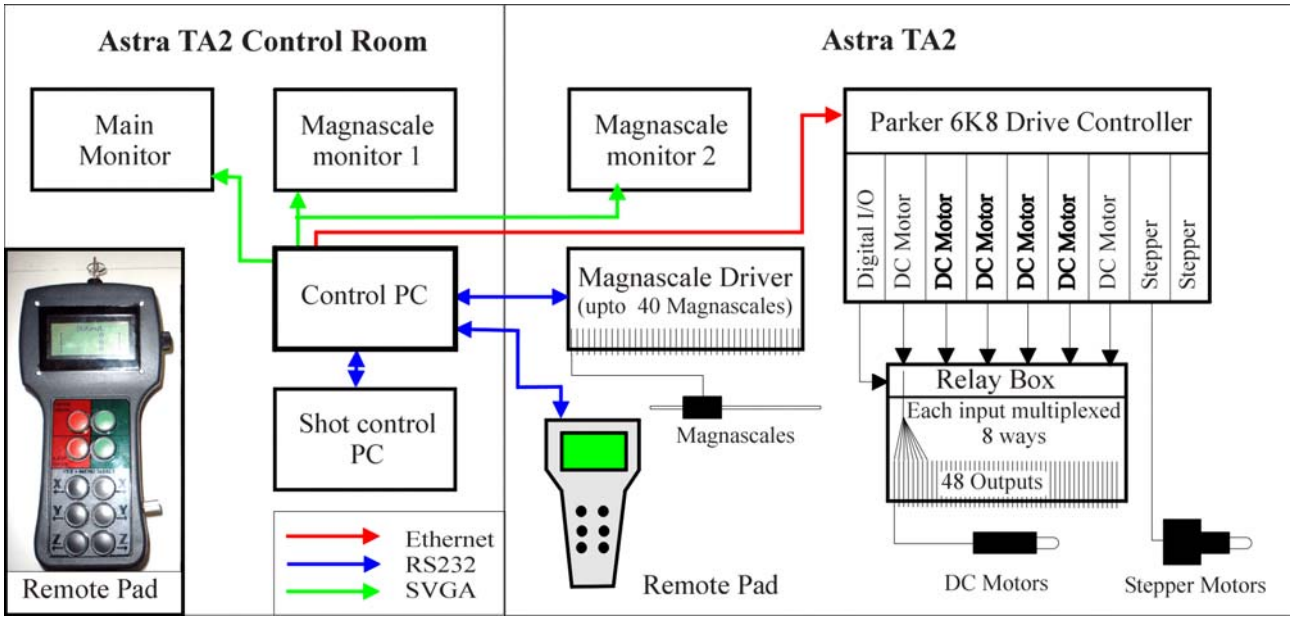

Figure 1. Schematic layout of hardware. Inset, the new remote pad.

Astra laser development

C J Hooker, A J Langley, E J Divall

Central Laser Facility, CLRC Rutherford Appleton Laboratory, Chilton, Didcot, Oxon, OX11 0QX, UK

Main contact email address: *A J Langley@rl.ac.uk*

Introduction

In the year covered by this report Astra has been heavily scheduled, and there has been neither time nor funding for major upgrades. Nevertheless, a number of improvements have been made to the laser, and this article describes these and their impact on its performance.

Prepulse control and monitoring

The configuration of the amplifier chain in Astra is such that several of the pulses in the continuous train from the oscillator are amplified in the first five passes of Amplifier 1. At that point a Pockels cell between crossed polarisers rejects all except the desired single pulse, which then makes another five passes of Amp 1 before proceeding, via a spatial filter and a second Pockels cell, to the second amplifier. As a consequence of leakage through the two Pockels cells, a small prepulse arrives at the target 13 ns before the main pulse. This is unimportant for gas-target experiments, but when solid targets are used it can be a serious problem. With the two Pockels cells as described, the best obtainable prepulse level was around 4 x 10^{-6} of the main pulse, resulting in a prepulse intensity on target of more than 10^{12} W.cm^{-2}, leading to pre-plasma formation on solid targets.

In preparation for a proton-production experiment using foil targets, it was decided to add a second Pockels cell in series with the one in Amp 1, to improve the rejection of unwanted pulses. The opportunity was taken to redesign the mounts of the Pockels cells, to make them occupy far less space on the table and also make them easier to adjust. The two cells are arranged not in a straight line, but offset with a pair of mirrors between them so that the beam can be accurately centred in each cell. A single high voltage pulser is used to drive both cells: as they both have the same quarter-wave voltage and need to be open simultaneously they can be connected in series to one pulser. The optics have been simplified as well: in the original set-up with a single Pockels cell, the output polarisation was 90 degrees from the input, and a periscope was used to rotate it back again. In the arrangement with two cells the input and output polarisations are the same, so the periscope was replaced by a single mirror.

A new prepulse monitor was constructed so the effect of the additional Pockels cell could be measured. The layout of the monitor is shown in Figure 1: it consists of a fast photodiode and a lens of 100 mm focal length, a diffuser, and a red filter to eliminate stray green light from the pump lasers. The diode signal is read out on an oscilloscope. The monitor is positioned near the output of the second amplifier, so the prepulse level into TA1 can be measured. A kinematically mounted drop-in mirror sends the beam into the monitor, so the prepulse can be measured at any time, and the Pockels cell adjusted to minimise it if necessary. When the full beam is present, the prepulse signal can be seen on the oscilloscope at a level of a few tens of millivolts. When the main pulse arrives 13 ns later it causes air breakdown at the focus of the lens, and the plasma scatters the light sufficiently for the diode not to be damaged, although it is heavily saturated. The prepulse level is compared with the main pulse by attenuating the beam with neutral density filters until the attenuated main pulse signal is comparable to the unfiltered prepulse signal. The ratio of the signals multiplied by the attenuation factor of the filters then gives the prepulse level in terms of the main pulse. With the second Pockels cell installed in Amp 1 a typical result is: main pulse 70 mV, prepulse 20 mV, attenuation factor 1.32 x 10^{7}.

Thus the main pulse is 1.32 x 10^{7} x 70/20 = 4.6 x 10^{7} times bigger than the prepulse; that is, the prepulse is 2.2 x 10^{-8} of the main pulse. This is a significant improvement over the performance with a single cell, and it ensured the success of the proton-production experiment described elsewhere in this report. Prepulse measurements were also made at the output of Amp 3, with the surprising result that the level was very similar to that after Amp 2. This is because the relative timing of the pump and the main pulse is such that the prepulse has completed two passes through the Ti:sapphire crystal before the pump beam arrives, so it experiences only two passes worth of gain compared to four passes for the main pulse. A measurement of prepulse after Amp 2 thus gives a good indication of the true level in both target areas.

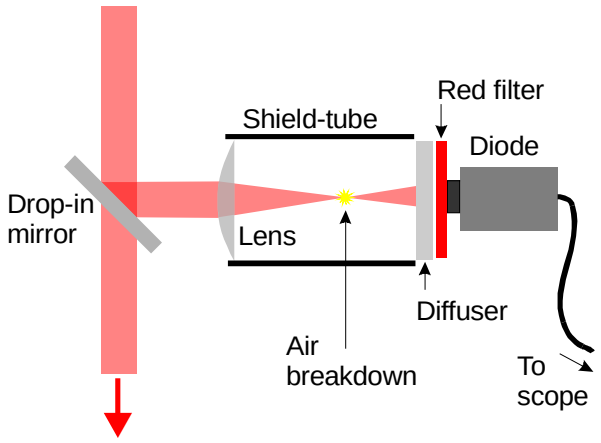

Figure 1. Prepulse monitor.

New Ti:sapphire crystal

The optical quality of the Amp 3 Ti:sapphire crystal is important for the beam uniformity in TA2, and also for the power level at which the amplifier can be operated. Small variations in refractive index occur as growth defects in many TiS crystals, and after the beam has propagated for a metre or more the result is an intensity modulation in the beam profile. As there are four passes through the crystal, it is possible for the modulation to become quite severe, and for the hot spots to cause damage to downstream optics. The crystal that was in use for most of last year gave 2:1 intensity variations across the beam profile, so the overall output energy had to be kept to 800 mJ or less.

A new crystal was obtained at the end of 2001 which had fewer irregularities, and therefore promised to give better output beam profiles. It also had a slightly higher absorption coefficient at the pump wavelength, and thus potentially higher gain. This crystal was installed during a shutdown period. It was operated at a range of pump energies to determine its performance, and output energies up to 1.2 Joules were obtained with just over 4 J of pump energy. Near- and far-field profiles were measured, and are shown in Figures 2 and 3: the uniformity of the near-field is better than before, with a 3:2 variation across the beam, and in consequence the amplifier can be operated at higher output energy. The previous crystal has some damage to its antireflection coatings, due to the higher-intensity regions of the beam; it will be recoated and kept as a spare.

Compressor alignment techniques

During the year, various experiments in TA1 have required pulses of different lengths, and these have generally been obtained by adjusting the length of the compressor. Such adjustments have been made by the experimenters. After instruction by Astra staff; more experienced experimenter groups have occasionally made other adjustments to the compressor to change the quality of the pulse in other ways. Restoring the compressor to optimum performance after these changes was a lengthy process, because of the lack of alignment devices and reference points within the device. This problem was addressed during the year, and a set of alignment devices and techniques developed which now allow the compressor to be completely realigned and optimised in a few hours. The main additions were (a) additional apertures which allow accurate setting of the beam direction into the compressor, (b) a sliding mirror which retro-reflects either the incident beam or the beam that has been reflected from both gratings, and (c) a far-field monitor that can view the retro-reflected beam in either the input or output path. An alignment procedure was developed which first establishes the geometrically correct orientations of the gratings, ensuring they are parallel to one another and that the groove directions are also parallel. The grating spacing is then set approximately by maximising the intensity of second harmonic light generated by a KDP crystal in the output beam. By observing the focal spot of the output beam with the far-field monitor, residual dispersion can be corrected by adjusting the angle of the second grating and the rear mirror until the spot is not elongated in either direction. The final stage is to optimise the compression by changing the angle of incidence on the gratings to minimise the third-order dispersion. This is done by 'walking' the gratings, using the far-field monitor to keep their relative positions correct, and minimising the width of the compressed pulse observed with an autocorrelator. Using the new technique, compressed pulses with 34 fs duration were obtained in TA1. With some experience, the entire procedure can be completed in half a day.

A similar set of alignment devices and a corresponding technique were developed for use in TA2. There are a few differences due to the 60 mm beam size: in particular the slide for the movable mirror obstructs part of the beam, so it cannot be left in place permanently, but the procedure is essentially the same. The shortest pulses obtained in TA2 so far have been around 60 fs, which is disappointingly long, and further investigation will be carried out into the reasons why shorter pulses are not achieved.

Option to increase the energy in TA2

The pulse energy in TA2 is controlled in two ways: firstly by an attenuator consisting of two uncoated mirrors which transmits 1% of the light, and secondly by means of a half-wave plate and a pair of polarising mirrors, which provides a 200:1 range of transmission. The polarisers are coated on both sides, and although the coatings transmit 92% of the vertical polarisation, the overall transmission is only about 70%. This loss can be avoided by removing the polarisers, but if this is done the length of the compressor needs to be adjusted, as the 51 mm optical path in the material introduces significant dispersion. Adjusting the compressor is a lengthy operation, so as an alternative, a 51 mm thick plane-parallel block of BK-7 glass with anti-reflection coatings was obtained, which can be placed in the beam in place of the polarisers. The block has the same dispersion as the polarisers, but minimal losses, so the energy can be increased without the need to adjust the compressor. In a test, replacing the polarisers with the glass block yielded 30% more energy in the target chamber, as expected.

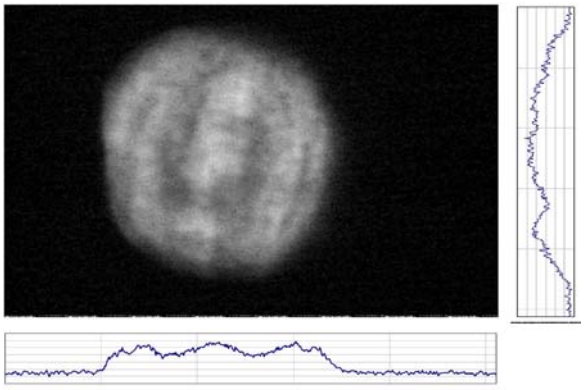

Figure 2. Near-field profile of output beam after the third amplifier and before compression. Amplified pulse energy was 1.2 J.

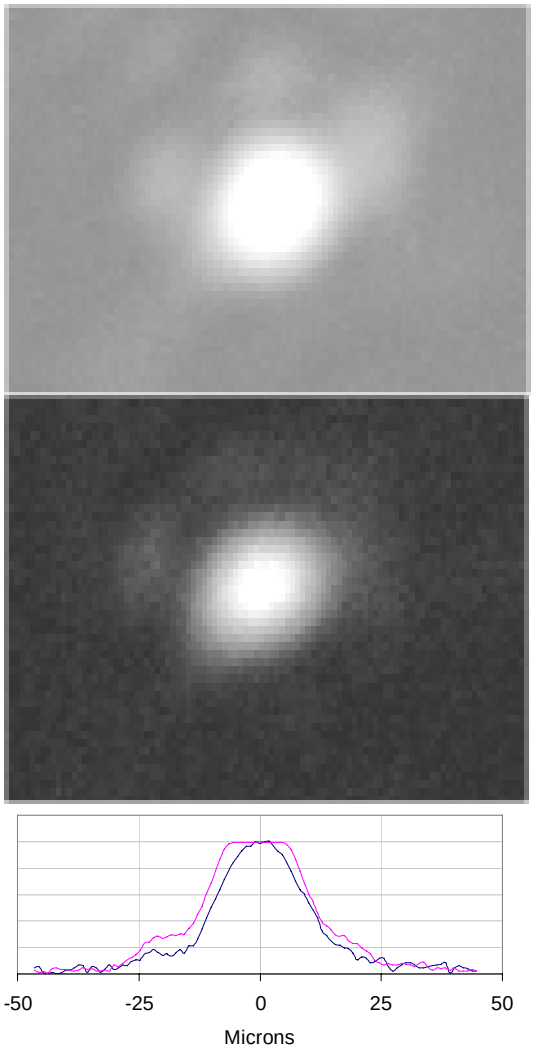

Figure 3. Far-field images of the compressor output beam. The cross-sectional intensity profiles (bottom) of the saturated far-field image (top) and unsaturated far-field image (middle) are shown as the purple and blue traces respectively.

The dependence of the specular reflectivity of plasma mirrors on laser intensity, pulse duration and angle of incidence

C Ziener, P S Foster, E J Divall, C J Hooker, M H R Hutchinson, A J Langley, D Neely

Central Laser Facility, CLRC Rutherford Appleton Laboratory, Chilton, Didcot, Oxon, OX11 0QX, UK

Main contact email address: *c.ziener@rl.ac.uk*

Introduction

Superintense lasers today approach peak intensities greater than 10^{21} W/cm^2. The intensity 1ns to 10 ps before the peak of the pulse is usually in the order of 10^{-8} to 10^{-6} times the main pulse intensity, due to either amplified spontaneous emission (ASE) from the various laser amplifiers or non ideal recompression of the pulse in chirped pulse amplification laser systems. An intensity of 10^{13} W/cm^2 creates a plasma on all known target materials. This in turn means that the main laser pulse interacts not with the solid target but with a preformed plasma. It was shown recently [1], that even nonionizing prepulses with intensities as low as 10^8 W/cm^2 can change the laser matter interaction considerably.

It is very hard to achieve an intensity contrast ratio better than 10^{-10} directly in the laser amplifier. One possible technique to "clean" the laser pulse after the amplification is the use of plasma mirrors [2]. If the laser intensity on a transparent material is chosen so that only the leading edge of the main ultrashort pulse is above the threshold for plasma production, prepulses or a pedestal with a lower intensity will be transmitted. The created plasma does not have sufficient time to expand during the rise time of the laser pulse. The main laser pulse therefore interacts with an overdense plasma with a very steep density gradient. These so called "plasma mirrors" can have very high reflectivity. The interaction of the laser pulse with the plasma mirror depends on a large number of parameters, e.g. angle of incidence, pulse duration, temporal pulse shape, and intensity on target.

Although there have been some experiments using dielectric materials as plasma mirrors [2,3], no systematic investigation concerning the specular reflectivity as a function of pulse duration and angle of incidence has been published to our knowledge. Since this is important for the design of almost every experiment involving plasma mirrors, we carried out an experiment measuring the specular reflectivity as function of intensity for two different laser pulse durations and three different angles of incidence.

Experimental setup

The experiments were carried out at the Astra laser facility of the CLF. By adjusting the length of the compressor, the pulse duration was changed to 90 fs and 500 fs respectively. The pulse shape was diagnosed with a scanning third-order autocorrelator. In the case of the shorter pulse, the intensity 1ps before the peak of the laser pulse was 10^{-5} times the peak intensity. No distinct pre-pulses have been found within 50ps before the laser pulse with a contrast ratio $>10^{-5}$. The contrast ratio of the pre-pulse 4 ns before the main pulse was measured with a photo diode to be 4 x10^{-8}.

To avoid averaging over a large angle of incidence, the 60mm diameter laser beam was focused by an off-axis parabolic mirror with a focal length of 1016 mm. This resulted in an F-number of 17, giving a cone of less than 3.5º opening angle.

The focal spot was 20 µm x 26 µm, thus the maximum intensity on target was 4 x 10^{17} W/cm^2. To vary the intensity on target either the target was moved out of focus to increase the area and decrease the intensity or the energy of the laser was adjusted by rotating a half wave plate, which is mounted between two polarisers. For each shot, the energy of the leak pulse of a high reflective mirror was measured with a calibrated photo diode to account for pulse-to-pulse fluctuations. The reflected energy was measured with an energy-meter. To avoid damage of the calorimeter, a calibrated neutral density (ND) filter was placed in front of it. The transmission of the ND filter was carefully checked to be constant over the whole energy range investigated.

A polished fused silica substrate mounted on an xyz-stage was used as target. It was moved after each shot to ensure that a fresh surface was hit by the next shot.

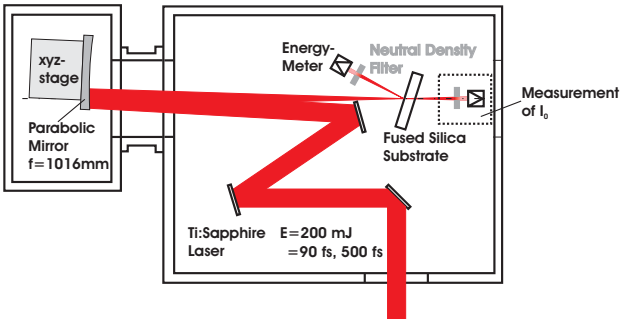

Figure 1. Experimental setup.

Results

In the figures, each data point represents a single laser shot. No averaging has been done. The specular reflectivity of the fused silica substrate as a function of intensity is shown in Figure 2. The pulse duration was 90 fs and the angle of incidence 6.5º.

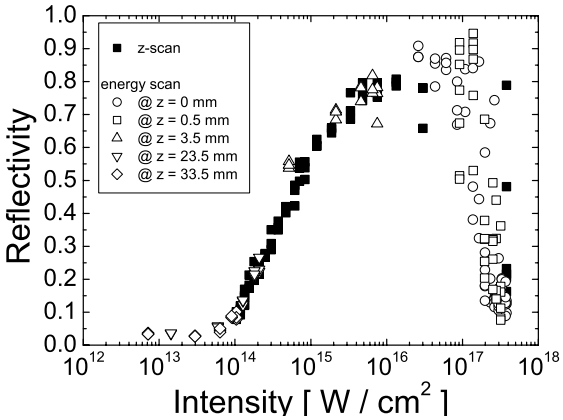

Figure 2. Specular reflectivity for a pulse duration of 90 fs and an angle of incidence of 6.5º . The intensity was varied by moving the target out of focus (full squares) and by decreasing the laser energy at different target positions (open symbols).

At intensities below 10^{14} W/cm^2 we measured a specular reflectivity of a few percent, which is the expected value for an uncoated fused silica substrate. Above a threshold intensity of 10^{14} W/cm^2 the specular reflectivity rises up to 80% at an intensity of about 3 x 10^{15} W/cm^2. It stays at this level and decreases for intensities above 3 x 10^{16} W/cm^2 very rapidly. The threshold intensity of 10^{14} W/cm^2 agrees very well with the damage threshold measurements of Kautek [4]. The rapid fall in specular reflectivity could be due to non specular reflection, scattering, or increased absorption. Since the size of the calorimeter was only slightly larger than the diameter of the beam and there was no additional measurement of transmission and non specular reflection, it is not possible to determine the reason for the

decrease in specular reflectivity. As can be seen, the specular reflectivity for intensities below 10^{16} W/cm^2 is independent of the way the intensity was reduced (increasing the beam diameter or decreasing the laser energy). That means, that the specular reflectivity is independent from the spot diameter for diameters bigger than 400 μm.

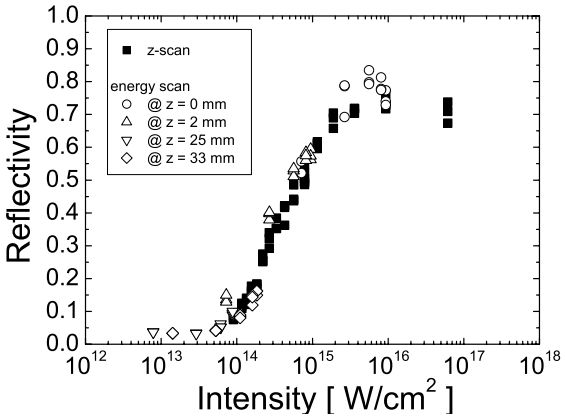

Figure 3. Specular reflectivity for a pulse duration of 90 fs and an angle of incidence of 18º.

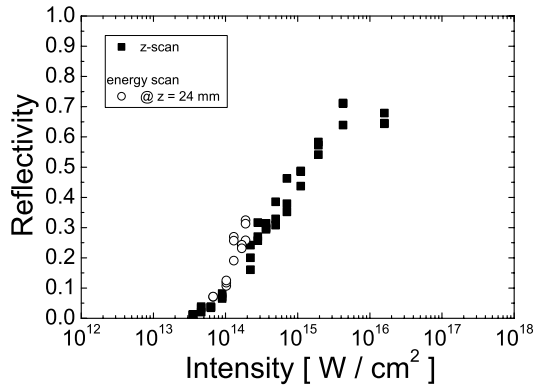

Figure 4. Specular reflectivity for a pulse duration of 90 fs and an angle of incidence of 45º.

The measurements with a pulse duration of 90 fs and an angle of incidence of 18º (Figure 3) and 45º (Figure 4) show the same behavior. The threshold where the specular reflectivity starts to increase is again at approximately 10^{14} W/cm^2. The intensity where the maximum of the specular reflectivity is reached is also about the same as for 6.5º. The maximum specular reflectivity measured for 18º was 75% and for 45º it was 65%. Smaller reflectivities for larger angles of incidence have been seen in previous measurements for various target materials. Mostly this behavior is due to an increased absorption (e.g. resonance absorption, vacuum heating) at higher intensities.

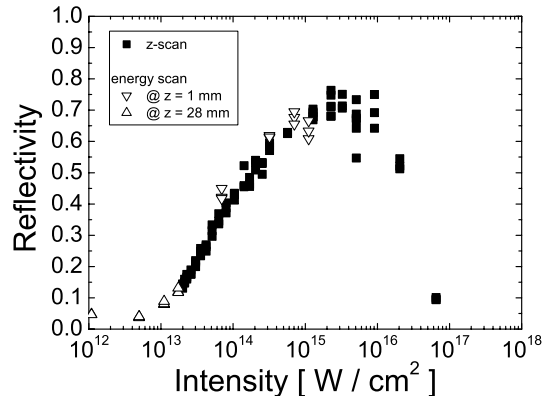

Figure 5. Specular reflectivity for a pulse duration of 500fs and an angle of incidence of 6º.

We also carried out measurements with a laser pulse duration of 500 fs. The results for an angle of incidence of 6º are shown in Figure 5, and the results for 19º in Figure 6 respectively. The specular reflectivity starts to increase at an intensity of about 10^{13} /cm^2. This is in very good agreement with the damage threshold measurements [4]. In this paper the damage threshold for 500 fs is about a factor of 8 smaller than in the case of 90 fs.

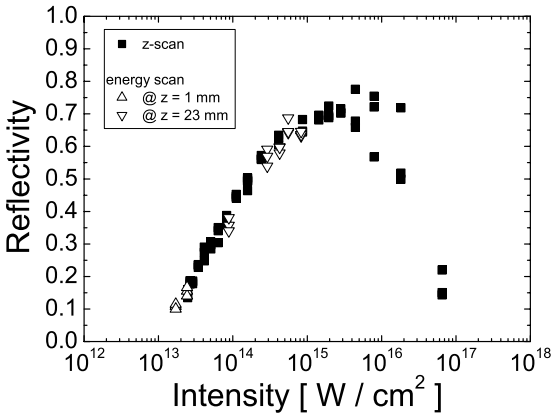

Figure 6. Specular reflectivity for a pulse duration of 500 fs and an angle of incidence of 19º.

The maximum specular reflectivity measured was 70% for both angles of incidence. For intensities larger than a few times 10^{16} W/cm^2 the same very rapid drop-off in specular reflectivity as for the 90 fs pulses was measured.

Discussion

To summarise our results, we have measured the specular reflectivity of a plasma mirror for 800 nm laser pulses for a large number of parameters. Pulses with durations of 90 fs and 500 fs were focused with an F/17 off-axis parabolic mirror onto a polished fused silica target. The specular reflectivity was measured for angles of incidence from 6º to 45º and for intensities from 10^{12} W/cm^2 to 4 x 10^{17} W/cm^2. In all cases the specular reflectivity increases if the intensity rises above a certain threshold intensity. This threshold intensity is about 10^{14} W/cm^2 for a pulse duration of 90 fs and 10^{13} W/cm^2 for 500 fs pulses. This difference is in very good agreement with former measurements of damage thresholds for fused silica. The maximum specular reflectivity measured was between 65% and 80%. For intensities above 5 x 10^{16} W/cm^2 the specular reflectivity dropped very rapidly to low values. This behavior can be explained with the increase in non-specular reflection and/or the increase in absorption.

The measurements clearly show that for the application of plasma mirrors the intensity necessary for a high reflectivity has to be within one order of magnitude.

References

1. K.B. Wharton, C.D. Boley, A.M. Komashko, A.M. Rubenchik, J. Zweiback, J. Crane, G. Hays, T.E. Cowan, and T. Ditmire; Phys Rev E, 64 (2): art. no. 025401 (2001)
2. H.C. Kapteyn, M.M. Murnane, A. Szoke, R.W. Falcone; Opt. Lett. 16, 490 (1991)
3. S. Backus, H.C. Kapteyn, M.M. Murnane, D.M. Gold, H. Nathel, and W. White; Opt. Lett. 18, 134 (1993)
4. W. Kautek, J. Krüger, M. Lenzner, S. Sartania, Ch. Spielmann, and F. Krausz; Appl. Phys. Lett. 69, 3146 (1996)

Time-of-Flight corroboration of “conventional” ultra high intensity measurement

C Ziener, P S Foster, E J Divall, C J Hooker, A J Langley, D Neely

Central Laser Facility, CLRC Rutherford Appleton Laboratory, Chilton, Didcot, Oxon, OX11 0QX, UK

Main contact email address: *c.ziener@rl.ac.uk*

Introduction

Measuring the intensity in the focal spot of a high intensity laser is a very demanding task. The conventional approach is to measure the energy distribution in the focal spot with the laser beam heavily attenuated. Then, the laser energy on target and pulse duration are measured. By combining these numbers, it is possible to calculate an average intensity. However, this “conventional” method has certain disadvantages. It is not possible to make all three measurements simultaneously at the focal plane. This results at least in an increased uncertainty of the intensity. Furthermore, the pulse duration is always measured in the near field of the laser beam. With laser beam diameters approaching 1 m it is very difficult to avoid pulse front distortions. These are not straightforward to measure with e.g. an autocorrelator and will result in lengthening the laser pulse in the focal volume, thus decreasing the intensity.

The mentioned difficulties are the reason for our attempt to measure the intensity in a more direct way.

Field ionisation of atoms and ions

At very high laser intensities, ionisation occurs either via multi-photon or via field (tunneling) ionisation. The so-called Keldysh parameter[1)]

$$\gamma = \sqrt{\frac{E_i}{2E_p}}$$

describes which mechanism is dominant. Here, E_I is the ionisation potential of the atom or ion and E_p is the ponderomotive or quiver energy of an electron in a laser field of field strength E_0

$$E_p = \frac{e^2 E_0^2}{4 m_e \omega^2}.$$

The ionisation potentials for different stages for various rare gases are shown in Figure 1.

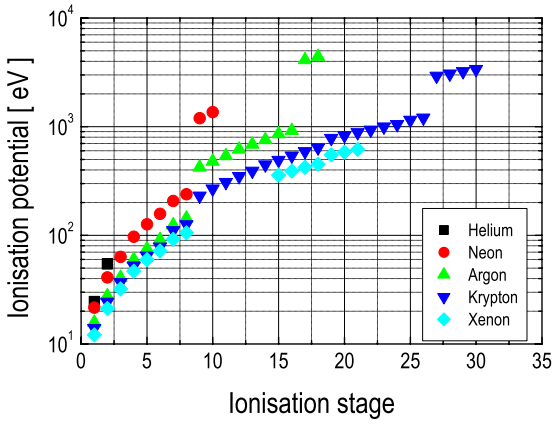

Figure 1. Ionisation potentials for rare gases.

Ammossov et al.[2)] calculated the ionisation rate for the field ionisation for complex atoms and ions:-

$$w = w_A \left((2\pi n^*)^{-1/2} \left(\frac{2e}{n^*} \right)^{n^*} \right)^{1/2} E_i \frac{(2l+1)(l+|m|)^{n^*}}{2^{|m|}(|m|)!(l-|m|)!} \times \left(\frac{2(2E_i)^{3/2}}{E_0} \right)^{2n^*-|m|-1} \left(\frac{3E_0}{\pi (2E_i)^{3/2}} \right)^{1/2} \exp\left[-\frac{2(2E_i)^{3/2}}{3E_0} \right]$$

with w_A the atomic unit of frequency, E_0 laser field strength, E_i the binding energy of the start state in atomic units, and n* the effective main quantum number

$$n^* = \frac{Z}{\sqrt{2E_i}}.$$

Using a simple barrier suppression model[3)], the saturation intensity, i.e. the intensity where the probability of ionisation is 1 is :-

$$I_{BSI} = 4.00 \times 10^9 \left(\frac{(E_i(eV))^4}{Z^2} \right) W/cm^2$$

Figure 2 shows the saturation intensities for rare gases. It can be seen that by carefully choosing the gas, almost the complete intensity range could be measured.

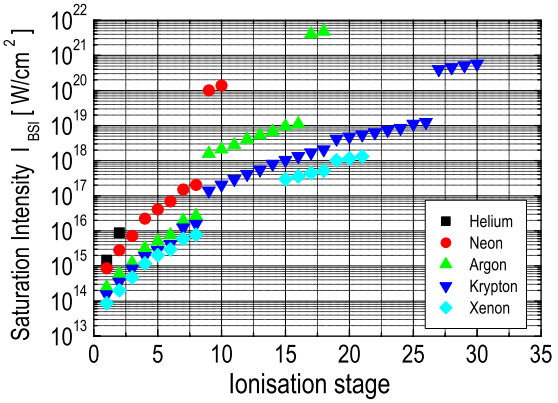

Figure 2. Saturation intensity calculated according to the barrier suppression model for rare gases.

A computer program was written to calculate the ion yield using the ADK formula. It solves the rate equations for the population density of the ground state (neutral atom) and the excited states (ionisation stages)[4)]. To account for the temporal and spatial intensity distribution of the laser pulse, the simulation has to be made in two steps. First, the rate equations are solved for laser pulses with different peak intensities. This emulates the ion production for different peak intensities within the spatial distribution of the focal spot. To get the ion numbers produced in the total focal volume, the ion numbers for the different intensities are integrated with spatial distribution weighting. Input parameters for the program are the peak intensity, the temporal shape of the pulse (Gauss or sech^2, FWHM) and the focal spot size as measured optically (FWHM).

Experimental setup

The experiments were carried out in Target Area 2 of the Astra laser system. Three flat Gold coated mirrors were used to steer the laser beam onto a Gold coated parabolic mirror. The latter has an effective focal length of 151.3 mm, a diameter of 75 mm and an off-axis distance of 55 mm resulting (for a 60 mm beam) in an F-number of approximately 2.5.

The ToF apparatus itself was a three-plate set-up of the Wiley-McLaren type[4]. An electron multiplier was used as the detector and the signal was stored by means of a fast digital oscilloscope. The position of the ToF plates as well as the position of the parabolic mirror could be adjusted by remote control with the vacuum chamber evacuated.

The target chamber was pumped down to a pressure less than $1x10^{-6}$ mbar by a combination of turbo pumps and a cold finger filled with liquid Nitrogen. It was then back filled with Argon to pressures in the range 3 to 6 x 10^{-6} mbar. A fine-control valve was used to regulate the flow of gas into the chamber. The feedline to this valve was pumped prior to use, to ensure a high purity of target gas at the interaction region. A field of strength 1.25 kVcm^{-1} was established across this region to extract the argon ions produced within the ionisation region of the laser focus towards the detector. This resulted in a temporal separation of the ions according to their mass-to-charge ratio (*m*/*z*) along the 100 cm flight-path. Each ionisation state detected was represented by a peak on a ToF spectrum recorded on a digital storage oscilloscope.

Determination of the intensity by means of measuring focal spot size, pulse length and energy in the focal spot

Using a second order autocorrelator, the pulse length was measured to be 60 fs.

At first the throughput of the compressor was measured. The energy in front of the entrance window of the compressor was 570 mJ, the energy right after the compressor was 225 mJ, thus giving a throughput of 40%.

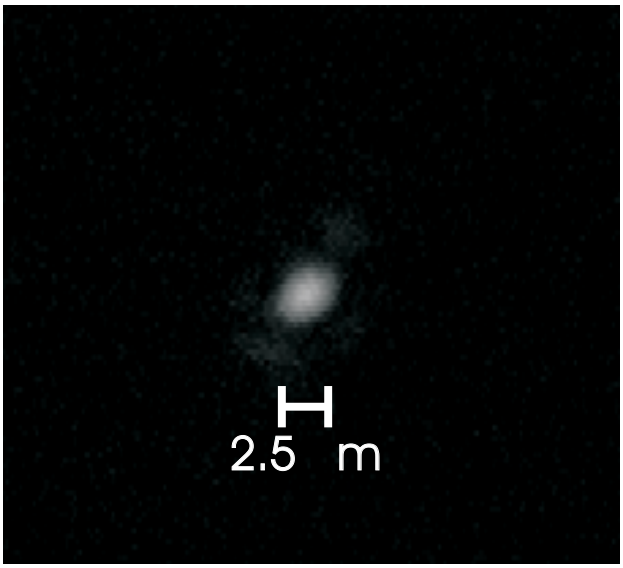

Figure 3. Focal spot imaged onto a CCD camera.

The size of the focal spot was measured by imaging the heavily attenuated low power beam with a microscope objective onto a CCD camera as shown in Figure 3. We then measured the spot size for different z-positions, to look for astigmatism. The result of the z-scan is shown in Figure 4. It can be seen that there is still a slight astigmatism, although it is not clear if it originates directly from the laser or from misalignment of the parabolic mirror. The spot size however is very small (about 2.5 μm), which is almost diffraction limited. About 40% of the energy is contained within the FWHM of the focal spot.

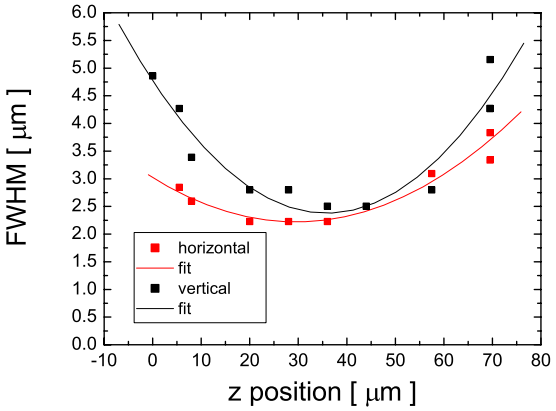

Figure 4. Focal spot size as a function of the longitudinal position.

Combining the three measurements (energy, intensity distribution, and pulse length) resulted in an optically measured peak intensity of 3.0 x 10^{19} W/cm^2.

Determination of the intensity by means of measuring the ion production of the focused laser beam with a ToF spectrometer

A typical time-of-flight spectrum for Argon is shown in Figure 5. The Ar pressure was $5.5x10^{-6}$ mbar. The optically measured laser intensity was $4.0x10^{17}$ W/cm^2. Clearly, Argon ionisation stages up to 8+ can be seen.

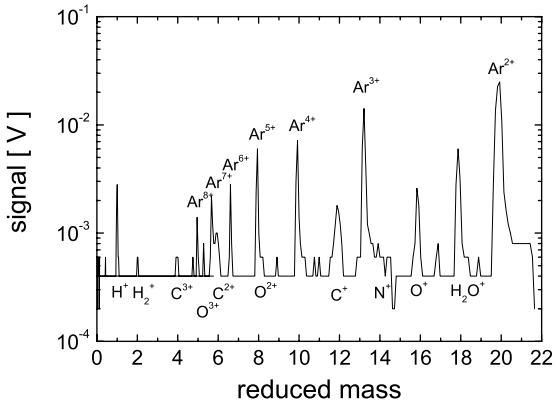

Figure 5. Typical time-of-flight spectrum for Argon. The peaks for ionisation stages up to Ar^{8+} and the main peaks for the background impurities are indicated.

For higher intensities (>$1.0x10^{18}$ W/cm^2), the peaks for the higher ionisation stages disappeared and only the lowest ionisation stages of Argon together with the background peaks could be measured. This unexpected behavior is probably the result of shielding effects. For high intensities, a great number of low charged ions are produced in the vicinity of the focal spot. If the ion density is high enough, the ions shield the focal region from the extraction field of the time-of-flight spectrometer. Thus for measuring ultra-high intensities it is necessary to go to ultra-high vacuum chambers (background pressure <10^{-9} mbar).

Since the lowest background pressure in our experiment was $7.0x10^{-7}$ mbar, it was not possible to measure the intensity at high power directly. We measured therefore the intensity in the low power operational mode of the Astra laser. The attenuation is achieved by inserting two AR coated mirrors instead of two HR coated mirrors. This takes place after the last transmissive optics. The influence of reflective optics including the compressor gratings is independent from the laser energy or intensity. It is

therefore possible to extrapolate the intensity measurements at low power to full power by simply measuring the ratio of the energy delivered to target in both operational modes.

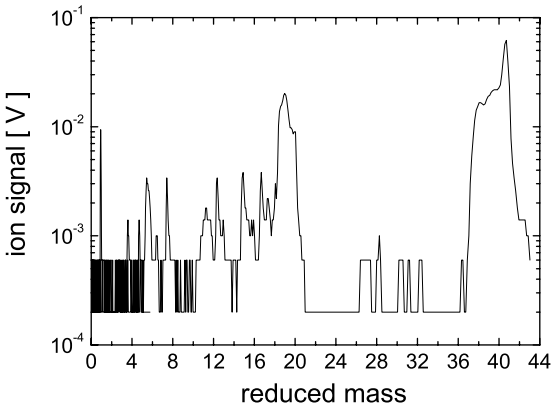

Figure 6. Time-of-flight spectrum for Argon for a laser intensity of 3.8×10^{18} W/cm^2.

The ion yield was measured by recording the time-of-flight spectra at a certain intensity and averaging over 10 laser shots. The area under the peaks for each ionisation stage were then integrated to get the total yield. Figure 7 shows the ion yield for an Argon pressure of 6×10^{-6} mbar.

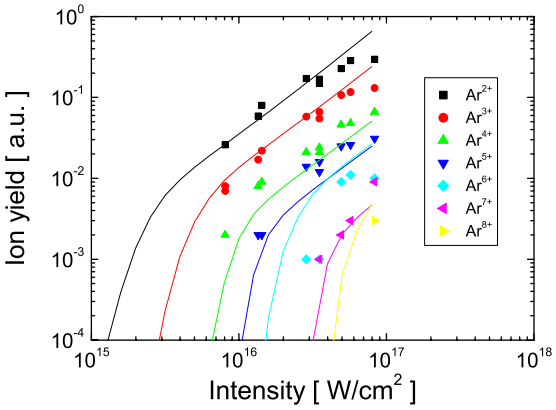

Figure 7. Ion yield as function of the peak intensity for Argon at a pressure of 6×10^{-6} mbar (symbols). Also shown are the ion yields as calculated with the simulation program (solid lines).

Also shown are the ion yields calculated with the simulation program mentioned above. The input parameter were $FWHM_{time}$ = 60 fs, pulse shape sech^2, focal spot size $FWHM_{spatial}$=2.5 µm. The calculated ion yields for the different ionisation stages were all multiplied by the same number to get the best fit with the simulated curves. The intensities of the measured data had to be scaled up by a factor of 1.5 also to provide the best fit as can be seen in Figure 7.

Discussion

Since measuring the intensity in the focal spot of an ultra-high intensity laser is an extremely difficult task, we made time-of-flight measurements to corroborate our "conventional" intensity measurement. We compared the intensity as calculated using "conventionally" measured pulse parameters to an intensity scale determined by fitting experimentally measured ion yields to an atomic ionisation model. The values are found to be in good agreement to within a factor of 1.5. Because of difficulties which stem from shielding effects within the ToF apparatus at very high intensities, the ToF spectra were recorded at an attenuated energy and hence the calibration was carried out at intensities up to 10^{17} W/cm^2. Since the attenuation occurred after the last transmissive optic in the laser system, no additional distortion of the pulse is expected as the pulse energy is scaled up to the maximum energy used. We can therefore justify scaling up the focused intensity. The full power intensity of the Astra laser system in this experiment was $(3.0 \pm 1.8) \times 10^{19}$ W/cm^2 on target.

References

1. L.V. Keldysh, JETP 20, 1307 (1965)

2. M.V. Ammossov, N.B. Delone, and V.P. Krainov, Sov. Phys. JETP 64, 1191 (1986)

3. H. Bethe and E. Salpeter; Quantum Mechanics of One-And Two-Electron Atoms, New York: Plenum, 1977

4. F. Dammasch, PhD Thesis, Berlin 2001

5. W. C. Wiley and I. H. McLaren, Rev. Sci. Inst. 26, 1150 (1955)

Fluorescence Suppression in Resonance Raman Spectroscopy using Combined Kerr Gated and SERDS Technique and Automated Spectrum Reconstruction

P Matousek, M Towrie, A W Parker

Central Laser Facility, CLRC Rutherford Appleton Laboratory, Chilton, Didcot, Oxon, OX11 0QX, UK

Main contact email address: *P.Matousek@rl.ac.uk*

Introduction

Resonance Raman spectra obtained using a probe beam wavelength matched to an electronic absorption band have exceptional sensitivity and selectivity that is particularly useful when studying complex samples as those found in biology. Unfortunately, fluorescence is often intense and limits observations to only strong Raman bands. In many cases, the probe beam may also induce fluorescence in contaminants or the solvent - and in biological or industrial cases particularly, the concentration of the molecule under study may be low.

Recently we have developed an efficient rejection device based on a 4 ps optical Kerr shutter[1,2], separating Raman light from fluorescence in the time domain. The fluorescence suppression ratio achievable by the technique depends on the fluorescence lifetime and can be up to ~10^5 for long lived fluorescence species (> 1 μs) and ~10^2 - 10^4 for lifetimes in the range of ~ 1 - 100 ns.

For the measurement of the most emissive samples we have advanced the Kerr gating method[3] by combining it with the conventional shifted excitation Raman difference spectroscopy[4,5] (SERDS). The SERDS technique relies on obtaining two Raman spectra using two slightly different probe wavelengths separated by an amount comparable with the bandwidth of the measured Raman bands (typically 10-20 cm^{-1}). The subtraction of the two spectra, S'_{λ} and $S'_{\lambda-\delta}$, from each other produces a difference spectrum, $D = S'_{\lambda} - S'_{\lambda-\delta}$, from which the Raman signal can be reconstructed. This technique has been shown to be able to reach the photon shot levels which otherwise are very difficult to attain with intense fluorescence backgrounds[4].

Experimental

The basic principle of the optical Kerr gate has been described in our earlier publications[1,2]. The Kerr gate setup consists of a 2 mm long cell filled with CS_2 and two 41x41 mm Glan Taylor polarisers. The Kerr gate is followed by a spectrometer (Triplemate). A home built filter stage by-pass option was used for better transmission. The probe laser line was blocked from entering the spectrometer using a glass edge absorbing filter. A concentrated solution of copper sulphate in water in a 1 cm thick optical cell was placed in front of the spectrometer to block the residual 800 nm gating beam. The spectrometer grating density was 600 lines per mm.

Raman scattered light was collected at 90° to the probe beam direction. A liquid nitrogen cooled, back illuminated CCD camera with an array 2000 x 800 pixels (Jobin Yvon Ltd) was used to record Raman spectra. The CCD was binned vertically across 400 pixels and horizontally across 5 pixels. One count corresponds to one photoelectron. The sample solution was re-circulated in an open liquid jet of 0.5 mm diameter.

The Raman spectra were collected by alternating every 10 s between the two shifted probe wavelengths. The probe wavelength and pulse duration were ~532 nm and 1 ps, respectively. The pulse energy was 5 μJ and repetition rate 1 kHz. The beam was focused to ~200 μm in the sample.

The versatile optical parametric generator/amplifier (OPG/OPA) technology adopted in our system[3] allowed us to generate the two excitation wavelengths in a very simple way. The OPG generated a broadband seed beam which was spectrally dispersed using a grating and the selected wavelength steered into the OPA stage using an optogalvanic mirror. The moving galvanometer mirror permits automatic alternation between the two spectrally shifted probe wavelengths, each cycle being synchronised with the CCD readout. The spectral shift δ was set to 28 cm^{-1}, which is well within the OPA acceptance bandwidth and no other adjustment to the OPG/OPA system was needed. The setup suffered from a slight pointing change but this would be eliminated if the optical path was reconfigured to enable the grating itself to be rotated between the two positions or by re-imaging the grating plane onto the optogalvanic mirror.

Results

To test the performance of the combined Kerr gated and SERDS approach we have chosen the laser dye rhodamine 6G (Rh6G), one of the most difficult samples a Raman spectroscopist can expect to be confronted with. The sample was prepared at concentration 1x10^{-3} mol.dm^{-3} in methanol and the probe was tuned to 532 nm providing an efficient means of fluorescence excitation. Under these conditions the Raman spectrum was measured under the maximum fluorescence emission of Rh6G. The fluorescence lifetime in methanol at this concentration is ~4 ns[7,8]. The fluorescence background without applying any rejection method was measured to be up to 20,000,000 counts/s (see Figure 1). First, each of the suppression techniques was used on their own demonstrating

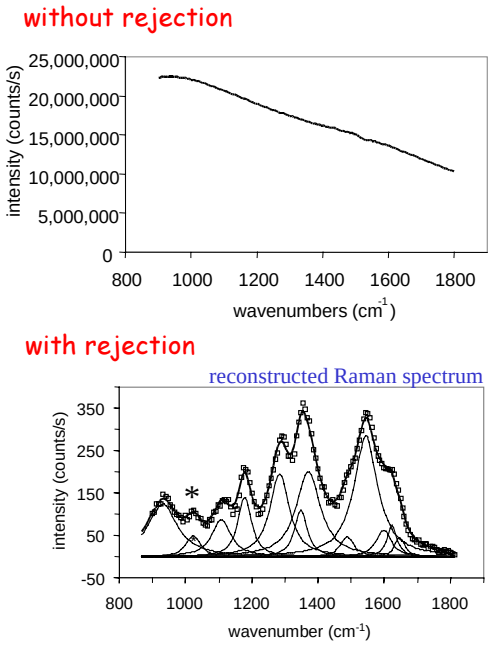

Figure 1. The resonance Raman spectrum of Rh6G in methanol without and with the combined Kerr gate & SERDS method with 532 nm excitation wavelength under the maximum of fluorescence emission. The bottom figure shows both the experimental data (o) and fit (solid line). The overall accumulation time was 800 s. The asterisk designates a methanol peak. The spectra were reconstructed using the fitting Method 1.

that if used individually they could not recover the Raman signal under these extreme conditions.

On the other hand, the combined Kerr gate and SERDS approach enabled us to observe clean resonance Raman signal of Rh6G (see Figure 1) with an S/N ratio of 1:0.1 to 1:1. This S/N level matches the calculated photon shot noise limit estimated from the remaining fluorescence after the Kerr gate and represents an improvement by more than a factor of 10 in S/N on what each technique could provide individually.

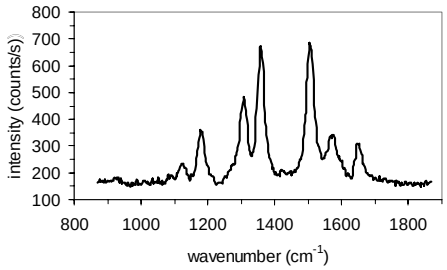

Figure 2. Pre-resonance Raman spectrum of Rh6G in methanol ($1x10^{-3}$ $mol.dm^{-3}$) obtained with Kerr gate approach only at an excitation wavelength of 595 nm on a tail of fluorescence emission. The accumulation time was 200 s. The solvent spectrum was subtracted.

In a separate experiment, for comparison, we have obtained a Raman spectrum of Rh6G measured at 595 nm under pre-resonance condition (see Figure 2). In this experiment only the Kerr gate was needed to suppress the tail of still intense fluorescence emission in the detection region ~ 650 nm. The Raman spectrum was obtained with good S/N and was found to be very similar to the non-resonance Raman spectrum of Rh6G obtained using FT-Raman technique by M. Majoube *et al*[9]. The pre-resonance Raman spectrum has also a close resemblance to our resonance Raman spectrum shown in Figure 1 below 1400 cm^{-1} region but differs substantially in the upper wavenumber region believed to be due to the resonance effect enhancing different sets of bands. A similar pattern was observed between surface enhanced Raman (@1064 nm) and surface enhanced resonant Raman (@458 nm) spectra of Rh6G in the above work[9].

Raman Spectrum Reconstruction

Method 1 - Numerical Fitting

The signal obtained from the described combined technique is in a form of difference spectrum, such as that obtained from the SERDS method alone, from which Raman spectrum needs to be reconstructed. To do this we fitted the measured difference spectrum to Lorentzian bands with purpose written software using a method described in Reference[4]. The reconstructed spectrum is shown in Figure 1. It is important to note that this procedure is subject to some uncertainty, particularly, in the regions where several bands overlap. A more thorough method was proposed by Bell et al[5] involving the measurement and data processing of three shifted spectra (0, δ and 2δ) instead of two.

Method 2 - Simple Linear Data Manipulation

To eliminate any subjective factors from the reconstruction process and to enable automation we have developed a new algorithm that performs the reconstruction in a very simple way. The spectrum is directly recovered from raw difference spectrum by performing only a linear data manipulation on the difference spectrum array. The algorithm is as follows:

$$S_n = S_{n-\Delta} + D_n \qquad (1)$$

where D_n and S_n are the intensities of the difference and reconstructed spectra, respectively, for the n-th data point of the array. The wavenumber separation between n-th and n-Δ -th data points is approximately equal to the down shift δ.

For this method to be applicable, the difference spectrum must have a 'blank' region with absence of any Raman bands that is substantially wider than the SERDS shift δ (in most cases ~100 cm^{-1} is sufficient). Conveniently, such a blank region can often be found just above the finger print region, i.e. at 1700-2800 cm^{-1}. The spectrum reconstruction must be initiated from the blank region of the spectrum moving towards the region containing Raman bands. In the Methods 2 and 3 (see later) we assume that the blank region is at lower array index values which correspond to higher wavenumbers. The array can be reversed prior to the analysis if this is not the case.

In this approach, we rely on the fact that by starting the reconstruction from the blank spectral region we are able to identify the first pixel in the differential spectrum that exhibits a rise due to a Raman peak and its intensity then originates solely from the intensity of the spectrum S'_{λ} which is 'closer' to the blank region than the downshifted spectrum $S'_{\lambda-\delta}$ that is still 'blank' at this point. Therefore the intensity of this pixel is directly equal to the corresponding intensity within the reconstructed spectrum. Also it is equal to the intensity of the pixel within $S'_{\lambda-\delta}$ spectrum downshifted by Δ and therefore we know how much to add to the difference spectrum D at the downshifted point to compensate for the effect of the subtraction of shifted spectrum $S'_{\lambda-\delta}$.

Method 2 however can only be used if the SERDS shift δ is approximately equal to the separation between some integral number of pixels within the spectrum array. If a reasonable match cannot be found then a more thorough method described below needs to be applied. Another solution is to increase the number of data points within the array using a linear interpolation until an acceptable match exists. One always has to bear in mind, however, that this is always an approximation as the inter-pixel separation is typically constant in nanometers, not wavenumbers. The Method 3 described below provides a solution to all of these limitations.

Method 3 - Linear Data Manipulation with Interpolation

A more rigorous approach applicable even to cases where mismatch between the inter-pixel separation and shift δ exists involves the refinement of the Method 2 by adding a data interpolation step. Let us assume that the spectral array D consists of two columns: wavenumbers and corresponding intensities, $[w_n,D_n]$. The computer routine then starts reconstructing the spectrum following the algorithm given below:

step 1 find a pair of points within the D array with indexes x and x+1 for which the following logical operation is true $(w_x > w_n + \delta)$ AND $(w_{x+1} \le w_n + \delta)$

step 2 calculate the value $S_{n-\Delta}$ by the linear interpolation between the data points S_x and S_{x+1}
$S_{n-\Delta} = (w_n+\delta-w_x)*(S_{x+1}-S_x)/(w_{x+1}-w_x)+S_x$

step 3 $S_n = S_{n-\Delta} + D_n$

step 4 perform the above starting from step 1 for the next data point n+1

The algorithm can be recast into a simple single formula:

$$S_n = D_n + \sum_{x=1}^{n-1}\{[(w_n+\partial-w_x)(S_{x+1}-S_x)/(w_{x+1}-w_x)+S_x]* \\ [(w_x > w_n+\partial)\ AND\ (w_{x+1} \le w_n+\partial)]\} \qquad (2)$$

The last term in the sum in the square brackets is a logical operation being 1 if TRUE and 0 if FALSE.

Figure 3 shows the resonance Raman spectrum of Rh6G reconstructed using the above methods from difference spectrum. All the three methods yielded virtually identical spectra. However, a superior S/N was obtained using the fitting Method 1 and linear manipulation with data interpolation Method 3. Out of these, the most convenient is clearly Method 3, linear manipulation with data interpolation, offering simplicity, high S/N and most importantly has none of the ambiguity involved in using fitting Method 1. In addition, Method 3 can be performed on line automatically at high speed, e.g. during data collection. Method 3 is also directly applicable to the conventional SERDS technique.

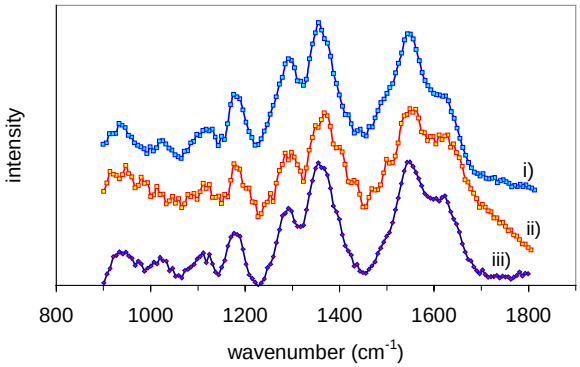

Figure 3. The Rh6G spectrum reconstructed from the difference spectrum using different methods: (i) numerical fitting (Method 1), (ii) simple linear data manipulation (Method 2) and (iii) linear data manipulation with interpolation (Method 3). The spectra are offset for clarity.

In the reconstructions shown in Figure 3 a residual curved background present in the reconstructed spectra was removed by fitting a second order polynomial function. This background is believed to originate from small pointing changes associated with changing wavelength by δ in our setup as discussed earlier and could be eliminated.

Conclusion

By combining the Kerr gating fluorescence suppression method with the conventional SERDS technique we have been able to obtain an exceptionally high level of fluorescence suppression not attainable using the two approaches individually. In a test experiment, the resonance Raman spectrum of Rh6G ($1x10^{-3}$ mol.dm^{-3} in methanol) was measured under its fluorescence maximum. The method allowed the photon shot noise level to be reached providing the detection limit for Raman spectra ~10^6 times lower than the level of fluorescence with an 800 s acquisition time. Its ultra high sensitivity holds great promise for selective probing of complex biological systems using resonance Raman in the near UV or visible, in cases, where selective resonance Raman enhancement of sample subcomponents or chromophores is desired.

We have also described a new, simple algorithm (Method 3) for reconstructing Raman spectrum from SERDS spectra with the absence of any subjective steps such as those present in the conventional fitting approach. Method 3 enables fast reconstruction in an automated way, for example, during data acquisition.

References

1. P Matousek, M Towrie, A Stanley and A W Parker Appl. Spectrosc., 53 1485, (1999)
2. P Matousek, M Towrie, C Ma, W M Kwok, D Phillips, W T Toner and A W Parker J. Raman Spectrosc, 32 983, (2001)
3. P Matousek, M Towrie and A W Parker J. Raman Spectrosc., 33 238, (2002)
4. A P Shreve, N J Cherepy and R A Mathies Appl. Spectrosc., 46 707, (1992)
5. S E J Bell, E S O Bourguignon and A Dennis Analyst, 123 1729, (1998)
6. M Towrie, A W Parker, W Shaikh and P Matousek Meas. Sci. Technol., 9 816, (1998)
7. J-C Gumy and E Vauthey J.Phys.Chem., 100 8628, (1996)
8. C Zander, M Sauer, K H Drexhage, D S Ko, A Schulz, J Wolfrum, L Brand, C Eggeling and C A M Seidel Appl. Phys. B-Lasers and Optics, 63 517, (1996)
9. M Majoube and M Henry Spectrochim. Acta A, 47 1459, (1991)

Appendix

An example of the computer routine for Method 3 written in Mathematica 4.0:

```
nx = 163; (*number of points in the spectrum*)
d = 28;   (*SERDS shift*)
scl = 1/1.1; (*correction factor accounting for differences in original
SERDS spectral intensities*)
init = 10;  (*starting pixel for data analysis*)
offst = 200;  (*enables offset within D to be corrected*)
a = -1500; (*polynomial background param - 0th*)
b = 16.8;  (*polynomial background param - 1st*)
c = 0.2;  (*polynomial background param - 2nd*)
dt = ReadList["d:\\kerrpls\\serdsraw.txt", {Number, Number}];
n = Table[{i, i^2}, {i, 1, nx}];
S = Table[0, {i, 1, nx}];
Do[S[[n]] =
   N[dt[[n]][[2]] - offst +
     scl*Sum[((dt[[n]][[1]] + d -
                dt[[ix]][[1]])*(S[[ix + 1]] -
                 S[[ix]])/(dt[[ix + 1]][[1]] - dt[[ix]][[1]]) +
            S[[ix]])*
       If[And[dt[[ix]][[1]] > dt[[n]][[1]] + d,
         dt[[ix + 1]][[1]] <= dt[[n]][[1]] + d], 1, 0], {ix, 1,
       n - 2}]], {n, init, nx - 1}]
Do[S[[n]] = S[[n]] - a - b*n - c*n*n, {n, 1, nx}];
RS = Table[{dt[[i]][[1]], S[[i]]}, {i, 1, nx}];
ListPlot[dt, PlotJoined -> True]
ListPlot[RS, PlotJoined -> True, PlotRange -> {All, {1000, 2000}}]
OUT1 = OpenWrite["SERDS.out", FormatType -> FortranForm,
PageWidth -> 200]
Do[Write[OUT1, RS[[i]][[1]], x, RS[[i]][[2]]], {i, nx}]
Close[OUT1]
Remove["Global`*"]
```

Development of Raman Tweezers

A D Ward, A W Parker, S W Botchway, M Towrie

Central Laser Facility, CLRC Rutherford Appleton Laboratory, Chilton, Didcot, Oxon, OX11 0QX, UK

Main contact email address: *a.d.ward@rl.ac.uk*

Introduction

The optical tweezers apparatus recently constructed in the laser Microscope Laboratory has been used successfully to capture, manipulate and measure forces on a wide range of particles, including mammalian cells, bacteria, spores and polymer beads[1,2]. This is possible through the generation of an optical potential using a high numerical aperture microscope objective lens to create a tightly focused laser beam. Recently, a number of new experimental studies have been reported[3] which combine optical tweezers with a range of spectroscopic techniques to allow the probing of individual cells. The

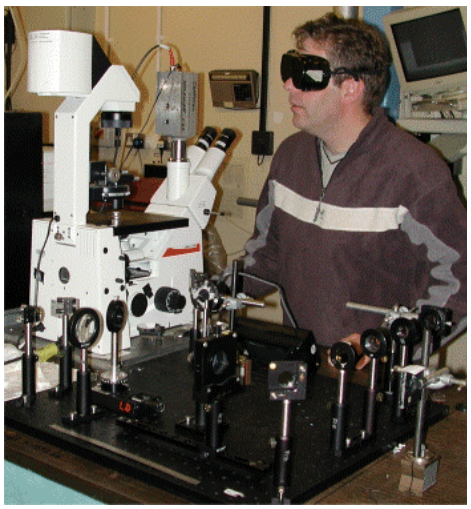

Figure 1. Photograph showing the Raman Tweezers apparatus being used by Dr Andy Ward, LSF.

wavelength of the trapping laser beam is selected to provide the spectroscopic light source and acquisition of the spectra is optimised by collection with a high power microscope objective. The techniques used to date include fluorescence and absorption, but of particular interest is the use of Raman spectroscopy to characterise the chemical species within single optically trapped microdroplets, beads and biological cells. This is potentially a powerful tool for use by biologists and biochemists and may provide a means of identifying abnormalities within living cells and also allow the monitoring of chemical changes that occur during cell death.

In this report we detail the combination of two areas of expertise within the LSF, namely optical tweezers and Raman spectroscopy, and detail our preliminary investigations on biological cells.

Experimental

The experimental set-up is shown in Figure 1 and schematically in Figure 2. Of particular note is that the system relies on a single near infrared CW laser to both produce the optical trap and generate the Raman spectra. For this there are two optical pathways. The first (solid lines) is primarily for conditioning and positioning the laser beam to create an optical trap. The second pathway (broken lines) directs the back scattered Raman light from the sample through the microscope and to the spectrometer.

The apparatus consists of a Ti:Sa laser (3900, Spectra-Physics) pumped with a cw Argon ion laser (Innova 90-5-UV, Coherent) to produce a beam at 785 nm, with an average power of 300 mW. The polarisation of the beam is rotated with a half wave plate to match the orientation of the spectrometer gratings. The beam is then passed through two sets of beam expansion optics (L1 to L4), reflected from a holographic notch filter (HNF-785, Kaiser Optical Systems) and directed into the microscope (Leica DM IRB). Here, a dichroic mirror reflects (> 750 nm) the beam through the objective lens (x63, NA 1.2, Leica Microsystems) where the optical trap is formed.

The Raman light scattered from the focal point is collimated by the objective lens and passes back along the same optical pathway but through the HNF-785 filter. This is used as a dichroic beam splitter, which at an incident angle of 18° reflects the 785 nm beam and transmits the Raman signal above 810 nm. A second edge filter is used to clean up the signal prior to focusing the beam onto the entrance slit of the spectrometer (SpectraPro-500, Acton Research Corporation) and detector (LN/CCD-1024, Princeton Instruments). To allow observation of the trapped particles, light (< 750 nm) from the microscope lamp is used to image the sample onto a CCD camera.

Results

Calibration of the spectrometer was performed by focusing in to a sample vial of toluene (Spectroscopic grade, Aldrich). Recorded wavenumbers are accurate to within 5 cm^{-1}. The

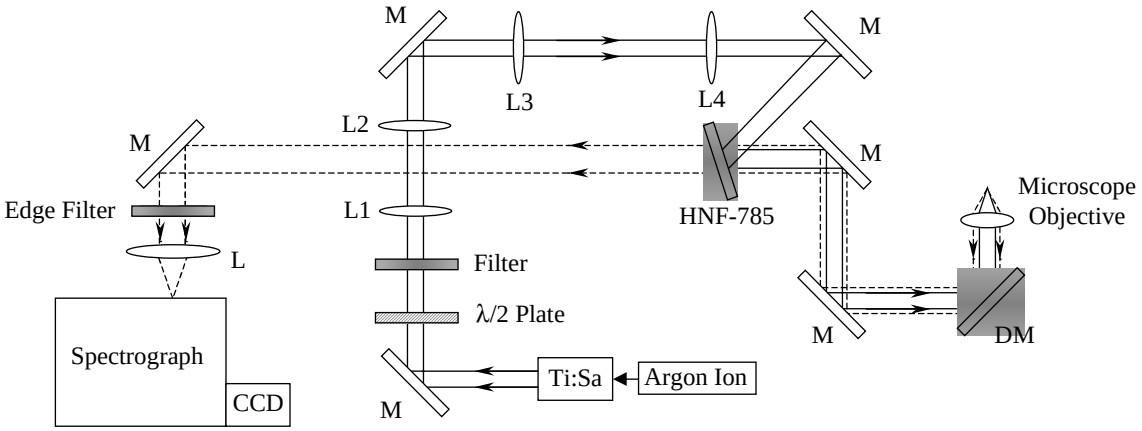

Figure 2. Schematic diagram of the Raman Tweezers optical set-up.

Raman collection optics were adjusted to optimise the signal, and assignment of the peaks was made from standard spectra.

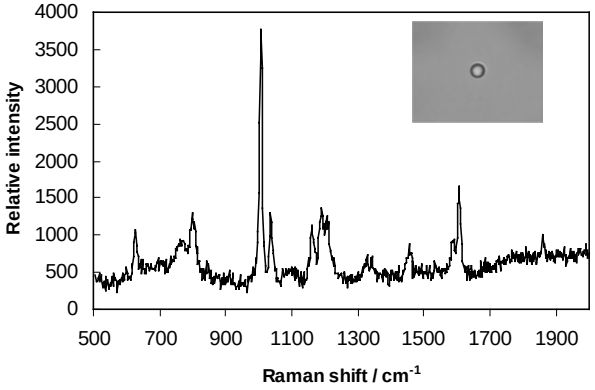

Figure 3. NIR Raman Spectrum and image (see inset) of an optically trapped polystyrene latex bead. The acquisition time is 10 seconds using an input laser power of 120 mW.

To demonstrate the system's ability to obtain a Raman spectrum from a trapped particle a polystyrene particle (2.6 μm diameter, Interfacial Dynamics Corporation) was captured in the optical tweezers and the trapping optics were adjusted to align the trapping position with the Raman detector optics. The spectrum, shown in Figure 3, has the background noise subtracted by acquiring a spectrum under identical conditions but without having a particle trapped. In practice it was found that blocking the laser for a short time allows the particle to diffuse away from the trapping location. The peak at 1001 cm^{-1} is in agreement with that of published spectra[3].

Having calibrated and aligned the spectrometer and optics, a solution of healthy yeast *cerevisae* and *sacromyces pombe* cells were examined using the Raman tweezers. Several cells were individually trapped and the Raman spectra recorded as described above. A typical spectrum is shown in Figure 4(A). Broad peaks are observed at 1085, 1309, 1444 and 1657 cm^{-1}. The spectra were noted to vary slightly in relative intensities between individual cells. To verify observations made in literature the yeast sample was denatured, by both boiling and bleaching. Confirmation of cell death was given from the lack of growth after overnight incubation and also observation of bacteria in the interior of the cells. The Raman signature from the dead cells is shown in Figure 4(B). Spectra A and B are similar, which is contrary to the literature findings where a complete loss of signal was reported for the dead cells[3]. The experiment was repeated to verify these findings.

Other biological materials that were characterised with the Raman tweezers include mammalian cells and bacteria. The spectra of these objects are shown in Figure 4(C) and 4(D). The mammalian cell whilst having similar peak positions has a much weaker signal suggesting that the composition of the cell membrane may play a significant part in generating the Raman signature.

Conclusions and future outlook

We have demonstrated that the combination of optical tweezers and Raman spectroscopy can be used to characterise single micron sized particles and biological cells. The apparatus developed here has trapped cells up to 20 microns in size. Our preliminary findings have cast doubt upon claims made in literature for distinguishing between dead and healthy cells[3] although the ability to use Raman spectroscopy at the intensities that can be readily achieved holds much future promise for utilizing the technique. New developments may lead to better fingerprinting of the biological cells and exciting new applications in the biosciences field. Future work may include studying the feasibility of creating enhanced resonance effects in an optical trapping environment by co-trapping cells with

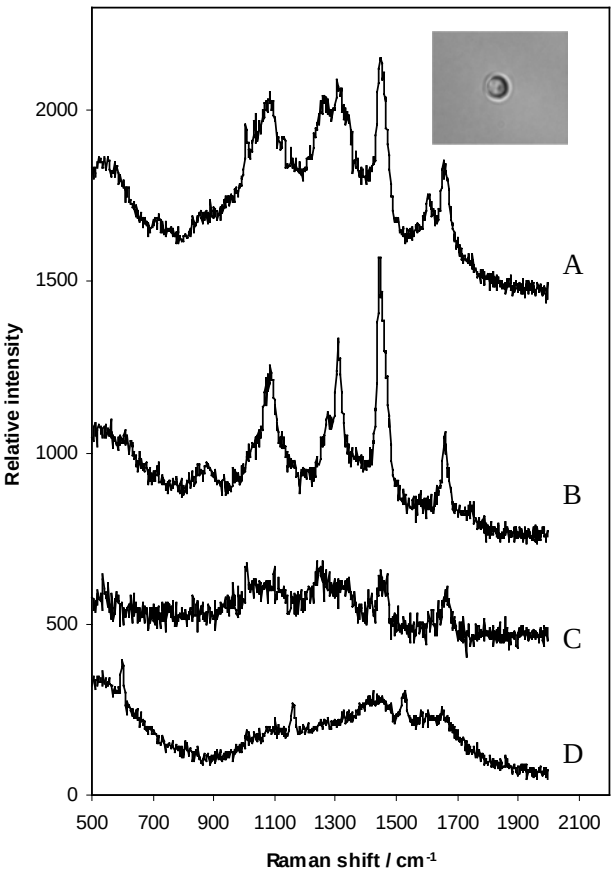

Figure 4. NIR Raman Spectra for a range of optically trapped biological specimens. A; a single healthy *cerevisae* yeast cell (see inset image); B; a yeast cell from the same sample after overnight bleaching; C; a mammalian cell and D; bacteria. All spectra were accumulated over 10 seconds and using an input laser power of 48 mW for A and B and 120 mW for C and D.

nanometer sized metal clusters. In addition, a Raman confocal microscope could be constructed, using a two-laser set-up, one to hold a cell and the second to scan areas within that cell for chemical identification. A range of hybrid optical tweezing techniques can now be envisaged to study dispersed biological specimens *in vitro* using spectroscopic methods that are currently available in the LSF.

Acknowledgement

Yeast cells were kindly provided by T. Humphery, MRC, Harwell.

References

1. Laser tweezers – Lattice forces in 2-D crystalline monolayers, R. Aveyard, B.P. Binks, J.H. Clint, P.D.I. Fletcher, B. Neumann V.N. Paunov, J. Annesley, D. Nees, A.W. Parker, A.D. Ward, A.N. Burgess, Central Laser Facility Annual Report 2000-2001, RAL-TR-2001-030, 107-108

2. Measurement of long range repulsive forces between charged colloidal particles adsorbed at an oil-water interface. R. Aveyard *et al*. Phys.Rev.Lett, 88 (24): art. no. 246102, 2002

3. Near-infrared Raman spectroscopy of single optically trapped biological cells, C. Xie, M.A. Dinno, Y. Li, Optics Letters 2001, 27(4), 249-251.

Self-Drilled Spatial Filter for a Multi-Pulse Picosecond Ultraviolet Laser System

A J Bodey, G J Hirst, W Shaikh

Central Laser Facility, CLRC Rutherford Appleton Laboratory, Chilton, Didcot, Oxon, OX11, UK

Main contact email address: *ns9ajb@bath.ac.uk*

Introduction

The Laser-Plasma X-ray Laboratory houses a powerful, pulsed UV laser system which, when its beam is focused onto a dense target, generates intense pulses of soft X-rays. The time structure of the laser beam consists of macropulses delivered at up to 100 Hz. Each macropulse contains eight 5 ps micropulses spaced over a 15 ns period. The laser system is a hybrid one, with a front end operating at 746 nm, followed by a frequency tripler and a final, double-passed krypton fluoride (KrF) amplifier, giving an average power of up to 12 W at 249 nm.

The frequency tripler effectively removes low-intensity components of the pulse train, delivering "clean" UV pulses to the KrF amplifier. However, as well as providing significant amplification of the picosecond pulses, the KrF laser also produces nanosecond background light in the form of amplified spontaneous emission (ASE). This can be sufficiently intense to preheat the target in advance of the picosecond pulses and can thereby affect the X-ray generation[1]. The ASE can also de-pump the laser medium, limiting the amplifier's gain[2].

The Spatial Filter

The ASE from the KrF laser is much less spatially coherent than the short pulse beam, so it can be reduced by spatial filtering, whereby the beam is focused through a pinhole which removes divergent components. A self-drilling spatial filter has been built with a number of features to enhance performance:

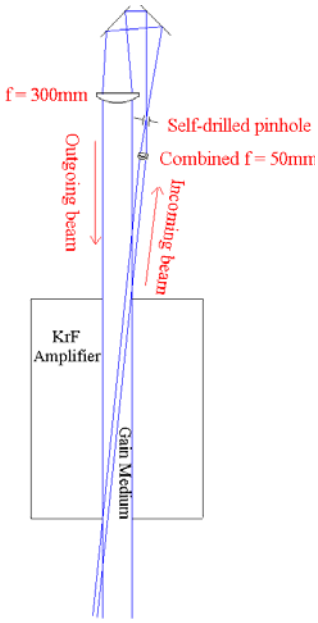

Figure 1. Spatial Filter Layout.

i) Spatial filtering can potentially achieve two aims: a reduction of nanosecond ASE, and an improvement in beam quality of the picosecond pulses. However, since the picosecond pulses are far more intense than the nanosecond ones, filtering them greatly increases the rate of pinhole damage. For this reason it was decided to concentrate on ASE removal and carry out only minimal short pulse filtering.

The best way to ensure that the bulk of the picosecond light passes through the pinhole is to allow the short pulses to drill their own hole in situ. The resulting pinholes have a typical diameter of 100 µm which, with f/16 focusing, corresponds to 10 times the diffraction-limited (first Airy minimum) spot size. Of course the expected depth of focus would be only ~60 µm, (significantly less than the substrate thickness). Furthermore the holes are drilled over many shots, with possible shot-to-shot variations in position. Therefore, the relatively large hole size does not necessarily reflect the beam quality of a single macropulse. Misalignment of the 8-beam multiplexer can also make the macropulse spot larger than the individual micropulses.

ii) Beam direction may drift in a laser system as a result of thermal fluctuation and vibration in optical components; if a fixed pinhole is used then the beam becomes misaligned. An advantage of self-drilled pinholes is that they maintain high short pulse transmission, irrespective of long term beam drifts.

iii) Irradiation at high intensities can ablate material from the pinhole, reducing the amount of ASE removed from the beam and limiting the pinhole lifetime. The conventional material for commercial pinholes is stainless steel, which absorbs UV light. However in initial tests (see below) their lifetime proved to be unacceptably short. A more successful approach is to refract and scatter the ASE without absorption in the pinhole material. A 200 µm thick fused silica substrate was used for its UV transparency and non-crystalline structure, which inhibits cracking during drilling. It was bead-blasted to texture both surfaces, increasing the scattering of unwanted light.

iv) The diameter of the beam on its first pass through the amplifier is kept low (~3 mm) to minimise overlap with the full-aperture return beam. The spatial filter also acts as the X6 beam expander which is needed to convert the beam size.

v) The gain of the amplifier lasts for approximately 25 ns. This is a relatively short time for each macropulse to travel through the gain medium, with a change in direction and beam size between the passes. Purpose-built lenses and mirror mounts have been used to minimise the path length in the spatial filter.

Results

In order to quantify the effect of filtering, the average power of the beam was measured ~1 m after the second pass through the amplifier with the short pulses both off and on. The two measurements were combined to give a ratio R (see Equation 1) which was near 1 if the beam was dominated by picosecond pulses and much lower if there was significant ASE.

$$R = \frac{\text{Power with short pulse on - Power with short pulse off}}{\text{Power with short pulse on}} \quad (1)$$

R was typically 0.3 when the spatial filter contained no pinhole, whereas a self-drilled pinhole increased it to 0.7. Although the pinhole caused a slight decrease in total laser power, an increase of up to 60% in X-ray yield was observed. This may have been due to increased power in the short pulses or, perhaps, to reduced plasma formation before their arrival.

Self-drilled steel pinholes were tried but their lifetime was less than an hour at a laser pulse rate of 12.5 Hz. By comparison, the fused silica pinholes lasted for tens of hours before a similar ASE increase was reached.

In conclusion, the use of a self-drilled fused silica pinhole leads to an increase in soft X-ray yield, probably due to a combination of increased picosecond pulse power and reduced pre-plasma from ASE. The pinhole needs no alignment, either initially or during use, and its lifetime is long enough for effective operation.

References

1. See for example J Yu, Z Jiang, J C Kieffer and A Krol Physics of Plasmas, 6 1318, (1999)

2. E C Harvey, C J Hooker, M H Key, A K Kidd, J M D Lister, M J Shaw and W T Leland J Appl Phys, 70 5238, (1991)

Progress in the construction of large-aperture adaptive mirrors

C J Hooker, J L Collier, C Spindloe

Central Laser Facility, CLRC Rutherford Appleton Laboratory, Chilton, Didcot, Oxon, OX11 0QX, UK

Main contact email address: *c.j.hooker@rl.ac.uk*

Introduction

In last year's Annual Report [1)] we described the development of 150 mm aperture bimorph adaptive mirrors using single wafers of piezoceramic (lead zirconate-titanate or PZT). These mirrors were made by the novel method of attaching the thinnest obtainable (2 mm) PZT discs to the Pyrex glass substrate, then thinning the PZT to the required 200 micron thickness by conventional optical grinding. This article describes further developments of the construction technique, which were needed to solve problems experienced with the first mirrors.

Failure of prototypes VP2 and VP3

The two single-wafer mirrors VP2 and VP3 were assembled, as were all previous mirrors in the CLF's adaptive optics programme, using a conductive fabric between the substrate and the PZT to act as the common ground for all the actuators. Inevitably it is hard to ensure that the adhesive layer in which the fabric lies is free from bubbles. VP2 and VP3 were assembled by an external contractor using a UV-curing adhesive, and both showed significant numbers of bubbles between the substrate and the fabric, as viewed through the face of the glass. It became clear that there were also bubbles between the fabric and the PZT, giving rise to areas of low adhesion. While the face of the mirror was polished, the PZT was covered with copper tape to prevent charge build-up which would have caused distortion of the figure. On VP2 the thinned PZT fractured while the tape was being removed, the piece which detached being the same shape as one of the bubbles on the PZT side, faintly visible from the front of the mirror. VP3 suffered a similar problem while being annealed to reduce the curvature induced by adhesive shrinkage: in this case a bubble expanded sufficiently to crack the PZT. Following these failures, an alternative assembly technique was devised to eliminate the fabric.

New assembly technique

The PZT discs as supplied have a conducting layer of silver on each face: this is applied so the manufacturer can polarise the material with an electric field. Provided electrical contact is made with this layer, it will act as the ground plane instead of the fabric.

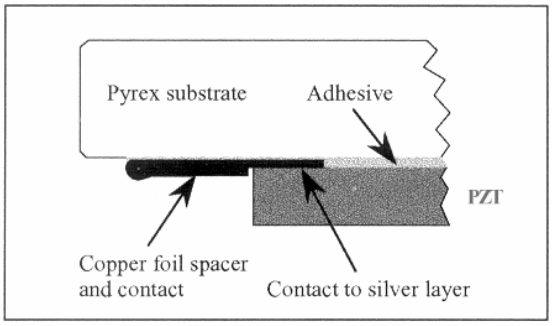

Figure 1. Cross-section of new design of adaptive mirror.

In the new technique, shown in Figure 1, the electrical connection is provided by pieces of copper screening tape, which has an electrically-conducting adhesive. The tape is stuck to one side of the PZT, then folded over on itself to form a tab, which is also glued to the substrate. The tape is 60 microns thick, and the PZT is 120 mm in diameter, so the volume of adhesive required to cover the area of the PZT can be calculated. The inner end of each piece of tape is cut to a 90 degree corner that faces the centre of the mirror: this divides the flow of adhesive near the edge of the PZT and prevents air becoming trapped. The PZT was laid on a flat surface (an old plane mirror) with the tape uppermost, and the required volume of adhesive, plus a 10% excess, was placed in the centre. The pool of adhesive was examined carefully, and any bubbles were removed with a needle. The substrate was lowered slowly onto the adhesive until contact was made and the adhesive began to flow outwards in an expanding circle. Initially, the weight of the substrate was sufficient to keep the film of adhesive spreading out, with gentle pressure being applied manually to keep it centred on the substrate, and to keep the substrate itself centred on the PZT. Once the film of adhesive had become too thin to flow under the weight of the substrate alone, the assembly was loaded with a second flat mirror and a 7 kilogram weight, and left for several hours, after which a bead of adhesive could be seen all round the edge of the PZT. The weight was removed, and the mirror assembly was given a 3 minute exposure on a UV light box to cure the adhesive. The excess cured adhesive was removed to avoid possible problems in the grinding stage. A few small bubbles were visible in the adhesive layer, but none of them was larger than 1 mm in diameter.

Formation of the electrodes

The original plan for forming the electrode pattern was to sputter copper onto the PZT, then form the desired pattern of electrodes in a layer of photoresist so the copper between them could be etched away. In practice, the resist did not have sufficient resistance to the etching solution, and large areas of the electrodes were removed as well. The reverse technique was then adopted, i.e. a photoresist mask was made in the form of the desired boundaries between electrodes, and the process of resist coating, exposure and development was repeated until a good mask was obtained. The PZT was then activated using hexamethyl disilazane (which fortunately does not dissolve the resist), and sputtered with copper. Typically, a copper layer of 1 to 1.5 microns can be put down in one or two minutes without overheating the assembly and melting the resist. When the coated side was washed with acetone, the resist dissolved, leaving the required electrode structure on the PZT. The pattern used was shown in Reference 1, Figure 4: it has 61 actuators, 49 of which are within the beam footprint and have equal areas. There are 12 larger actuators outside the beam area providing slope control at the beam edges. The electrical resistance between adjacent electrodes was greater than 20 MΩ.

Mirror housing and mounting

An improved housing was designed to hold the mirror and protect the connecting wires at the back. As the mirror has only 61 actuators, there are 3 spare channels in the driver box. Two of these were designated for tip and tilt, and were led out to BNC connectors on the back plate of the housing. The micrometers on the mirror mount were replaced with linear piezoelectric drivers having a range of +/- 10 microns: these were connected to the BNC sockets. Tip and tilt motions are thus incorporated into the mirror response, and can be corrected in the closed loop.

References

1. C J Hooker, L Coffey and J L Collier, CLF Annual Report 2000-2001, RAL-TR-2001-030, pg 175

The Performance of a Stable High-gain Diode-pumped Nd:YLF Amplifier

I N Ross

Central Laser Facility, CLRC Rutherford Appleton Laboratory, Chilton, Didcot, Oxon, OX11 0QX, UK

M Csatari

Department of Optical and Quantum Electronics, University of Szeged, dom ter 9, H-6720 Szeged, Hungary

Main contact email address: *i.n.ross@rl.ac.uk*

Introduction

The work reported here is directed towards meeting the requirements for a photo-injector laser to generate the electron bunches suitable for injection into the proposed future CERN linear accelerator (CLIC). Table 1. indicates the principal performance specification for this photo-injector laser.

UV energy/pulse	5 μJ
Pulse duration	10 ps
Wavelength	<270 nm
Time between pulses	2.13 ns
Pulse train duration	91.6 μs
Repetition rate	100 Hz
Energy stability	<0.1%

Table 1. Photo-cathode specifications.

Figure 1 illustrates the basic system design to meet the specification in Table 1.

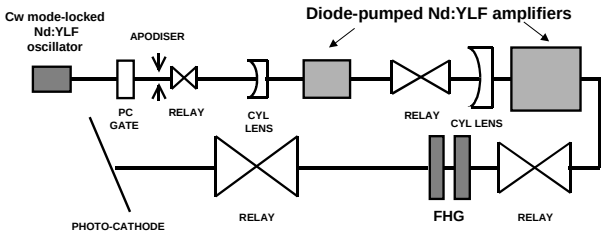

Figure 1. Basic design of the photo-injector laser system.

A high average power cw mode-locked Nd:YLF laser operating at 500MHz serves as the oscillator. The oscillator pulses are amplified and frequency converted to the fourth harmonic before relaying to the photo-cathode of the accelerator.

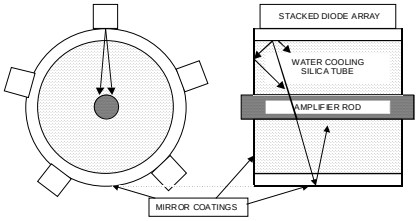

Figure 2. Schematic of the amplifier head.

The principal aspect of this laser system requiring development is the design and operation of the amplifiers. These must be efficient to minimise the cost of the pump diode arrays, have high gain to minimise the number of amplifiers and must show a very high degree of output stability. For cost and simplicity a cylindrical pumping cavity design is used as shown in Figure 2.

Such a design is best matched to a rod diameter of about 10mm but can work well for smaller rods if a simple lens is inserted in front of each diode array.

The average power limit of this Nd:YLF amplifier is given by its fracture limit of approximately 18W/cm, this being the maximum rate of deposition of heat per unit length of rod. Since the thermal dissipation into Nd:YLF due to the quantum defect is 32% of the excited state pump rate then it follows that the maximum extractable power is a factor (1-0.32)/0.32 higher than the fracture limit, or 56W/cm. For example a 10cm rod could give a maximum output power of about 500W. Techniques to increase the fracture limit, such as that used for Nd:YAG[1], may enable this limit to be extended.

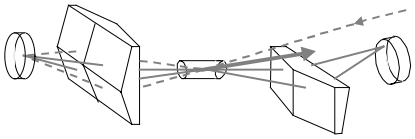

Figure 3. The four-pass amplifier geometry.

The amplifier must be operated to give a high gain but also with heavy gain saturation in order to achieve high efficiency and stability of the output power. We used a four pass geometry as shown in Figure 3. However for such a high gain system it will be important to establish the gain limit set by pump depletion resulting from amplified spontaneous emission. Such a limit could be a serious problem if too many passes are used with too close an optical coupling between passes.

For optimisation of the performance a multi-pass analysis of this amplifier was carried out.

Analysis

The analysis is given for Nd:YLF but can readily be used for other materials and amplifier designs. The examples used will be for the test amplifier as used for all the experimental results given below.

The amplifier is most stable when it is operated in a 'quasi-steady-state' mode in which the excited state population levels reach an equilibrium level during the pump pulse, this being a balance between the input pump power reaching the upper laser level (pump rate) and the sum of the power lost to the amplified beam and to amplified spontaneous emission (ASE), or:

$$I_p = I_{out} - I_{in} + \frac{F_{sat}.\ln G}{\eta_R}\frac{1+B}{\tau_{fl}} \qquad (1)$$

where: I_p, I_{out}, I_{in} are the pump rate, output intensity and input intensity respectively

F_{sat} = saturation fluence; G = amplifier gain

η_R = splitting ratio in the upper laser level

τ_{fl} = fluorescence lifetime of the excited state

and where B is the increase in the excited state decay rate resulting from ASE. B_P for any position P in the rod can be calculated from:

$$B_P = f\alpha \int_{rod} \frac{\exp(\alpha r)}{4\pi r^2} dV \qquad (2)$$

where: f = fraction of excited state population fluorescing at the laser wavelength; α = gain coefficient; and the integral is evaluated over the volume of the rod and must include surface reflections.

Equation 1 needs to be reformulated to apply to our 4-pass test amplifier. Assuming a constant beam size from pass to pass and an intra-pass loss of L, Equation 1 can be re-written as:

$$I_p = f_1(G) I_{in} + f_2(G) \qquad (3)$$

Where:

$$f_1(G) = (1-L)^3 G^4 + (1-L)^2 LG^3 + (1-L) LG^2 + LG - 1 \quad \text{and}$$

$$f_2(G) = \frac{F_{sat} \ln G}{\eta_R} \frac{(1+B)}{\tau_{fl}}$$

and where: G = single pass gain of amplifier

For a 4-pass amplifier with good decoupling (for example a long distance) between passes and for a rod with a diffuse barrel surface, an approximate expression for *B* is:

$$B = 0.05(d/l)^{0.3} G \qquad (4)$$

for a rod of length l and diameter d.

For the pulse trains being considered valid results can be obtained by assuming a cw input beam.

The extraction efficiency (η_{ex}) of the amplifier, is defined here as the ratio of the intensity increase of the amplified beam to the pump rate:

$$\eta_{ex} = \frac{I_{out} - I_{in}}{I_p} \qquad (5)$$

Since the ASE loss increases with gain, there will necessarily be a compromise between efficiency and gain.

For our 4-pass test amplifier Figure 4 shows the calculated variation of efficiency with 4-pass gain and predicts that gains of more than 10^4 can be obtained with Nd:YLF without a major reduction in efficiency.

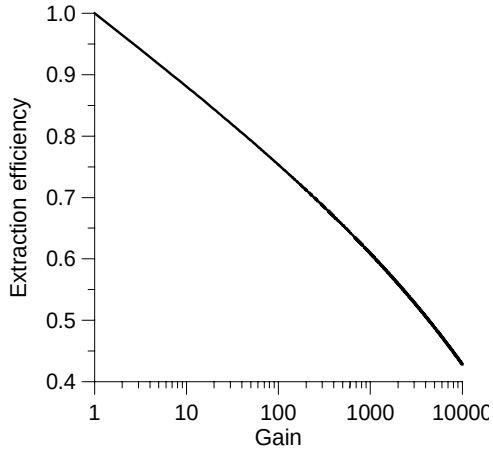

Figure 4. The variation of the efficiency of extraction of pump power with the amplifier gain.

Two measures of stability can also be assessed in steady state operation by differentiating Equation 1 to give:

$$dI_p = (f_1' I_{in} + f_2') dG + f_1 dI_{in} \qquad (6)$$

Use of the substitution $I_{out} = (1-L)^3 . G^4 . I_{in}$ leads to an equation for the interdependence between changes in input, pump and output intensities:

$$I_p \frac{dI_p}{I_p} = \frac{G}{4}(f_2' + f_1' I_{in}) \frac{dI_{out}}{I_{out}} - \left[\frac{G}{4}(f_2' + f_1' I_{in}) - f_1 I_{in} \right] \frac{dI_{in}}{I_{in}} \qquad (7)$$

where f_1', f_2' are the differentials of f_1 and f_2 respectively with respect to G. For the test amplifier with measured values of 9 for G, 4.7kW/cm^2 for I_{out}, and 0.2 for *L* this reduces to:

$$\frac{dI_{out}}{I_{out}} = 1.85 \frac{dI_p}{I_p} + 0.163 \frac{dI_{in}}{I_{in}} \qquad (8)$$

The stability for the laser system is consequently largely determined by the stability of the pumping rate of the final amplifier and can support much larger variations for the input.

Having established the expected performance in the steady state mode it is useful to consider the dynamics of reaching the steady state. To do this we calculate the response of the amplifier in the presence of a time-varying pump and input signal beam. This is described by the spatial and temporal changes to the amplifier gain coefficient. For an input pulse train with a time separation of τ_s between pulses the incremental change in the gain coefficient from one pulse to the next has three contributions: the increase due to pumping; the loss due to fluorescence enhanced by amplified spontaneous emission; and the depletion by the previous pulse. The net change is given by:

$$\Delta\alpha(z,t) = \frac{\eta_R}{F_{sat}} \frac{I_p(z,t)\tau_S}{l} - \frac{\alpha(z,t)\tau_S(1+B)}{\tau_{fl}} - \frac{\alpha(z,t)\eta_R F(z,t)}{F_{sat}} \qquad (9)$$

where: η_R = level splitting ratio in the upper laser state and it is assumed that the equilibrium in the level populations is re-established in a time short compared with τ_S.

and where $F(z,t)$ = the sum of the pulse fluences in all passes at position z and time t. and is given by

$$F(z,t) = F_{in}(t) \begin{bmatrix} \exp \int_0^z \alpha(z,t)dz \\ + L \exp\left(\int_0^l \alpha(z,t)dz + \int_z^l \alpha(z,t)dz \right) \\ + L^2 \exp\left(2\int_0^l \alpha(z,t)dz + \int_0^z \alpha(z,t)dz \right) \\ + L^3 \exp\left(3\int_0^l \alpha(z,t)dz + \int_z^l \alpha(z,t)dz \right) \end{bmatrix} \qquad (10)$$

Solving these equations for the test 4-pass amplifier with a constant fluence input pulse train gives an output fluence of the form shown in Figure 5.

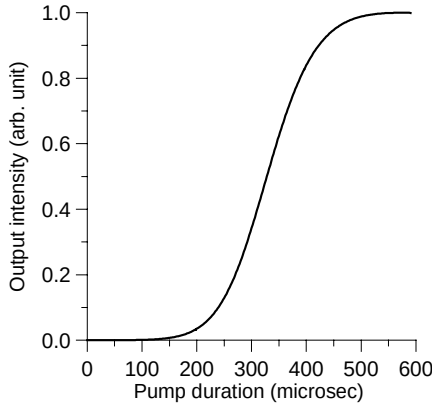

Figure 5. Calculated evolution of amplified beam.

It can be seen that perfectly steady-state operation is achieved.

Test amplifier performance

An amplifier head was constructed to the design shown in Figure 2 and used to pump a 5mm diameter by 50mm long rod of Nd:YLF. 5 QCW 1kW stacked diode arrays (Thales) were distributed around the rod as shown in Figure 2 and an additional lens in front of each array ensured efficient optical coupling to the rod. The diode wavelengths were in the range 798 to 802 nm to provide good absorption efficiency for both polarisations[2)] . Repetition rate was normally 5Hz with pump duration in the range 400 - 800μs.

The input seed beam was provided by an 800mW CW Nd:YLF laser (Crystalaser) and the injection optics of the 4-pass geometry gave a beam size of 4mm in the first pass and adjustable down to 1mm in the final pass. The propagation distance between passes of 1m ensured low ASE pass-to-pass coupling and good beam overlap in all passes.

Gain and saturation

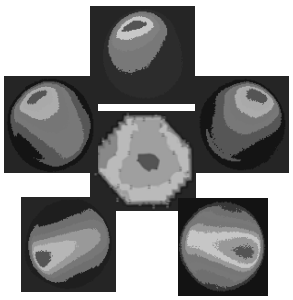

Figure 6. Pump distributions for individual and all 5 diodes.

Figure 6 shows the fluorescence distribution in the rod for pumping with individual diode arrays and with all five arrays together. The effect of pump polarisation is seen since the top diode polarisation at the rod is 's' which is more strongly absorbed by the rod, and the bottom diodes are mostly 'p' polarisation at the rod and the absorption is less. The combined effect of all diodes provides quite uniform pumping as illustrated in the centre 'saturated gain' distribution.

The ability of the amplifier to generate high gain is shown in Figure 7 by the measured evolution of the small signal gain during the 600μs pump duration. Also shown is a calculated profile for which the best match to the measured curve gave a combined pump cavity transfer and rod absorption efficiency of 53%. The peak gain achieved was $5x10^5$ with a background ASE intensity measured at the 10^{-3} level.

At an input power of 450mW into the first pass it was possible to strongly saturate the amplifier, giving the evolution of output intensity shown also in Figure 7. This is seen to be in good agreement with the calculated profile, and in this case the steady state is reached after 350μs as expected, with an output intensity at 7kW/cm^2 which is 8x the saturation intensity for Nd:YLF. The amplified beam has a flat-top of diameter 2.5mm containing a peak power of 380W, in comparison with the un-amplified approximately Gaussian profile with FWHM of 1mm.

Stability

The output pulse train stability is a critical requirement for this type of laser system (Table 1), and this must be maintainable over periods of perhaps several hours. The proposed design aims to achieve the best possible stability by using diode pumping and by relying on heavy saturation of the amplifiers to provide a strong clamp on the output intensity. As indicated by the earlier 'steady-state' analysis such a design largely confines

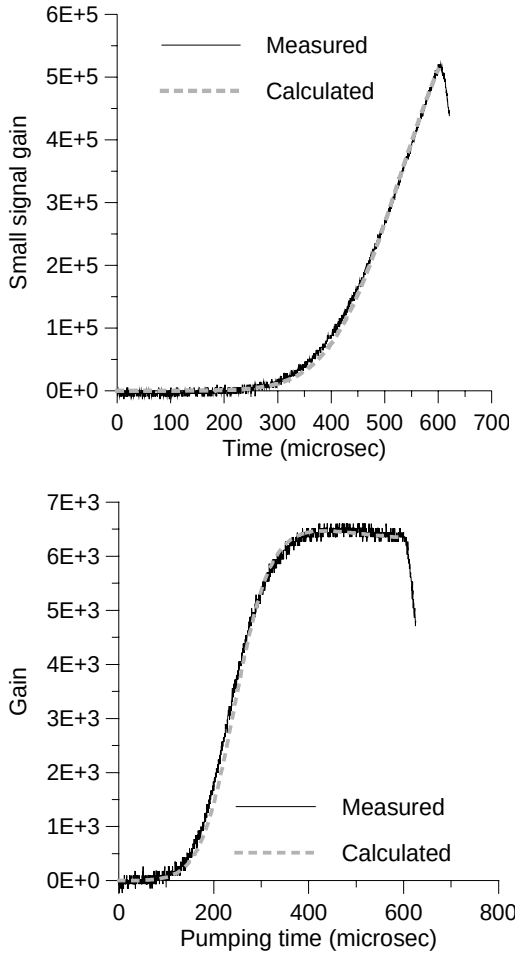

Figure 7. The calculated and measured gain of the amplifier for small signal and under heavy saturation.

the problem to stabilising the pump rate in the final amplifier. This is dependent on two principal factors: the current to the diode array, and the temperature of the coolant, the latter having a strong influence on the diode spectrum and hence the absorption efficiency of the laser rod. In our system the diode driver was stable to about 0.5% long term and the temperature of the coolant was maintained to 0.5deg. Evidently both of these could be improved.

Stability measurements were conducted using an InGaAs photodiode which has a very low temperature coefficient at 1047nm and is not sensitive to background visible radiation, together with an oscilloscope with stability in the region of 0.1%. Allowing a period of at least 30 minutes for stabilisation, the long term stability of the output power was measured and is shown in Figure 8.

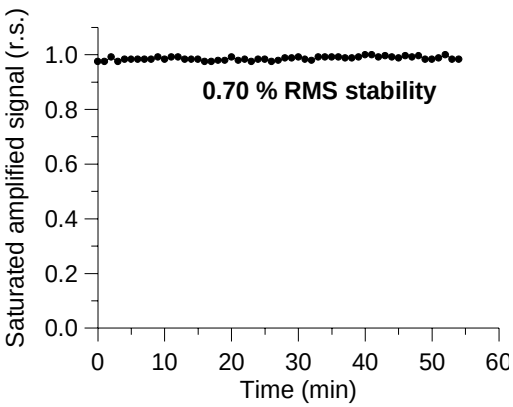

Figure 8. Long-term stability of the amplified beam.

The rms stability was measured at less than 0.7% over a period of one hour. This excellent performance was achieved without special precautions to stabilise the mechanics and environment and without any feedback stabilisation system. A demonstration of the insensitivity to variations of the amplifier input power is shown in Figure 9. A factor of 10 attenuation of the input led to a reduction of only a few % in the output of the amplifier in this heavily saturated mode.

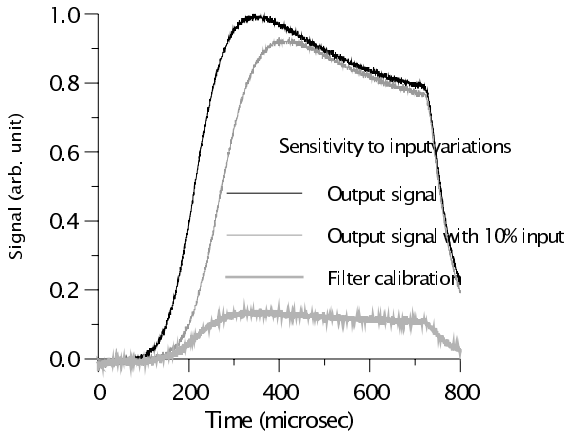

Figure 9. Low sensitivity of the amplified signal to a large attenuation of the input signal.

Thermal aberrations in the amplifier

For many potential applications the optical integrity of the amplified beam is important and one reason for selecting Nd:YLF as the gain medium was its much reduced thermal lensing in comparison with materials such as Nd:YAG[3]. A radial shear Sagnac interferometer placed in the amplified beam was used to assess the thermal lensing, and the recorded interferograms were analysed using a CCD, frame store and software package (OFA). Examples of interferograms recorded for the pumped amplifier and for both orientations are shown extrapolated up to the fracture limit of the rod in Figure 10 for 10 watts average thermal power dissipated in the rod.

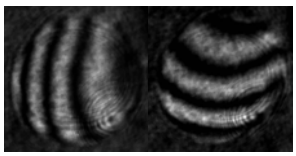

Figure 10. Interferograms of the output beam for both orientations and for 10 watts power of thermally deposited power.

A Zernike analysis of these interferograms yielded significant coefficients only for primary astigmatism and defocus, indicating that the aberration can be effectively compensated using cylindrical lenses. Using the measured Zernike coefficients, the Strehl ratio was calculated and plotted in Figure 11 with an extrapolation to higher powers. This allows calculation of the maximum power which is possible without astigmatic compensation.

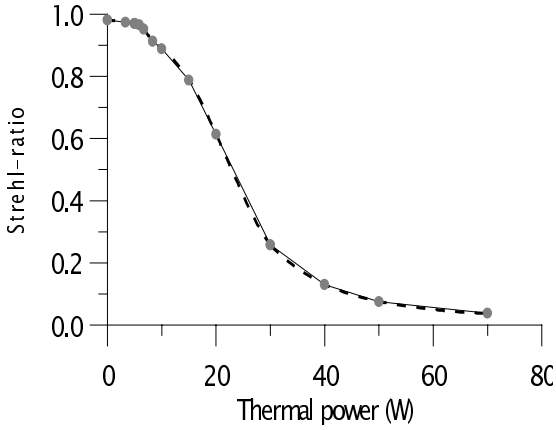

Figure 11. Dependence of Strehl Ratio on thermal power.

Conclusions

We have proposed and analysed a 'quasi-steady-state' mode of operation for a QCW diode-pumped laser amplifier for use in a photo-injector system. Under heavy saturation this amplifier has high extraction efficiency and is highly stable, being only sensitive to changes in its diode pump power and temperature. In multi-pass operation the amplifier also has high gain and is very insensitive to changes in input beam energy or power.

A simple design of amplifier based on Nd:YLF has been constructed and tested. Its performance provided good verification for the analytical predictions for gain and efficiency, and the optical quality of the amplifier at high average power was assessed. The most promising aspect of this amplifier has been the measured output pulse stability. At 0.7%rms over 1 hour this competes favourably with the previously best lasers and can be improved using a more stable diode-laser power supply and coolant temperature.

References

1. J.Marion Appl.Phys.Lett. 47, 694, (1985)
2. N.P.Barnes, M.E.Storm, P.L.Cross, M.W.Skolaut IEEE JQE QE-26, 558, (1990)
3. J.E.Murray IEEE J.Q.E.19, 488, (1983)

Applications of OPCPA in Compact High Average and Peak Power (CHAPP) Lasers

I N Ross

Central Laser Facility, CLRC Rutherford Appleton Laboratory, Chilton, Didcot, Oxon, OX11 0QX, UK

Main contact email address: *I.N.Ross@rl.ac.uk*

Introduction

There has been a strong and increasing development of diode-pumped lasers over the last few years to meet the increasing demands for high average power laser systems. Much of this work has focused on applications in engineering which are both of immediate commercial interest and place less difficult requirements on the laser. In general the highest powers have been generated at a wavelength of about 1micron as continuous beams or Q-switched pulse trains. However there are of course many applications which place more difficult requirements on the laser output in terms of wavelength, pulse duration, peak power and beam quality, and there is an increasing need to develop such systems.

The current most successful diode-pumped lasers for gain, efficiency and average power are neodymium-doped. These will be developed further and will be able to generate high average power with high efficiency at 1 micron for pulse durations down to approximately 1ps. This pulse duration limit, determined by the gain bandwidth of neodymium, will restrict the maximum peak power available and there is of course no tuneability. Thermal distortion can be large and make it difficult to generate close-to-diffraction-limited beams.

Ytterbium-doped materials are also being strongly developed and will be able, also at a wavelength of 1 micron, to achieve both higher average powers as a result of the smaller thermal deposition rate and shorter pulses by virtue of the larger gain bandwidth. However the low gain and high saturation fluence do not allow efficiency extraction of stored energy.

Optical parametric amplifiers (OPAs) however are well matched to the requirements for high average and peak power lasers and can simultaneously generate excellent beam quality.

The properties of OPAs

Using suitably selected OPA crystals there is no linear absorption at the wavelengths present. Consequently there is little thermal heating of the crystal and little beam distortion. Any residual absorption is minimised as a result of the high gain possible in an OPA which leads to very short lengths of material in the beam path.

The potential of the OPA for very high peak power is a result of the large gain bandwidth, which enables them to amplify ultra-short pulses. The optimum selection of crystal and geometry leads to gain bandwidths in excess of $5000cm^{-1}$ and amplified pulse durations of less than 5fs. Such short pulses can give high peak power even when the energy is not large, as is often the case in high average power systems which generally operate at low energy and high repetition rate.

The third property of note for some applications using high average power is the wide tuneability of OPAs and hence the ability to select the optimum wavelength. As an example, a number of future applications involve the generation of fast particles from laser plasma, and efficient particle generation requires high peak power, or more strictly high $I\lambda^2$. The OPA allows the possibility to select a longer wavelength for which it is easier to achieve high values of $I\lambda^2$. In addition to this advantage, a longer wavelength also benefits from higher laser damage threshold and lower B-integral, and can enable the selection of the highest average power lasers for OPA pumping.

An application in Positron Emission Tomography (PET)

This cancer scanning technique requires the availability of the F^{18} isotope which is currently generated using 5MeV protons from a large centralised accelerator. The 20 minute half-life of the F^{18} isotope restricts the use of the PET technique to hospitals within only a short radius of the accelerator. There is evidently a considerable incentive to develop a laser system with the average and peak power sufficient to efficiently produce the 5MeV protons from a laser-plasma source and with a 'table-top' size to allow it to be sited within the hospital.

An estimate of the specification of the laser system suggests that it would need to generate hundreds of watts with a peak pulse power given by $I\lambda^2 = 10^{20}W/cm^2\ \mu m^2$. This level of $I\lambda^2$ has been demonstrated for Ti:sapphire lasers but such systems would need considerable development up to repetition rates of hundreds of Hz instead of the current maximum of 10Hz.

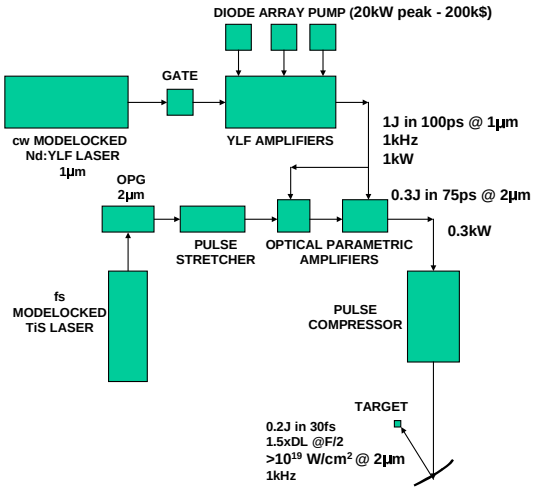

Figure 1. Proposed OPCPA laser design for PET.

A perhaps more accessible scheme is designed around OPAs operating as chirped pulse amplifiers (or OPCPAs). Such a scheme is shown in Figure 1. An OPA pump wavelength of 1μm is selected to optimise the efficiency of the pump laser and the OPA signal (or operating) wavelength is chosen as 2μm to minimise the requirement on focused intensity. A mode-locked Nd:YLF oscillator provides the source pulses for the pump beam. These are amplified using diode-pumped Nd:YLF amplifiers to a level of 1J in 100μs at 1kHz, or an average power of 1kW. Such a system looks feasible without exceeding the B-integral and thermal limits of the amplifiers and at an acceptable pump diode cost estimated to be $200k. These pulses are then used as pump beams for the OPAs. The OPCPA system has a short pulse source at 2μm which is stretched to about 75μs, amplified in the OPAs and re-compressed before focusing onto a suitable target for generating the proton beam. Maximum bandwidth and efficiency for the OPCPA system is obtained using BBO as the nonlinear crystal and the predicted re-compressed pulse duration is 30fs with efficiency 20%. Using F/2 focusing optics and assuming the beam is 1.5x diffraction limit gives an expected $I\lambda^2$ of $10^{20}W/cm^2\ \mu m^2$ with an average power of 200W, as required.

Summary

Optical parametric amplifiers have attractive possibilities in applications requiring high average power, high peak power or a combination of the two. One immediate prospect is a laser system for PET scanning and a scheme is proposed to meet the requirements of this application. It is expected that the technique can be scaled to still higher power and intensity.

LaNSA project: Filling process for BC505 liquid scintillator

K L Lancaster, H Habara, P Norreys, J Govans, C Cornish, A Jackson, T Strange

Central Laser Facility, CLRC Rutherford Appleton Laboratory, Chilton, Didcot, Oxon, OX11 0QX, UK

G Mant

Lawrence Livermore national Laboratory, Livermore, California, USA

Main contact email address: *K.L.Lancaster@rl.ac.uk*

Introduction

The Large area Neutron Scintillator Array, LaNSA, is a highly sensitive 800-element neutron detection system for high intensity Laser-plasma interactions. The instrument gathers time of flight data to produce neutron energy spectra.

A single LaNSA module consists of 16 photomultiplier tubes optically coupled to 16 Aluminium compartments containing a 'proton knock-on' liquid scintillator. The compartments are coated in a reflective paint to maximize the light input into the photomultiplier tubes. The scintillator fluid BC505 fluoresces in the blue region of the visible spectrum.

The modules are filled with the liquid scintillator in a precise way using a custom made filling system to prevent wastage and contamination of the BC505.

Method of filling

The custom made filling station consists of a large tank connected to a system of valves to deposit the fluid. A fill line is used to transfer the fluid to the tank. Argon and Nitrogen lines are connected to the tank via regulators set at 2 psi. The station can fill three modules simultaneously via gravitational fill.

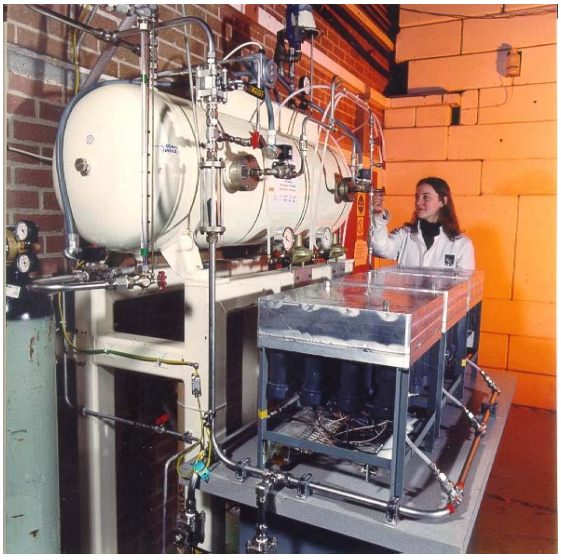

Figure 1. The filling rig in R2 with three modules attached.

The scintillator liquid was introduced into the main tank via a pump mechanism. Once the liquid was added to the tank it was bubbled through with nitrogen to remove any air for 1.5 hours.

The modules were secured via swagelok fittings to the fill header and the fill and vent valves on the modules were opened. The modules were purged with argon to remove air and condensation for 5 minutes before filling with liquid. The liquid was then allowed to flow into the module via the fill header until no bubbles emerged from the vent valve on the module. Underneath the rear legs of the module shims were placed to introduce a small argon layer into the compartments. This acts as an expansion region for the fluid if the temperature changes, to prevent damage.

Once the modules were filled, the fill and vent valves were closed, and the modules were disconnected from the headers. Filled modules were then installed straight into three frames designed to be installed into Vulcan Target Area West and the Petawatt target area.

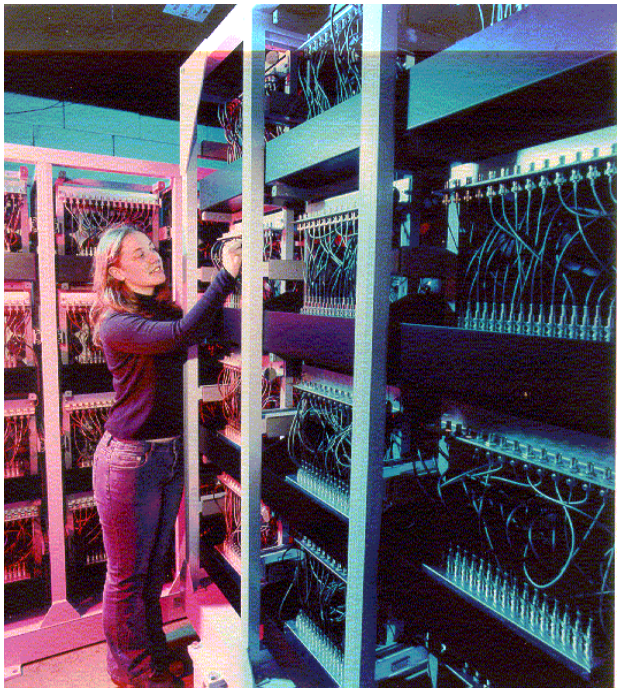

Figure 2. The modules installed into the arrays for testing in building R2.

Acknowledgements

The custom made filling station was constructed by G.Mant at Lawrence Livermore National Laboratory. G.Mant also provided assistance in the reconstruction of the filling station at RAL.

References

1. Notes on filling procedures - G. Mant, private communication.

Neutron Spectroscopy with Large Area TIME-of-FLIGHT Detector Array

H Habara, K L Lancaster, P A Norreys

Central Laser Facility, CLRC Rutherford Appleton Laboratory, Chilton, Didcot, Oxon, OX11 0QX, UK

Main contact email address: *H.Habara@rl.ac.uk*

Introduction

Recent developments in high power lasers have allowed the study of new regimes of laser-matter interactions relevant to astrophysics[1)], nuclear physics[2)], and fusion energy research[3,4)]. In the context of inertial fusion energy research, the 'fast ignitor' (FI) concept[5)] was proposed in order to relax the strict conditions for ignition in terms of plasma instability injecting an energy driver such as fast electrons and ions. It is therefore important for FI to understand how to accelerate the electrons and ions generated in ultra-intense laser-plasma interactions and also how the particles propagate into the super-critical.

There have already been many reports in both simulation and experiment that demonstrate a number of different acceleration mechanisms. Some of these suggest the acceleration strongly depends upon the laser and the plasma conditions, such as the laser polarization, intensity and the density scale-length[6)]. In particular, recent simulations predict that the energy of the accelerated ions suddenly increases with higher laser intensity and that the ion acceleration direction is changed from the longitudinal (or laser) direction to the transverse direction as plasma density scale-length is increased[7)]. Therefore, measurement of the accelerated ion momentum distribution helps us to understand the laser-plasma interactions under various controlled conditions.

Neutron spectroscopy is one of the most fascinating methods to investigate the accelerated ion distribution processes generated by ultra-intense laser-plasma interactions (using beam-fusion neutron spectroscopy)[8,9)]. For this purpose, we are re-constructing the multi-channel neutron spectrometer, LaNSA[10,11)]. The system records the timing when the neutrons are detected at each scintillator in the array. These timings are converted into neutron spectrum via the time-of-flight (TOF) method. Neutron energy spectra taken at several different directions can then be used to determine the momentum distribution of the accelerated ions by taking into account the Doppler shifts of neutron spectra from 2.45MeV for each viewing angle. In this paper, we discuss the re-commissioning of the LaNSA system and the future experiments that are planned for the RAL PW laser system.

Neutron Spectroscopy

Usually in measuring the ion momentum distribution, direct observation of ions with plastic nuclear track detectors such as a CR-39 was used. However, the ion motion is likely to be strongly affected by large electric and/or magnetic fields in the plasma. Neutron spectroscopy, on the other hand, has the advantage that neither the target potential nor the self-generated magnetic fields can affect the motion of neutrons generated in the target. Unfortunately, the measurement of the neutron spectrum from just one direction does not give us the three-dimensional ion momentum distribution. It is necessary to measure the neutron spectra from at least two different directions to obtain the ion momentum distribution in the target.

Figure 1 shows an example of neutron spectra generated by beam-fusion nuclear reactions from three different viewing angles. The s-polarized, 1μm laser light was obliquely incident onto a CD 5μm target from 40 degrees from target normal at an intensity of 10^{19}W/cm^2. The solid lines in all figures show the observed neutron spectra.

Figure 1(a) shows experimental spectra at three observation angles: 90° or parallel to the target surface (solid line), 56° (dashed line) and 1° (dotted line) to the target normal, respectively. The peak of the spectra from the front side of the target shifts to lower energy (2.2MeV at 56°, 1.9MeV at 1°) from 2.45 MeV given by D-D thermal neutron energy while there is almost no shift in the spectra along the target surface direction (solid line). These shifts suggest that ions are accelerated into the target inside taking account of the momentum conservation, which is similar to a Doppler effect on the neutron spectra. To investigate the precise momentum distribution of the ions, we performed 3D Monte-Carlo simulations to compare the calculated spectra with the experimental results. Figure 1(b) shows the well fitted calculated spectra at the same viewing angle as the experiments, which indicates that the ions are accelerated into the target, exactly opposite to the target normal direction. The ion distribution is shown in Figure 1(c) as a contour plot projected on the x-y plane from the 3-D distribution. The distribution collimation in the target rear direction is given as a momentum ratio of P_x:P_y:P_z=2.3:1:1. The ion energy to the x-direction corresponding to the direction into the target is 330keV whereas the energy to the y and z-direction is about 70keV.

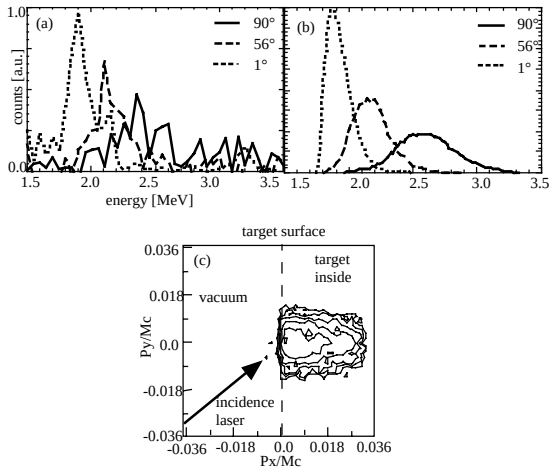

Figure 1. An example of (a) neutron spectra, (b) well-fitted calculated spectra (same energy units) and (c) the well-fitted ion momentum. distribution.

Large area Neutron Spectroscopy Array (LaNSA)

The neutron detector that we are re-constructing for the next generation experiments is the multi-channel spectrometer, LaNSA[10,11)], which originally consisted of 960 channels of scintillator-photo-multiplier detectors. In order to measure the neutron angular distribution, these modules will be divided into three separate units, each of which has 240 channels. The neutron detectors consist of an array of Thorn-EMI9902KB05 photo-multipliers coupled to BC505 liquid scintillator. The electrical signals are delivered to a Time-Digital-Converter (TDC), which records the arrival time of the signal via a discriminator. These timings are collected and then converted into a neutron spectrum through the time-of-flight (TOF) method. The data acquisition of the system is based on a PC to control all CAMAC and Fastbus modules.

These three modules will be positioned in target area PetaWatt (TAP) and target area west (TAW) of the Vulcan laser facility at the Rutherford Appleton Laboratory. Figure 2 shows a schematic image of the neutron array for one spectrometer in

TAP together with an overview of the setup for PW laser and the neutron spectrometers. An image of chamber and the module at TAW is also shown in Figure 3. The neutron detector modules are represented by a yellow box and the neutron flow is given by the green gimlet area in both images. The distance between the two modules and the chamber centre in TAP is about 12m and 5m. The distance of the array in TAW is about 8m from the chamber centre.

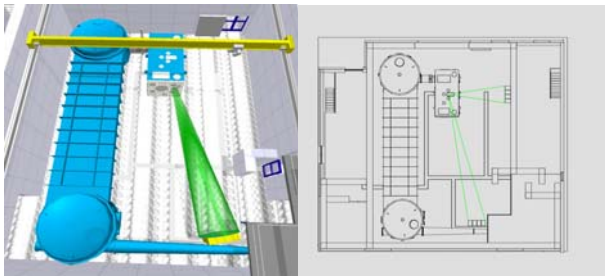

Figure 2. Image for one module at PW laser chamber room (TAP) and overview of PW laser and the neutron spectrometers**.**

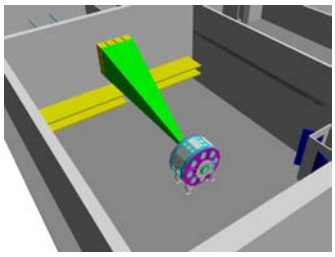

Figure 3. Image of neutron detection at TAW.

The energy resolution for each module as a function of distance from the target is shown in Figure 4 for different neutron energies. The shorter the distance between the spectrometer and the focal position, the worse the energy resolution of the neutron spectrum becomes. For example, at 5m distance, the module has 300keV of energy resolution for 2.45MeV neutrons, whereas there is only 800keV resolution for 14MeV neutrons. On the other hand, at 12m distances, the energy resolution of the module becomes much smaller (100keV for 2.45MeV neutron and 350keV for 14MeV neutron). Therefore, the module that is nearest the target will be set up so that it views an angle that is perpendicular to the expected ion acceleration direction. By adjusting the target rotation and the incident laser direction, the energy resolution of both modules can remain at a comparably low level. On the other hand, the dynamic range to detect the neutrons can be set by adjusting the voltage of the photo-multipliers and the discriminator threshold.

Summary

Using these neutron spectrometers, we plan experiments to measure the ion acceleration distribution for incident intensities up to 10^{21} Wcm^{-2}. It will be possible to change plasma density to determine the effect of scale-length on the ion acceleration mechanisms. Measurement of neutron spectra generated by a number of different nuclear fusion reactions has other interesting applications. In particular, B-D and Li-D reactions generate higher energy neutrons and have higher energy cross sections than those of the DD reaction - this may lead to the simultaneous observation of the high energy part of the ion momentum distribution.

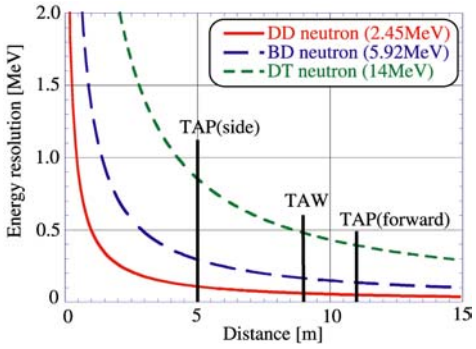

Figure 4. Energy resolution for different neutron energies as a function of the distance between the spectrometer and laser focal position.

Acknowledgements

The work is supported by the UK Engineering and Physical Science Research Council. The LaNSA array is on loan from the U.S. Department of Energy to the UK Ministry of Defence.

References

1. B A Remington, D Arnet, R P Drake and H Takabe
Science, 284 1488, (1999)
2. E P Liang, S C Wilks and M Tabak
Phys. Rev. Lett., 81 4887, (1998)
3. J Nuckolls, L Wood, Z Thiessen, and G Zimmerman
Nature, 239 139, (1972)
4. J. Lindl, R. L. McCrory, and E. M. Campbell
Phys. Today**,** 45 32, (1992)
5. M Tabak *et al.*,
Phys. Plasmas, 1 1626, (1994)
6. M I K Santala *et al.*
Phys. Rev. Lett., 84 1459, (2000)
7. C Toupin, E Levebvre and G Bonnaud
Phys. of Plasmas, 8 1011, (2001)
8. P A Norreys *et al.*
Plasma Phys. Control. Fusion, 40 175, (1998)
9. H Habara *et al*
Proceedings of SPIE, 3886 513, (2000)
10. M D Cable, S P Hatchett and M B Nelson
Rev. Sci. Instrum., 63 4823, (1992)
11. M B.Nelson and M D Cable,
Rev. Sci. Instrum., 63 4874, (1992)

Schedules and Operational Statistics

1) **Vulcan**
2) **Astra**
3) **Lasers for Science Facility**

Vulcan Operational Statistics

A Kidd, T Boland, C Danson

Central Laser Facility, CLRC Rutherford Appleton Laboratory, Chilton, Didcot, Oxon. OX11 0QX, UK

Main contact email address *A.K.Kidd@rl.ac.uk*

Vulcan has completed an active experimental year, with 12 full experiments taking place between April 2001 and March 2002 in the two main target areas, East (TAE) and West (TAW). The period followed the Vulcan scheduled downtime to install the capacitor bank in preparation for the arrival of components from LLNL for the Petawatt upgrade. The schedule slipped by two weeks at the start of this period in order to complete capacitor bank testing.

Table 1 below shows the operational schedule for the year, and illustrates the shot rate statistics for each experiment. Numbers in parentheses indicate the total number of full energy laser shots delivered to target, followed by the number of these that failed.

The total number of full disc amplifier shots that have been fired this year is 1,029 with 94 of these failing to meet user requirements. The EPSRC Facility Access Agreement (FAA) requires Vulcan to be at least 90% reliable. The overall shot failure rate to target for the year is 9.1%. This compares with 4.6% during both 2000-2001 and 1999-2000 and 5.4% for the previous year. Analysis of the reasons for failure of the individual shots enables a breakdown of these causes into specific categories.

The FAA also requires that the laser system be available, during the four week periods of experimental data collection, from 09:00 to 17:00 hours, Monday to Thursday, and from 09:00 to 16:00 hours on Fridays (a total of 156 hours). The laser has not always met the startup target of 9:00 am but it has been common practice to operate the laser well beyond the standard contracted finish time on several days during the week and to operate during some weekends.

On average, Vulcan has been available for each experiment for approximately 118 hours during contracted hours and 164 hours overall. However, each experiment has also experienced an average of 5 hours of laser downtime.

Figure 1 (next page) shows the identified failure modes and their individual failure rates.

This information enables servicing and equipment refurbishment to be focused on the most serious sources of system downtime. Figure 1 shows the most serious causes of failed shots to be the 9mm amplifiers (36%), oscillators (23%) and timing (22%). Improvements to the system continue to be made by targeting the main causes of failure. The three main causes of failure for 2000-2001 were the oscillators (25%), energy low (unspecified) (16%) and the disk amplifiers (13%).

PERIOD	TAE	TAW
23 Apr – 3 June	GR/N36806 – *C Lewis* Non-linear XRL (83, 27)	GR/L79151 – *AE Dangor* Beat-wave (72, 3)
11 Jun – 22 Jul	GR/L72718 – *J Wark* Radiation transport (142, 10)	GR/M82936 – *K Krushelnick* Magnetic fields with CPA (116, 6)
30 Jul – 9 Sep	GR/R12626 – *N Woolsey* Astrophysics simulations (88, 14)	Euro – *M Koenig* Electron deposition with CPA (71, 2)
24 Sep – 4 Nov	GR/R09572 – *D Riley* X-ray scattering (64, 7)	GR/N36554 – *G Tallents* TW X-ray laser (81, 7)
12 Nov – 23 Dec	LLNL – *G Collins* Equation of state (73, 3)	GR/N33188 – *K Ledingham* Solid targets (63, 6)
14 Jan – 24 Feb	Direct Access – *D Riley* Thomson scattering with an X-ray laser (77, 9)	GR/M82936 – *K Krushelnick* Magnetic fields with CPA (99, 5)

Table 1. Experimental schedule for the period April 2001 – March 2002.

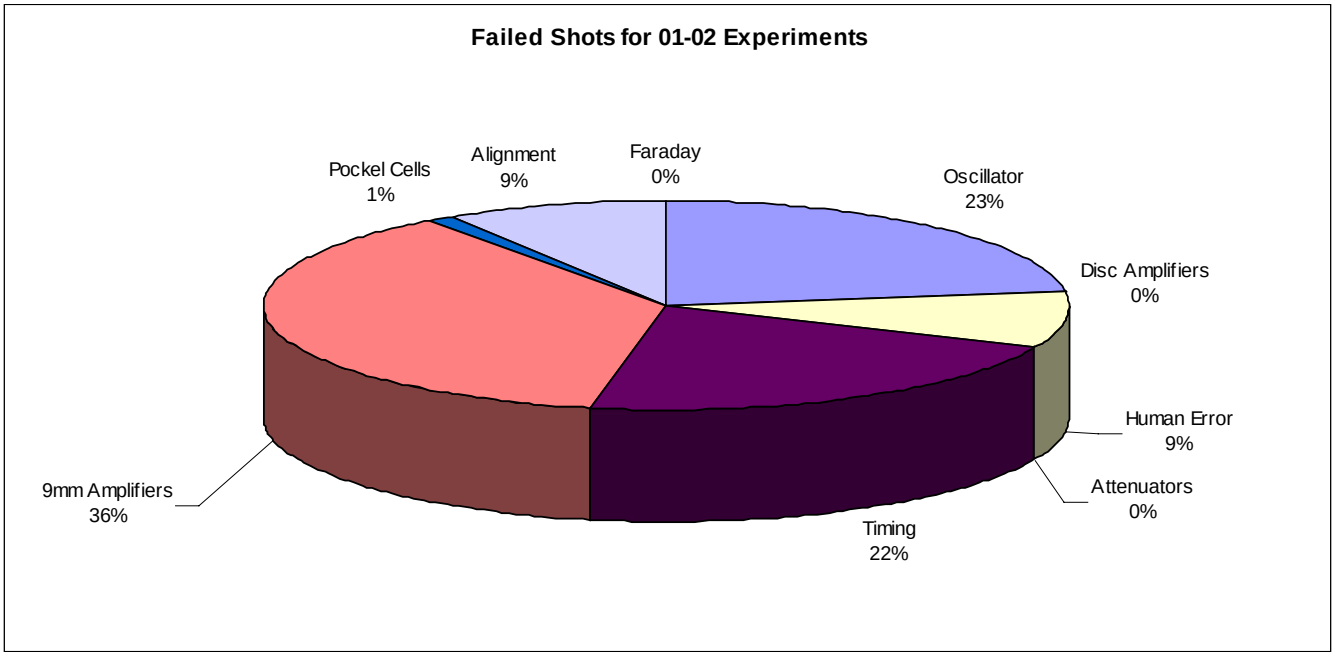

Figure 1. Analysis of Vulcan failure modes.

Astra Operational Statistics

A J Langley

Central Laser Facility, CLRC Rutherford Appleton Laboratory, Chilton, Didcot, Oxon., OX11 0QX, UK

Main contact email address: *A.J.Langley@rl.ac.uk*

A total of 30 scheduled experiment weeks were carried out with the Astra laser during the reporting period April 2001 to March 2002. The EPSRC sponsored 63 % of the experiments whilst the remainder were sponsored by the EU. All of the experiments were physics based.

The Astra laser was available for experiments for an average of 90 % of the time in normal daytime hours during scheduled experiments. In all experiments 100 % of daytime down-time was made up in out-of-hours working. Reliability defined as the time the laser was available as a percentage of the total time provided to scheduled experiments was 93 %.

We have had the opportunity to carry out about 10 weeks of laser optimisation this year. The details of the upgrades implemented in this time are described in detail elsewhere in this report.

In summary though we have improved the contrast ratio of the laser's 13 ns pre-pulse to 2 x 10^{-8} of the main pulse – an important improvement for all surface plasma experiments. A new TiS crystal was also installed during the year. The laser is now capable of providing over 1 J into target area. Partly due to diffraction grating inefficiencies, only 25-30% of this energy reaches target and it is the aim of next year's development work to install new and more efficient gratings.

Astra has proved itself to be an efficient and effective operational facility this year capable of delivering 5 TW pulses of 50 fs duration with focused intensities up to 10^{19} Wcm^{-2}. A suite of diagnostics are in place to support experiments – a single-shot autocorrelator to monitor pulse duration, laser energy, far and near-field detectors are in place to monitor the laser through the day. A third-order correlator is also available.

Date	Target Area 1 (ATA1)	Target Area 2 (ATA2)
2 Apr		Maintenance
9 Apr		
16 Apr		**Krushelnick** (IC) Wakefield studies
23 Apr		
30 Apr		
7 May		
14 May		
21 May		
28 May		**Krushelnick**
4 Jun		
11 Jun		
18 Jun		**Hooker** (Oxford) Capillary waveguides for driving short-wavelength lasers
25 Jun		
2 Jul		
9 Jul		
16 Jul		
23 Jul		
30 Jul		
6 Aug		**Riley** (QUB) Plasmon correlation studies
13 Aug		
20 Aug		
27 Aug		
3 Sep -24 Sep		System optimisation
1 Oct		
8 Oct		
15 Oct		**Ledingham** (Glasgow) Proton generation
22 Oct		
29 Oct		
5 Nov		
12 Nov – 31 Dec		System optimisation
7 Jan		Maintenance
14 Jan		
21 Jan		**Costello** (Dublin) X-ray spectroscopy
28 Jan		
4 Feb	**Mitchell** (University of Rennes) Laser ionisation studies of prepared ions	
11 Feb		
18 Feb		
25 Feb		
4 Mar		**Training**
11 Mar		
18 Mar		**Costello**
25 Mar		

Table 1. Astra Experiment Schedule 2001/2002.

LSF Operational Statistics

S M Tavender, M Towrie, A W Parker

Central Laser Facility, CLRC Rutherford Appleton Laboratory, Chilton, Didcot, Oxon., OX11 0QX, UK

Main contact email address *S.M.Tavender@rl.ac.uk*

RAL-based experiments

In the reporting period (April 2001 to March 2002), 21 different User groups performed a total of 54 experiments in the LSF laboratories at RAL. A total of 3814 hours laser time was scheduled throughout the year and 4348 hours delivered with only 186 hours downtime. Across the funding Councils the weeks scheduled were 80 to EPSRC, 3 to the MRC, 1 to BBSRC, 10 to Commercial Users and 14 to European Users giving 108 weeks delivered to the User community overall. Once again, a wide spread of disciplines was covered and a breakdown is shown in Figure 1 with the RAL-Based schedule Table 1. A total of 19 publications, 9 conference papers, and 2 PhD theses were published during the reporting year.

Loan Pool

The Loan Pool delivered 349 weeks of laser time in the reporting period. Downtime was 27 weeks and was mainly due to teething problems and misalignment of the new laser systems and the fluoride excimer being unallocated for 14 weeks. In the laser loans there were 5 groups new to the Loan Pool. The chemistry community was once again the biggest user with nearly 80% of allocated time but there were also applications for the cw lasers to study biological systems using LIF and confocal imaging. The breakdown is shown in Figure 2. The Loan Pool schedule is shown in Table 2. There was a total of 19 publications, 4 conference papers and 1 PhD theses published during the reporting year.

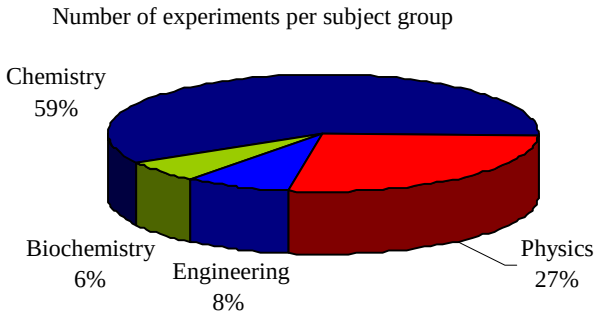

Figure 1. RAL-based experiments.

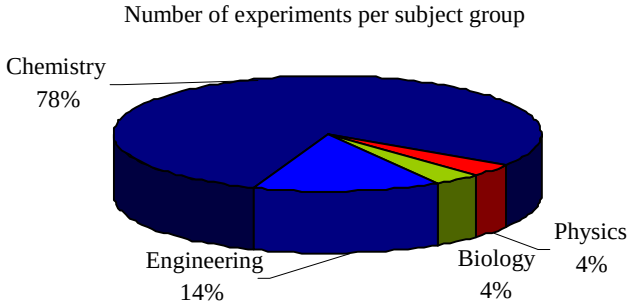

Figure 2. Loan Pool RAL-based experiments.

Table 1. LASERS *for* SCIENCE FACILITY RAL-BASED SCHEDULE: 2001-2

Date	Laser Microscope Laboratory	Nanosecond Science Laboratory	Ultrafast Spectroscopy Laboratory	X-Ray and UV Laboratory
02-Apr-01	MAINTENANCE	**D PHILLIPS** (IC) GR/L84001 NL1C1/01	**K REID** (Nottingham)	
09-Apr-01	**COMMERCIAL**		*Photoelectron angular distributions as*	MAINTENANCE
16-Apr-01			*a probe of intramolecular*	
23-Apr-01			*dynamical processes*	**COMMERCIAL** Q00/165
30-Apr-01			GR/M83759 US5C1/01	
07-May-01	**LSF USER MEETING AND WORKSHOP**			
14-May-01		**MAINTENANCE**	**P MATOUSEK** *Beam development* US3P1/01	**C WHARTON** (Birmingham)
21-May-01	**C WHARTON** (Birmingham)		**MAINTENANCE**	*Intracellular dynamics*
28-May-01	*Intracellular dynamics* GR/N19052 CM3P1/01		**A VLCEK** (QMWC) *Dynamics of*	GR/N19052 XU2P1/01
04-Jun-01			*organometallics* GR/N11414 US2C1/01	
11-Jun-01	**MAINTENANCE**		**D PHILLIPS** (Imperial College)	**H REEHAL** (SBU)
18-Jun-01	**K BRINDLE** (C'bridge) 8/E11895 CM2B1/01A		*Dynamics of Charge Transfer*	*TFCS Photovoltaics*
25-Jun-01	**COMMERCIAL**	MAINTENANCE	*Reactions* GR/L84001 US7C1/01	EPSRC ABT GR/N19052 XU2P1/01
02-Jul-01			**J J McGARVEY** (QUB) DNA Interactions	
09-Jul-01			GR/M45696 US1C1/01	**J CAIRNS** (Dundee) *Production*
16-Jul-01			**J KELLY** (Ireland)	*of X-ray masks* GR/M41223 XU1E1/01
23-Jul-01			*DNA photoxidation by Rhenium Carbonyl*	**COMMERCIAL** Q00/165

Date	Laser Microscope Laboratory	Nanosecond Science Laboratory	Ultrafast Spectroscopy Laboratory	X-Ray and UV Laboratory
30-Jul-01		**J MOORE** (York)	*Compounds*	
06-Aug-01		*Ns TR^3 spectroscopy of functional*	*USEV7C1/01*	
13-Aug-01		*(diimine) Re $(CO)_3$ complexes*	**M GEORGE (**Nottingham)	
20-Aug-01	**C WHARTON (**B'ham) *Multiphoton irradiation*	EPSRC ABT GR/R01316 NL2C1/01	P.I.R.A.T.E.	**C WHARTON (**B'ham) *Multiphoton irradiation*
27-Aug-01	*of cellular components to investigate*			*of cellular components to investigate*
03-Sep-01	*intra-cellular dynamics* GR/N19052 CM4P2/01		GR/M40486 US11C2/01	*intra-cellular dynamics* GR/N19052 XU2P2/01
10-Sep-01	MAINTENANCE	MAINTENANCE	**D PHILLIPS** (Imperial College)	
17-Sep-01			*Reorganisation Dynamics accompanying Charge*	
24-Sep-01	**A WARD** (CLF) *Characterisation of*		*Transfer Reactions and relaxation*	MAINTENANCE
01-Oct-01	*Tweezers CM5P2/01 EPSRC DA*		GR/L84001 US10C2/01	
08-Oct-01	**R BISBY** E*xcitation of free radicals CM6B2/01*		**MAINTENANCE**	
15-Oct-01		**R BISBY** (Salford) NL6C2/01 EPSRC DA	**J McGARVEY** (QUB) *DNA Interactions*	**R De BRUIJN** (The Netherlands)
22-Oct-01			GR/M45696 US8C2/01	Dynamics of EUV emitting
29-Oct-01	**A WARD** Tweezer *Characterisation* CM5P2/01		**A VLCEK** (QMWC) *Organometallic complexes*	*micro-droplet plasmas*
05-Nov-01			GR/N11414 US9C2/01	XUEV25P2/01
12-Nov-01			**D STUFKENS** (The Netherlands)	**J CAIRNS** (Dundee) *Production*
19-Nov-01			*Metal-Metal bond splitting of*	*of X-ray masks* GR/M41223 XU5E2/01
26-Nov-01	**COMMERCIAL DTI SMART**	**M CHESTERS** (Nottingham)	*Os carbonyl clusters*	
03-Dec-01	**A WARD** Tweezer *Characterisation* CM5P2/01	*UV Resonance Raman Studies of*	USEV13C2/01	
10-Dec-01	**C WHARTON** (B'ham) GR/N19052 CM8P3/01	*Adsorbates on Metal Surfaces*	**M GEORGE (**Nottingham)	MAINTENANCE
17-Dec-01	COMMERCIAL DTI SMART	NL3C1/01 EPSRC DA	P.I.R.A.T.E.	
	XMAS/NEW YEAR			
07-Jan-02	MAINTENANCE		GR/M40486 US18C3/01	
14-Jan-02	**C WHARTON** (B'ham) GR/N19052 CM8P3/01		MAINTENANCE	**C WHARTON** (B'ham) GR/N19052 CM8P3/01
21-Jan-02		MAINTENANCE	**J McGARVEY** (QUB *DNA Interactions*)	
28-Jan-02	**COMMERCIAL**		GR/M45696 US15C3/01	**J CAIRNS** *X-ray masks* GR/M41223 XU9E3/01
04-Feb-02	**COMMERCIAL DTI SMART**	**E TUITE** *(Newcastle) DNA damage*	**A VLCEK** (QMWC) *Photochemical dynamics*	
11-Feb-02			*of organometallic complexes* GR/N11414 / US16C3/01	**P O'NEILL** (MRC) *Energy dependence*
18-Feb-02			**S SCHNEIDER** *Photophysical processes in*	*for the induction of base damage in DNA*
25-Feb-02	**S FAULKNER** CM7C3/01 *Macrophage Luminescence*	**D PHILLIPS** (IC) *Dynamics of charge*	*organic electron donor-acceptor systems*	*by low energy photons* XU8B3/01
04-Mar-02		*Transfer* GR/R29062/ NL7C3/01	**K REID** (Nottingham)	
11-Mar-02			*Photoelectron angular distributions as a*	**A MICHETTE** (Kings)
18-Mar-02			*probe of intramolecular dynamical processes*	*Development of the laboratory scanning x-ray*
25-Mar-02			GR/M83759 US17C3/01	*microscope* GR/N28061/01 XU7P3/01

Table 2. LASERS *for* SCIENCE FACILITY LOAN POOL SCHEDULE: 2001-2

Date	NSL1 POWERLITE/ SIRAH + DFG	NSL2 SURELITE III-10/SIRAH	NSL3 SURELITE III-10/ SIRAH	NSL4 Continuum 8010/ND6000	NSL5 Fluoride Excimer	NSL6 Nd:YAG/ Dye/SHG	CWL2 VERDI/MIRA + SHG & THG	CW3 Frequency Doubled Argon Ion
Apr 2	**LACZIK**	**STACE**	**REID**	**SMITH**		**SIMONS**	**LINFIELD**	**LEGGATT**
9	**(Oxford)**	Cluster Spectroscopy	**(Nottingham)**	**(Birmingham)**		**(Oxford)**	**(Cambridge)**	**(UMIST)**
16	LP22E3/00	in Helium			**UNALLOCATED**			
23		Nanodroplets	LP18C3/00	State-				
30		LP19C3/00		selected		Zwitterions in	Development	Nanometre
May 7	**BELMONT**			and state-		The gas phase	of an	Scale
14	**(Exeter)**	**SPECTRON/ PDL2 RETIRED**	**ALEXANDER**	to-state			all-optical	Photolithography
21	A study of the	**AWARDED TO WHEELER Leicester**	**(Edinburgh)**	rotational	**SERVICE**		high power	
28	shallow angle			energy	**AT**		terahertz	
Jun 4	scattering and	**STACE**	"Molecular	transfer	**RAL**		source	
11	Transmission	**(Sussex)**	Young's Slits":	in				
18	Characteristics in		understanding	$OH(X^2\Pi)$		LP6C1/01	LP21P3/00	
25	the sea's **INSTALL/**	NO Rydberg	interference in					
Jul 2	Near **COMMISS-IONING**	Spectroscopy	dissociation					LP23C3/00
9	Surface **Powerlite**	in Helium	dynamics	LP3C1/01		**SIMONS**	**INSTALLATION/**	
16	Volume **Sirah+**	Nanodroplets				**(Oxford)**	**COMMISSIONING**	
23	**DFG**				**SUN**		**Verdi/ MIRA**	**LEGGATT**
30	**McK'RICK**	**Surelite**		**SMITH**	**(City)**		**+ SHG & THG**	**(UMIST)**
Aug 6	**Herriot-Watt)**	**Installation**		**(Birmingham)**			**TAYLOR**	
13	LP1E1/01				Fabrication of		**(IC)**	
20	**GCR11 RETIRED**		LP5C1/01	State-	Bragg gratings	Structure and		
27	**AWARDED TO**			selected	using high pulsed	conformation of	Spectroscopic	Nanometre
Sept 3	**MACKENZIE**	LP4C1/01		and state-	laser power	adrenaline and	and dynamic	Scale
10	**(Warwick)** Dynamics		**SPECTRON RETIRED**	to-state	in rare-earth	noradrenaline	SHG studies of	Photolithography
17	of the		**AWARDED TO COSTEN (H'Watt)**	rotational	doped optical		the	LP11C2/01
24	Reaction of			energy	fibre, for		electrochemical	
Oct 1	$O(^3P)$	**STACE**		transfer	sensing and		oxidation of	
8	with	**(Sussex)**	**SERVICE &**	in	communications		silicon	
15	Vibrationally		**REALIGNMENT**	$OH(X^2\Pi)$	applications	LP10C1/01		
22	Excited	Electronic	**GERMANY/**					
29	Methane	spectra	**RAL**		LP9E1/01			LP11C2/01
Nov 5		of benzene				**SIMONS**		
12		molecules		LP13C1/01		**(Oxford)**		
19		trapped					LP8B1/00	**CHESTERS**
26	LP2C1/01	in helium			**CRANTON**	An investigation		**(RAL/Nottingham)**
Dec 3		droplets		**SMITH**	**(NTU)**	of the IR and UV		UV Resonance
10				**(Birmingham)**		spectra of	**DEVONSHIRE**	Raman Studies
17	**McKENDRICK**		**FROST**			multiply	**(Sheffield)**	Adsorbates on
24	**(Herriot-Watt)**		**(Herriot-Watt)**	State-Selected	Laser processing	hydrated 4-		Metal Surfaces
31				State-to-State	of thin film	and 5-phenyl:		NL3C1/01
Jan 7		LP12C2/01		Rate	phosphors	imidazole		
14				Constants for	for flat	A model for	Novel Plasma	
21			REMPI-LIF	Inelastic and	screen displays	proton	Diagnostic	**LEGGATT**
28		**STACE**	studies of simple	Reactive		wires?	Techniques	**(UMIST)**
Feb 4	Dynamics of the	**(Sussex)**	ion-molecule	Collisions			which exploit the	
11	Reaction of $0(^3P)$	Electronic	Reactions	of $CN(X^2\Sigma)$		LP17C3/01	precise,	
18	with vibrationally	spectra					microscopic	Nanometre
25	excited methane	of benzene					scale, spatial	Scale
Mar 4		molecules			LP15E2/01	**SIMONS**	extent	Photolithography
11		trapped		LP16C3/01		**(Oxford)**	of fs laser pulses	
18		in helium						
25		droplets			**CRANTON**			

Publications

1) **High Power Laser Progamme - Vulcan Laser**
2) **High Power Laser Progamme - Astra Laser**
3) **Lasers for Science Facility Programme**
4) **Laser Science and Development**

High Power Laser Programme
Vulcan Laser

JOURNAL PUBLICATIONS, BOOKS AND PUBLISHED PROCEEDINGS

K M Aggarwal, F P Keenan, S J Rose
Electron impact excitation of Al XIII: collision strengths and rate coefficients
Proc X-Ray Lasers 2000, J de Phys IV 11 (Pr2) 309-312 (2001)

K M Aggarwal, P H Norrington, K L Bell, F P Keenan, G J Pert, S J Rose
Electron impact excitation of Gd XXXVII and radiative rates for Ni-like ions with $60 \leq Z \leq 90$
Proc X-Ray Lasers 2000, J de Phys IV 11 (Pr2) 313-316 (2001)

I R Al'Miev, S J Rose, J S Wark
Further simulations of the gain in a K XIX/Cl XVII resonantly photopumped X-ray laser
J Quant Spectr & Rad Trans 70 (1) 11-24 (2001)

D Batani, F Pisani, A Bernardinello, A Antonicci, F Amiranoff, M Koenig, E Martinolli, S Baton, T Hall, C Rousseaux, W Nazarov, PA Norreys, A Djaoui, D Neely
Fast electron transport in dense matter
Proc Int Conf Lasers 2000, 409-416, publ STS Press, McLean, VA, USA (2001)

A Bernardinello, D Batani, A Antonicci, F Pisani, M Koenig, L Gremillet, F Amiranoff, S Baton, E Martinolli, C Rousseaux, T A Hall, P Norreys, A Djaoui
Effects of self-generated electric and magnetic fields in laser-generated fast electron propagation in solid materials: Electric inhibition and beam pinching
Laser and Particle Beams 19 (1) 59-65 (2001)

G A Blair, J Frisch, K Honhavaara, T Kamps, F Poirier, I N Ross, M Ross, H Schlarb, P Schmuser, S Schreiber, D Sertore, N Walker, M Wendt, K Wittenburg
Proposing a laser based beam size monitor for the future linear collider
Proc 2001 Particle Accelerator Conference, vol 2, 1339-1341, publ IEEE, Piscataway, NJ, USA (2001)

M Borghesi, H D Campbell, M Galimberti, L A Gizzi, A J MacKinnon, W Nazarov, A Schiavi, O Willi
Propagation issues and fast particle source characterization in laser-plasma interactions at intensities exceeding 10^{19} W/cm^2
Proc SPIE 4424 414-417 (2001)

M Borghesi, D H Campbell, A Schiavi, H Gessner, O Willi, A J MacKinnon, P K Katel, R Snavely, S Hatchett, L A Gizzi, M Galimberti, R J Clarke, R Allott, S Hawkes, H Ruhl
Fast particle generation in ultra-intense interaction experiments and applications
Proc Int Conf Lasers 2000, 451-458, publ STS Press, McLean, VA, USA (2001)

M Borghesi, A Schiavi, D H Campbell, M G Haines, O Willi, A J MacKinnon, L A Gizzi, M Galimberti, R J Clarke, H Ruhl
Proton imaging: a diagnostic for inertial confinement fusion/fast ignitor studies
Plasma Physics & Controlled Fusion 43 (12A) A267-A276 (2001)

R D Edwards, M A Sinclair, T J Goldsack, K Krushelnick, F N Beg, E L Clark, A E Dangor, Z Najmudin, M Tatarakis, B Walton, M Zepf, K W D Ledingham, I Spencer, P A Norreys, R J Clarke, R Kodama, Y Toyama, M Tampo
Characterization of a gamma-ray source based on a laser-plasma accelerator with applications to radiography
Appl Phys Letts 80 (12) 2129-2131 (2002)

M Galimberti, A Giulietti, D Giulietti, L A Gizzi, M Borghesi, H D Campbell, A Schiavi, O Willi
Gamma-ray measurements in relativistic interactions with underdense plasmas
Proc SPIE 4424 512-515 (2001)

L A Gizzi, M Galimberti, A Giulietti, D Giulietti, P Tomassini, M Borghesi, D H Campbell, A Schiavi, O Willi
Relativistic laser interactions with preformed plasma channels and gamma-ray measurements
Laser & Particle Beams 19 (2) 181-186 (2001)

J Hawreliak, D Chambers, S Glenzer, R S Marjoribanks, M Notley, P Pinto, O Renner, P Sondhauss, R Steel, S Topping, E Wolfrum, P Young, J S Wark
A Thomson scattering post-processor for the MEDUSA hydrocode
J Quant Spectr & Rad Trans 71 (2-6) 383-395 (2001)

R Keenan, C L S Lewis, S J Topping, G J Tallents, F Strati, G J Pert, A Klisnick, D Ros, J Kuba, R Smith, P V Nickles, K A Janulewicz, F Bortolotto, A G MacPhee, R J Clarke, R Allott
Developments in X-ray laser pumping with travelling wave at Vulcan
Proc X-Ray Lasers 2000, J de Phys IV 11 (Pr2) 47-50 (2001)

R E King, G J Pert, S P McCabe, P A Simms, A G MacPhee, C L S Lewis, R Keenan, R M N O'Rourke, G J Tallents, S J Pestehe, F Strati, D Neely, R Allott
Saturated X-ray lasers at 196 and 73 Å pumped by a picosecond traveling-wave excitation
Phys Rev A 64 (5) 053810 (2001)

A Klisnick, J Kuba, D Ros, R Smith, P Fourcade, G Jamelot, J-L Miquel, J F Wyart, C Chenais-Popovics, R Keenan, S J Topping, C L S Lewis, F Strati, G J Tallents, D Neely, R Clarke, J Collier, A G MacPhee, F Bortolotto, P V Nickles, K A Janulewicz
Generation of a transient short pulse X-ray laser using a traveling-wave sub-ps pump pulse
Proc X-Ray Lasers 2000, J de Phys IV 11 (Pr2) 11-17 (2001)

A Klisnick, J Kuba, D Ros, R Smith, G Jamelot, C Chenais-Popovics, R Keenan, S J Topping, C L S Lewis, F Strati, G J Tallents, D Neely, R Clarke, J Collier, A G MacPhee, F Bortolotto, P V Nickels, K A Janulewicz
Demonstration of a 2-ps transient X-ray laser
Phys Rev A 65 (3) 033810 (2002)

R Kodama, P A Norreys, K Mima, A E Dangor, R G Evans, H Fujita, Y Kitagawa, K Krushelnick, T Miyakoshi, N Miyanaga, T Norimatsu, S J Rose, T Shozaki, K Shigemori, A Sunahara, M Tampo, K A Tanaka, Y Toyama, Y Yamanaka, M Zepf
Fast heating of ultrahigh-density plasma as a step towards laser fusion ignition
Nature 412 (6849) 798-802 (2001)

J Kuba, A Klisnick, D Ros, R Smith, G Jamelot, C Chenais Popovics, R Keenan, S J Topping, C L S Lewis, F Strati, G J Tallents, D Neely, A G MacPhee, R J Clarke, J Collier, P V Nickles, K A Janulewicz, F Bortolotto
Temporal resolution of a transient pumping X-ray laser
Proc X-Ray Lasers 2000, J de Phys IV 11 (Pr2) 43-46 (2001)

K W D Ledingham
From single ion to single pion
Proc 10th International Symposium on Laser ionization and Applications Incorporating RIS, AIP Conf Proc 584 67-72 (2001)

R W Lee, H A Baldis, R C Cauble, O L Landen, J S Wark, A Ng, S J Rose, C Lewis, D Riley, J-C Gauthier, P Audebert
Plasma-based studies on 4th generation light sources
Proc 19th Advanced ICFA beam Dynamics Workshop, AIP Conf Proc 581 45-58 (2001)

Z Najmudin, M Tatarakis, A Pukhov, E L Clark, R J Clarke, A E Dangor, J Faure, V Malka, D Neely, M I K Santala, K Krushelnick
Measurements of the inverse Faraday effect from relativistic laser interactions with an underdense plasma
Phys Rev Letts 87 (21) 215004 (2001)

G J Pert
X-ray lasers pumped by ultra-short light pulses
Proc X-Ray Lasers 2000, J de Phys IV 11 (Pr2) 181-187 (2001)

G J Pert
The transition from uni-directional to bi-directional behaviour in amplified spontaneous emission lasers
Opt Comm 191 (1-2) 113-23 (2001)

S J Pestehe, G J Tallents
A model for opacity measurements across expanding X-ray laser media
Proc X-Ray Lasers 2000, J de Phys IV 11 (Pr2) 333-336 (2001)

S J Pestehe, G J Tallents
Escape factors for laser-plasmas
J Quant Spectr & Rad Trans 72 (6) 853-878 (2002)

S J Rose
The radiative opacity at the Sun centre - a code comparison study
J Quant Spectr & Rad Trans 71 (2-6) 635-638 (2001)

I Spencer, K W D Ledingham, R P Singhal, T McCanny, E L Clark, K Krushelnick, M Zepf, F N Beg, M Tatarakis, C Escoda, M Norrefeldt, A E Dangor, P A Norreys, R J Clarke, R M Allott
High-intensity laser generation of proton beams for the production of β^+ sources used in positron emission tomography
Proc 10th International Symposium on Laser ionization and Applications Incorporating RIS, AIP Conf Proc 584 73-78 (2001)

I Spencer, K W D Ledingham, R P Singhal, T McCanny, P McKenna, E L Clark, K Krushelnick, M Zepf, F N Beg, M Tatarakis, A E Dangor, P A Norreys, R J Clarke, R M Allott, I N Ross
Laser generation of proton beams for the production of short-lived positron emitting radioisotopes
Nucl Instr & Meth in Phys Res B 183 (3-4) 449-458 (2001)

F Strati, G J Tallents
Group speed effects in saturated soft X-ray lasers in transient collisional excitation regime driven with travelling wave pumping
Proc X-Ray Lasers 2000, J de Phys IV 11 (Pr2) 297-300 (2001)

F Strati, G J Tallents
Analytical modeling of group-velocity effects in saturated soft-X-ray lasers pumped with a picosecond traveling-wave excitation
Phys Rev A 64 (1) 013807 (2001)

G J Tallents, F Strati, J Y Lin, R Smith, S J Pestehe, G J Pert, C L S Lewis, A G MacPhee, R Keenan
Short pulse pumped X-ray lasers
Proc X-Ray Lasers 2000, J de Phys IV 11 (Pr2) 59-66 (2001)

M Tatarakis, I Watts, F N Beg, E L Clark, A E Dangor, A Gopal, M G Haines, P A Norreys, U Wagner, M S Wei, M Zepf, K Krushelnick
Laser technology - Measuring huge magnetic fields
Nature 415 (6869) 280-280 (2002)

S J Topping, R Keenan, C L S Lewis, R M N O'Rourke, A G MacPhee, S Dobosz, G J Tallents, M Notley, D Neely
Progress in FWSD non-linear effects with XRLs
Proc X-Ray Lasers 2000, J de Phys IV 11 (Pr2) 487-490 (2001)

L M Upcraft, G J Pert
Computational modelling of a Ne-like-Ar collisionally pumped OFI X-ray laser
Proc X-Ray Lasers 2000, J de Phys IV 11 (Pr2) 205-208 (2001)

W Wei, J Zhang, S J Rose
Effects of the radiation field on the physical processes of laser-produced plasmas
Acta Physica Sinica 50 (8) 1517-1520 (2001)

O Willi, D H Campbell, A Schiavi, M Borghesi, M Galimberti, L A Gizzi, W Nazarov
Propagation of an ultra intense laser beam through underdense and overdense plasmas
Proc Int Conf Lasers 2000, 425-432, publ STS Press, McLean, VA, USA (2001)

E Wolfrum, A M Allen, I Al'Miev, T W Barbee, P D S Burnett, A Djaoui, C Iglesias, D H Kalantar, R W Lee, R Keenan, M H Key, C L S Lewis, A M Machacek, B A Remington, S J Rose, R O'Rourke, J S Wark
Measurements of the XUV mass absorption coefficient of an overdense liquid metal
J Phys B – At Mol Opt Phys 34 (17) L565-L570 (2001)

N C Woolsey, Y A Ali, R G Evans, R A D Grundy, S J Pestehe, P G Carolan, N J Conway, R O Dendy, P Helander, K G McClements, J G Kirk, P A Norreys, M M Notley, S J Rose
Collisionless shock and supernova remnant simulations on VULCAN
Physics of Plasmas 8 (5) 2439-2445 (2001)

N C Woolsey, Y Abou-Ali, R Evans, R A Grundy, S J Pestehe, P Carolan, N Conway, R O Dendy, P Helander, K G McClements, J G Kirk, P A Norreys, M M Notley, S J Rose
Supernova remnant simulation experiments on VULCAN
Proc SPIE 4424 484-491 (2001)

N C Woolsey, Y A Ali, R G Evans, R A D Grundy, S J Pestehe, P G Carolan, N J Conway, R O Dendy, P Helander, K G McClements, J G Kirk, P A Norreys, M Notley, S J Rose
Response to "Comment on 'Collisionless shock and supernova remnant simulations on VULCAN'" [Phys. Plasmas 9, 727 (2002)]
Physics of Plasmas 9 (2) 729-730 (2002)

M Zepf, E L Clark, K Krushelnick, F N Beg, C Escoda, A E Dangor, M I K Santala, M Tatarakis, I F Watts, P A Norreys, R J Clarke, J R Davies, M A Sinclair, R D Edwards, T J Goldsack, I Spencer, K W D Ledingham
Fast particle generation and energy transport in laser-solid interactions
Physics of Plasmas 8 5 2323-2330 (2001)

PUBLISHED DURING 2000/2001

C L S Lewis, G J Tallents
A review of Ni-like X-ray laser experiments undertaken using the VULCAN laser at the Rutherford Appleton Laboratory
Comptes Rendus Serie IV 1 (8) 1053-1065 (2000)

IN PRESS AT END OF 2001/2002

M Borghesi, S Bulanov, D H Campbell, R J Clarke, T Z Esirkepov, M Galimberti, L A Gizzi, A J MacKinnon, N M Naumova, F Pegoraro, H Ruhl, A Schiavi, O Willi
Macroscopic evidence of soliton formation in multiterawatt laser-plasma interaction
Phys Rev Letts 88 (13) 135002 (2002)

M Borghesi, D H Campbell, A Schiavi, M G Haines, O Willi, A J MacKinnon, P Patel, L A Gizzi, M Galimberti, R J Clarke, F Pegoraro, H Ruhl, S Bulanov
Electric field detection in laser-plasma interaction experiments via the proton imaging technique
Physics of Plasmas 9 (5) 2214-2220 (2002)

M Tatarakis, A Gopal, I Watts, F N Beg, A E Dangor, K Krushelnick, U Wagner, P A Norreys, E L Clark, M Zepf, R G Evans
Measurements of ultrastrong magnetic fields during relativistic laser-plasma interactions
Physics of Plasmas 9 (5) 2244-2250 (2002)

I Watts, M Zepf, E L Clark, M Tatarakis, K Krushelnick, A E Dangor, R M Allott, R J Clarke, D Neely, P A Norreys
Dynamics of the critical surface in high-intensity laser-solid interactions: Modulation of the XUV harmonic spectra
Phys Rev Letts 88 (15) 155001 (2002)

CONFERENCE PRESENTATIONS

OECD Global Science Forum Workshop on Compact High-Intensity Short-Pulse Lasers, Kyoto, Japan (May 2001)

K W D Ledingham
Nuclear physics with high intensity lasers

UK Workshop on Positron Physics and Applications, Swansea, UK (Jun 2001)

K W D Ledingham, P McKenna, I Spencer, R P Singhal, T McCanny, E L Clark, K Krushelnick, M Zepf, F N Beg, M Tatarakis, M-S Wei, A Gopal, A E Dangor, P A Norreys, R J Clarke, R M Allott, I N Ross
Laser-induced nuclear physics and applications

21st ICFA Beam Dynamics Workshop, Stony Brook, USA (Jun 2001)

P A Norreys
Vulcan PW laser, review on electron and ion acceleration and X-ray experiments in Europe

Euroconference on Advanced Diagnostics for Magnetic and Inertial Fusion, Varenna, Italy (Sept 2001)

M Borghesi
Imaging of plasmas using proton beams generated by ultra-intense laser pulses

P A Norreys, K L Lancaster, H Habara
Advanced concepts in fast ignition and the relevant diagnostics

2nd International Conference on Fusion Sciences and Applications, Kyoto, Japan (Sept 2001)

P M Celliers, G W Collins, D Hicks, L B Da Silva, A McKinnon, R Cauble, S J Moon, R J Wallace, B A Hammel, M Koenig, A Benuzzi, G Huser, E Henry, D Batani, I Masclet, B Marchet, M Rebec, Ch Reverdin, N Dague, O Willi, J Pasley, H Gessner, D Neely, M Notley, C Danson
Shock Hugoniot and optical measurements of strongly shocked water

G W Collins, P M Celliers, D Bradley, D Hicks, L B Da Silva, A McKinnon, R Cauble, S J Moon, H Baldis, W Hsing, B A Hammel, M Koenig, A Benuzzi, G Huser, R Jeanloz, K Lee, L R Benedetti, E Henry, D Batani, P Loubeyre, O Willi, J Pasley, H Gessner, D Neely, M Notley, C Danson
Recreating planetary cores with high intensity lasers

M H R Hutchinson
High power laser applications research in the EU

S Jacquemot, G Jamelot, E Fill, P Nickles, G Tallents, G Pert, C L S Lewis
The European X-ray laser network

M H Key, F Amiranoff, C Andersen, D Batani, S D Baton, T Cowan, N Fisch, R Freeman, L Gremillet, T Hall, S Hatchett, J Hill, J King, J Koch, M Koenig, B Lasinski, B Langdon, A MacKinnon, E Martinolli, P Norreys, P Parks, E Perelli-Cippo, M Rabec le Gloahec, M Rosenbluth, C Rousseaux, J J Santon, F Scianitti, R Snavely, R Stephens
Studies of energy transport by relativistic electrons in the context of fast ignition

Z Najmudin, K Krushelnick, A E Dangor, B Walton, A Gopal, U Wagner, S Fritzler, V Malka, R J Clarke
Studies on electron acceleration in plasmas at Rutherford Appleton Laboratories

P A Norreys, K Krushelnick, A E Dangor, M Tatarakis, E L Clark, M Zepf, K Ledingham
Relativistic laser-plasmas & fast ignition studies at the Rutherford Appleton Laboratory

J R Pasley, O Willi, A Iwase, W Nazarov
Tamping of indirectly-driven targets

O Renner, P K Patel, D M Chambers, S H Glenzer, R S Marjoribanks, J Hawreliak, E Wolfrum, J S Wark
Line reversal between components of the A1 Ly α doublet

A Schiavi, D H Campbell, O Willi, M Borghesi, H Ruhl
E-field structures and anomalous proton stopping in laser produced plasmas

K A Tanaka, R Kodama, Y Kitagawa, K Fujita, H Fujita, M Heya, N Izumi, T Jitsuno, K Mima, N Miyanaga, H Nishimura, T Norimatsu, Y Sentoku, K Shigemori, A Sunahara, S Akamatsu, T Matsusita, T Miyakoshi, F Otani, T Shozaki, M Tanpo, S Tohyama, T Yamanaka, P A Norreys, M Zepf
Review of fast ignition related research at ILE Osaka university

N C Woolsey, R O Dendy, R A D Grundy, J G Kirk, K G McClements, P Helander, P A Norreys, S J Rose
Collisionless shock experiments with applications to astrophysics

Euroconference on Short Pulse Superstrong Laser Plasma Interactions, San Feliu de Guixols, Spain (Sept-Oct 2001)

M Borghesi
Laser-generated protons and applications

R Grundy
Collisionless shock and supernova remnant simulations on Vulcan

P McKenna
Laser induced nuclear physics

P Norreys
Advanced geometries for fast ignition

J Pasley
Tamped ablation in indirectly driven target

G Tallents
Advancement in X-ray laser

N Woolsey
Collisionless shock experiments with application to astrophysics

43rd Annual Meeting of the APS Division of Plasma Physics, Los Angeles, USA (Nov 2001)

E Clark, M Zepf, F Beg, M Tatarakis, R Clarke, M Wei, A Gopal, U Wagner, A E Dangor, P A Norreys, K Krushelnick
Proton measurements from ultra intense laser plasma interactions

D G Hicks, P M Celliers, G W Collins, L B Da Silva, A J Mackinnon, R Cauble, S J Moon, R J Wallace, B A Hammel, M Koenig, A Benuzzi, G Huser, E Henry, D Batani, P Loubeyre, O Willi, J Pasley, H Gessner, R Jeanloz, K M Lee, L R Benedetti, D Neely, M M Notley, C Danson
Laser-driven shocks in water pre-compressed by diamond anvil cells

K Krushelnick, F N Beg, A Gopal, M Tatarakis, M-S Wei, E L Clark, A E Dangor, U Wagner, P A Norreys, M Zepf
Polarimetry measurements of high order harmonics from intense laser solid interactions

B R Walton, Z Najmudin, M-S Wei, C Marle, K Krushelnick, A E Dangor, R J Clarke, M J Poulter, C Hernandez-Gomez, S Hawkes, D Neely, C N Danson, J L Collier, S Fritzler, V Malka
Short pulse laser beatwave experiments using the VULCAN laser facility

4th International Conference on High Energy Density Laboratory Astrophysics, Ann Arbor, USA (Feb 2002)

P A Norreys, C Courtois, R A D Grundy, R O Dendy, R G Evans, P Helander, K G McClements, J G Kirk, J L Collier, M M Notley, N C Woolsey
Experimental studies of collisionless shocks with applications to astrophysics

P A Norreys, U Wagner, D Neely, R Clarke, M Tatarakis, I Watts, M Zepf, E Clark, M Haines, A E Dangor, K Krushelnick
Measurement of superstrong magnetic fields with PW lasers

29th Annual UK Plasma Physics Conference, Belfast, UK (Mar 2002)

M Borghesi
Point-projection probing with laser-produced protons

E Clark
Proton and ion acceleration in ultra intense laser plasma interactions

E L Clark, M Zepf, F N Beg, M Tatarakis, M Wei, A Gopal, U Wagner, A E Dangor, P A Norreys, K Krushelnick
Proton and ion acceleration in ultra intense laser plasma interactions

R Evans
Simulations of DC magnetic fields produced by ultra high intensity

A Gopal, M Tatarakis, F N Beg, E L Clark, A E Dangor, K W D Ledingham, P McKenna, P A Norreys, I Spencer, M-S Wei, M Zepf, K Krushelnick
Magnetic field measurements during high intensity short pulse laser solid target interactions

R Keenan, C L S Lewis, S J Topping, J S Wark, E Wolfrum
Development of X-ray lasers for radiogrphic applications

D Riley, C Lewis, F Khattak, R Keenan, S Topping, A McEvoy, J Angulo
X-ray laserThomson scattering

S J Topping, R Keenan, C L S Lewis, R O'Rourke, S Dobosz
FWSD non-linear effects with XRLs in a gas jet plasma

M Wei, F N Beg, E L Clark, A E Dangor, A Gopal, K W D Ledingham, P McKenna, P A Norreys, I Spencer, M Tatarakis, M Zepf, K Krushelnick
Study of electron and proton beam generation from double side illumination of solid targets with high intensity laser pulses

M Zepf, R Kodama, P A Norreys, K Mima, A E Dangor, R G Evans, H Fujita, Y Kitagawa, K Krushelnick, T Miyagoshi, N Miyanaga, T Norimatsu, S J Rose, T Shozaki, K Shigemori, A Sunahara, M Tampo, K A Tanaka, Y Toyama, T Yamanaka
CPA laser heating of cone guided implosion targets

THESES

J Pestehe
Spectroscopy of X-ray laser media
Ph D, University of York

I Spencer
Laser induced nuclear physics
Ph D, University of Glasgow

F Strati
Experimental and theoretical characterisation of short pulse X-ray lasers
Ph D, University of York

High Power Laser Programme – Astra Laser

JOURNAL PUBLICATIONS, BOOKS AND PUBLISHED PROCEEDINGS

A A A El-Zein, P McKenna, W A Bryan, I M G Johnston, T R J Goodworth, J H Sanderson, I D Williams, W R Newell, P F Taday, E J Divall, A J Langley
A detailed study of multiply charged ion production within a high intensity laser focus
Proc 10th International Conferecnce on the Physics of Highly Charged Ions, Physica Scripta T92 119-121 (2001)

P Graham, K W D Ledingham, R P Singhal, S M Hankin, T McCanny, X Fang, C Kosmidis, P Tzallas, P F Taday, A J Langley
On the fragment ion angular distributions arising from the tetrahedral molecule CH_3I
J Phys B – At Mol Opt Phys 34 (20) 4015-4026 (2001)

P Graham, K W D Ledingham, R P Singhal, S M Hankin, T McCanny, X Fang, P F Taday, A J Langley, C Kosmidis
Angular distributions of fragment ions arising from tetrahedral CH_3I and isomer identification using intense laser fields
Laser and Particle Beams 19 (2) 187-193 (2001)

S M Hankin, L Robson, A D Tasker, K W D Ledingham, T McCanny, R P Singhal, C Kosmidis, P Tzallas, A J Langley, P F Taday, E J Divall
Ultrafast laser time-of-flight mass analysis of laser-desorbed atoms and molecules
Proc 10th International Symposium on Laser ionization and Applications Incorporating RIS, AIP Conf Proc 584 14-19 (2001)

L Robson, A D Tasker, S M Hankin, K W D Ledingham, R P Singhal, X Fang, T McCanny, C Kosmidis, P Tzallas, A J Langley, P F Taday, E J Divall
Analysis of polycyclic aromatic hydrocarbons (PAHs) using nanosecond laser desorption/femtosecond ionization laser mass spectrometry (FLMS)
Proc 10th International Symposium on Laser ionization and Applications Incorporating RIS, AIP Conf Proc 584 291-296 (2001)

D J Spence, A Butler, S M Hooker
First demonstration of guiding of high-intensity laser pulses in a hydrogen-filled capillary discharge waveguide
J Phys B - At Mol Opt Phys 34 (21) 4103-4112 (2001)

D J Spence, A Butler, S M Hooker
Investigation of a novel hydrogen plasma waveguide for high-intensity laser pulses
Proc Applications of High-Field and Short Wavelength Sources IX, OSA Trends in Optics & Photonics 65 TuE21 (2001)

A D Tasker, L Robson, S M Hankin, K W D Ledingham, R P Singhal, X Fang, T McCanny, C Kosmidis, P Tzallas, A J Langley, P F Taday, E J Divall
Ultrafast laser analysis of nitro-PAHs using laser desorption/femtosecond ionization mass spectrometry
Laser and Particle Beams 19 (2) 205-208 (2001)

P Tzallas, C Kosmidis, J G Philis, K W D Ledingham, T McCanny, R P Singhal, S M Hankin, P F Taday, A J Langley
Ionization/dissociation of thiazole and thiazolidine induced by strong laser fields
Chem Phys Letts 343 (1-2) 91-98 (2001)

I D Williams, P McKenna, B Srigengan, I M G Johnston, W A Bryan, J H Sanderson, A El-Zein, T R J Goodworth, W R Newell, P F Taday, A J Langley
Intense laser field studies of positive ions
Proc 16th International Conference on Application of Accelerators in Research & Industry, AIP Conf Proc 576 44-47 (2001)

IN PRESS AT END OF 2001/2002

J B Greenwood, I M G Johnston, P McKenna, I D Williams, T R J Goodworth, J H Sanderson, W A Bryan, A A A El-Zein, W R Newell, A J Langley, E J Divall
Suppression of multiple ionization of atomic ions in intense ultrafast laser pulses
Phys Rev Letts 88 (23) 233001 (2002)

J H Sanderson, T R J Goodworth, A El-Zein, W A Bryan, W R Newell, A J Langley, P F Taday
Coulombic and pre-Coulombic geometry evolution of carbonyl sulfide in an intense femtosecond laser pulse, determined by momentum imaging
Phys Rev A 65 (4) 043403 part B (2002)

CONFERENCE PRESENTATIONS

221st American Chemical Society National Meeting, San Diego, USA (Apr 2001)

K W D Ledingham, A D Tasker, L Robson, S M Hankin, R P Singhal, P McKenna, X Fang, T McCanny, C Kosmidis, P Tzallas, A J Langley, P F Taday, E J Divall
Intense laser irradiation of molecules

CLEO/Europe-EQEC Focus Meeting, Munich, Germany (Jun 2001)

K Osvay, G Kurdi, J Klebniczki, M Csatári, I N Ross, E J Divall, C J Hooker, A J Langley
Noncollinear optical paramteric amplification of femtosecond UV pulses

Workshop on 2nd Generation Laser & Plasma Accelerators, Presqu'ile de Giens, France (Jun 2001)

D J Spence, A Butler, S M Hooker
Guiding of high-intensity laser pulses in a hydrogen-filled capillary discharge

D J Spence, S M Hooker
Investigation of a hydrogen plasma waveguide

Ultrafast Optics 2001, Montebello, Canada (Jul 2001)

K Osvay, G Kurdi, J Klebniczki, M Csatári, I N Ross, E J Divall, C J Hooker, A J Langley
Broadband amplification of ultraviolet laser pulses

Applications of High Field and Short Wavelength Sources IX, Palm Springs, USA (Oct 2001)

D J Spence, A Butler, S M Hooker
Investigation of a novel hydrogen plasma waveguide for high-intensity laser pulses

12th Conference on Ultrafast Processes in Spectroscopy, Florence, Italy (Oct-Nov 2001)

K Osvay, G Kurdi, J Klebniczki, M Csatári, I N Ross
Optical parametric amplification of femtosecond laser pulses at 400 nm

Science of Superstrong Laser Interactions, Hayama, Japan (Mar 2002)

K W D Ledingham, P McKenna, I Spencer, R P Singhal, T McCanny, E L Clark, K Krushelnick, M Zepf, F N Beg, M Tatarakis, M-S Wei, A Gopal, A E Dangor, P A Norreys, R J Clarke, R M Allott, I N Ross
Laser induced nuclear physics

15th Dutch Physical Society Symposium on Plasma Physics and Radiation Technology, Lunteren, The Netherlands (Mar 2002)

S M Hooker, A Butler, A J Gonsalves, C M McKenna
The hydrogen-filled capillary discharge waveguide

29th Annual UK Plasma Physics Conference, Belfast, UK (Mar 2002)

C Ziener, P S Foster, E J Divall, C J Hooker, M H R Hutchinson, A J Langley, D Neely
Specular reflectivity of plasma mirrors as a function of intensity, pulse duration and angle of incidence

Lasers for Science Facility Programme

JOURNAL PUBLICATIONS, BOOKS AND PUBLISHED PROCEEDINGS

S Ameer-Beg, S M Ormson, R G Brown, P Matousek, M Towrie, E T J Nibbering, P Foggi, F V R Neuwahl
Ultrafast measurements of excited state intramolecular proton transfer (ESIPT) in room temperature solutions of 3-hydroxyflavone and derivatives
J Phys Chem A 105 (15) 3709-3718 (2001)

S W Botchway, I Barba, K Brindle, A W Parker
Development of a time correlated single photon counting multiphoton laser scanning confocal microscope – studies in biological fluorescence lifetime imaging
9th European Conference on the Spectroscopy of Biological Molecules, Eds V Kopecky, K Ruszova, J Stepanek, vol 2, 158, ISBN 80-238-7356-3, Charles University, Prague (2001)

C G Coates, P Callaghan, J J McGarvey, J M Kelly, L Jacquet, A Kirsch-De Mesmaeker
Spectroscopic studies of structurally similar DNA-binding ruthenium (II) complexes containing the dipyridophenazine ligand
J Molec Struct 598 (1) 15-25 (2001)

C G Coates, J Olofsson, M Coletti, J J McGarvey, B Onfelt, P Lincoln, B Norden, E Tuite, P Matousek, A W Parker
Picosecond time-resolved resonance Raman probing of the light-switch states of $[Ru(Phen)_2dppz]^{2+}$
J Phys Chem B 105 (50) 12653-12664 (2001)

J P Connelly, S W Botchway, L Kunz, D Pattison, A W Parker, A J MacRobert
Time-resolved fluorescence imaging of photosensitiser distributions in mammalian cells using a picosecond laser line-scanning microscope
J Photochem Photobiol A – Chem 142 (2-3) 169-175 (2001)

N Everall, T Hahn, P Matousek, A W Parker, M Towrie
Picosecond time-resolved Raman spectroscopy of solids: capabilities and limitations for fluorescence rejection and the influence of diffuse reflectance
Appl Spectr 55 (12) 1701-1708 (2001)

W M Kwok, I Gould, C Ma, M Puranik, S Umapathy, P Matousek, A W Parker, D Phillips, W T Toner, M Towrie
Vibrational studies of ground state 4-dimethylaminobenzonitrile (DMABN) and its ring deuterated isotopomer DMABN-d_4
Phys Chem Chem Phys 3 (12) 2424-2432 (2001)

W M Kwok, C Ma, A W Parker, D Phillips, M Towrie, P Matousek, X Zheng, D L Phillips
Picosecond time-resolved resonance Raman observation of the iso-CH_2Cl-I and iso-CH_2I-Cl photoproducts from the "photoisomerization" reactions of CH_2ICl in the solution phase
J Chem Phys 114 (17) 7536-7543 (2001)

W M Kwok, C Ma, D Phillips, A W Parker, M Towrie, P Matousek, D L Phillips
Picosecond time-resolved resonance Raman observation of iso-CH_2Br-I following A-band photodissociation of CH_2BrI in the solution phase
Chem Phys Letts 341 (3-4) 292-298 (2001)

C Ma, W M Kwok, P Matousek, A W Parker, D Phillips, W T Toner, M Towrie
Resonance Raman study of ring deuterated 4-dimethylaminobenzonitrile (DMABN-d_4): the ground, ICT and triplet states
J Photochem Photobiol A – Chem 142 (2-3) 177-185 (2001)

C Ma, W M Kwok, P Matousek, A W Parker, D Phillips, W T Toner, M Towrie
Time-resolved study of the triplet state of 4-dimethylaminobenzonitrile (DMABN)
J Phys Chem A 105 (19) 4648-4652 (2001)

A Malnasi-Csizmadia, M Kovacs, R J Woolley, S W Botchway, C R Bagshaw
The dynamics of the relay loop tryptophan residue in the Dictyostelium myosin motor domain and the origin of spectroscopic signals
J Biol Chem 276 (22) 19483-19490 (2001)

P O'Neill, A W Parker, M A Plumb, L D A Siebbeles
Guanine modification following ionisation of DNA occurs predominantly via intra- not interstrand charge migration: An experimental and theoretical study
J Phys Chem B 105 (22) 5283-5290 (2001)

S Schneider, J Kurzawa, A Stockmann, R Engl, J Daub, P Matousek, M Towrie
Photoinduced electron transfer in phenothiazine and pyrene based dyades studied by picosecond time-gated Raman spectroscopy
Chem Phys Letts 348 (3-4) 277-284 (2001)

L C Snoek, R T Kroemer, M R Hockridge, J P Simons
Conformational landscapes of aromatic amino acids in the gas phase: infrared and ultraviolet ion dip spectroscopy of tryptophan
Phys Chem Chem Phys 3 (10) 1819-1826 (2001)

A Vlcek, I R Farrell, D J Liard, P Matousek, M Towrie, A W Parker, D C Grills, M W George
Early photochemical dynamics of organometallic compounds studied by ultrafast time-resolved spectroscopic techniques
J Chem Soc Dalton Trans 2002 (5) 701-712 (2002)

J A Weinstein, D C Grills, M Towrie, P Matousek, A W Parker, M W George
Picosecond time-resolved infrared spectroscopic investigation of excited state dynamics in a Pt^{II} diimine chromophore
Chem Comms 2002 (4) 382-383 (2002)

S M A Wright, I R Sims, I W M Smith
Vibrational relaxation of highly excited NCNO in collisions with He, Ar and N_2
Phys Chem Chem Phys 3 (12) 2203-2208 (2001)

PUBLISHED DURING 1999/2000

E A Mastio, C B Thomas, W M Cranton, E Fogarassy
The effects of multiple KrF laser irradiations on the electroluminescence and photoluminescence of rf-sputtered ZnS:Mn-based electroluminescent thin film devices
Appl Surf Sci 157 (1-2) 61-66 (2000)

C J Randall, C Murray, K G McKendrick
State-specific collisional coupling of the CH $A\,^2\Delta$ and $B\,^2\Sigma$ states
Phys Chem Chem Phys 2 (4) 461-472 (2000)

PUBLISHED DURING 2000/2001

R H Bisby, A W Parker
Structure of the radical from one-electron oxidation of 4-hydroxycinnamate
Free Radical Res 35 (1) 85-91 (2001)

D Chastaing, S D Le Picard, I R Sims, I W M Smith, W D Geppert, C Naulin, M Costes
Rate coefficients and cross-sections for the reactions of $C(^3P_J)$ atoms with methylacetylene and allene
Chem Phys Letts 331 (2-4) 170-176 (2000)

W D Geppert, D Reignier, T Stoecklin, C Naulin, M Costes, D Chastaing, S D Le Picard, I R Sims, I W M Smith
Comparison of the cross-sections and thermal rate constants for the reactions of $C(^3P_J)$ atoms with O_2 and NO
Phys Chem Chem Phys 2 (13) 2873-2882 (2000)

D C Koutsogeorgis, E A Mastio, W M Cranton, C B Thomas
Pulsed KrF laser annealing of ZnS:Mn laterally emitting thin film electroluminescent displays
Thin Solid Films 383 (1-2) 31-33 (2001)

M Mons, I Dimicoli, B Tardivel, F Puizzi, E G Robertson, J P Simons
Energetics of the gas phase hydrates of trans-formanilide: a microscopic approach to the hydration sites of the peptide bond
J Phys Chem A 105 (6) 969-973 (2001)

E G Robertson, M R Hockridge, P D Jelfs, J P Simons
IR-UV ion-depletion and fluorescence spectroscopy of 2-phenylacetamide clusters: hydration of a primary amide
Phys Chem Chem Phys 3 (5) 786-795 (2001)

E G Robertson, J P Simons
Getting into shape: conformational and supramolecular landscapes in small biomolecules and their hydrated clusters
Phys Chem Chem Phys 3 (1) 1-18 (2000)

IN PRESS AT END OF 2001/2002

J Dyer, D C Grills, P Matousek, A W Parker, M Towrie, J A Weinstein, M W George
Revealing the photophysics of fac-[(dppz-12-NO_2)Re$(CO)_3$(4-Me_2Npy)]$^+$: a picosecond time-resolved IR study
Chem Comms 2002 (8) 872-873 (2002)

C Ma, W M Kwok, P Matousek, A W Parker, D Phillips, W T Toner, M Towrie
Excited states of 4-aminobenzonitrile (ABN) and 4-dimethylaminobenzonitrile (DMABN): time-resolved resonance Raman, transient absorption, fluorescence and ab initio calculations
J Phys Chem A 106 (14) 3294-3305 (2002)

P Mojzes, P Praus, V Baumruk, P-Y Turpin, P Matousek, M Towrie
Structural features of two distinct molecular complexes of copper(II) cationic porphyrin and deoxyribonucleotides
Biopolymers 67 (4-5) 278-281 (2002)

S J Pestehe, G J Tallents, I C E Turcu, Y Abou-Ali, G Hirst, M Powers, W Shaikh
Efficiency of 1.5 - 4.5 keV x-ray production from 2 ps duration KrF laser pulses incident onto solid targets
J Phys D 35 (11) 1117-1122 (2002)

F W Vergeer, F Hartl, P Matousek, D J Stufkens, M Towrie
First direct observation of a CO-bridged primary photoproduct of [$Ru_3(CO)_{12}$] by picosecond time-resolved IR spectroscopy
Chem Comms 2002 (11) 1220-1221 (2002)

CONFERENCE PRESENTATIONS

9th European Conference on the Spectroscopy of Biological Molecules, Prague, Czech Republic (Sept 2001)

S W Botchway, I Barba, K Brindle, A W Parker
Development of a time correlated single photon counting multiphoton laser scanning confocal microscope – studies in biological fluorescence lifetime imaging

Laser Science and Development

JOURNAL PUBLICATIONS, BOOKS AND PUBLISHED PROCEEDINGS

J Collier, C Hernandez-Gomez, R Allott, C Danson, A Hall
A single-shot third-order autocorrelator for pulse contrast and pulse shape measurements
Laser & Particle Beams 19 (2) 231-235 (2001)

M H R Hutchinson, D Neely, B E Wyborn
Vulcan Upgrade: a petawatt laser facility for experiments at 10^{21} W cm^{-2}
Proc SPIE 4424 63-69 (2001)

P Matousek, M Towrie, C Ma, W M Kwok, D Phillips, W T Toner, A W Parker
Fluorescence suppression in resonance Raman spectroscopy using a high-performance picosecond Kerr gate
J Raman Spectr 32 (12) 983-988 (2001)

K Osvay, G Kurdi, J Klebniczki, M Csatári, I N Ross
Demonstration of high gain amplification of femtosecond ultraviolet laser pulses
Appl Phys Letts 80 (10) 1704-1706 (2002)

I N Ross, C J Hooker, P Dombi
Efficient generation of large diffraction gratings with a grating interferometer
Appl Opt 40 (34) 6153-6156 (2001)

IN PRESS AT END OF 2001/2002

P Matousek, M Towrie, C Ma, W M Kwok, D Phillips, W T Toner, A W Parker
Fluorescence background suppression in Raman spectroscopy using combined Kerr gated and shifted excitation Raman difference techniques
J Raman Spectr 33 (4) 238-242 (2002)

CONFERENCE PRESENTATIONS

10th International Conference on Time-Resolved Vibrational Spectroscopy, Okazaki, Japan (May 2001)

P Matousek, M Towrie, A W Parker, W M Kwok, C Ma, D Phillips, W T Toner
Fluorescence suppression in picosecond TR^3 spectroscopy

OECD Global Science Forum Workshop on Compact High-Intensity Short-Pulse Lasers, Kyoto, Japan (May 2001)

M H R Hutchinson
Evolution toward "user facility" role

M H R Hutchinson
High intensity laser programme at the Rutherford Appleton Laboratory

I Ross
New approach toward ultrahigh power generation

21st ICFA Beam Dynamics Workshop, Stony Brook, USA (Jun 2001)

I N Ross
A laser system for the CLIC drive beam photo-injector option

International Adaptive Optics Workshop, Albuquerque, USA (July 2001)

J Collier, C Hooker, S Hawkes, I Ross, C B Edwards, C Reason, C N Danson, C Hernandez-Gomez, C Haefner, P Neumayer
Adaptive correction of an ultra-high intensity laser system

QEP15, Glasgow, UK (Sept 2001)

S Hawkes, J Collier, C Hooker, C Danson, C Edwards, C Hernandez-Gomez, C Haefner, C Reason, I Ross
Adaptive optics development for ultra high intensity lasers

C Hernandez-Gomez, C Aldis, R Allott, P Brummitt, R Clarke, J Collier, C N Danson, C B Edwards, A Frackiewicz, J Govans, S Hancock, M Harman, P Hatton, S Hawkes, P Holligan, C Hooker, M H R Hutchinson, A Jackson, A Kidd, T Knott, W Lester, D Neely, M Notley, D Pepler, M Pitts, C Reason, D Rodkiss, I Ross, R Wellstood, G Wiggins, T Winstone, R Wyatt, B Wyborn, C Zeiner
Vulcan: a petawatt laser facility for experiments at 10^{21} W/cm^2

2nd International Conference on Fusion Sciences and Applications, Kyoto, Japan (Sept 2001)

C N Danson, C B Edwards, M H R Hutchinson, D Neely, B Wyborn
The Vulcan Petawatt interaction facility

AILU Technical Meeting, RAL, UK (Sept 2001)

C N Danson
Introduction to the Vulcan Petawatt

Diffractive Optics 2001 – EOS Topical Meeting 30, Budapest, Hungary (Oct 2001)

D A Pepler, P M Godfrey, C N Danson
Axial line-focus with a binary-phase Fresnel zone plate

Raman Spectroscopy in Archaeology and Art History, London, UK (Nov 2001)

P Matousek, M Towrie, A W Parker
Fluorescence suppression in resonance Raman spectroscopy

The Pittsburgh Conference – PITTCONN 2002, New Orleans, USA (Mar 2002)

P Matousek, M Towrie, A W Parker
Fluorescence suppression in resonance Raman spectroscopy by optical Kerr gating

29th Annual UK Plasma Physics Conference, Belfast, UK (Mar 2002)
C N Danson, C B Edwards, M H R Hutchinson, D Neely, B Wyborn
The Vulcan petawatt interaction facility

PANEL MEMBERSHIP AND CLF STRUCTURE

PANEL MEMBERSHIP

HIGH POWER LASER DIRECT ACCESS PANEL 2001/02

Professor G J Pert (Chairman)
Department of Physics
University of York

Professor W Graham
Plasma & Laser Interaction Physics
Queens University, Belfast

Dr J-C J Gauthier
LULI
Paris, France

Mr D A Pepler (Secretary)
Rutherford Appleton Laboratory

Mr P C Thompson
AWE
Aldermaston

Dr P A Norreys
Rutherford Appleton Laboratory

Professor M G Haines
Plasma Physics Group
Imperial College

Research Council Representative:
Mrs C Exton (until November 2001)
Ms J Nicholson (from November 2001)
EPSRC

VULCAN SCHEDULING ADVISORY PANEL 2001/02

Professor D D Burgess (Chairman)
Imperial College, London

Professor C L S Lewis
Department of Pure and Applied Physics
Queen's University of Belfast

Professor J Wark
Oxford Universsity

Dr K Krushelnick deputising for Professor M G Haines
Plasma Physics Group
Imperial College

Mr C N Danson (Secretary)
Rutherford Appleton Laboratory

Mr P C Thompson
AWE
Aldermaston

Dr P A Norreys
Rutherford Appleton Laboratory

Professor G Pert
University of York

Research Council Representative:
Ms J Nicholson
EPSRC

LASERS *for* SCIENCE FACILITY PANEL 2001/02

Dr R Bisby (Chairman)
Department of Biological Sciences
University of Salford

Professor J A Cairns
Department of Electronic Engineering & Physics
University of Dundee

Dr R Devonshire
Department of Chemistry
Sheffield University

Dr I P Clark (Secretary) (until October 2001)
Ms S Tavender (Secretary) (from October 2001)
Rutherford Appleton Laboratory

Dr K G McKendrick
Department of Chemistry
Herriot-Watt University

Dr W R Newell
Department of Physics & Astronomy
University College London

Research Council Representatives:
Dr A Bramley
EPSRC
Mrs C Exton (until October 2001)
Dr A McCaig (from October 2001
Ms J Nicholson (from October 2001)
EPSRC
Dr C Thompson
BBSRC

CLF EURO EXPERIMENTS PANEL 2001/02

Professor C L S Lewis (Chairman)
Department of Pure and Applied Physics
Queen's University of Belfast

Professor C Fotakis
Institute of Electronic Structure and Laser
FORTH, Greece

Professor D Phillips
Department of Chemistry
Imperial College

Dr S W Botchway (Secretary)
Rutherford Appleton Laboratory

Mr C N Danson (Contract Manager)
Rutherford Appleton Laboratory

Dr G Matthieussent
Laboratoire Physique Gaz et Plasmas, Universite Paris XI - CNRS, France

Professor J Meyer-ter-Vehn
Max-Planck-Institut für Quantenoptik
Garching, Germany

Dr Karel Rohlena
Institut of Physics
Prague

Professor J Kossanyi
CNRS – Laboratoire des Materiaux Moléculaires
Thiais, France

CENTRAL LASER FACILITY STRUCTURE 2001/02

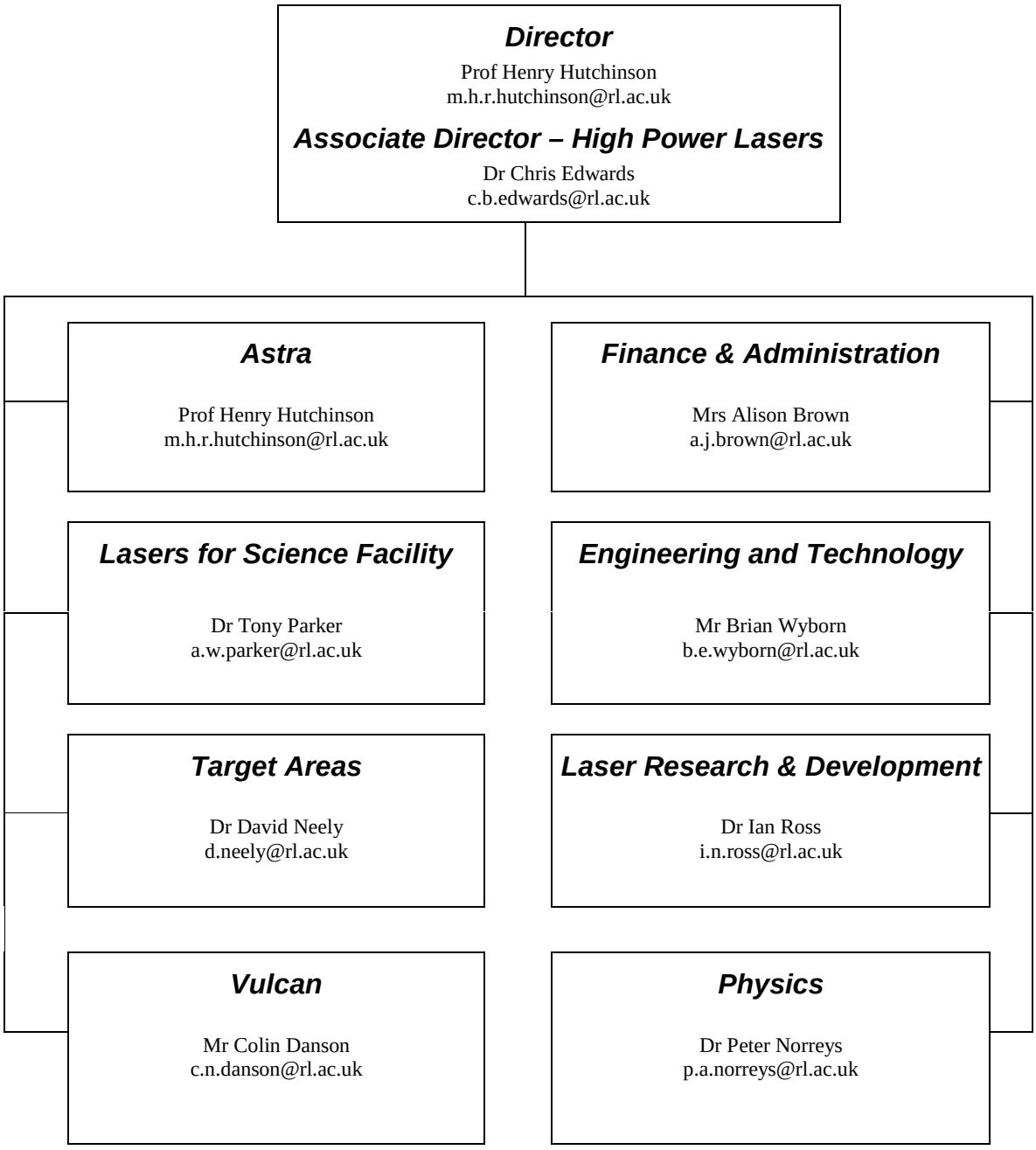

Author Index